VNIVERSITAT DE VALÈNCIA

FACULTY OF BIOLOGICAL SCIENCES

Department:
Biochemistry and Molecular Biology

Doctoral Program:
Biomedicine and Biotechnology

PRINCIPE FELIPE
CENTRO DE INVESTIGACION

POLYMER THERAPEUTICS LABORATORY

POLYMER-BASED COMBINATION CONJUGATES FOR THE TREATMENT OF TRIPLE NEGATIVE BREAST CANCER: FROM RATIONAL DESIGN TO PRECLINICAL EVALUATION

Juan José Arroyo Crespo

Doctoral Thesis - University of Valencia

July 2018

Thesis Directors: **Dr. María J. Vicent Docón** and **Dr. Ana Armiñán de Benito**

Dr. María J. Vicent Docón, Ph.D. in Chemistry and Head of the Polymer Therapeutics Laboratory at the Centro de Investigación Príncipe Felipe (Valencia Spain), and Dr. Ana Armiñán de Benito, Ph.D. in Biology and senior researcher of the same laboratory CERTIFY, that the work

"POLYMER-BASED COMBINATION CONJUGATES FOR THE TREATMENT OF TRIPLE NEGATIVE BREAST CANCER: FROM RATIONAL DESIGN TO PRECLINICAL EVALUATION"

has been developed by Juan José Arroyo Crespo under their supervision in the Centro de Investigación Príncipe Felipe in Valencia, as a thesis project to obtain a Ph.D degree in Biomedicine and Biotechnology from the University of Valencia, Faculty of Biological Sciences, Biochemistry and Molecular Biology Department.

A mis padres,

a Nacho y a Marta

“I was like a boy playing on the sea-shore, and diverting myself now and then finding a smoother pebble or a prettier shell than ordinary, whilst the great ocean of truth lay all undiscovered before me”

Sir Isaac Newton (1642-1727)

INDEX

CHAPTER III.

ANTICANCER ACTIVITY DRIVEN BY DRUG LINKER MODIFICATION IN A POLYGLUTAMIC ACID-BASED COMBINATION-DRUG CONJUGATE 179

ACKNOWLEDGEMENTS

"*Ningún mar en calma hizo experto marinero*" (Bunbury)

El laboratorio no es un lugar fácil. La decepción y el desánimo son fieles compañeros gran parte del tiempo en todo laboratorio de investigación exigente. Siempre faltan horas, reinan las prisas, el estrés y la impaciencia. Casi nunca hay una relación directa entre las horas invertidas y la calidad de los resultados, y la cabeza no desconecta cuando termina la *jornada laboral*. Muchas veces resulta imposible encontrar motivación para continuar *viviendo* en el laboratorio, y los fracasos experimentales acumulados suelen sumar ganas de desistir…

Sin embargo, he tenido la inmensa suerte de contar con la gran familia del I-36. Una familia cambiante a lo largo de los años, pero siempre formada por miembros de un tremendo valor personal y científico. Me acogieron con agradable fraternidad desde el primer día y me permitieron desarrollarme como investigador. Ellos me han ayudado a crecerme ante la adversidad, a enfrentarme a mis monstruos y a sacar energía del fondo del mar para continuar. Quiero expresar, por tanto, unas palabras de profunda gratitud a todos aquellos que me han hecho este camino más llevadero, científica y personalmente, y sin cuya inestimable ayuda me hubiera resultado imposible llegar hasta aquí, hoy.

Mis primeras palabras de agradecimiento sólo pueden ser para mis directoras de Tesis: María Jesús y Ana. Gracias, María Jesús, por apostar y confiar en mí desde el día en que nos conocimos, a pesar de que mi escasa experiencia no me avalara demasiado. Gracias por abrirme las puertas de tu laboratorio en aquel diciembre de 2012, cuando el CIPF y con él, el I-36, sufrían la resaca de la crisis y del ERE y ninguna nueva incorporación era una apuesta fácil. Gracias también, por tus innumerables charlas, siempre instructivas, por tus malabares para mantenerme en el laboratorio y por enseñarme a aportar mil enfoques distintos a un mismo resultado, incluso convirtiéndolo en positivo cuando *a priori* no lo era. Gracias por todo lo que me has enseñado, por contagiarme tu inagotable ambición y por tu paciencia conmigo. GRACIAS.

Ana, con el paso de los meses y los años, te has convertido en un pilar fundamental, no sólo para mi Tesis, sino para mi supervivencia en el laboratorio y has sido una compañera de fatigas inmejorable. Gracias por sacar adelante esas jornadas interminables de animalario, incluso en los días con los ánimos por los suelos. Ahí se demuestra la calidad de un investigador!! Gracias por toda la Biología y Oncología que me has enseñado y me has hecho aprender. Gracias por las largas tardes/noches

discutiendo resultados y organizando experimentos. Gracias por aportarme tu espíritu crítico, detallista y organizado, por sembrarme la cabeza de dudas interesantes y por aportar grandes ideas a mi investigación. Tienes un valor incalculable! GRACIAS por todo!!!

Continuando con mi Breast Team, tengo que dar unas enormes GRACIAS a mi chico, David. Compañero, has sido una persona clave para mí en el laboratorio. Nunca olvidaré cuánto me asusté cuando, en mis primeras semanas, me dijeron que venía un estudiante francés a trabajar conmigo, y lo mucho que me alegré cuando te conocí y me dijiste que preferías el español al inglés! Eres un currante como no he conocido otro y es un absoluto placer trabajar contigo. Tienes la capacidad envidiable de contagiar buen rollo que espero, mantengas siempre! Y lo más importante, te has ganado una confianza científica (muy difícil de ganar y muy fácil de perder!) espectacular en el Lab. (siento no poder decir lo mismo de la mecánica! :-P). *Merci beaucoup pour tout, mon ami*!

Vicent, a pesar de que nos ampararon en el I-36 casi a la vez, tu recorrido científico ya era largo y completo. Gracias por tus enseñanzas supramoleculares y, sobre todo, por enseñarme a avistar la presencia de *black holes* antes (o casi antes!) de caer en ellos. Gracias por tu infinita paciencia conmigo y por cambiar mi perspectiva de la caracterización físicoquímica! Te debo todo lo que sé de NMR! Tu amplitud de miras, tu constante crítica constructiva y tus grandes ideas han supuesto un indiscutible adelanto para mi ciencia y por ello te estaré siempre agradecido!

Esther, gracias por estar constantemente dispuesta a echarme una mano siempre que lo he necesitado, en todos los aspectos, y ofrecer profesionalidad y un gran criterio científico en todo lo que haces. Gracias, entre otras muchas cosas, por tu cursillo personalizado de NTA! Eres una compañera de lujo! María Helena, nunca olvidaré tu amable permanentemente buena disposición a colaborar hasta en las tareas más inesperadas. Aunque muchas veces te desesperemos y te hagamos ser la policía del Lab, sabes cuánto apreciamos tu inestimable trabajo y que te queremos un montón! Gracias a ti también, Zoraida, por tu inestimable contribución a nuestro ERC-Team, por tu buen humor y tus constantes palabras de ánimo. Stuart, gracias por ayudarnos a organizar y sacar adelante tanta producción científica. Gracias por tu infinita paciencia con mi inglés abulense, por todas las horas extra para pulir los artículos, muchas veces *in extremis*, y por enseñarme tantos trucos de expresión escrita.

No puedo pasar por aquí sin plasmar un profundo agradecimiento a mis primeras profes en el Lab. Gracias infinitas, Coralie, por acogerme en tu proyecto y ofrecerme la posibilidad de seguir tus pasos en el Lab. Fueron unos meses intensos, en los que te

preocupaste por mí, me aconsejaste y vaticinaste cosas que poco a poco han ido ocurriendo después en el Lab. Gracias por tus enseñanzas, trucos y reflexiones sobre el Lab y la vida. Por cierto… ya te he perdonado que dijeras a Ana que yo era "un poco mujer" porque podía hacer bien varias cosas a la vez! ;-P Muchas gracias a ti también, Marina, por ser mi primera toma de contacto con el inglés científico, con un polímero, un *vivaspín* y un liofilizador. Convivimos poco tiempo en el Lab, pero nunca olvidaré mis primeras clases de conjugación y tu enorme paciencia conmigo! Muchas gracias también a ti, Gaby, por tus consejos y tus sabias palabras en mis inicios en el I-36. Hemos compartido pocos momentos en el Lab, pero aquellos tiempos fueron de gran importancia para mí!

Por supuesto, merece un especial agradecimiento la próxima hornada de doctorandas del I-36. Las tres Supernenas!! Siempre os agradeceré vuestro apoyo y ha sido un placer haberos podido echar una mano y enseñar algún truquillo de veterano de guerra. Gracias por alegrar las jornadas de trabajo con vuestro buen humor, y vuestras historias. El I-36 es mejor desde que lo habitáis vosotras! Sonia, gracias por todas las experiencias compartidas, por las aventuras durante el congreso de Graná y por todo tu apoyo en esta larga carrera! Irene, muchas gracias por tu buen humor permanente, tus ánimos, tu confianza en mí, por ser una gran compañera de despacho y por tus clases magistrales de pellejos! Fer, ha sido un grandísimo honor girar en órbitas similares y compartir una gran parte de nuestro tiempo en el Lab. Conserva tu gran tesón! No me cabe ninguna duda de que ni esas estrellitas ni esos ratoncillos van a poder contigo! Eres una máquina! Además quisiera dar las gracias a Álex, por tus interesantes ideas y discusiones experimentales y por aguantar sin mucha queja mis condiciones climáticas ideales veraniegas en el despacho!

Debo hacer un alto en el camino para agradecer a mis doctoras favoritas todo su apoyo durante todo este tiempo. Elena, nunca olvidaré tus esfuerzos para comunicarte conmigo en mis inicios y tu inmejorable disposición siempre. Muchas gracias por tu apoyo incondicional! Has sido una gran compañera dentro y fuera del Lab. *Grazie mille per tutto*! Inma, a pesar de que contigo sólo sinteticé mi primer (y único!) dibloque, allá por 2013, y de que pasaste una buena parte de mi Tesis fuera del I-36, recibí tu reentrada en el Lab como un soplo de aire fresco. Gracias infinitas por tu capacidad organizativa, tu inagotable afán por hacer las cosas bien y tu infinita resistencia a la tempestad. Gracias, también, por iluminarme más allá del laboratorio y por obligarme a poner las cosas en perspectiva. Pequeña Gran Aroa, muchísimas gracias por transmitirme tu capacidad de trabajo inimitable, tu espíritu crítico y tu insaciable sed de aprender. Muchas gracias por cuidar de mí desinteresadamente desde mi llegada y en cada una de mis etapas en el I-36. Has sido siempre un ejemplo a seguir para mí y para el Lab, como científica y como

persona y espero tenerte cerca pronto de nuevo! Mi querida compañera Castellana, Amaya, te estaré eternamente agradecido por tu simpatía desde el primer minuto que pisé el I-36 y me ofreciste tu teléfono para que no comiera solo aquél día. Has sido una excelente compañera de fatigas en el Lab y en el despacho! Muchísimas gracias por tu comprensión y apoyo constante!

Tal y como me repitió mil veces un gran profesor, "no puedes considerar que comprendes completamente un concepto hasta que no eres capaz de conseguir que lo entiendan los demás". Por eso, quiero dar las gracias también a los estudiantes Erasmus que he supervisado estos años, Frauke, Lowie y Marie Julie. Gracias por obligarme a organizar ideas, por trasladarme vuestras inquietudes y por hacerme dudar de muchas cosas que yo creía que sabía bien. Ha sido muy instructivo tener la oportunidad de enseñaros y habéis supuesto un gran reto y una fuente de inspiración en mi trabajo.

No me puedo olvidar de brindar un gran agradecimiento a la pequeña gran familia de PTS. Desde tiempos inmemoriales (cuando Richard e Ismael eran los únicos pobladores) habéis ido creciendo como un esqueje del I-36 y ya tenéis una poderosa identidad propia! Mi especial agradecimiento va dirigido a Dani y Luz, en primer lugar, por ser los estudiantes favoritos del I-36, y por todas las experiencias vividas con vosotros en estos años, vuestro apoyo y vuestra ayuda. Y más recientemente, las "nuevas" incorporaciones, Lola, Jose, Sergio, Jaciel, que siempre habéis estado dispuestos a aconsejarme y echarme una mano cuando he necesitado ayuda.

Me gustaría también dar las gracias a varios jefes de grupo, cuya colaboración ha sido esencial en el desarrollo de esta Tesis. Gracias, con especial entusiasmo a Jerónimo Forteza y a su equipo. Gracias a sus interesantes reuniones, me he podido asomar por un agujerito al apasionante mundo de la patología clínica. Gracias por todas tus sugerencias, consejos y críticas, que me han ayudado a sacar adelante la caracterización de los modelos preclínicos. Dentro de su laboratorio, también quiero dar las gracias a Irene Borredá, sin cuyas preparaciones histológicas, no hubiera sido posible caracterizar los modelos. Eternamente agradecido! Gracias también a Ana Conesa y a su equipo, por tu vital visión transcriptómica de nuestros tejidos tumorales y por tu excelente interpretación de los resultados. También quiero dar las gracias a Antonio Pineda y a Martina Palomino, por sus consejos y sus sabias discusiones sobre metabolómica. Finalmente, quiero dar las gracias a los compañeros de Oncovisión (Bruker) por su eterna paciencia e inmejorable disposición para desarrollar y analizar los experimentos de imagen PET/CT. En especial a César, Emilio y Luisa.

El CIPF es una nave espacial dotada con unas instalaciones y unas *facilities* envidiables, que también me han permitido sacar adelante todo este trabajo. Quiero mostrar mi agradecimiento a todo el personal que mantiene la nave a flote, con especial mención al departamento de mantenimiento (en especial a Jesús), cafetería (en especial a Merche), limpieza (en especial a Estrella) e informática (en especial a Jhos y Vicent).

No me puedo olvidar de los interesantes investigadores que he conocido durante mi estancia en la Facultad de Química de la Universidad de Bolonia. He tenido varios supervisores y estudiantes a quienes quiero también dar las gracias: Valentina, Andrea, Bárbara, Sara y Pierluigi. Gracias por vuestra acogida, vuestro apoyo y vuestra contribución científica! *Grazie mille a tutti!*

Por último, quisiera dar las gracias a tres personas importantes que han contribuido y me han ayudado directa o indirectamente desde Salamanca. En primer lugar, gracias a Manuel Fuentes, del Lab. 11 del Centro de Investigación del Cáncer, que me ofreció la oportunidad desinteresada de introducirme en el mundo de la investigación y del cáncer, acogiéndome en su laboratorio para hacer prácticas, y, finalmente, facilitó mi puesta en contacto con María Jesús. Gracias por tu hospitalidad, tu confianza y tus sabios consejos! Quiero dar las gracias igualmente al Catedrático de Química Orgánica de la Facultad de Química, Quino, por tus consejos y lecciones de química telemáticos cuando me volví loco tratando de derivatizar uno de los fármacos comprendidos en la Tesis. Finalmente, merece un agradecimiento mi profesor de Biología Molecular y Bioquímica David. Gracias por tu apoyo, tu recibimiento y tu dedicación más allá de las clases de la carrera. Gracias también por ofrecerme una visión panorámica del mundo de la investigación.

Pero esta Tesis no sólo se ha forjado en los laboratorios…

Quiero brindar mi mayor agradecimiento, un GRACIAS con mayúsculas, a mis padres y a mi hermano. Vosotros habéis sido los principales sufridores de la distancia y de la Tesis. Si he llegado hasta aquí ha sido gracias a la oportunidad que me habéis ofrecido vosotros, a vuestro soporte, a vuestros cuidados, a vuestra paciencia y a vuestra comprensión. Muchas gracias por aguantarme y por permitirme alcanzar esta meta. Nunca podré devolveros todo lo que habéis hecho por mí todos estos años. Media Tesis es vuestra!

También desde Salamanca (y Suiza) ha jugado un papel esencial mi Comité de Sabios. Los irrepetibles Pedro, Álvaro y Juantxi. Muchas gracias por vuestra confianza, vuestra motivación y por creer en mí. En especial quiero resaltar tu esencial soporte, Álvaro. Has sido un faro en mi noche de temporal, y me has enseñado mucho más de mí mismo de lo que nunca hubiera aprendido sólo. Has conseguido que recuperara la confianza en mí que había perdido, y eso ha sido una labor hercúlea. Haré lo posible por devolverte todo lo que has hecho por mí, amigo! No me puedo olvidar de darte las gracias a ti, Luís. Aunque te debo mil llamadas, que a partir de ahora empezaré a devolver, siempre has hecho grandes esfuerzos por estar pendiente de mí, por animarme y por conseguir que saliera un poco del Lab. Muchas gracias por todo!

Quiero poner el colofón a estos agradecimientos dándote las GRACIAS a ti, Marta. Como sabes, mi Gran Hallazgo de estos últimos años no ha sido científico! Espero vivir lo suficiente para agradecerte toda tu confianza, paciencia, cariño, dedicación, comprensión y ánimo de todos estos años. Sólo tú y yo sabemos lo que hemos pasado para llegar hasta aquí. Has sido la única terapia que me ha permitido sacar la cabezota del laboratorio, y la estabilidad mental que he conseguido mantener te la debo a ti! Ahora comienza el momento de recuperar ésta inversión vital. Por cierto… te lo repito: Media Tesis es tuya!

ABBREVIATIONS

wt%	Drug loading in weight percent
aa	Amino acid
Ab	Antibody
ACN	Acetonitrile
AD	Alzheimer's disease
AGM	Aminoglutethimide
AIDS	Acquired immunodeficiency syndrome
Ala	Alanine
ALL	Acute lymphoblastic leukemia
ALN	Alendronate
AML	Acute myeloid leukemia
Amph B	Amphotericin B
Anh	Anhydrous
APAF-1	Apoptotic protease activating factor-1
APP	Amyloid precursor protein
Ar	Argon
Asp	Aspartate
ATP	Adenosine triphosphate
AUC	Area under the curve
BBB	Blood brain barrier
BCS	Breast conservative surgery
BDMC	Bisdemethoxycurcumi
Boc	Tertiary-butyloxycarbonyl
BSA	Bovine serum albumin
BTB	Blood tumor barrier
Bz	Benzyloxycarbonyl

CAA	Cancer Associated Adipocyte
CAC	Critical aggregation concentration
CD	Circular dichroism
CD	Cyclodextrin
CDCl3	Deuterated chloroform
CHO	Chinese hamster ovary
CMC	Critical micelle concentration
CNS	Central nervous system
COSY	Correlated spectroscopy
CPT	Camptothecin
CsA	Cyclosporine A
CTC	Circulating tumor cell
Cys	Cysteine
DCC	N,N´-dicyclohexylcarbodiimide
ddH2O	Deionized water
DDS	Drug delivery system
DIC	N,N’-Diisopropyl carbodiimide
DIEA	N,N-Diisopropylethylamine
DLS	Dynamic light scattering
DMEM	Dulbecco’s modified eagle’s medium
DMF	N,N'-Dimethyl formamide
DMSO	Dimethyl sulphoxide
DMTMM	4-(4,6-Dimethoxy-1,3,5-triazin-2-yl)-4- methylmorpholinium
DNA	Deoxyribonucleic acid
DOSY	Diffusion-ordered spectroscopy
DOTA	1,4,7-tetrazacyclododecane-1,4,7-10-tetraacetic acid
Dox	Doxorubicin
DP	Degree of polymerization

DTT	1,4-dithiothreitol
EC	European commission
ECM	Extracellular matrix
EDC	1-Ethyl-3-(-3-dimethylaminopropyl) carbodiimide
EDTA	Ethylenediaminetetraacetic acid
EG	Ethylene glycol
EGFR	Epidermal growth factor receptor
EMT	Epithelial-mesenchymal transition
EPI	Epirubicin
ER	Estrogen receptor
EPR	Enhanced permeability and retention
eq	Equivalents
ESF	European science foundation
FACS	Fluorescence activated cell sorting
FBS	Fetal bovine serum
FCS	Fluorescence correlation spectroscopy
FDA	Food and drug administration
FDC	Free drug content
FITC	Fluorescein Isothiocyanate
FT-IR	Fourier transform infrared spectroscopy
G-CSF	Granulocyte colony stimulating factor
GAU	Glutamic acid units
GFLG	Gly-Phe-Leu-Gly
Gly	Glycine
GO	Gene ontologies
GPC	Gel permeation chromatography
GSH	Glutathione
HCl	Hydrochloride Acid

HDL	High Density Lipoprotein
HER2	Human epidermal growth factor receptor-2
HES	Hydroxyethylstarch
HEWL	Hen egg white lysozyme
HGH	Human growth hormone
HOBt	Hydroxybenzotriazole
HPLC	High pressure liquid chromatography
HPMA	N-(2'-Hydroxypropyl)methacrylamide
hrGCSF	Human recombinant granulocyte-colony stimulating factor
i.m.	Intramuscular
i.p.	Intraperitoneal
i.v.	Intravenous
ID	Injected dose
IGF1R	Insulin-like growth factor-1 receptor
IHC	Immunohistochemistry
IL	Interleukin
KDa	Kilodalton
Leu	Leucine
Lys	Lysine
LSGS	Low serum growth supplement
m/z	Mass/charge
mAb	Monoclonal antibody
MBq	Mega Becquerel
MCR	Mean count rate
MDR	Multidrug resistance
ME	Macrophage elastase
MMP	Matrix metalloproteinase
MRI	Magnetic resonance imaging

MS	Mass spectrometry
MTT	3-(4,5-dimethyl-2-thiazolyl)-2,5-diphenyl-2H-tetrazolium
MTX	Methotrexate
MWCO	Molecular weight cut off
N2	Nitrogen
NaOH	Sodium hydroxide
nBu	N-Butylamine
NCA	N-Carboxyanhydride
NCE	New chemical entity
NGF	Nerve growth factor
NHS	N-Hydroxysuccinimide
NIR	Near infra red
NMR	Nuclear Magnetic Resonance
NOESY	Nuclear Overhauser Effect Spectroscopy
NPs	Nanoparticles
OG	Oregon green cadaverine
PAA	Poly amino acid
PAMAM	Poly(amido amine)
PB	Phosphate buffer
PBS	Phosphate buffer saline
PBLG	Phosphate buffer saline
pCR	Pathologic complete remission rate
PD	Pharmacodynamics
PDC	Polymer drug conjugate
PDI	Polydispersity index
PEG	Poly(ethylene glycol)
PEI	Poly(ethylene imine)
PEO	Poly(ethylene oxide)

PET	Positron emission tomography
PGA	Poly(L-glutamic acid)
PGG	Poly(L-γ-glutamyl-glutamine)
Phe	Phenylalanine
PK	Pharmacokinetics
PLA	Polylactic acid
PMMA	Poly(methyl methacrylate)
PNS	Peripheral nervous system
PPC	Polymer protein conjugate
PR	Progesterone receptor
PT	Polymer therapeutics
PTX	Paclitaxel
RES	Reticulum endothelium system
RFU	Relative fluorescence units
Rg	Gyration radius
RGD	Arginylglycylaspartic
Rh	Hydrodynamic radius
RI	Refractive index
ROCK	Rho associated kinase
ROP	Ring opening polymerization
ROS	Reactive oxygen species
RT	Radiation treatment
r.t.	Room temperature
RTKs	Receptor tyrosine kinases
RM	Radical mastectomy
SANS	Small angle neutron scattering
SAS	Small angle scattering
SAR	Structure-activity relationship

SEC	Size exclusion chromatography
SEM	Standard error of the mean
SGLT1	Sodium-glucose linked transporter
SPECT	Single photon emission computed tomography
STAT	Signal transducer and activator of transcription
TDC	Total drug content
Tf	Transferrin
TKI	Tyrosine-kinase inhibitor
TI	Topoisomerase inhibitor
TNBC	Triple-negative breast cancer
TFA	Trifluoroacetic acid
TJ	Tight junction
TNF	Tumor necrosis factor
UV	Ultraviolet
v/v	Volume/volume
VEGF	Vascular endothelial growth factor

ABSTRACT

Among breast cancer subtypes, triple negative breast cancer (TNBC) represents around 15-20% of newly diagnosed cancer cases. Together with heterogeneous behavior among single patients, TNBC presents with a complex molecular landscape, low detection rate, and an aggressive and highly proliferative profile and these characteristics provide for the poor prognosis of TNBC patients. The lack of hormonal receptor (ER, PR, and HER2) expression impedes the administration of targeted therapies, and for this reason, the development of novel therapies for TNBC represents a primary clinical need.

Research into the development of polymer conjugates for the treatment of TNBC falls into four main areas:

i) The detailed study and comprehension of relevant preclinical mouse models that faithfully mimic the clinical scenario as a nanomedicine evaluation platform.

ii) The development of new polymer-drug combination conjugates with optimized drug ratio and stimuli-responsive polymer-drug linker(s) in order to achieve adequate drug(s) pharmacokinetics at the site of action.

iii) The exhaustive physicochemical characterization that allowed the establishment of structure-activity relationships (SAR). Additionally, the integration of -omics in order to identify pharmacological biomarkers to better design and monitor the activity of selected nanoconjugates.

We now address these main points in this Thesis, which aimed to design polymer-drug combination conjugates for the treatment of TNBC. Drug combination therapies have emerged as a valid option for the treatment of breast cancer, as this approach permits synergistic drug targeting of multiple pathways.

Studies employing animal models of disease allow for the understanding of disease development and progression, the search for therapeutic targets, and the validation of therapeutic strategies; however, the lack of accurately characterized research models that faithfully mimic the pathological features of human TNBC frequently hampers research aims. We now present the broad and detailed characterization of preclinically relevant spontaneously metastatic TNBC murine models that faithfully

reproduce the human clinical scenario. Our comparisons have uncovered important descriptors (some coming from –omics analysis) regarding the interconnected tissular/molecular processes driving disease progression towards metastasis. These descriptors include metastatic spread via the lymphatic route, immune system remodeling, cancer-associated adipocytes, and crucial metabolomic alterations.

As part of the development of a polymer-based therapy for TNBC, we present a versatile and straightforward methodology for the preparation of well-defined polyglutamate-based drug combination conjugates based on the well-established properties of the poly-glutamic acid (PGA) as a multivalent and biodegradable polymer carrier. We synthesized and characterized a family of conjugates containing amino acid-based proteolytic drug linkers including Gly, Gly-Gly, Gly-Phe-Leu-Gly as key drivers in the final macromolecule solution conformation (which drives the biological fate). These new drug delivery systems incorporate both chemotherapy (doxorubicin) and endocrine therapy (the aromatase inhibitor aminoglutethimide) as a synergistic combination. Overall, we demonstrate how the presence of a small flexible Gly linker can drastically modify the spatial conformation of the entire polymer–drug macromolecule, promoting the synergistic release of both drugs and significantly improving the biological activity.

The release of drug combinations conjugated to the polymer backbone via protease-cleavable drug linkers, such as those noted above, relies on the heterogeneous expression levels (at both the patient and tumor level) of various proteolytic enzymes some of them not found within the tumor microenvironment, target we wish to reach to be able to modulate metastatic processes. To improve drug release intracellularly but also at the tumor microenvironment, we developed a new family of conjugates incorporating the pH-sensitive hydrazone linker. These conjugates provided improved antitumor and antimetastatic activity (supported by histology and transcriptomic analysis); however, we noted that the pH-sensitive drug-linker length significantly influences the cell death mechanism involved.

Finally, we applied the knowledge acquired from the development of the previous polymer-drug combination conjugates, together with the selection of a more powerful combination of synergistic drugs for TNBC treatment (including a tyrosine-kinase inhibitor, TKI and a topoisomerase inhibitor, TI) for the development of an even more

effective family of polymer-drug conjugates. This novel system demonstrated enhanced antitumor activity in a human TNBC mice model, leading to a 50% primary tumor growth reduction and the almost complete remission of lung metastasis.

Overall, the findings exhibited throughout this Thesis highlight the need for a deeper understanding of polymer-drug conjugates at supramolecular level, including the need for a complete physicochemical characterization to allow the design of more effective polymer-drug conjugates. Additionally, we highlight the importance of the full characterization of the animal models employed and the parameters driving primary tumor development and the pathways modulating metastatic spread and tumor-side pathologies.

OBJECTIVES OF THE RESEARCH

The main objective of this Thesis is the design and development of biocompatible and biodegradable polypeptide-based-drug combination conjugates for the treatment of advanced stage / metastatic triple-negative breast cancer (TNBC). Strategy to be always performed by using well-controlled synthetic approaches, validated by exhaustive characterization techniques and tested in relevant preclinical models in order to accelerate bench to bedside process.

This global aim frames the following specific objectives:

1. The development and full characterization of two spontaneously metastatic and preclinically relevant orthotopic triple negative breast cancer animal models as platforms for advanced therapeutics validation.

2. Synthesis, full physico-chemical characterization and biological evaluation of poly-L-glutamic acid(PGA)-drug combination conjugates that incorporate drugs at an adequate ratio as well as bioresponsive polymer-drug(s) linkers to achieve synergism in TNBC models.

The rational designed of the combination conjugates will involve:

i) Exploring linkers of different bioresponsive nature (protease *vs.* pH responsive).
ii) Structure-activity relationship studies in biologically relevant media.
iii) *In vitro* and *in vivo* studies (safety, pharmacokinetics and anticancer activity) in preclinically relevant models (Objective 1).

3. Implementation of –omics techniques (metabolomics and transcriptomics) in the development of polymer combination conjugates in order to understand not only molecular mechanism of action but also identify relevant biomarker and physicochemical descriptors that would help us to move toward personalized approaches.

Chapter I

GENERAL INTRODUCTION AND BACKGROUND

I.1. Breast Cancer

Breast cancer is a group of systemic diseases involving abnormal cell growth within breast tissue, with the potential to invade or spread to other parts of the body [1]. The most frequent clinical signs of breast cancer include the appearance of different sized-lumps in the breast, a sudden change in breast size, form, or aspect, dimpling of the skin, fluid exudate from the nipple, and red or scaly patches of skin [2]. As breast cancer develops, metastasis can occur, leading to clinical symptoms such as bone pain, swollen lymph nodes, shortness of breath, and yellow skin [3].

I.1.1. Characteristics, Prevalence, Staging, and Molecular Subtypes

Breast cancer represents the most common invasive cancer in women and the leading cause of cancer-related deaths among women in the world [4]. Breast cancer development is staged into five phases (**Table 1**) according to the tumor size, location, involvement of lymph node, and spread. Breast cancer and clinical outcome directly correlates with the stage (**Figure 1A**) at diagnosis and with patient age (**Figure 1B**). While recent advances in screening and treatment have improved survival rates, data from 2008 still demonstrates a 20% increase in breast cancer incidence (**Figure 2**) and an associated 14% increase in cancer-related mortality [5].

Disease stage	Clinical characteristics
Stage 0	Abnormal cells found in the lining of breast ducts or sections of the breast or nipple discharge
Stage I	Tumor of 2 cm or less that has not spread beyond point of origin (in situ)
Stage II	Tumor size of 2 cm to 5 cm with presence of small carcinomas in two or three auxiliary lymph nodes, tumor has not spread outside the breast
Stage III	Tumor size no larger than 5 cm with invasion of four to nine auxiliary lymph nodes with a possibility of growth into the chest wall, additional signs include possible dimpling, inflammation, or change in skin color
Stage IV	Cancer of any size that has spread to distant organs (invasive)

Table 1. Stages of breast cancer and clinical characteristics

A

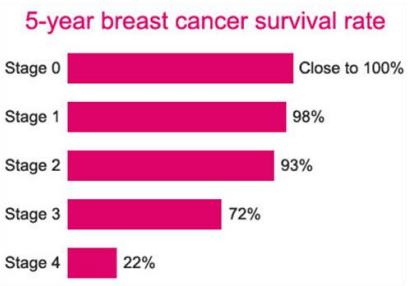

B

	In Situ Cases		Invasive Cases		Deaths	
Age	**Number**	**%**	**Number**	**%**	**Number**	**%**
<40	1,610	3%	11,160	4%	990	2%
40-49	12,440	20%	36,920	15%	3,480	9%
50-59	17,680	28%	58,620	23%	7,590	19%
60-69	17,550	28%	68,070	27%	9,420	23%
70-79	10,370	16%	47,860	19%	8,220	20%
80+	3,760	6%	30,080	12%	10,910	27%
All ages	**63,410**		**252,710**		**40,610**	

Figure 1. A) Five-year survival rates for women by breast cancer stage (after initial diagnosis), US, 2014. **B)** Estimated new female breast cancer cases and deaths by age, USA, 2017.

Breast cancer has been historically classified according to tumor size, morphology, and nodal involvement, with the immunohistochemical expression of three membrane proteins (progesterone receptor (PR), estrogen receptor (ER) and epidermal growth factor (EGFR) receptor 2 (HER2)) in biopsies employed as means to assess patient prognosis and manage treatment approaches.

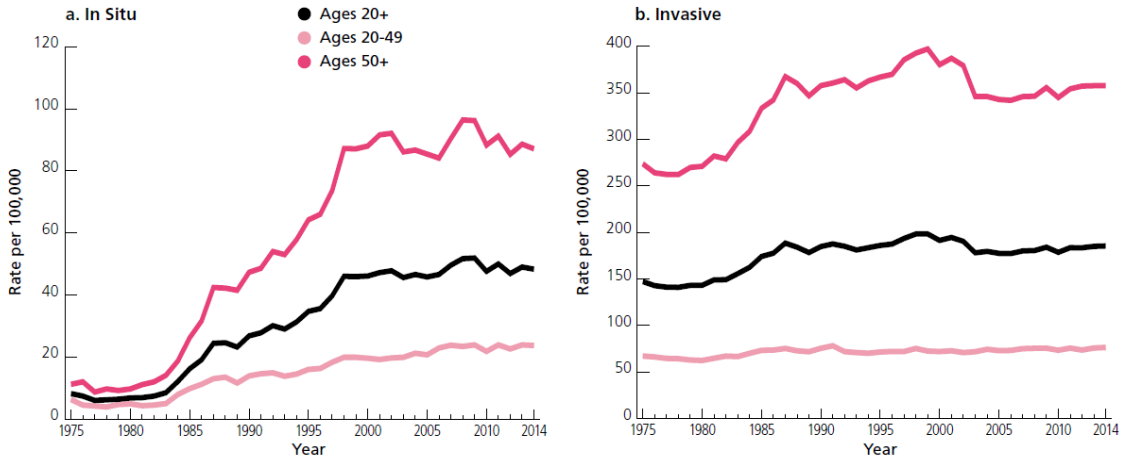

Figure 2. Trends in incidence rates of invasive and in situ female breast cancer by age, 1975-2014, USA [6]**.**

However, the recent development of new expression-profiling tools, including protein microarrays, has uncovered additional heterogeneity within breast cancer patients, with classifications now expanded past PR/ER/HER2 expression status [7]. This conceptual shift has led to advances in patient treatment stratification due to increased diagnostic accuracy and more successful therapeutic decision-making [8].

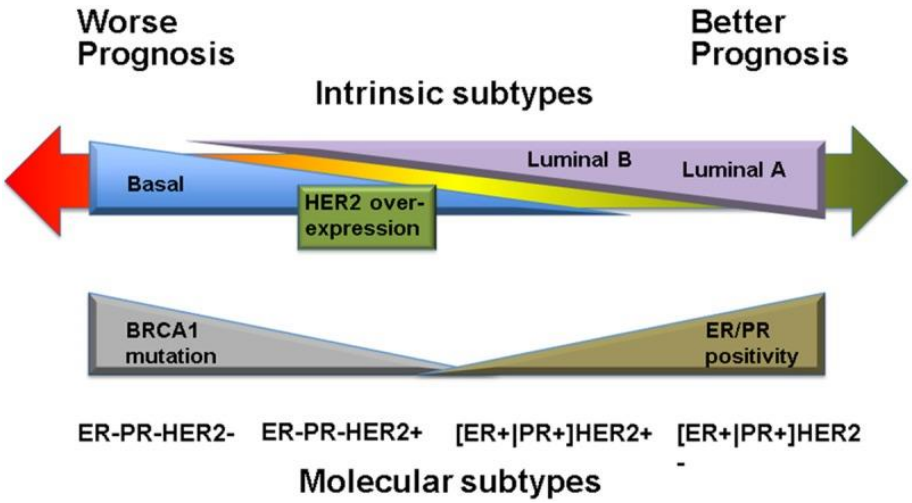

Figure 3: Patient outcome based on breast tumor intrinsic subtypes. Adapted from [7].

Studies now highlight six major molecular/transcriptional subtypes (**Figure 3**) of breast cancer: basal-like, luminal A, luminal B, HER2-enriched, normal-like, Claudin-low and triple negative [7]. Each subtype correlates with differential histopathological features, tumor evolution, therapeutic response, overall patient management, and clinical outcome (**Table 2**). Namely:

Luminal A represents a relatively common subtype of breast cancer, defined by high expression of ER and PR and low expression of the Ki67 proliferation marker and the HER2 oncoprotein. Luminal A tumors tend to be low grade, slow growing, and less aggressive and normally associate with the best prognosis, particularly in the short term, due to elevated responsiveness to anti-hormone therapy [9, 10].

Luminal B tumors also exhibit ER and/or PR expression, but with higher levels of Ki67 (indicative of a large proportion of actively dividing cells) or HER2 with high histologic grade [11]. Luminal B tumors tend to exhibit an aggressive clinical behavior with prognosis similar to non-luminal cancers (including basal-like subtype) [12] and an associated poorer survival rate than luminal A cancers [10]. Patients with luminal B tumors are often diagnosed at a younger age, exhibit slightly quicker growing tumors, and tend to display factors (including poorer tumor grade, larger tumor sizes, and frequent lymph node involvement) that lead to a poorer prognosis when compared to patients with luminal A tumors.

HER2-enriched tumors exhibit heterogeneous biology and clinic behaviors and tend to grow and spread more aggressively than other subtypes. This translates to

an associated poorer short-term prognosis compared to hormone receptor (HR)-positive breast cancers. Although the majority of HER2-positive tumors are HR-negative by immunohistochemistry, ~30% are typically HR-positive [13]. Within HR-positive tumors, 40-50% are HER2-positive with Luminal A and B tumors representing the bulk of the remainder. Within the HR-negative disease, 80-90% are HER2+ and 10-20% are Basal-like [13]. Thus, HR status does not fully describe these molecular subtypes.

Normal-like tumors present with similarities to normal breast tissue. The significance of this subtype has yet to be determined, and some argue that it may represent contamination of samples with normal breast tissue [14]. Studies have discovered some similarities to luminal A disease (HR-positive, HER2-negative, and low Ki-67 expression). While normal-like tumors suffer from a prognosis slightly worse than luminal A, the classification of this infrequent subtype remains unclear due to high molecular heterogeneity.

Claudin-low represents the latest subtype identified by gene expression profiling studies [15], mainly characterized by the lack of expression of claudin proteins (components of tight junctions between adjacent epithelial cells) and epithelial cell adhesion molecules. Claudin-low tumors are typically triple negative (61–71%), while 25 to 39% of triple negative breast cancers are considered claudin-low. Claudin-low tumors differ from basal-like tumors by the inconsistent expression of basal keratins and significantly lower expression of proliferation-associated genes [15]. Accordingly, claudin-low tumors have a lower pathologic complete remission rate (pCR) with neoadjuvant chemotherapy than basal-like tumors, but higher than luminal tumors. The identification of the claudin-low subtype provides further evidence of the broad underlying biology of TNBC and the need for a better understanding of the different subtypes of breast cancer and the associated therapeutic implications.

Triple-Negative tumors lack the expression of ER, PR, and HER2 and represent around 15-20% of the new diagnosed cancer cases [16]. The following section discusses the importance of triple-negative breast cancer (TNBC) in further detail.

Intrinsic subtype	IHC status	Grade	Outcome	Prevalence$^{\Delta}$
Luminal A*	[ER+, PR+] HER2-,KI67-	1|2	Good	23.7%
Luminal B*	[ER+, PR+] HER2-,KI67+	2|3	Intermediate	38.8%
HER2 over-expression*	[ER-,PR-] HER2+	2|3	Poor	11.2%
TNBC/Basal-like*	[ER-,PR-] HER2-, basal marker+	3	Poor	18.3%
Normal-like*	[ER+, PR+] HER2-,KI67-	1|2|3	Intermediate	7.8%
Claudin-low*	[ER-,PR-] HER2-, claudin -	1|2|3	Poor	~70% of TNBCs

Table 2: Summary of breast tumor molecular subtypes. *Subtypes with detailed expression patterns and clinical implications discussed in the text, which represent the majority of the breast tumor cases. $^{\Delta}$The prevalence of each subtype derives from [17].

I.1.2. Triple-Negative Breast Cancer: Molecular Landscape and Clinical Characteristics

Together with a highly aggressive nature and heterogeneous behavior in patients, the characteristics of TNBC include a complex molecular landscape, low detection rate, and an aggressive/highly proliferative profile, which combine to give the worse prognosis of all subtypes. Additionally, TNBC patients suffer from significantly reduced survival rates when compared to non-TNBC (nTNBC) patients (**Figure 4**). Pathologically, TNBC displays rapid growth rates with prominent lymphoplasmacytic inflammatory infiltrate with visceral metastasis expected at late stages (mainly in lungs, liver, and brain). Furthermore, frequent lymphatic system compromise impedes focused treatment and favors tumor recurrence [18]. Rapid tumor evolution leads to the development of an inner hypoxic and/or necrotic core [19] associated with multiple drug resistance (MDR) and overall worse prognostic [20].

Unfortunately, TNBC currently lacks targeted therapeutics [21-23], patients usually respond to treatment heterogeneously [24], and the lack of standardized treatment for TNBC in the metastatic scenario makes TNBC treatment an unmet clinical need [25]. Nevertheless, TNBC does display sensitivity to chemotherapeutic agents, such as anthracyclines and taxanes [26], leading to reduced recurrence in some cases [27]. However, the role of chemotherapeutic agents in TNBC treatment remains unclear, with more advances required to improve drug delivery and reduce unwanted side effects.

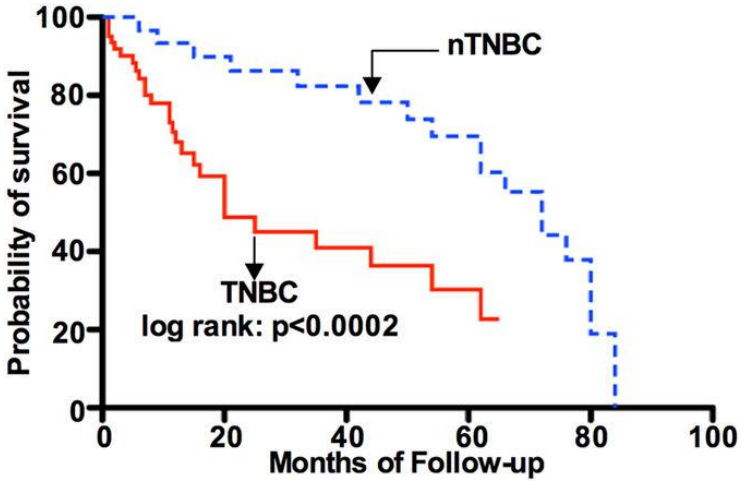

Figure 4: TNBC survival compared to nTNBC survival [28]

I.1.3. Classification and Subtypes of Triple-Negative Breast Cancer

TNBC encompasses a wide spectrum of entities with different biological characteristics and clinical behavior [29]. The American College of Pathology [30], American Society of Clinical Oncology [31], and St. Gallen guidelines [11] define TNBC as breast cancer with less than 1% of tumor cells expressing ER and PR via immunohistochemistry (IHC). However, the high prevalence of uncommon histopathological subtypes, such as metaplastic (90%), medullary (95%), adenoid cystic (90-100%), and apocrine (40-60%) carcinomas [24] typifies the heterogeneous nature of TNBC. While molecular assessments also demonstrate a wide range of heterogeneity, breast cancer characterization applies the detection of common markers such as basal cytokeratin (CK) 5/6 and EGFR [32].

Attempts to distinguish TNBC subtypes at the molecular levels have employed a wide range of characterization tools, including cDNA microarrays [33], in situ mRNA

hybridization [34], histopathological quantification, laser-capture microdissection [35], and reverse phase protein arrays [36]. Transcriptional analyses employing these tools has now highlighted the existence of up to six distinct TNBC subtypes.

Basal-Like (BL1 and BL2) Subtypes

The enrichment for genes from cell cycle, cell division, and DNA damage response (ATR/BRCA) pathways characterizes the BL1 subtype. High Ki67 mRNA expression and nuclear Ki67 staining by ICH (> 70%) further supports the proliferative nature of this subtype. The BL2 subtype also involves growth factor signaling (EGF, NGF, MET, Wnt/β-catenin, and IGF1R), glycolysis, and gluconeogenesis pathways [37].

Immunomodulatory (IM) Subtype

The high expression of factors involved in immune cell processes, including immune cell signaling, characterizes the immunomodulatory (IM) subtype. Immune signaling genes within the IM subtype substantially overlap with the gene signature for medullary breast cancer: a rare, histologically distinct TNBC form that, despite its high-grade histology, is associated with a favorable prognosis. This subtype also exhibits activation of signal transducer and activator of transcription (STAT) transcription factor-mediated pathways and has the best prognosis of TNBC subtypes.

Mesenchymal (M) and Mesenchymal Stem-Like (MSL) Subtypes

The mesenchymal (M**)** subtype expressed components and pathways involved in cell motility, extracellular receptor interaction, and cell differentiation pathways. The mesenchymal stem-like (MSL) subtype shares many characteristics of the M subtype; however, the MSL subtype also expresses genes related to growth factor signaling pathways.

Luminal Androgen Receptor (LAR) Subtype

The luminal androgen receptor (LAR) subtype represents the most differential TNBC subtype; while this subtype is ER-negative, highly expressed genes are present in gene ontologies (GO) including hormonally regulated

pathways (steroid synthesis, porphyrin metabolism, and androgen/estrogen metabolism) [38]. Tumors exhibit AR, ER, prolactin, and ErbB4 signaling, but ERα-negative IHC staining; however, gene expression profiling demonstrates the expression of *ESR1* (the gene encoding ERα) and other estrogen-regulated genes (*PGR, FOXA, XBP1, GATA3*). Thus, these 'ER-negative' tumors demonstrate molecular evidence of ER activation. Tumors within the LAR group also express numerous downstream AR targets and coactivators, with AR expression by IHC more than 10-fold higher compared to other TNBC subtypes.

I.1.4. Metastasis in Breast Cancer and Triple Negative Breast Cancer

The metastatic process comprises the spread of malignant cells from a primary tumor to distant sites through the blood or lymphatic system (**Figure 5**) [39]. Metastasis is considered the major breast cancer complication and represents the main cause of death in breast cancer patients. Primary tumor crosstalk with other organs via systemic factors (cytokines, chemokines, soluble proteins, exosomes, etc.) to promote primary tumor growth and metastasis and may promote systemic inflammation and a variety of other non-metastatic systemic complications such as cachexia, osteoporosis, osteopetrosis, and paraneoplastic syndromes. The most recent studies have shown that gene expression profile of breast tumors can predict the expected site of distant metastasis [40, 41].

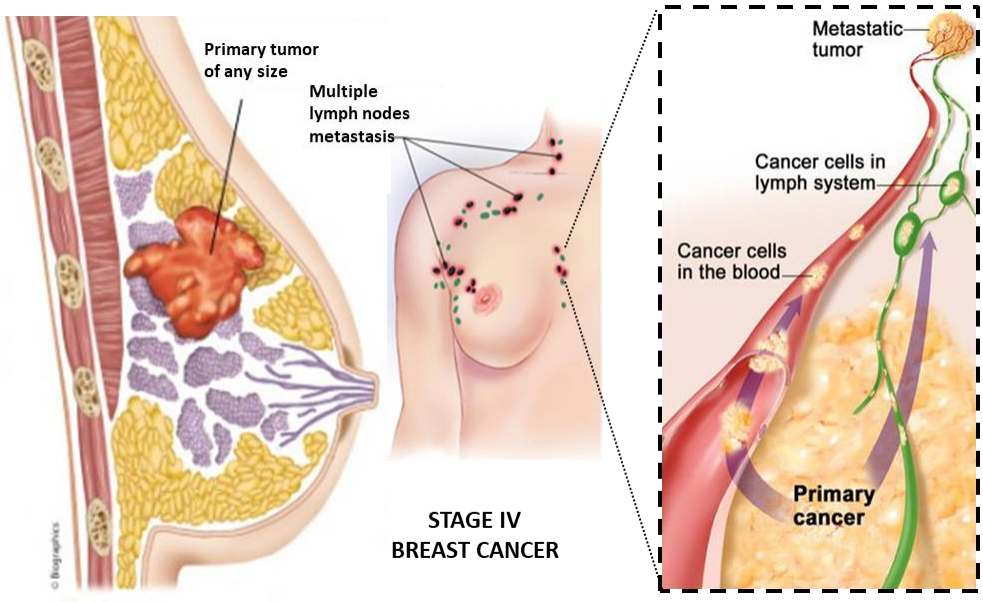

Figure 5: Representation of the process of metastasis (adapted from National Cancer Institute, Ref [42])

While the rate of bone metastases is similar between TNBC and other breast cancer subtypes, TNBC patients are four times more likely to develop visceral metastases than patients with non-TNBC subtypes [43]. Once a patient develops a primary tumor with distant metastasis, variables other than the number of affected organs and the locations involved have no bearing on outcome and patients with visceral metastasis generally have a poor outcome.

The analysis of survival in patients suffering from TNBC metastasis revealed that the route of first metastasis correlates significantly with survival of TNBC patients: distant metastases to the brain being the poorest survival indicator, followed by liver, pleura, bone, and lung [44].

Metastasis occurs in a series of discrete steps known as the "metastatic cascade" (**Figure 6**). If the tumor cell completes the metastatic cascade, the process can repeat, with the metastatic secondary tumor the origin for a secondary metastatic cascade [45].

STAGE 1: Tumor Cell Dissemination and Epithelial-Mesenchymal Transition

Epithelial tissues, representing the origins of most solid tumors, usually form relatively rigid sheets of epithelial cells. The separation from the tumor stroma by the basement membrane organizes the structure by lateral belts of cell–cell adhesion complexes, building the extracellular matrix (ECM). Invasive tumor cells must first alter cell-to-cell adhesion and cell adhesion to the ECM, considered as a first barrier to invasion.

During the evolution of an *in situ* tumor into an *invasive* carcinoma, epithelial tumor cells release from their neighbors within the tumor stroma and breach the basement membrane barrier. To overcome this and other impediments to invasion, carcinoma cells trigger an epithelial-mesenchymal transition (EMT), a critical process for diverse aspects of normal embryonic development. The EMT program, which involves dissolution of adherents and tight junctions and a loss of cell polarity, dissociates the cells within epithelial cell sheets into individual cells that exhibit multiple mesenchymal attributes, including enhanced motility and invasiveness [46, 47]. Multiple signaling pathways and molecules, including Receptor Tyrosine Kinases (RTKs), the transforming growth factor β (TGFB) superfamily, WNT, and NFκB [48], orchestrate the EMT. Cells undergoing EMT also secrete protein-degrading enzymes like matrix metalloproteinases (MMPs)

[49] to aid invasion of surrounding tissues and vessels and many tumor overexpress such MMPs. Of note, TNBCs display a higher tendency for early distant metastasis and cancer recurrence due to enhanced EMT when compared to other breast cancer subtypes [50].

STAGE 2: Tumor Cell Passage through Lymph Node or Blood Vessel Walls

To invade tissues and vessels, cells must acquire the ability to migrate. Cell migration starts with the extension of cell membrane protrusions, driven by a continuous cycle of actin polymerization. Invasive tumor cells migrate either as single cells or collectively in the form of files, clusters, or sheets. Studies have observed collective invasion of tumor cells in tumors with incomplete or no EMT. Single cell migration occurs slowly, through "mesenchymal" migration or more rapidly, via an "amoeboid" form that does not require ECM remodeling [51].

Structural features of tumor-associated blood and lymphatic vessels drive the mechanics of cancer cell intravasation. Through a variety of ECM-remodeling mechanisms, tumor cells stimulate the generation and development of new blood vessels within their local microenvironment (neoangiogenesis) to provide themselves with nutrients and an oxygen supply. However, tumor-derived neovasculature tends to be weak, incomplete, tortuous, prone to leakiness, and under a continuous state of reconfiguration [52] when compared to blood vessels present in normal tissues. The weak nature of the tumor-associated microvasculature and the absence of adequate pericyte coverage combine to facilitate cancer cell intravasation. Again, a wide variety of signaling pathways and molecules control intravasation, including cyclooxygenase-2 (COX-2), epiregulin (EREG), MMP-1, and MMP-2. The presence of these factors synergistically promotes breast carcinoma intravasation and stimulates neoangiogenesis and the formation of weak and leaky blood vessels.

STAGE 3: Survival and Travel through the Lymphatic System and Bloodstream to Distant Sites

After cancer cell intravasate into the blood vessel lumen, they can propagate widely through the venous/arterial and lymphatic vessel circulation. Circulating tumor cells (CTC) detected [53] within the bloodstream of carcinoma patients provide crucial information regarding metastatic stage. However, CTCs in blood circulation must survive multiple stresses (anoikis processes, capillaries entrapment, the hemodynamic shear forces, etc.) to reach distant organ sites, and, therefore, survival rate is low. The main

difference between metastatic and non-metastatic cells in breast cancer lies not with migration capacity, but rather migration direction: non-metastatic mammary tumor cells move randomly and appear unpolarized, while metastatic cells polarize towards blood vessels and migrate directionally [54, 55].

STAGE 4: Arrival in Distant Small Blood Vessels, Invasion of Blood Vessel Walls, and Movement into the Surrounding Tissue/the Role of Exosomes in Metastatic Dissemination

Generally, individual tumor cell types preferentially form metastases in specific target organs [56, 57]. Tissue specific tropism may be a product of vasculature layout and size restrictions (passive targeting), homing via ligand-receptor recognition (active targeting), or via the production of pre-metastatic niches for CTCs. In addition to mediating migration and invasion [58, 59], spherical nanovesicles of 40-100 nm in diameter known as exosomes play an important role in the modulation of pre-metastatic niche [60]. Exosomes, found in most body fluids, contribute to cell−cell communication and may represent diagnostic/prognostic markers for cancer intensive investigation.

Advanced imaging techniques in orthotopic breast cancer models demonstrated the movement of breast cancer cell exosomes to metastatic sites [61-63] and tumor cell-derived exosome driven increases in vascular permeability *in vitro* and *in vivo [64]*. *Furthermore,* breast cancer cell-derived exosomes induce proinflammatory cytokines in distant macrophages [65] and promote metastasis via immunosuppressive activities [66].

STAGE 5. Extravasation through Blood/Lymphatic Vessels

Once lodged in the microvasculature of distant organs, CTCs invade the vascular basement membrane and ECM initiating intraluminal growth and forming discrete groups of cells that eventually ruptures the walls of surrounding vessels, thereby placing tumor cells in direct contact with the tissue parenchyma [67]. To overcome physical barriers to extravasation in tissues with low intrinsic microvessel permeability, primary tumors secrete factors (e.g. EREG, COX-2, MMP-1, and MMP-2 [68]) that perturb distant microenvironments and induce vascular hyperpermeability. Ultimately, these tumor cells will attach at a new location and proliferate to produce the secondary tumor.

STAGE 6. Micrometastasis Formation

Extravasated carcinoma cells must survive in the new microenvironment of the invaded parenchyma of distant tissues in order to form micrometastasis. The microenvironment at the metastatic locus usually differs widely from the original TME. These microenvironmental differences may include the type and amount of stromal cells, ECM constituents, available growth factors and cytokines, nutrients/oxygen supply and even the microarchitecture of the tissue itself.

Cancer cells may solve the problem of a discordant microenvironment at the invaded site via the establishment of a "pre-metastatic niche". Thanks to the release systemic signals including lysyl oxidase (LOX), [69] or MMP-9 [70] the mobilization of VEGF receptor 1-positive (VEGFR1+) hematopoietic stem cells is induced from the bone marrow to these future sites of metastasis. Additional mechanisms may include the stimulation of various integrins as well as liberation of molecules that have been sequestered in the ECM, such as the carcinoma cell chemoattractant stromal cell-derived factor 1 (SDF-1) [71]. Once more, the secretion of cancer cell-derived exosomes may be crucial to the generation of a pre-metastatic niche [72] by converting distant microenvironments into more hospitable sites for disseminated tumor cells.

STAGE 7. Blood Vessel Growth Creates a Blood Supply that Allows Continuing Tumor Growth. Metastasis Colonization.

Once disseminated cancer cells have survived the initial interaction with the microenvironment of a foreign tissue, how the cancer cell then proliferates and forms large macroscopic metastases remains unclear. In fact, these occult micrometastases may persist in one of two ways. The spread tumor cells may hold largely quiescent, with their proliferation at metastatic sites greatly impaired due to incompatibilities with the foreign microenvironments that surround them [73]. Alternatively, the cancer cells in occult micrometastases may proliferate continuously; however, a net increase in their overall number may not occur due to the counterbalancing effects of a high apoptotic rate [74].

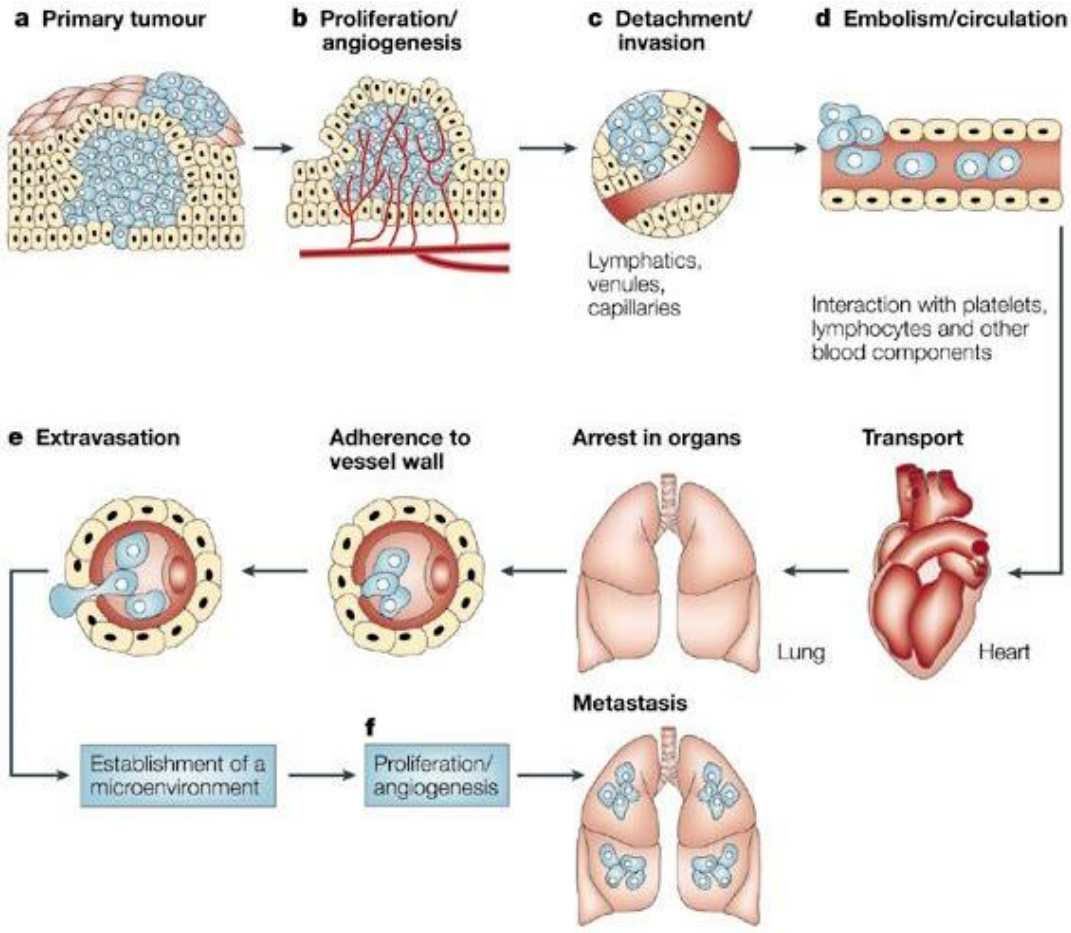

Figure 6: Metastatic cascade representation. Adapted from Ref [75].

I.1.5. Current Therapeutic Approaches for Triple Negative Breast Cancer

Due to the intrinsic lack of expression of target receptors in tumor cells, TNBC patients do not benefit from hormonal-based therapy. Current treatment options for TNBC include breast conservative surgery (BCS) followed by radiation treatment (RT) and systemic chemotherapy.

Despite the fact that TNBC tends to be more aggressive, surgical decision making often depends on traditional clinico-pathological variables and ultimately on patient preference [25]. Freedman *et al* [76] concluded that local recurrence rate after BCS in TNBC patients were lower than in other aggressive subtypes of breast cancer, so they remain appropriate candidates for breast conservation. However, the risk of local and regional recurrence after surgery still represents a significant problem [77].

TNBC patients receive conventional adjuvant radiotherapy following radical mastectomy (RM) or breast conserving surgery (BCS), as for other breast cancer subtypes; however, there still exists controversy regarding this issue among oncologists [78]. Given the rapid growth rates and aggressiveness of TNBC, BCS followed by radiotherapy could not lead to equivalent outcome than RM as in other types of breast cancer. Although radiotherapy decreases local recurrence after mastectomy in TNBC, overall patient survival failed to improve [79].

Chemotherapeutic drugs represent the only systemic treatment currently available for TNBC, even though this approach is only curative in a subset of patients with chemotherapy-sensitive disease (indicated by the 30% to 35% rates of pathologic complete response (pCR) [80]). While some reports suggest that TNBC responds to chemotherapy better than other types of breast cancer, prognosis remains poor [81]. Chemotherapeutic strategies for the management of TNBC include targeting DNA repair (platinum compounds and taxanes), p53 (taxanes), or cell proliferation (anthracyclines), and targeted therapies [82]. Platinum-derived anticancer treatments have demonstrated promising activity, but up to 70–80% of patients still suffer from residual disease following neoadjuvant cisplatin-based treatment strategies [83]. Besides, taxanes display certain activity in TNBC in most cases, they have not shown particular benefit over non-TNBC [84]. The chemosensitivity of TNBC tumors displaying p53 mutations remains a controversial point, given the reported resistance of p53-mutated breast cancers to anthracycline chemotherapy [85]. Currently, taxane/anthracycline sequential chemotherapy regimens provide the highest pCR rates (~40% to 45%). However, the inclusion or substitution of other chemotherapeutic drugs (capecitabine, gemcitabine, vinorelbine, or ixabepilone) resulted in little or no improvement in pCR rates [86].

As mentioned before, TNBC patients with high rates of visceral metastases suffer from a relatively short median survival (7-13 months) and a limited duration of response to successive chemotherapeutic regimens. TNBC is typically associated with an initially higher response rate to chemotherapeutics, but lacks of proper response following treatment with existing chemotherapy agents, resulting a shorter overall survival [87]. The underlying molecular mechanisms for this inconsistency are yet to be elucidated, although the inherent genomic instability of TNBC could support the possibility of stronger resistance to chemotherapeutic cytotoxicity.

I.1.6. Potential Therapeutic Approaches for Triple Negative Breast Cancer

While several clinical trials have tested small molecule inhibitors and monoclonal antibodies against crucial cellular pathways in TNBC patients, none have entered clinical practice due to limited efficacy. A better understanding of the underlying biology of TNBC may identify new therapeutic targets and allow TNBC patient stratification. Classification of tumors at the molecular level via microarray and DNA sequencing analysis may facilitate drug development.

SRC Proto-oncogene Tyrosine-protein Kinase Inhibitors

The SRC proto-oncogene tyrosine-protein kinase plays roles in cell adhesion and motility [88], both of which represent crucial mechanisms for cancer progression and invasiveness. In preclinical studies, TNBC cell lines displayed high sensitivity to Dasatinib, a small molecule kinase inhibitor of the Src, Abl, and KIT protein kinases [89]. Additional studies indicated heightened sensitivity of mesenchymal-like TNBC subtypes to Src inhibitors [90], which may be explained by the overexpression of genes related to cell motility in mesenchymal-like TNBC subtypes and the crucial role of Src in cell migration.

Poly ADP-ribose Polymerase (PARP) Inhibitors

TNBC generally displays a high prevalence of mutations in the breast cancer-1 (BRCA1) gene [90], which codes for an enzyme that mediates DNA damage repair such as that caused by chemotherapy. The poly (ADP-ribose) polymerase (PARP) family of proteins regulate DNA repair, genomic stability, and programmed cell death. Therefore, PARP therapy alone or in combination with chemotherapy/radiotherapy may enhance DNA damage levels and promote cancer cell death [91]. Of note, the US Food and Drug Administration (FDA) approved the first PARP inhibitor, olaparib (Formerly, Lynparza), for the treatment of metastatic, HER2-negative breast cancer in patients with BRCA1or BRCA2 mutation that had previously undergone chemotherapy [92].

Androgen Receptor (AR) Inhibitors

While normal breast development requires androgen receptor (AR) signaling, deregulated signaling has been implicated in breast cancer development [91]. Gene

expression studies have identified TNBC subsets (particularly the LAR subfamily) enriched for AR signaling-related factors. Furthermore, preclinical and proof-of-concept clinical studies have demonstrated potential for AR-signaling inhibition as a treatment option for TNBC [93]. To this end, recent studies discovered that a combination of AR inhibition with the antiandrogen drugs enzalutamide and bicalutamide significantly reduced proliferation, anchorage-independent growth, migration, and invasion, and increased apoptosis in LAR and three non-LAR TNBC molecular subtypes (mesenchymal-like, mesenchymal stem-like, and basal-like 2) [94, 95].

Epigenetic Targets

There exists evidence of gene silencing in patients suffering from TNBC by DNA methylation and/or histone deacetylation [96, 97], and so, epigenetic silencing may be involved in the lack of hormone receptor expression in TNBCs. Treatment with DNA methyltransferase (DNMT) inhibitors or histone deacetylase (HDAC) inhibitors may reactivate genes involved in the endocrine pathway and subsequently restore sensitivity to endocrine therapy. Treatment with the 5-aza-2'-deoxycytidine (decitabine) DNMT inhibitor has proven effective in treating hematological neoplasms [98].

Vascular Endothelial Growth Factor (VEGF) Inhibitors

As stated above, BL-2 and MSL subtypes of TNBC express higher levels of VEGF pathway genes [99], which aid tumor cells in the development of new blood vessels (angiogenesis) to acquire the oxygen and nutrient supply required for growth and spread. Bevacizumab (formerly Avastin) interferes with VEGF activity by preventing VEGF from interacting with receptors on blood vessel walls [21], thereby, inhibiting VEGF-mediated angiogenesis.

Epidermal Growth Factor Receptor (EGFR)-targeted therapies

While the overexpression of EGFR in TNBC can promote cancer cell growth, Cetuximab (Formerly, Erbitux) inhibits both EGFR signaling and cancer cell growth. Of note, Cetuximab has been used in combination therapies for TNBC [100].

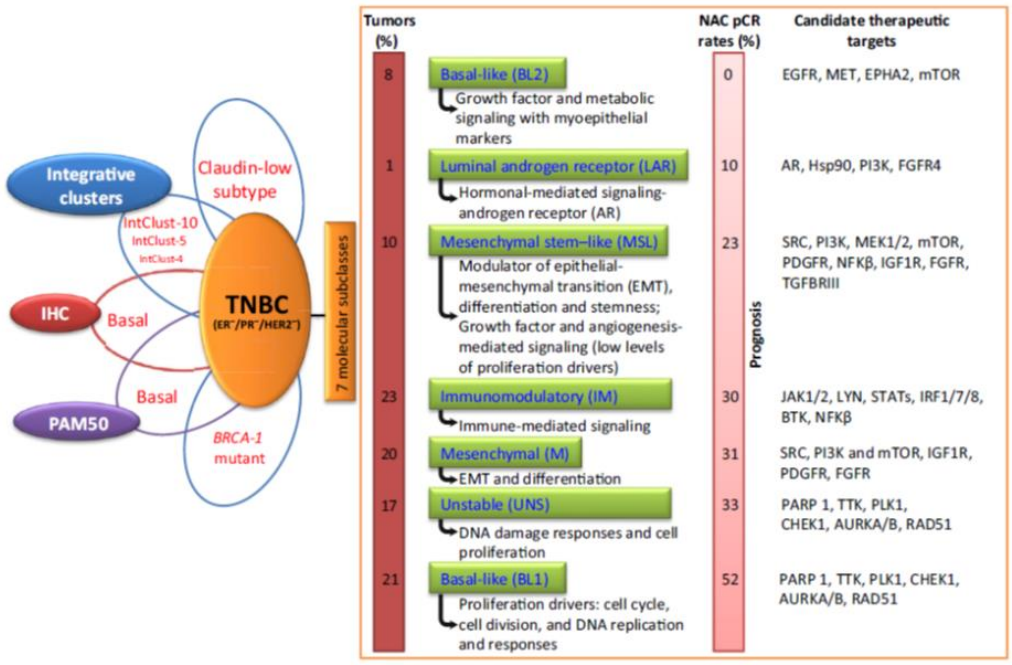

Figure 7: Classification of TNBC and candidate therapeutic targets. Adapted from Ref [22]

Potential therapeutic strategies	Agent examples
Src inhibition	Dasatinib; Saracatanib
PARP inhibition	Olaparib; ABT-888
Androgen receptor inhibition	Bicalutamide
Targeting epigenetics	Decitabine LBH589
EGFR pathway inhibition	Cetuximab
PI3K pathway inhibition	NVP-BEZ235; Everolimus

Figure 8. Potential therapeutic strategies and agent examples for TNBC. Adapted from Ref [14]

I.1.7. Nuclear Magnetic Resonance-Metabolomics and Transcriptomics as Tools for Biomarker Identification in Triple Negative Breast Cancer

NMR-Metabolomics

Nuclear magnetic resonance (NMR)-mediated metabolomic analysis permits the study of small molecules (<1500 Da) in complex mixtures, providing information

regarding their metabolic networks and interactions, with a high potential for precisely describing the physiological state of a tissue or entire organism [101]. Metabolomic analysis of metastasized organs and/or tissues, and tumor biopsies provides information in two different areas:

Firstly, given the wide range of applications, metabolomics permits the identification of metabolic alterations in different tissues as a consequence of cancer development. Thus, metabolomics enables the understanding of disease progression and describes the complex pathways driving the disease. Additionally, "metabolomics signatures" of ongoing disease can be considered as a prognostic/diagnostic tool and may promote the discovery of potential biomarkers for cancer development or metastasis (see **Chapter II**). Recent studies have identified "metabolic vulnerabilities" in TNBC, which represent new and potentially exciting therapeutic targets for TNBC [102].

Secondly, metabolomics can aid our understanding of the molecular mechanisms involved in the response to new drugs/drug-delivery systems (DDS) [103]. The applicability of this experimental approach to cell cultures and animal models makes metabolomics a useful tool for establishing direct connections between in vitro and in vivo data, thus providing a reliable platform for the characterization of the biological output of anticancer agents.

Transcriptomics through mRNA sequencing

Transcriptomics has become an essential instrument for both basic and clinical research, and the incorporation of transcriptomic mRNA analysis as a characterization tool for TNBC subtypes has identified several new modulators of TNBC, as genes driving TNBC development and aggressivity [104]. Similarly to NMR-metabolomics, transcriptomics also aids the comprehension of the pathways involved in spontaneous cancer-related processes, such as invasion and metastasis. The elucidation of differential gene expression in metastatic tumors is a key step to understand the complex mechanisms controlling tumor adaptability [105].

Remarkably, transcriptomics has allowed to unveil distinctive features of the transcriptional regulation program in breast cancer, including the discovery of inter-chromosomal relationships between genes strikingly scarce in a cancer network, [106]

the profile of immune cells in primary breast cancers [107] and the analysis of breast cancer recurrence risk from a wide set of patients [108].

Transcriptomic analysis provides an opportunity to simultaneously analyze a large number of genes/targets and identify the mechanisms of action of different antitumor drugs after treatments [109]. Additionally, the differentially expressed genes after anticancer DDS administration can reflect the differential pharmacokinetics/pharmacodynamics thus helping in the better design of this advanced therapeutics (see **Chapter IV**). The main efforts in this field are focused on the integrative understanding of transcriptional regulation in the establishment and modification of the cancer cellular landscape, particularly how the regulatory program of a "healthy" cell drifts towards a "cancerous" phenotype [110]. In this context, high-throughput omic technologies have provided us unprecedented tools to study the alterations found in cancer at a deeper level.

I.2. Nanomedicine-based Approaches for Breast Cancer Treatment

The goal of chemotherapy, the only systemic treatment available for TNBC, is to deliver high-efficacy drugs to a specified location at a required concentration for a set period. Pharmacokinetic control is difficult to achieve due to the different transient states of drugs in adhesion, distribution, metabolism, and excretion. Additionally, cancer cells tend to develop drug resistance (e.g., MDR [111]) during the course of treatment, eventually leading to failure of chemotherapy.

Nanomedicine advances hope to overcome many of the limitations of current chemotherapeutic formulations, including low efficacy, unwanted side-effects, and low bioavailability [112, 113]. Nanocarriers with controlled surface charge and surface modifications (e.g., polyethylene glycol (PEG)) and fixed sizes (e.g., 100–200 nm in diameter), may serve as efficient vehicles for anticancer agents with higher selectivity for primary tumor and metastases, and reduced drug resistance and side effects. More than 40 nanomedicines including nanocristals, polymer therapeutics, liposomes, inorganic or viral nanoparticles are already used in routine clinical cancer care with more than 70 clinical trials ongoing [114] (**Figure 9**).

In particular, nanomedicines as treatment options for TNBC may provide early diagnosis, accurate cancer imaging, and controlled drug delivery [115]. The combination of drugs and nanocarriers permits high drug loading, high transportation efficiency across the cell membrane and tunable pharmacokinetics [116], allowing controlled drug release with minimal side effects. Furthermore, such formulations aid escape clearance by the reticuloendothelial system (RES), thereby promoting longer blood half-life, and help to overcome resistance mechanisms [117].

Finally, the multivalency offered by many nanomedicine approaches also permits the design of efficient combination therapy by ensuring the concomitant delivery of two or more anticancer agents with synergistic effects. This is a very promising strategy towards advanced therapeutics with already one combination liposomal formulation, Combiplex® approved by FDA [118-120] (**See Section 3.4**).

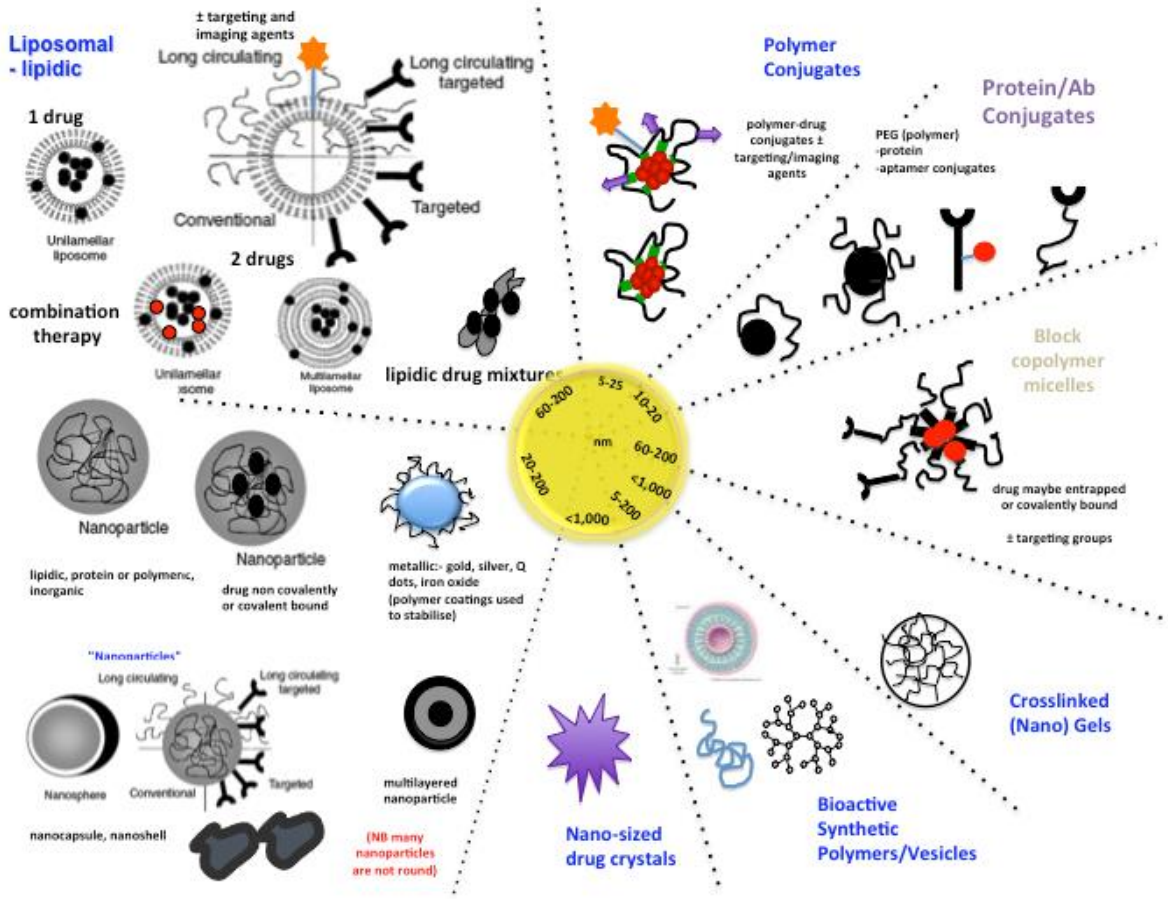

Figure 9. Schematic illustration of established nanotherapeutic platforms. Redrawn from Ref [121]

Also to note that, systemic administration of nanomedicines usually relies on passive accumulation (EPR effect), exclusively due to their intrinsic size within the blood pool on arrival the tumor stroma [122] (**See Section 3.2)**. However, the rapid development of solid tumors often leads to hypoxic and necrotic regions, which represent difficult targets for systemic treatments [123]. Active targeting has been not a very successful strategy so far but it is believe with omics and molecular technics novel targets to be use as adequate vectors would be identify in the near future that could push active targeting approaches forward [124].

I.2.1. Currently used Nanomedicines for Breast Cancer Treatment

A limited number of FDA-approved nanomedicines exist for breast cancer treatment [125], the most well-known include paclitaxel (PTX) protein-bound nanoparticles (Abraxane or nab-paclitaxel) and liposome-encapsulated doxorubicin (Doxil).

Abraxane comprises paclitaxel non-covalently bound to a 130 nm nanoparticle processed from human serum albumin (**Figure 10**) and permits safer patient administration due to the absence of the excipient cremophor®, as well as a rapid accumulation of paclitaxel at the tumor site [126, 127]. Compared to the parental "free" drug, Abraxane permits a 9-fold greater permeation of paclitaxel into tissues via transporter-mediated pathways, a 33% higher intratumoral drug concentration, a 10-fold higher mean maximal concentration of free paclitaxel, and a 4-fold lower elimination ratio [128]. In clinical trials, Abraxane demonstrated comparable or better efficacy over paclitaxel for locally advanced breast cancer or inflammatory breast cancer [129] and can be safely combined with ordinary chemotherapy or targeted therapies.

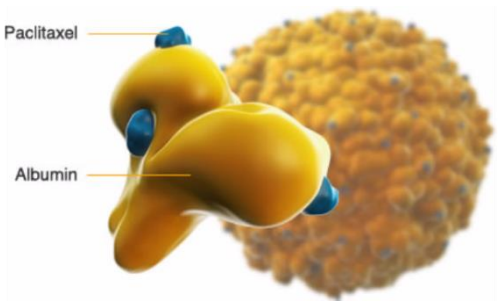

Figure 10. Schematic representation of Abraxane

Doxil represents the first FDA-approved anticancer nanodrug (1995) and consists of a PEGylated liposomal formulation of around 85 nm in diameter of the anthracycline drug doxorubicin (**Figure 11**) [130]. Three unconnected principles drove Doxil development; (i) long circulation time and evasion of RES via the PEGylated liposomes; (ii) high doxorubicin loading determined by a transmembrane gradient, which also permits specific drug release at the tumor; and (iii) the liposome lipidic bilayer that exhibits a dynamic phase composed of phosphatidylcholine and cholesterol.

Doxil permits doxorubicin tumor accumulation via EPR-mediated passive targeting [131], leading to improved tumor growth suppression rates and overall survival. Although the maximum tolerated dose (MTD) for Doxil is similar to free doxorubicin (Dox), due to the appearace of foot and hand disease as side effect, Doxil led to a major (~3-fold) reduction in anthracycline-associated cardiotoxicity when compared to free Dox [132]. Generally, Doxil studies provide the precedents for the safe and effective application of nanomedicines in combination with standard drug therapy [125].

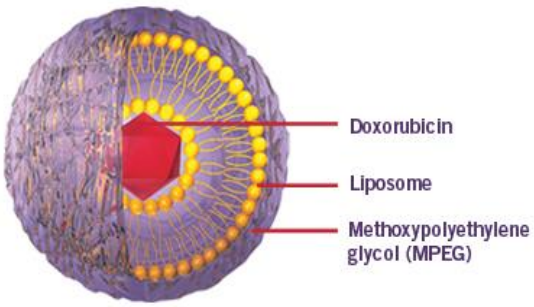

Figure 11. Schematic representation of Doxil

I.3. Polymer Therapeutics

The term “Polymer Therapeutics” (PT) describes a wide family of nano-sized medicines (5-100 nm in diameter) considered the first polymeric nanomedicines [133]. Of note, the polymeric drug glatiramer acetate for the treatment of multiple sclerosis (Copaxone®, Teva Pharm), and the polymer conjugate polyethylene glycol (PEG)-filgrastim for the treatment of neutropenia (Neulasta®, Amgen) have appeared in the top 10 best-selling drugs in the USA [133].

Polymer therapeutics are comprised of a wide-range of nano-sized constructs whose common feature is the incorporation of a rationally designed covalent chemical bond between a water-soluble polymeric carrier (with or without inherent activity) and the bioactive molecule(s). Although only these three characteristics define PT, the incorporation of site-specific targeting moieties or/and imaging molecules and even its capability of self-assembled in larger nanoconstructs has extended the initial term [134].

I.3.1. Classification of Polymer Therapeutics

PTs comprise polymeric drugs [135], polymer-drug conjugates (PDCs) [136-138], polymer-protein conjugates [139, 140], polymeric micelles, in which the drug is attached by covalent bonding [141, 142], and multicomponent polyplexes (polyelectrolyte complexes) which are being developed as non-viral vectors [143, 144]. The development of polymer-drug conjugates represents one of the aims of the present Thesis, and will be described in detail (**Section 4**).

PTs allow for tailored drug loading, the incorporation of drug combinations, and intelligent bio-responsive linkers that release drugs under specific biological conditions, such as those found at tumor sites [145].

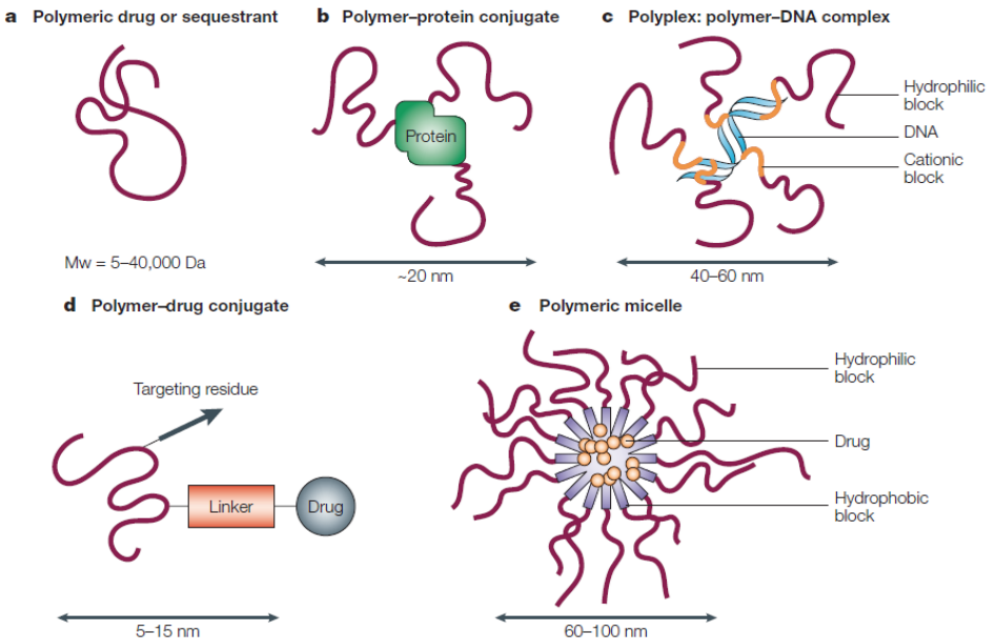

Figure 12. Schematic representation of polymer therapeutics families, their main characteristics, and the average hydrodynamic diameter. Adapted from Ref [145].

All the described PT subtypes use specific water-soluble polymers, either as the bioactive agent itself or as an inert functional part of a multifaceted construct for improved drug, protein, or gene delivery. The versatility of synthetic chemistry in PT and the incorporation of bioresponsive moieties and biomimetic features enhances the scope for PT in comparison with other nanomedicines [145].

The therapeutic approach in which PT are based is built on two relevant foundations. Firstly, controlled and sustained drug release within a suitable therapeutic window, and secondly, targeting drug release at the desired site of action. Intravenous administration (i.v.) is the preferred route of administration for most of the polymer-drug conjugates in the clinics, with the purpose of faster bioavailability within the bloodstream in comparison with other administration routes and the avoidance of tissue-specific biological barriers [146, 147].

PT offers many advantages over other nanomedicines, such as (i) greater water solubility (appropriate for very hydrophobic drugs such as Dox or paclitaxel PTX); (ii) improved plasma half-life by means of a higher hydrodynamic volume, which decreases kidney clearance; (iii) protection against proteolytic enzymes, or unspecific cellular uptake; (iv) reduction or prevention of aggregation, immunogenicity and antigenicity; and (v) improved pharmacokinetics (PK) at the whole body, cellular, and subcellular level.

More than 30 years of PT development has led to 24 products entering the market (**Table 3**), with a growing number entering clinical development (**Tables 4 and 5**). The improved understanding of biodistribution, clearance, mechanism of action, and stability of the first generation of PTs, as well as improved physicochemical characterization, has prompted a second generation of better quality PTs with promising characteristics.

I.3.2. Passive Targeting of PT by the Enhanced Permeability and Retention Effect

The advantages of nanomedicines, in particular PT, relate to their controllable sizes and their size-dependent macromolecular properties. Following i.v. administration, a given nanomedicine can passively extravasate more selectively at tumor tissues due to the increased permeability of the angiogenic tumor vasculature and defective lymphatic

drainage. This selective effect, first described by Maeda and Matsumura [148], is known as the “enhanced permeability and retention (EPR) effect”. EPR-mediated targeting also function within inflamed areas, thereby justifying the development and use of this class of macromolecular carriers in infectious and inflammatory conditions [149].

EPR-mediated targeting is finally determined by circulating plasma concentration, stability, and plasma half-life of the PT [150]. However, the EPR effect is also influenced by tumor type, tumor region, presence of intratumoral necrotic or inflamed area, and tumor vascularization. Therefore, poorly-vascularized damaged tissues are less suitable for nanomedicine-based treatments [151], demonstrating for a requirement for new PT-based therapeutic approaches incorporating targeting moieties.

The EPR effect also suffers from several additional limitations that promote the application of active targeting strategies [152]. These include (i) the inability of the nanomedicine to interact with blood components or blood vessels; (ii) the requirement for weakly negative to near neutral total surface charges; (iii) a requirement for systemic circulation times of several hours/days; and (iv) interactions of the nanomedicine with serum proteins and the subsequent alteration in size profiles.

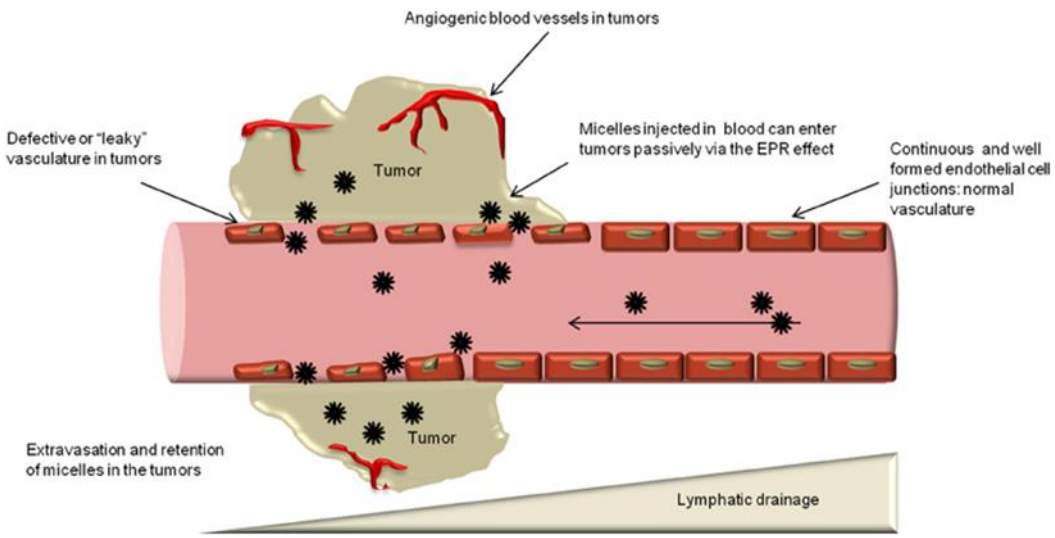

Figure 13. Enhanced permeability and retention (EPR) effect and passive targeting representation. Adapted from Ref [156]

The EPR effect in human patients also presents with patient-to-patient variability, depending on a patient's pathological and physiological characteristics and clinical condition [153, 154], and has provoked diverse opinions regarding the real value of the

EPR effect. Some studies support EPR-mediated accumulation of nanomedicines within tumors, while others show that the EPR effect depends on the tumor model, suggesting that the EPR effect alone may not provide the entire solution. Maeda himself recognizes this heterogeneity and has developed methods to enhance the EPR effect in order to overcome the heterogeneity and improve drug delivery to tumors [155][34].

I.3.3. Cellular Internalization Pathways of Polymer Therapeutics

Following tumor accumulation by the EPR effect, endocytic mechanisms control uptake of PTs into the tumor cell. Of note, water-soluble polymer-drug conjugates (PDCs) limit cellular uptake to the endocytic pathway looking for a lysosomotropic delivery, [145] and this fact has allowed to bypass drug resistance mechanisms. Following capture of nanomedicines at the cell membranes and the formation of intracellular vesicles called endosomes, a complex sequence of fusion events leads to the formation of the lysosome, which displays low pH (5.5) and high concentration of proteolytic enzymes [157]. The vast majority of PDCs rely on this pathway to finally release the conjugated drug from the polymer, though polymer backbone or polymer-drug linker degradation by low pH or proteolytic enzyme activity. A detailed analysis of enzyme- and pH-responsive PDCs can be found in **Section 5.**

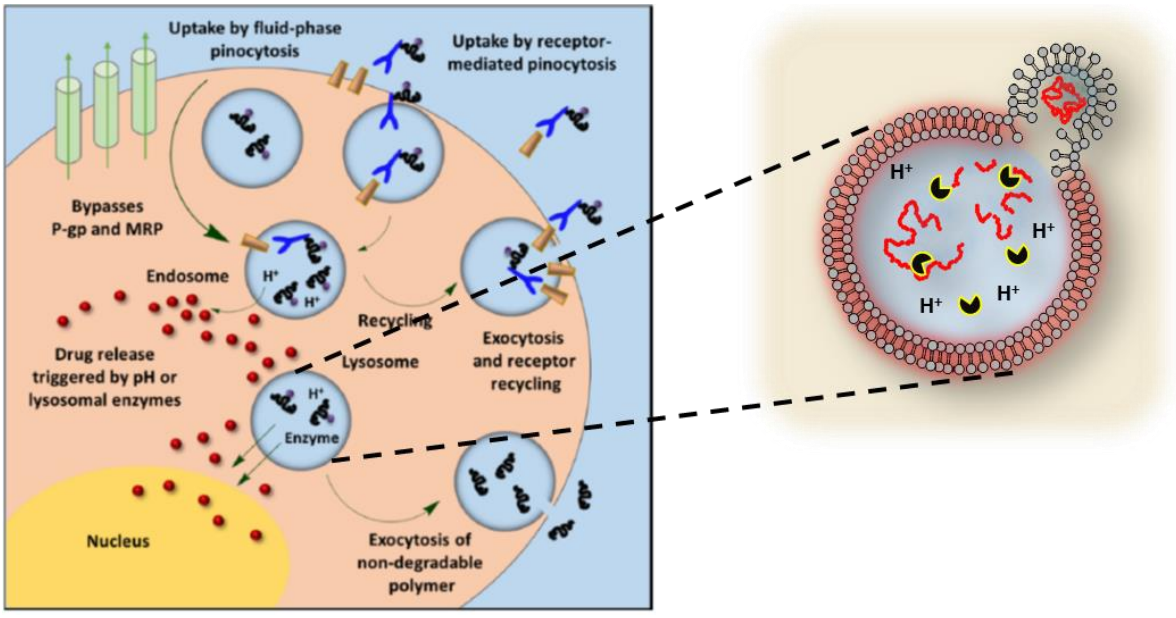

Figure 14. Lysosomotropic intracellular drug delivery process followed by Polymer-Drug conjugates. Adapted from Ref [158]

I.3.4. Polymer-based Combination Therapy

The multivalent nature of many polymeric carriers allows the incorporation of more than one active moieties to promote synergistic combinatorial effects. Four types of polymer-based combination therapy have been proposed (**Figure 15**), encompassing the administration of:

I. Polymer-drug conjugate + free drug(s) (Type I)
II. Polymer-drug conjugate + polymer-drug conjugate (Type II)
III. Single polymeric carrier bearing the combination of drugs (Type III)
IV. Polymer-directed enzyme prodrug therapy (PDEPT) or polymer-enzyme liposome therapy (PELT)

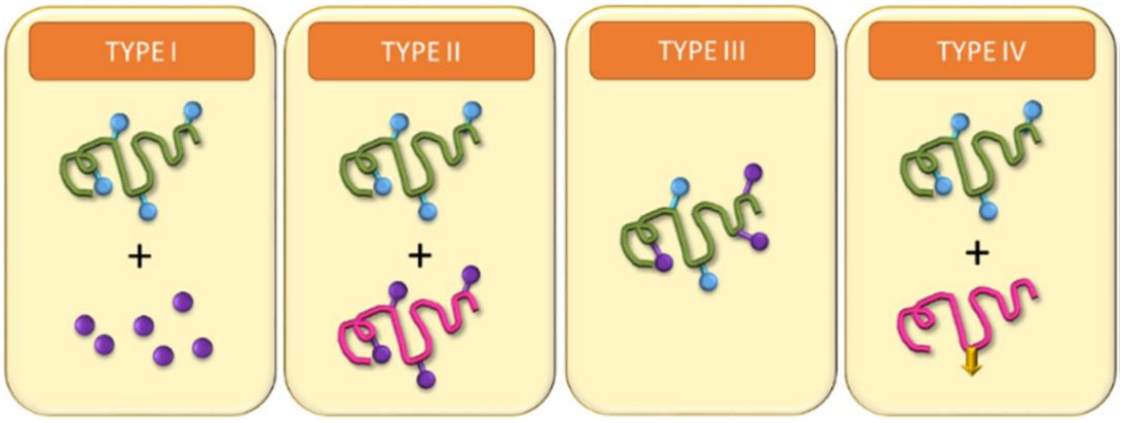

Figure 15. Polymer-based combination therapy strategies.

During this thesis, we synthesized, characterized, and biologically evaluated three different Type III polymer-based combination therapies for the treatment of TNBC (**Chapters 3, 4 and 5**).

Type III polymer-based combination therapy offers several benefits in comparison with single polymer-drug conjugates:

I. Guaranteed simultaneous (controlled) delivery of both drugs to the same site of action.
II. The presence of rationally designed linker allow us to tune the relative pharmacokinetics that allow to achieve synergism.
III. Allows administration as a single dose, which translates into benefits in patience compliance and manufacturing.

However, the enhanced complexity of the systems brings new challenges, including:

I. The previous identification of appropriate drug combinations and ratios to achieve synergistic effects.
II. The requirement for more controlled drug release kinetics.
III. The possibility of reduced loading capacity due to steric impediments at the molecular level.
IV. The requirement for a more detailed physico-chemical characterization as the incorporation of two active agents significantly enhances the complexity of the nanosystem [120].

I.4. Polymer Conjugates as Therapeutics

Polymer-drug conjugates have long been considered the backbone of the drug delivery field, and the successful translation of several of these conjugates into clinical practice has demonstrated the potential of this approach to improve patient outcomes. The most recent advances in this field include DDS with ultra-high drug loadings, biodegradable polymeric backbones, and new drug conjugation chemistries, as well as the use of polymeric carriers as "platforms" that enable the incorporation of different therapeutic and imaging agents for applications in multifunctional therapies.

I.4.1. Polymer-protein Conjugates

The first polymer-protein conjugates (PPC), pioneered by Abuchowski *et al*. in 1977, demonstrated how polyethylene glycol (PEG) conjugation (or PEGylation) could ameliorate protein immunogenicity, improve solubility, and extend plasma half-life [159, 160]. PEG is a highly water-soluble, flexible, uncharged, and biocompatible polymer that has been widely used as an excipient and starting product in the pharmaceutical industry. When bound to a therapeutic protein, PEG shields antigenic epitopes via steric repulsion, thus reducing immunogenicity [161]. Furthermore, steric repulsion prevents degradation by proteolytic enzymes and opsonization and subsequent clearance by the mononuclear

phagocyte system (MPS). The increase in molecular weight and hydrodynamic radius conferred by PEG conjugation further reduces plasma clearance by renal filtration. Accordingly, the improvements in protein stability, plasma half-life, and immunogenicity reduce the required frequency of dosing and improve the overall safety profile of the therapeutic agent. The clinical impact of PEGylation has been established by several clinically approved PEG-protein conjugates as therapies for hepatitis C, acute lymphatic leukemia, and rheumatoid arthritis (**Table 3)** [162]. Furthermore, nucleic acids can also be PEGylated to reduce renal clearance and extend the circulation half-life of, for example, aptamer therapeutics, including the approved drug Macugen for macular degeneration [163-165]. These successes have encouraged the clinical evaluation of various PEGylated proteins, including enzymes, cytokines, growth factors, and antibodies **(Table 3, 4 and 5).**

However, the non-biodegradable nature of PEG represents an important limitation to clinical application. Currently approved PEGylated protein therapeutics employ PEGs of ≤40 kDa molecular weight, close to the glomerular filtration threshold of approximately 50 kDa [165]. While increased molecular weight generally affords extended circulation time, concerns regarding the accumulation of non-biodegradable PEG limit the optimization of polymer molecular weight and resultant pharmacokinetics. However, new biodegradable alternatives to PEG such as polyoxazolidines or polypept(o)ides can enhance protein pharmacokinetics, and present an exciting opportunity in the development of the next generation of polymer-protein conjugates [166-168].

Additionally, conflicting reports on the immunogenicity and antigenicity of PEG have further provoked interest in the development of non-fouling and biocompatible PEG replacements [169]**.** Notably, a heparin-mimicking polymer affords stabilization to a heparin-binding protein-basic fibroblast growth factor, which is otherwise unstable even after PEGylation [170]. In addition to the traditional advantages of polymer conjugation, the ligation of responsive polymers affords “smart” conjugates in which protein activity and release can be modulated [171]. Additionally, amphiphilic polymer-protein conjugates can be incorporated into sophisticated superstructures to alter their pharmacokinetic profile and to increase functionality via the entrapment and co-delivery of additional active agents [172].

I.4.2. Polymer-drug Conjugates

PDCs represent one of the most successful and oldest polymeric DDS. The first attempts to enhance the therapeutic output of drugs by conjugation to macromolecules were performed in the 50s-60s, when Jatzkewitz focused on a variety of soluble polymers, in particular poly(vinylpyrrolidone) [173]. Mathé et al. conjugated drugs to immunoglobulins for the first time in 1958, establishing the first platform for PDCs [174]. The field of PDCs underwent a paradigm shift in 1975, when Ringsdorf conceptualized the application of biocompatible polymers as efficient drug carriers and thus encouraged the rational design of PT candidates that would entered in clinical testing years later (Kopecek, Duncan, Ulbrich and Rihova) [175, 176].

Rational design, a key requisite for the successful development of PDCs, encompasses three components: a water-soluble polymeric carrier, a bioresponsive linker, and a bioactive agent [175]. However, due to the multivalency of polymers applied in PDC development, more than one compound can be conjugated to the polymeric backbone, allowing the introduction of targeting residues (in order to trigger active targeting-receptor-mediated endocytosis) [177] or more than one drug (polymer-based combination therapy, see **Section 3.4**) [119]. Furthermore, the conjugation of imaging agents for theranostic purposes[178] could enhance the therapeutic value of a given PDC. Within the first generation of PDCs only a few polymeric carriers have shown success in clinical trials, including:

- Poly(*N*-hydroxypropyl methacrylamide) (polyHPMA)-Dox Developed and described for the first time by Kopeček, Ulbrich and Duncan, with (PK2) and without (PK1) galactosamine as active residue [177, 179-181].
- Poly(glutamic acid) conjugates of paclitaxel (Xyotax^{TM} or Opaxio^{TM}) or camptothecin (CT-2106) – First synthesized by Li and Wallace [182-184].
- PEG-cyclodextrin-camptothecin nanoparticulated conjugate of 30 nm (CRLX101 or IT-101) - Developed by Davis [185, 186].
- PEG-polypeptide block copolymer conjugated with SN-38 (NK-012), Doxorubicin (NK-911) or Cisplatin (NC-6004) – Developed by Kataoka [187-189].

Name	Polymer carrier	Drug	Company	Indication(s)	Year approved
Adagen	PEG	Adenosine deaminase	Enzon Pharmaceuticals	ADA-SCID	1990
SMANCS	Poly(styrene -co-maleic acid)	Neocarzinostatin	Astellas Pharma	Liver and renal cancer	1993
Oncaspar	PEG	L-asparaginase	Enzon Pharmaceuticals	Acute lymphoblastic leukemia	1994
PegIntron	PEG	Interferon α-2b	Merck	Hepatitis C	2000
Pegasys	PEG	Interferon α-2a	Genentech	Hepatitis B and hepatitis C	2002
Neulasta	PEG	G-CSF	Amgen	Chemotherapy induced neutropenia	2002
Somavert	PEG	HGH receptor antagonist	Pfizer	Acromegaly	2003
Macugen	PEG	Anti-VEGF aptamer	Bausch & Lomb	Neovascular age-related Macular degeneration	2004
Mircera	PEG	Epoetin beta	Roche	Anemia associated with chronic kidney disease	2007
Cimzia	PEG	Anti-TNFα Fab' fragment	UCB Pharma	Crohn's disease, rheumatoid arthritis, psoriatic arthritis, and ankylosing spondylitis	2008
Krystexxa	PEG	Uricase	Horizon Pharma	Chronic gout	2010
Plegridy	PEG	Interferon β-1a	Biogen	Relapsing multiple sclerosis	2014
Movantik	PEG	Naloxone	AstraZeneca	Opioid-induced constipation	2014
Adynovate	PEG	Factor VIII	Baxalta	Hemophilia A	2015
Palynziq	PEG	Phenylalanine ammonia lyase	BioMarin	Phenylketonuria	2018

Table 3. Marketed polymer conjugates. PEG, polyethylene glycol. G-CSF, granulocyte-colony stimulating factor.

Table 4. Polymer-protein conjugates in clinical development.

Name	Polymer carrier	Drug	Company	Indication(s)*	Stage (ClinicalTrials.gov identifier)
Damoctocog alfa	PEG	Factor VIII	Bayer	Hemophilia A	Pre-registration (NCT01580293)
Turoctocog alfa pegol	PEG	Factor VIII	Novo Nordisk	Hemophilia A	Pre-registration (NCT01480180)
Calaspargase pegol	PEG	Asparaginase	Shire	Acute lymphoblastic leukemia and lymphoblastic lymphoma	Pre-registration (NCT01574274)
Pegvorhyaluronidase alfa	PEG	Hyaluronidase	Halozyme Therapeutics	Pancreatic cancer	Phase 3 (NCT02715804)
TransCon Growth Hormone	PEG	Human growth hormone	Ascendis Pharma	Growth hormone deficiency	Phase 3 (NCT03344458)
Pegilodecakin	PEG	IL-10	ARMO BioSciences	Pancreatic cancer	Phase 3 (NCT02923921)
Elapegademase	PEG	Adenosine deaminase	Leadiant Biosciences	ADA-SCID	Phase 3 (NCT01420627)
Pegargiminase	PEG	Arginine deiminase	Polaris Pharmaceuticals	Mesothelioma	Phase 2/3 (NCT02709512)
BCT-100	PEG	Arginase 1	Bio-Cancer Treatment International	Acute myeloid leukemia	Phase 2 (NCT02899286)
Pegsiticase	PEG	Uricase	Selecta Biosciences	Chronic gout	Phase 2 (NCT02959918)
Sanguinate	PEG	Carboxyhemoglobin	Prolong Pharmaceuticals	Sickle cell disease	Phase 2 (NCT02411708)
Pegzilarginase	PEG	Arginase I	Aeglea BioTherapeutics	Arginase I deficiency	Phase 2 (NCT03378531)
BMS-986036	PEG	FGF21	Bristol-Myers Squibb	Nonalcoholic steatohepatitis	Phase 2 (NCT03486899)

Name	Polymer carrier	Drug	Company	Indication(s)*	Stage (ClinicalTrials.gov identifier)
NKTR-214	PEG	IL-2	Nektar Therapeutics	Solid tumors	Phase 1/2 (NCT02869295)
Olaptesed pegol	PEG	Anti-CXCL12 aptamer	NOXXON Pharma	Colorectal cancer and pancreatic cancer	Phase 1/2 (NCT03168139)
Fovista	PEG	Anti-PDGF-B aptamer	Ophthotech Corporation	Ocular von Hippel-Lindau syndrome	Phase 1/2 (NCT02859441)
BMS-986171	PEG	FGF21	Bristol-Myers Squibb	Nonalcoholic steatohepatitis	Phase 1 (NCT02538874)
NKTR-358	PEG	IL-2	Nektar Therapeutics	Autoimmune diseases	Phase 1 (NA)
NKTR-214	PEG	IL-2	Nektar Therapeutics	Solid tumors	Phase 1/2 (NCT02869295)
Zimura	PEG	Aptamer complement C5 inhibitor	Ophthotech Corporation	Neovascular age-related Macular degeneration	Phase 2 (NCT03362190)
Dapirolizumab pegol	PEG	Anti-CD40L Fab' fragment	UCB Pharma	Systemic lupus erythematosus	Phase 2 (NCT02804763)

Table 4. Polymer-protein conjugates in clinical development (continuation)

Name	Polymer carrier	Drug	Company	Indication(s)	Stage (ClinicalTrials.gov identifier)
Onzeald	PEG	Irinotecan	Nektar Therapeutics	Breast cancer	Pre-registration (NCT02915744)
PEX168	PEG	Loxenatide	Jiangsu Hansoh Pharmaceutical	Type 2 diabetes	Pre-registration (NCT02477969)
NKTR-181	PEG	μ-opioid receptor agonist	Nektar Therapeutics	Chronic low back pain and chronic noncancer pain	Phase 3 (NCT02367820)
NC-6004	PEG-bpoly(glutamic acid) micelle	Cisplatin	NanoCarrier	Pancreatic cancer	Phase 3 (NCT02043288)
Opaxio	Polyglutamic acid	Paclitaxel	CTI BioPharma	Ovarian cancer, Peritoneal cancer, and fallopian tube cancer	Phase 3 (NCT00108745)
APL-2	PEG	Cyclic peptide complement C3 inhibitor	Apellis Pharmaceuticals	Paroxysmal nocturnal hemoglobinuria	Phase 3 (NCT03500549)
CRLX101	Cyclodextrin-PEG that Selfassembles into nanoparticles	Camptothecin	BlueLink Pharmaceuticals	Ovarian cancer, peritoneal cancer, and fallopian tube cancer	Phase 2 (NCT01652079)
NK012	PEG-bpoly(glutamic acid) micelle	SN-38	Nippon Kayaku	Breast cancer	Phase 2 (NCT00951054)
OsteoDex	Dextran	Alendronate	DexTech Medical	Prostate cancer	Phase 2 (NCT02825628)
Somadex	Dextran	Somatostatin	DexTech Medical	Neuroendocrine tumors and acromegalia	Phase 2 (NA)
BP-C1	Benzo-polycarbonic Acid polymer	Platinum(II)	Meabco A/S	Breast cancer	Phase 2 (NCT02783794)

Table 5. Polymer-drug conjugates in clinical development.

Name	Polymer carrier	Drug	Company	Indication(s)	Stage (ClinicalTrials.gov identifier)
Pegcantratinib	PEG	TrkA inhibitor	Sienna Biopharmaceuticals	Pruritus	Phase 2 (NCT03322137)
NC-6300	PEG-bpoly(aspartic acid) micelle	Epirubicin	NanoCarrier	Solid tumors and soft tissue sarcoma	Phase 1/2 (NCT03168061)
CRLX301	Cyclodextrin-PEG that selfassembles Into nanoparticles	Docetaxel	BlueLink Pharmaceuticals	Solid tumors	Phase 1/2 (NCT02380677)
DEP cabazitaxel	PEGpolylysine dendrimer	Cabazitaxel	Starpharma	Solid tumors	Phase 1/2 (NA)
DEP docetaxel	PEGpolylysine dendrimer	Docetaxel	Starpharma	Solid tumors	Phase 1 (NCT02442531)
NC-4016	PEG-bpoly(glutamic acid) micelle	Oxaliplatin	NanoCarrier	Solid tumors and lymphoma	Phase 1 (NCT03168035)
RadProtect	PEG-bpoly(glutamic acid) chelating Complex micelle	Amifostine	Original BioMedicals	Acute radiation syndrome	Phase 1 (NCT02587442)
SER-214	Poly(2-ethyl-2-oxazoline)	Rotigotine	Serina Therapeutics	Parkinson's disease	Phase 1 (NCT02579473)
DFP-13318	PEG	SN-38	ProLynx	Solid tumors	Phase 1 (NCT02646852)

Table 5. Polymer- drug conjugates in clinical development (continuation)

The first polymer- drug conjugates to reach clinical trials employed copolymers of HPMA, poly-L-glutamic acid (PGA), or PEG as carriers of cytotoxic chemotherapeutic agents. PK1, the first clinically investigated water-soluble polymer-small molecule drug conjugate, comprises Dox bound to an HPMA copolymer via a lysosomally cleavable peptidyl linker [145]. Given the non-biodegradability of the HPMA copolymer, the authors chose a size of 30 kDa to ensure renal elimination. In preclinical animal models, PK1 demonstrated a 15-fold improvement in plasma half-life, an enhanced safety profile, and greater anti-tumor efficacy compared to unconjugated doxorubicin [190]. Notably, PK1 displayed 17-77x greater tumor accumulation of drug relative to free doxorubicin in these models. Furthermore, a 45-250x higher drug concentrations in tumor relative to healthy tissues suggested the relative importance of passive tumor targeting [190]. However, PK1 testing in clinical trials in the late 1990s found marginal efficacy and tumor accumulation of the conjugate in only a small subset of patients and efficacy was marginal. While PK1 displayed extended circulation time and an overall improved safety profile[191], its development was abandoned.

Given their lack of biodegradability and subsequent limitations on molecular weight, first generation conjugates of PEG and HPMA exhibit suboptimal pharmacokinetics. Hence, current research efforts focus on the evaluation of conjugates employing new biodegradable and backbone-degradable water-soluble polymers. New water-soluble, biocompatible, and biodegradable polymers, such as polycarbonates or polypeptides, are likewise being synthesized and evaluated, expanding the repertoire of polymers available for drug conjugation [192, 193]. Additionally, biologically active polymers, such as peptide molecular transporters, are being employed as drug carriers due to the added biological functionality they afford.

Molecular architecture is also emerging as an important modulator of PDC *in vivo* fate and subsequent therapeutic efficacy, with circular and branched structures generally exhibiting extended plasma half-lives and greater efficacy than their linear counterparts [194-197]. Importantly, polymer branching affords an alternative approach to the synthesis of high molecular weight conjugates without compromising the drug loading efficiency of di-end-functional polymers such as PEG. In addition to polymer molecular weight and architecture, linker chemistry modulation can achieve optimized drug release profiles and enhanced therapeutic efficacy. For example, the incorporation of hydrazone and hydrazone benzyl ester linkers promotes slow and fast drug release from HPMA-

dexamethasone constructs, respectively [198]. In an *in vivo* rat model of arthritis, the slow releasing conjugate exhibited sustained anti-inflammatory activity, leading to an improved therapeutic outcome compared to the fast releasing formulation.

The vast majority of PDCs synthesized, characterized, and evaluated throughout this Thesis have been based on polypeptides, in particular polyglutamates (PGA). We present a deep review on the rational design, key design features, physico-chemical properties, and controlled drug release in polypeptide conjugates in **Section 5.**

I.5. Polypeptide-Based Conjugates as Therapeutics

Polyamino acids (PAA or polypeptide)-based materials have gained much attention in the field of biomedicine over recent decades. [199-201] PAAs mimic natural proteins and demonstrate remarkable biocompatibility and biodegradability due to the endogenous nature of the building monomers. Development of polymerization techniques (mainly N-carboxyanhydride ring-opening polymerization (NCA-ROP)) [20] and synthetic chemistry have permitted the production of polypeptides with narrow polydispersity, minimal side product formation, high reproducibility, and precise functionalization of the polypeptide backbone. [202]

The suitability of polypeptide-based materials for drug delivery applications is also confirmed through the steady increase in the number of polypeptide-based compounds reaching preclinical studies and clinical trials. [200] In this section, we will mainly focus on polypeptide drug-conjugates and their key design features; further reading on polypeptide-based materials can be found in the literature. [200, 203, 204]

Applicability of synthetic polypeptide-based conjugate development has reached multiple areas of medicine, including the elaboration of anti-microbial, [205-207] anti-virus, [208, 209] anti-cancer, [209-215] anti-diabetic, [216] anti-apoptotic, [217] and anti-tuberculosis drugs,[218] magnetic resonance imaging (MRI) agents, [219] and theranostic agents. [36] The great advantage of polypeptides is their structural versatility which allows the generation of a myriad of architectures with differential physico-chemical features, allowing high loading rates and the possibility to conjugate drugs of different origin, polarity, and hydrophilicity. Poly-L-glutamate (P(L-Glu)), for example,

has been used for the delivery of highly lipophilic drugs (PTX, [213] 4-(N-hydroxyphenyl)retinamide, [220] camptothecin (CPT), [221] N,N-dimethylsphingosine), [222] hydrophilic drugs (dopamine), [223] peptoids, [224] metal complexes (Gd(III)-DO3A, [225] VO, [226] and Cu [227]), and nucleic acids. [228] Structural versatility of polypeptide conjugates is also exemplified by the wide range of delivery systems in which P(L-Asp), P(L-Glu), or P(L-Lys), for example, are present. [208, 229, 230]

Engineering polypeptide complexity is an accepted approach in order to mimic nature and cross many biological barriers in a target pathology. This has led to the identification of interconnected systems selected from a rather wide, complex, and diverse toolbox. Advanced polypeptide conjugates are complex systems with several structural levels and diverse architectures. Even though each conjugate is a unique system, its final physico-chemical properties comply with strictly explicit and determined trends.

Existing key design features can be described at three distinct levels: primary, selection of structural elements before the synthesis of the polymer (e.g., polymer matrix nature and architecture, linker design and responsiveness, active molecule nature); secondary, optimization of the physico-chemical properties of the synthesized conjugates (e.g., size, charge, conformation, geometry, topology); and tertiary, modulating the biological properties through fine tuning of the previous two levels in reiterative design cycles.

However, precise design of advanced polypeptide-based conjugates toward the pursued biological output remains a serious challenge due to several related points:

1. Multiple different parameters involved in the design can significantly alter the final properties of the conjugate.

2. Lack of scientific data devoted to the strategic and logical design of sophisticated polypeptide systems.

3. Lack of appropriate characterization tools and techniques to disclose the interaction of the nanocarriers with biological interfaces. [231]

4. Structural complexity and molecular mass inhomogeneity have made computer simulations of such systems highly challenging and so, only a few examples has been reported. [232] However, extensive practical work has

revealed some correlations between structure of the conjugate and its properties. [114]

Herein, we will focus on the role of structural elements (especially stimuli responsive polymer-drug linkers) and the physico-chemical parameters that determine a given system biological performance and, therefore, their successful applicability and transferability. Throughout the following sections, we will endeavor to illustrate the role of different parameters affecting the final physico-chemical properties, the responsive nature, and the biological performance of the conjugate.

I.5.1. Rational Design of Polypeptide-Based Conjugates

The rational design of polypeptide-based therapeutics for the treatment of a given pathology must be holistically driven using a step-wise design following the pathway taken by the therapeutic through the body. [233] Therefore, the administration route, the biological barriers to be crossed, and the target site of action all require scrutiny for the successful selection and design of the conjugate with selected properties. The physico-chemical parameters of the drug delivery systems determine their inherent ability to cross the required biological barriers. [234] Another important aspect to be considered for appropriate biological activity is the specific response to the different physiological environments encountered in the body. This knowledge would ensure an adequate overall stability, optimal response, and thus, delivery of the cargo in the target site of action at the desired timing. Furthermore, the administration route and the dose schedule in the target patient population are key issues for the successful translation of a drug delivery system. [235, 236]

I.5.1.1. Biological Barriers and Administration Routes

“Biological barriers” is a generalized term for a group of specific protective mechanisms present throughout the body. All the known biological barriers can be classified into five hierarchical levels (**Figure 16**).

Level 1 (absorption: reaching the bloodstream). Independent of the administration route, the first obstacle for most conjugates is the bloodstream to allow adequate body distribution and to reach the selected molecular target. Design of effective conjugates must ensure their chemical stability and integrity during blood circulation at physiological conditions (ionic strength, redox potential, pH, presence of proteases, etc.) until arrival at the desired site of action. The easiest administration strategy for a given drug conjugate is intravenous injection, which represents the most widely used route due to rapid onset and high bioavailability. For polypeptide-based therapeutics, alternative routes of administration include topical, [237, 238] oral, [239] and pulmonary, [240] delivery through different mucus barriers (buccal, nasal, vaginal, ocular, etc.), [36, 219, 240] and through direct injection to the site of disease (intraocular, intraperitoneal etc.). However, in this context, these administration routes have not yet been fully exploited.

Level 2 (circulatory barriers). In the bloodstream, the immune, reticuloendothelial (RES), and hepatic systems are the main obstacles for adequate delivery. Recognition of foreign entities is implemented by a family of proteins known as opsonins which absorb to the surface of the nanosystem and promote phagocytosis. While the exact mechanisms behind opsonization have yet to be fully delineated, certain physico-chemical and surface properties which affect the level of opsonization have been ascertained. [241, 242] Furthermore, as macromolecules, some conjugates will trigger the activation of the complement system, the innate immune response, limiting the effectiveness of the treatment besides the subsequent development of hypersensitivity reactions or allergies. [243]

Level 3 (tissue-specific barriers and tumor stroma). Some organs are provided with highly specific blood tissue barriers (blood-brain, blood-ocular, blood-retinal, blood-testis, blood-thymus and blood-air). Crossing the blood-brain barrier (BBB) using polypeptide conjugates has only recently gained much attention following the publication of the so-called “Trojan Horse” strategy. [244, 245] However, to the best of our knowledge, there is currently no reported evidence for polypeptide conjugates crossing any other of the above-mentioned barriers apart from our own recently patented work on the BBB. [245] However, solid tumors develop a deficient lymphatic drainage and an abnormal architecture of neovasculature with wide fenestration within the stroma, allowing permeation of macromolecules. In this scenario, passive targeting by the so-called enhanced permeability and retention (EPR) effect [246] has stimulated the

development of anti-cancer polypeptide conjugate therapies. [215, 247, 248] However, for future developments, it is important to take into account that the EPR effect is a rapidly evolving concept. [249]

Level 4 (cellular barriers). The passive diffusion of molecules with a molecular mass above 1 kDa is efficiently blocked by the cell membrane. Conjugates can enter the cell through endocytosis (including clathrin-mediated, caveolin-mediated and clathrin-and-caveolin-independent), phagocytosis, or macropinocytosis. [250, 251] To enhance endocytic cell internalization, different ligands can be conjugated to the surface of the polypeptides (e.g., folic acid, cholesterol, or Arginylglycylaspartic acid (RGD) based peptides). [252, 253]

Level 5 (subcellular barriers). Targeting of specific organelles (e.g., the nucleus or mitochondrion) represents the least researched area within drug delivery. Endocytic processes define the trafficking of a given agent to different subcellular vesicles or organelles. Most polypeptide-drug conjugates are designed to enter the cell by clathrin-mediated endocytosis to be actively transported to lysosomes for further degradation, a process which is advantageous for bioresponsive-drug release. [251, 254] In clathrin-mediated endocytosis, endosomal escape is the only way to ensure access of the carrier to targeted organelle. In this case, the incorporation of bioresponsive elements in the conjugate backbone or specific targeting sequences are required.

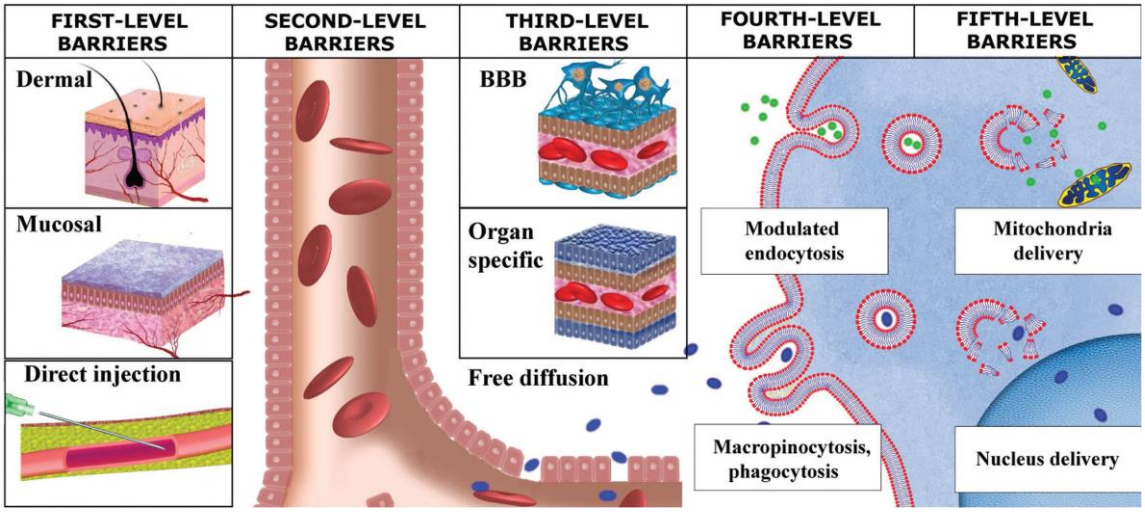

Figure 16. General representation of biological barriers present in the body. [255]

I.5.2. Key Design Features of Polypeptide Conjugates

In general, polypeptide conjugates used in drug delivery consists of four parts: the biodegradable polymer matrix, the active agent (e.g., small molecules), the linker, and targeting (and/or imaging) moieties. However, the linking and targeting moieties are not always essential conjugate design features **Figure 17.**

Conjugation of active agents to the polypeptidic carrier can have a prominent effect on the final physico-chemical properties. However, conjugates do tend to replicate the biodistribution and pharmacokinetic behavior of the original polymer matrix if no major conformational changes are induced by the conjugated drug(s) (importance of drug(s) nature and loading). [256] This topic is thoroughly discussed in section 5.3. Conversely, the polypeptide matrix itself can affect the activity of the conjugated agent, especially when functional groups determining activity are blocked or utilized for conjugation. The chemotherapeutic agent paclitaxel (PTX), for example, is connected to the polypeptide through the 2′-hydroxyl position which is essential for tubulin binding. [257] Thus, PTX conjugated to P(L-Glu) is inactive and needs to be degraded within the cell to provide its therapeutic effect. [258] Polymer conjugates of Dox, also require in-cell degradation, as the anti-tumorigenic effect requires Dox interaction with the DNA and the polymer conjugate cannot penetrate the nuclear membrane. [36] However, polymer conjugation prevents Dox-related cardiotoxic effects. [259] Nevertheless, polymer conjugation does not always alter the activity of the conjugated agent and, in some cases (e.g., phloridzin (Prz), [260] doxycycline [261]), drug activity is increased.

The versatility of PAAs is demonstrated by the diversity of developed systems to date; ranging from linear or branched homopolypeptides to block (and random) copolypeptides capable of generating hierarchically assembled nanostructures from synthesized polypeptide conjugates (e.g., micelles and core cross-linked micelles, vesicles, cross-linked networks and hydrogels). [200, 262, 263] In each case amino acid building block choice is driven by the required functionality. Additionally, ROP of NCAs renders polypeptides with conserved N-terminal ends and can be used to introduce functionalities at the C-terminal site for latter conjugation strategies. Synthetic aspects of polypeptide production are outside of the scope of this Chapter and can be found elsewhere. [202, 220, 264, 265] In the context of Polypeptide Therapeutics, amino acids can be classified from two different points of view.

(1) Functional classification: According to the chemical reactivity of the associated side chains, amino acids can be classified as functional (where side chains contain functional groups suitable for active molecule conjugation) and non-functional (where side chain modification is unpractical or inaccessible). (2) Structural classification: According to the structural or architectural properties brought to the scaffold, amino acids can be grouped as hydrophobic (e.g., Ala, Val, Leu, Ile, Phe, Tyr, Trp), α-helix forming (e.g., Leu, Phe), β-sheet forming (e.g., Ala, Val), random coil promoters (mainly ionizable side chains in their charged state), or polar (or ionizable). [266]

Although the conjugation of active agents to the polypeptide backbone does not necessarily need to occur through side-chain functionalities, most of the examples in the literature operate within this strategy. This fact is attributed to the multivalency of PAA backbones and high cargo loading attainable. There are a number of amino acids with functional side groups that have yet to be thoroughly explored for polypeptide therapeutic design, including methionine, serine, threonine, and cysteine. [267] In practice, glutamic acid, aspartic acid, and lysine are the most exploited amino acids in polypeptide conjugate synthesis.

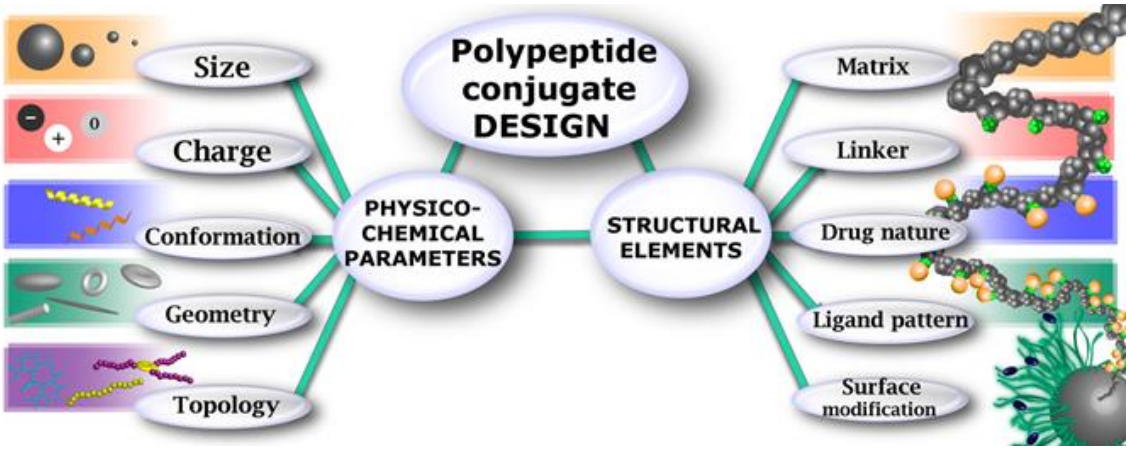

Figure 17. Schematic representation of the key design features related to structural levels and physico-chemical properties in the design of polypeptide therapeutics. [255]

I.5.3. Physico-Chemical Properties Driving the Bio-Nano Interface

Interaction of a polypeptide conjugate with the bio-nano interface is driven by a complex system of simultaneous interactions which requires the step-wise design of experimental conditions in relevant physiological environments to completely reveal the material's performance in a biological milieu. [231] Polypeptide conjugates are discussed in the following section in relation to the influence of active agent incorporation on the final physico-chemical properties and the impact on their biological output.

I.5.3.1. Effect of Size

The size of the conjugate is an important parameter that determines its fate in the bloodstream, its targeting ability, and mechanisms of cellular uptake. In the bloodstream, nanosystems smaller than 5 nm rapidly penetrate capillary fenestrae, equilibrate with the extracellular matrix, and become rapidly cleared by renal glomerular capillaries. Larger particles exhibit prolonged circulation (except in cases when clearance is guided by factors other than size), although the RES eliminates nanosystems larger than 200 nm from the circulation. Thus, the diameter of the nanosized therapeutics suitable for in vivo application should lie in the range from 5 to 200 nm. It is important to note that even in this size range, nanomedicines display non-uniform size-behavior, unique for each material. [268] This fact is often disregarded and few studies have investigated size optimization for the nanosystems.

A serious problem with passive size-dependent accumulation of nanoconstructs is similar capillary porosity in different tissues. Studies into the anti-cancer efficiency of amphiphilic block copolymer PEG-P(L-Asp)-Dox found that micelles demonstrated tissue cytotoxicity that was probably related to accumulation specificity and retention time in the specific tissue. [269, 270] As shown in **Figure 18**, the conjugate concentrated in the spleen, liver, and tumor because of the corresponding size of fenestrae (approx. 100–200 nm). Thus, highly selective tissue targeting with polypeptide conjugates (and nanomedicines in general) remains a great challenge.

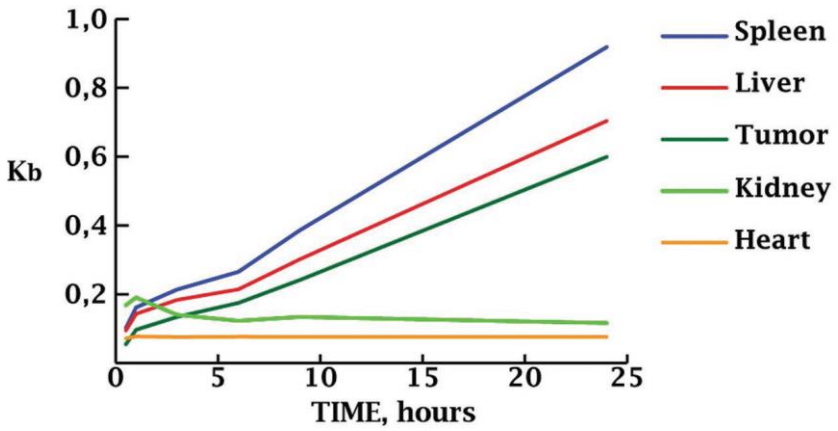

Figure 18. Tissue-to-blood concentration ratio (Kb = C_{tissue}/C_{blood}) of PEG-PAsp-Dox. Adapted from Ref [270]

Self-assembly of nanoconstructs is highly dependent on the nature of the assembling polymers and conjugated drug(s) and many different driving forces specific for each system are involved in its regulation. Self-assembly is regulated by the minimization of the interfacial energy directed by hydrophobic/hydrophilic balance, ∏–∏ stacking, dipole interactions, and hydrogen bonding among different domains. The balanced forces determine the compactness, conformation, and size of the conjugate.

Of note, many hydrophilic polypeptides and related copolymers do not aggregate in water and self-assembly of such systems is often induced by simple conjugation with a hydrophobic drug. For example, both PEG-P(L-Asp) and PEG-P(L-Glu) form nanosized systems after conjugation with Dox, while non-conjugated polymers do not aggregate in aqueous solution. [271]

When highly hydrophobic drugs are conjugated to self-assembled PAA (co)polymers, or when the content of the hydrophobic drug increases, the size of the resulting polymer-drug conjugate usually rises significantly. The size increase is in direct non-linear proportion to the drug conjugation ratio. The assessment of a series of CPT conjugated PEG_{5000}-P(L-Glu) graft-copolymers demonstrated that an increased CPT content led to an increase in final nanosystem size from 30 nm (15.2 wt% of CPT) to 65 nm (25.1 wt% of CPT). [272] Zhou *et al*. obtained similar results for a synthesized series of PEG_{45}-$P(L\text{-}Lys)_{25}$-SS-CPT*x* (*x*=3, 6, and 8), where all of the conjugates formed spherical particles with diameters of 85, 118, and 152 nm, respectively. [273] Analogous trends were observed for other hydrophobic drugs such as Dox. For PEG-P(L-Asp) copolymer conjugates with the anti-tuberculosis drugs Pyrazinamide and Isoniazid,

conjugation with Pyrazinamide (86% conjugation) resulted in the formation of micelles with an average diameter of 78.2 nm [218] while Isoniazid conjugation (65% modification) led to the formation of significantly larger micelles (266 ±27 nm). [274]

Post-synthetic modification with hydrophobic moieties through coordination bonds leads to nanosystem compaction, as was shown for many metal-containing drugs. For example, spherical nanoconjugates of γ-P(LGlu)-(citric acid)-Cisplatin (CDDP) displayed an average size of 107±6.3 nm while free γ-P(L-Glu) was larger, at 212±8.6 nm. [274] The same trend is typical for physical encapsulation of hydrophobic drugs. Some drugs have changeable effects on the size of the conjugate. Assessment of γ-P(L-Glu) series with different anti-diabetes drug Prz content, demonstrated that all conjugates formed spherical nanoconstructs with average sizes of 149±23 (P(L-Glu)-Prz-7%), 187±4.0 (P(L-Glu)-Prz-15%), and 170±19 (P(L-Glu)-Prz-25%) nm. [260] However, some drugs have a less pronounced effect on size. This includes P(L-Glu)-Dox conjugates with 15% and 30% loading, which demonstrated even less pronounced size dependence with nanosystem sizes of 6.2±1.3 nm and 7.5±0.7 nm, respectively. [261]

Molecules for active targeting are conjugated either at the polymer side-chains [241] or at the terminal ends of the polymer and only a few targeting molecules per chain are present. Nevertheless, the effect of even a low conjugation level on conjugate size can be pronounced depending on residue nature. Targeting moieties are usually hydrophilic and, in most cases, conjugation results in an increase in nanosystem size independently of the polymer matrix nature, mainly if terminal conjugation is used. For terminal end modification of PEG-poly(γ-benzyl-L-Glutamate) (PEG-P(L-Glu-Bz)) with glycyrrhetinic acid (GA), the size of the modified micelles was higher than for the non-modified copolymer (181.1 and 175.4 nm, respectively). [241] An increase in size also occurred for dendrimeric P(L-Lys) nanosystems modified with folic acid [275] or galactose [276] and for PEG-P(L-Asp) nanosystems modified with biotin. [277] In general, terminal modification resulted in a size increase from 3% to 70%.

The effect of conjugation on size when more than one drug or a drug and a targeting moiety are used is often more significant than that observed for single component conjugation, possibly due to both intra- and inter-molecular interactions. P(L-Glu) dendrimers with oligomeric silsesquioxane core with a size of 3 nm grew to 135 nm after conjugation with Dox and Biotin. The conjugated nanoassembly displayed an

unusual morphology, as each nanoassembly was an aggregate of smaller nanoobjects of 2–3 nm (the size of single dendrimers). This suggests that hydrophobic interactions within the conjugates, due to the presence of Dox molecules on the periphery of the nanosystem, drove the self-assembly process.[278] Dox and Wortmannin conjugation to PEG-P(L-Asp-hydrazide) block copolymers generated nanosystems of less than 70 nm in diameter, although when the amount of Wortmannin increased, nanoassembly size also increased gradually. The only exception was observed for micelles with a 50:50 ratio which displayed a size of 91 nm. [279] In some reports, molecular weight (*M*w), is used to explain biological performance and can affect biodistribution in a similar way to size. For tumor targeting, the EPR effect is most pronounced for agents with an *M*w above 50 kDa (either single molecule or self-assembled nanosystem). [280] For P(L-Glu)-CPT conjugates, an increase in *M*w from 33 to 50 kDa enhanced anti-tumor efficacy against B16 melanoma cancer cells without significant changes in the maximal tolerated dose. [221] Similar results were also obtained for P(L-Glu)-CDDP conjugates with different *M*w. [281]

The *M*w of the matrix is a crucial parameter for polypeptide conjugates suitable for MRI as it affects T1 relaxivity, water exchange rate, accumulation in target tissues, and rotational correlation lifetime of Gd(III) species (so far only Gd-containing polypeptide conjugates have been investigated). [282] Polymeric P(L-Glu)-diethylenetriaminepentaacetic acid (DTPA)-Gd conjugates displayed sustained signal enhancement from necrotic tissues, while oligomeric P(L-Glu)-DTPA-Gd and low *M*w conjugates showed a much shorter signal. [283] The *M*w of each conjugate also affected the speed of signal disappearance -the quicker clearance of lower *M*w conjugates resulted in quicker signal disappearance-. The 50 and 87 kDa conjugates demonstrated prolonged signal increase duration in the tumor periphery and interstitium with no significant difference when compared to each other. [284]

I.5.3.2. Effect of Charge

Nanosystem surface charge has a prominent effect on the *in vivo* fate of conjugates, determining the recognition in and clearance from the circulation, interactions with cell membranes, cellular uptake, and toxicity. Surface charge also determines the physical stability of the system and aggregation tendency after exposure to biological

media. [285] In the blood, zeta (ξ) potential determines the pharmacokinetic properties of the conjugate and the possibility of phagocytosis.

Conjugates with a positive zeta potential such as (P(L-Glu-hydrazide)-*b*-poly(*N*,*N*-dimethylaminopropylmethacrylamide))3-g-PEG-Dox (ξ=+46.3 mV) are not directly applicable in vivo, because of charge-associated toxicity, but can be transformed to negatively charged nanoconstructs by conjugation or complexation with anionic molecules (e.g., siRNA). It is generally accepted that polypeptide conjugates suitable for *in vivo* application should carry a small negative or neutral charge in order to inhibit opsonization and RES elimination.

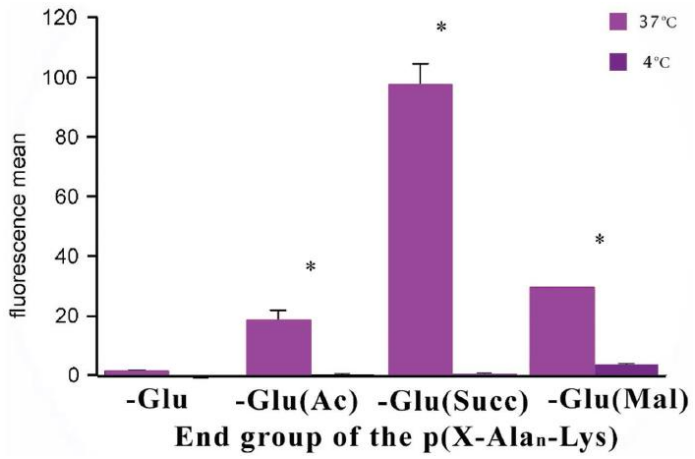

Figure 19. Effect of the terminal group of p(X-Alam-Lys) on the cellular uptake. Adapted from Ref [286]

Effect of Zeta Potential on Cellular Uptake

Nanosystem binding to the lipid cell membrane is the first step in cellular uptake and is greatly affected by nanosystem surface charge. Variations in zeta potential can be used to control binding to the cell both in vitro and *in vivo*. Cellular surface charge is usually negative due to sulfated proteoglycans (core proteins anchored in the lipid bilayer and glycosaminoglycan side chains of dermatan, keratin, or chondroitin sulfate). [287] Nanosystems with higher surface charges tend to bind strongly to the membrane, and this increases cellular uptake. However, moderate cationic polymers have shown high insertion efficiency in negatively charged films, whereas highly cationic and anionic polymer displayed reduced interaction with such monolayer films. [288] Even though cellular uptake is higher for polycations, negatively charged conjugates can also penetrate cellular membranes and are preferential for biomedical use due to lower toxicity profiles.

For anionic polypeptides, uptake is also dependent on the absolute value of the zeta potential. For a p(X-Alam-Lys) series, where X is either free, acetylated, succinylated, or maleilated Glu, polypeptides (**Figure 19**) with a larger negative charge density (Suc-Glu) displayed greater uptake by murine macrophages when compared to the less negatively charged acetylated and malariated conjugates since the C=C double bond in maleic acid residue is conjugated with C=O, and this influences the state of the terminal carboxylic group. [288]

Zeta Potential in Polymer Conjugate Design

During conjugation, the zeta potential value of the system changes according to the charge of the modifying moiety. For example, CDDP conjugates of PEG_{114}-*b*-$P(L\text{-}Glu)_{12}$ block copolymer (10% CDDP) displayed a relatively low zeta potential of −3.93±0.5 mV due to the conjugation of the carboxylate anion with platinum. [287] The drug loading influences the charge density of the nanosystem in direct non-linear proportion. For example, zeta potentials for two samples of $P(L\text{-}Glu)_{160}$-PEG_{5000} with 10% and 20% loadings of CDDP was of −17.7±1.0 mV and −8.5±1.3 mV, respectively. [281] This trend seems logical from an electrostatic point of view, although its mathematical expression is often complicated and rarely reported. In some cases, zeta potential behavior does not follow expected trends. Tsai *et al.* demonstrated unusual changes in zeta potential for γ-P(L-Glu) conjugated with Dox and galactose. When conjugated with Dox, the zeta potential of the system increased from −37 to −27 mV and after conjugation with galactose, zeta-potential slightly decreased (−32 mV). This was expected because Dox bears a slightly positive charge while the hydroxyl groups of galactose are slightly negative. However, conjugation of Dox and galactose significantly decreased the zeta potential to −75 mV with no obvious reason. [289] Thus, prediction of synergistic effect on zeta potential remains a serious challenge in the preliminary design of polypeptide conjugates. Zeta potential can also be controlled by changing the ratio of monomers of opposite charge. For a series of random P(L-Glu)-P(L-Lys) polymers by varying lysine/glutamate content it was possible to change the value of zeta potential from −30.3 to +4.9 mV. [290] Further CDDP loading increased the zeta potential of all nanosystems. For example, a study found that the zeta potentials of aggregates for three compounds (Glutamate/Lysine molar ratio of 4/1, 1.5/1, and 1/1) to be −30.3, −21.8, and −15.5 mV before and −21.0, −19.8, and −10.8 mV after CDDP conjugation, respectively.

However, each conjugate displayed different zeta potential changes at different pH. By careful manipulation of drug loading and monomer ratio, the authors managed to tune pH-dependent surface charge reversion at high level of precision. [290]

I.5.3.3. Effect of Conformation

The conformation of the polymer chain is not usually considered as a key parameter determining applicability of a conjugate as a drug delivery system. Compared to size and charge, chain conformation has minimal influence on recognition and elimination from the bloodstream. However, conformation strongly affects nanosystem stability, interaction with cellular membranes, and biological activity. [291] For example, PEG-*b*-P(L-Glu)-CDDP and PEG-*b*-P(D-Glu)-CDDP, which adopt helical conformations with different handedness, displayed no differences in biodistribution or anti-cancer activity. However, micelles with a random P(D,L-Glu) copolymer matrix, which are unable to form helical conformation, were less active and cleared faster, even though the nanosystem size was similar. The authors concluded that an α-helical structure additionally stabilized micelles and extended their bioavailability. [292] Additionally, polypeptides containing amino acids that stimulate α-helical conformation (Ala, Phe, Leu) are generally much stronger membrane disrupting agents than amino acids stimulating β-sheet conformation (Ile, Val). The conformation of polypeptides and polypeptide based conjugates is very sensitive to pH of the solution and to conjugation or, more generally, to the electrostatically equilibrated structure of the nanosystem. Upon pH change, functional groups in the amino acid residues become ionized/neutralized and polymers undergo conformational transitions. [293]

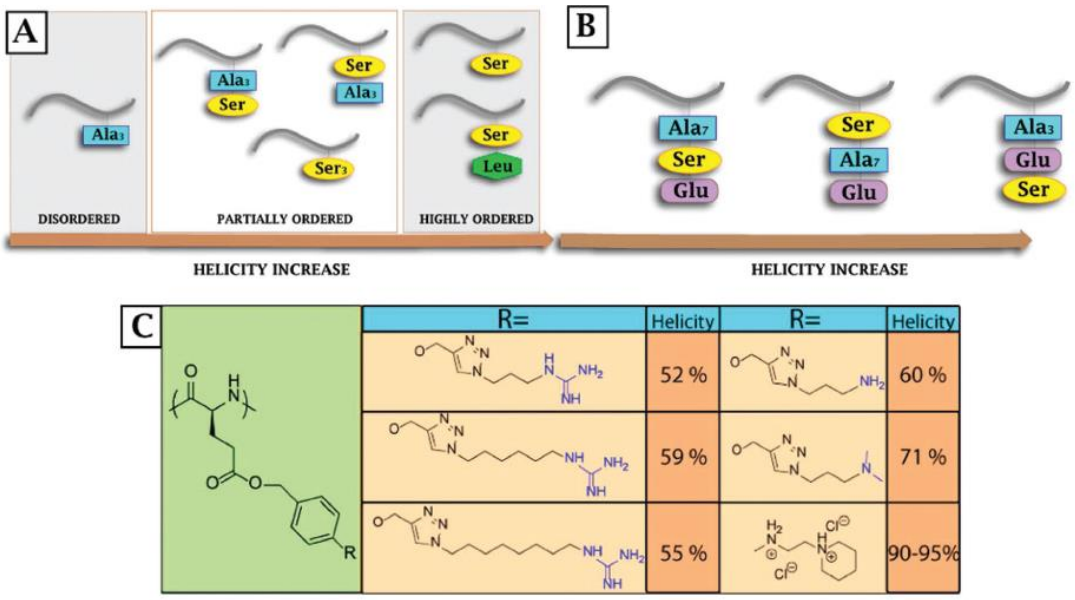

Figure 20. A, B) Effect of the terminal amino acid sequence on the helicity of the PLys adapted from Refs [125, 126]; **C)** effect of terminal group on helicity of γ-4-((2-(piperidin-1-yl)ethyl)aminomethyl)benzyl-PGA. Adapted from Ref [294] and Ref [295]

In some cases, conformation is concentration dependent. For example, PEG-P(L-Glu) complexes with polylysines at concentrations of 0.02, 0.05, and higher than 0.1 mg mL^{-1}, micelles existed as random coil, mixed, and β-sheet conformation, respectively. Most probably, PEG chains suppress the collapse of the nanosystems into a random coil due to increased surface area/volume ratio. [296]

Effect of Conjugation on Conformation

Conjugation has a complex effect on conformation because, in addition to utilizing the functional groups of the polypeptide, conjugated moieties introduce new spatial and charged elements that change the electrostatic equilibrium. Conjugated molecules can be thus classified as stabilizing or destabilizing. Serine, for example, has a tendency to stabilize ordered structures (either α-helix or β-sheet) as was shown for a series of branched P(L-Lys). The incorporation of terminal Ser and Leu in the side-chains of branched P(L-Lys) led to the acquisition of a more ordered (α-helical) conformation in comparison with Ala (**Figure 20**). [297] Glutamate replacement of leucine in P[L-Lys($Leu_{1.0}$-$Ser_{0.9}$-$DLAla_{7.0}$)] changed the tendency to form helical structure, with a dependence on the amino acid position in the sequence as shown in the **Figure 21**. Under

acidic conditions glutamate-containing polymers tended to stabilize or destabilize helical structures depending on the surroundings.

Under appropriate conditions, polymers with both serine and glutamate formed β-sheet structures. [298] Conjugated moieties allows stabilization of the conjugate conformation in the organism that is especially important for polypeptides with a narrow pH range of conformational stability such as P(L-Glu) that tends to form α-helix at pH=4.5. Conjugation with the hydrophilic anti-cancer agent D-penicillamine stabilized the helix conformation even in a completely water soluble state at pH 7.4 (normal pH of blood plasma). [299, 300] The secondary structure of P(L-Glu) can also be stabilized as a helix when functionalized with amine/guanidine as shown in **Figure 20**. [294] Remarkably, one study achieved stable helicity of up to 90%–95% following α-4-((2-(piperidin-1-yl)ethyl) aminomethyl)benzyl incorporation into the P(L-Glu) structure. Interestingly, the helical structure remained even after around 40% addition of the other functionalized moieties. [295] Many active agents have minimal effect on conformation change after conjugation and nanosystem can display behavior similar to a non-modified polypeptide. An illustrative example of such systems is P(L-Glu)-Dox which is negatively charged at pH 7.6 and displays a random coil conformation. At acidic pHs, the charge is neutralized and the conjugate adopts an α-helical conformation, similar to that observed for control P(L-Glu). [301] However, upon Dox conjugation, such conformational change occurs at slightly less acidic environments (pH 5.7 *vs.* 4.5 for P(L-Glu)-Dox and P(L-Glu), respectively).

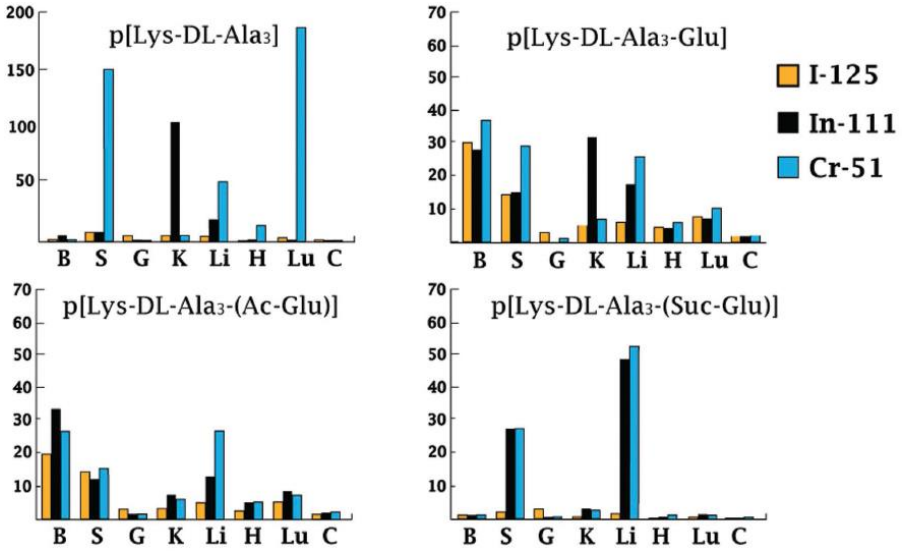

Figure 21. Effect of the terminal group and radioisotope nature on biodistribution. Adapted from Ref. [256]

When a conjugated drug destabilizes secondary structure, additional moieties may be incorporated in order to achieve the necessary conformation. Methotrexate (MTX), for example, has a tendency to destabilize the secondary structure of P(Lys-DL-Ala*x*) but the conjugate can be further stabilized with helix-stabilizing amino acids (such as Leu) or destabilized with Glu. [297] The study also found that the incorporation of D-amino acids into polypeptide polymers with L-chirality mediates the destabilization of secondary structure. Even small changes to a polypeptide backbone can destabilize polymer conjugate conformation. For example, polycysteine molecules modified with galactose or glucose adopt a predominantly α-helical conformation. The oxidation of the thiol group to sulfone destabilized the α-helix and causes a transition to a disordered conformation, perhaps due to the strong interaction of sulfone groups with water molecules. This results in the disruption of peptide hydrophobic packing and the increase of steric crowding that consequently results in the destabilization of the helix. Interestingly, separation of the thioester group by an additional methylene group led the conjugate to retain an α-helical conformation even after oxidation to sulfone. [302] Chain topology also influences the amount of secondary structure defects. For example, linear and 3-arm star P(γ-carbobenzyloxy-L-Lys) and P(L-Glu-Bz) both displayed an α-helix conformation. However, smaller star-copolymers displayed smaller helix persistence length which may affect the binding sites. [303] Due to increased steric effects and charge repulsion, the helicity of star copolypeptides is usually lower than that of linear analogues. [304]

I.5.3.4. Effect of Geometry

While geometry is an important characteristic to consider during nanomedicine design, there have been few extensive studies on this topic until recent times. However, it is now evident that many nanoconjugate properties, including transport, degradation and release profile, are shape-dependent. [305] Conjugate diameter affects nanosystem velocity, diffusion, and adhesion to the blood vessels, airways, and intestine. However, shape has more complex effect on these characteristics because non-spherical nanosystems demonstrate flow-dependent alignment. Shape can also affect the targeting ability, as local curvature affects ligand and opsonin adsorption and the degree to which nanosystems fit to the contours of cellular membrane. Conjugate shape changes may lead to increased cell attachment, resistivity to detachment, as well as increased cell

internalization. However, nanodisks, as compared to nanospheres, have a tendency to localize within phospholipid bilayers, but not to penetrate the membrane. [306] Shape may even be the main driving attribute in some biological scenarios. [307] Several studies have demonstrated that shape, and in particular local particle shape, and not size, has a dominant influence on phagocytosis when alveolar macrophages where exposed to non-spherical particles of different sizes and shapes. [305] This was due to the influence of local shape on macrophage actin structure [308-310] and is an important issue to take into account in the rational design of a given immunotherapy.

Geometry of Conjugates

It has been long understood in polymer chemistry that altering synthetic conditions can generate polypeptidebased polymers with multiple different morphologies. [311] However, there are only a few reports on polypeptide conjugates with a shape other than spherical. Many researchers have synthesized conjugates with ellipsoidal geometry based on P(L-Glu-Bz). This includes the synthesis of nanosystems with ellipsoidal morphology from different γ-P(L-Glu-Bz)-PEG-60 and γ-P(L-Glu-Bz)-Bz-50 copolymers in different ratios. [312] The formation of such mixed nanosystems occurs without conformation change of the initial polymer molecules, as shown for γ-P(L-Glu-Bz)-Bz-50 and P(L-Glu-Bz)-β-CD-50 (cyclodextrin). Both polymers remained in an α-helical conformation before and after nanosystem formation. For P(L-Glu-Bz)-P(L-Glu) conjugates with CDDP, the polymer and the conjugate adopted ellipsoidal shapes (aspect ratio of 1.3, 37±7 nm x 27±6 nm) with a hydrodynamic diameter of 49–58 nm. The authors observed no significant changes in the morphology with CDDP loading up to 8.3%. [313] However, terminal modifications with small targeting molecules do not affect the shape of polymer nanoassemblies. When comparing P(L-Glu-Bz) with benzyl, MeO-PEG, or PEG-biotin as a terminal groups or with benzyl and fluorescein isothiocyanate (FITC isomer I) as terminal groups, nanosystem morphology was dependent on polymer nature. Constructs containing PEG formed spherical species while other nanosystems displayed an ellipsoidal morphology. [312] Finally, one recent study found that P(L-Glu)-Dox conjugates formed fibril aggregates of approximately 40 nm in diameter and two to tens of micrometres in length. [301]

I.5.3.5. Effect of Composition

Influence of Stereoisomery

Stereoisomery of amino acids affects the conformation, biodegradability, and activity of conjugates on the cellular level. For branched P[L-Lys-DL-Ala-X-cAD] (cAD = cisaconityl daunomycin), conjugates with D- and L-Leu had similar cytotoxicity, while conjugates with D-Glu were seven times less toxic and conjugates with L-Glu were four times more toxic than Leu-containing nanosystems. Stereochemically controlled toxicity is thus dependent on amino acid type and is specific for each system. [314] For corresponding MTX conjugates, replacement of L-Leu and L-Glu with D-analogues produced a four to five fold decrease in activity. Polypeptides conjugated with D-amino acid sequences behave identically to the L-analogues due to identical physico-chemical properties (except conformation handedness). Poly-D-amino acids, however, are not in-cell degradable as was shown for P(L-Glu) and P(D-Glu) conjugates with the NIR-813 fluorescent dye. [315] Another study found no differences in P(L-Glu)-DTPA-Gd using D- or L-PGlu, indicating that affinity to necrotic tissues is not mediated by specific processes whether an enzymatic or a receptor-mediated transport mechanism is taking place. [283]

Effect of Active Agent Characteristics

The biodistribution of micelles is considerably more affected by size, charge, and surface properties than by the nature of the drug to be delivered, as the drug is usually concentrated in the core. [297] However, upon conjugation, the nature of the drug can determine chain topology leading to different biodistribution and pharmacokinetics when compared to the non-modified polypeptide. One interesting study constructed a series of conjugated radioactive metals (125I, 51Cr and 111In) and branched P(L-Lys) with short side chains of $(DL\text{-}Ala)_3$, amphoteric $(DL\text{-}Ala)_3$-Glu, polyanionic $(DL\text{-}Ala)_3$-(Ac-Glu), and highly polyanionic $(DL\text{-}Ala)_3$-(Suc-Glu). Similar elution profiles suggested structural similarity of the conjugates independent of the radiolabel used. Interestingly, polymers labeled with different metals demonstrated similar blood levels but different organ distribution as shown on **Figure 21**. [316] Unfortunately, the reason for these differences in behavior remains undetermined. Despite the fact that radiometals are retained at a

higher level at the clearance sites of the matrix polypeptide, the degree of retention depended on both the nature of the polymer and the radiometal used. [316] This study revealed another challenging problem for polypeptide conjugate design, namely understanding how the nature of the drug affects biodistribution of the whole conjugate. A further study assessed two other conjugates: P[LLys-Ala-Suc-Glu]-Dau with and without terminally conjugated 5(6)-carboxyfluorescein. Remarkably, the conjugate with Dau and 5(6)-carboxyfluorescein was more effective than the Dau conjugate, suggesting that even negligible modification (one to two molecules per conjugate) can play a crucial role in cellular uptake. [314] In the case of the previously discussed γ-P(L-Glu)-Prz conjugates, the polymer matrix did not interfere with the activity of the drug or its binding to the Prz target, the SGLT1 sodium-glucose linked transporter. [239, 260]

Effect of Topology

Although scarcely reported, conjugate topology can affect conjugate cellular uptake. In a recent study, star-shape polyglutamates St-P(L-Glu) were directly compared with their linear analogues P(L-Glu) with regards to cell trafficking as well as in vivo biodistribution and pharmacokinetics. [317] Importantly, a 3-fold cell uptake enhancement for the St-P(L-Glu) was demonstrated when compared to a linear counterpart. Both polyglutamates showed similar biodistribution profiles with renal excretion and no specific accumulation in any organ. However, the star-shaped polymer displayed longer retention times and greater distribution volume. [317] Investigations into the cytotoxicity of synthesized poly(γ-4-((2-(piperidin-1-yl)ethyl)aminomethyl) benzyl-L-glutamate) (P(PA-L-Glu-Bz))-containing polymers demonstrated the highest FITC uptake for star copolymer 8-arm PEG_{113}-*b*-$P(PA\text{-}L\text{-}Glu\text{-}Bz)_{91}$ and the lowest for a graft-copolymer. These findings correlated to the capability of the polypeptide to trigger membrane pore formation and suggests that the cytotoxicity of polymer/DNA complexes is cell-dependent and signifies that topology of the polymer affects cytotoxicity.

I.5.3.6. Effect of the Linker

In drug design, the scrutiny of the linker role is rarely extended above the cleavage mechanism and stimuli responsibility for controlled release applications. Nevertheless, in addition to its direct function, the linker influences physico-chemical parameters, toxicity,

drug loading, and conjugate solubility. For example, incorporation of glutamyl linkers into the P(L-Glu)-PTX conjugate to yield poly(L-γ-glutamyl-glutamine)-paclitaxel nanoconjugate (PGG-PTX) drastically increased conjugate water solubility and showed a better therapeutic index in preclinical models. Maximum tolerated dose for PGG-PTX versus P(LGlu)-PTX was found to be 350 versus 160 mg PTX kg^{-1}, respectively.

For P(L-Lys citramide) conjugates with Norfloxacin, studies demonstrated spacer-dependent effects on aggregation behavior. Of the three linking strategies used (lysine linker, carbamate linkers, or direct linking to polymer), conjugates with the lysine linker tended to form aggregates. This may be due to electrostatic interactions between the residual primary amine group and the carboxyl groups present as pendent groups along the polymer chain or covalent amide bonds between amine and carboxylic acid groups. The carbamate space did not lead to detectable levels of aggregation. [316]

Linkers also affect the hydrodynamic radius and zeta potential of the nanosystems. An increase in the number of carbons in the acid motif of the backbone results in a decrease in the hydrodynamic radius and an increase in zeta-potential in the following order Ami >Asp >Glu. [318] The structure of the linker can also affect conjugate cytotoxicity. When analyzed using the MCF-7 breast cancer cell line, PEG45-P(L-Lys), PEG_{45}-$P(L\text{-}Lys)_{25}$-CPT_6, and PEG_{45}-$P(L\text{-}Lys)_{25}$-SS-CPT_6 (additionally incorporated disulfide bond) displayed IC_{50} values of 500.0, 6.8, and 0.88 μg mL−1, respectively. In general, conjugates were more active against OVCAR-3 cell line and less active against MCF-7, SKOV-3, and MDA-MB-468 cells when compared with free CPT. [273] Additionally, a γ-P(D-Glu)-vancomycin (Van) conjugate demonstrated linker-dependent anti-bacterial behavior. P(D-Glu)-Van, P(D-Glu)-*N*-succinylethane 1.2-diamine-Van, and free Van displayed an anti-bacterial activity against *Bacillus subtilis* equal to an 8, 9, and 14 mm zone of inhibition at 1 mg mL^{-1}, respectively, using a filter disk assay. Similar results were obtained against Van-resistant strains of *Lactobacillus casei* with inhibition area of 5 and 3 mm for conjugated and free Van, respectively. [319]

I.5.3.7. Effect of Ligand Patterning

Simultaneous binding to multiple ligands often occurs in biological systems. The application of polyvalent interactions may be beneficial in drug delivery system design

as it allows strong binding from low surface area ligands, increased binding specificity, the creation of conformational contact between large biological surfaces, macroscopic reorganization, and redistribution of molecules. [320] Typical drug conjugate design includes the synthesis of constructs with random surface distribution of ligands that limit or completely restrict manipulations on ligand grouping, cluster size, and spacing. Even though many studies devoted to ligand patterning of small olygolysine with mannose and diglycoside clusters have been published, [321, 322] this topic remains scarcely investigated for polypeptide conjugates. Optimal cluster arrangement results in better targeting properties due to longer binding time on the cell surface and binding of more conjugates, all of which increase the probability of endocytosis. In cells overexpressing folate receptors, these receptors exist in the membrane as clusters of three or more molecules. Quite recently, Poon *et al*. prepared mixed micelles from nonfunctionalized and functionalized linear dendritic polymer (P(L-Asp)-Bz)$_{12}$-PED (polyester Dendron)-PEG$_{600}$-FAx, where x = 1–16 with 0%–100% folate functionalization providing micelles with different cluster arrangement. Maximum activity corresponded to the 20%F-60% mix micelles (**Figure 22**). The binding energy increased with an increase in folate modification, from 10% to 40% (1.5 = 0.4 to 6.9 = 0.9 folates/Dendron) and then starts to decrease due to steric binding interference due to an excess of ligands clustered in a small binding area. [323] Another study demonstrated that P(L-Lys)-catechin conjugates displayed significant enhancement of concentration-dependent inhibition against collagenase from *Clostridium histolyticum* (ChC) compared to free catechin. This may occur due to efficient multivalent interactions between collagenase and catechin from P(L-Lys)-catechin. Catechin conjugates also inhibit hyaluronidase in contrast with non-conjugated catechin. [324]

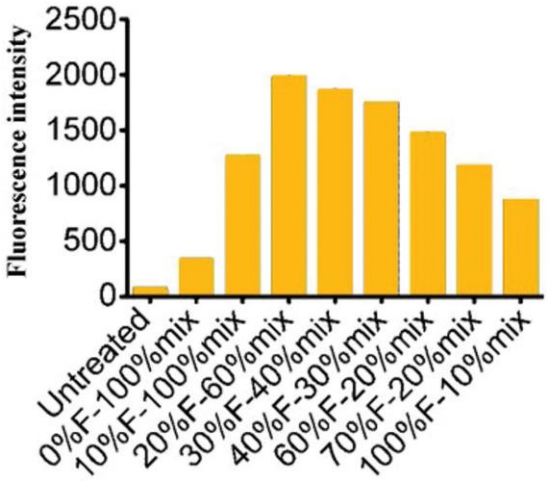

Figure 22. Effect of ligand pattern on the cellular uptake obtained by usage of polymer mixtures. Reprinted with permission from Ref [323].

I.5.4. Stimuli-Triggered Drug Release

Smart stimuli responsive materials have greatly evolved over the last few decades. The potential for molecular programming of nanomaterials to respond to small changes in the environment has led to the synthesis of materials in different fields including materials science [325] and biomedicine. [262] The human body represents a multitude of intrinsic microenvironments appropriate for the spatio-temporal control of drug release. A multitude of systems have so far been described which have the ability to deliver a cargo or to activate the therapeutic effect, in response to an endogenous environmental factor [326] (e.g., pH, redox potential, enzyme availability, or reactive oxygen species) or external stimuli (e.g., magnetic field, temperature, light). [262] Relevant examples of polypeptide conjugates described so far as drug delivery vehicles with inbuilt endogenously stimulated triggered release mechanisms are discussed within this section. [262, 326, 327]

I.5.4.1. pH-Responsive Drug Release

pH in Relevant Physiological Environments

pH-responsive macromolecules are developed taking into account the pH gradients experienced depending on their pharmacokinetics and pharmacodynamics

following the route of administration and arriving to the site of action. In addition, their design should also consider the differential physiological pH environments comparing normal against pathological conditions. The design of active nanosystems responding to pH changes at the tissue level plays a special role for the treatment of solid tumors (and inflammation related pathologies) [328] where many regions are transiently or chronically acidic, playing an important role in tumor progression and metastasis, and therefore highlighting the need of non-invasive techniques for in vivo imaging and measurement of pH. [327, 329] At the cellular level, a mildly acidic pH gradient is encountered following endocytic uptake pathway. [250, 251]

Polypeptide-Based pH-Responsive Drug Release Systems

Considering that the vast majority of amino acids employed to design polypeptide conjugates are limited to Glu, Asp, and Lys, the chemical toolbox for pH-responsive systems for direct drug conjugation to polypeptide backbone employed up to date is reduced to compatible chemistries with amines and carboxylic acids (e.g., esters, carbamates). However, rationally designed linkers offer the opportunity to expand the toolbox to different pH-labile groups such as hydrazone, acetal, cis-acotinyl, Schiff-base or α-thiopropionate among others, which have all been introduced into pH-responsive polymer–drug conjugates to date. [330]

Pioneering the development of amphiphilic block copolypeptide-drug conjugate micelles, Prof. Kataoka designed a series of PEG-P(L-Asp) block copolymer drug conjugates with the ability to assemble into micelles after conjugation to anthracycline derivatives through pH labile hydrazine bonds (Dox and Epirubicin (Epi)). [270, 332] In one remarkable example, Bae *et al*. modified the surface of PEG-P(L-Asp-hyd-Dox) block copolymer micelles, with an already proven outstanding pH-control on drug release profile (**Figure 23A**), [270] with piloting residues of folate for cancer cell-targeting. In vitro evaluation in human pharyngeal cancer cells proved the advantage of active targeting and an outstanding control of the release profile as a function of pH. [270] Of note, the NC-6300 system, which relies on a similar design, but incorporating Epi without active targeting residues, displayed an improved anti-tumor activity against hepatocellular carcinoma compared to the native Epi with significantly reduced

cardiotoxicity. [212] Further proof-of-concept studies also validated NC-6300 against triple negative breast and liver tumors [332] and so granted the enrolment of this candidate into phase I clinical trials for advanced or metastatic tumors. Phase I trials are currently ongoing in Japan with NC-6300. [230] Modulation of the pH-lability, and as a consequence, the responsiveness to pH, depends on the bond's chemical environment.

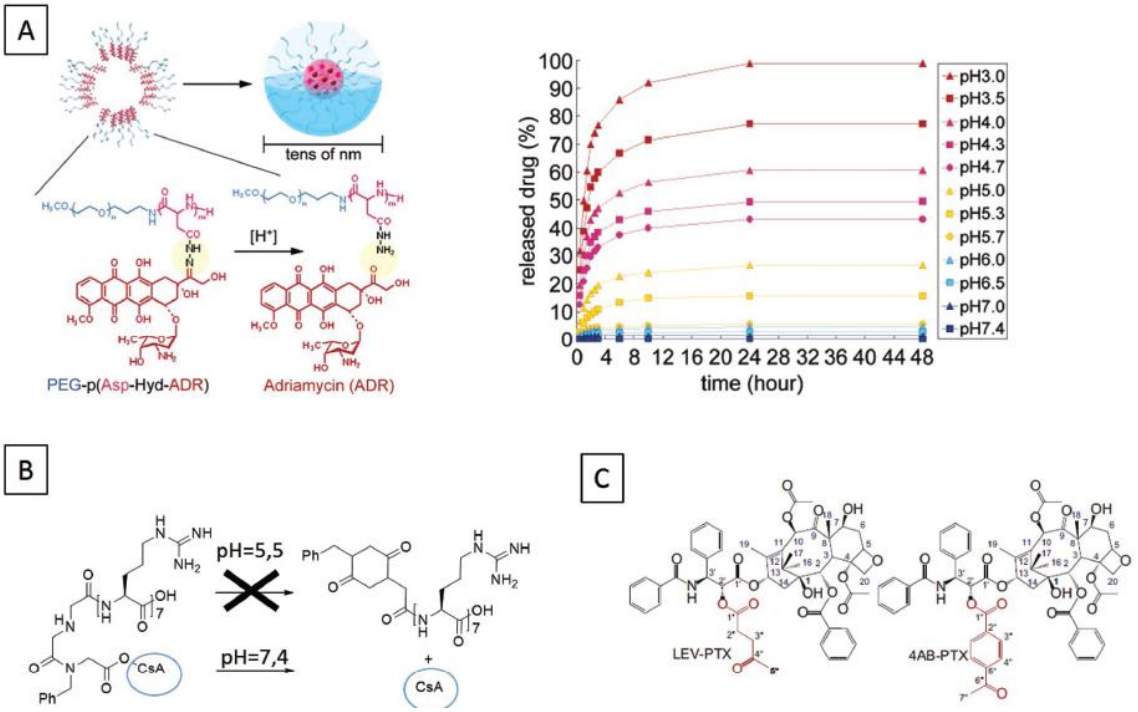

Figure 23. A) Schematic representation of PEG-P(L-Asp-hyd-Dox) block copolymer micelles showing the chemical structure and drug release profile. Reprinted with permission from Ref [270]. **B)** Chemical structures of PEG-p(Asp-Hyd-LEV-PTX) and PEG-p(Asp-Hyd-4AB-PTX), adapted from Ref [331]; C) Chemical structure of P(L-Arg-CsA) conjugated through a pH-responsive self-immolative linker adapted from Ref [237].

Following this approach, different PTX prodrugs with modulated release characteristics have been recently published by Alani *et al*. (**Figure 23B**). [331] They synthesized two micelle-forming conjugates of PTX: PEG-p(Asp-Hyd-LEV-PTX) and PEG-p(Asp-Hyd-4AB-PTX) using two different modifications of the drug. In one, the hydrazone moiety is modulated through the use of alkylic (LEV), while the other uses aromatic (4AB) ketones. Micelles displayed a notable release rate of LEV-PTX under acidic pH, although they observed no 4AB-PTX release after 24 h. The authors took advantage of such behavior to modulate the release profile of LEV-PTX by co-assembling mixed micelles of PEG-p(Asp-Hyd-4AB-PTX) and PEGp(Asp-Hyd-LEV-PTX), so

illustrating an alternative pharmacokinetictuning solution for PTX-prodrug strategies. Satchi-Fainaro and co-workers recently reported a polyglutamate-based combination conjugate bearing Dox through a hydrazone linker (EMCH) and PTX through direct conjugation (ester bond) as drugs in a synergistic ratio. The combination conjugate was highly effective in inhibiting the growth of mammary tumors compared to a combination of free drugs and drugs conjugated to polymers separately. [333] In an additional study, a comparative evaluation of linear P(L-Glu) vs. dendritic PEG-Polyglycerol bearing the abovementioned combination therapy revealed that activity against mammary tumors for the combination P(L-Glu) conjugate was superior to the dendritic polymer carrier which showed no differences in activity compared to the combination of drugs conjugated to the dendrimer separately. [333]

Aside from hydrazone as a pH-labile linker, other chemical entities such as cis-aconityl moiety have been incorporated into polypeptidic carriers such as P(D-Lys). Shen and Ryser prepared the first model of pH-sensitive linkage for Dau release from a lysosomotropic P(D-Lys) conjugate. [334] In spite of a lack of polypeptidic carriers designed for topical administration, Rothbard *et al*. have very elegantly conjugated the immunosuppressor drug cyclosporine A (CsA) to P(L-Arg) oligomers through a pH-labile linker for use in the topical delivery in inflammatory skin diseases. [237] In contrast with the typical release upon acidification, this self-immolative linker (**Figure 22C**) is stable under acidic pH (skin barrier) and takes advantage of an intramolecular nucleophilic attack of the secondary amine in the neighboring carbonyl group. This is enabled at neutral pH through the deprotonation of the amine. They proved how, in contrast to free CsA which cannot penetrate the skin, R7-CsA could reach dermal T lymphocytes and inhibit cutaneous inflammation in mouse.

I.5.4.2. Redox Responsive Drug Release

Redox Characteristics of Relevant Physiological Environments

In general, redox microenvironments at different extracellular and intracellular regions are caused by the presence of reducing/oxidizing agents, as well as redox proteins, providing an opportunity for the controlled delivery of different active agents. At the extracellular level, cysteine and cystine constitute the major source of thiol/disulfide pairs

in mammalian plasma (8×10^{-3} M). This is one of the main redox control nodes for protein signaling that, together with glutathione (GSH) marginal levels (2×10^{-6} M), represents the main pathways for disulfide bond reduction in a mildly oxidizing extracellular environment. [335, 336] Although systemic circulation of polymeric vehicles are thought to progress under relative oxidizing environment, the above mentioned conditions might promote the inactivation of disulfide-based drug delivery systems with prolonged blood half-life. [337] The intracellular environment, in contrast, provides a highly reductive environment, mediated by the action of multiple proteins (e.g., thioredoxin, glutaredoxin, protein disulfide isomerase) and small reductant molecules, mainly represented by GSH. [232] Noticeably, the redox environment in endosomes has been reported to be mildly oxidizing when compared to other organelles and cellular environments, suggesting the need for late lysosomal digestion or escape from endosomes in order to efficiently deliver the cargo for reductive dependent strategies. [335] In addition, the tumor microenvironment has been reported to be a highly reductive environment and so represents an attractive target for the development of redox-responsive anti-cancer nanomedicines. [338]

Polypeptide-Based Redox-Triggered Drug Release Systems

Several examples of different redox-sensitive linkers for targeted controlled drug delivery are present in the literature, [339] but the field is dominated by the employment of disulfide bonds. The fact that disulfide-containing carriers can take advantage of the large intra/extracellular redox gradient, renders them very attractive for the design of drug and gene-delivery systems.

In the context of polypeptidic conjugates, an interesting study based on P(D-Lys) structures has been developed by Shen and co-workers. They have conjugated MTX to P(D-Lys) using two different types of spacers and have evaluated its cytotoxic activity in Chinese Hamster Ovary (CHO) cells. [334] In the P(D-Lys)-SS-MTX conjugate, MTX was conjugated to the polymer using a disulfide spacer as a probe to study the reducing cytoplasmic environment. The fact that disulfide reduction did not demonstrate any dependence on GSH led the authors to hypothesize that the conjugate experienced an enzymatic degradation in a prelysosomal compartment. Based on these studies, Feener *et*

al, synthesized an analogue conjugate in which [125I]iodotyramine, instead of MTX, was again linked to P(D-Lys) through a disulfide linker.[340] The resultant P(D-Lys)-SS-[125I]tyn conjugate was used as a probe to detect disulfide cleavage in the endocytic pathway. Several analyses of subcellular fractionations allowed the authors to hypothesize that instead of the cytosol, as would be expected, the redox environment of the Golgi apparatus was the most probable place of disulfide cleavage. Using a different approach, Zhou and collaborators recently designed a complex redox-responsive high drug-loaded, tumor targeted nanosystem. [273] This nanoconstruct is based on PEG-P(L-Lys) in which the folate is covalently attached to P(L-Lys) amines through the PEG moiety. The system was FITC-labeled and conjugated CPT to the amine groups of block-PLys via disulfide bonds.

Carrying all these different moieties, the CPT-conjugate formed stable nanoparticulate systems in the bloodstream with uniform sizes and experienced enhanced accumulation and both passive and active tumor uptake. These self-assembled conjugates could also be loaded with a secondary active agent (Dox) physically encapsulated inside the core. Following FA-receptor mediated endocytosis, the conjugate was disassembled in the reductive environment of the cytosol via the cleavage of the disulfide linkers releasing CPT and Dox and leading to excellent in vitro anti-tumor activity in various cancer cell lines.

Looking for efficient gene silencing, Takemoto *et al*. grafted siRNA to the side chains of a PAsp (PAsp-SS-siRNA) polymer through disulfide bonding. [341] This released conjugated siRNA into the cytosolic milieu due to the reductive conditions. Subsequent P(Asp-SS-siRNA) complexation with a poly-L-aspartamide containing 1,2-diaminoethane side chains aimed to enhance biodegradability. Using this strategy, they achieved strong target-specific gene silencing in vitro employing the mouse melanoma B16F10-Luc cell line. Another interesting example is the polymer-protein conjugate based on P(L-Glu) reported by Talelli and Vicent (**Figure 24A**). [342, 343] In this system, P(L-Glu) is covalently bounded to lysozyme, used as a model protein, through disulfide bonds and was used for the design of a reduction sensitive PUMPT (Polymer Masked− Unmasked Protein Therapy) system. The P(L-Glu) cover protected and masked the protein efficiently, but disulfide reduction and therefore protein unmasking, restored lysozyme activity. Very recently, this strategy has been validated via the use of a PEG-P(L-Glu) block copolymer for the intraperoxisomal delivery of engineered human

alanine:glyoxylate aminotransferase liver peroxisomal enzyme. [342] This can be used to treat primary hyperoxaluria type I, a rare genetic disease characterized by an abnormally high concentration of urinary oxalate that can progress to end-stage-renaldisease and to a potentially fatal condition called systemic oxalosis. The self-immolative disulfide carbonate (and carbamate) represents another interesting linker for polypeptide conjugate design (**Figure 24B**). [344] This linker has been employed for the development of a luciferin-releasable system based on a cell penetrating motif, octaarginine. The study conjugated this probe system through the selfimmolative disulfide carbonate linker designed for quantification of carrier uptake. Following disulfide cleavage, intramolecular nucleophilic attack of thiol on carbonyl atom at the intermediate specie yields a cyclic product releasing the native probe; a very interesting approach to consider for future designs.

I.5.4.3. Enzyme Responsive Release

Enzymes have long been identified as powerful biological targets for site-specific design of drug delivery systems. [345] Many disorders are associated with an enzyme imbalance, mainly overexpression of proteases, including cancer [346] or inflammatory diseases, amongst many notable others. For example, following polypeptide conjugates pathway throughout the body, extracellular proteases such as matrix metalloproteases (MMPs) play an important role in the degradation of extracellular matrix components and cell membrane proteins and are overexpressed in damaged tissues. [347, 348] Intracellularly, cathepsins represent the major family of proteases involved in the degradation and turnover of intracellular proteins. Due to their higher activity under acidic pH, endosomal and lysosomal locations are particularly relevant for triggering polypeptide conjugates degradation. [349] Therefore, proteases have constituted a powerful alternative for the design of specific stimuli responsive polypeptide conjugates and their use as a trigger for drug delivery relies on their ability to promote polypeptide matrix degradation and hence facilitation of drug release in a site-specific manner.

The anti-cancer polypeptide-drug P(L-Glu)-PTX (Opaxio) in Phase III clinical trials represents one of the best examples in this class as, although PTX is covalently bound through an ester bond, its 37 wt% loading makes its release highly depending on cathepsin B levels. [213] A correlation between estrogen levels and cathepsin B activity has now been reported [149] and therefore only patients with baseline estradiol levels >25

pg mL−1 would benefit from this conjugate.[350] P(L-Glu)-CPT is another example of a P(L-Glu)-drug conjugate to reach Phase I clinical trials for ovarian and colorectal carcinomas. [351] CPT was also conjugated via an ester bond but in this case through a Gly linker in order to stabilize the CPT lactone ring.

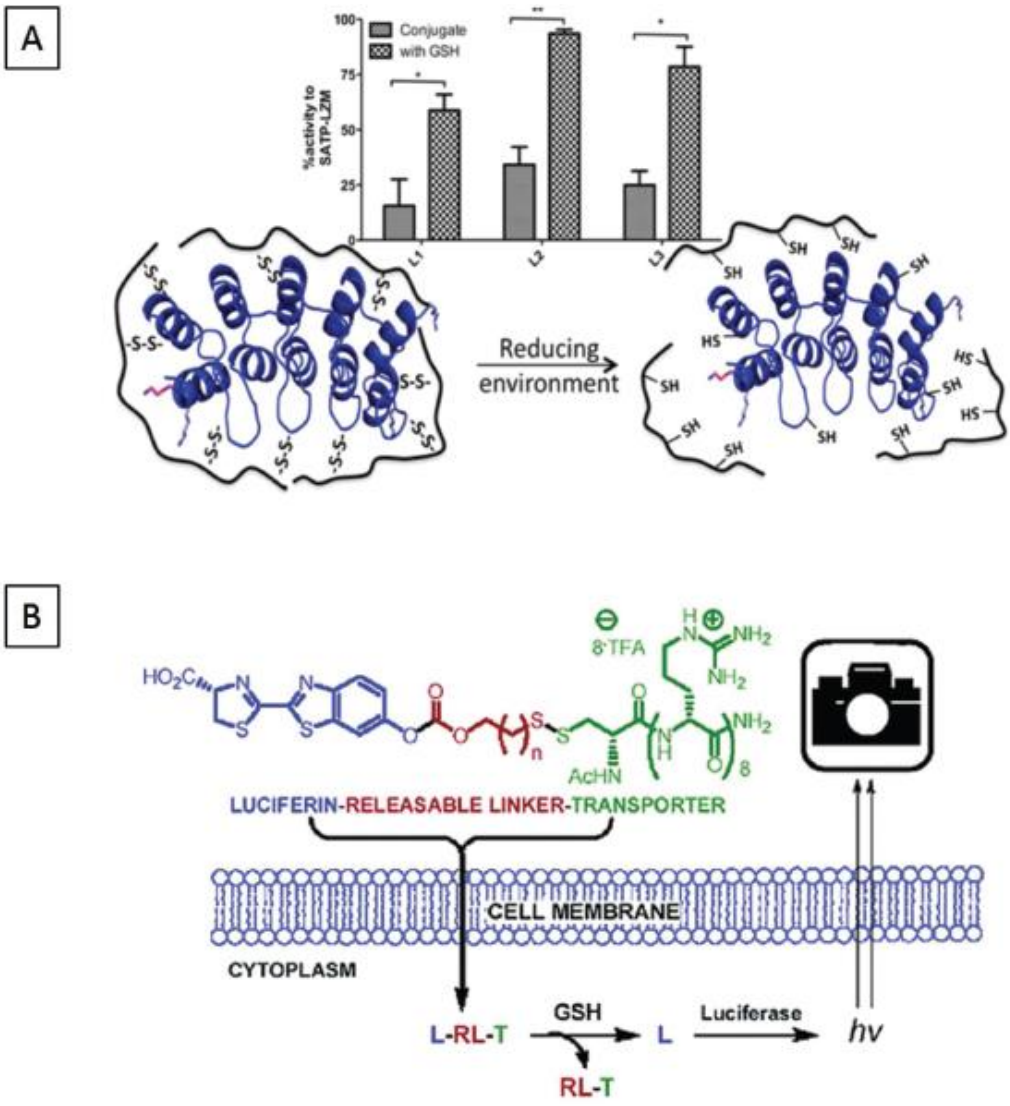

Figure 24. A) Schematic representation of the PUMPT strategy developed with P(L-Glu)-lysozyme polypeptide-protein conjugate sensitive to intracellular GSH levels. Reprinted with permission from Ref [343] **B)** Chemical structure and representation of the Luciferin releasable probe conjugated through a self-immolative disulfide-carbonate. Reprinted with permission from Ref [344].

I.5.5. Perspectives and Outlook

The physico-chemical parameters of the conjugate, and hence the biological performance, are defined by an intricate interplay of multiple structural factors. This

highlights the need for detailed structure-activity relationship studies to develop the hierarchical strategies of polypeptide conjugate design. However, structural complexity also represents a unique opportunity, since small changes at the structural level might endow nanomedicines with outstanding and unexpected biological performance. Future development of polypeptide-drug conjugates may proceed toward the determination of dependencies between physico-chemical parameters and biological activity and to the elaboration of careful synthetic strategies for the design of conjugates with preliminary designated characteristics. Extensive research in the adjacent areas of nanomedicine and polypeptide chemistry has allowed us to delineate possible future trends and opportunities to fully exploit the potential of polypeptide therapeutics:

(1) Different polarity of amino acids and enormous possibilities of side chain modification allow for the synthesis of a variety of architectures. A recent study reports that a combination of soft and rigid helix turns in γ-P(L-Glu-Bz)-block-poly(O-benzyl-L-hydroxyproline) results in the formation of lamellar structures with a "zig-zag" morphology. [352] Additionally, several interesting aggregation modes have been described for polypeptide-based polymers. These include helical rods and rings, [353] disk-like micelles with cylindrical pores, [354] bilamellar vesicles, and bicells. [355] The transfer of different geometries achieved for polypeptide-based polymers to the area of conjugates will allow the expansion of conjugate applicability and, in theory, reveal unknown effects of the geometry on the in vivo response in various pathological conditions. Many polyamino acids display tunable secondary conformation transformation from α-helix to β-sheet [356] and studies show that this conformation can be controlled via a multitude of factors as discussed in **Section 4**. [352] Future development directed toward the synthesis of stimuli-tunable conformation drug conjugates together with full exploitation of amino acids chemical diversity might allow for a step-wise adaption of the polypeptidic vehicle upon interface with biological media allowing for highly specific targeting site and release of the cargo within the body. For example, recent reports have shown the ability of short amphiphilic polyproline fragments to target mitochondria probably due to the specific characteristics of the polyproline helix conformation. [7, 357, 358] Another interesting approach toward organelle specific delivery relies on an adaptive response through the different stimuli gradients along the body of a P(L-Lys)-block–poly(L-Leu) diblock copolymer with β-carboxylic amidated lysine residues using 2,3-dimethylmaleic anhydride, rendering anionic micelles at neutral

solution. As a result, the system demonstrated step-wise hydrolysis following the endocytic uptake pathway resulting in an adaptive charge reversal of the nanosized micelles optimal for systemic circulation and endocytic uptake, followed by endosomal escape and nuclei internalization.

(2) The shift to increased conjugate biodegradability is not a new paradigm in nanomedicine, but improvements in the in vivo degradability are not always possible. PEGylation remains the main strategy in the synthesis of stealth polypeptide conjugates even though PEG is not biodegradable and could present serious problems associated and hypersensitive reactions (e.g., anaphylactic reactions). [359] Several alternatives to PEG, such as polysarcosine, have recently been proposed, [203, 265, 360] although their use in the field of polymer conjugates has yet to be reported.

(3) There is a generalized trend to explore novel nanosized delivery systems with increasing complexity and chemical functionality. This is rationally motivated by various factors: the complexity of human body, the underlying biochemical mechanisms in life threatening pathologies, which requires engineered nanomedicines capable of adaptation to a multitude of environments, and the bio-nano interface interactions which exist along the voyage to the site of action. However, there is now a consensus to reach a compromise between complexity, required to achieve highly specific and efficient activity against the target disease, and chemical simplicity, required for translation into real therapies. This necessitates that a given conjugate can be produced in a robust, reproducible, and scalable manner to ensure industrial feasibility and avoid premature failure at clinical trials. [361]

(4) Incorporation of novel chemical functionalities have proven their value in different contexts, and beyond the increase in manufacturing complexity, potential opportunities to improve and complement polypeptide therapeutics toolbox are conceptualized in the following scientific examples with other polymeric drug delivery systems:

a. Despite strong evidence for specific protease-sensitive linkers as powerful biological targets for drug release, this concept has not been widely exploited in polypeptide conjugates. However, some polymer-drug conjugates can serve as interesting examples to illustrate this approach and might be adapted through the proper chemistry to polypeptide conjugate design. As relevant examples, Cathepsins B and D cleave

specific tetrapeptide sequences, [362] in particular Gly-Phe-Leu-Gly (GFLG) and Gly-Phe-Ala-Leu (FAL), in tumor cells. [363-366] Other studies have exploited the presence of enzymes in the extracellular environment, such as short peptide sequences (MMP2 cleavable linker = H_2N-GPLGIAGQ-COOH), cleavable by MMPs. [367] While these representative examples highlight the potential of enzyme triggered drug delivery, further studies are still required to obtain precise information of the target enzyme levels at the desired site to fine-control cell uptake and to demonstrate that in vivo drug release is correlated to enzymatic activity.

b. Although poorly explored in polymer (and polypeptide) conjugate design, reactive oxygen species (ROS), mainly generated in the mitochondria through diverse endogenous sources, represent an important trigger for stimulated release. [368, 369] A number of existing responsive functionalities have proven the great potential for ROS-mediated drug release via appropriate linker design (or model compounds) as well as ROS-mediated degradation or response of polymeric materials.

These include phenylboronic acids and esters, [370] thioketals, [371, 372] poly-L-methionine [373] and poly-L-proline [374, 375] among others. As an example, proline is the only natural-occurring amino acid capable of forming a tertiary amide bond. This bond is more easily oxidized as compared to secondary amide bonds and, therefore, could be applied for ROS triggered release of active molecules within polypeptidic conjugates. Although there are still no examples with conjugates, its benefits have been already demonstrated by Sung and co-workers who synthesized different types of ROS cleavable scaffolds based on poly(L-proline) and investigated their applications in tissue engineering. [375] They prepared porous polymeric scaffolds via crosslinking a PEG-poly(ε-caprolactone)-poly(carboxyl-ε-caprolactone) (PEG-PCL-cPCL (4%-86%–10%)) block copolymer with biaminated PEG-oligo(proline)-PEG. Treatment with hydrogen peroxide cleaved all proline residues within 6 days and addition of the ROS generator SIN-1 accelerated this further. This proof of concept study suggests that it may be feasible to adapt synthetic strategies for the incorporation of such responsive linkers toward the development of ROS mediated polypeptide conjugates delivery platforms.

c. Molecular recognition of specific molecules in biological media represents a highly challenging task, mainly due to the complex composition of the physiological environment which requires highly specific and efficient interactions. In this context, the

intrinsic ability of phenyl boronic acids and derivatives to interact selectively with diols is of significant note. [376] This approach is highly attractive for the development of glucose sensitive systems toward an on-demand insulin release in response to changes in blood glucose levels. To this end, Zhao *et al*. have developed a polypeptidic nanogel based on PEG-block-γ-P(L-Glu-Bz)-co-(γ-propargyl-LGlu-graft-glucose). [377] This system can release physically entrapped insulin in response to specific levels of glucose in phosphate buffered saline. The construct displayed appropriate cytocompatibility and hematocompatibility allowing us to envisage the potential and feasibility of this approach for the chronic treatment of diabetes with on-demand insulin release systems following a polypeptidic conjugate design.

As shown in this Chapter, the multivalency of the different polypeptides together with their biodegradability, the tunable architectural properties including size, shape, zeta potential, conformation, and rationally designed polymer-drug(s) linkers, have already been used in many different clinical applications upon conjugation of drugs or imaging agents as single agents or in combination therapy ranging from intravenous to topical administration. However, an even better understanding of polypeptide chemistry together with the clinical knowledge of the pathological environments to target (enzyme type and concentration, pH, ROS, GSH level, etc.), would allow us to improve the already available medicine armory and more importantly, to identify novel therapeutic approaches for unmet clinical needs. However, we must remember to take into account the robustness and industrial feasibility of polypeptide conjugate production in order to facilitate the transfer from bench to bedside.

I.6. Physico-chemical Characterization of Polymer-drug Conjugates

The intrinsic molecular complexity and the multiple dynamic interactions with the multiple biological environments encountered following delivery to a biological system hamper the design of new DDS. There exists a general agreement for the need of characterization methodologies that, beyond quality control parameters, allow the identification and study of representative physicochemical descriptors [119]. These findings will be useful for the determination of structure-activity relationships (SARs) which themselves will enable the rational design of nanomedicines towards improved

biological performance. This strategy requires a deeper and more comprehensive approach to the study of conformation, dimensions, dynamics, and interactions with the biological environment to provide robust tools towards rational design of DDS to overcome biological barriers.

Following the successful achievement of nanomedicine characterization in terms of identity, molecular weight, composition, purity, solubility, and stability, DDS performance in relevant physicochemical environments must now be addressed. A progressive increase in media complexity would allow a more complete understanding of DDS performance based on the physicochemical descriptors extracted in solvated states. Characterization in hydrated states and relevant physiological media is accessible through a battery of complementary techniques entailing a multitude of different principles. **Table 6** summarizes several of the most important techniques used in physicochemical characterization of the different nanosystems, some of which will be explained in detail during the present thesis.

I.7. The Importance of Faithful Preclinical Triple Negative Breast Cancer Models

Development of novel nanomedicine strategies for TNBC (and most cancers) requires profuse preclinical studies in mouse cancer models in order to identify and validate novel cancer drivers and therapeutic targets, to determine *in vivo* drug pharmacokinetics and pharmacodynamics (PK/PD), and to evaluate *in vivo* anti-cancer efficacy of these novel therapeutics. Following promising preclinical results, phase I–III clinical trials evaluate the tolerability and anti-cancer efficacy of these drugs in human patients. A proportion of patients will show poor response due to intrinsic or acquired resistance, which may be studied mechanistically in preclinical mouse models to identify response biomarkers and combination therapies to prevent or overcome resistance. The close alignment of mouse studies and human clinical trials will lead to better patient stratification, identification of novel biomarkers, and development of optimal combination therapies, culminating in improved cancer patient care. However, the field currently lacks adequately described spontaneously metastatic breast cancer preclinical models that faithfully reproduce the clinical scenario to develop advanced therapeutics.

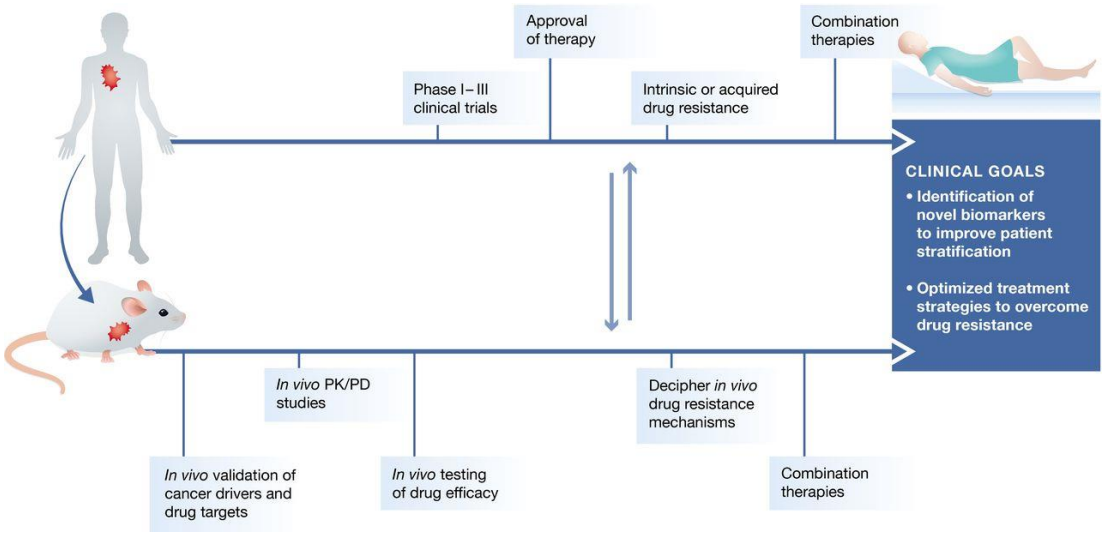

Figure 25. Applications of preclinical murine models in basic cancer research and translational oncology. Adapted from Ref [378].

During the development of this thesis, we have established and described the development and characterization of two clinically relevant spontaneously metastatic TNBC orthotopic murine models (an immunodeficient human MDA-MB231-Luc model and an immunocompetent mouse 4T1 model) with a special focus on their use as in vivo platforms for the development of anticancer nanomedicines. Importantly, we identified distinctive features that may represent functional biomarkers for disease progression or as molecular diagnostic tools. Chapter II explains the details of these models.

Technique	Strenghts	Drawbacks	Descriptor Measured
UV-Vis	Quantitative, non-destructive, fast measurements, time-course studies, physiological conditions (aqueous, pH, ionic strength)	Necessity of chromophores, signal overlapping	Composition, conformation, non-covalent interactions
Differential Refractometry	Quantitative, non-destructive, fast measurements, time-course studies, physiological conditions (aqueous, pH ionic strenght), universal	Reference cell, not specific	Concentration
FS	Quantitative, selective, time-course studies, non-destructive, physiological conditions (aqueous, pH, ionic strength)	Necessity of fluorophores, fluorescence quenching	Concentration, composition, CMC stability
FRET	Quantitative, selective, low sample concentration, physiological conditions (aqueous, pH, ionic strength)	Insufficient spectral separation (false negatives), donor reabsorbs emission, high background noise	Structure, binding affinities, stability conformational change
FCS	Sensitive to single-entities, very small sample volumes, fast measurement, in vivo measurement possible	Dimerization not observable, high preparation time, requires fluorophore	Size (R_h), Size distribution
IR	Fast measurement, small sample volumes, time-course studies	Water masks part of the spectra, signal overlapping	Composition, conformation, non-covalent interactions
ATR-FTIR	Fast measurement, small sample volumes, null sample preparation, aqueous samples, time-course studies	Needs ATR correction software, signal overlapping	Composition, conformation, interactions
RS	Quantitative, minimal sample preparation, relative fast measurements, physiological conditions (pH, ionic strength, biological fluids), mapping of biological tissues	Auto-fluorescence, signal overlapping	Composition, conformation, Interaction with biological environment
CD	Quantitative, non-destructive, fast measurement, minimal sample preparation, time-course studies, physiological conditions (aqueous, pH ionic strength)	Signal overlapping	Conformation, non-covalent interactions, binding affinities
1D-NMR ^{1}H NMR	Non-destructive, minimal sample preparation, semi-quantitative, time-course studies, physiological conditions (aqueous, pH, ionic strength), highly selective, water signals can be eliminated	Relatively long measurments, expertise required, relatively large concentration required, signal overlapping	Composition, binding affinities, interactions
^{19}F NMR	Biological samples, tissues	Long measurement time, biological sample preparation	Quantification in tissues
NOESY NMR	Non-destructive, minimal sample preparation, semi-quantitative, physiological conditions (aqueous, pH, ionic strength), highly selective, water signals can be eliminated	Very long measurement times, expertise required, relatively large concentration required, signal overlapping	Conformation at the molecular level, non-covalent interactions, epitope mapping, dynamics
PGSE NMR	Non-destructive, minimal sample preparation, semi-quantitative, complex mixtures, physiological conditions (aqueous, pH, ionic strength), highly selective, water signals can be eliminated, biological fluids	Relatively long measurement times, expertise required, relatively large concentration required, signal overlapping	Size (R_h), conformation, non-covalent interactions, co-assembling systems, fast screening of interacting components within complex mixtures dynamics

Table 6. Summary of the most relevant techniques used to elucidate physicochemical descriptors in physiological media. Adapted from Ref [231].

Technique	Strenghts	Drawbacks	Descriptor Measured
STD NMR	Non-destructive, minimal sample preparation, semi-quantitative, physiological conditions (aqueous, pH, ionic strength), highly selective, water signals can be eliminated	Long measurement times, expertise required, relatively large concentration required, signal overlapping	Binding affinities, epitope maping, screening of interacting components within complex mixtures, dynamics
NMR Relaxometry	Non-destructive, minimal sample preparation, semi-quantitative, physiological conditions (aqueous, pH, ionic strength), highly selective, water signals can be eliminated	Long measurement times, expertise required, relatively large concentration required, signal overlapping	Conformation, mobility, flexibility (or rigidity, structure topology, dynamics
SANS	Non-destructive, minimal sample preparation, physiological conditions (aqueous, pH, ionic strength), possibility of contrast variation scattering studies	Long measurments, expertise required, relativelly large concentration required	Size , conformation, flexibility (or rigidity), 3D shape
SAXS	Non-destructive, minimal sample preparation, physiological conditions (aqueous, pH, ionic strength)	Relatively long measurement time, expertise required, relatively large concentration required, heavier elements mask the scattering from lighter elements	Size, conformation, flexibility (or rigidity), 3D shape
SLS	Non-destructive, small sample volumes, physiological conditions (aqueous, pH, ionic strength)	Requires sample preparation, interferences (dust, aggregation)	Size (R_h, Rg), size distribution, form factor (ρ), molecular weight
DLS	Non-destructive, small sample volumes, physiological conditions (aqueous, pH, ionic strength), biological fluids	Requires sample preparation, interferences (dust, aggregation), can't differentiate similar sized populations	Size (R_h), size Distribution
ITC	Quantitative, aqueous samples	High preparation time, high precision in sample preparation is required	Non-covalent interactions, binding affinities and associated thermodynamic data
ESEM	Non-destructive, 3D mapping , physiological conditions	Expertise required	Size, size distribution, surface morphology, shape
Cryo-TEM	Physiological conditions, 3D mapping	Expertise required	Size, size distribution, surface morphology, shape
AFM	Non-destructive, 3D mapping, minimal sample preparation	Overestimation of measurements	Size, size distribution, surface morphology, shape
PT	Non-destructive, aqueous sample	Salts and pH might interfere the measurements	Salt ratio, ionization state, pKa
Z-potential	Non-destructive, physiological conditions (aqueous, pH, ionic strength)	Salts and pH might interfere the measurements	Surface charge, stability Binding affinities
NTA	Small sample volumes, minimal sample preparation, physiological conditions (aqueous, pH, ionic strength), selective measuremen through fluorescent labelling	Interferences (Dust, aggregation), limited particle concentration range	Size (R_h) distribution, particle size concentration, selective filtering through fluorescence
SPR	Quantitative, small sample volumes, physiological conditions	Artefacts	Interactions, binding rates

Table 6. Summary of the most relevant techniques used to elucidate physicochemical descriptors in physiological media (continuation).

I.8. References

[1] http://www.cancer.gov DCNCIRM.
[2] Camacho-Rivera M, Kalwar T, Sanmugarajah J, Shapira I, Taioli E. Heterogeneity of breast cancer clinical characteristics and outcome in US black women--effect of place of birth. The breast journal. 2014;20:489-95.
[3] Board PDQATE. Breast Cancer Treatment (PDQ(R)): Patient Version. PDQ Cancer Information Summaries. Bethesda (MD): National Cancer Institute (US); 2002.
[4] McGuire A, Brown JA, Malone C, McLaughlin R, Kerin MJ. Effects of age on the detection and management of breast cancer. Cancers. 2015;7:908-29.
[5] Torre LA, Siegel RL, Ward EM, Jemal A. Global Cancer Incidence and Mortality Rates and Trends--An Update. Cancer epidemiology, biomarkers & prevention : a publication of the American Association for Cancer Research, cosponsored by the American Society of Preventive Oncology. 2016;25:16-27.
[6] Duggan MA, Anderson WF, Altekruse S, Penberthy L, Sherman ME. The Surveillance, Epidemiology and End Results (SEER) Program and Pathology: Towards Strengthening the Critical Relationship. The American journal of surgical pathology. 2016;40:e94-e102.
[7] Dai X, Li T, Bai Z, Yang Y, Liu X, Zhan J, et al. Breast cancer intrinsic subtype classification, clinical use and future trends. American journal of cancer research. 2015;5:2929-43.
[8] Pusztai L, Broglio K, Andre F, Symmans WF, Hess KR, Hortobagyi GN. Effect of molecular disease subsets on disease-free survival in randomized adjuvant chemotherapy trials for estrogen receptor-positive breast cancer. Journal of clinical oncology : official journal of the American Society of Clinical Oncology. 2008;26:4679-83.
[9] Blows FM, Driver KE, Schmidt MK, Broeks A, van Leeuwen FE, Wesseling J, et al. Subtyping of breast cancer by immunohistochemistry to investigate a relationship between subtype and short and long term survival: a collaborative analysis of data for 10,159 cases from 12 studies. PLoS medicine. 2010;7:e1000279.
[10] Haque R, Ahmed SA, Inzhakova G, Shi J, Avila C, Polikoff J, et al. Impact of breast cancer subtypes and treatment on survival: an analysis spanning two decades. Cancer epidemiology, biomarkers & prevention : a publication of the American Association for Cancer Research, cosponsored by the American Society of Preventive Oncology. 2012;21:1848-55.
[11] Harbeck N, Thomssen C, Gnant M. St. Gallen 2013: brief preliminary summary of the consensus discussion. Breast care (Basel, Switzerland). 2013;8:102-9.
[12] Tran B, Bedard PL. Luminal-B breast cancer and novel therapeutic targets. Breast cancer research : BCR. 2011;13:221.
[13] Llombart-Cussac A, Cortes J, Pare L, Galvan P, Bermejo B, Martinez N, et al. HER2-enriched subtype as a predictor of pathological complete response following trastuzumab and lapatinib without chemotherapy in early-stage HER2-positive breast cancer (PAMELA): an open-label, single-group, multicentre, phase 2 trial. The Lancet Oncology. 2017;18:545-54.
[14] Peddi PF, Ellis MJ, Ma C. Molecular basis of triple negative breast cancer and implications for therapy. International journal of breast cancer. 2012;2012:217185.
[15] Herschkowitz JI, Simin K, Weigman VJ, Mikaelian I, Usary J, Hu Z, et al. Identification of conserved gene expression features between murine mammary carcinoma models and human breast tumors. Genome biology. 2007;8:R76.
[16] Bianchini G, Balko JM, Mayer IA, Sanders ME, Gianni L. Triple-negative breast cancer: challenges and opportunities of a heterogeneous disease. Nature reviews Clinical oncology. 2016;13:674-90.
[17] Cheang MC, Chia SK, Voduc D, Gao D, Leung S, Snider J, et al. Ki67 index, HER2 status, and prognosis of patients with luminal B breast cancer. Journal of the National Cancer Institute. 2009;101:736-50.

[18] Rakha EA, Chan S. Metastatic triple-negative breast cancer. Clinical oncology (Royal College of Radiologists (Great Britain)). 2011;23:587-600.
[19] Brouckaert O, Wildiers H, Floris G, Neven P. Update on triple-negative breast cancer: prognosis and management strategies. International journal of women's health. 2012;4:511-20.
[20] Jia H, Truica CI, Wang B, Wang Y, Ren X, Harvey HA, et al. Immunotherapy for triple-negative breast cancer: Existing challenges and exciting prospects. Drug resistance updates : reviews and commentaries in antimicrobial and anticancer chemotherapy. 2017;32:1-15.
[21] Zeichner SB, Terawaki H, Gogineni K. A Review of Systemic Treatment in Metastatic Triple-Negative Breast Cancer. Breast cancer : basic and clinical research. 2016;10:25-36.
[22] Kalimutho M, Parsons K, Mittal D, Lopez JA, Srihari S, Khanna KK. Targeted Therapies for Triple-Negative Breast Cancer: Combating a Stubborn Disease. Trends in pharmacological sciences. 2015;36:822-46.
[23] Andreopoulou E, Kelly CM, McDaid HM. Therapeutic Advances and New Directions for Triple-Negative Breast Cancer. Breast care (Basel, Switzerland). 2017;12:21-8.
[24] Elsawaf Z, Sinn HP, Rom J, Bermejo JL, Schneeweiss A, Aulmann S. Biological subtypes of triple-negative breast cancer are associated with distinct morphological changes and clinical behaviour. Breast (Edinburgh, Scotland). 2013;22:986-92.
[25] Wahba HA, El-Hadaad HA. Current approaches in treatment of triple-negative breast cancer. Cancer biology & medicine. 2015;12:106-16.
[26] Carey LA, Dees EC, Sawyer L, Gatti L, Moore DT, Collichio F, et al. The triple negative paradox: primary tumor chemosensitivity of breast cancer subtypes. Clinical cancer research : an official journal of the American Association for Cancer Research. 2007;13:2329-34.
[27] Liedtke C, Mazouni C, Hess KR, Andre F, Tordai A, Mejia JA, et al. Response to neoadjuvant therapy and long-term survival in patients with triple-negative breast cancer. Journal of clinical oncology : official journal of the American Society of Clinical Oncology. 2008;26:1275-81.
[28] Noman AS, Uddin M, Rahman MZ, Nayeem MJ, Alam SS, Khatun Z, et al. Overexpression of sonic hedgehog in the triple negative breast cancer: clinicopathological characteristics of high burden breast cancer patients from Bangladesh. Scientific reports. 2016;6:18830.
[29] Pareja F, Geyer FC, Marchio C, Burke KA, Weigelt B, Reis-Filho JS. Triple-negative breast cancer: the importance of molecular and histologic subtyping, and recognition of low-grade variants. NPJ breast cancer. 2016;2:16036.
[30] Wolff AC, Hammond MEH, Hicks DG, Dowsett M, McShane LM, Allison KH, et al. Recommendations for Human Epidermal Growth Factor Receptor 2 Testing in Breast Cancer: American Society of Clinical Oncology/College of American Pathologists Clinical Practice Guideline Update. Archives of pathology & laboratory medicine. 2014;138:241-56.
[31] Denduluri N, Somerfield MR, Eisen A, Holloway JN, Hurria A, King TA, et al. Selection of Optimal Adjuvant Chemotherapy Regimens for Human Epidermal Growth Factor Receptor 2 (HER2) -Negative and Adjuvant Targeted Therapy for HER2-Positive Breast Cancers: An American Society of Clinical Oncology Guideline Adaptation of the Cancer Care Ontario Clinical Practice Guideline. Journal of clinical oncology : official journal of the American Society of Clinical Oncology. 2016;34:2416-27.
[32] Rakha EA, El-Sayed ME, Green AR, Lee AH, Robertson JF, Ellis IO. Prognostic markers in triple-negative breast cancer. Cancer. 2007;109:25-32.
[33] Perou CM, Sorlie T, Eisen MB, van de Rijn M, Jeffrey SS, Rees CA, et al. Molecular portraits of human breast tumours. Nature. 2000;406:747-52.
[34] Wu S, Liu Y, Jiang Y, Luo Y, Cui Q, Liang Z, et al. [HER2 mRNA expression in breast cancers with equivocal immunohistochemical results using in situ mRNA hybridization]. Zhonghua bing li xue za zhi = Chinese journal of pathology. 2015;44:725-8.
[35] Lehmann BD, Jovanovic B, Chen X, Estrada MV, Johnson KN, Shyr Y, et al. Refinement of Triple-Negative Breast Cancer Molecular Subtypes: Implications for Neoadjuvant Chemotherapy Selection. PloS one. 2016;11:e0157368.

[36] Xing T, Yang X, Wang F, Lai B, Yan L. Synthesis of polypeptide conjugated with near infrared fluorescence probe and doxorubicin for pH-responsive and image-guided drug delivery. Journal of Materials Chemistry. 2012;22:22290.
[37] Prat A, Adamo B, Cheang MC, Anders CK, Carey LA, Perou CM. Molecular characterization of basal-like and non-basal-like triple-negative breast cancer. The oncologist. 2013;18:123-33.
[38] Rampurwala M, Wisinski KB, O'Regan R. Role of the Androgen Receptor in Triple-Negative Breast Cancer. Clinical advances in hematology & oncology : H&O. 2016;14:186-93.
[39] Geiger TR, Peeper DS. Metastasis mechanisms. Biochimica et biophysica acta. 2009;1796:293-308.
[40] Fertig EJ, Lee E, Pandey NB, Popel AS. Analysis of gene expression of secreted factors associated with breast cancer metastases in breast cancer subtypes. Scientific reports. 2015;5.
[41] Albiges L, Andre F, Balleyguier C, Gomez-Abuin G, Chompret A, Delaloge S. Spectrum of breast cancer metastasis in BRCA1 mutation carriers: highly increased incidence of brain metastases. Annals of oncology : official journal of the European Society for Medical Oncology. 2005;16:1846-7.
[42] https://www.nih.gov/about-nih/what-we-do/nih-almanac/national-cancer-institute-nci.
[43] Dent R, Hanna WM, Trudeau M, Rawlinson E, Sun P, Narod SA. Pattern of metastatic spread in triple-negative breast cancer. Breast cancer research and treatment. 2009;115:423-8.
[44] Tseng LM, Hsu NC, Chen SC, Lu YS, Lin CH, Chang DY, et al. Distant metastasis in triple-negative breast cancer. Neoplasma. 2013;60:290-4.
[45] Talmadge JE, Fidler IJ. AACR centennial series: the biology of cancer metastasis: historical perspective. Cancer research. 2010;70:5649-69.
[46] Christofori G. New signals from the invasive front. Nature. 2006;441:444-50.
[47] Thiery JP. Epithelial-mesenchymal transitions in tumour progression. Nature reviews Cancer. 2002;2:442-54.
[48] Pires BR, Mencalha AL, Ferreira GM, de Souza WF, Morgado-Diaz JA, Maia AM, et al. NF-kappaB Is Involved in the Regulation of EMT Genes in Breast Cancer Cells. PloS one. 2017;12:e0169622.
[49] Mehner C, Hockla A, Miller E, Ran S, Radisky DC, Radisky ES. Tumor cell-produced matrix metalloproteinase 9 (MMP-9) drives malignant progression and metastasis of basal-like triple negative breast cancer. Oncotarget. 2014;5:2736-49.
[50] Lampa M, Arlt H, He T, Ospina B, Reeves J, Zhang B, et al. Glutaminase is essential for the growth of triple-negative breast cancer cells with a deregulated glutamine metabolism pathway and its suppression synergizes with mTOR inhibition. PLOS ONE. 2017;12:e0185092.
[51] Friedl P, Wolf K. Tumour-cell invasion and migration: diversity and escape mechanisms. Nature reviews Cancer. 2003;3:362-74.
[52] Carmeliet P, Jain RK. Molecular mechanisms and clinical applications of angiogenesis. Nature. 2011;473:298-307.
[53] Stott SL, Hsu CH, Tsukrov DI, Yu M, Miyamoto DT, Waltman BA, et al. Isolation of circulating tumor cells using a microvortex-generating herringbone-chip. Proceedings of the National Academy of Sciences of the United States of America. 2010;107:18392-7.
[54] Sahai E. Illuminating the metastatic process. Nature reviews Cancer. 2007;7:737-49.
[55] Deryugina EI, Kiosses WB. Intratumoral Cancer Cell Intravasation Can Occur Independent of Invasion into the Adjacent Stroma. Cell reports. 2017;19:601-16.
[56] Obenauf AC, Massagué J. Surviving at a distance: organ specific metastasis. Trends in cancer. 2015;1:76-91.
[57] Brown DM, Ruoslahti E. Metadherin, a cell surface protein in breast tumors that mediates lung metastasis. Cancer cell. 2004;5:365-74.
[58] Fu H, Yang H, Zhang X, Xu W. The emerging roles of exosomes in tumor-stroma interaction. Journal of cancer research and clinical oncology. 2016;142:1897-907.
[59] Singh R, Pochampally R, Watabe K, Lu Z, Mo YY. Exosome-mediated transfer of miR-10b promotes cell invasion in breast cancer. Molecular cancer. 2014;13:256.

[60] Weidle HU, Birzele F, Kollmorgen G, RÜGer R. The Multiple Roles of Exosomes in Metastasis. Cancer Genomics & Proteomics. 2017;14:1-16.
[61] Suetsugu A, Honma K, Saji S, Moriwaki H, Ochiya T, Hoffman RM. Imaging exosome transfer from breast cancer cells to stroma at metastatic sites in orthotopic nude-mouse models. Advanced drug delivery reviews. 2013;65:383-90.
[62] Mittelbrunn M, Gutierrez-Vazquez C, Villarroya-Beltri C, Gonzalez S, Sanchez-Cabo F, Gonzalez MA, et al. Unidirectional transfer of microRNA-loaded exosomes from T cells to antigen-presenting cells. Nature communications. 2011;2:282.
[63] Luga V, Zhang L, Viloria-Petit AM, Ogunjimi AA, Inanlou MR, Chiu E, et al. Exosomes mediate stromal mobilization of autocrine Wnt-PCP signaling in breast cancer cell migration. Cell. 2012;151:1542-56.
[64] Tominaga N, Kosaka N, Ono M, Katsuda T, Yoshioka Y, Tamura K, et al. Brain metastatic cancer cells release microRNA-181c-containing extracellular vesicles capable of destructing blood-brain barrier. Nature communications. 2015;6:6716.
[65] Chow A, Zhou W, Liu L, Fong MY, Champer J, Van Haute D, et al. Macrophage immunomodulation by breast cancer-derived exosomes requires Toll-like receptor 2-mediated activation of NF-kappaB. Scientific reports. 2014;4:5750.
[66] Deng Z, Cheng Z, Xiang X, Yan J, Zhuang X, Liu C, et al. Tumor cell cross talk with tumor-associated leukocytes leads to induction of tumor exosomal fibronectin and promotes tumor progression. The American journal of pathology. 2012;180:390-8.
[67] Jiang WG, Sanders AJ, Katoh M, Ungefroren H, Gieseler F, Prince M, et al. Tissue invasion and metastasis: Molecular, biological and clinical perspectives. Seminars in cancer biology. 2015;35 Suppl:S244-s75.
[68] Padua D, Zhang XH, Wang Q, Nadal C, Gerald WL, Gomis RR, et al. TGFbeta primes breast tumors for lung metastasis seeding through angiopoietin-like 4. Cell. 2008;133:66-77.
[69] Erler JT, Bennewith KL, Cox TR, Lang G, Bird D, Koong A, et al. Hypoxia-induced lysyl oxidase is a critical mediator of bone marrow cell recruitment to form the premetastatic niche. Cancer cell. 2009;15:35-44.
[70] Psaila B, Lyden D. The metastatic niche: adapting the foreign soil. Nature reviews Cancer. 2009;9:285-93.
[71] Peinado H, Zhang H, Matei IR, Costa-Silva B, Hoshino A, Rodrigues G, et al. Pre-metastatic niches: organ-specific homes for metastases. Nature reviews Cancer. 2017;17:302-17.
[72] Lobb RJ, Lima LG, Moller A. Exosomes: Key mediators of metastasis and pre-metastatic niche formation. Seminars in cell & developmental biology. 2017;67:3-10.
[73] Wells A, Griffith L, Wells JZ, Taylor DP. The dormancy dilemma: quiescence versus balanced proliferation. Cancer research. 2013;73:3811-6.
[74] Mazzieri R, Pucci F, Moi D, Zonari E, Ranghetti A, Berti A, et al. Targeting the ANG2/TIE2 axis inhibits tumor growth and metastasis by impairing angiogenesis and disabling rebounds of proangiogenic myeloid cells. Cancer cell. 2011;19:512-26.
[75] Valastyan S, Weinberg RA. Tumor metastasis: molecular insights and evolving paradigms. Cell. 2011;147:275-92.
[76] Sarsenov D. True Local Recurrences after Breast Conserving Surgery have Poor Prognosis in Patients with Early Breast Cancer.8.
[77] Yagata H, Kajiura Y, Yamauchi H. Current strategy for triple-negative breast cancer: appropriate combination of surgery, radiation, and chemotherapy. Breast cancer (Tokyo, Japan). 2011;18:165-73.
[78] Dawood S. Triple-negative breast cancer: epidemiology and management options. Drugs. 2010;70:2247-58.
[79] Kyndi M, Sorensen FB, Knudsen H, Overgaard M, Nielsen HM, Overgaard J. Estrogen receptor, progesterone receptor, HER-2, and response to postmastectomy radiotherapy in high-risk breast cancer: the Danish Breast Cancer Cooperative Group. Journal of clinical oncology : official journal of the American Society of Clinical Oncology. 2008;26:1419-26.

[80] Rouzier R, Perou CM, Symmans WF, Ibrahim N, Cristofanilli M, Anderson K, et al. Breast cancer molecular subtypes respond differently to preoperative chemotherapy. Clinical cancer research : an official journal of the American Association for Cancer Research. 2005;11:5678-85.
[81] Sharma P, Kimler BF, Ward C, O'Dea A, Hoffmann MS, Klemp JR, et al. Prognosis of triple negative breast cancer patients who attain pathological complete response with neoadjuvant carboplatin/docetaxel and do not receive adjuvant anthracycline chemotherapy. Journal of Clinical Oncology. 2016;34:1015-.
[82] Berrada N, Delaloge S, Andre F. Treatment of triple-negative metastatic breast cancer: toward individualized targeted treatments or chemosensitization? Annals of oncology : official journal of the European Society for Medical Oncology. 2010;21 Suppl 7:vii30-5.
[83] Silver DP, Richardson AL, Eklund AC, Wang ZC, Szallasi Z, Li Q, et al. Efficacy of neoadjuvant Cisplatin in triple-negative breast cancer. Journal of clinical oncology : official journal of the American Society of Clinical Oncology. 2010;28:1145-53.
[84] Bhattacharyya A, Ear US, Koller BH, Weichselbaum RR, Bishop DK. The breast cancer susceptibility gene BRCA1 is required for subnuclear assembly of Rad51 and survival following treatment with the DNA cross-linking agent cisplatin. The Journal of biological chemistry. 2000;275:23899-903.
[85] Varna M, Bousquet G, Plassa LF, Bertheau P, Janin A. TP53 Status and Response to Treatment in Breast Cancers. Journal of Biomedicine and Biotechnology. 2011;2011.
[86] Tian M, Zhong Y, Zhou F, Xie C, Zhou Y, Liao Z. Effect of neoadjuvant chemotherapy in patients with triple-negative breast cancer: A meta-analysis. Oncology Letters. 2015;9:2825-32.
[87] Foulkes WD, Smith IE, Reis-Filho JS. Triple-negative breast cancer. The New England journal of medicine. 2010;363:1938-48.
[88] Gelman IH. Src-family tyrosine kinases as therapeutic targets in advanced cancer. Frontiers in bioscience (Elite edition). 2011;3:801-7.
[89] Qian XL, Zhang J, Li PZ, Lang RG, Li WD, Sun H, et al. Dasatinib inhibits c-src phosphorylation and prevents the proliferation of Triple-Negative Breast Cancer (TNBC) cells which overexpress Syndecan-Binding Protein (SDCBP). PloS one. 2017;12.
[90] Lehmann BD, Bauer JA, Chen X, Sanders ME, Chakravarthy AB, Shyr Y, et al. Identification of human triple-negative breast cancer subtypes and preclinical models for selection of targeted therapies. The Journal of clinical investigation. 2011;121:2750-67.
[91] Geenen JJJ, Linn SC, Beijnen JH, Schellens JHM. PARP Inhibitors in the Treatment of Triple-Negative Breast Cancer. Clinical pharmacokinetics. 2018;57:427-37.
[92] Robert M, Frenel JS, Gourmelon C, Patsouris A, Augereau P, Campone M. Olaparib for the treatment of breast cancer. Expert opinion on investigational drugs. 2017;26:751-9.
[93] Rahim B, O'Regan R. AR Signaling in Breast Cancer. Cancers. 2017;9.
[94] Barton VN, D'Amato NC, Gordon MA, Lind HT, Spoelstra NS, Babbs BL, et al. Multiple molecular subtypes of triple-negative breast cancer critically rely on androgen receptor and respond to enzalutamide in vivo. Molecular cancer therapeutics. 2015;14:769-78.
[95] Zhu A, Li Y, Song W, Xu Y, Yang F, Zhang W, et al. Antiproliferative Effect of Androgen Receptor Inhibition in Mesenchymal Stem-Like Triple-Negative Breast Cancer. Cellular physiology and biochemistry : international journal of experimental cellular physiology, biochemistry, and pharmacology. 2016;38:1003-14.
[96] Sharma P. The prognostic value of BRCA1 promoter methylation in early stage triple negative breast cancer. 2014;3:1-11.
[97] Comprehensive molecular portraits of human breast tumors. Nature. 2012;490:61-70.
[98] Hennessy BT, Garcia-Manero G, Kantarjian HM, Giles FJ. DNA methylation in haematological malignancies: the role of decitabine. Expert opinion on investigational drugs. 2003;12:1985-93.
[99] Nielsen TO, Hsu FD, Jensen K, Cheang M, Karaca G, Hu Z, et al. Immunohistochemical and clinical characterization of the basal-like subtype of invasive breast carcinoma. Clinical cancer research : an official journal of the American Association for Cancer Research. 2004;10:5367-74.

[100] Tanei T, Choi DS, Rodriguez AA, Liang DH, Dobrolecki L, Ghosh M, et al. Antitumor activity of Cetuximab in combination with Ixabepilone on triple negative breast cancer stem cells. Breast cancer research : BCR. 2016;18:6.
[101] Markley JL, Bruschweiler R, Edison AS, Eghbalnia HR, Powers R, Raftery D, et al. The future of NMR-based metabolomics. Current opinion in biotechnology. 2017;43:34-40.
[102] Lanning NJ, Castle JP, Singh SJ, Leon AN, Tovar EA, Sanghera A, et al. Metabolic profiling of triple-negative breast cancer cells reveals metabolic vulnerabilities. Cancer & metabolism. 2017;5:6.
[103] Arminan A, Palomino-Schatzlein M, Deladriere C, Arroyo-Crespo JJ, Vicente-Ruiz S, Vicent MJ, et al. Metabolomics facilitates the discrimination of the specific anti-cancer effects of free- and polymer-conjugated doxorubicin in breast cancer models. Biomaterials. 2018;162:144-53.
[104] Eswaran J, Cyanam D, Mudvari P, Reddy SDN, Pakala SB, Nair SS, et al. Transcriptomic landscape of breast cancers through mRNA sequencing. Scientific reports. 2012;2.
[105] McBryan J, Fagan A, McCartan D, Bane FT, Vareslija D, Cocchiglia S, et al. Transcriptomic Profiling of Sequential Tumors from Breast Cancer Patients Provides a Global View of Metastatic Expression Changes Following Endocrine Therapy. Clinical cancer research : an official journal of the American Association for Cancer Research. 2015;21:5371-9.
[106] Espinal-Enríquez J, Fresno C, Anda-Jáuregui G, Hernández-Lemus E. RNA-Seq based genome-wide analysis reveals loss of inter-chromosomal regulation in breast cancer. Scientific reports. 2017;7.
[107] Chung W, Eum HH, Lee HO, Lee KM, Lee HB, Kim KT, et al. Single-cell RNA-seq enables comprehensive tumour and immune cell profiling in primary breast cancer. 2017;8:15081.
[108] Sinicropi D, Qu K, Collin F, Crager M, Liu ML, Pelham RJ, et al. Whole transcriptome RNA-Seq analysis of breast cancer recurrence risk using formalin-fixed paraffin-embedded tumor tissue. PloS one. 2012;7:e40092.
[109] Lin KH, Huang MY, Cheng WC, Wang SC, Fang SH, Tu HP. RNA-seq transcriptome analysis of breast cancer cell lines under shikonin treatment. 2018;8:2672.
[110] Espinal-Enriquez J, Fresno C, Anda-Jauregui G, Hernandez-Lemus E. RNA-Seq based genome-wide analysis reveals loss of inter-chromosomal regulation in breast cancer. 2017;7:1760.
[111] O'Reilly EA, Gubbins L, Sharma S, Tully R, Guang MH, Weiner-Gorzel K, et al. The fate of chemoresistance in triple negative breast cancer (TNBC). BBA clinical. 2015;3:257-75.
[112] Hartshorn CM, Bradbury MS. Nanotechnology Strategies To Advance Outcomes in Clinical Cancer Care. 2018;12:24-43.
[113] Wang M, Thanou M. Targeting nanoparticles to cancer. Pharmacological research. 2010;62:90-9.
[114] Duncan R, Gaspar R. Nanomedicine(s) under the Microscope. Molecular pharmaceutics. 2011;8:2101-41.
[115] Mendes TF, Kluskens LD, Rodrigues LR. Triple Negative Breast Cancer: Nanosolutions for a Big Challenge. Advanced science (Weinheim, Baden-Wurttemberg, Germany). 2015;2:1500053.
[116] Kutty RV, Wei Leong DT, Feng SS. Nanomedicine for the treatment of triple-negative breast cancer. Nanomedicine (London, England). 2014;9:561-4.
[117] Shi J, Kantoff PW, Wooster R, Farokhzad OC. Cancer nanomedicine: progress, challenges and opportunities. Nature reviews Cancer. 2017;17:20-37.
[118] Tolcher AW, Mayer LD. Improving combination cancer therapy: the CombiPlex((R)) development platform. Future oncology (London, England). 2018;14:1317-32.
[119] Duncan R, Vicent MJ. Polymer therapeutics-prospects for 21st century: the end of the beginning. Advanced drug delivery reviews. 2013;65:60-70.
[120] Greco F, Vicent MJ. Combination therapy: opportunities and challenges for polymer-drug conjugates as anticancer nanomedicines. Advanced drug delivery reviews. 2009;61:1203-13.

[121] Wicki A, Witzigmann D, Balasubramanian V, Huwyler J. Nanomedicine in cancer therapy: challenges, opportunities, and clinical applications. Journal of controlled release : official journal of the Controlled Release Society. 2015;200:138-57.
[122] Maeda H, Tsukigawa K, Fang J. A Retrospective 30 Years After Discovery of the Enhanced Permeability and Retention Effect of Solid Tumors: Next-Generation Chemotherapeutics and Photodynamic Therapy--Problems, Solutions, and Prospects. Microcirculation (New York, NY : 1994). 2016;23:173-82.
[123] Kobayashi H, Watanabe R, Choyke PL. Improving conventional enhanced permeability and retention (EPR) effects; what is the appropriate target? Theranostics. 2013;4:81-9.
[124] Eldar-Boock A, Miller K, Sanchis J, Lupu R, Vicent MJ, Satchi-Fainaro R. Integrin-assisted drug delivery of nano-scaled polymer therapeutics bearing paclitaxel. Biomaterials. 2011;32:10.1016/j.biomaterials.2011.01.073.
[125] Wu D, Si M, Xue HY, Wong HL. Nanomedicine applications in the treatment of breast cancer: current state of the art. International journal of nanomedicine. 2017;12:5879-92.
[126] Li Y, Chen N, Palmisano M, Zhou S. Pharmacologic sensitivity of paclitaxel to its delivery vehicles drives distinct clinical outcomes of paclitaxel formulations. Molecular pharmaceutics. 2015;12:1308-17.
[127] Chen N, Li Y, Ye Y, Palmisano M, Chopra R, Zhou S. Pharmacokinetics and pharmacodynamics of nab-paclitaxel in patients with solid tumors: disposition kinetics and pharmacology distinct from solvent-based paclitaxel. Journal of clinical pharmacology. 2014;54:1097-107.
[128] Gardner ER, Dahut WL, Scripture CD, Jones J, Aragon-Ching JB, Desai N, et al. Randomized crossover pharmacokinetic study of solvent-based paclitaxel and nab-paclitaxel. Clinical cancer research : an official journal of the American Association for Cancer Research. 2008;14:4200-5.
[129] Nahleh ZA, Barlow WE, Hayes DF, Schott AF, Gralow JR, Sikov WM, et al. SWOG S0800 (NCI CDR0000636131): addition of bevacizumab to neoadjuvant nab-paclitaxel with dose-dense doxorubicin and cyclophosphamide improves pathologic complete response (pCR) rates in inflammatory or locally advanced breast cancer. Breast cancer research and treatment. 2016;158:485-95.
[130] Barenholz Y. Doxil(R)--the first FDA-approved nano-drug: lessons learned. Journal of controlled release : official journal of the Controlled Release Society. 2012;160:117-34.
[131] Vail DM, Amantea MA, Colbern GT, Martin FJ, Hilger RA, Working PK. Pegylated liposomal doxorubicin: proof of principle using preclinical animal models and pharmacokinetic studies. Seminars in oncology. 2004;31:16-35.
[132] Tahover E, Patil YP, Gabizon AA. Emerging delivery systems to reduce doxorubicin cardiotoxicity and improve therapeutic index: focus on liposomes. Anti-cancer drugs. 2015;26:241-58.
[133] Duncan R. Polymer therapeutics: Top 10 selling pharmaceuticals - what next? Journal of controlled release : official journal of the Controlled Release Society. 2014;190:371-80.
[134] Duncan R. Polymer therapeutics as nanomedicines: new perspectives. Current opinion in biotechnology. 2011;22:492-501.
[135] Li J, Yu F, Chen Y, Oupicky D. Polymeric drugs: Advances in the development of pharmacologically active polymers. Journal of controlled release : official journal of the Controlled Release Society. 2015;219:369-82.
[136] Canal F, Sanchis J, Vicent MJ. Polymer--drug conjugates as nano-sized medicines. Current opinion in biotechnology. 2011;22:894-900.
[137] Kopecek J. Polymer-drug conjugates: origins, progress to date and future directions. Advanced drug delivery reviews. 2013;65:49-59.
[138] Feng Q. Anticancer nanoparticulate polymer-drug conjugate. 2016;1:277-96.
[139] Grover GN, Maynard HD. Protein-Polymer Conjugates: Synthetic Approaches by Controlled Radical Polymerizations & Interesting Applications. Current opinion in chemical biology. 2010;14:818-27.

[140] Qi Y, Chilkoti A. Protein-Polymer Conjugation—Moving Beyond PEGylation. Current opinion in chemical biology. 2015;28:181-93.
[141] Yang Y, Pan D, Luo K, Li L, Gu Z. Biodegradable and amphiphilic block copolymer-doxorubicin conjugate as polymeric nanoscale drug delivery vehicle for breast cancer therapy. Biomaterials. 2013;34:8430-43.
[142] Li N, Li N, Yi Q, Luo K, Guo C, Pan D, et al. Amphiphilic peptide dendritic copolymer-doxorubicin nanoscale conjugate self-assembled to enzyme-responsive anti-cancer agent. Biomaterials. 2014;35:9529-45.
[143] Nino-Pariente A, Arminan A, Reinhard S, Scholz C, Wagner E, Vicent MJ. Design of Poly-l-Glutamate-Based Complexes for pDNA Delivery. Macromolecular bioscience. 2017;17.
[144] Osada K. Development of functional polyplex micelles for systemic gene therapy. Polymer Journal. 2014;46:469.
[145] Duncan R. The dawning era of polymer therapeutics. Nature reviews Drug discovery. 2003;2:347-60.
[146] Muheem A, Shakeel F, Jahangir MA, Anwar M, Mallick N, Jain GK, et al. A review on the strategies for oral delivery of proteins and peptides and their clinical perspectives. Saudi Pharmaceutical Journal : SPJ. 2016;24:413-28.
[147] Hamman JH, Enslin GM, Kotze AF. Oral delivery of peptide drugs: barriers and developments. BioDrugs : clinical immunotherapeutics, biopharmaceuticals and gene therapy. 2005;19:165-77.
[148] Matsumura Y, Maeda H. A new concept for macromolecular therapeutics in cancer chemotherapy: mechanism of tumoritropic accumulation of proteins and the antitumor agent smancs. Cancer research. 1986;46:6387-92.
[149] Greish K, Fang J, Inutsuka T, Nagamitsu A, Maeda H. Macromolecular therapeutics: advantages and prospects with special emphasis on solid tumour targeting. Clinical pharmacokinetics. 2003;42:1089-105.
[150] Vicent MJ, Ringsdorf H, Duncan R. Polymer therapeutics: clinical applications and challenges for development. Advanced drug delivery reviews. 2009;61:1117-20.
[151] Danquah MK, Zhang XA, Mahato RI. Extravasation of polymeric nanomedicines across tumor vasculature. Advanced drug delivery reviews. 2011;63:623-39.
[152] Maeda H, Nakamura H, Fang J. The EPR effect for macromolecular drug delivery to solid tumors: Improvement of tumor uptake, lowering of systemic toxicity, and distinct tumor imaging in vivo. Advanced drug delivery reviews. 2013;65:71-9.
[153] Nichols JW, Bae YH. EPR: Evidence and fallacy. Journal of controlled release : official journal of the Controlled Release Society. 2014;190:451-64.
[154] Tang Y, Soroush F, Sheffield JB, Wang B, Prabhakarpandian B, Kiani MF. A Biomimetic Microfluidic Tumor Microenvironment Platform Mimicking the EPR Effect for Rapid Screening of Drug Delivery Systems. Scientific reports. 2017;7:9359.
[155] Maeda H. Toward a full understanding of the EPR effect in primary and metastatic tumors as well as issues related to its heterogeneity. Advanced drug delivery reviews. 2015;91:3-6.
[156] Jhaveri AM, Torchilin VP. Multifunctional polymeric micelles for delivery of drugs and siRNA. Frontiers in Pharmacology. 2014;5:77.
[157] El-Sayed ME, Hoffman AS, Stayton PS. Smart polymeric carriers for enhanced intracellular delivery of therapeutic macromolecules. Expert opinion on biological therapy. 2005;5:23-32.
[158] Duncan R. Polymer conjugates as anticancer nanomedicines. Nature Reviews Cancer. 2006;6:688.
[159] Abuchowski A, McCoy JR, Palczuk NC, van Es T, Davis FF. Effect of covalent attachment of polyethylene glycol on immunogenicity and circulating life of bovine liver catalase. The Journal of biological chemistry. 1977;252:3582-6.
[160] Davis FF, Abuchowski A, van Es T, Palczuk NC, Chen R, Savoca K, et al. Enzyme-Polyethylene Glycol Adducts: Modified Enzymes with Unique Properties. Enzyme Engineering: Springer US; 1978. p. 169-73.

[161] Caliceti P. Pharmacokinetic and biodistribution properties of poly(ethylene glycol)–protein conjugates. Advanced drug delivery reviews. 2003;55:1261-77.
[162] Ulbrich K, Holá K, Šubr V, Bakandritsos A, Tuček J, Zbořil R. Targeted Drug Delivery with Polymers and Magnetic Nanoparticles: Covalent and Noncovalent Approaches, Release Control, and Clinical Studies. Chemical Reviews. 2016;116:5338-431.
[163] Keefe AD, Pai S, Ellington A. Aptamers as therapeutics. Nature Reviews Drug Discovery. 2010;9:537-50.
[164] Ni S, Yao H, Wang L, Lu J, Jiang F, Lu A, et al. Chemical Modifications of Nucleic Acid Aptamers for Therapeutic Purposes. International Journal of Molecular Sciences. 2017;18:1683.
[165] Turecek PL, Bossard MJ, Schoetens F, Ivens IA. PEGylation of Biopharmaceuticals: A Review of Chemistry and Nonclinical Safety Information of Approved Drugs. Journal of Pharmaceutical Sciences. 2016;105:460-75.
[166] Gao W, Liu W, Christensen T, Zalutsky MR, Chilkoti A. In situ growth of a PEG-like polymer from the C terminus of an intein fusion protein improves pharmacokinetics and tumor accumulation. Proceedings of the National Academy of Sciences. 2010;107:16432-7.
[167] Gao W, Liu W, Mackay JA, Zalutsky MR, Toone EJ, Chilkoti A. In situ growth of a stoichiometric PEG-like conjugate at a protein's N-terminus with significantly improved pharmacokinetics. Proceedings of the National Academy of Sciences. 2009;106:15231-6.
[168] Steinbach T, Wurm FR. Degradable Polyphosphoester-Protein Conjugates: "PPEylation" of Proteins. Biomacromolecules. 2016;17:3338-46.
[169] Schellekens H, Hennink WE, Brinks V. The Immunogenicity of Polyethylene Glycol: Facts and Fiction. Pharmaceutical Research. 2013;30:1729-34.
[170] Nguyen TH, Kim S-H, Decker CG, Wong DY, Loo JA, Maynard HD. A heparin-mimicking polymer conjugate stabilizes basic fibroblast growth factor. Nature Chemistry. 2013;5:221-7.
[171] Luginbuhl KM, Schaal JL, Umstead B, Mastria EM, Li X, Banskota S, et al. One-week glucose control via zero-order release kinetics from an injectable depot of glucagon-like peptide-1 fused to a thermosensitive biopolymer. Nature Biomedical Engineering. 2017;1:0078.
[172] Vanparijs N, De Coen R, Laplace D, Louage B, Maji S, Lybaert L, et al. Transiently responsive protein–polymer conjugates via a 'grafting-from' RAFT approach for intracellular co-delivery of proteins and immune-modulators. Chemical Communications. 2015;51:13972-5.
[173] Kopeček J. Biomaterials and Drug Delivery: Past, Present, and Future. Molecular pharmaceutics. 2010;7:922-5.
[174] Mathe G, Tran Ba LO, Bernard J. [Effect on mouse leukemia 1210 of a combination by diazo-reaction of amethopterin and gamma-globulins from hamsters inoculated with such leukemia by heterografts]. Comptes rendus hebdomadaires des seances de l'Academie des sciences. 1958;246:1626-8.
[175] Ringsdorf H. Structure and properties of pharmacologically active polymers. Journal of Polymer Science: Polymer Symposia. 1975;51:135-53.
[176] Duncan R, Ringsdorf H, Satchi-Fainaro R. Polymer therapeutics--polymers as drugs, drug and protein conjugates and gene delivery systems: past, present and future opportunities. Journal of drug targeting. 2006;14:337-41.
[177] Seymour LW, Ferry DR, Anderson D, Hesslewood S, Julyan PJ, Poyner R, et al. Hepatic drug targeting: phase I evaluation of polymer-bound doxorubicin. Journal of clinical oncology : official journal of the American Society of Clinical Oncology. 2002;20:1668-76.
[178] Melancon MP. Challenges to effective cancer nanotheranostics. 2012;164:177-82.
[179] Duncan R. Biological effects of soluble synthetic polymers as drug carriers. Critical reviews in therapeutic drug carrier systems. 1985;1:281-310.
[180] Kopecek J, Kopeckova P, Minko T, Lu Z. HPMA copolymer-anticancer drug conjugates: design, activity, and mechanism of action. European journal of pharmaceutics and biopharmaceutics : official journal of Arbeitsgemeinschaft fur Pharmazeutische Verfahrenstechnik eV. 2000;50:61-81.

[181] Seymour LW, Ferry DR, Kerr DJ, Rea D, Whitlock M, Poyner R, et al. Phase II studies of polymer-doxorubicin (PK1, FCE28068) in the treatment of breast, lung and colorectal cancer. International journal of oncology. 2009;34:1629-36.
[182] Li C, Yu DF, Newman RA, Cabral F, Stephens LC, Hunter N, et al. Complete regression of well-established tumors using a novel water-soluble poly(L-glutamic acid)-paclitaxel conjugate. Cancer research. 1998;58:2404-9.
[183] Singer JW. Paclitaxel poliglumex (XYOTAX, CT-2103): a macromolecular taxane. Journal of controlled release : official journal of the Controlled Release Society. 2005;109:120-6.
[184] Homsi J, Simon GR, Garrett CR, Springett G, De Conti R, Chiappori AA, et al. Phase I trial of poly-L-glutamate camptothecin (CT-2106) administered weekly in patients with advanced solid malignancies. Clinical cancer research : an official journal of the American Association for Cancer Research. 2007;13:5855-61.
[185] Davis ME. Design and development of IT-101, a cyclodextrin-containing polymer conjugate of camptothecin. Advanced drug delivery reviews. 2009;61:1189-92.
[186] Pham E, Birrer MJ, Eliasof S, Garmey EG, Lazarus D, Lee CR, et al. Translational impact of nanoparticle-drug conjugate CRLX101 with or without bevacizumab in advanced ovarian cancer. Clinical cancer research : an official journal of the American Association for Cancer Research. 2015;21:808-18.
[187] Cabral H, Kataoka K. Progress of drug-loaded polymeric micelles into clinical studies. Journal of controlled release : official journal of the Controlled Release Society. 2014;190:465-76.
[188] Koizumi F, Kitagawa M, Negishi T, Onda T, Matsumoto S, Hamaguchi T, et al. Novel SN-38-incorporating polymeric micelles, NK012, eradicate vascular endothelial growth factor-secreting bulky tumors. Cancer research. 2006;66:10048-56.
[189] Uchino H, Matsumura Y, Negishi T, Koizumi F, Hayashi T, Honda T, et al. Cisplatin-incorporating polymeric micelles (NC-6004) can reduce nephrotoxicity and neurotoxicity of cisplatin in rats. British journal of cancer. 2005;93:678-87.
[190] Stirland DL, Nichols JW, Miura S, Bae YH. Mind the gap: a survey of how cancer drug carriers are susceptible to the gap between research and practice. Journal of controlled release : official journal of the Controlled Release Society. 2013;172:1045-64.
[191] Vasey PA, Kaye SB, Morrison R, Twelves C, Wilson P, Duncan R, et al. Phase I clinical and pharmacokinetic study of PK1 [N-(2-hydroxypropyl)methacrylamide copolymer doxorubicin]: first member of a new class of chemotherapeutic agents-drug-polymer conjugates. Cancer Research Campaign Phase I/II Committee. Clinical cancer research : an official journal of the American Association for Cancer Research. 1999;5:83-94.
[192] Cho S, Heo GS, Khan S, Gonzalez AM, Elsabahy M, Wooley KL. Functionalizable Hydrophilic Polycarbonate, Poly(5-methyl-5-(2-hydroxypropyl)aminocarbonyl-1,3-dioxan-2-one), Designed as a Degradable Alternative for PHPMA and PEG. Macromolecules. 2015;48:8797-805.
[193] Tsai F-T, Wang Y, Darensbourg DJ. Environmentally Benign CO2-Based Copolymers: Degradable Polycarbonates Derived from Dihydroxybutyric Acid and Their Platinum–Polymer Conjugates. Journal of the American Chemical Society. 2016;138:4626-33.
[194] Chen B, Jerger K, Fréchet JMJ, Szoka FC. The influence of polymer topology on pharmacokinetics: Differences between cyclic and linear PEGylated poly(acrylic acid) comb polymers. Journal of Controlled Release. 2009;140:203-9.
[195] Nasongkla N, Chen B, Macaraeg N, Fox ME, Fréchet JMJ, Szoka FC. Dependence of Pharmacokinetics and Biodistribution on Polymer Architecture: Effect of Cyclic versus Linear Polymers. Journal of the American Chemical Society. 2009;131:3842-3.
[196] Etrych T, Strohalm J, Chytil P, Říhová B, Ulbrich K. Novel star HPMA-based polymer conjugates for passive targeting to solid tumors. Journal of drug targeting. 2011;19:874-89.
[197] Etrych T, Šubr V, Strohalm J, Šírová M, Říhová B, Ulbrich K. HPMA copolymer-doxorubicin conjugates: The effects of molecular weight and architecture on biodistribution and in vivo activity. Journal of Controlled Release. 2012;164:346-54.

[198] Quan L, Zhang Y, Crielaard BJ, Dusad A, Lele SM, Rijcken CJF, et al. Nanomedicines for Inflammatory Arthritis: Head-to-Head Comparison of Glucocorticoid-Containing Polymers, Micelles, and Liposomes. ACS nano. 2013;8:458-66.
[199] Deming TJ. Synthetic polypeptides for biomedical applications. Progress in Polymer Science. 2007;32:858-75.
[200] Duro-Castano A, Conejos-Sánchez I, Vicent M. Peptide-Based Polymer Therapeutics. Polymers. 2014;6:515-51.
[201] Hehir S, Cameron NR. Recent advances in drug delivery systems based on polypeptides prepared fromN-carboxyanhydrides. Polymer International. 2014;63:943-54.
[202] Hadjichristidis N, Iatrou H, Pitsikalis M, Sakellariou G. Synthesis of Well-Defined Polypeptide-Based Materials via the Ring-Opening Polymerization of α-Amino AcidN-Carboxyanhydrides. Chemical Reviews. 2009;109:5528-78.
[203] Gangloff N, Ulbricht J, Lorson T, Schlaad H, Luxenhofer R. Peptoids and Polypeptoids at the Frontier of Supra- and Macromolecular Engineering. Chemical Reviews. 2015;116:1753-802.
[204] Luxenhofer R, Han Y, Schulz A, Tong J, He Z, Kabanov AV, et al. Macromol. Rapid Commun. 19/2012. Macromolecular Rapid Communications. 2012;33:1724-.
[205] Engler AC, Shukla A, Puranam S, Buss HG, Jreige N, Hammond PT. Effects of Side Group Functionality and Molecular Weight on the Activity of Synthetic Antimicrobial Polypeptides. Biomacromolecules. 2011;12:1666-74.
[206] Cohen CR, Brown J, Moscicki A-B, Bukusi EA, Paull JRA, Price CF, et al. A Phase I Randomized Placebo Controlled Trial of the Safety of 3% SPL7013 Gel (VivaGel®) in Healthy Young Women Administered Twice Daily for 14 Days. PLoS ONE. 2011;6:e16258.
[207] McGowan I, Gomez K, Bruder K, Febo I, Chen BA, Richardson BA, et al. Phase 1 randomized trial of the vaginal safety and acceptability of SPL7013 gel (VivaGel) in sexually active young women (MTN-004). AIDS. 2011;25:1057-64.
[208] Price CF, Tyssen D, Sonza S, Davie A, Evans S, Lewis GR, et al. SPL7013 Gel (VivaGel®) Retains Potent HIV-1 and HSV-2 Inhibitory Activity following Vaginal Administration in Humans. PLoS ONE. 2011;6:e24095.
[209] Feng Z, Lai Y, Ye H, Huang J, Xi XG, Wu Z. Poly (γ, L-glutamic acid)-cisplatin bioconjugate exhibits potent antitumor activity with low toxicity: A comparative study with clinically used platinum derivatives. Cancer Science. 2010;101:2476-82.
[210] Fox ME, Guillaudeu S, Fréchet JMJ, Jerger K, Macaraeg N, Szoka FC. Synthesis andIn VivoAntitumor Efficacy of PEGylated Poly(l-lysine) Dendrimer−Camptothecin Conjugates. Molecular Pharmaceutics. 2009;6:1562-72.
[211] Senzer N, Bedell C, Nemunaitis J. OncoVEX(GM-CSF). Drugs of the Future. 2010;35:449.
[212] Kiew L-V, Cheong S-K, Sidik K, Chung L-Y. Improved plasma stability and sustained release profile of gemcitabine via polypeptide conjugation. International Journal of Pharmaceutics. 2010;391:212-20.
[213] Langer CJ, O'Byrne KJ, Socinski MA, Mikhailov SM, Leśniewski-Kmak K, Smakal M, et al. Phase III Trial Comparing Paclitaxel Poliglumex (CT-2103, PPX) in Combination with Carboplatin Versus Standard Paclitaxel and Carboplatin in the Treatment of PS 2 Patients with Chemotherapy-Naïve Advanced Non-small Cell Lung Cancer. Journal of Thoracic Oncology. 2008;3:623-30.
[214] O'Brien MER, Socinski MA, Popovich AY, Bondarenko IN, Tomova A, Bilynsky˘ı BT, et al. Randomized Phase III Trial Comparing Single-Agent Paclitaxel Poliglumex (CT-2103, PPX) with Single-Agent Gemcitabine or Vinorelbine for the Treatment of PS 2 Patients with Chemotherapy-Naïve Advanced Non-small Cell Lung Cancer. Journal of Thoracic Oncology. 2008;3:728-34.
[215] Paz-Ares L, Ross H, O'Brien M, Riviere A, Gatzemeier U, Von Pawel J, et al. Phase III trial comparing paclitaxel poliglumex vs docetaxel in the second-line treatment of non-small-cell lung cancer. British Journal of Cancer. 2008;98:1608-13.

[216] Karmaker S, Saha TK, Yoshikawa Y, Yasui H, Sakurai H. A novel drug delivery system for type 1 diabetes: Insulin-mimetic vanadyl-poly(γ-glutamic acid) complex. Journal of Inorganic Biochemistry. 2006;100:1535-46.
[217] Vicent MJ, Pérez-Payá E. Poly-l-glutamic acid (PGA) Aided Inhibitors of Apoptotic Protease Activating Factor 1 (Apaf-1): An Antiapoptotic Polymeric Nanomedicine. Journal of Medicinal Chemistry. 2006;49:3763-5.
[218] Silva M, Ricelli NL, El Seoud O, Valentim CS, Ferreira AG, Sato DN, et al. Potential Tuberculostatic Agent: Micelle-forming Pyrazinamide Prodrug. Archiv der Pharmazie. 2006;339:283-90.
[219] Islam MA, Bajracharya P, Kang S-K, Yun C-H, Kim E-M, Jeong H-J, et al. Mucoadhesive Alginate/Poly (L-Lysine)/Thiolated Alginate Microcapsules for Oral Delivery of <I>Lactobacillus Salivarius</I> 29. Journal of Nanoscience and Nanotechnology. 2011;11:7091-5.
[220] Zou C, Brewer M, Cao X, Zang R, Lin J, Deng Y, et al. Antitumor activity of 4-(N-hydroxyphenyl)retinamide conjugated with poly(l-glutamic acid) against ovarian cancer xenografts. Gynecologic Oncology. 2007;107:441-9.
[221] Singer JW, Bhatt R, Tulinsky J, Buhler KR, Heasley E, Klein P, et al. Water-soluble poly-(l-glutamic acid)–Gly-camptothecin conjugates enhance camptothecin stability and efficacy in vivo. Journal of Controlled Release. 2001;74:243-7.
[222] Ghosh SC, Auzenne E, Khodadadian M, Farquhar D, Klostergaard J. N,N-Dimethylsphingosine conjugates of poly-l-glutamic acid: Synthesis, characterization, and initial biological evaluation. Bioorganic & Medicinal Chemistry Letters. 2009;19:1012-7.
[223] Fante C, Eldar-Boock A, Satchi-Fainaro R, Osborn HMI, Greco F. Synthesis and Biological Evaluation of a Polyglutamic Acid–Dopamine Conjugate: A New Antiangiogenic Agent. Journal of Medicinal Chemistry. 2011;54:5255-9.
[224] Vicent MJ. Polymer-drug conjugates as modulators of cellular apoptosis. The AAPS Journal. 2007;9:E200-E7.
[225] Vaidya A, Sun Y, Feng Y, Emerson L, Jeong E-K, Lu Z-R. Contrast-Enhanced MRI-Guided Photodynamic Cancer Therapy with a Pegylated Bifunctional Polymer Conjugate. Pharmaceutical Research. 2008;25:2002-11.
[226] Hu R, He C, Liu J, Wu Y, Li J, Feng Z, et al. Effects of Insulin-Mimetic Vanadyl-Poly(γ-Glutamic Acid) Complex on Diabetic Rat Model. Journal of Pharmaceutical Sciences. 2010;99:3041-7.
[227] Karmaker S, Saha TK, Sakurai H. Investigation of a CuII–Poly(γ-Glutamic Acid) Complex in Aqueous Solution and its Insulin-Mimetic Activity. Macromolecular Bioscience. 2007;7:456-66.
[228] Cui J, De Rose R, Best JP, Johnston APR, Alcantara S, Liang K, et al. Mechanically Tunable, Self-Adjuvanting Nanoengineered Polypeptide Particles. Advanced Materials. 2013;25:3468-72.
[229] Phase II and Phase III Trials: Docetaxel/Irinotecan versus Docetaxel/Cisplatin in Advanced Non–Small-Cell Lung Cancer (WJTOG 9803). Clinical Lung Cancer. 2001;2:178-9.
[230] Takahashi A, Yamamoto Y, Yasunaga M, Koga Y, Kuroda J-i, Takigahira M, et al. NC-6300, an epirubicin-incorporating micelle, extends the antitumor effect and reduces the cardiotoxicity of epirubicin. Cancer Science. 2013;104:920-5.
[231] Nino-Pariente A, J. Nebot V, J. Vicent M. Relevant Physicochemical Descriptors of "Soft Nanomedicines" to Bypass Biological Barriers. Current Pharmaceutical Design. 2016;22:1274-91.
[232] Cai C, Wang L, Lin J. Self-assembly of polypeptide-based copolymers into diverse aggregates. Chemical Communications. 2011;47:11189.
[233] Cheng CJ, Tietjen GT, Saucier-Sawyer JK, Saltzman WM. A holistic approach to targeting disease with polymeric nanoparticles. Nature Reviews Drug Discovery. 2015;14:239-47.
[234] Mitragotri S, Lahann J. Physical approaches to biomaterial design. Nature Materials. 2009;8:15-23.
[235] Duncan R, Izzo L. Dendrimer biocompatibility and toxicity. Advanced Drug Delivery Reviews. 2005;57:2215-37.
[236] Dobrovolskaia MA. Pre-clinical immunotoxicity studies of nanotechnology-formulated drugs: Challenges, considerations and strategy. Journal of Controlled Release. 2015;220:571-83.

[237] Rothbard JB, Garlington S, Lin Q, Kirschberg T, Kreider E, McGrane PL, et al. Conjugation of arginine oligomers to cyclosporin A facilitates topicaldelivery and inhibition of inflammation. Nature Medicine. 2000;6:1253-7.
[238] Sahu K, Sharma M, Bansal H, Dube A, Gupta PK. Topical photodynamic treatment with poly-l-lysine–chlorin p6 conjugate improves wound healing by reducing hyperinflammatory response in Pseudomonas aeruginosa-infected wounds of mice. Lasers in Medical Science. 2012;28:465-71.
[239] Ikumi Y, Kida T, Sakuma S, Yamashita S, Akashi M. Polymer–phloridzin conjugates as an anti-diabetic drug that Inhibits glucose absorption through the Na+/glucose cotransporter (SGLT1) in the small intestine. Journal of Controlled Release. 2008;125:42-9.
[240] Mignani S, El Kazzouli S, Bousmina M, Majoral J-P. Expand classical drug administration ways by emerging routes using dendrimer drug delivery systems: A concise overview. Advanced Drug Delivery Reviews. 2013;65:1316-30.
[241] Li S-D, Huang L. Stealth nanoparticles: High density but sheddable PEG is a key for tumor targeting. Journal of Controlled Release. 2010;145:178-81.
[242] Owensiii D, Peppas N. Opsonization, biodistribution, and pharmacokinetics of polymeric nanoparticles. International Journal of Pharmaceutics. 2006;307:93-102.
[243] Moghimi SM. Cancer nanomedicine and the complement system activation paradigm: Anaphylaxis and tumour growth. Journal of Controlled Release. 2014;190:556-62.
[244] Tamai I, Tsuji A. Transporter-Mediated Permeation of Drugs Across the Blood–Brain Barrier. Journal of Pharmaceutical Sciences. 2000;89:1371-88.
[245] Duro-Castano A, Nebot VJ, Niño-Pariente A, Armiñán A, Arroyo-Crespo JJ, Paul A, et al. Nanocarriers: Capturing “Extraordinary” Soft-Assembled Charge-Like Polypeptides as a Strategy for Nanocarrier Design (Adv. Mater. 39/2017). Advanced Materials. 2017;29.
[246] Maeda H, Wu J, Sawa T, Matsumura Y, Hori K. Tumor vascular permeability and the EPR effect in macromolecular therapeutics: a review. Journal of Controlled Release. 2000;65:271-84.
[247] Canal F, Sanchis J, Vicent MJ. Polymer–drug conjugates as nano-sized medicines. Current Opinion in Biotechnology. 2011;22:894-900.
[248] Bonomi P. Paclitaxel poliglumex (PPX, CT-2103): macromolecular medicine for advanced non-small-cell lung cancer. Expert Review of Anticancer Therapy. 2007;7:415-22.
[249] Wang AZ. EPR or no EPR? The billion-dollar question. Science Translational Medicine. 2015;7:294ec112-294ec112.
[250] Canton I, Battaglia G. Endocytosis at the nanoscale. Chemical Society Reviews. 2012;41:2718.
[251] Duncan R, Richardson SCW. Endocytosis and Intracellular Trafficking as Gateways for Nanomedicine Delivery: Opportunities and Challenges. Molecular Pharmaceutics. 2012;9:2380-402.
[252] Bareford L, Swaan P. Endocytic mechanisms for targeted drug delivery☆. Advanced Drug Delivery Reviews. 2007;59:748-58.
[253] Eldar-Boock A, Miller K, Sanchis J, Lupu R, Vicent MJ, Satchi-Fainaro R. Integrin-assisted drug delivery of nano-scaled polymer therapeutics bearing paclitaxel. Biomaterials. 2011;32:3862-74.
[254] Biswas S, Torchilin VP. Nanopreparations for organelle-specific delivery in cancer. Advanced Drug Delivery Reviews. 2014;66:26-41.
[255] Zagorodko O, Arroyo-Crespo JJ, Nebot VJ, Vicent MJ. Polypeptide-Based Conjugates as Therapeutics: Opportunities and Challenges. Macromolecular bioscience. 2016;17:1600316.
[256] Pimm MV, Perkins AC, Gribben SJ, Mezö G, Gaál D, Hudecz F. Gamma scintigraphy of111In-labelled branched chain polypeptides (BCP) with a poly(L-lysine) backbone in mice with mammary carcinoma: Effect of charge on biodistribution and tumour imaging potential. Annals of Nuclear Medicine. 1995;9:247-51.
[257] Jamieson C, Moir EM, Rankovic Z, Wishart G. Medicinal Chemistry of hERG Optimizations: Highlights and Hang-Ups. Journal of Medicinal Chemistry. 2006;49:5029-46.

[258] Shaffer SA, Baker-Lee C, Kennedy J, Lai MS, de Vries P, Buhler K, et al. In vitro and in vivo metabolism of paclitaxel poliglumex: identification of metabolites and active proteases. Cancer Chemotherapy and Pharmacology. 2006;59:537-48.
[259] Gada KS, Patil V, Panwar R, Hatefi A, Khaw B-A. Bispecific antibody complex pre-targeted delivery of polymer–drug conjugates for cancer therapy. Drug Delivery and Translational Research. 2012;2:65-76.
[260] Sakuma S, Sagawa T, Masaoka Y, Kataoka M, Yamashita S, Shirasaka Y, et al. Stabilization of enzyme-susceptible glucoside bonds of phloridzin through conjugation with poly(γ-glutamic acid). Journal of Controlled Release. 2009;133:125-31.
[261] Conejos-Sánchez I, Cardoso I, Oteo-Vives M, Romero-Sanz E, Paul A, Sauri AR, et al. Polymer-doxycycline conjugates as fibril disrupters: An approach towards the treatment of a rare amyloidotic disease. Journal of Controlled Release. 2015;198:80-90.
[262] Shen Y, Fu X, Fu W, Li Z. Biodegradable stimuli-responsive polypeptide materials prepared by ring opening polymerization. Chemical Society Reviews. 2015;44:612-22.
[263] Deming TJ. Preparation and development of block copolypeptide vesicles and hydrogels for biological and medical applications. Wiley Interdisciplinary Reviews: Nanomedicine and Nanobiotechnology. 2014;6:283-97.
[264] Duro-Castano A, England RM, Razola D, Romero E, Oteo-Vives M, Morcillo MA, et al. Well-Defined Star-Shaped Polyglutamates with Improved Pharmacokinetic Profiles As Excellent Candidates for Biomedical Applications. Molecular Pharmaceutics. 2015;12:3639-49.
[265] Barz M, Luxenhofer R, Zentel R, Vicent MJ. Overcoming the PEG-addiction: well-defined alternatives to PEG, from structure–property relationships to better defined therapeutics. Polymer Chemistry. 2011;2:1900.
[266] He D, Wagner E. Defined Polymeric Materials for Gene Delivery. Macromolecular Bioscience. 2015;15:600-12.
[267] Deming TJ. Synthesis of Side-Chain Modified Polypeptides. Chemical Reviews. 2015;116:786-808.
[268] Cabral H, Matsumoto Y, Mizuno K, Chen Q, Murakami M, Kimura M, et al. Accumulation of sub-100 nm polymeric micelles in poorly permeable tumours depends on size. Nature Nanotechnology. 2011;6:815-23.
[269] Bae Y, Fukushima S, Harada A, Kataoka K. Design of Environment-Sensitive Supramolecular Assemblies for Intracellular Drug Delivery: Polymeric Micelles that are Responsive to Intracellular pH Change. Angewandte Chemie International Edition. 2003;42:4640-3.
[270] Bae Y, Nishiyama N, Fukushima S, Koyama H, Yasuhiro M, Kataoka K. Preparation and Biological Characterization of Polymeric Micelle Drug Carriers with Intracellular pH-Triggered Drug Release Property: Tumor Permeability, Controlled Subcellular Drug Distribution, and Enhanced in Vivo Antitumor Efficacy. Bioconjugate Chemistry. 2005;16:122-30.
[271] Vega J. Pharmaceutical Research. 2003;20:826-32.
[272] Tai W, Mo R, Lu Y, Jiang T, Gu Z. Folding graft copolymer with pendant drug segments for co-delivery of anticancer drugs. Biomaterials. 2014;35:7194-203.
[273] Zhou Z, Tang J, Sun Q, Murdoch WJ, Shen Y. A multifunctional PEG–PLL drug conjugate forming redox-responsive nanoparticles for intracellular drug delivery. Journal of Materials Chemistry B. 2015;3:7594-603.
[274] Xiong Y, Jiang W, Shen Y, Li H, Sun C, Ouahab A, et al. A Poly(γ, l-glutamic acid)-citric acid based nanoconjugate for cisplatin delivery. Biomaterials. 2012;33:7182-93.
[275] Jain K, Gupta U, Jain NK. Dendronized nanoconjugates of lysine and folate for treatment of cancer. European Journal of Pharmaceutics and Biopharmaceutics. 2014;87:500-9.
[276] Agrawal P, Gupta U, Jain NK. Glycoconjugated peptide dendrimers-based nanoparticulate system for the delivery of chloroquine phosphate. Biomaterials. 2007;28:3349-59.
[277] Lee M, Jeong J, Kim D. Intracellular Uptake and pH-Dependent Release of Doxorubicin from the Self-Assembled Micelles Based on Amphiphilic Polyaspartamide Graft Copolymers. Biomacromolecules. 2014;16:136-44.

[278] Pu Y, Chang S, Yuan H, Wang G, He B, Gu Z. The anti-tumor efficiency of poly(L-glutamic acid) dendrimers with polyhedral oligomeric silsesquioxane cores. Biomaterials. 2013;34:3658-66.
[279] Bae Y, Diezi TA, Zhao A, Kwon GS. Mixed polymeric micelles for combination cancer chemotherapy through the concurrent delivery of multiple chemotherapeutic agents. Journal of Controlled Release. 2007;122:324-30.
[280] Singer JW. Paclitaxel poliglumex (XYOTAX™, CT-2103): A macromolecular taxane. Journal of Controlled Release. 2005;109:120-6.
[281] Yu H, Tang Z, Zhang D, Song W, Zhang Y, Yang Y, et al. Pharmacokinetics, biodistribution and in vivo efficacy of cisplatin loaded poly(l-glutamic acid)-g-methoxy poly(ethylene glycol) complex nanoparticles for tumor therapy. Journal of Controlled Release. 2015;205:89-97.
[282] Chen Z, Yu D, Liu C, Yang X, Zhang N, Ma C, et al. Gadolinium-conjugated PLA-PEG nanoparticles as liver targeted molecular MRI contrast agent. Journal of Drug Targeting. 2010;19:657-65.
[283] Jackson EF, Esparza-Coss E, Wen X, Ng CS, Daniel SL, Price RE, et al. Magnetic Resonance Imaging of Therapy-Induced Necrosis Using Gadolinium-Chelated Polyglutamic Acids. International Journal of Radiation Oncology*Biology*Physics. 2007;68:830-8.
[284] Ye F, Ke T, Jeong E-K, Wang X, Sun Y, Johnson M, et al. Noninvasive Visualization of in Vivo Drug Delivery of Poly(l-glutamic acid) Using Contrast-Enhanced MRI. Molecular Pharmaceutics. 2006;3:507-15.
[285] Mahmoud NN, Al-Qaoud KM, Al-Bakri AG, Alkilany AM, Khalil EA. Colloidal stability of gold nanorod solution upon exposure to excised human skin: Effect of surface chemistry and protein adsorption. The International Journal of Biochemistry & Cell Biology. 2016;75:223-31.
[286] Szabó R, Peiser L, Plüddemann A, Bösze S, Heinsbroek S, Gordon S, et al. Uptake of Branched Polypeptides with Poly[l-Lys] Backbone by Bone-Marrow Culture-Derived Murine Macrophages: The Role of the Class A Scavenger Receptor. Bioconjugate Chemistry. 2005;16:1442-50.
[287] Nadel S, Klein N, Heyderman R, Levin M. Endotoxin antibody for sepsis in infants. The Lancet. 1992;339:678.
[288] Nagy IB, Hudecz F, Alsina MA, Reig F. Physicochemical characterization of branched chain polymeric polypeptide carriers based on a poly-lysine backbone. Biopolymers. 2003;70:323-35.
[289] Tsai W-B, Lai H-Y, Lee J-L, Lo C-W, Chen W-S. Enhancement of the Cytotoxicity and Selectivity of Doxorubicin to Hepatoma Cells by Synergistic Combination of Galactose-Decorated γ-Poly(glutamic acid) Nanoparticles and Low-Intensity Ultrasound. Langmuir. 2014;30:5510-7.
[290] Huang Y, Tang Z, Zhang X, Yu H, Sun H, Pang X, et al. pH-Triggered Charge-Reversal Polypeptide Nanoparticles for Cisplatin Delivery: Preparation and In Vitro Evaluation. Biomacromolecules. 2013;14:2023-32.
[291] Giménez V, James C, Armiñán A, Schweins R, Paul A, Vicent MJ. Demonstrating the importance of polymer-conjugate conformation in solution on its therapeutic output: Diethylstilbestrol (DES)-polyacetals as prostate cancer treatment. Journal of Controlled Release. 2012;159:290-301.
[292] Mochida Y, Cabral H, Miura Y, Albertini F, Fukushima S, Osada K, et al. Bundled Assembly of Helical Nanostructures in Polymeric Micelles Loaded with Platinum Drugs Enhancing Therapeutic Efficiency against Pancreatic Tumor. ACS Nano. 2014;8:6724-38.
[293] Shukla SC, Singh A, Pandey AK, Mishra A. Review on production and medical applications of ε-polylysine. Biochemical Engineering Journal. 2012;65:70-81.
[294] Zhang R, Zheng N, Song Z, Yin L, Cheng J. The effect of side-chain functionality and hydrophobicity on the gene delivery capabilities of cationic helical polypeptides. Biomaterials. 2014;35:3443-54.
[295] Yin L, Tang H, Kim KH, Zheng N, Song Z, Gabrielson NP, et al. Light-Responsive Helical Polypeptides Capable of Reducing Toxicity and Unpacking DNA: Toward Nonviral Gene Delivery. Angewandte Chemie International Edition. 2013;52:9182-6.

[296] Mutaf OF, Kishimura A, Mochida Y, Kim A, Kataoka K. Induction of Secondary Structure through Micellization of an Oppositely Charged Pair of Homochiral Block- and Homopolypeptides in an Aqueous Medium. Macromolecular Rapid Communications. 2015;36:1958-64.
[297] Hudecz F, Pimm MV, Rajnavölgyi É, Mezo Gb, Fabra A, Gaál D, et al. Carrier Design: New Generation of Polycationic Branched Polypeptides Containing OH Groups with Prolonged Blood Survival and Diminished in Vitro Cytotoxicity. Bioconjugate Chemistry. 1999;10:781-90.
[298] Mezö G, Reményi J, Kajtár J, Barna K, Gaál D, Hudecz F. Synthesis and conformational studies of poly(l-lysine) based branched polypeptides with Ser and Glu/Leu in the side chains. Journal of Controlled Release. 2000;63:81-95.
[299] Wadhwa S, Mumper RJ. Polypeptide conjugates of d-penicillamine and idarubicin for anticancer therapy. Journal of Controlled Release. 2012;158:215-23.
[300] Wadhwa S, Mumper RJ. Intracellular Delivery of the Reactive Oxygen Species Generating Agentd-Penicillamine upon Conjugation to Poly-l-glutamic Acid. Molecular Pharmaceutics. 2010;7:854-62.
[301] Lai J, Huang Y. Fibril aggregates of the poly(glutamic acid)–drug conjugate. RSC Advances. 2015;5:48856-60.
[302] Kramer JR, Deming TJ. Glycopolypeptides with a Redox-Triggered Helix-to-Coil Transition. Journal of the American Chemical Society. 2012;134:4112-5.
[303] Gitsas A, Floudas G, Mondeshki M, Butt HJ, Spiess HW, Iatrou H, et al. Effect of Chain Topology on the Self-Organization and Dynamics of Block Copolypeptides: From Diblock Copolymers to Stars. Biomacromolecules. 2008;9:1959-66.
[304] Yin L, Song Z, Kim KH, Zheng N, Tang H, Lu H, et al. Reconfiguring the architectures of cationic helical polypeptides to control non-viral gene delivery. Biomaterials. 2013;34:2340-9.
[305] Champion JA, Katare YK, Mitragotri S. Particle shape: A new design parameter for micro- and nanoscale drug delivery carriers. Journal of Controlled Release. 2007;121:3-9.
[306] Zhang Y, Tekobo S, Tu Y, Zhou Q, Jin X, Dergunov SA, et al. Permission to Enter Cell by Shape: Nanodisk vs Nanosphere. ACS Applied Materials & Interfaces. 2012;4:4099-105.
[307] Truong NP, Whittaker MR, Mak CW, Davis TP. The importance of nanoparticle shape in cancer drug delivery. Expert Opinion on Drug Delivery. 2014;12:129-42.
[308] Paul D, Achouri S, Yoon Y-Z, Herre J, Bryant Clare E, Cicuta P. Phagocytosis Dynamics Depends on Target Shape. Biophysical Journal. 2013;105:1143-50.
[309] Köster DV, Husain K, Iljazi E, Bhat A, Bieling P, Mullins RD, et al. Actomyosin dynamics drive local membrane component organization in an in vitro active composite layer. Proceedings of the National Academy of Sciences. 2016;113:E1645-E54.
[310] Masters TA, Pontes B, Viasnoff V, Li Y, Gauthier NC. Plasma membrane tension orchestrates membrane trafficking, cytoskeletal remodeling, and biochemical signaling during phagocytosis. Proceedings of the National Academy of Sciences. 2013;110:11875-80.
[311] Zhang L, Eisenberg A. Multiple Morphologies of "Crew-Cut" Aggregates of Polystyrene-b-poly(acrylic acid) Block Copolymers. Science. 1995;268:1728-31.
[312] Segura-Sánchez F, Montembault V, Fontaine L, Martínez-Barbosa ME, Bouchemal K, Ponchel G. Synthesis and characterization of functionalized poly(γ-benzyl-l-glutamate) derivates and corresponding nanoparticles preparation and characterization. International Journal of Pharmaceutics. 2010;387:244-52.
[313] de Miguel L, Popa I, Noiray M, Caudron E, Arpinati L, Desmaele D, et al. Osteotropic Polypeptide Nanoparticles with Dual hydroxyapatite Binding Properties and Controlled Cisplatin Delivery. Pharmaceutical Research. 2014;32:1794-803.
[314] Hudecz F, Embleton MJ, Clegg JA, Kajtár J, Pimm MV, Szekerke M, et al. Branched polypeptide-daunomycin conjugates: Synthesis, conformation, cytotoxicity and biodistribution. Peptides 1990: Springer Netherlands; 1991. p. 806-7.

[315] Melancon MP, Wang W, Wang Y, Shao R, Ji X, Gelovani JG, et al. A Novel Method for Imaging In Vivo Degradation of Poly(L-Glutamic Acid), a Biodegradable Drug Carrier. Pharmaceutical Research. 2007;24:1217-24.
[316] Pimm MV, Gribben SJ, Bogdán K, Hudecz F. The effect of charge on the biodistribution in mice of branched polypeptides with a poly(l-lysine) backbone labelled with 125I, 111In or 51Cr. Journal of Controlled Release. 1995;37:161-72.
[317] Duro-Castano A, Movellan J, Vicent MJ. Smart branched polymer drug conjugates as nano-sized drug delivery systems. Biomaterials Science. 2015;3:1321-34.
[318] Xue Y, Tang X, Huang J, Zhang X, Yu J, Zhang Y, et al. Anti-tumor efficacy of polymer–platinum(II) complex micelles fabricated from folate conjugated PEG-graft-α,β-poly [(N-amino acidyl)-aspartamide] and cis-dichlorodiammine platinum(II) in tumor-bearing mice. Colloids and Surfaces B: Biointerfaces. 2011;85:280-8.
[319] Prodhomme EJF, Tutt AL, Glennie MJ, Bugg TDH. Multivalent Conjugates of Poly-γ-d-glutamic Acid fromBacillus licheniformiswith Antibody F(ab') and Glycopeptide Ligands. Bioconjugate Chemistry. 2003;14:1148-55.
[320] Mammen M, Choi S-K, Whitesides GM. Polyvalent Interactions in Biological Systems: Implications for Design and Use of Multivalent Ligands and Inhibitors. Angewandte Chemie International Edition. 1998;37:2754-94.
[321] Biessen EAL, Noorman F, van Teijlingen ME, Kuiper J, Barrett-Bergshoeff M, Bijsterbosch MK, et al. Lysine-based Cluster Mannosides That Inhibit Ligand Binding to the Human Mannose Receptor at Nanomolar Concentration. Journal of Biological Chemistry. 1996;271:28024-30.
[322] Frison N, Taylor ME, Soilleux E, Bousser M-T, Mayer R, Monsigny M, et al. Oligolysine-based Oligosaccharide Clusters. Journal of Biological Chemistry. 2003;278:23922-9.
[323] Poon Z, Chen S, Engler AC, Lee H-i, Atas E, von Maltzahn G, et al. Ligand-Clustered "Patchy" Nanoparticles for Modulated Cellular Uptake and In Vivo Tumor Targeting. Angewandte Chemie International Edition. 2010;49:7266-70.
[324] Ihara N, Schmitz S, Kurisawa M, Chung JE, Uyama H, Kobayashi S. Amplification of Inhibitory Activity of Catechin against Disease-Related Enzymes by Conjugation on Poly(ε-lysine). Biomacromolecules. 2004;5:1633-6.
[325] Aida T, Meijer EW, Stupp SI. Functional Supramolecular Polymers. Science. 2012;335:813-7.
[326] Chen H, Liu D, Guo Z. Endogenous Stimuli-responsive Nanocarriers for Drug Delivery. Chemistry Letters. 2016;45:242-9.
[327] Bhatnagar S, Venuganti VVK. Cancer Targeting: Responsive Polymers for Stimuli-Sensitive Drug Delivery. Journal of Nanoscience and Nanotechnology. 2015;15:1925-45.
[328] Lee ES, Gao Z, Bae YH. Recent progress in tumor pH targeting nanotechnology. Journal of Controlled Release. 2008;132:164-70.
[329] Hashim AI, Zhang X, Wojtkowiak JW, Martinez GV, Gillies RJ. Imaging pH and metastasis. NMR in Biomedicine. 2011:n/a-n/a.
[330] Pang X, Jiang Y, Xiao Q, Leung AW, Hua H, Xu C. pH-responsive polymer–drug conjugates: Design and progress. Journal of Controlled Release. 2016;222:116-29.
[331] Alani AWG, Bae Y, Rao DA, Kwon GS. Polymeric micelles for the pH-dependent controlled, continuous low dose release of paclitaxel. Biomaterials. 2010;31:1765-72.
[332] Harada M, Bobe I, Saito H, Shibata N, Tanaka R, Hayashi T, et al. Improved anti-tumor activity of stabilized anthracycline polymeric micelle formulation, NC-6300. Cancer Science. 2010;102:192-9.
[333] Markovsky E, Baabur-Cohen H, Satchi-Fainaro R. Anticancer polymeric nanomedicine bearing synergistic drug combination is superior to a mixture of individually-conjugated drugs. Journal of Controlled Release. 2014;187:145-57.
[334] Zhang S, Chen C, Li Z. Effects of molecular weight on thermal responsive property of pegylated poly-l-glutamates. Chinese Journal of Polymer Science. 2013;31:201-10.

[335] Samiec PS, Drews-Botsch C, Flagg EW, Kurtz JC, Sternberg P, Reed RL, et al. Glutathione in Human Plasma: Decline in Association with Aging, Age-Related Macular Degeneration, and Diabetes. Free Radical Biology and Medicine. 1998;24:699-704.
[336] Jones DP, Carlson JL, Mody VC, Cai J, Lynn MJ, Sternberg P. Redox state of glutathione in human plasma. Free Radical Biology and Medicine. 2000;28:625-35.
[337] Ishida T, Kirchmeier MJ, Moase EH, Zalipsky S, Allen TM. Targeted delivery and triggered release of liposomal doxorubicin enhances cytotoxicity against human B lymphoma cells. Biochimica et Biophysica Acta (BBA) - Biomembranes. 2001;1515:144-58.
[338] Policastro LL, Ibañez IL, Notcovich C, Duran HA, Podhajcer OL. The Tumor Microenvironment: Characterization, Redox Considerations, and Novel Approaches for Reactive Oxygen Species-Targeted Gene Therapy. Antioxidants & Redox Signaling. 2013;19:854-95.
[339] Liu L, Liu P. Synthesis strategies for disulfide bond-containing polymer-based drug delivery system for reduction-responsive controlled release. Frontiers of Materials Science. 2015;9:211-26.
[340] Wei-Chiang S, Xiantang D, Feener EP, Ryser HJP. The intracellular release of methotrexate from a synthetic drug carrier system targeted to fc receptor-bearing cells. Journal of Controlled Release. 1989;10:89-96.
[341] Takemoto H, Ishii A, Miyata K, Nakanishi M, Oba M, Ishii T, et al. Polyion complex stability and gene silencing efficiency with a siRNA-grafted polymer delivery system. Biomaterials. 2010;31:8097-105.
[342] Roncador A, Oppici E, Talelli M, Pariente AN, Donini M, Dusi S, et al. Use of polymer conjugates for the intraperoxisomal delivery of engineered human alanine:glyoxylate aminotransferase as a protein therapy for primary hyperoxaluria type I. Nanomedicine: Nanotechnology, Biology and Medicine. 2017;13:897-907.
[343] Talelli M, Vicent MJ. Reduction Sensitive Poly(l-glutamic acid) (PGA)-Protein Conjugates Designed for Polymer Masked–Unmasked Protein Therapy. Biomacromolecules. 2014;15:4168-77.
[344] Jones LR, Goun EA, Shinde R, Rothbard JB, Contag CH, Wender PA. Releasable Luciferin−Transporter Conjugates: Tools for the Real-Time Analysis of Cellular Uptake and Release. Journal of the American Chemical Society. 2006;128:6526-7.
[345] Puente XS, Sánchez LM, Overall CM, López-Otín C. Human and mouse proteases: a comparative genomic approach. Nature Reviews Genetics. 2003;4:544-58.
[346] Littlewood-Evans A, Kokubo T, Ishibashi O, Inaoka T, Wlodarski B, Gallagher JA, et al. Localization of cathepsin K in human osteoclasts by in situ hybridization and immunohistochemistry. Bone. 1997;20:81-6.
[347] Egeblad M, Werb Z. New functions for the matrix metalloproteinases in cancer progression. Nature Reviews Cancer. 2002;2:161-74.
[348] Iyer RP, Patterson NL, Fields GB, Lindsey ML. The history of matrix metalloproteinases: milestones, myths, and misperceptions. American Journal of Physiology-Heart and Circulatory Physiology. 2012;303:H919-H30.
[349] Turk B, Turk D, Turk V. Lysosomal cysteine proteases: more than scavengers. Biochimica et Biophysica Acta (BBA) - Protein Structure and Molecular Enzymology. 2000;1477:98-111.
[350] Beer TM, Ryan C, Alumkal J, Ryan CW, Sun J, Eilers KM. A phase II study of paclitaxel poliglumex in combination with transdermal estradiol for the treatment of metastatic castration-resistant prostate cancer after docetaxel chemotherapy. Anti-Cancer Drugs. 2010;21:433-8.
[351] Springett GM, Takimoto C, McNamara M, Doroshow JH, Syed S, Eastham E, et al. Phase I study of CT-2106 (polyglutamate camptothecin) in patients with advanced malignancies. Journal of Clinical Oncology. 2004;22:3127-.
[352] Gkikas M, Haataja JS, Seitsonen J, Ruokolainen J, Ikkala O, Iatrou H, et al. Extended Self-Assembled Long Periodicity and Zig-Zag Domains from Helix–Helix Diblock Copolymer Poly(γ-

benzyl-l-glutamate)-block-poly(O-benzyl-l-hydroxyproline). Biomacromolecules. 2014;15:3923-30.
[353] Cai C, Lin J, Chen T, Wang X-S, Lin S. Super-helices self-assembled from a binary system of amphiphilic polypeptide block copolymers and polypeptide homopolymers. Chemical Communications. 2009:2709.
[354] Lin X, He X, Hu C, Chen Y, Mai Y, Lin S. Disk-like micelles with cylindrical pores from amphiphilic polypeptide block copolymers. Polymer Chemistry. 2016;7:2815-20.
[355] Marsden HR, Handgraaf J-W, Nudelman F, Sommerdijk NAJM, Kros A. Uniting Polypeptides with Sequence-Designed Peptides: Synthesis and Assembly of Poly(γ-benzyll-glutamate)-b-Coiled-Coil Peptide Copolymers. Journal of the American Chemical Society. 2010;132:2370-7.
[356] Chen C, Wu D, Fu W, Li Z. Peptide Hydrogels Assembled from Nonionic Alkyl-polypeptide Amphiphiles Prepared by Ring-Opening Polymerization. Biomacromolecules. 2013;14:2494-8.
[357] Kalafut D, Anderson TN, Chmielewski J. Mitochondrial targeting of a cationic amphiphilic polyproline helix. Bioorganic & Medicinal Chemistry Letters. 2012;22:561-3.
[358] Li L, Geisler I, Chmielewski J, Cheng J-X. Cationic amphiphilic polyproline helix P11LRR targets intracellular mitochondria. Journal of Controlled Release. 2010;142:259-66.
[359] Sahiner UM, Yavuz ST, Gökce M, Buyuktiryaki B, Altan I, Aytac S, et al. Anaphylactic reaction to polyethylene-glycol conjugated-asparaginase: Premedication and desensitization may not be sufficient. Pediatrics International. 2013;55:531-3.
[360] Klinker K, Barz M. Polypept(o)ides: Hybrid Systems Based on Polypeptides and Polypeptoids. Macromolecular Rapid Communications. 2015;36:1943-57.
[361] Farokhzad OC, Langer R. Impact of Nanotechnology on Drug Delivery. ACS Nano. 2009;3:16-20.
[362] Choe Y, Leonetti F, Greenbaum DC, Lecaille F, Bogyo M, Brömme D, et al. Substrate Profiling of Cysteine Proteases Using a Combinatorial Peptide Library Identifies Functionally Unique Specificities. Journal of Biological Chemistry. 2006;281:12824-32.
[363] Soyez H, Schacht E, Vanderkerken S. The crucial role of spacer groups in macromolecular prodrug design. Advanced Drug Delivery Reviews. 1996;21:81-106.
[364] Minko T, Kopečková P, Kopeček J. Pharmaceutical Research. 1999;16:986-96.
[365] Kopeček J, Kopečková P. HPMA copolymers: Origins, early developments, present, and future☆. Advanced Drug Delivery Reviews. 2010;62:122-49.
[366] Veronese FM, Schiavon O, Pasut G, Mendichi R, Andersson L, Tsirk A, et al. PEG−Doxorubicin Conjugates: Influence of Polymer Structure on Drug Release, in Vitro Cytotoxicity, Biodistribution, and Antitumor Activity. Bioconjugate Chemistry. 2005;16:775-84.
[367] Zhu L, Kate P, Torchilin VP. Matrix Metalloprotease 2-Responsive Multifunctional Liposomal Nanocarrier for Enhanced Tumor Targeting. ACS Nano. 2012;6:3491-8.
[368] Song C-C, Du F-S, Li Z-C. Oxidation-responsive polymers for biomedical applications. J Mater Chem B. 2014;2:3413-26.
[369] Xu Q, He C, Xiao C, Chen X. Reactive Oxygen Species (ROS) Responsive Polymers for Biomedical Applications. Macromolecular Bioscience. 2016;16:635-46.
[370] Zhang Y, Yin Q, Yin L, Ma L, Tang L, Cheng J. Chain-Shattering Polymeric Therapeutics with On-Demand Drug-Release Capability. Angewandte Chemie International Edition. 2013;52:6435-9.
[371] Wilson DS, Dalmasso G, Wang L, Sitaraman SV, Merlin D, Murthy N. Orally delivered thioketal nanoparticles loaded with TNF-α–siRNA target inflammation and inhibit gene expression in the intestines. Nature Materials. 2010;9:923-8.
[372] Shim MS, Xia Y. A Reactive Oxygen Species (ROS)-Responsive Polymer for Safe, Efficient, and Targeted Gene Delivery in Cancer Cells. Angewandte Chemie International Edition. 2013;52:6926-9.
[373] Rodriguez AR, Kramer JR, Deming TJ. Enzyme-Triggered Cargo Release from Methionine Sulfoxide Containing Copolypeptide Vesicles. Biomacromolecules. 2013;14:3610-4.

[374] Yu SS, Koblin RL, Zachman AL, Perrien DS, Hofmeister LH, Giorgio TD, et al. Physiologically Relevant Oxidative Degradation of Oligo(proline) Cross-Linked Polymeric Scaffolds. Biomacromolecules. 2011;12:4357-66.
[375] Lee SH, Boire TC, Lee JB, Gupta MK, Zachman AL, Rath R, et al. ROS-cleavable proline oligomer crosslinking of polycaprolactone for pro-angiogenic host response. J Mater Chem B. 2014;2:7109-13.
[376] Ma R, Shi L. Phenylboronic acid-based glucose-responsive polymeric nanoparticles: synthesis and applications in drug delivery. Polym Chem. 2014;5:1503-18.
[377] Zhao L, Xiao C, Ding J, Zhuang X, Gai G, Wang L, et al. Competitive binding-accelerated insulin release from a polypeptide nanogel for potential therapy of diabetes. Polymer Chemistry. 2015;6:3807-15.
[378] Kersten K, de Visser KE, van Miltenburg MH, Jonkers J. Genetically engineered mouse models in oncology research and cancer medicine. EMBO Molecular Medicine. 2017;9:137-53.

Chapter II

TRIPLE-NEGATIVE BREAST CANCER PRECLINICAL MODELS PROVIDE FUNCTIONAL EVIDENCE OF METASTATIC PROGRESSION AND SUITABILITY FOR NANOMEDICINE EVALUATION

II.1. Antecedents and Background

Triple negative breast cancer (TNBC, lacking ER, PR, and HER2 expression) represents around 15-20% of newly diagnosed cases [1], and the complex molecular landscape, low detection rate, and aggressive/highly-proliferative nature result in poor prognosis and heterogeneous behavior in patients. Rapid growth rates and prominent lymphoplasmacytic inflammatory infiltrates because of host immune responses promote metastasis to the lungs, liver, and brain and frequent lymphatic system involvement that impedes focal treatment favors recurrence, aggravates the clinical situation, and lowers survival rates [2]. Rapid tumor evolution also leads to the development of an inner hypoxic and further necrotic core [3] and the associated development of multiple drug resistance (MDR) and poorer prognosis [4].

TNBC currently lacks targeted therapeutics [5], and current treatment strategies provide heterogeneous patient responses/outcomes [6]. Additionally, no standardized treatment for metastatic TNBC exists, therefore representing a critical unmet clinical need [7]. Studies have indicated the efficacy of certain chemotherapeutic agents, including anthracyclines and taxanes [8], with reduced tumor recurrence observed [9]; however, accurate tumor targeting and reduced side effects remain as important goals.

Nanopharmaceuticals can enhance therapeutic outcomes by passive tumor targeting via the enhanced permeability and retention (EPR) effect [10], active targeting employing membrane receptors, optimized pharmacokinetics [11], enhanced cell membrane transport, and controlled drug release in the tumor microenvironment or tumor cell. Therefore, full characterization of preclinical models may identify functional descriptors and biomarkers translatable to the rational design of advanced nanomedicine-based treatments for TNBC [12].

Multistage animal models represent crucial translational research platforms for testing and validation of experimental therapies. However, the relative lack of accurately characterized models that faithfully mimic the pathological features of human TNBC, including spontaneous metastasis or multiple side alterations, frequently hampers research [13, 14]. Currently employed metastatic mouse models mimic advanced stage disease, but the requirement for infusions of high concentrations of aggressive BC cells

[13], the need to resect the primary tumor to allow metastasis, or slow metastatic development limits the application of this model.

Here, we present the differential features of two clinically relevant spontaneously metastatic TNBC mice models, representing the murine (the well-established 4T1 model) [15], developed in an immunocompetent (BALB/c) background, and human (MDA-MB-231-Luc model) disease, established, for the first time, in the immunodeficient (NOD/SCID) mice. Within this study, we focused on fully characterizing disease progression in each model and identifying functional biomarkers, key metabolites and differential cytokines considered crucial for prognostic potential. Furthermore, we analyzed the potential for these models in the development and clinical translation of advanced therapeutics, including nanomedicines, for TNBC [8].

II.2. Results

II.2.1. Comparison of Primary Tumor Development in TNBC Models

Primary morphological analysis demonstrated that 4T1 tumors grew exponentially and homogeneously, reaching a cylindrical form after day (D)24 (**Figure 1**). Subsequent analysis demonstrated slower initial growth kinetics for MDA-MB-231-Luc tumors compared to 4T1 up to around D30, finally acquiring an amorphous cylindrical shape at D42 (**Figure 1**). Primary tumors in both models exhibited the typical stromal progression of most solid tumors, including inner necrotic region development [16], although with marked differences in growth kinetics and stromal arrangement (**Figure 4**).

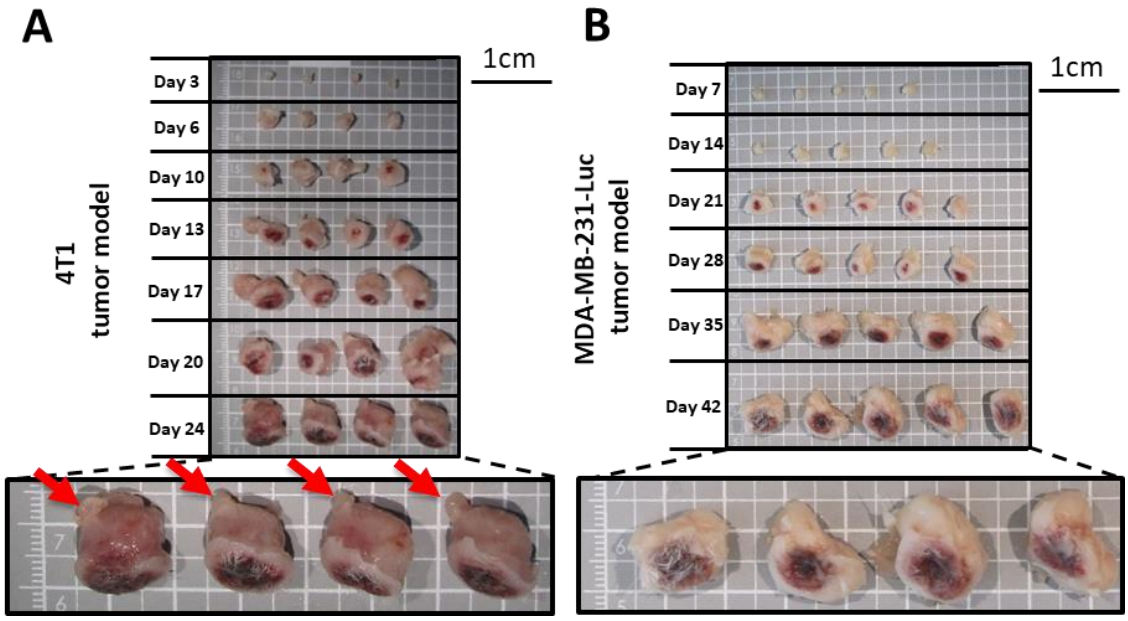

Figure 1: Tumor growth after cell inoculation appeared as a stiff solid mass of a similar volume after (**A**) three days (4T1) and (**B**) one week (MDA-MB-231-Luc). In general, 50% of 4T1 tumors invaded the proximal inguinal lymph node (ILN) around day 13 of tumor growth, and all ILNs became metastasized at day 24 (red arrows). Invasion of the proximal lymph nodes occurred to a lesser extent in the MDA-MB-231-Luc model.

Analysis of tumors at the experimental endpoints demonstrated that the internal necrotic tissue presented cellular debris with diffuse margins, pyknotic nuclei, and karyorrhexis in both models (See H&E sections in **Figure 2A, B**). While H&E tumor sections in 4T1 tumors identified a spheroidal concentric necrotic core surrounded by

homogeneous concentric transition rings followed by a concentric proliferative region, MDA-MB-231-Luc tumors presented a more gelatinous necrotic core with heterogeneous spread of necrosis throughout the tumor stroma (**Figure 2**).

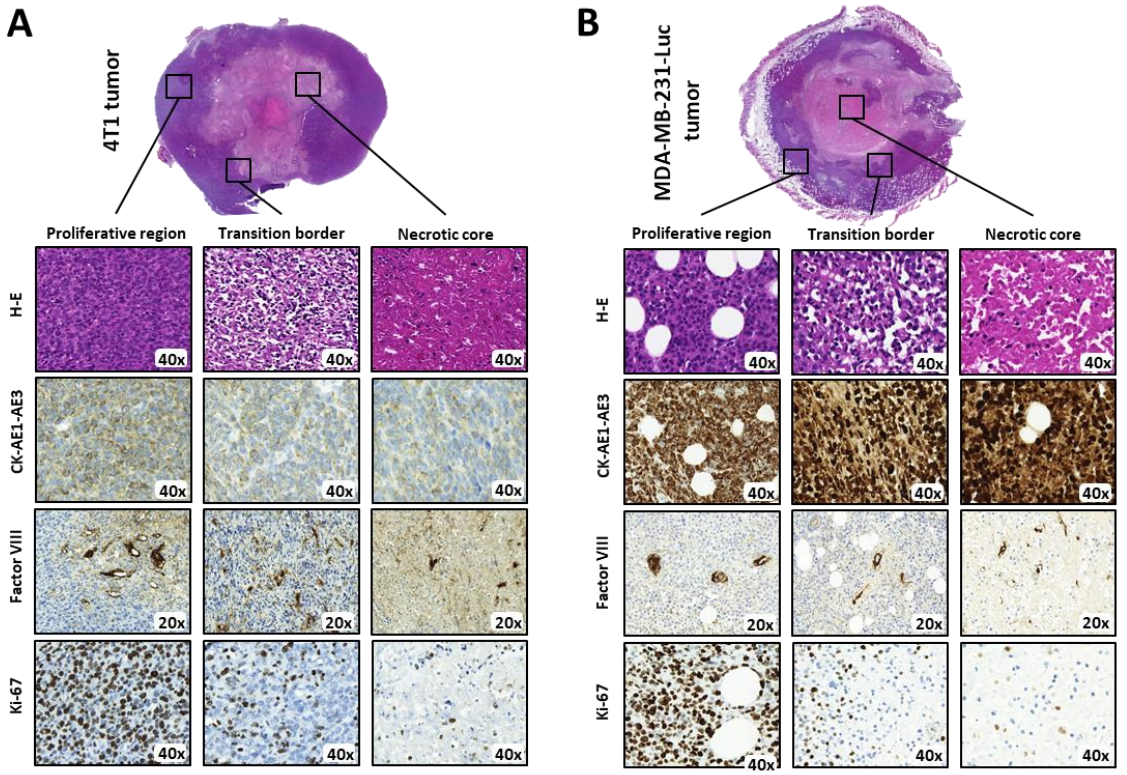

C

	4T1 model			MDA-MB-231-Luc model		
	Proliferative region	Transition border	Necrotic core	Proliferative region	Transition border	Necrotic core
CD-31	++ (myeloid cells)	++	+++	+ (myeloid cells)	-	-
FLI-1	+ (mesechymal cells)	+	++	+ (mesenchymal cells)	-	-
Factor VIII	+++ (Vessels)	++ (Vessels)	+	+++ (Vessels)	+++ (Vessels)	++ (Vessels)
Cytokeratin 19	-	+	++	-	-	-
Cytokeratin AE1/AE3	++	-	+	++	-	-
Ki-67	+++	+	-	+++	+	-

Figure 2. Primary tumor development and immunohistological analysis of features. For the **A)** 4T1 model and MDA-MB-231 model **B),** axial tumor H-E staining, demonstrating the stromal arrangement and an immunohistochemical study of tumor regions. Original magnification displayed in each image. **C)** Summary table of the most relevant immunohistological markers evaluated. Qualitative scale ranging from hyperchromatic (+++) to negative (-).

Overall, the stroma surrounding MDA-MB-231-Luc tumors presented lower cellular density and tumors evolved as soft and flexible solid masses. Both animal models developed fungating lesions (round, non-bleeding skin ulcerations with firm inflamed borders above the mammary gland) that appeared during the first week of 4T1- and the second week of MDA-MB-231-Luc-tumor development, in line with human wound development subtypes [17] (**Figure 1**).

Cytokeratin (CK)-AE1/AE3 immunostaining confirmed the epithelial nature of tumor cells, with expression varying between both region and model. Factor VIII immunostaining demonstrated similar tumor neovasculature and undamaged endogenous blood vessels in both models, indicating a slightly vascularized tumor stroma **(Figure 2A, B)**. We subsequently evaluated region-dependent proliferative rates by Ki-67 immunostaining and confirmed increased cell growth rates in outer regions of both tumors. We summarize data on immunohistochemical tumor markers in **Figure 2C.**

We also morphometrically evaluated volume during tumor development in both models, discovering marked differences in growth kinetic profiles (**Figure 3**). We observed around 2-fold greater tumor growth rate for the 4T1 model (reaching around 1.0 cm^3 at D24) when compared to the MDA-MB-231-Luc model (reaching around 1.0 cm^3 at D42), despite notable differences in the number of inoculated cells (5 x 10^5 vs. 3 x 10^6, respectively).

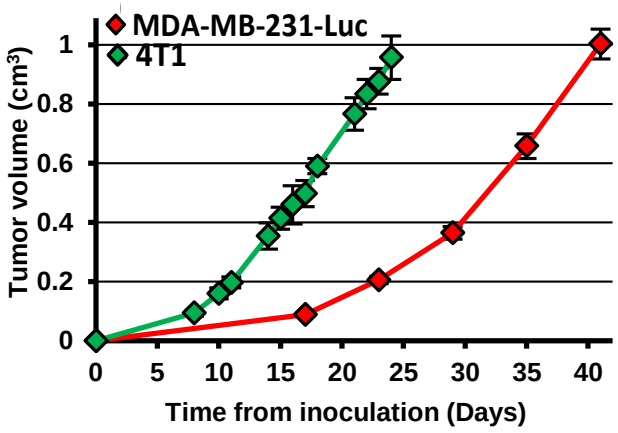

Figure 3. Morphometric tumor analysis demonstrating differential grow kinetics of primary tumors in both models.

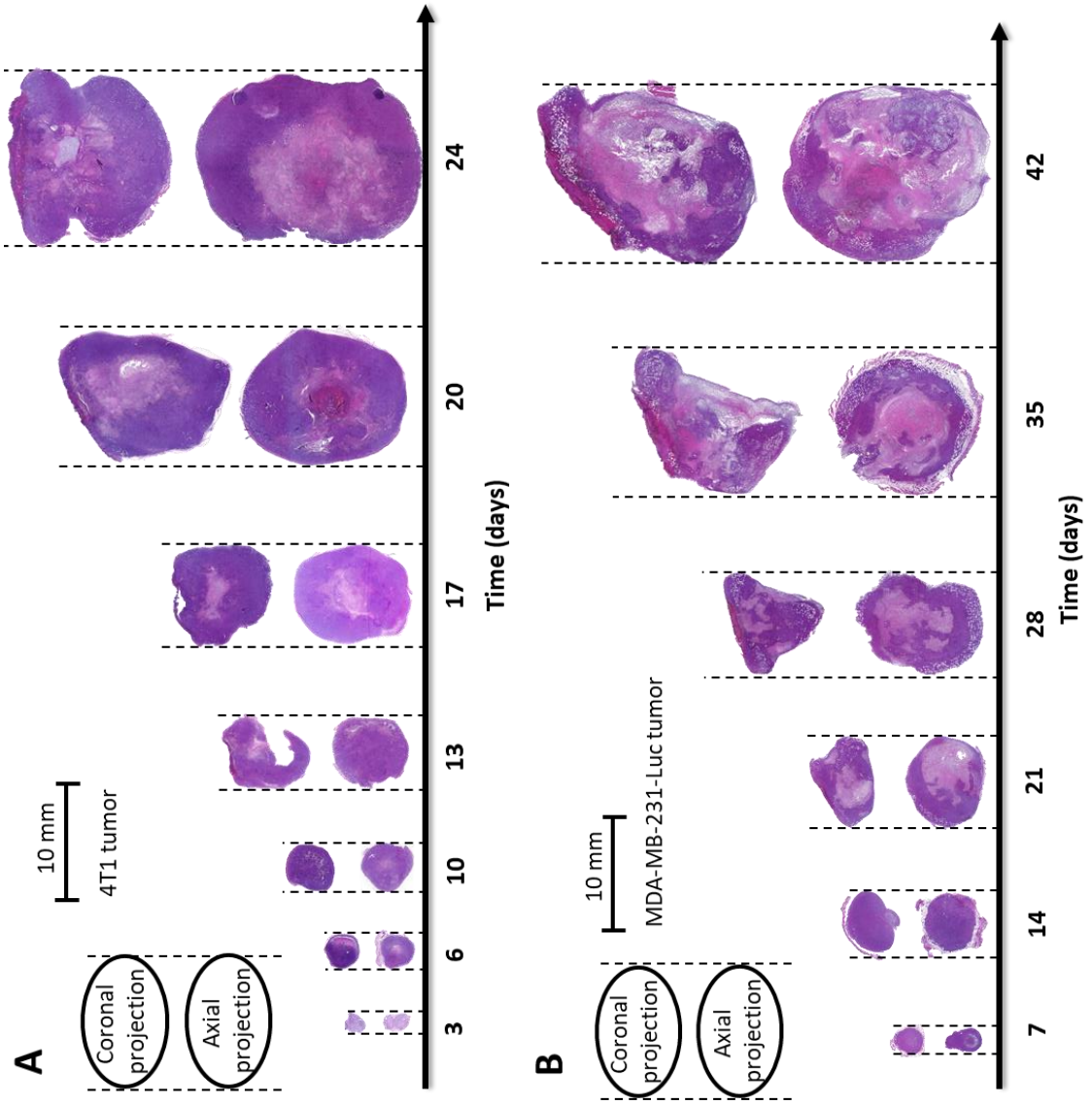

Figure 4. H-E histological staining of primary tumors during development. **A)** From 3-6 days, 4T1 tumors appeared as a dense and compact population of viable cells in a solid, high-pressure region that pushed the tumor mass to grow against the abdominal wall and hypodermis. By Day 10, the first evidence of hypoxia and necrosis in the tumor core emerged, as result of massive blood vessel collapse. From days 10-17, the histological study demonstrated a central necrotic core surrounded by a concentric hypoxic, transition ring. **B)** MDA-MB-231-Luc tumors developed slower, taking seven days to acquire the same volume as the 4T1 tumors at day 3. The first hypodense regions appeared non-concentrically at day 14 of development, with heterogeneously distributed small necrotic areas throughout the tumor. From day 20, several larger disperse necrotic zones emerged, and tumors appeared approximately 80% necropsied at the endpoint.

Subsequent quantification of maximum tumor permeability (related to the enhanced permeability and retention [EPR] effect [18]) established three-fold greater permeability for the MDA-MB-231-Luc model when compared to the 4T1 model (33% injected dose (ID)/gram of tumor (g) at around D14 vs. 13% ID/g at D10, respectively, when analyzing tumors at around 0.1 cm^3) (**Figure 5)**.

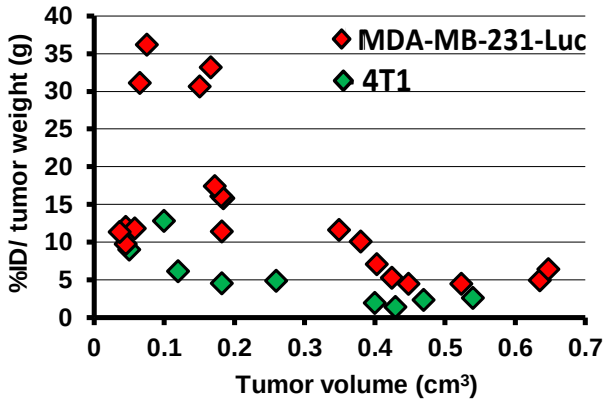

Figure 5. EPR effect quantification of primary tumors. EPR_{Max} was around 0.1 cm^3 for both tumor models, corresponding to day 8 and day 14 for 4T1 and MDA-MB-231-Luc, respectively.

Tumor density analyses reflected differential stromal arrangements, as previously noted (**Figure 6**). 4T1 tumors initially displayed high density at early development time points (around 3 g/cm^3), which then decreased progressively over two weeks to around 1.5 g/cm^3. In contrast, MDA-MB-231-Luc tumors displayed a more homogeneous density during tumor development, rising from 1.0 g/cm^3 to 1.4 g/cm^3 over the experimental time frame.

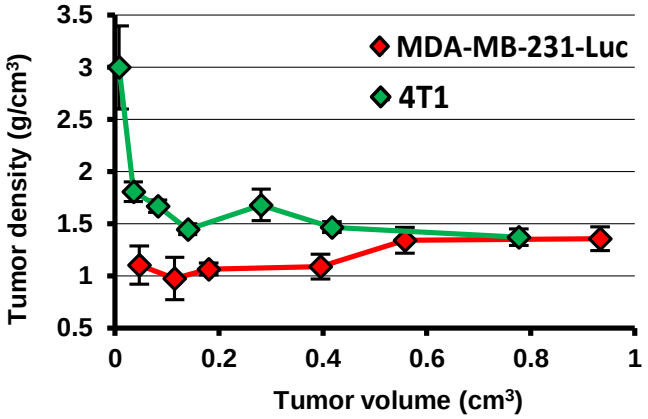

Figure 6. Tumor density determined by simple arithmetic calculation demonstrating a lighter stroma as a result of lower cell density and higher lipid content in the MDA-MB-231-Luc model.

Additional metabolomics analysis supported differences in tumor growth kinetics observed between models; 4T1 tumors displayed increased levels of guanosine and uracil (metabolites related to cell growth and proliferation, **Figure 7C, D**) and cholesterol and phospholipids (critical cell membrane components, **Figure 7D**) when compared to the MDA-MB-231-Luc tumors.

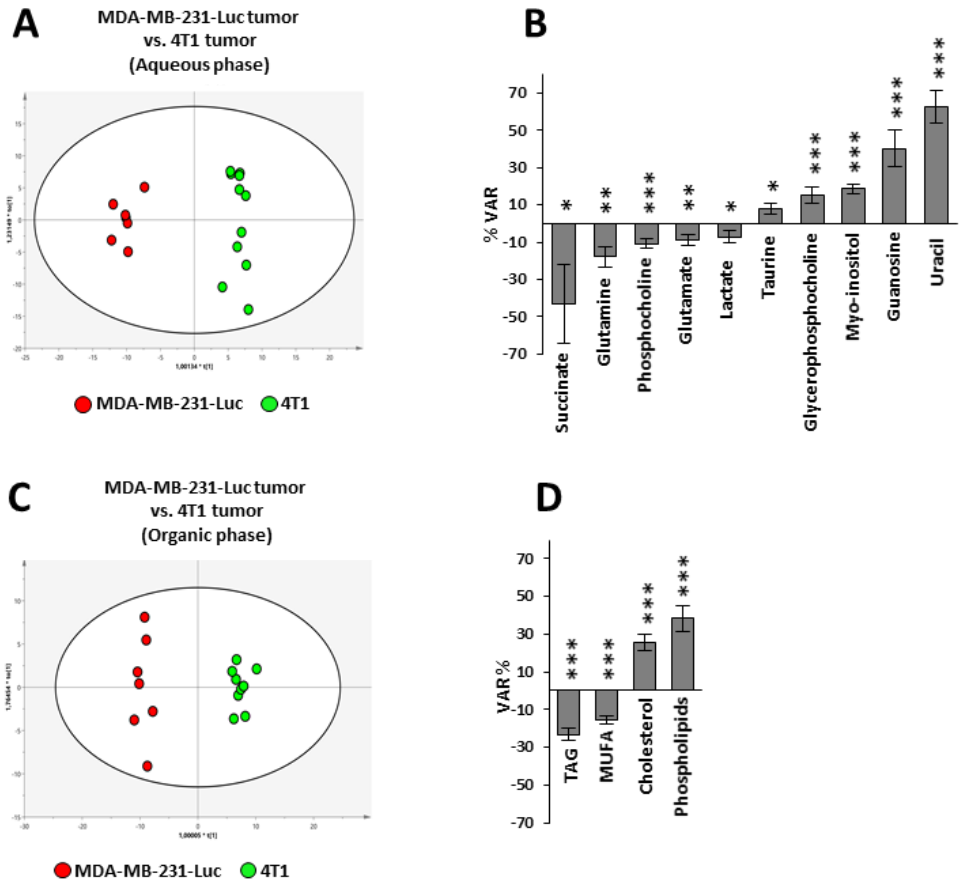

Figure 7. Multivariate modeling resulting from the analysis of primary tumors. (**A** and **B**) OPLS-DA score plot representing the comparison between MDA-MB-231- Luc vs. 4T1 primary tumors (aqueous phase) (R^2 = 0.976 / Q2 = 0.925) and organic phase (R2 = 0.982 / Q2 = 0.936), respectively. **C** and **D**) Metabolic changes for MDA-MB-231-Luc vs. 4T1 primary tumor (aqueous phase) and MDA-MB-231-Luc vs. 4T1 primary tumors (organic phase) comparisons. Statistical significance determined via ANOVA t-test, (*** p<0.001, ** p<0.01, *p<0.05).

Importantly, the tumor histopathological study at model endpoints also demonstrated a relationship between MDA-MB-231-Luc tumors, but not 4T1 tumors, and lipid burden (**Figure 8**). We observed disperse accumulation of adipocyte lobes from early stages of MDA-MB-231-Luc tumor development, with adipocytes distributed throughout the proliferative tumor region **(Figure 4).** According to their reduced size and

distribution pattern within the tumor stroma and further Interleukin (IL)-6 and IL-1β immunostaining[19] (**Figure 8**), we consider these adipocytes as cancer-associated adipocytes (CAA). Interestingly, metabolomic comparisons revealed significantly increased triacylglycerol (TAG) levels for MDA-MB-231-Luc tumors, a lipid whose synthesis/hydrolysis is controlled by adipocytes, agreeing with histopathological findings (**Figure 7**).

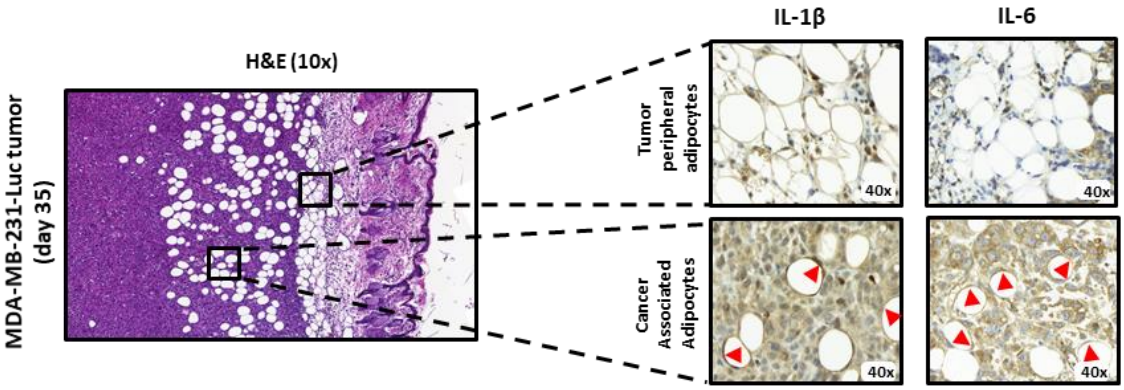

Figure 8. CAAs from MDA-MB-231-Luc tumors exhibited extensive phenotypic changes. Subpopulations of tumor stroma infiltrated adipocytes expressed IL-1β and IL-6 (IL-6 to a lesser extent) (indicated with red arrows). Note the diminished averaged sizes, a known characteristic feature of CAA.

II.2.2. Comparison of the Spontaneous Metastatic Landscape in TNBC Models

4T1 tumors metastasize to liver, lungs, bones, and brain at advanced stages, and we employed intrinsic resistance to 6-thioguanine (6-TG) to quantify metastatic cells[20]**.** MDA-MB-231-Luc tumors produce multiple organ metastasis after intravenous cancer cell inoculation or after tumor resection [21]; however, to the best of our knowledge, no study has reported spontaneous metastatic spread from unresected MDA-MB-231-Luc tumors in NOD/SCID mice (e.g., see Iorns *et al*. [22]). In both models, we observed a very low incidence of brain, bone, and liver metastases, but high levels of lung and axillary lymph node (ALN) metastasis, a finding that correlates with the TNBC clinical scenario. Therefore, our studies focused on these two major metastatic sites**.**

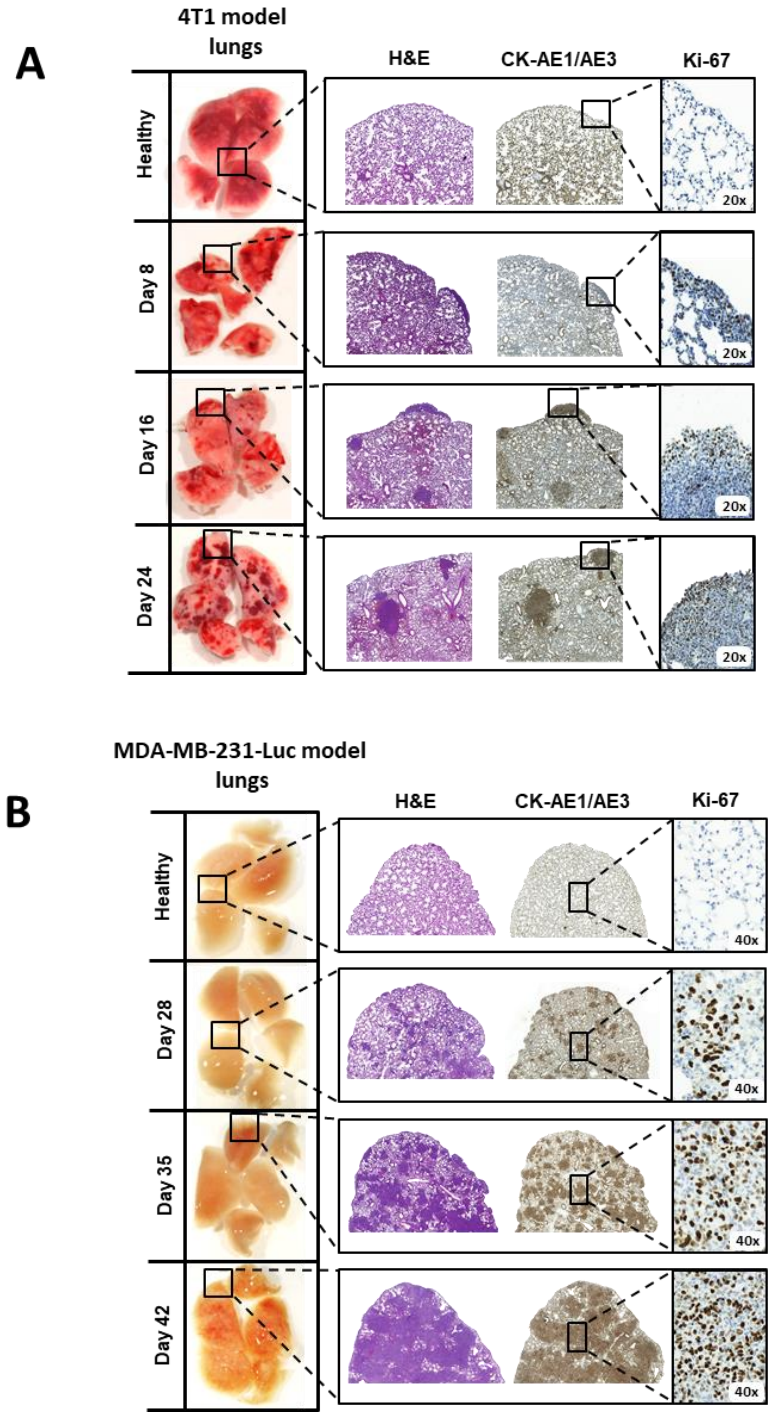

Figure 9. A) 4T1 model lungs presented with prominent subpleural metastasis from day eight after tumor cell inoculation. Further analysis confirmed predominant pleural invasion, although intraparenchymal regions also appeared metastasized. Metastatic regions within the lungs as evidenced by CK-AE1/AE3 immunostaining and highly proliferative nature evidenced by Ki-67 immunostaining. **B)** The MDA-MB-231-Luc model developed metastasis later (day 28) and the metastatic nodules appears disseminated throughout the lung parenchyma with predominant bronchioloalveolar pattern.

Lungs from the 4T1 model revealed evident sub-pleural metastases from D8, although we discovered the first evidence of discrete micro-metastasis from D3 (**Figure 10A**). Between D8 to D16, lungs presented with perivascular metastatic nodules following a predominantly sub-pleural pattern[23]. H&E staining identified prominent metastatic progression leading to disperse necrotic regions from D14 (**Figure 9A**). Additionally, macroscopic examination identified increased tissue hyperemia concomitant with metastasis progression; however, we did not observe this trend in MDA-MB-231-Luc lungs (**Figure 9B).**

Metastatic burden in MDA-MB-231-Luc appeared later than in the 4T1 and exhibited higher variability. Macroscopic lung evaluation uncovered first signs of lung metastases at around D28 as homogeneously disperse nodes, with intraalveolar and intrabronchiolar metastatic infiltrations present throughout the lung parenchyma (**Figure 9B**). Subsequently, lungs became slightly hyperemic and displayed signs of damage. We confirmed metastasis and enhanced proliferation in both models using CK-AE1/AE3 and Ki-67 immunostaining, respectively (**Figure 9**). Overall, we observed higher lung metastasis and lesser implication of the subpleural region in the MDA-MB-231-Luc compared to the 4T1 model.

Comparisons of healthy and metastatic lungs at the metabolomics levels established significant alterations in both models. Analysis of corresponding Orthogonal Projections to Latent Structures Discriminant Analysis (OPLS-DA) models revealed similar metabolic changes for the 4T1 and MDA-MB-231-Luc models (e.g., taurine, glutamate, UDP-N-acetylglucosamine), while other metabolites experienced variations of opposite sign (e.g., lysine, tyrosine). Furthermore, comparisons between metastatic and healthy lungs also uncovered several unique metabolic changes (e.g., 4T1: phenylalanine, arginine, aspartate; MDA-MB-231-Luc: glutathione, glycerophosphocholine) (**Figure 11**).

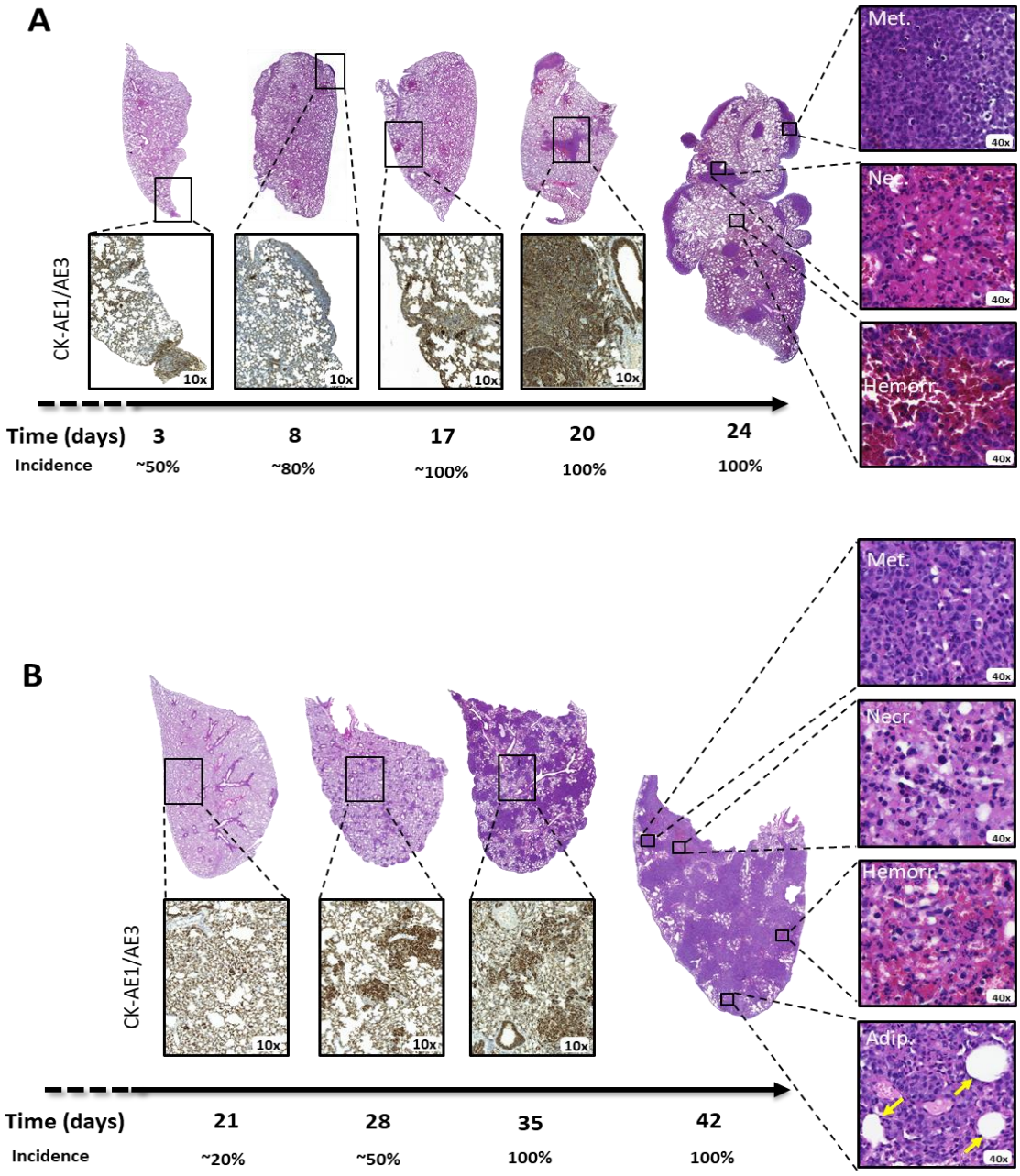

Figure 10: A) H-E staining of representative 4T1 lung lobes allowed the detection of initiated metastasis around days 3-8 after cell inoculation. CK-AE1/AE3 confirmed the presence of tumorigenic cells. Endpoint lung analysis revealed the presence of metastasis-derived massive hemorrhages, parenchymal karyorrhexis, and loss of cell morphology. In later stages, the invaded regions covered around 60% of the whole lung tissue and mainly appeared in subpleural location. **B)** First signs of metastasis appeared around day 21 in the MDA-MB-231-Luc model and evolved to cover most of the lung tissue at the endpoint. Metastasis presented with a mainly intraparenchymatous pattern with low subpleural compromise. Several adipocytic regions were found associated with lung metastasis (yellow arrows).

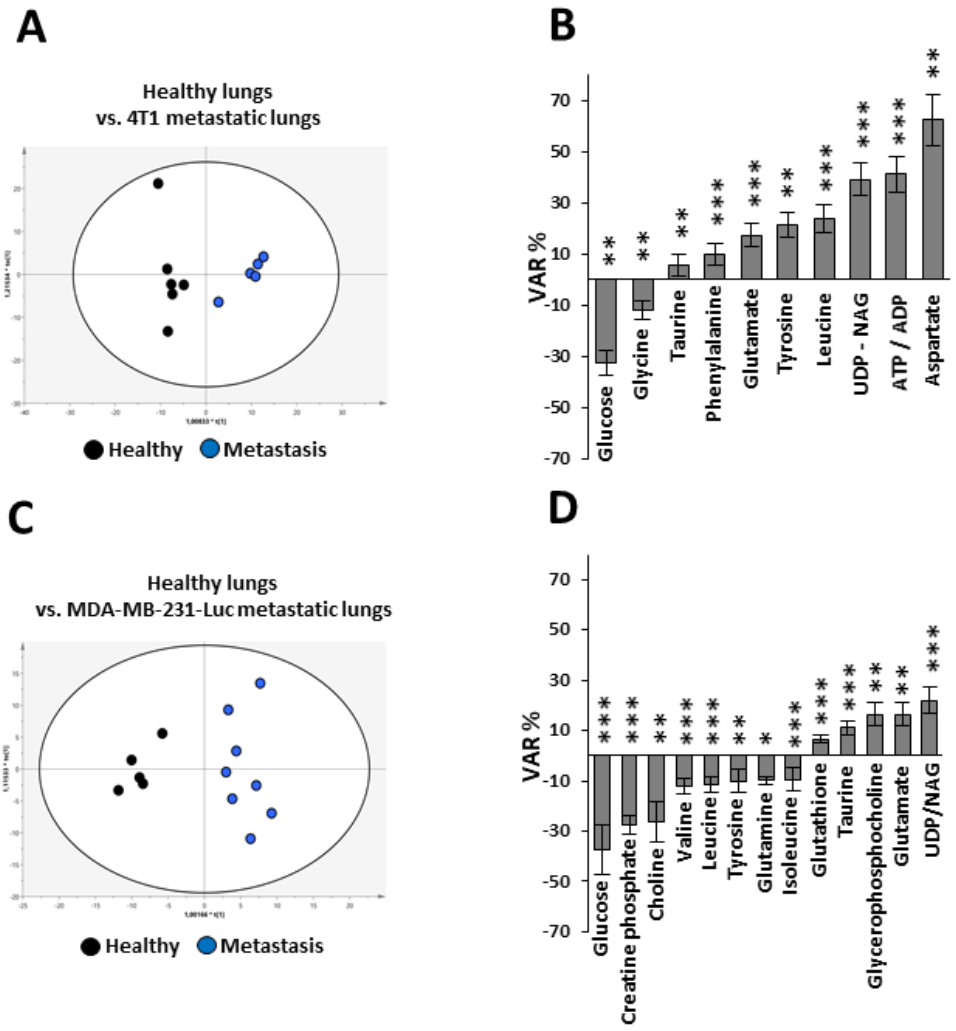

Figure 11: Multivariate modeling resulting from the analysis of lung metastases. (**A** and **C**) OPLS-DA score plot representing comparisons between healthy lung tissue vs. metastatic lung (4T1) (aqueous phase; R^2 = 0.913 / Q^2 = 0.890) and healthy lung tissue vs. metastatic lung (MDA-MB-231-Luc) (aqueous phase; R^2 = 0.921 / Q^2 = 0.806), respectively. **B**) and **D**) Metabolic changes in healthy lung tissue vs. metastatic lung (4T1) (aqueous phase) and healthy lung tissue vs. metastatic lung (MDA-MB-231-Luc) (aqueous phase) comparisons, respectively. Statistical significance determined via ANOVA t-test, (***p<0.001, ** p<0.01, *p<0.05).

At the macroscopic level, inguinal lymph node (ILN) metastases appeared in most 4T1 animals, and those with ILN metastases suffered from rapid ALN spread. Direct ALN metastasis without ILN involvement rarely occurred (**Figure 13**). However, we seldom found metastases on the right side of the body (side of inoculation) and so we focused on metastatic development from tumor to left ALN following the afferent lymphatic vessel. 4T1 ALNs appeared macroscopically normal until D17, after which we observed metastasis (**Figure 13**). Histopathological studies revealed nodes with varying

degrees of physiological activation and swelling in the absence of metastasis until D10, and the majority of mice displayed similar characteristics by the endpoint. However, some 4T1 tumor-bearing mice exhibited paracortical metastatic foci within the node hilus from D13. Mice with similar characteristics displayed widespread metastatic invasion of the ALN at D20 of tumor development. By D24, mice exhibited almost complete ALN invasion with normal morphology loss.

MDA-MB-231-Luc model macroscopic studies discovered lower variability in ALN invasion when compared to the 4T1 (**Figure 13)**. We observed no signs of metastatic spread in the first three weeks of MDA-MB-231-Luc tumor development; however, all ALNs presented with signs of medullary sinusoidal metastasis at D21-28. As expected, ALN swelling directly correlated to metastasis due to the lack of lymph node immunoreactivity and immune-related swelling. We also discovered more prominent metastasis to the left ALN in the MDA-MB-231-Luc model at advanced tumor development stage (**Figure 13**). **Figure 12** depicts time-frame metastatic spread in MDA-MB-231 ALNs.

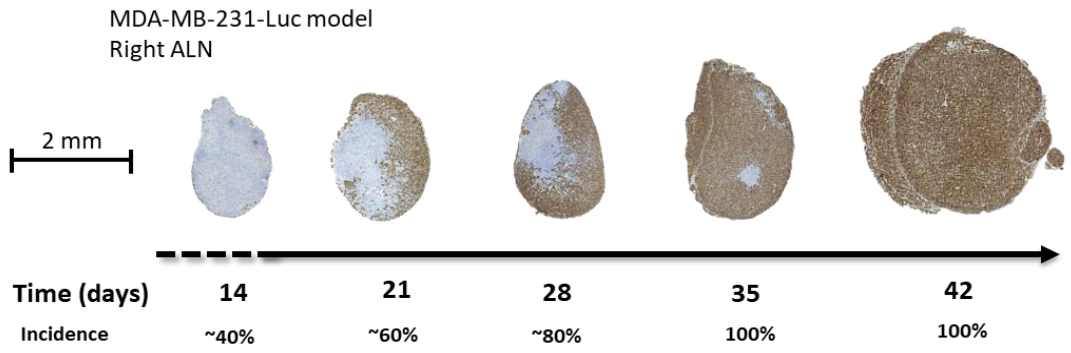

Figure 12: Right ALN metastasis progressed slowly in the MDA-MB-231-Luc model without significant node swelling. Within 14 days, tumor cells accumulated in the subcapsular sinus, and during the following weeks, tumor cells progressed along the LN stromal network toward the center of the ALN.

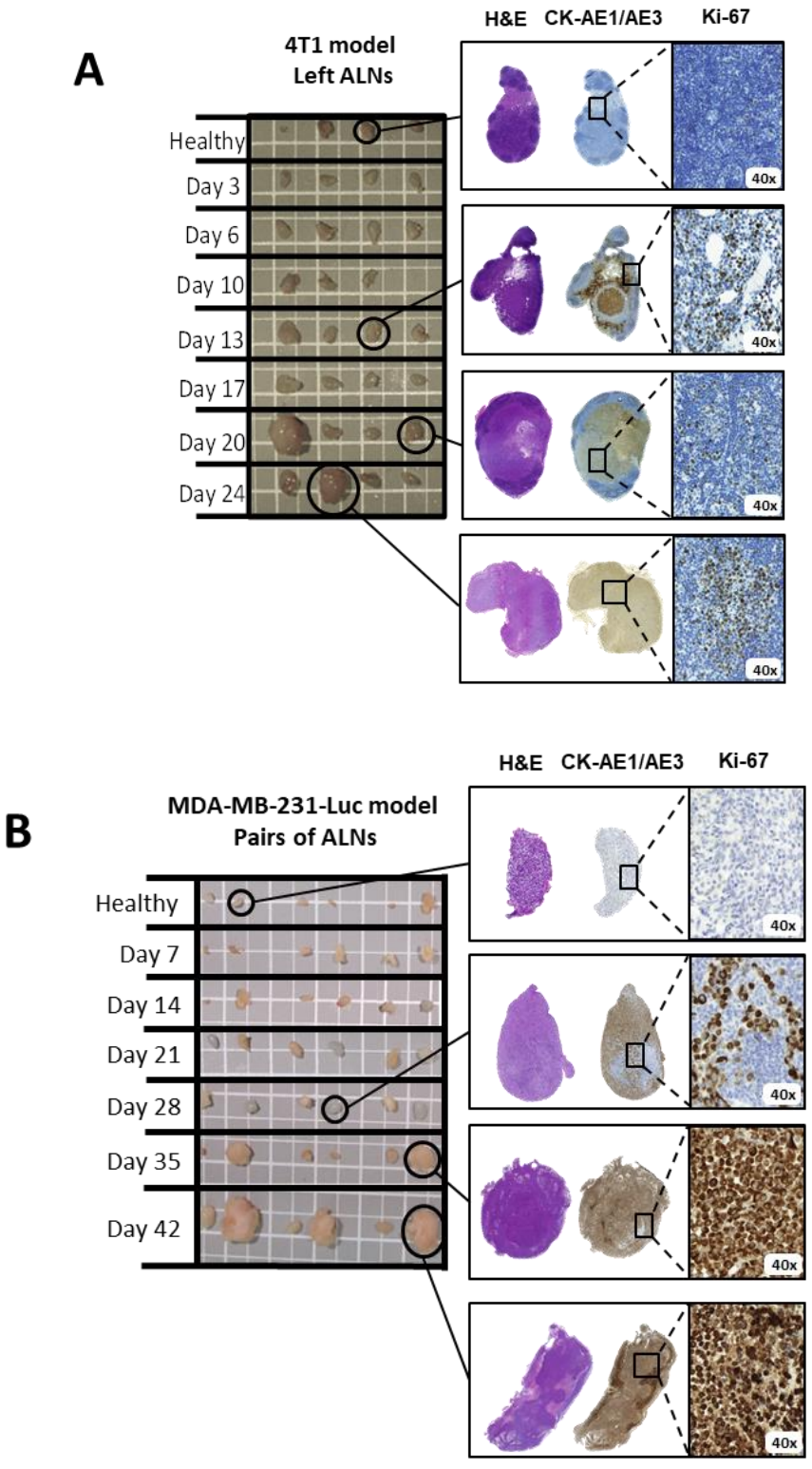

Figure 13: Evolution of ALN metastasis by H&E staining and CKAE1/AE3 and Ki-67 immunostaining. **A)** The 4T1 model displayed heterogeneous metastatic invasion in ALN, and the vast majority of animals presented metastasis in the left ALN at the experimental endpoint **B)** The MDA-MB-231-Luc model exhibited homogeneous ALN metastasis distribution. Figure displays left and right ALN.

II.2.3 Non-invasive imaging of Primary Tumor and Metastasis Development in TNBC Models

^{18}F-fluorodeoxyglucose uptake by positron emission tomography (^{18}F-FDG-PET) and computed tomography (CT) permitted *in vivo* analysis of 4T1 tumor progression[24]. **Figure 14A** depicts a three-dimensional view of 4T1 tumor development displaying uniform radiotracer uptake by the spheroidal tumor mass until D3. ^{18}F-FDG-PET also allowed the measurement of the tumor similarly to caliper measurements (**Figure 14 C**). We observed the development of an inner tumor core from D10, growing concentrically within the tumor mass, confirming previous findings and coinciding with maximal EPR effect (**Figure 5**). Analysis displayed in **Figure 14A** confirmed tumor core necrosis via the lack of radiotracer uptake. At endpoint, the necrotic region constituted around 80% of total tumor volume, and PET analysis confirmed metastasis in the left ALN only (**Figure 14B**).

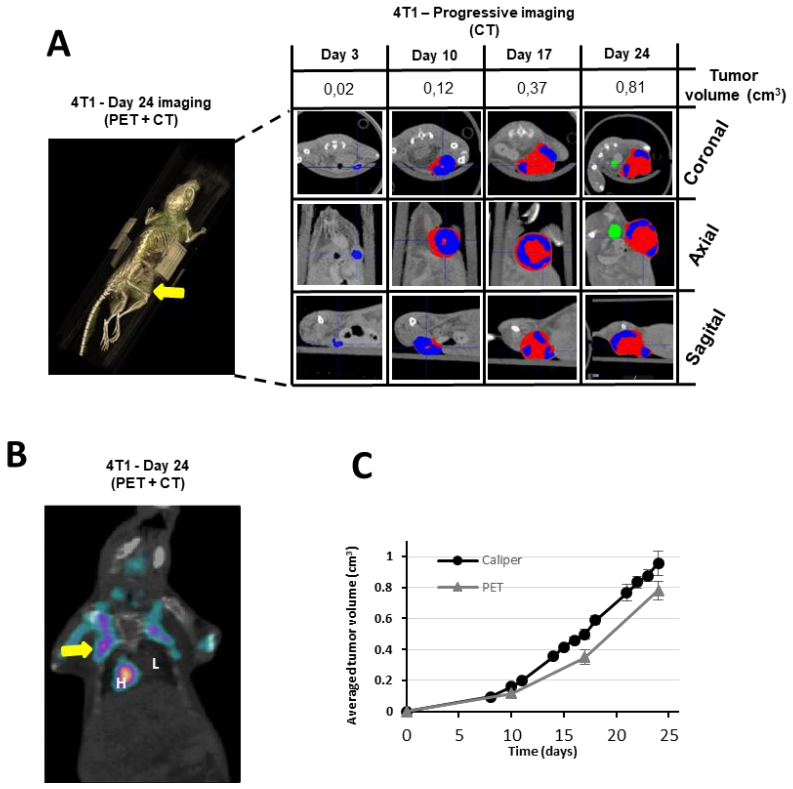

Figure 14: A) PET/CT combination permitted in vivo monitoring of 4T1 primary tumor progression. Note the increasing hypodense region developing in the tumor core corresponding to the necrotic core. **B)** Detail on metastatic spread to ALN **C)** Morphometric evaluation of 4T1 tumor comparing traditional caliper measurement with PET/CT measurement.

Inherent luciferase activity in MDA-MB-231-Luc cells permitted the *in vivo* tracking of tumor progression and quantification of distal metastasis by bioluminescence imaging (BLI) using the IVIS® system (**Figure 15**). Tumors grew uniformly until D28, after which they became amorphous, with a loss of bioluminescence, again evidencing the necrotic core. **Figure 15** also confirmed the uniform appearance of left ALN metastasis at D28 as demonstrated by histopathology (**Figure 13A**). BLI analysis at D35 revealed increased left ALN metastasis with extravasation to the right ALN, the advancement of tumor core necrosis, and metastatic spread to surrounding tissues. At endpoint, all mice displayed increased metastatic growth to the left ALN, invasion of the right ALN, and metastatic growth development in abdominal and thoracic regions.

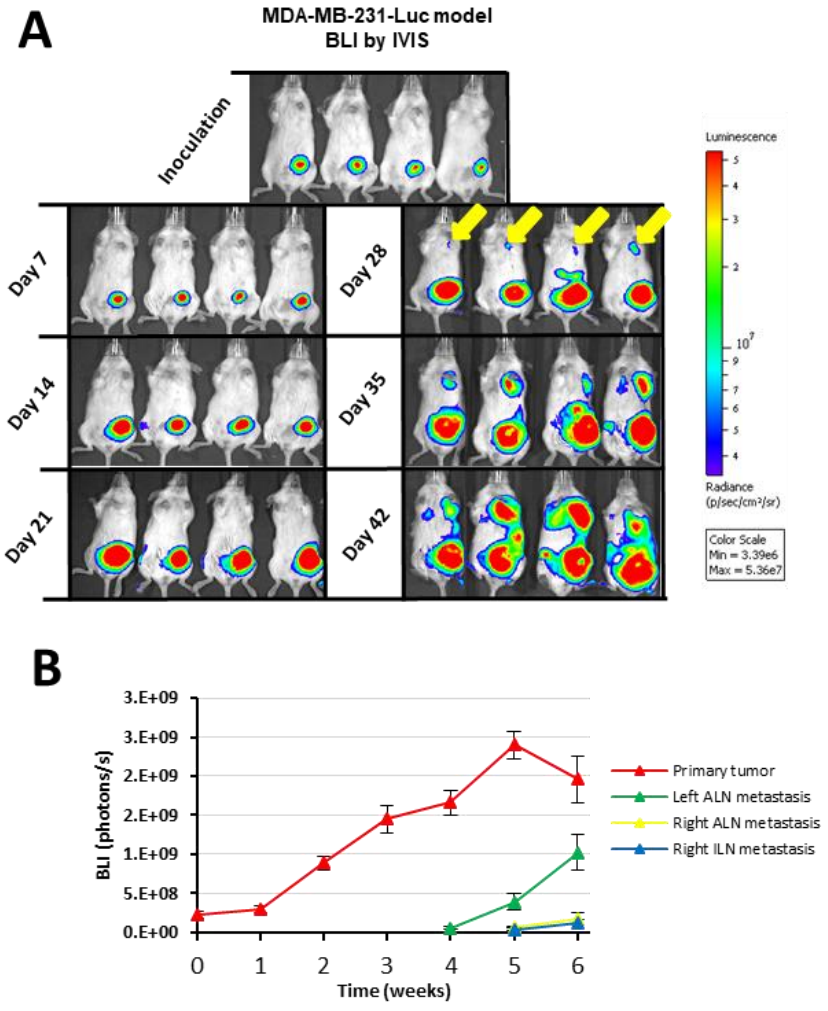

Figure 15: **A)** Tumor growth and metastatic landscape demonstrated by BLI in the MDA-MB-231-Luc tumor model. ALN metastasis noted from day 28, and necrotic tumor core noted from day 35. **B)** Quantification of ^{18}F-FDG by BLI in terms of emitted radiation.

Dynamic PET/CT analyses demonstrated a hypodense region within MDA-MB-231-Luc tumors at endpoint (**Figure 16** - red arrow); however, we observed a thinner ^{18}F-FDG labeled ring in the peritumoral region indicative of lower glucose metabolism at the tumor site. Additionally, we observed evidence of radiotracer uptake in abdominal lymph nodes around the tumor site (**Figure 16** inset). **Figure 17** shows significantly swollen left ALNs by CT. By PET, we detected the expected metastatic growth with the highest uptake located close to the afferent region of the left ALN and metastatic spread to the right ALN in the absence of swelling (as shown by CT) (**Figure 17** - yellow arrows). By CT, we also observed lung metastasis following the so-called miliary pattern[25], which describes innumerable small metastases of variable-size within the parenchyma (**Figure 17**; consistent with **Figure 9**).

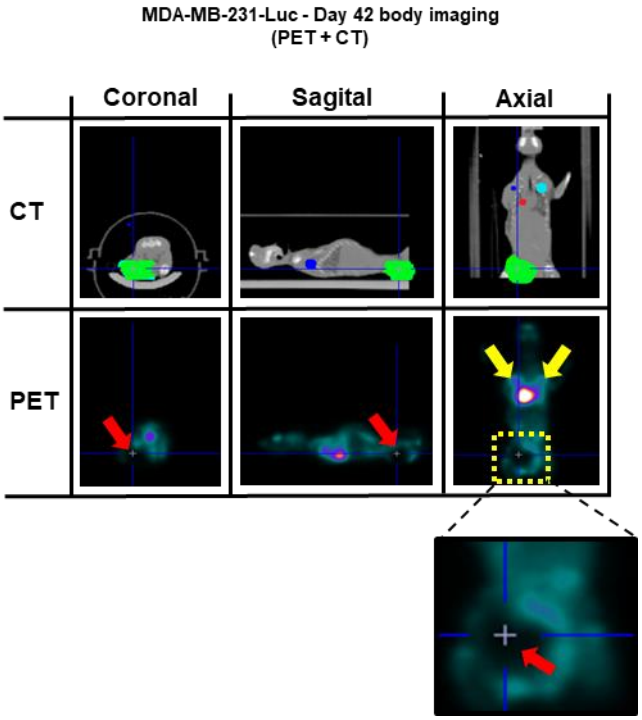

Figure 16. Three-dimensional projections of an MDA-MB-231-Luc representative mouse at the experimental endpoint. CT allowed for the delimitation of the tumor region (green region). Further PET analysis permitted the visualization of the peritumoral region, displaying a dark hollow indicative of tumor necrosis (inset, red arrow). Moreover, ILN metastasis was detectable with higher prominence on the left side (yellow arrows).

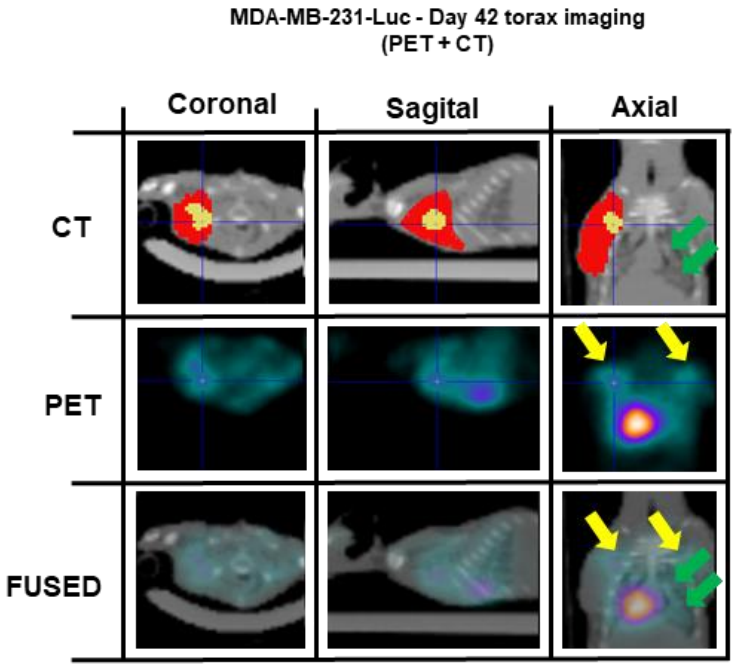

Figure 17. Thoracic region in detail. Characteristic intraparenchymatous lung metastasis detected by CT (green arrows). In addition, the swollen left ALN detected by CT (red region), but only an active metastatic region was detected by PET (yellow region) within the ALN mass.

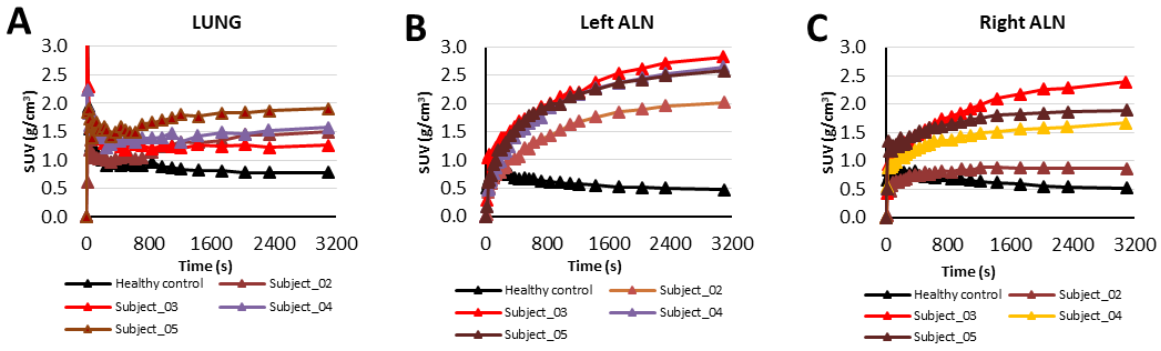

Figure 18. Quantification of ^{18}F-FDG emission in lung (**A**), left ALN (**B**) and right ALN (**C**) by dynamic PET/CT experiment over 60min.

II.2.4. Comparisons of Hematological Parameters in TNBC Models

The hematological study depicted the development of systemic pathologies during tumor growth in both models, including a marked tumor-derived inflammatory response with anemia, thrombocytosis, reticulocytosis, leukocytosis, and subsequent lymphocytosis (**Figures 19 and 20**). This profile evolved during tumor development,

although we observed model-specific alterations related to immune system status with significantly higher levels of leukocytes/lymphocytes at later stages in the 4T1 model (**Figure 20A)**. Both models exhibited reduced erythrocyte levels (around 8-10%) during tumor development, correlating to imbalanced medullary/extra-medullary hematopoiesis. We found more pronounced anemia in the 4T1 model with hemoglobin levels diminishing gradually (**Figure 20A)**. Although more pronounced in the 4T1 model, we also discovered a robust increase in reticulocytes in both models; however, in contrast, we found significantly higher thrombocyte levels in the MDA-MB-231-Luc model (around 800 $g.L^{-1}$ vs. around 400 $g.L^{-1}$) at endpoints (**Figure 20A, B)**.

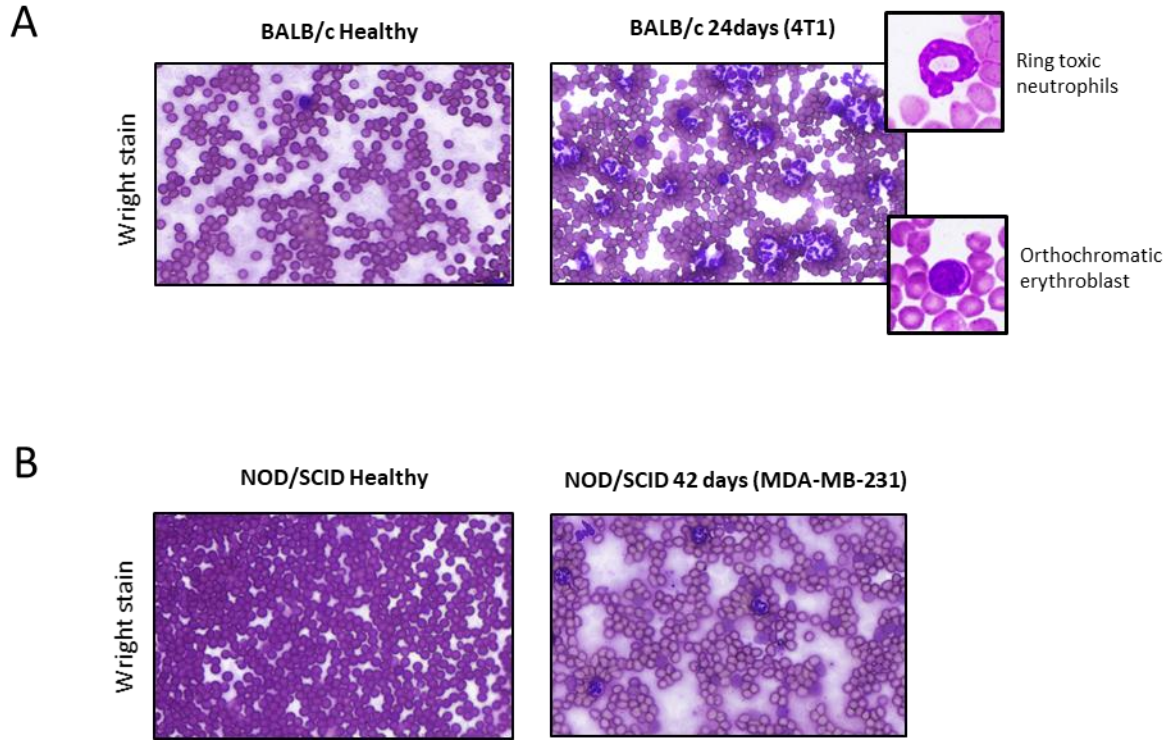

Figure 19. Comparisons of blood smears from healthy and endpoint animals in the (**A**) 4T1 and (**B**) MDA-MB-231-Luc models. Stronger acute leukocytosis stronger is appreciable in the 4T1 model. Abnormal and immature cells can occasionally be found (e.g., immature neutrophils or orthochromatic erythroblasts). Magnification: 30x

While a severe leukemoid reaction occurred from D10 in the 4T1 model (around 160 $g.L^{-1}$), we only observed a slight effect in the MDA-MB-231-Luc model (around 27 $g.L^{-1}$) close to endpoint (**Figure 20B**). In both models, segmented neutrophils accounted for around 33% of leukocyte number before tumor cell inoculation and around 85% at the endpoints. We also observed a differential lymphoid reaction between the models, in

agreement with leukocyte counts. Wright-stained blood smears confirmed results by allowing comparisons with data from healthy mice with tumor model endpoint data (**Figure 19**). Although we observed a more moderate response in MDA-MB-231-Luc, both models exhibited extensive granulocytosis (left shift) with predominant levels of polynuclear-segmented leukocytes.

Immunophoretic analysis of blood serum revealed a significant and sudden increase in gamma globulin and alpha 2 globulin levels and a decrease in albumin levels at D42 in the MDA-MB-231-Luc model (**Figure 21**). Moreover, we found increased beta globulin bands in 4T1 (D3) and MDA-MB-231-Luc (D35) models, coinciding with the first evidence of lung metastasis (**Figure 21**).

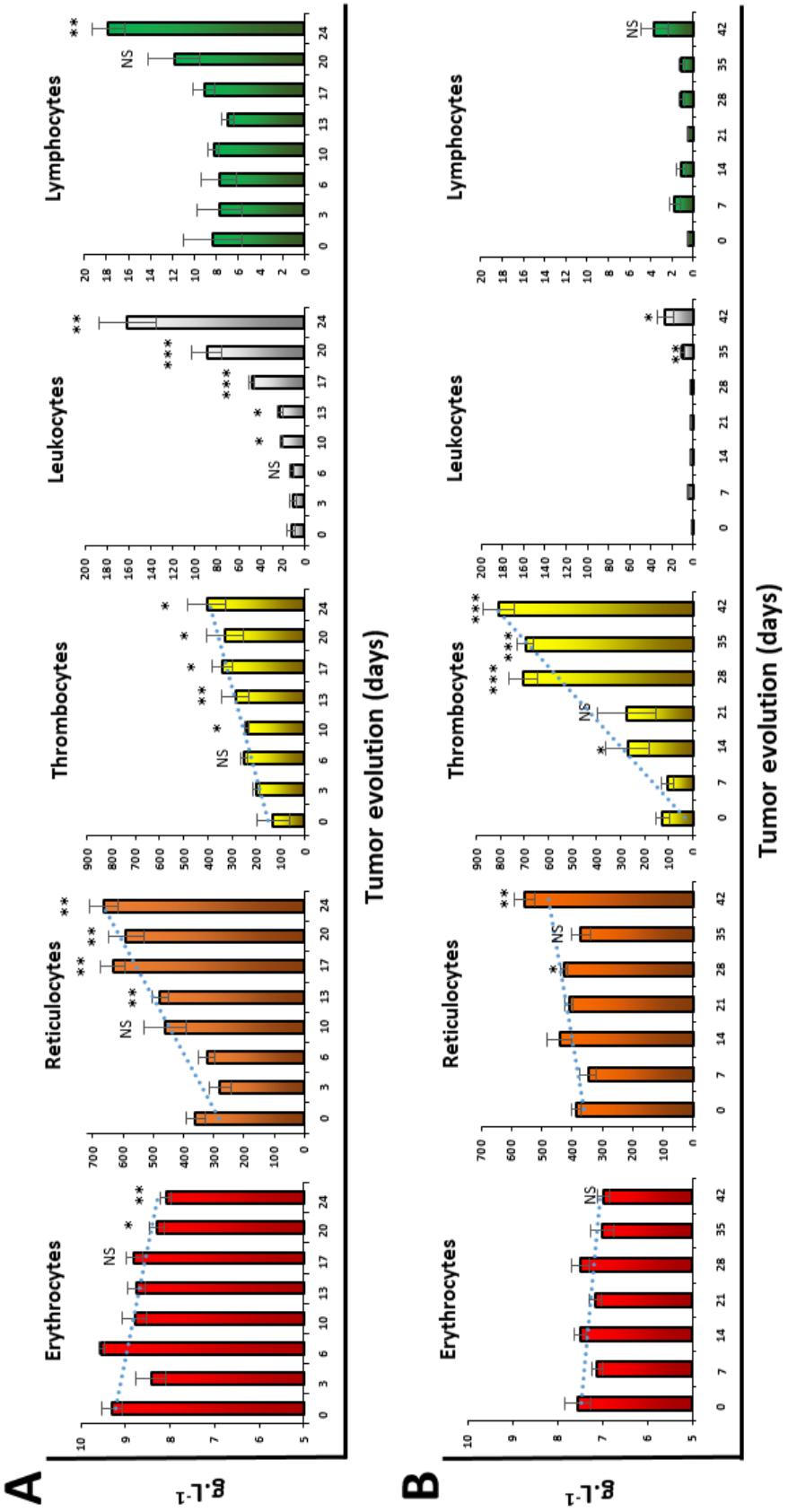

Figure 20: Complete hemogram of (**A**) 4T1 and (**B**) MDA-MB-231-Luc model

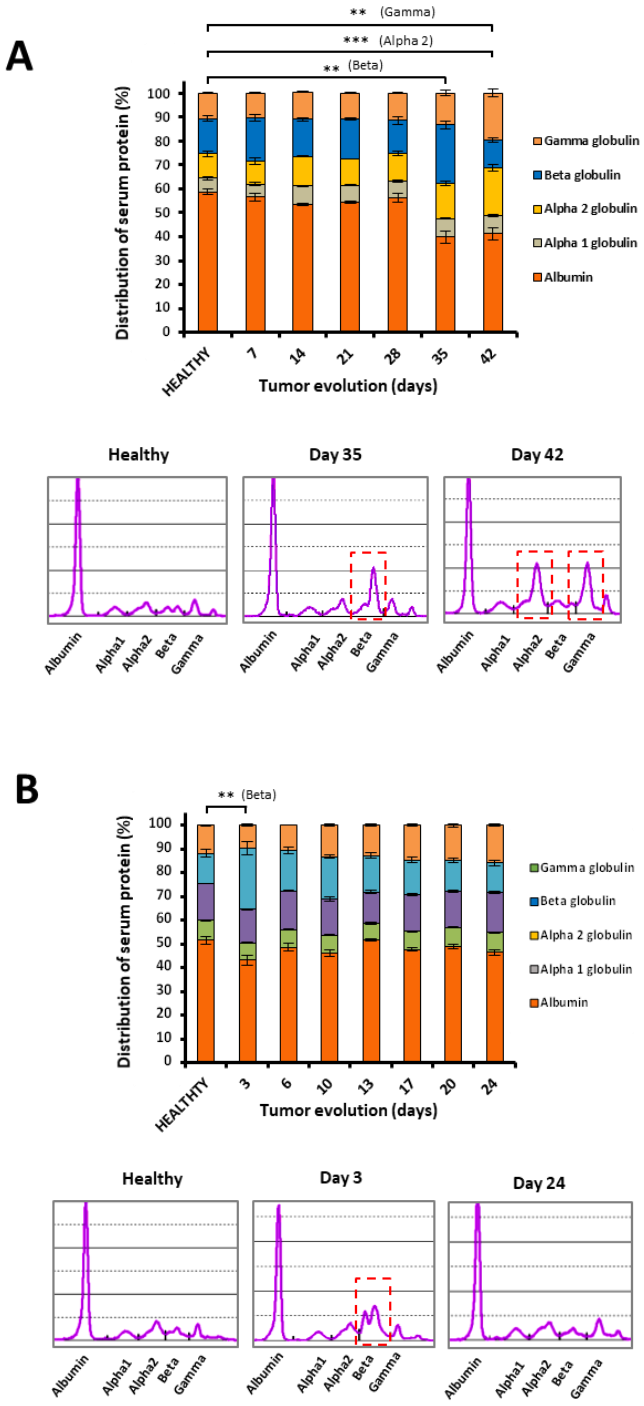

Figure 21. Proteinograms of peripheral blood in both models during tumor progression displayed in **A)** 4T1 and **B)** MDA-MB-231-Luc models. Beta hyperglobulinemia found in both models at the same time that lung metastasis evolved (D3 for the 4T1 model and D35 for the MDA-MB-231-Luc model). Data represent mean ± SEM. Statistical significance was determined via ANOVA t-test, (*** $p<0.001$, ** $p<0.01$, *$p<0.05$). The MDA-MB-231-Luc model displayed acute bands in the alpha immunoglobulin and gamma immunoglobulin, a profile compatible with ongoing inflammatory processes (increased alpha-2 globulin), while the unspecific hypoalbuminemia is consistent with previously mentioned pathologies in a chronic scenario.

Exosomes play crucial roles in conditioning the pre-metastatic niche[26], and we employed NTA of peripheral blood serum to assess exosomal dynamics during tumor progression. We discovered peak exosome levels on the first appearance of metastasis (D3) in 4T1 (**Figure 22**), before returning to basal levels. However, we did not observe any fluctuations during tumor progression in the MDA-MB-231-Luc model.

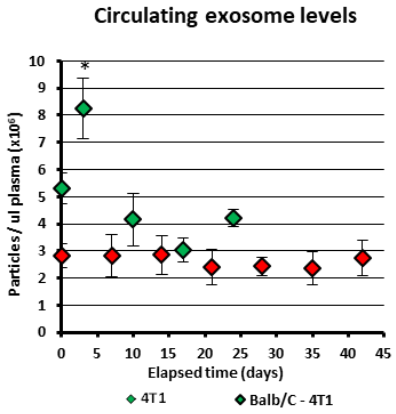

Figure 22: Comparisons of circulating exosome levels during tumor progression for both tumor models.

Directly correlated with the immune system status, inflammatory response markers may predict clinical outcomes in cancer patients, and so, we evaluated the neutrophil-lymphocyte-ratio (NLR), finding a rapid increase from D6 in the 4T1 model (**Figure 23A**). As an innate immune system effector, the complement system constitutes the first barrier against non-self-cells and plays a decisive role in tumor growth [27]. In agreement, 4T1 animals displayed increasing levels of C-3 protein from D20 (**Figure 23B).**

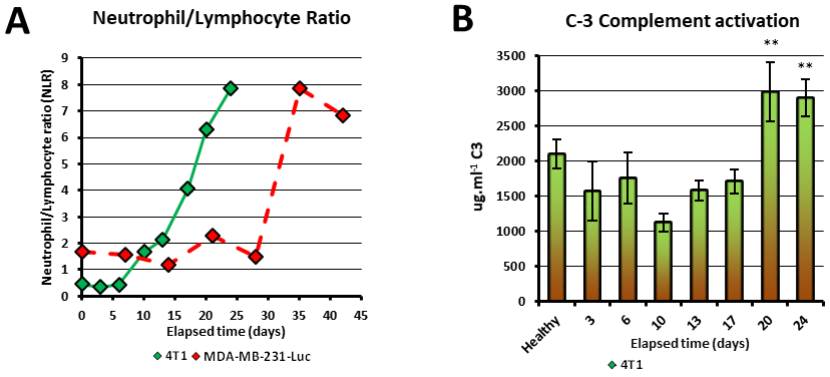

Figure 23: **A)** Neutrophil/Lymphocyte ratio (NLR). The MDA-MB-231-Luc mouse NLR is included for comparative purposes, although the immunocompromised character of the NOD/SCID mice does not permit a proper comparison. **B)** Complement system activation of the 4T1 tumor model.

II.2.5. Dysregulated Bone Marrow Hematopoiesis in TNBC Models: A role for G-CSF in Extramedullary Hematopoiesis

Initial macroscopic organ analysis indicated acute splenomegaly (0.6% to 4% total body weight from D6 to D24) and slight hepatomegaly (4.8% to 6% total body weight over 24 days) (**Figure 24**) in the 4T1 model, but not the MDA-MB-231-Luc model.

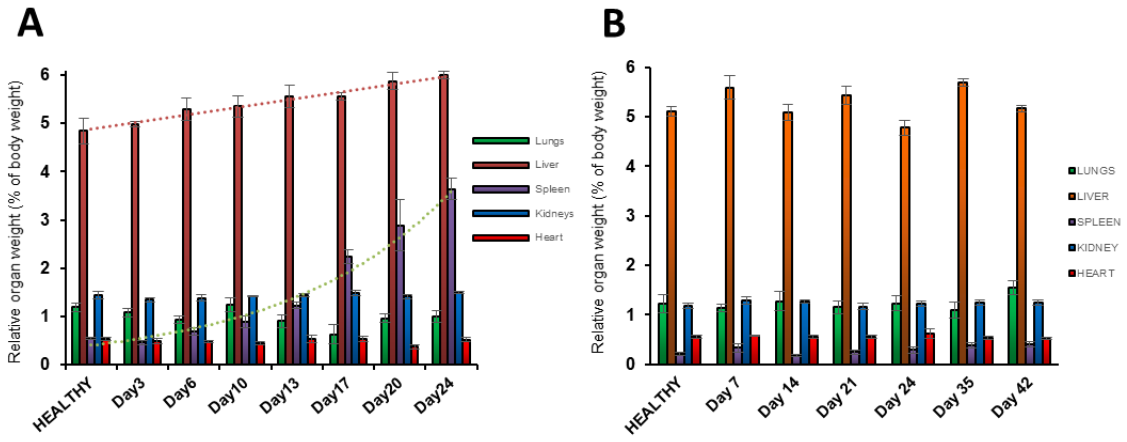

Figure 24: **A)** Analysis of major organs weight in the 4T1 model revealed slight hepatomegaly and acute splenomegaly along tumor progression. **B**) No significant alterations in organ weight observed in the MDA-MB-231- tumor model.

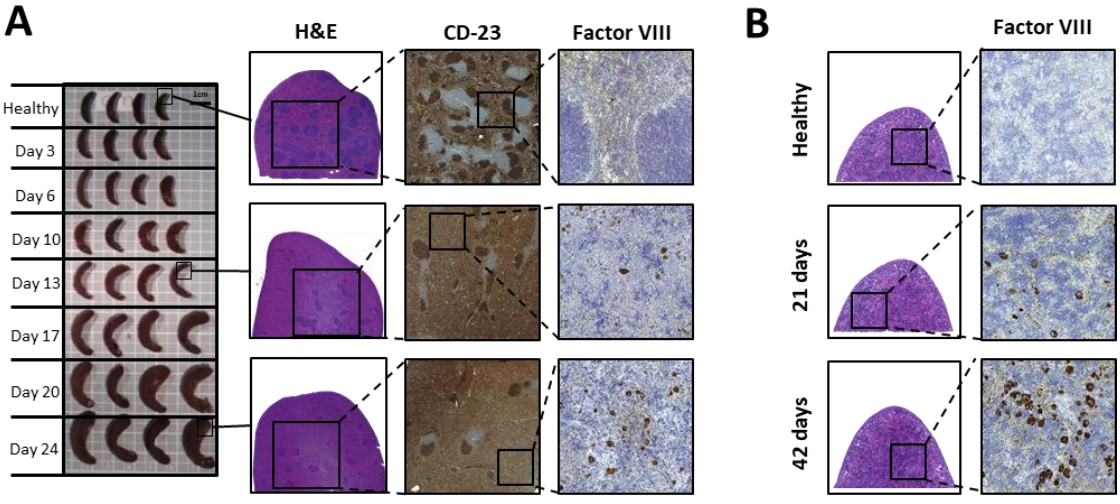

Figure 25 A) Congestion of the spleen red pulp as consequence of the adaptive HE and megakaryocytosis revealed by Factor VIII immunostaining. **B)** Spleen in MDA-MB-231-Luc animals did not suffer from splenomegaly. However, an acute megakaryopoiesis was revealed by Factor VIII immunostaining.

Histopathological studies of bone marrow uncovered reduced megakaryocytosis (Factor VIII), reduced myeloid cell precursors (myeloperoxidase), and enhanced granulocytosis (CD-15) compared to healthy tissues (**Figure 26)**, supporting extramedullary hematopoiesis (EH) promoted by bone marrow myelosuppression (in agreement with previous hematological findings).

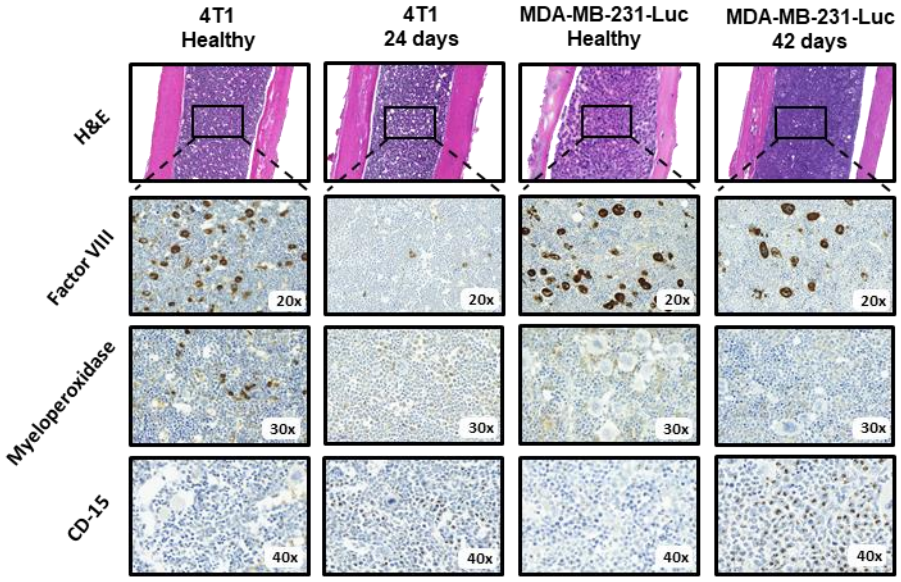

Figure 26: G-CSF impedes the normal maturation of myeloid cell precursors in bone marrow. Factor VIII immunostaining demonstrates the severely reduced megakaryocyte production of the 4T1 model in comparison with healthy animals in contrast to the slight reduction observed in the MDA-MB-231-Luc model. The loss of myeloid cells in both models was observed by myeloperoxidase staining. Presence of granulocytes in bone marrow at endpoints in both models is depicted by CD-15 immunostaining.

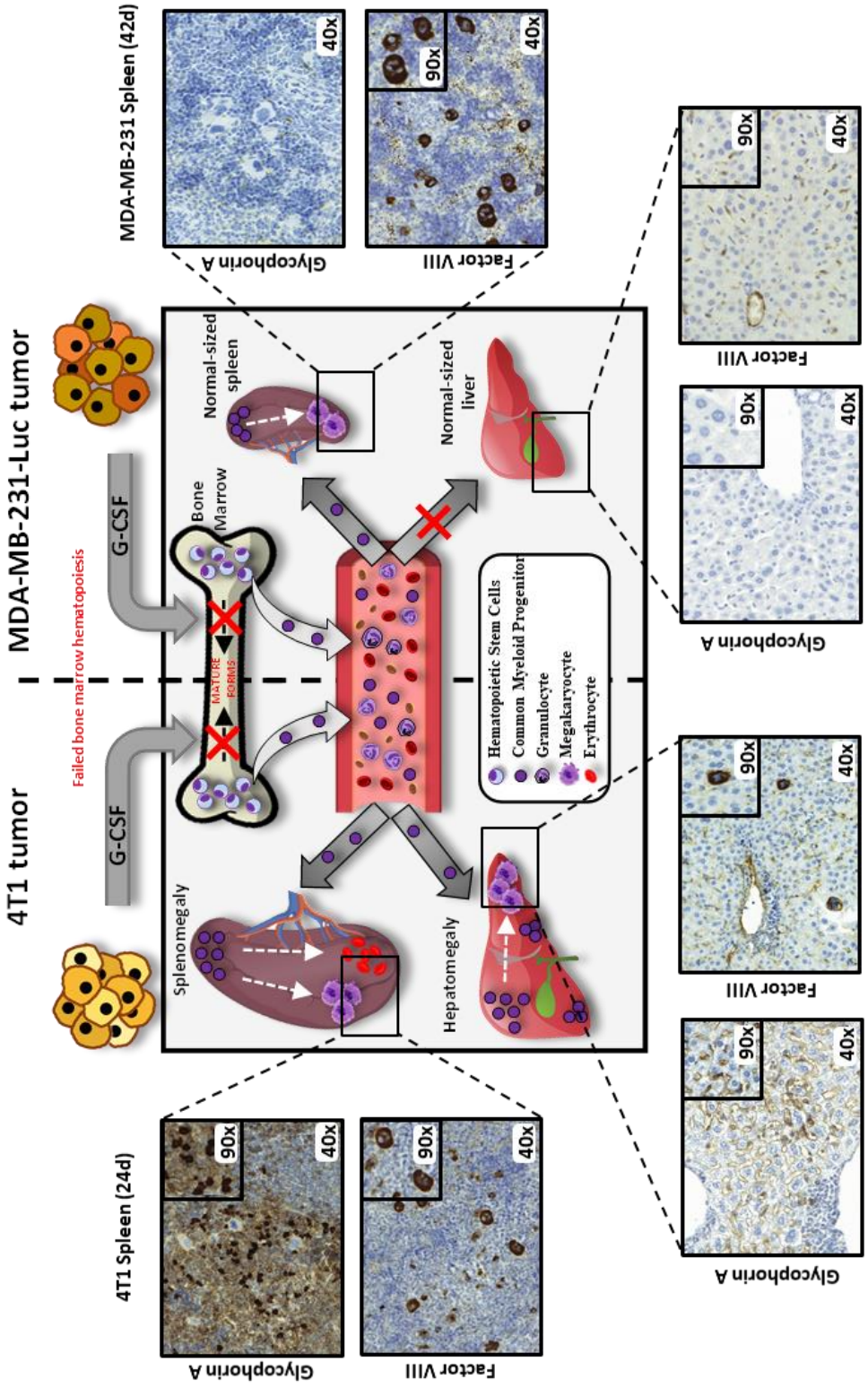

Figure 27 (**A**). 4T1 and MDAMB-231-Luc cells secrete G-CSF, which activates extramedullary hematopoiesis by stimulating the release of immature myeloid precursors. The 4T1 model presented hepatosplenomegaly as result of erythropoiesis and megakaryopoiesis in the spleen and megakaryopoiesis in the liver. Multiple colonies of myeloid cell precursors found in the liver. (**B**). The MDA-MB-231-Luc model does not present with hepatosplenomegaly; however, megakaryopoiesis takes place in the spleen.

Analysis of the enlarged spleen of the 4T1 model supported EH by reactive megakaryocytic hyperplasia, as evidenced by large numbers of Factor VIII-positive megakaryocytes, and ongoing erythropoiesis, as evidenced by Glycophorin A-positive erythroid-precursors and mature erythrocytes (**Figure 27**). Further studies revealed increased cellularity and congested red pulp with hyperplasia due to elevated reactive hematopoiesis (**Figure 25**). Studies of the MDA-MB-231-Luc model normal-sized spleen highlighted reactive megakaryocytic hyperplasia as the unique pathological consequence of EH (**Figure 27**).

In the 4T1 model, we observed overt signs of EH in the liver, as evidenced by increased myeloid precursor cell (MPC) perivascular infiltration into the surrounding hepatic arteries starting from D3. At later stages, MPCs entered the liver parenchyma to induce reactive megakaryocytic hyperplasia (**Figure 27**). In contrast, MDA-MB-231-Luc model liver developed no significant macroscopic or histopathological abnormalities.

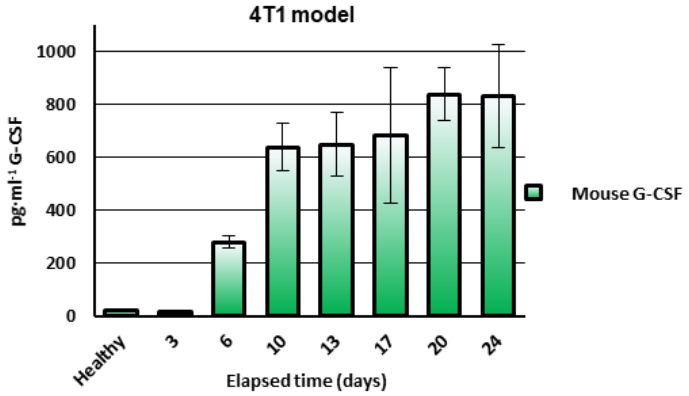

Figure 28: G-CSF levels in the 4T1 tumor model during tumor progression

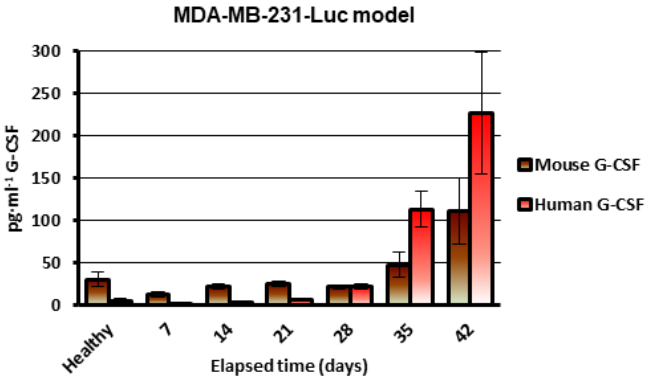

Figure 29: Human and mouse-derived G-CSF levels in the MDA-MB-231 tumor model during tumor progression.

To understand EH origin, we conducted immunoassays to analyze circulating granulocyte colony stimulating factor (G-CSF) levels[28]. We discovered increasing levels of total G-CSF in 4T1 model peripheral blood at early stages of tumor development (**Figure 28**), in agreement with previous studies in immunocompetent mouse models[29]. We also discovered increasing levels of tumor- and host-derived G-CSF during MDA-MB-231-Luc tumor progression **(Figure 29)**. Of note, only *in vitro* studies have previously shown G-CSF secretion from MDA-MB-231 cells[30]. High human G-CSF levels in MDA-MB-231-Luc started increasing from D28 (**Figure 29**) and correlated to the previously observed leukemoid/lymphoid reactions.

II.3. Discussion

The accelerated development of advanced anti-cancer therapies requires adequate preclinical models and the identification of functional biomarkers to facilitate clinical translation [31] and identification of patients that would benefit from said therapies [32]. In this study, we report the exhaustive characterization of relevant preclinical TNBC mouse models regarding systemic landscape, metastatic foci, and metabolic alterations, paying particular attention to functional biomarkers. Both models develop homogeneous primary tumors with subsequent ALN and lungs metastasis, faithfully mimicking critical features of the human disease. Therefore, these models offer a useful platform for testing/validation of advanced anticancer therapeutics, especially for the treatment of patients presenting with both primary tumors and metastasis.

II.3.1. Modeling Capacities of the 4T1 and MDA-MB-231-Luc TNBC Models

The rapid tumorigenic development encountered for the 4T1 model offers a rapid and straightforward means to assess treatment outcomes in an immunocompetent model. Model characteristics include aggressive primary tumor evolution as densely packed masses with slight anemia, thrombocytosis, and reticulocytosis in the short term, and an acute leukemoid reaction with lymphocytosis and complement system activation in the mid-to-long term. In comparison, the MDA-MB-231-Luc model displayed slower tumor growth with marked spontaneous inclusion of CAAs, known to exhibit an activated

phenotype linked to the acquisition of a pro-invasive effect of surrounding tumor cells [19]. Therefore, high CAA content of MDA-MB-231-Luc tumors may serve as a faithful model to study this phenomenon and develop treatments to avoid adipocytic pro-tumorigenic effects. Furthermore, high lipid content and low cellular density in the tumor stroma generated a softer tumor mass with a three-fold higher EPR effect, thereby providing a model to assess EPR-related passive tumor accumulation, especially important for the effectiveness of nanomedicinal approaches to cancer treatment [18]. The flexibility and permeability of the MDA-MB-231-Luc model stroma may also provide a means to assess intratumoral administration strategies [33].

The metabolomic comparison of 4T1 and MDA-MB-231-Luc primary tumors suggests that specific metabolic alterations could explain the differences observed in growth rates, with guanosine and uracil (a pyrimidine derivative) the two most relevant soluble metabolites contributing to model discrimination. Interestingly, Tayyari *et al*. [34] reported that TNBC tumors displayed increased pyrimidine synthesis and elevated levels of myoinositol and taurine, similar to findings in our 4T1 primary tumors. Metabolomic analysis of organic extracts provided further evidence for lipidic reprogramming in TNBC development and progression; in particular, 4T1 primary tumors displayed higher concentrations of cholesterol and phospholipids. These alterations reflect the avidity of proliferative cancer cells for lipids and cholesterol [35], a characteristic now considered a hallmark of cancer aggressiveness [35, 36]. MDA-MB-231-Luc primary tumors also displayed high levels of TAGs, whose hydrolysis in adipocytes adjacent to cancer cells generates free fatty acids for use as an energy source by tumor cells for tumor progression [35].

We observed spontaneous lung and ALN metastasis in both models; however, while studies suggest that the 4T1 model develops lung metastasis via the hematogenous route [20], we discovered earlier evidence of distal metastasis and subsequent rapid development predominantly through the lymphatic system, as observed in two recent studies [37, 38]. Therefore, the 4T1 mouse model is ideal for the development and validation of lymph-targeted anti-cancer therapies [39]. Additionally, alterations to the complement system in the 4T1 model may provide a prognostic marker of disease progression or even a sign of treatment efficiency when using non-immunogenic therapeutics (a safety requirement for systemic administration).

II.3.2. Role of G-CSF as a Critical Functional Biomarker of Metastatic Progression

The colony-stimulating factor (CSF) subfamily of glycoproteins play crucial roles in inflammatory cell activation [40], bone marrow cell mobilization into the peripheral blood, and immune system activation [41]. Increasing levels of G-CSF during 4T1 tumor progression [29] may trigger passive compensatory EH and the concomitant leukemoid reaction with prominent hepatosplenomegaly [29]. The leukemoid reaction is a well-described paraneoplastic affection, arising in around 15% of cancer patients, proposed as a prognostic marker for BC [42] thereby ratifying the suitability of our 4T1 model as preclinical BC model.

The MDA-MB-231-Luc model presented similar hematological parameters to the 4T1 model at early stages; however, we did not observe a leukemoid reaction accompanying tumor growth, and the first evidence of metastasis occurred at later time points through the hematological pathway. Importantly we observed that tumor- and host-derived G-CSF release concomitant with metastasis, led to the partial restoration of the immune system (granulocytosis and lymphocytosis) suggesting a "metastatic switch" appearing from the fourth week to trigger an immunological response in the immunosuppressed NOD/SCID mouse model. This suggests that stromal cells and/or host tumor-infiltrating cells also represent a significant G-CSF source [43]. Although the reduced immunological competency of the host does not permit extended adaptive splenomegaly or hepatomegaly in this model, we observed slight passive EH in the spleen as a response to bone marrow myelosuppression. Surprisingly, we only observed lung metastasis from D28, concomitant with human G-CSF release. Studies have proposed the indirect role of G-CSF in pre-metastatic niche formation [44], a finding supported by our MDA-MB-231-Luc model discoveries. Therefore, we propose circulating G-CSF levels as a prognostic indicator of disease and more importantly, the inhibition of cytokines such as CSFs as a promising therapeutic approach alone or in combination with metastatic inhibitors. We do note that the possible role of either human or host G-CSF in the immune system reactivation of the NOD/SCID mice remains unresolved; although the leukemoid reaction triggered by the release of G-CSF may be responsible for metastasis spread.

Our work emphasizes the active role of the immune system in metastatic spread in both models [45]. We suggest, after the sudden changes at week four, that a quiescent MDA-MB-231-Luc tumor subpopulation reactivates through a likely "metastatic switch". Several tumor-derived factors could be involved in the generation of pre-metastatic niche, and their overexpression could be a prerequisite for metastasis development.

II.3.3. Other Biomarkers and Predictive Factors

Exosomes have emerged as regulators of inter- and intra-cellular communication and can "tailor" the pre-metastatic niche for engraftment of cancer cells [26]. Interestingly, the 4T1 model displayed significantly increased circulating blood exosomes at D3, simultaneous with the first evidence of lung metastasis, suggesting its active role in lung metastasis establishment [26]. However, we did not find any modulation in exosome levels in MDA-MB-231-Luc.

The prompt hyper-β-immunoglobulinemia detected in both models coincided with first signs of lung metastasis. Transferrin overexpression may be connected to neovascularization to influence metastatic capacity in BC [46]. Transferrin-like lipoproteins can specifically stimulate metastatic cell growth [47]. Similarly, β-lipoprotein (LDL) is intimately involved in angiogenic regulation, with a direct connection between LDL levels and metastatic progress [48]. In this context, our metabolomics analyses confirmed that lipid metabolism alterations closely associates with TNBC malignancy and metastatic progression to the lungs.

Finally, studies have demonstrated that NLR associates with poorer prognosis in human cancers [49]; high NLR associates with reduced disease-free survival (DFS). Applying this prognostic factor in our 4T1 model, NLR values indicate worse prognosis from D6-10, mimicking advanced stages of the disease and providing a tool to develop therapeutics devoted to recurrent or metastatic scenarios.

II.3.4. Metabolomic Metastatic Signature

Metabolomic analysis of lung tissues revealed distinct signatures for both models. Some metabolites exhibited the same trend when comparing metastatic and healthy lung tissues (taurine, glutamate, UDP-NAG, glucose), reflecting common alterations. For example, the metabolism of glutamate/glutamine and taurine/hypotaurine plays a significant role in TNBC [34], and UDP-derivatives have been linked to metastasis [50]. A second important group of metabolites, mostly composed of amino acids, exhibited changes in the opposite direction when comparing metastatic and healthy lung tissues. The differences in amino acids levels may relate to different growth kinetics; much faster for the 4T1 model, therefore, requiring more energy. Of note, several amino acids that exhibited lower concentrations in the MDA-MB-231-Luc model metastatic lung (i.e., leucine, isoleucine, and valine) are branched amino acids (BCAA), and studies have indicated an association between increased concentrations of BCAA and chemotherapy-induced apoptotic processes [51]. Interestingly, the ratio of choline/GPC indicates the acidic nature of metastatic tumors, since lower pH (typical of tumor cells) leads to decreased PC and increased GPC [52]. High glutamine consumption correlates with the essential function of glutaminase in TNBC development [53]. Decreased creatine phosphate levels, perhaps related to hypoxic regions within the metastasis [54], also correlate with the reduced pH characteristic of tumors.

We also found several unique metabolic changes for each model. In 4T1 metastatic lungs, we discovered increased phenylalanine levels [55] (related with advanced stages of the disease), aspartate [51] (upregulated glutaminolysis) and ATP+ADP (fueling metastatic survival). Analysis of MDA-MB-231-Luc metastatic lungs revealed a specific increase in glutathione levels, a molecule that plays protective and pathogenic roles and promotes chemoresistance [56], and GPC levels. Overall, the metabolomic signature for lung metastases in each model reflects the different molecular and biochemical mechanisms associated with metastatic spread, which could be employed as a biomarker for disease monitoring during preclinical evaluation.

Finally, we note certain limitations to our study. Our human model only represents one subtype (representing around 15% of all TNBC); similar analyses of additional major TNBC subtypes could uncover clinically relevant information. We also note the lack of tumor resection during the study of metastasis (which would more closely follow the

clinical situation); however, we believe that studying metastasis in the presence of the primary tumor can aid the development of therapies aimed at patients presenting with both tumor modalities.

BALB/cOlaHsd 4T1 breast carcinoma cell line (murine)	NOD.CB17-Prkdcscid/NCrHsd MDA-MB-231-Luc breast carcinoma (human)
→ Early stage drug discovery (screening)	→ Mid-to-late stage drug discovery (screening)
→ Necrosis and tumor microenvironment studies	→ Studies on relationship between metastasis spread and stromal CAA
→ Faithfully mimicking of stage-specific histological and biochemical aspects of human disease	→ Mimics human disease in immunosuppressed conditions
	→ Adequate for intratumor administration
→ Similar human immune response to tumor	→ Metastatic spread by non-invasive imaging techniques (BLI and PET/CT)
→ Suitability for cancer-induced leukocytosis study	→ Increased passive accumulation of nanotherapeutics via greater EPR effect
→ Preferential lymphatic route for metastatic spread to lung	→ Preferential hematic route for metastatic spread to lung
→ Ideal for evaluation of effects on immune surveillance	→ Facilitates assessment of human biomarkers and predictors

Table 1. Suggested suitability for different aspects of therapy development, demonstrating evident complementarity of the models for TNBC drug discovery and validation.

II.4. Conclusions

Within this present study, we describe the progression of two preclinical spontaneously metastatic TNBC models relevant for the development of anti-cancer therapeutics. We concentrated on the pathological features that ultimately drive anti-cancer treatment and, therefore, patient outcomes. Our exhaustive characterization demonstrated MDA-MB-231-Luc metastatic progression in the NOD/SCID model. We also discovered a metastatic switch in both models (MDA-MB-231-Luc and 4T1) with immune system activation and serum-protein profile reconfiguration, which may support resistance to treatment and recurrence in TNBC. The detailed characterization of relevant models such as these will help to foster the rational design of anti-cancer therapeutics. Importantly, we identified critical functional biomarkers including the EPR effect, G-CSF, CAA infiltration, NLR, complement activation, and metabolomic signatures for metastasis progression that may further facilitate the development of anti-cancer therapeutics.

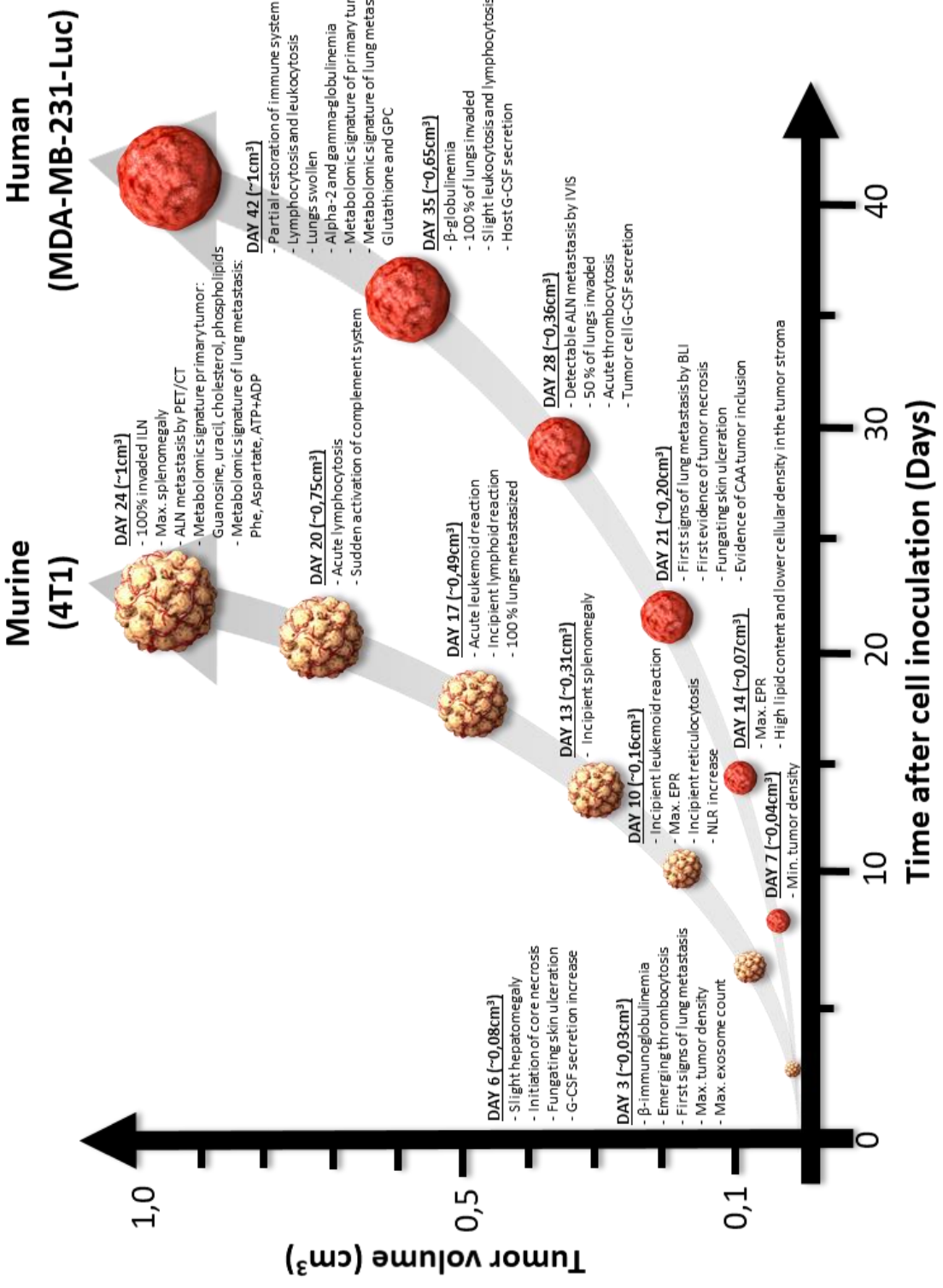

Figure 30: Timeline of TNBC tumor progression indicating main differential features between 4T1 and MDA-MB231-Luc regarding primary tumor, including stroma and metastatic sites. CAA. Cancer-Associated Adipocytes, EPR: Enhanced Permeability and Retention Effect, G-CSF: Granulocyte colony-stimulating factor, GPC: glycerylphosphorylcholine, TGA: Triacylglycerol.

II.5. Materials and Methods

II.5.1. Cell culture and Cell Characterization

The 4T1 breast cancer cell line was obtained from ATTC ® (EU) and maintained in RPMI (Roswell Park Memorial Institute) Media 1640 supplemented with 10% heat-inactivated Fetal Bovine Serum (FBS) using standard tissue culture conditions. The MDA-MB-231-Luc cell line was obtained and characterized at the Functional Validation & Preclinical Research (FVPR) of CIBBIM-Nanomedicine working as the Unit 20 of the ICTS "NANBIOSIS" (http://www.nanbiosis.es/portfolio/u20-in-vivo-experimental-platform/) (Barcelona, Spain). The cells were routinely maintained in Dulbecco's modified Eagle's medium / Nutrient Mixture F-12 (DMEM/F12, Gibco) supplemented with 10% FBS and 500 μg/mL Geneticin (Gibco) at 37 °C in a humidified atmosphere with 5% CO_2. In both cases, media was replaced every 2 - 3 days and underwent passaging once cells reached 80% cell confluence. The MDA-MB-231-Luc cell line was fully characterized by western blotting in terms of HER2 (ErbB2, BioVision Ref 3783-100), Estrogen Receptor (ER-alpha, Cell Signaling #8644), and Progesterone Receptor (PR-beta, Cell Signaling #3157) expression. Luciferase transfection efficiency and bioluminescence maintenance were analyzed before proceeding.

II.5.2. Mouse Strains

The 6 to 8 week-old female inbred immunocompetent BALB/c (BALB/cOlaHsd) mice or the immunodeficient non-obese diabetic NOD/SCID (NOD.CB17-*Prkdc*^{scid}/NCrHsd) mice used for all the experimental procedures were purchased from Envigo Laboratories Inc. (Spain, EU).

II.5.3. Ethical Considerations

Animal experiments were performed in accordance with the European Communities Council Directive (86/609/ECC) guidelines and by the Spanish Royal Decree 1201/2005. All the experimental procedures were approved by the Institutional

Animal Care and Use Committee and accomplished by accredited and trained staff, meeting the animal care rules. All mice were maintained in a specific-pathogen-free facility, under temperature, humidity, and using a 12h light-dark cycle. Food pellets and water were provided ad-libitum during the whole experiments in all cases and general aspect, grooming conduct, tumor size, body weight, and behavior were evaluated daily from the beginning of the experiment to ensure animal wellness. Tumor development did not lead to weight loss in the animals, nor pain-related behavior.

II.5.4. Establishment of Spontaneously Metastatic Primary Tumor Models

4T1 orthotopic tumors were induced by the subdermal inoculation of 5×10^5 4T1 early passage cells suspended in 100 µl of Matrigel (10%) in the second left mammary fat pad of BALB/c females under inhalatory anesthesia (3% sevoflurane in 100% oxygen). Following the same experimental conditions, MDA-MB-231-Luc tumors were established by injecting 3×10^6 early passage cells in NOD/SCID female's mammary fat pad. Tumors were morphometrically evaluated daily with an electronic caliper and tumor volumes were obtained by considering tumor shape as spheroidal. At progressive periods, representative mice were sacrificed under CO_2 atmosphere and the blood, main organs, and tumor were extracted, weighed, and preserved for later hematological and histopathological analysis. The experiments were terminated when tumors reached 1.0 cm^3 (or 24 days after the inoculation in case of 4T1 tumors and 42 days after inoculation in case of MDA-MB-231-Luc).

II.5.5. Study of Enhanced Permeability and Retention Effect

To study vascular permeability, 200 µl of Evans blue – albumin macromolecular complex (10mg/Kg) was administered intravenously (i.v.) (4 mice/group). After 60 minutes, mice were sacrificed under CO_2 atmosphere and tumors were resected, washed, and submerged in 3 ml of formamide (Sigma-Aldrich). Tissues were allowed to release accumulated dye preserved from light, at 60°C for 48h and the final concentration of Evans-blue was determined spectrophotometrically at 620 nm [57, 58].

II.5.6. Non-invasive Imaging Techniques to Monitor Metastasis

Bioluminescence (BLI) by IVIS

Luciferase-transfected MDA-MB-231-Luc cells present in the animal body were tracked using IVIS technology. For bioluminescence imaging (BLI), mice were anesthetized with 3% sevoflurane in oxygen and received a subdermal injection of 150 mg/kg D-luciferin (Gold BioTechnology, USA). BLI was performed with the IVIS spectrum system 10 min after D-luciferin administration. Images were acquired using the automatic camera settings and BLI data were quantified with the Living Image (PerkinElmer, Japan) software in terms of photons per second.

Positron Emission Tomography-Computed Tomography (PET-CT) Analysis

PET-CT analysis employed the Albira equipment (Bruker, USA) located within the CIPF. Animals were kept without food for 14h prior to radiotracer administration for PET and housed at constant temperature of 21ºC to minimize the influence of external factors on glucose uptake. The average mouse weight was 19.2±0.7g, while the average blood glucose level was 47.2±10.1mg.dl^{-1}. Anesthesia was induced by inhalation of isoflurane (4% in 100% oxygen) and maintained at (1.5% in 100% oxygen). The resolution of the hybrid PET/CT tomography was fixed at 1.5mm with an axial field of 9 cm and transaxial of 8 cm. Once the parameters were fixed, animals were i.v. injected with ^{18}F-FDG (IBA Molecular, Spain) with an activity of 4.5±0.1MBq through a tail vein catheter. The average 18F-FDG dosage was 4516.2 KBq±236.3. Dynamic PET experiments were performed by the acquisition of 28 frames of 60 min of total length (6 x 10 s, 6 x 30 s, 6 x 60 s, 5 x 120 s, 4 x 300 s and 1 x 1200 s). CT scans were performed immediately after PET acquisitions, allowing the overlap of both images. PET images were reconstituted using the algorithm Maximum Likelihood Estimation Method (MLEM, 12 iterations) and decay, scatter, and random corrections were applied where required. CT scans were performed at 45 KV and 0.4 mA, with further reconstruction using the FBP algorithm.

Acquired images were semi-quantitatively analyzed through the Standard Uptake Values (SUVs), which allowed the definition of the volumes of interests (VOIs) and establishment of time-activity curves (TACs) for different regions of interest. 18F-FDG uptake in the time point of the dynamic assay (40-60min) was employed for the static

analysis. 18F-FDG accumulation in different VOIs was measured by the same way as for the SUVs. To minimize the uptake fluctuations due to factors including animal weight or slight differences in i.v. administration, SUVs were normalized using the relationship between radioactivity in tissue (KBq/ml) at different acquisition time points and injected doses in the PET acquisition (KBq) divided by each mouse weight, obtaining a SUV (g/ml) as presented in the graphs.

PET and CT data were processed using the PMOD software suite (ver3.6) (Pmod Technologies, Zurich, Switzerland). 18F-FDG uptake was quantified by registering anatomic images of CT and corresponding PET normalized to SUV. Spherical VOIs were established in axillar lymph nodes (diameter = 2mm) and lungs (diameter = 1mm). The obtained VOIs were transferred to the PET image, resulting in the TACs standardized to SUVs (g/ml) for each different areas of interest.

II.5.7. Blood Collection and Analysis

At defined time points, mice were sacrificed under a CO_2 atmosphere. Blood was immediately extracted by cardiac puncture with a 1.0 ml heparinized syringe and transferred to a 2.0 ml Eppendorf tube. Serum was isolated and analyzed through an automated hematologic analyzer (Sysmex XT-2000i). Serum protein content was measured using an automated capillary electrophoresis system (Capillarys Sebia 2). For the blood smear preparation, a small drop of blood was placed near the frosted end of a clean glass slide. The blood was streaked in a thin film over a slide and then it was allowed to air-dry for 60 min. Commercial Wright's staining procedure was performed afterward.

II.5.8. Histopathological Analysis and Imaging

Histopathological analysis were carried out in the Instituto Valenciano de Patología, Tumors, major organs, and areas expected to develop metastasis or pathological alterations, were removed from euthanized mice at relevant time points. All the tissues were washed in fresh PBS, carefully dried, weighed, and fixed in 4% paraformaldehyde (PFA). PFA was eliminated by successive washing with PBS.. Bone

marrow samples were derived from femurs decalcified by immersion in Osteodec (BioOptica) for 8 h. A common dehydration and paraffin-inclusion procedure was carried out leading to blocks that were sliced into 4-µm sections. Hematoxylin-Eosin (H-E) staining and immunostaining were performed as required (Dako Autostainer 48, US) and the slides were finally assembled with Eukitt. Tissue slides were observed under the microscope and those of interest were scanned with a Panoramic 250 Flash III slide scanner and processed with CaseViewer software (both from (3DHISTECH Ltd, Budapest, Hungary). A detailed list of the antibodies used can be found in the Supplementary Figure S11.

II.5.9. Metabolomic profiling by NMR

Samples corresponding to tumors and metastatic lungs, collected at the experimental endpoints, as well as healthy lungs (control samples) were removed following the procedures indicated above, washed in PBS, immediately frozen in liquid nitrogen, and stored at – 80ºC until analysis. Tissue samples were powdered and the metabolites were extracted and analyzed by NMR using previously described methods [59]. Following sample preparation, NMR spectra were recorded at 300 K (27 ºC) on a Bruker AVII-600 using a 5 mm TCI cryoprobe and processed using Topspin 3.5 (Bruker GmbH, Karlsruhe, Germany). Acquisition parameters for these experiments were optimized to achieve an optimal signal to noise and resolution [59]. Multivariate data analysis was performed with SIMCA-P 14.1 (Umetrics, Sweden). Specifically, PCA models were generated for the different comparisons to evaluate the intrinsic variability of the data and to observe clustering or separation trends. OPLS-DA models were built for minimizing the contribution of variability within and between the samples, and to further improve the separation between the groups. Identification of the most relevant metabolites included the analysis of the OPLS-DA loadings S-plot, that provides information on the relative contribution of spectral variables to the separation between groups. Finally, main metabolites contributing to group discrimination were integrated using the global spectral deconvolution tool in MestreNova.

II.5.10. Statistical Analysis

All graphs present mean ± SEM from $n \geq 3$ assays. Animal assays were performed with 4-7 animals per group. Statistical analysis was performed using one-way ANOVA test and Mann–Whitney U test; comparisons with $p<0.05$ were considered statistically significant with a 95% confidence interval.

II.5.11. Exosome Isolation from Mouse Blood Serum

Fresh serum was isolated from blood through centrifugation (4000 rpm, 10 min, 4 ºC). Serum was purified by differential centrifugation (500g, 10min; 3000g, 20min and 10000g, 20min at 10°C). Volume was adjusted to 4ml with PBS. Then, an ultracentrifugation was performed (100000g, 70min, rotor MLS-50, UC Optimamax). The pellet was suspended in 1ml of PBS and adjusted to 4ml and the ultracentrifugation procedure was repeated. Finally, the pellet was suspended in 50ul and kept at 4ºC until analysis.

II.5.12. Sizing and Quantification of Exosomes by NTA

Purified exosomes were diluted with PBS buffer (100 – 5000 times) in order to reach the particle concentration ($2*10^8$ to $2*10^9$ particles/ml) in the operational range for the NTA. Exosomes were then quantified and sized using the Nanosight NS300 (Malvern Instruments, UK). For image acquisitions, the focus was fixed to -1 and camera level set to 8 in all experiments. For image processing and analysis, the threshold level was established to 8. Five statistically representative movies were recorded and processed for each sample.

II.6. References

[1] Bianchini G, Balko JM, Mayer IA, Sanders ME, Gianni L. Triple-negative breast cancer: challenges and opportunities of a heterogeneous disease. Nature Reviews Clinical Oncology. 2016;13:674-90.
[2] Tseng LM, Hsu NC, Chen SC, Lu YS, Lin CH, Chang DY, et al. Distant metastasis in triple-negative breast cancer. Neoplasma. 2013;60:290-4.

[3] Brouckaert O, Wildiers H, Floris G, Neven P. Update on triple-negative breast cancer: prognosis and management strategies. International journal of women's health. 2012;4:511-20.
[4] Boichuk S, Galembikova A, Sitenkov A, Khusnutdinov R, Dunaev P, Valeeva E, et al. Establishment and characterization of a triple negative basal-like breast cancer cell line with multi-drug resistance. Oncol Lett2017. p. 5039-45.
[5] Andreopoulou E, Kelly CM, McDaid HM. Therapeutic Advances and New Directions for Triple-Negative Breast Cancer. Breast care (Basel, Switzerland). 2017;12:21-8.
[6] Elsawaf Z, Sinn HP, Rom J, Bermejo JL, Schneeweiss A, Aulmann S. Biological subtypes of triple-negative breast cancer are associated with distinct morphological changes and clinical behaviour. Breast (Edinburgh, Scotland). 2013;22:986-92.
[7] Wahba HA, El-Hadaad HA. Current approaches in treatment of triple-negative breast cancer. Cancer Biol Med. 2015;12:106-16.
[8] Bakrania AK, Variya BC, Patel SS. Novel targets for paclitaxel nano formulations: Hopes and hypes in triple negative breast cancer. Pharmacol Res. 2016;111:577-91.
[9] Liedtke C, Mazouni C, Hess KR, Andre F, Tordai A, Mejia JA, et al. Response to neoadjuvant therapy and long-term survival in patients with triple-negative breast cancer. Journal of clinical oncology : official journal of the American Society of Clinical Oncology. 2008;26:1275-81.
[10] Maeda H, Tsukigawa K, Fang J. A Retrospective 30 Years After Discovery of the Enhanced Permeability and Retention Effect of Solid Tumors: Next-Generation Chemotherapeutics and Photodynamic Therapy--Problems, Solutions, and Prospects. Microcirculation (New York, NY : 1994). 2016;23:173-82.
[11] Kutty RV, Wei Leong DT, Feng SS. Nanomedicine for the treatment of triple-negative breast cancer. Nanomedicine (London, England). 2014;9:561-4.
[12] Atkinson SP, Andreu Z, Vicent MJ. Polymer Therapeutics: Biomarkers and New Approaches for Personalized Cancer Treatment. J Pers Med. 2018;8.
[13] Manning HC, Buck JR, Cook RS. Mouse Models of Breast Cancer: Platforms for Discovering Precision Imaging Diagnostics and Future Cancer Medicine. J Nucl Med. 2016;57 Suppl 1:60s-8s.
[14] Francia G, Cruz-Munoz W, Man S, Xu P, Kerbel RS. Mouse models of advanced spontaneous metastasis for experimental therapeutics. Nat Rev Cancer. 2011;11:135-41.
[15] Kaur PaNGMaZHaGDaGMaKSaAA. A mouse model for triple-negative breast cancer tumor-initiating cells (TNBC-TICs) exhibits similar aggressive phenotype to the human disease. BMC cancer. 2012;12:120.
[16] Kobayashi H, Watanabe R, Choyke PL. Improving Conventional Enhanced Permeability and Retention (EPR) Effects; What Is the Appropriate Target? Theranostics. 2014;4:81-9.
[17] Tilley C, Lipson J, Ramos M. Palliative Wound Care for Malignant Fungating Wounds. Nursing Clinics of North America. 2016;51:513-31.
[18] Maeda H, Tsukigawa K, Fang J. A Retrospective 30 Years After Discovery of the Enhanced Permeability and Retention Effect of Solid Tumors: Next-Generation Chemotherapeutics and Photodynamic Therapy-Problems, Solutions, and Prospects. Microcirculation. 2016;23:173-82.
[19] Lee J, Hong BS, Ryu HS, Lee H-B, Lee M, Park IA, et al. Transition into inflammatory cancer-associated adipocytes in breast cancer microenvironment requires microRNA regulatory mechanism. PLOS ONE. 2017;12:e0174126.
[20] H Heppner G, R Miller F, Malathy Shekhar PV. Nontransgenic models of breast cancer. Breast Cancer Research. 2000;2.
[21] Milsom CC, Lee CR, Hackl C, Man S, Kerbel RS. Differential Post-Surgical Metastasis and Survival in SCID, NOD-SCID and NOD-SCID-IL-2Rγnull Mice with Parental and Subline Variants of Human Breast Cancer: Implications for Host Defense Mechanisms Regulating Metastasis. PLoS ONE. 2013;8:e71270.
[22] Iorns E, Drews-Elger K, Ward TM, Dean S, Clarke J, Berry D, et al. A New Mouse Model for the Study of Human Breast Cancer Metastasis. PLoS ONE. 2012;7:e47995.

[23] Donnem T, Hu J, Ferguson M, Adighibe O, Snell C, Harris AL, et al. Vessel co-option in primary human tumors and metastases: an obstacle to effective anti-angiogenic treatment? Cancer medicine. 2013;2:427-36.
[24] Marini C, Ravera S, Buschiazzo A, Bianchi G, Orengo AM, Bruno S, et al. Discovery of a novel glucose metabolism in cancer: The role of endoplasmic reticulum beyond glycolysis and pentose phosphate shunt. Scientific Reports. 2016;6:25092.
[25] Schaller A, Beau-Faller M, Mennecier B, Renaud-Picard B, Weingertner N, Massard G, et al. Lung Adenocarcinoma with Pulmonary Miliary Metastases and Complex Somatic Heterozygous EGFR Mutation. Case Reports in Oncology. 2014;7:769-73.
[26] dos Anjos Pultz B, Andrés Cordero da Luz F, Socorro Faria S, Peixoto Ferreira de Souza L, Cristina Brígido Tavares P, Alonso Goulart V, et al. The multifaceted role of extracellular vesicles in metastasis: Priming the soil for seeding. International Journal of Cancer. 2017;140:2397-407.
[27] Pio R, Corrales L, Lambris JD. The Role of Complement in Tumor Growth. Advances in Experimental Medicine and Biology: Springer New York; 2013. p. 229-62.
[28] Inra CN, Zhou BO, Acar M, Murphy MM, Richardson J, Zhao Z, et al. A perisinusoidal niche for extramedullary haematopoiesis in the spleen. Nature. 2015;527:466-71.
[29] duPre SA, Hunter KW. Murine mammary carcinoma 4T1 induces a leukemoid reaction with splenomegaly: Association with tumor-derived growth factors. Experimental and Molecular Pathology. 2007;82:12-24.
[30] Hollmén M, Karaman S, Schwager S, Lisibach A, Christiansen AJ, Maksimow M, et al. G-CSF regulates macrophage phenotype and associates with poor overall survival in human triple-negative breast cancer. OncoImmunology. 2015;5:e1115177.
[31] Dhandapani M, Goldman A. Preclinical Cancer Models and Biomarkers for Drug Development: New Technologies and Emerging Tools. Journal of Molecular Biomarkers & Diagnosis. 2017;08.
[32] Duncan R. Polymer therapeutics at a crossroads? Finding the path for improved translation in the twenty-first century. Journal of Drug Targeting. 2017;25:759-80.
[33] Tchou J, Zhao Y, Levine BL, Zhang PJ, Davis MM, Melenhorst JJ, et al. Safety and Efficacy of Intratumoral Injections of Chimeric Antigen Receptor (CAR) T Cells in Metastatic Breast Cancer. Cancer Immunology Research. 2017;5:1152-61.
[34] Tayyari F, Gowda GAN, Olopade OF, Berg R, Yang HH, Lee MP, et al. Metabolic profiles of triple-negative and luminal A breast cancer subtypes in African-American identify key metabolic differences. Oncotarget. 2018;9.
[35] Beloribi-Djefaflia S, Vasseur S, Guillaumond F. Lipid metabolic reprogramming in cancer cells. Oncogenesis. 2016;5:e189-e.
[36] Manning HC, Buck JR, Cook RS. Mouse Models of Breast Cancer: Platforms for Discovering Precision Imaging Diagnostics and Future Cancer Medicine. Journal of Nuclear Medicine. 2016;57:60S-8S.
[37] Pereira ER, Kedrin D, Seano G, Gautier O, Meijer EFJ, Jones D, et al. Lymph node metastases can invade local blood vessels, exit the node, and colonize distant organs in mice. Science. 2018;359:1403.
[38] Brown M, Assen FP, Leithner A, Abe J, Schachner H, Asfour G, et al. Lymph node blood vessels provide exit routes for metastatic tumor cell dissemination in mice. Science. 2018;359:1408.
[39] Zhang XY, Lu WY. Recent advances in lymphatic targeted drug delivery system for tumor metastasis. Cancer biology & medicine. 2014;11:247-54.
[40] Liu Z, Zhu Y, Wang Y, Fu Q, Fu H, Wang Z, et al. Prognostic value of granulocyte colony-stimulating factor in patients with non-metastatic clear cell renal cell carcinoma. Oncotarget. 2017;8.
[41] Metcalf D. The colony-stimulating factors and cancer. Nature Reviews Cancer. 2010;10:425-34.

[42] Lin C-H, Yu J-C, Ou J-J, Lee Y-T, Wu H-S. Leukemoid Reaction as a “Tumor Marker” in Breast Cancer. Surgical Science. 2012;03:271-3.
[43] Kowanetz M, Wu X, Lee J, Tan M, Hagenbeek T, Qu X, et al. Granulocyte-colony stimulating factor promotes lung metastasis through mobilization of Ly6G+Ly6C+ granulocytes. Proceedings of the National Academy of Sciences. 2010;107:21248-55.
[44] Jablonska J, Lang S, Sionov RV, Granot Z. The regulation of pre-metastatic niche formation by neutrophils. Oncotarget. 2017;8.
[45] Kitamura T, Qian B-Z, Pollard JW. Immune cell promotion of metastasis. Nature Reviews Immunology. 2015;15:73-86.
[46] Cavanaugh PG, Jia LB, Zou YY, Nicolson GL. Transferrin receptor overexpression enhances transferrin responsiveness and the metastatic growth of a rat mammary adenocarcinoma cell line. Breast Cancer Research and Treatment. 1999;56:201-15.
[47] Nicolson GL, Menter DG, Herrmann J, Cavanaugh P, Jia L, Hamada J-i, et al. Tumor Metastasis to Brain: Role of Endothelial Cells, Neurotrophins, and Paracrine Growth Factors. Critical Reviews™ in Oncogenesis. 1994;5:451-71.
[48] Rodrigues dos Santos C, Fonseca I, Dias S, Mendes de Almeida JC. Plasma level of LDL-cholesterol at diagnosis is a predictor factor of breast tumor progression. BMC Cancer. 2014;14.
[49] Wei B, Yao M, Xing C, Wang W, Yao J, Hong Y, et al. The neutrophil lymphocyte ratio is associated with breast cancer prognosis: an updated systematic review and meta-analysis. OncoTargets and Therapy. 2016;Volume 9:5567-75.
[50] Johnson CH, Santidrian AF, LeBoeuf SE, Kurczy ME, Rattray NJW, Rattray Z, et al. Metabolomics guided pathway analysis reveals link between cancer metastasis, cholesterol sulfate, and phospholipids. Cancer & Metabolism. 2017;5.
[51] Armiñán A, Palomino-Schätzlein M, Deladriere C, Arroyo-Crespo JJ, Vicente-Ruiz S, Vicent MJ, et al. Metabolomics facilitates the discrimination of the specific anti-cancer effects of free- and polymer-conjugated doxorubicin in breast cancer models. Biomaterials. 2018;162:144-53.
[52] Galons J-P, Job C, Gillies RJ. Increase of GPC Levels in Cultured Mammalian Cells during Acidosis. A31P MR Spectroscopy Study Using a Continuous Bioreactor System. Magnetic Resonance in Medicine. 1995;33:422-6.
[53] Lampa M, Arlt H, He T, Ospina B, Reeves J, Zhang B, et al. Glutaminase is essential for the growth of triple-negative breast cancer cells with a deregulated glutamine metabolism pathway and its suppression synergizes with mTOR inhibition. PLOS ONE. 2017;12:e0185092.
[54] Tsai IL, Kuo T-C, Ho T-J, Harn Y-C, Wang S-Y, Fu W-M, et al. Metabolomic Dynamic Analysis of Hypoxia in MDA-MB-231 and the Comparison with Inferred Metabolites from Transcriptomics Data. Cancers. 2013;5:491-510.
[55] Puchades-Carrasco L, Jantus-Lewintre E, Pérez-Rambla C, García-García F, Lucas R, Calabuig S, et al. Serum metabolomic profiling facilitates the non-invasive identification of metabolic biomarkers associated with the onset and progression of non-small cell lung cancer. Oncotarget. 2016;7.
[56] Balendiran GK, Dabur R, Fraser D. The role of glutathione in cancer. Cell Biochemistry and Function. 2004;22:343-52.
[57] Maeda H, Sawa T, Konno T. Mechanism of tumor-targeted delivery of macromolecular drugs, including the EPR effect in solid tumor and clinical overview of the prototype polymeric drug SMANCS. J Control Release. Netherlands2001. p. 47-61.
[58] Maeda H. Tumor-Selective Delivery of Macromolecular Drugs via the EPR Effect: Background and Future Prospects. Bioconjugate Chem. 2010;21:797-802.
[59] Arminan A, Palomino-Schatzlein M, Deladriere C, Arroyo-Crespo JJ, Vicente-Ruiz S, Vicent MJ, et al. Metabolomics facilitates the discrimination of the specific anti-cancer effects of free- and polymer-conjugated doxorubicin in breast cancer models. Biomaterials. 2018;162:144-53.

Chapter III

ANTICANCER ACTIVITY DRIVEN BY DRUG LINKER MODIFICATION IN A POLYGLUTAMIC ACID-BASED COMBINATION-DRUG CONJUGATE

The experimental research presented within this Thesis Chapter has been carried out in tight collaboration with Dr. Coralie Deladriere, who also presented part of it in her thesis dissertation. As a result of this collaboration, we are both co-first authors of the publication [1] in the journal Advanced Functional Materials [Journal impact factor: 12.12, scored 7 of 87 in Nanoscience and Nanotechnology (JCR, 2016), Q1], Volume 28, Issue 22 (DOI: 10.1002/adfm.201800931)("Anticancer Activity Driven by Drug Linker Modification in a Polyglutamic Acid-based Combination-drug Conjugate").

As stated in the Introduction Chapter, the polymeric carrier provides an ideal platform for delivery of a cocktail of drugs simultaneously [2], and so the pursuit for novel polymer-based combination conjugates more defined and better characterized is currently on first line of investigation in the polymer therapeutics field.

In the earlies 2000, it was reported the first endocrine-chemotherapy combination in the form of the model compound HPMA-copolymer-aminoglutethimide-doxorubicin [3]. It was then hypothesized that combination of endocrine therapy and chemotherapy by simultaneous attachment to the same polymer would bring significant advantages. The combination was suitable to be administered as a single dose, leading to the benefits of manufacture of a single conjugate and improved patience compliance.

After EPR-mediated targeting, arrival of both covalently conjugated drugs to the tumour cells at the same time can be guaranteed. This strategy also provides the opportunity to tailor polymer-drug linkers to impart different rates of drug release for each compound, allowing the incorporation of optimal drug loadings at optimal drug ratios to act synergistically. The conjugate was evaluated *in vitro* using MCF-7 cells and an aromatase-transfected cell line MCF-7Ca. It was found that conjugates containing both drugs (aminoglutethimide and doxorubicin) showed markedly enhanced cytotoxicity compared to PK1 (HPMA-GFLG-Dox, the conjugate that has already shown activity in breast cancer patients clinically), while mixtures of polymer conjugates containing only aminoglutethimide or only doxorubicin did not show synergistic benefit.

These observations underlined the exciting possibility of designing polymer-drug combinations for improved treatment of breast and prostate cancer, including the use or more active anticancer drugs, more effective stimuli-responsive drug linkers and safer and biodegradable polymeric carrier.

III.1. Antecedents and Background

As stated in previous Thesis Chapters, combination anti-cancer strategies within nanomedicine may represent an efficient means to treat breast cancer, [4-6] a molecularly complex and heterogeneous disease that often metastasizes and/or becomes drug resistant. [7] There currently exist a wide range of strategies under investigation, including the liposomal entrapment of Cytarabine and Daunorubicin (FDA approved Vyxeos™, formerly CPX-351), which has improved all efficacy parameters, including overall survival, in a Phase 3 clinical trial of high-risk acute myeloid leukemia patients. [8]

Polymeric Therapeutics (PT) as single agent or as combination therapeutics offer numerous advantages over conventional drugs, including the possibility of an enhanced passive accumulation via the Enhanced Permeability and Retention (EPR) Effect on those tumors adequately vascularized, [9-11] or the ability to cross specific biological barriers. [12, 13] Moreover, drug(s) conjugation to a polymeric carrier benefits from several additional advantages [14, 15] as an optimized drug pharmacokinetics, multivalence that allows the conjugation of multiple active/imaging agents and targeting moieties, [6, 16] and the ability to target drug activity to tumors via bioresponsive polymer-drug linkers. [17] One issue limiting the widespread use of polymer conjugates is the current lack of understanding of the complex interplay of dynamic physicochemical factors, such as size, shape, surface chemistry, roughness, rigidity, and the influence of linkers and active agents, which characterize the interaction of nanosized PTs with the biological interface. [18]

We developed the first polymer-drug combination conjugate, an N-(2-Hydroxypropyl) methacrylamide copolymer carrying both Aminogluthetimide and Doxorubicin (HPMA-AGM-Dox), with the aim of combining an aromatase inhibitor with a chemotherapeutic agent for the treatment of chemotherapy-resistant breast cancer. [19-21] HPMA-AGM-Dox displayed enhanced *in vitro* breast cancer cell toxicity compared to a combination of the unconjugated drugs or individual polymer-drug conjugates. [20, 21] Recently, *in vivo* proof of concept for antitumor drug synergism with the combination conjugate has been also achieved in an aggressive metastatic 4T1 murine breast cancer model. [19] The mechanism of the enhanced activity appeared primarily due to the kinetics of drug release and the fact that both drugs were made 'bioavailable' in the same

cell at the same time. Importantly, when protein expression of tumor tissue samples were analyzed, strong differences were observed in tumor-associated angiogenesis pathways, which could only be explained by the simultaneous estrogen inhibition induced by AGM, only made available at the appropriate cell and time with the combination conjugate. This effect was enhanced by an autophagic cell death mechanism only associated with the combination conjugate. [19] These results demonstrated for the first time that the rational design of a combination PT could significantly enhance drug therapeutic output while also significantly reducing the side effects and tissue damage observed when applying the unconjugated forms of these active agents. This concept has been further explored and reinforced both *in vitro* and *in vivo* through studies in our laboratory and other research groups. [6]

However, despite these promising findings, preclinical evidence of detrimental side effects derived from the use of biopersistent polymer carriers (i.e. HPMA or Polyethylene glycol (PEG)) [22] have led to an exponentially growing research interest on biodegradable polymers, in particular, polypeptides such as poly-glutamic acid (PGA) [17, 23] as clinical benefits have been achieved with polypeptide based polymeric drugs, such as Copaxone [24] (one of the Top Ten selling drugs) [25, 26] and the lessons learnt with polypeptide/PGA-based anti-cancer PTs such as Opaxio. [27, 28]

Encouraged by the successful application of PGA to conjugate chemotherapy as single agents [27, 28] and in combination, [29-31] as well as our prior data combining endocrine and chemotherapy, [19-21] we now describe the first PGA-based combination conjugates bearing chemotherapy and estrogen modulator agents for the treatment of breast cancer. Furthermore, we took this opportunity to explore how the incorporation of different polymer-drug linkers influences conjugate characteristics and biological fate. Implementing a rational experimental design, we systematically prescreened a family of single and combination conjugates, provided with different drug loadings and linkers, *in vitro* in a breast cancer cell line, and then selected successfully screened conjugates for further assessments in an aggressive orthotopic 4T1 breast cancer murine model. We also studied the spatial conformation and physical structure of our conjugate family in biological milieu to predict and better understand intrinsic interactions with the nano-bio interface and therefore, therapeutic effect and mechanisms of action. Parameters assessed included drug release kinetics in the presence of lysosomal enzymes as well as

tridimensional conformation including secondary structure, size, and shape by Dynamic Light Scattering (DLS), Small Angle Neutron Scattering (SANS), and Circular Dichroism (CD). We present the selected PGA-based drug-combination conjugate as an exciting therapeutic candidate, underlining that the choice and/or design of drug-polymer linkers may allow tight spatiotemporal control of drug release and the enhanced personalized treatment of aggressive breast cancer.

III.2. Results and Discussion

III.2.1. Synthesis and Characterization of Polymer-drug Conjugates

We employed optimized and scalable synthetic methodologies to develop a rationally designed family of polymer-based combination anticancer conjugates using n-butyl poly-L-glutamic acid (PGA) (100 units, Mw ~13 kDa) as a biodegradable carrier, with the aim of achieving drug synergism. Aromatase inhibitors, such as Aminoglutethimide (AGM), induce apoptosis [32] and can act synergistically when combined with chemotherapeutics, [33] as previously shown in our studies with N-(2-Hydroxypropyl) methacrylamide (HPMA)-based combination conjugates. [19-21] Although HPMA has demonstrated its suitability as carrier for anticancer treatments, we expected that replacing HPMA with PGA would improve safety issues specially in chronic administrations given its enhanced biodegradability. This improved characteristic would reduce unwanted side effects related to polymer accumulation as seen with other non-biodegradable carrier such as PEG. [22, 29, 34]

Therefore, we developed a library of well-defined PGA-conjugates via carbodiimide coupling (**Figure 1**). [21, 35] We also synthesized and fully characterized single-agent PGA conjugates bearing Dox or AGM for comparative purposes (**Table 1** summarizes data on all conjugates assessed). We introduced Dox directly and AGM via direct amide conjugation, a Gly linker (G), [36] a Gly-Gly linker (GG), [37, 38] or the well-known tetrapeptidic Gly-Phe-Leu-Gly linker (GFLG), which is cleaved by the lysosomal thiol-dependent protease Cathepsin B. [39] To explore the effect of two different therapeutic scenarios, we fixed Dox content within the polymer conjugate at 5% mol, but varied AGM from 5% mol (Low Loading [$_{LL}$]) to 10% mol (High Loading [$_{HL}$]) (**Figure 1**). Additionally, we also incorporated both drugs within the same PGA chain to create a family of combination conjugates. Importantly, the robust methodology

employed and tight controls on drug loading permitted the scale-up of this process to gram-scale batches without losses in either conjugation efficiency or yield. Prior to characterization, we isolated and purified all conjugates by Size Exclusion Chromatography (SEC) to remove any excess of salts, activating agents or traces of unreacted drugs (See **section III.4. Materials and Methods** for a detailed synthetic methodology).

^{1}H-NMR characterization of the synthesized products was used to determine their identity and purity. As demonstrated in **Figure 2**, which displays spectra of representative conjugates, the covalent incorporation of a single drug (PGA-(G-AGM)$_{LL}$, PGA-Dox) or the drug combination (PGA-(G-AGM)$_{LL}$-Dox) into the polymer backbone resulted in the expected widening of characteristic drug signals (See **section III.4.3 of Materials and Methods** for details on family characterization). The signal of the Dox methylene group at 1.2 ppm and the signals corresponding to the aromatic ring (0.75 ppm) and ethylene group (7.4 ppm) of AGM permitted identity verification for both the single and combination nanoconjugates. As shown in **Figure 3**, representative conjugates displayed a homogeneous distribution of drug content along the polymer population (as derived from the SEC elution profiles in UV-Vis at 260 nm). These profiles conformed to the expected behavior according to size, as different conjugates exhibited slightly shorter retention times and broader peaks when compared with parental unconjugated/unmodified PGA (**Figure 3**), in accordance with the enhanced Mw due to the incorporation of drugs.

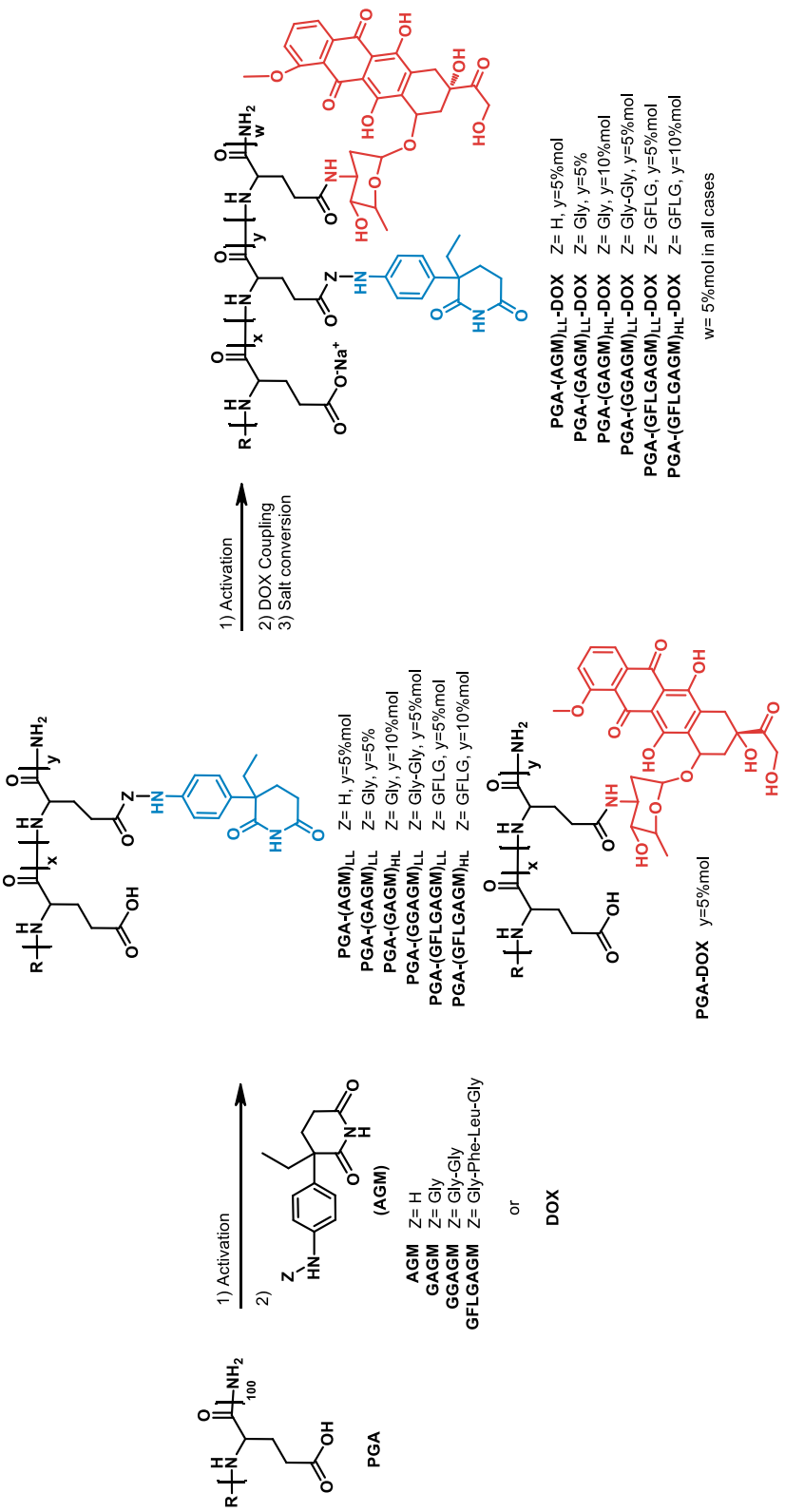

Figure 1. Synthetic route for the preparation of single and combination PGA-drug conjugates: 1) Carbodiimide-based carboxylic group activation. 2) Attachment of Dox or AGM (or derivatives) for single conjugates, and Dox coupling as the second drug in the combination conjugates. 3) Conversion into polycarboxilate form.

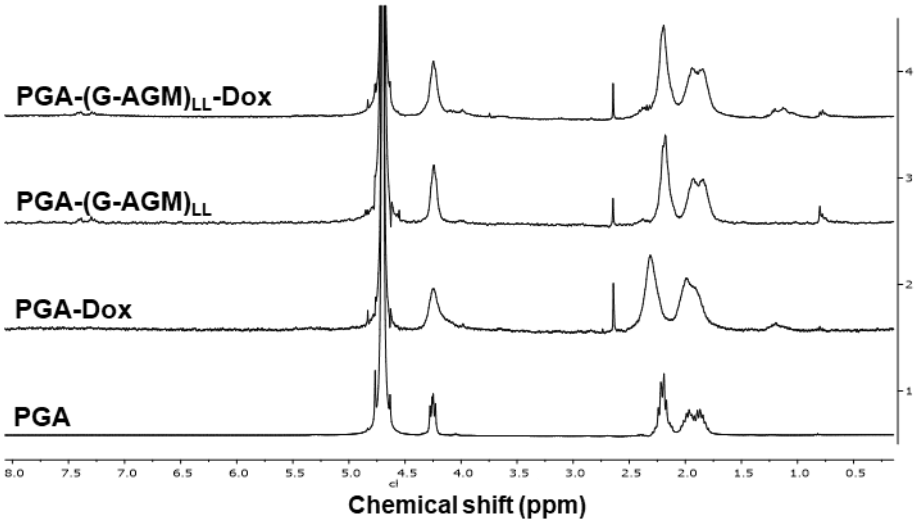

Figure 2. Representative 1H-NMR spectra (D2O, 500MHz) of single and combination conjugates.

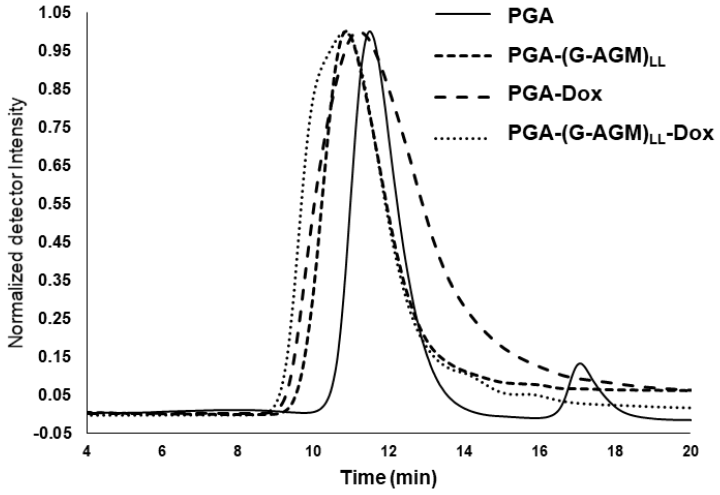

Figure 3. Representative SEC chromatograms for parental PGA (RI detection, peak at 17.1 min corresponds to the counter-cation Na^+) and PGA-Dox, PGA-(G-AGM)$_{LL}$, and PGA-(G-AGM)$_{LL}$-Dox conjugates (UV at 260nm).

III.2.2. Quantitative Characterization of Total Drug Loading and Free Drug Content in PGA-drug Conjugates

Despite the lower reactivity of the aromatic amine present in AGM, we found the synthetic carbodiimide-activation methodology to be a good and reproducible approach (**Table 1**) for both the single and combination conjugates. We noted that conjugation yield improved significantly when we first incorporated AGM with different peptidic linkers, and so we performed amide coupling through a primary peptidic amine rather than

through the primary aromatic amine of the drug. We also noted efficient conjugation of Dox, except for combination conjugates bearing the GFLG-AGM moiety. Lower Dox loading in the presence of the bulky GFLG-AGM moiety may be due to steric hindrance, which can limit high levels of Dox incorporation. We also found that a SEC-based purification procedure ensured low levels of free-drug in the final conjugates ranging from 0.1-0.7% w/w for Dox and 0.2-1.1% w/w for AGM (**Table 1**). Absolute Mw analysis by analytical tandem SEC-MALS-RI proved difficult due to heterogeneity in drug loadings and the inherent nature of the conjugates, so we calculated the theoretical molecular weight of PGA conjugates according to the percentage of modification (range: 12.7 – 18.6 KDa).

	Total drug[a] (%w/w)		Free drug[b] (%w/w to total drug)		Mw[c] (Da)	Total drug (%mol)	
Compound	**AGM**	**Dox**	**AGM**	**Dox**	-	**AGM**	**Dox**
PGA	-	-	-	-	12700	-	-
PGA-$(AGM)_{LL}$	6.8	-	1.1	-	13600	4.0	-
PGA-$(G\text{-}AGM)_{LL}$	9.1	-	0.9	-	13900	4.7	-
PGA-$(G\text{-}AGM)_{HL}$	17.8	-	0.7	-	15450	9.5	-
PGA-$(GG\text{-}AGM)_{LL}$	10.8	-	0.9	-	14200	4.4	-
PGA-$(GFLG\text{-}AGM)_{LL}$	10.4	-	0.2	-	14800	2.5	-
PGA-$(GFLG\text{-}AGM)_{HL}$	18.8	-	0.4	-	15650	4.8	-
PGA-(Dox)	-	14.2	-	0.1	14800	-	3.9
PGA-$(AGM)_{LL}$-Dox	8.1	15.8	0.8	0.4	16700	5.8	4.8
PGA-$(G\text{-}AGM)_{LL}$-Dox	7.8	20.1	1.1	0.3	17600	5.61	6.5
PGA-$(G\text{-}AGM)_{HL}$-Dox	20.1	12.7	1.0	0.4	18900	13.1	4.4
PGA-$(GG\text{-}AGM)_{LL}$-Dox	7.6	18.9	0.9	0.2	17300	3.8	6.0
PGA-$(GFLG\text{-}AGM)_{LL}$-Dox	12.4	7.1	0.3	0.7	15800	3.2	2.0
PGA-$(GFLG\text{-}AGM)_{HL}$-Dox	24.2	7.6	0.4	0.7	18600	7.4	2.6

Table 1. Characteristics of PGA-AGM-Dox polymer-drug conjugates. (a Determined by UV-Vis (AGM) and HPLC (Dox). b Determined by HPLC. C Determined by aqueous SEC MALLS-RI for the sodium salt form of PGA. Mw of -the polymer – drug conjugates were estimated from total drug loading)

III.2.3. Preliminary in vitro Evaluation and Drug Release Kinetics of PGA Conjugates

To assess the biological implications of different drug linkers and drug ratios in the synthesized conjugates, we undertook a wide-ranging preliminary *in vitro* screening of the PGA-AGM-Dox family of conjugates. This analysis also compared treatment with

the various PGA-AGM conjugates and PGA-Dox as two separate species added simultaneously (i.e. drugs were not present in the same polymeric chain).

Cell viability assays in the MCF-7ca breast cancer cell line demonstrated higher cytotoxicity for the combination conjugates PGA-(GG-AGM)$_{LL}$-Dox (**Figure 4B**), PGA-(G-AGM)$_{LL}$-Dox (**Figure 4C**), and PGA-(G-AGM)$_{HL}$-Dox (**Figure 4D**) when compared with the single PGA-Dox and PGA-AGM parent conjugates alone or in a physical combination (**Table 2).** The PGA-(AGM)$_{LL}$-Dox (**Figure 4A**), PGA-(GFLG-AGM)$_{LL}$-Dox (**Figure 4E**), and PGA-(GFLG-AGM)$_{HL}$-Dox (**Figure 4F**) did not display high toxicity compared to PGA-Dox at tested concentrations. We found evidence of poor Dox release in the conjugates bearing the tetrapeptide GFLG for AGM, which is a requisite for cell toxicity, probably due to restricted linker access. Of note, the physical combination of single drug conjugates administered at the same time (**Figure 4A, E, and F**) did mediate an enhanced cytotoxic effect when compared to the combination conjugates. However, the administration of two different conjugates to a patient will not ensure that both drugs will arrive at the target cell at the desired ratio and within the required period, making this treatment strategy ultimately inefficient for our selected molecular targets.

As previous studies demonstrated significant synergism between AGM and Dox in the different breast cancer cells when incorporated within the same non-biodegradable polymeric carrier, [19-21] we computed the Combination Index (CI) for our new biodegradable systems against MCF7-ca. [40] These calculations discovered no synergistic effects when we treated cells with both drugs as separate single conjugates (**Table 2** - PGA-(AGM)$_{LL}$ + PGA-Dox, PGA-(GG-AGM)$_{LL}$+ PGA-Dox, PGA-(G-AGM)$_{LL}$ + PGA-Dox, and PGA-(G-AGM)$_{HL}$ + PGA-Dox), except for the PGA-(GFLG-AGM)$_{LL}$ and PGA-Dox treatment, which provided the lowest CI value of 0.3. However, we did observe high levels of synergism (CI < 1) for the PGA-(G-AGM)$_{LL}$-Dox (0.32), PGA-(G-AGM)$_{HL}$-Dox (0.32), and PGA-(GG-AGM)$_{LL}$-Dox (0.33) combination conjugates, with a weaker synergistic effect observed for PGA-(GFLG-AGM)$_{LL}$-Dox (0.56).

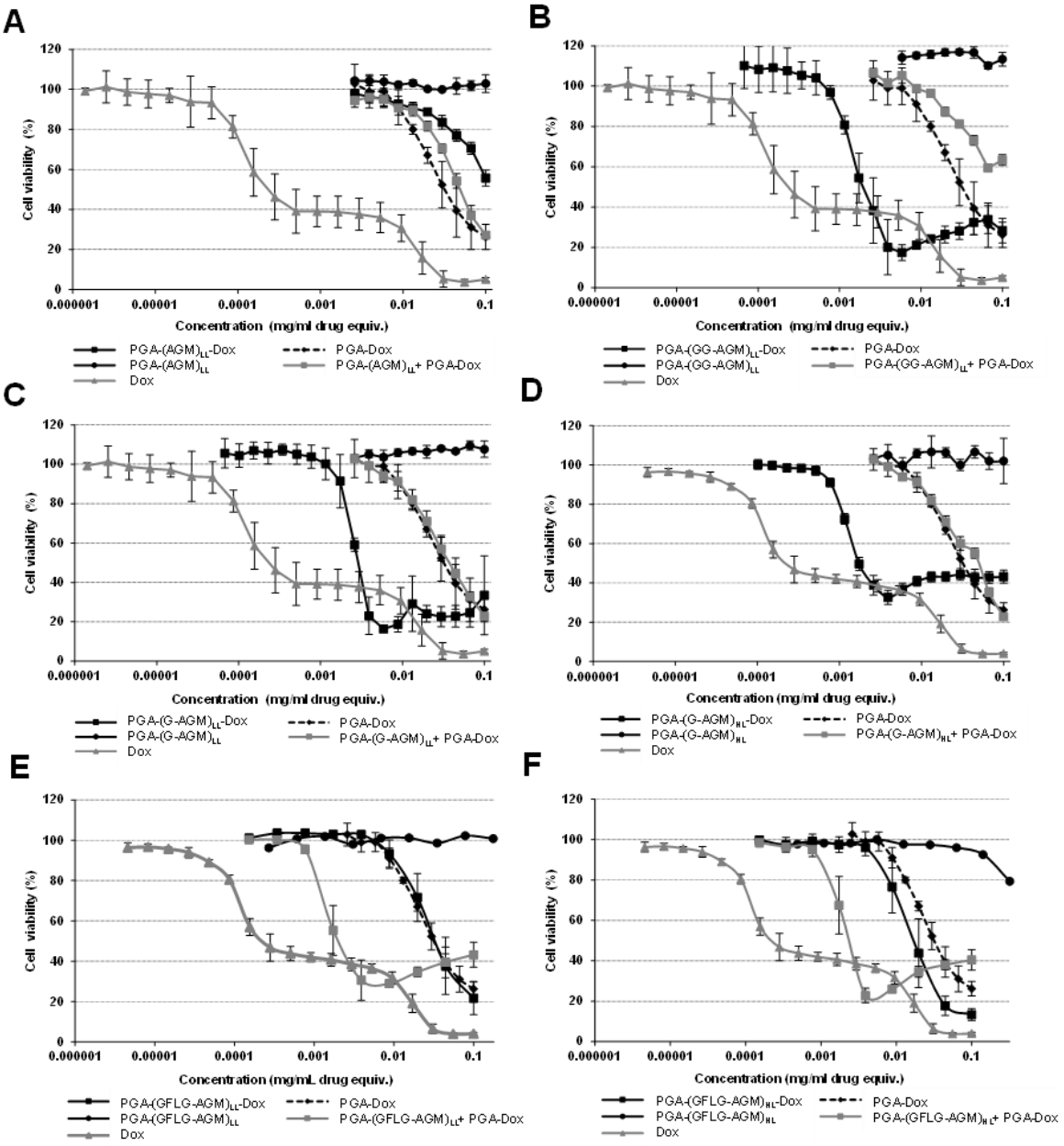

Figure 4. Cell toxicity study of polymer drug conjugates in MCF-7ca cells. Cell viability measured by MTS assay after 72 hours of treatment. PGA-$(AGM)_{LL}$-Dox (**A**), PGA-$(GG\text{-}AGM)_{LL}$-Dox (**B**), PGA-$(G\text{-}AGM)_{LL}$-Dox (**C**), PGA-$(G\text{-}AGM)_{HL}$-Dox (**D**), PGA-$(GFLG\text{-}AGM)_{LL}$-Dox (**E**) and PGA-$(GFLG\text{-}AGM)_{HL}$-Dox (**F**). Every assay is displayed with its corresponding single conjugates and Dox as free drug control. Data expressed as mean ± SEM, at least n = 3 experiments per treatment.

Treatment	*IC50* (mg/ml)*	*CI***
Dox	**0,00024**	**N/A**
PGA-Dox	**0,028**	**N/A**
PGA-$(AGM)_{LL}$-Dox	**0,53**	**>1**
PGA-$(AGM)_{LL}$	**N/A**	**N/A**
PGA-$(AGM)_{LL}$ + PGA-Dox	**0,05**	**>1**
PGA-$(GG\text{-}AGM)_{LL}$-Dox	**0,0011**	**0,32**
PGA-$(GG\text{-}AGM)_{LL}$	**N/A**	**N/A**
PGA-$(GG\text{-}AGM)_{LL}$+ PGA-Dox	**N/A**	**>1**
PGA-$(G\text{-}AGM)_{LL}$-Dox	**0,003**	**0,33**
PGA-$(G\text{-}AGM)_{LL}$	**N/A**	**N/A**
PGA-$(G\text{-}AGM)_{LL}$ + PGA-Dox	**1**	**1**
PGA-$(G\text{-}AGM)_{HL}$-Dox	**0,0017**	**0,33**
PGA-$(G\text{-}AGM)_{HL}$	**N/A**	**N/A**
PGA-$(G\text{-}AGM)_{HL}$ + PGA-Dox	**0,055**	**1**
PGA-$(GFLG\text{-}AGM)_{LL}$-Dox	**0,035**	**>1**
PGA-$(GFLG\text{-}AGM)_{LL}$	**N/A**	**N/A**
PGA-$(GFLG\text{-}AGM)_{LL}$ + PGA-Dox	**0,0027**	**0.32**
PGA-$(GFLG\text{-}AGM)_{HL}$-Dox	**0,022**	**0,56**
PGA-$(GFLG\text{-}AGM)_{HL}$	**N/A**	**N/A**
PGA-$(GFLG\text{-}AGM)_{HL}$+ PGA-Dox	**0,0026**	**0,3**

Table 2. IC50 and Combination Index (CI) values for free Dox and the polymer drug conjugates in human MCF-7ca cells (N/A: non-applicable, *IC50 values obtained graphically, **Combination Index estimated by Compusyn.

We noted that the presence of the linker drastically modified the *in vitro* cytotoxic effects; the addition of small, short, and flexible Gly or Gly-Gly linkers led to enhanced results when compared to direct linkage of AGM or through the more bulky GFLG linker. Additionally, we assessed cell toxicity of two highly synergistic conjugates found in the previous study in murine 4T1 breast cancer cells as a first step towards studying conjugate antitumor activity in an orthotopic immunocompetent mammary tumor mouse model. The PGA-$(G\text{-}AGM)_{LL}$-Dox (IC50 = 0.0034) and PGA-$(G\text{-}AGM)_{HL}$-Dox (IC50 = 0.0033) conjugates presented higher cytotoxicity compared to the single conjugate PGA-Dox

(IC50 = 0.0084) (**Figure 5A and B**. We also assessed cell toxicity of PGA-$(AGM)_{LL}$-Dox as a control for non-synergistic effect (**Figure 5C**) and, as expected, this combination conjugate displayed a higher IC50 value (0.012 mg/ml) than the combination conjugates bearing the Gly spacer. In general, we observed a more pronounced cytotoxic activity in 4T1 cells than in MCF-7ca, probably due to the higher level of Cathepsin B activity in 4T1 cells, [19] which degrades the peptidic polymer-drug linkers and the poly-L-glutamic acid carrier. Subsequent CI value calculations found strong synergism for the PGA-$(G\text{-}AGM)_{HL}$-Dox conjugate (CI = 0.176) (**Table 3**).

Treatment	*IC50 (mg/ml)*	*CI*
Dox	**0,000085**	**N/A**
PGA-Dox	**0,0084**	**N/A**
PGA-$(G\text{-}AGM)_{LL}$-Dox	**0,0034**	**0,388**
PGA-$(G\text{-}AGM)_{LL}$	**N/A**	**N/A**
PGA-$(G\text{-}AGM)_{LL}$+ PGA-Dox	**0,019**	**>1**
PGA-$(G\text{-}AGM)_{HL}$-Dox	**0,0033**	**0,176**
PGA-$(G\text{-}AGM)_{HL}$	**N/A**	**N/A**
PGA-$(G\text{-}AGM)_{HL}$+ PGA-Dox	**0,012**	**>1**
PGA-$(AGM)_{LL}$-Dox	**0,012**	**>1**

Table 3. Determination of IC50 and Combination Index (CI) values for free Dox and the polymer-drug conjugates in mouse 4T1 breast cancer cell line.

We also evaluated drug release kinetics in presence of Cathepsin B for the PGA-$(G\text{-}AGM)_{LL}$-Dox, PGA-$(G\text{-}AGM)_{HL}$-Dox, and PGA-$(AGM)_{LL}$-Dox conjugates (**Figure 6A-C**), finding three different release profile scenarios as a consequence of drug loadings and linker type. The PGA-$(G\text{-}AGM)_{LL}$-Dox conjugate displayed a significantly faster and higher release of AGM (13% after 72h) in contrast to Dox (7%) during the same time period. However, the PGA-$(G\text{-}AGM)_{HL}$-Dox conjugate released higher amount of Dox (12% at 72 hours) as compared to lower levels of AGM (3%) over the same time. Meanwhile, the PGA-$(AGM)_{LL}$-Dox conjugate displayed a simultaneous release profile for both drugs (~10%) over 72 hours. PGA-$(G\text{-}AGM)_{HL}$-Dox and PGA-$(G\text{-}AGM)_{LL}$-Dox differ only in their level of AGM loading, with higher loading significantly diminishing drug release kinetics, perhaps due to structural modifications in the polymer chain.

However, we noted a similar cytotoxic effect for both LL and HL conjugates, possibly mediated through different molecular mechanisms. While high Dox release from the PGA-(G-AGM)$_{HL}$-Dox can enhance cytotoxicity, high AGM release from the PGA-(G-AGM)$_{LL}$-Dox conjugate may enhance cell sensitivity to Dox [19, 20] and provide a synergistic effect even given the lower levels of Dox release. Aromatase inhibitors such as AGM promote apoptosis [41] and this may also sensitize cancer cells to Dox treatment. In a direct comparison between PGA-(AGM)$_{LL}$-Dox and PGA-(G-AGM)$_{LL}$-Dox conjugates, which only differ in the addition of the small flexible Gly linker, enhanced AGM release seems to be related with structural alteration promoted by Gly. In terms of drug synergism, we found that Gly presence induced synergism while the absence of Gly brings drug antagonism.

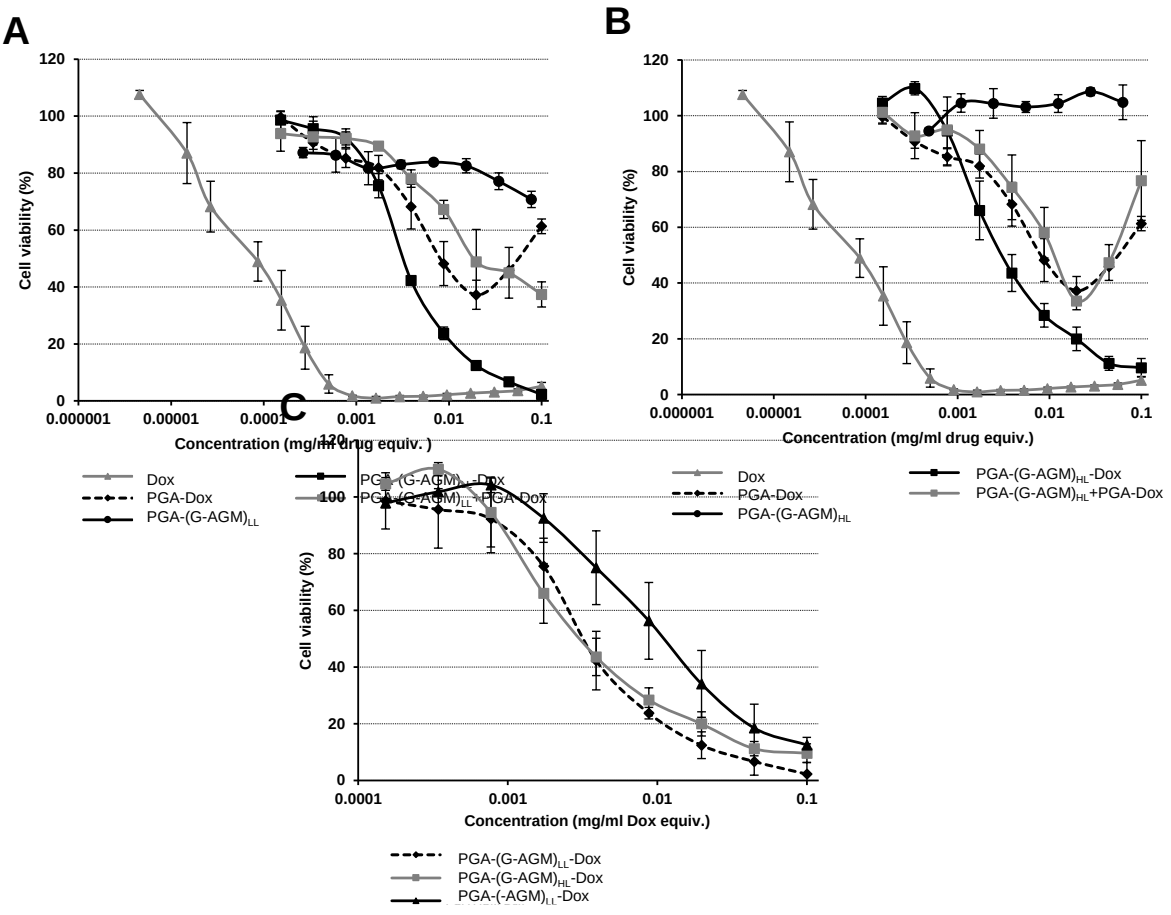

Figure 5. Cell toxicity analysis of the polymer drug conjugates PGA-(G-AGM)$_{LL}$-Dox (**A**), and PGA-(G-AGM)$_{HL}$-Dox (**B**) in 4T1 cells. **C**) Comparative study of cell toxicity of PGA-(G-AGM)$_{LL}$-Dox, PGA-(G-AGM)$_{HL}$-Dox and PGA-(AGM)$_{LL}$-Dox. Cell viability measured by MTS assay after 72 hours of the treatment.

Drug release required the strategic design of the family of polypeptide-drug conjugates towards lysosomotropic delivery, where the enzymatic degradation of the polymeric chain will release the active agents at the desired site of action. This not only improves therapeutic efficiency, but also reduces unwanted off-target side effects. The degradation process requires efficient cellular uptake and adequate access of the endopeptidase to the linker, [42] with accessibility directly related with the three-dimensional spatial disposition of the polypeptide. This in turn is influenced by structural factors such as conjugated moieties, [43] based branched polypeptides with Ser and Glu/Leu in the side chains} drug loadings, [44] drug ratios, [45] linking chemistry, and physico-chemical descriptors mediating the nano-bio interface. [17, 46] At this point, *in vitro* behavior of the conjugates cannot be explained by taking into account drug loadings and linking chemistry solely, although it seems clear that under the same PGA-Dox linking chemistry and drug loading, incorporation of AGM at different ratios or through different linkers could explain the observed results.

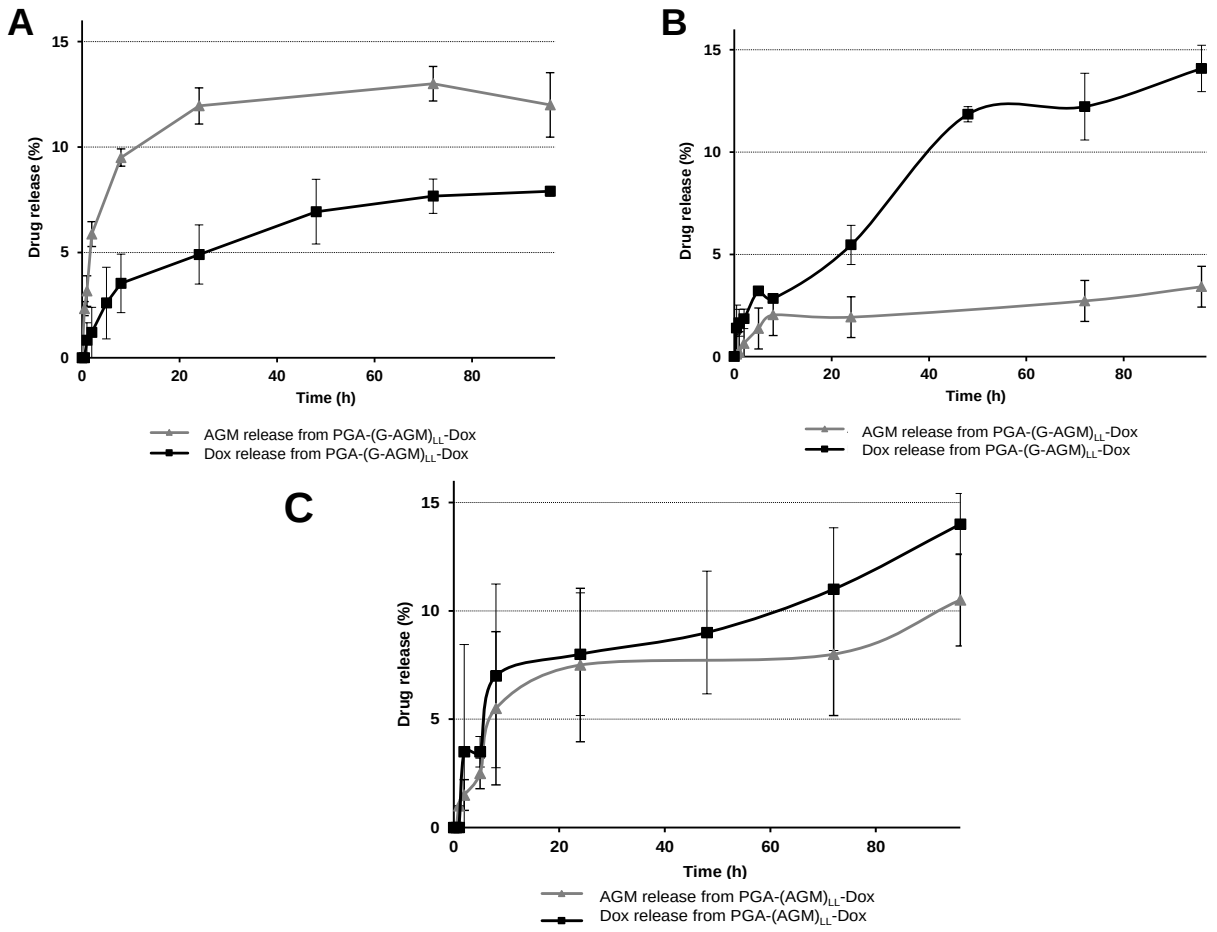

Figure 6. Drug release kinetics in presence of Cathepsin B of PGA-(G-AGM)$_{LL}$-Dox (D), PGA-(G-AGM)$_{HL}$-Dox (E) and PGA-(AGM)$_{LL}$-Dox (F). Data expressed as mean ± SEM, at least n = 3 experiments per treatment.

III.2.4. Antitumor Evaluation and Biodistribution of Selected Conjugates in a 4T1 Orthotopic Breast Cancer Murine Model

The conjugation of active agents to a biodegradable polymer provides distinct advantages over conventional monotherapy strategies. These include passive accumulation of the combination conjugate in solid tumors thanks to the EPR effect [9, 10] as well as the simultaneous delivery of both drugs at the tumor site of action. [16] Given tumor complexity, modulating the activity of two pathways will often provide greater therapeutic effects than monotherapies. In addition, polymer conjugation permits enhanced blood circulation times that allows sustained bioavailability and conjugate accumulation in tumor vessels, so leading to enhanced therapeutic output. The orthotopic mouse 4T1 breast tumor model has several characteristics that make an attractive experimental model to mimic breast cancer [47] including the well vascularized nature of the tumor, [48] which is a prerequisite for the EPR effect.

In order to explore the antitumor effect of the nanosystems under study, we randomly split mice inoculated with 4T1 cells into representative groups and scheduled three treatments every three days with selected combination conjugates and their corresponding single conjugates at 10 mg/kg Dox equiv. We administered Dox as a free agent in a control group at the maximum non-lethal dose (3 mg/kg). [19] Analysis of tumor growth along time (**Figure 7**) demonstrated high intragroup uniformity allowing us to effectively evaluate the antitumor effect of different treatments. Treatment with the single conjugates bearing AGM, Dox, the addition of either single conjugate, or free Dox did not significantly affect tumor growth. However, we observed a synergistic antitumor effect in animals treated with the PGA-(G-AGM)$_{LL}$-Dox and PGA-(G-AGM)$_{HL}$-Dox combination conjugates, as compared with the single conjugates (alone or added simultaneously) and controls (unconjugated PGA or PBS) (**Figure 7**).

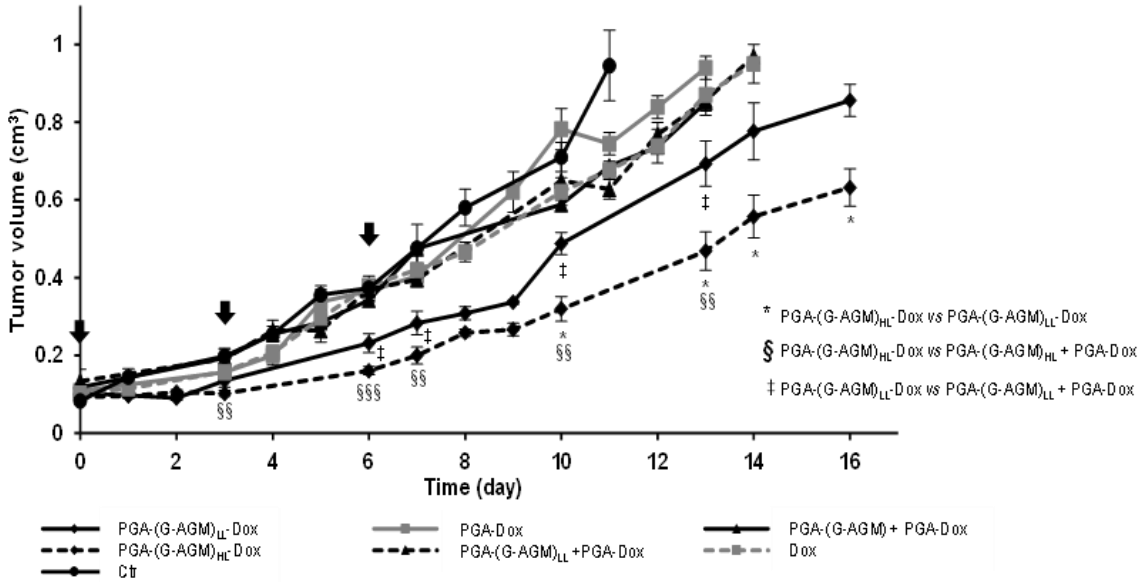

Figure 7. Antitumor activity and safety of PGA-(G-AGM)$_{LL}$-Dox and PGA-(G-AGM)$_{HL}$-Dox in an orthotopic 4T1 breast tumor mice model (A) The combination conjugates PGA-(G-AGM)$_{HL}$-Dox inhibited tumor volume growth more than PGA-(G-AGM)$_{LL}$-Dox, the simple conjugate or the combination of the simple conjugates (PGA-(G-AGM)$_{HL}$ + PGA-Dox). Data represents mean ± SEM. Statistical significance was determined using an ANOVA t-test, (*** $p<0.005$, ** $p<0.01$).

We also assessed safety profiles for all tested polymer-drug conjugates via the study of body weight, general wellbeing, behavior, and histopathology of specific organs. We did not observe significant alterations in body weight of treated animals (**Figure 8**) and histological study of the kidney and liver displayed no pathological tissue alterations related with any conjugate-based treatment, confirming the *in vivo* safety of this family of polymer-drug conjugates (**Figure 10**). Subsequent analysis of survival rates (**Figure 8**) demonstrated that PGA-(G-AGM)$_{LL}$-Dox and PGA-(G-AGM)$_{HL}$-Dox treated mice survived longer than other treated mice (controls or single treatments).

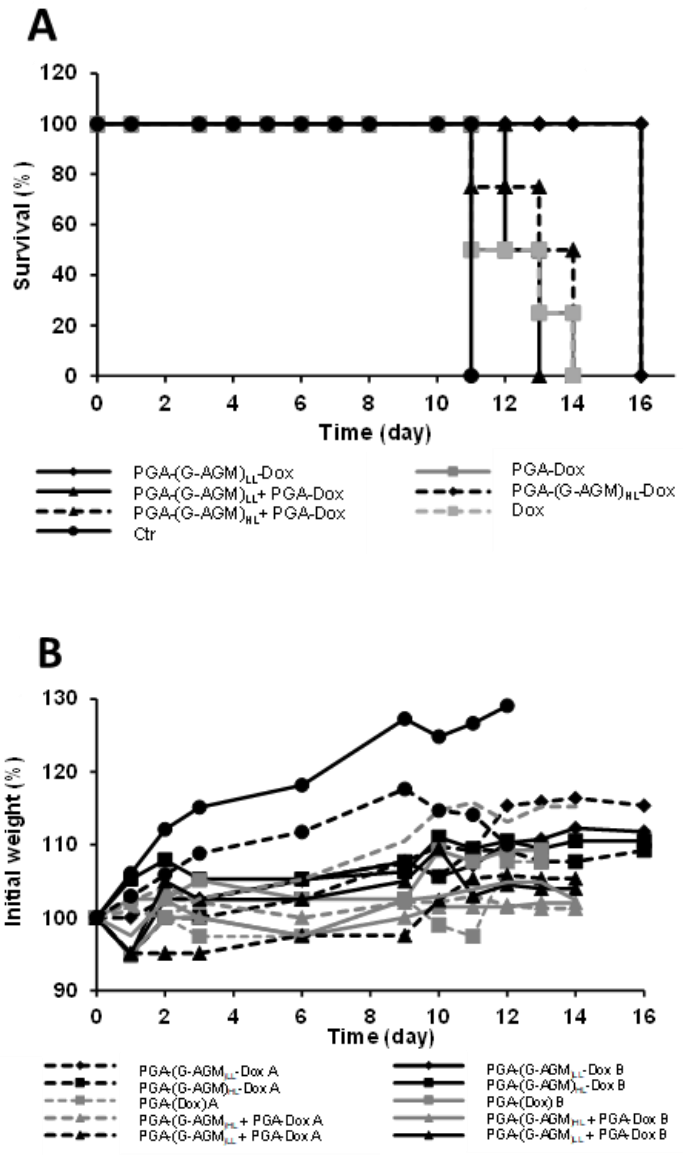

Figure 8. A) Kaplan–Meier survival curves by treatment demonstrating improved overall survival for PGA-(G-AGM)$_{HL}$-Dox and PGA-(G-AGM)$_{LL}$-Dox. The long-rank test demonstrated significant differences ($p < 0.0001$). **B)** Animal body weight did not significantly decrease along the experiment.

We next studied biodistribution and pharmacokinetics for a representative conjugate with high antitumor activity (PGA-(G-AGM)$_{HL}$-Dox) and compared the treatment with conventional Dox intravenous (i.v.) administration as a monotherapy in the 4T1 tumor model.

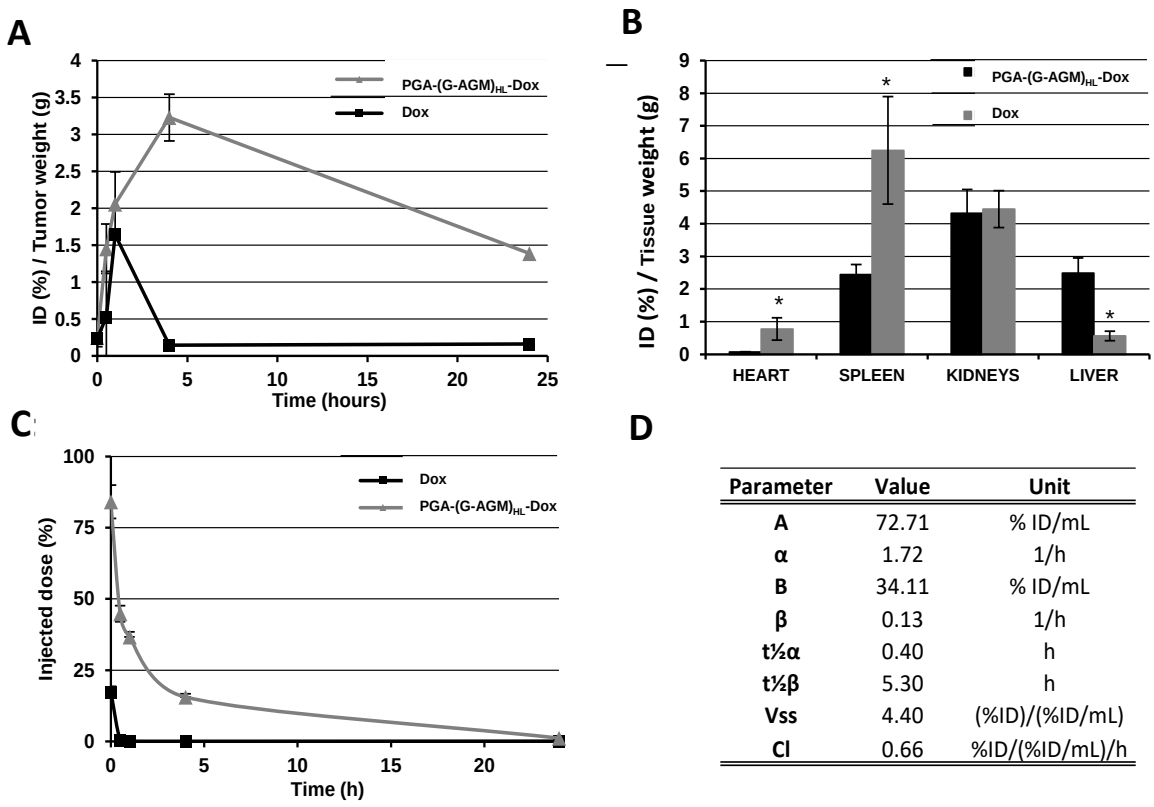

Parameter	Value	Unit
A	72.71	% ID/mL
α	1.72	1/h
B	34.11	% ID/mL
β	0.13	1/h
t½α	0.40	h
t½β	5.30	h
Vss	4.40	(%ID)/(%ID/mL)
Cl	0.66	%ID/(%ID/mL)/h

Figure 9. Biodistribution study of PGA-(G-AGM)$_{HL}$-Dox and Dox was studied in an orthotopic 4T1 breast tumor mice following iv injection in a tumor (**A)** and in blood and in heart, spleen, kidney and liver at 24h (**B**). The conjugate remained longer than Dox in the bloodstream (**C**) allowing sustained state for better tumor accumulation **D)** Pharmacokinetic parameters obtained from blood sample of mice i.v. administered with PGA-(G-AGM)$_{HL}$-Dox analyzed by a bi-compartment model (n=5).

Passive tumor accumulation reached a maximum accumulation time at 4 hours after i.v. administration (59-fold in comparison with free Dox, **Figure 9A**). We also detected conjugate accumulation in the heart and spleen, although at a significantly lower level (**Figure 9B**). Given the small size of the conjugate tested, we also expected kidney and liver accumulation due to renal excretion, as well as clearance by the reticuloendothelial system (**Figure 9B**, which may be promoted by the altered conformation of the combination conjugate. [49] To perform the pharmacokinetics study, we analyzed plasma samples of treated animals at different times (basal, 0.5, 1, 4 and 24 hours) and quantified Dox accumulation by HPLC (**Figure 9C**). We observed a similar blood circulation time profile for the combination polymer conjugate in comparison with free Dox. However, while we did not detect Dox at 30 min post administration of the free Dox form, we did detect Dox following combination conjugate treatment, resulting in a 9-times higher PGA-(G-AGM)$_{HL}$-Dox accumulation half-life (t½α=0.4h) when compared to free Dox (t½α=0.09h) (**Figure 9D**). These data agree with previous studies. [19, 49]

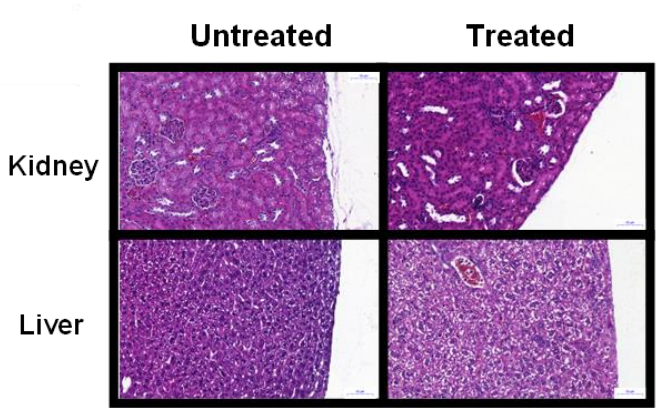

Figure 10. H&E staining of representative histological samples showed no pathological alterations associated with PGA-(G-AGM)$_{HL}$-Dox treatment in clearance related organs (kidney and liver) when compared to untreated control mice

III.2.5. Physico-chemical evaluation of selected conjugates and cellular uptake

The conjugation of single drugs and combinations of drugs influences conjugate size and conformation, and these effects modify the biophysical properties and thus the pharmacokinetic and biodistribution profile of the resultant conjugate. Conjugated moieties introduce new spatial and charged elements that change the electrostatic equilibrium of the whole anionic polypeptide. [17] While the behavior of our conjugates in the animal model can be explained by the drug release kinetics, drug synergism profiles, and the *in vitro* analyses, any correlation between drug loadings, linking chemistry, and *in vivo* fate remains unsolved. Such correlations are driven by an intricate and complex interplay of interconnected factors. The lack of descriptive elements to predict biological output within this family of polymer-drug conjugates motivated us to carry out a more detailed physico-chemical characterization of the conjugates, looking at conformational and structural/morphological features that might allow us to rationalize the observed biological performance.

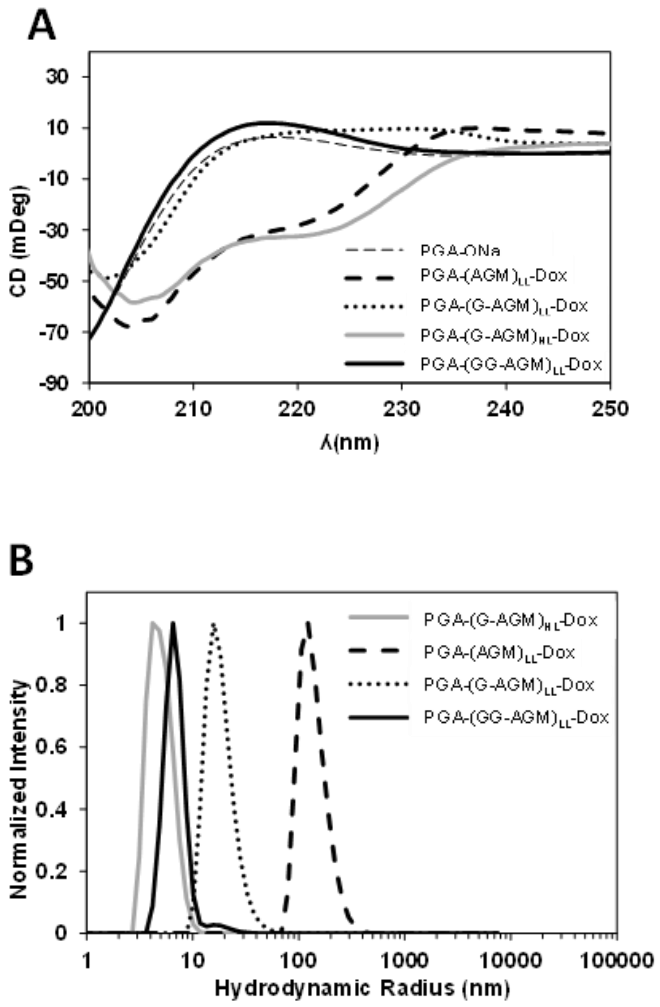

Figure 11. Physico-chemical characterization of selected combination conjugates PGA-$(AGM)_{LL}$-Dox, PGA-$(G\text{-}AGM)_{LL}$-Dox and PGA-$(G\text{-}AGM)_{HL}$-Dox. **A)** Circular Dichroism data on selected conjugates in phosphate buffer 10mM, pH=7.4 at 0,6mg/ml; **B)** Size distribution graphs in Number obtained by DLS in PBS at 2mg/ml.

At the molecular level, secondary structure analysis by Circular Dichroism (CD) (**Figure 11A**) demonstrated that PGA-$(G\text{-}AGM)_{LL}$-Dox clearly deviated from the expected random coil conformation of the polyanionic PGA towards a partial alpha-helix conformation. [50] We performed measurements in 10 mM phosphate buffer (pH=7.4) in order to avoid the influence of pH on PGA secondary structure. Therefore, we attributed the observed changes in conformation exclusively to the modifications performed. [51] PGA-$(AGM)_{LL}$-Dox, demonstrated a trend towards an alpha-helix conformation. The native secondary structure expected for PGA backbone seems to govern the overall conformation with increasing hydrophilic Gly linker length. Interestingly, the percentage of modification also influenced the disruptive effect of the linker; comparisons between

PGA-(G-AGM)$_{LL}$-Dox and PGA-(G-AGM)$_{HL}$-Dox demonstrated that the significant trend to partial alpha-helix structure can only be attributable to the increase of G-AGM moiety loading. G-AGM appears to partially shift the secondary structure to alpha-helix again, even more markedly than in the parent conjugate with direct attachment of drugs.

In order to ascertain how these observations at molecular level correlate with the polymer-drug conjugate conformations adopted in solution, we studied selected samples by SANS. The scattering data obtained for PGA-(AGM)$_{LL}$-Dox, PGA-(G-AGM)$_{LL}$-Dox, PGA-(G-AGM)$_{HL}$-Dox and PGA-(GG-AGM)$_{LL}$-Dox are shown on a log-log plot in **Figure 12**. We fitted the data according to a broad peak model [52] (See section **Materials and Methods III.4.6** for fitting details and complete analysis).

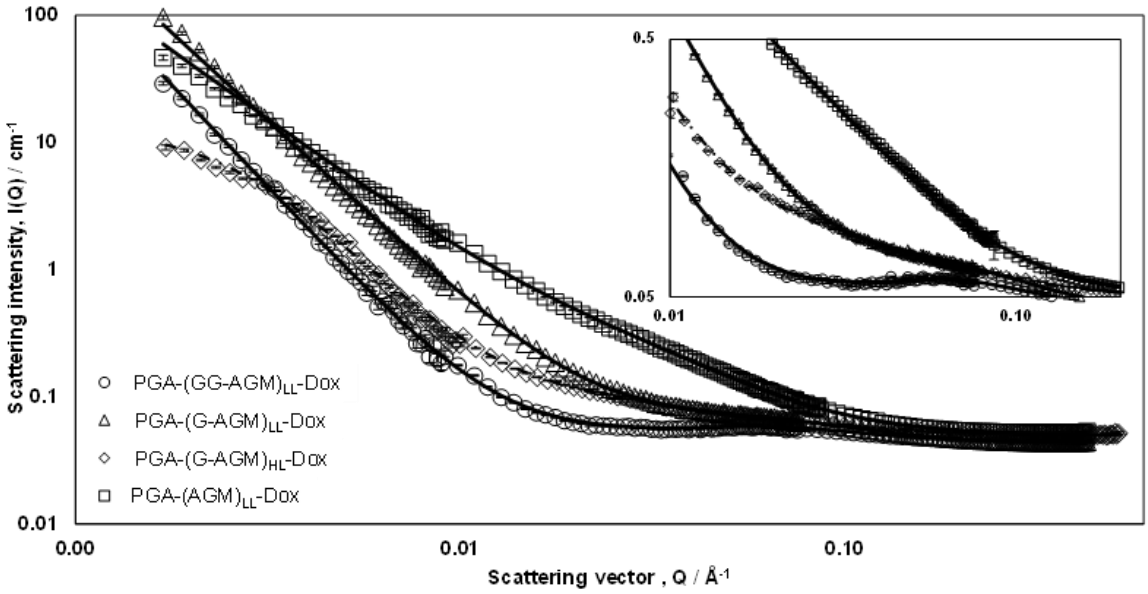

Figure 12. SANS profiles and fitting.

The predominant conformation of PGA in its protonated state in solution at low concentration is a helical structure at the molecular scale, giving rise to rod-like molecules at acidic pH, while random coil is the preferred conformation in the carboxylate form (pH>pKa). [51] These helixes associate in solution to form larger clusters that have an internal structure arising from alignment of the individual rod-like PGA molecules. Apart from the conjugate PGA-(G-AGM)$_{HL}$-Dox (68 nm), the total size of the clusters is outside of the accessible Q range for SANS, in agreement with the Volume and/or Intensity data obtained by DLS where the large-sized aggregates population has a much pronounced contribution to the overall size distribution (**section III.4.7 of Materials and Methods**).

However, detailed information can be provided on the alignment and spacing of molecules within the clusters. Due to the low drug loading and the single contrast (H-conjugate in D_2O), the PGA polymer backbone dominated the observed scattering. Hence, the SANS data provides information on how the drug and linker conjugation affect the PGA solution structure. The higher slope of the low Q scattering data (n) for the PGA-$(GG\text{-}AGM)_{LL}$-Dox, PGA-$(G\text{-}AGM)_{LL}$-Dox and PGA-$(G\text{-}AGM)_{HL}$-Dox conjugates, compared to PGA-$(AGM)_{LL}$-Dox suggests a fundamental difference in structure of the aggregates formed by these conjugates. Fitting parameters for PGA-$(GG\text{-}AGM)_{LL}$-Dox, PGA-$(G\text{-}AGM)_{LL}$-Dox and PGA-$(G\text{-}AGM)_{HL}$-Dox are indicative of more collapsed clusters (i.e. in the globular state with less free space within the scattering body). For the PGA-$(AGM)_{LL}$-Dox conjugate, fitting data suggested a more open Gaussian-like structure at this length scale (i.e. that the clusters are likely to be less densely internally packed). This would be in agreement with the measured size distributions by number shown in **Figure 11B**, where the large aggregates are outweighed, and hence the predominant clusters sizing follow the trend PGA-$(GG\text{-}AGM)_{LL}$-Dox < PGA-$(G\text{-}AGM)_{HL}$-Dox < PGA-$(G\text{-}AGM)_{LL}$-Dox < PGA-$(AGM)_{LL}$-Dox with the latter showing R_h size distributions of 100 nm in both number or intensity plots, in agreement with cryo-transmission electron microscopy (TEM) (**Figure 13A**).. The Gly linker introduces a hydrophilic character in the AGM construct, and computed LogP values (a measure of hydrophobicity or hydrophilicity) for AGM (1.46), G-AGM (0.09) and GG-AGM (-1.06) demonstrated a significant reduction of hydrophobicity of AGM upon Gly incorporation. Hence, PGA-$(AGM)_{LL}$-Dox had the highest hydrophobic character, displayed the highest propensity to aggregate (**section III.4.8 of Materials and Methods**), and also had the largest cluster size.

In the high Q region of the SANS data, the experiment probes the arrangement of chains within the cluster. Conjugates with low loading of AGM attached by a Gly-Gly and Gly linker both gave a small, broad peak (centered at Q_0 = 0.062 and 0.043 $Å^{-1}$, respectively) in the scattering data (Inset in **Figure 12**). This peak corresponds to a length scale of around 100-140 Å ($2\pi/Q_0$) within the structure, which is attributed to regular spacing of adjacent rigid molecules within the cluster. The absence of a peak for PGA-$(AGM)_{LL}$-Dox and PGA-$(G\text{-}AGM)_{HL}$-Dox indicated a loss of short range order within the aggregate, presumably as the effect of chain-chain charge interactions is outweighed by the excluded volume requirements, and drug solvent effect of the attached drugs. The

smaller Q_0 value for PGA-(G-AGM)$_{LL}$-Dox agrees with the lower flexibility of the linking group (compared to PGA-(GG-AGM)$_{LL}$-Dox) causing a greater perturbation of the PGA conformation. The peak observed in PGA-(G-AGM)$_{LL}$-Dox is lost when increasing the AGM loading to form PGA-(G-AGM)$_{HL}$-Dox. This further highlights drug-caused perturbation of PGA clusters.

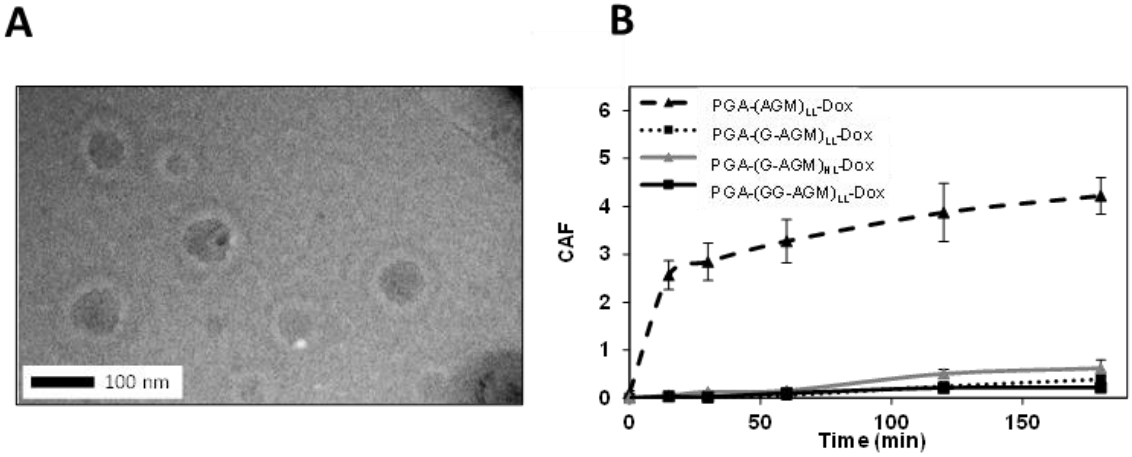

Figure 13. A) Representative Cryo-TEM image of PGA-(AGM)$_{LL}$-Dox in H2O at 2mg/ml, scale bar is 100 nm. **B)** Cellular uptake study of the selected conjugates by flow cytometry. Results are represented as the average of Cell associated fluorescence (CAF) ± SEM. (n=3).

Taken together, these data indicate that direct conjugation of the AGM molecules (in addition to the Dox present in all conjugates) disrupts the ability of the PGA to adopt its preferred solution conformation. [37, 38] The flexibility introduced by the Gly-Gly linker allows the character of the polymer backbone to dominate the structures formed, with the conjugate containing Gly-Gly linker (most flexible) showing the scattering most similar to that of pure PGA (peak is present). [37, 38] With the Gly linker, at low G-AGM loading the Gly affords sufficient flexibility for the PGA to retain its internal ordering (peak), and the overall aggregated morphology (n^{-3}). These data are consistent with CD spectroscopy that reports a range of helical content of the conjugates as discussed above (**Figure 11A**). Comparing the SANS data for these two conjugates, we start to see the influence of the additional G-AGM on the secondary structure. At low G-AGM loading the overall structure remains broadly similar to that expected for pure PGA, as described above. At high loading PGA-(G-AGM)$_{HL}$-Dox, packing of the individual molecules in the clusters is less ordered, (loss of peak). This is presumably due to a reduction in PGA-PGA charge repulsions, which keep the molecules separated by the characteristic distance

indicated by the peak at high Q. This lessened repulsion allows for closer association of the conjugate molecules, and the clusters become smaller and more globular (turnover at low Q). This smaller globular structure is a favorable result, as it is apparent that conjugates with such morphologies, as shown by SANS, give lowest IC_{50} values (**Tables 2 and 3**).

For the PGA-$(AGM)_{LL}$-Dox, PGA-$(G\text{-}AGM)_{LL}$-Dox and PGA-$(G\text{-}AGM)_{HL}$-Dox the CD, DLS and SANS data can help to correlate structure, conformation and drug release studies with the biological output (**Table 4**). Results from *in vitro* and *in vivo* experiments suggest that the drug release profile is the main factor in the antitumor activity of this family of conjugates. However, for PGA-$(AGM)_{LL}$-Dox exists evidence of a higher helical conformation and propensity to aggregate with the biggest cluster sizes and degradation of the PGA-(±G)-drug links is not (or certainly is less) inhibited. However, although this conjugate also displays by far the most efficient cellular uptake along the family, the simultaneous drug release and subsequent drug antagonism translates into low cytotoxicity. Combined with the identical polymer-drug linkages this accounts for the similar release profiles for both drugs. For the PGA-$(G\text{-}AGM)_{LL}$-Dox, AGM was released preferentially to Dox. The more strongly helical structure of the individual PGA-$(G\text{-}AGM)_{LL}$-Dox conjugate molecules indicated by CD supports the lower accessibility of Dox, and ordered spacing structures within the clusters suggests structure with greater accessibility for the cathepsin B cleaving group. It is more difficult to reconcile the release data for the PGA-$(G\text{-}AGM)_{HL}$-Dox conjugate: lower release of AGM and high release of Dox. CD reports a helical structure at the molecular level, SANS reports disordered clusters of molecules that are smaller and more densely packed than PGA-$(G\text{-}AGM)_{LL}$-Dox. Neither technique probes the detailed packing of the AGM around the PGA helix, but SANS assessments indicate that, at high G-AGM content, inter-molecular interactions are AGM, rather than PGA, dominated. Intra-molecular or indeed inter-molecular AGM-AGM interactions may somehow be screening the linkers. This might also be indicative of non-random distribution of the drug along the PGA chain at the higher loading either at outset, or induced as the drug loading changes at very low release levels. More detailed structural studies at key time-points would be required to resolve these possibilities.

Polymer-drug conjugate	Cytotoxicity human MCF-7ca	Cytotoxicity murine 4T1	Size (R_H) (By number)	Cellular Uptake	Secondary structure trend	Antitumor activity	Drug release	SANS
PGA-$(AGM)_{LL}$-Dox	Low (IC50 = 0.53)	Sparingly (IC50 = 0.012)	~100nm	High	Alpha-helix	Non-effective	Simultaneous	Larger, non-compact aggregates. No evidence of internal ordering
PGA-$(G\text{-}AGM)_{LL}$-Dox	High (IC50=0.003)	High (IC50=0.0034)	~20nm	Low	Random coil	Effective	AGM first and faster	Larger compact aggregates. Some internal ordering
PGA-$(G\text{-}AGM)_{HL}$-Dox	High (IC50=0.0017)	High (IC50=0.0033)	~4nm	Low	Alpha-helix	Highly effective	Dox first and faster	Smaller, more compact aggregates. No evidence of internal ordering
PGA-$(GG\text{-}AGM)_{HL}$-Dox	High (IC50=0.0011)	N/A	~7nm	Low	Random coil	N/A	N/A	Large compact aggregates. Internally ordered

Table 4. Summary of main physico-chemical and biological descriptors of the selected polymer-drug conjugates.

III.3. Conclusions

We have designed a wide family of single and combination polymer-drug conjugates aiming for efficient antitumor treatment for breast cancer. Within the present family of PGA-AGM-Dox conjugates, we ratify the importance of the presence of both drugs in the same polymeric carrier that secures their co-delivery to the same cell. Of note, we paid special attention to the interplay between biological behavior and determinant physico-chemical properties. As expected drug ratio is a key feature ruling conjugate activity as seen for PGA-$(G\text{-}AGM)_{HL}$-Dox *vs.* PGA-$(G\text{-}AGM)_{LL}$-Dox in this case. More importantly, we discovered that the presence of the small and flexible Gly linker (the smallest amino acid, involving less than 1% of the total molecular weight of the conjugate) plays a decisive role in the structure of the whole macromolecule and hence significantly influences biological activity. The introduction of Gly induces a significant shift in drug release kinetics, size, secondary structure, and internal arrangement of the polypeptidic backbone as derived from the intensive CD, DLS, and SANS studies. The different configuration for Gly linker introduction (G or GG) between the polymer and AGM seems to modify the spatial disposition of the conjugate in such a way as to modify the disposition of the conjugate for the protease cleavage allowing a differential release of AGM *vs.* Dox and consequently determining the final therapeutic output. It is clear

that the kinetics of drug release is one of the major physicochemical descriptors to take into account when designing combination therapeutics.

As seen within this work, the choice of linkers employed in the conjugation of active agents in a combination-polymer-drug conjugate can endow the complex macromolecular system with enhanced properties. In our family of conjugates the best performance was seen with PGA-(G-AGM)$_{HL}$-Dox, conjugate bearing a 2:1 (AGM:Dox) drug ratio and Gly as AGM linker. This combination conjugate showed significantly greater antitumor effects than PGA-(G-AGM)$_{LL}$-Dox (1:1 AGM:Dox ratio) and even more remark performance if compared with those with a direct AGM conjugation.

Our results lay the groundwork to move towards the efficient design of newer conjugates with more adequate linkers allowing enhanced spatio-temporal control on release profiles, seeking for synergistic effects and, therefore, improved antitumor effects. Our results also highlight the importance of an exhaustive supramolecular characterization to adequately compare *in vitro* and *in vivo* assessments.

III.4. Materials and Methods

III.4.1. Materials

All organic solvents were of analytical grade purchased from Scharlab and used without further purification. All chemicals were of reagent grade and used without further purification and were purchased from Sigma-Aldrich otherwise stated. Poly-(alpha-L-glutamic acid) (Mw: 12900Da, PDI: 1.2, 100 subunits per polymer, PGA100u) was obtained from Polypeptide Therapeutic Solutions SL (Valencia, Spain). Doxorubicin hydrochloride salt was purchased from Xingcheng Chempharm Co. Ltd (Zhejiang, China). Aminoglutethimide was purchased from Sigma-Aldrich. Anhydrous N,N-Dimethylformamide (DMF, ≥99.8% anhydrous) was purchased from Scharlab SL (Sentmenat, Spain). 1-Hydroxibenzotriazol monohydrate (HOBt) was purchased from Iris Biotech GmbH (Marktredwitz, Germany). Deuterated dimethyl sulfoxide (d6-DMSO) and deuterium oxide were purchased from Deutero GmbH. Ultrapure water with resistivity of 18 MΩ.cm was used in all aqueous preparations (Milli-Q® ultrapure).

Preparative SEC was performed using either Sephadex® G-25 or Sephadex® LH-20 and were purchased from GE Healthcare Bio-Sciences AB (Uppsala, Sweden). Phenazinemethosulfate (PMS) was supplied by Sigma (Sp). Dulbecco's Modified Eagle's Medium (DMEM), Leibovitz, Phosphate buffer saline (PBS), Fetal bovine serum (FBS) Medium 200, Low Serum Growth Supplement (LSGS) and Trypsin, were provided from Gibco. (3-(4,5-dimethylthiazol-2-yl)-5- (3-carboxymethoxyphenyl)-2-(4-sulfophenyl)-2H-tetrazolium) (MTS) was supplied by Promega (Sp). Oregon Green was purchased from Invitrogen.

III.4.2. Physico-chemical characterization methods

III.4.2.1. Ultraviolet-Visible Spectroscopy (UV-VIS)

UV-VIS measurements were performed using JASCO V-630 spectrophotometer at 25 °C with 1.0 cm matched quartz cells and with spectral bandwidth of 0.5 nm.

Determination of total AGM content by UV Spectroscopy.

AGM or the corresponding amino acid-AGM derivative, X-AGM, were first prepared for use as calibration standards. A stock solution of AGM derivative in HPLC grade MeOH was prepared (1 mg/mL). To obtain a calibration curve samples were diluted using MeOH to give a concentration range of 0-50 μg/mL for AGM or 0-130 μg/mL for X-AGM. The total drug loading of the conjugates was determined by measuring the optical density at 254 nm in milliQ H_2O. PGA in the same concentration range as the conjugates analyzed (0-5 mg/mL) was used as blank.

III.4.2.2. High Performance Liquid Chromatography (HPLC)

Analytical determination of total drug loadings and free drugs was performed on a Waters HPLC system provided with 2x515 binary pumps, autosampler 717 Plus, FLD 2475 and PDA 2996. RP C-18 Lichrospher analytical column was employed (Scharlab). Chromatograms were treated with Empower 2.0 software (Waters).

Determination of total Dox loading by HPLC.

Aqueous solutions of PGA-X-AGM-Dox conjugates (1 mg/mL) were prepared, and an aliquot (100 mL) was added to a polypropylene tube and made up to 1 mL with

water. Then 1 mL of 2 M HCl was added and the tubes were heated at 80°C for 30 min in order to get Dox aglycone. After cooling down to RT. 1 mL 2 M NaOH and the pH of the samples was adjusted to 8,5 with ammonium formate buffer (100 μL, 1.0 M, pH 8,5). In parallel the same procedure was carried out for the parent compound Dox (using 100 mL of a 1 mg/mL stock aqueous solution). Daunorubicin (Dau) was used here as internal standard; 100 mL of a 1 mg/mL stock aqueous solution was added to each sample. Samples were then thoroughly extracted by vortexing (3x10 sec). The upper aqueous layer was carefully removed and the solvent was evaporated under reducer pressure (speedvac). The dry residue was dissolved in 100 mL of HPLC grade methanol. Addition of 100 mL of methanol to redissolve the product gave a 100 mg/mL stock from which a range of concentrations were prepared (2-60 mg/mL). The amount of total drug was determined by HPLC using RP18 column (125x4 mm), with a flow rate of 1 mL/min and using a gradient elution [solvent A: 2-propanol/H_2O 12:88 (v/v), solvent B: 2-propanol/H2O 29:71 (v/v)] adjusted to pH=3,2 with orthophosphoric acid. The total run time was 25 min and the gradient profile was: t = 0 A 0%, t = 1 A 60%, t = 3 A 60%, t = 8 A 0%, t = 18 A 0%, t = 20 A 100%, t = 20 A 100%. To monitor Dox and Dau standard a fluorescence detection at λ= 485 nm for excitation and λ= 560 nm for emission was used. Retention time (tr) was 15 min for Dox aglycone and 20 min for Dau aglycone.

Determination of free Dox content by HPLC.

100 μL of a known concentration of PGA-X-AGM-Dox conjugate was added with 100 μL of NaHCO3 and 100 μL of Dau (1 mg/mL) as internal standard. Free Dox and Dau were thoroughly extracted with CHCl3:Isopropyl alcohol 4:1 (3x30 sec). The upper aqueous layer was carefully removed and the organic phase dried through N_2 flow. The dry residue was dissolved in 100 μL of HPLC grade MeOH. In parallel the same process was also carried out with a mixture of Dox and Dau to construct a standard curve. The standards were dissolved in 1 mL of HPLC grade MeOH to give a 100 mg/mL stock solution from which a range of concentration were prepared (5-100 mg/mL). The amount of free drug was determined by HPLC using RP18 column (125x4 mm), with a flow rate of 1 mL/min and using a gradient elution [A: 2-propanol/H2O 12:88 (v/v), solvent B: 2-propanol/H2O 29:71 (v/v)] adjusted to pH 3,2 with o-phosphoric acid. Total run time was 42 min and the gradient profile was: t = 0 A 0%, t = 1 A 0%, t = 26 A 100%, t = 27 A 50%, t = 37 A 50%, t = 40 A 0%, t = 42 A 0%. To monitor Dox and Dau standard, a

fluorescence detection at λ_{ex} = 485 nm for excitation and λ_{em} = 560 nm for emission was used. The tr was 20 min for Dox and 30 min for Dau.

Determination of total AGM loading by HPLC, indirect analysis.

The dried residue obtained from the conjugation reactions was dissolved in CH_2Cl_2 and all remaining precipitate was filtered off. AGM is completely soluble in CH_2Cl_2. The solvent was evaporated under reduced pressure and MeOH (10 mL) was added to make the stock solution. 3 different concentrations were injected to the HPLC (after filtered through 0,45 μm). The free amount of drug in the conjugate residues was determined by HPLC using a RP18 column (125x4 mm), with a flow rate of 1 mL/min and using a gradient elution [A: H_2O milliQ+0,1%TFA, solvent B: ACN+0,1%TFA]. Total run time 25 min and the gradient profile was: t=0 A 90%, t=4 A 90%, t=19 A 10%, t=21 A=90%, t=25 A=90%, t=40 A 0%, t=42 A 0%. Oestradiol (1 μg/mL) was used as internal standard. A UV-Vis diode array (DAD) was used as detector. The retention time was 2 min for GGAGM, 6 min for G-AGM and 5 min for AGM.

Determination of free AGM content by HPLC

To evaluate the free drug, 100 μL of a known concentration of polymer conjugate was added with 100 μL of sodium bicarbonate and 100 μL of oestradiol (1 μg/mL) as internal standard. Free X-AGM and oestradiol were thoroughly extracted with a mixture (5 mL) of AcOEt : Isopropyl alcohol 4:1 (3x10 s). The upper organic layer was carefully removed and dried through N2 flow. The dried residue was dissolved in 100 μL of HPLC grade ACN. In parallel to construct a standard curve, the same concentrations used for the determination of the total drug loading were used to obtain an HPLC standard curve. 100 μL of each concentration was added to a mixture of 100 μL of bicarbonate, 100 μL of oestradiol and 700 μL of milliQ H2O and thoroughly extracted as described above. The amount of free drug was determined by HPLC using the same HPLC protocol described for the determination of the total drug loading by HPLC (indirect measurement, see below). Retention time was 2 min for GG-AGM, 6 min for G-AGM, 5 min for AGM and 12 min for oestradiol.

III.4.2.3. Matrix Assisted Laser Desorption/Ionization–Time Of Flight (MALDI-TOF)

1 μL of sample was spotted into the MALDI target plate. After droplets were air-dried at room temperature, 0.5 μL of matrix (5 mg/mL CHCA (Sigma) in 0.1% TFA-ACN/H_2O (1:1, v/v)) was added and allowed to air-dry at room temperature. The samples were analyzed in a 4700 Proteomics Analyzer (ABSciex) in positive reflection mode (3000 shots every position) in a suitable range of mass. The samples were also analyzed in a 4700 Proteomics Analyzer (ABSciex) in linear mode (3000 shots every position) in a suitable range of mass. A matrix sample was analyzed under the same experimental conditions.

III.4.2.4. Nuclear Magnetic Resonance (NMR) Spectroscopy

NMR spectra were recorded at 27 °C (300 K) on an Avance III 500 MHz Bruker spectrometer equipped with a 5 mm TBI broadband probe or a 300 Ultrashield^{TM} from Bruker (Billerica MA, USA). Data were processed with the software Mestrenova (Bruker GmbH, Karlsruhe, Germany). Samples were prepared tipically at 5mg/ml in deuterated solvents.

III.4.2.5. Size Exclusion Chromatography (SEC) in aqueous media.

SEC measurements in aqueous media containing 0.5 M of $NaNO_3$ and 0.005%(w/w) azide as an additive were performed in a AF2000 system from Postnova Analytics (Landsberg, Germany). The system was configured to work on SEC mode with an isocratic pump (PN1130) an autosampler (PN5300), a refractive index (RI, PN3150), 21 angle-multi angle light scattering (MALS, PN3621) and a UV-Visible (PN3211) detectors. A working flow rate of 0.7 $mL \cdot min^{-1}$ at 30 °C was employed with one TSKgel G3000PWXL column.

III.4.2.6. Circular Dichroism (CD).

CD Spectroscopy was performed with a J-815 CD Spectrometer (JASCO Corporation) using a Peltier thermostated cell holder (PTC-423, JASCO Corporation) with a recirculating cooler (JULABO F250, JASCO Corporation). A nitrogen flow (~2.7

L·min-1) was lead through the spectrometer and controlled with a nitrogen flow monitor (Afriso Euro-Index). The samples were dissolved under different conditions (ddH_2O or PB, and different concentrations ranging from 0.6mg·mL^{-1}). Samples were measured repeatedly (n= 3) in a quartz cuvette with d= 0.1 cm.

III.4.2.7. Dynamic Light Scattering (DLS).

DLS measurements were performed using a Malvern ZetasizerNanoZS instrument, equipped with a 532 nm laser at a fixed scattering angle of 173°. Solutions were sonicated for 10 min and allowed to age for the required time, filtered through a 0.45 μm cellulose membrane filter and measured. Size distribution was measured (radius, nm) for each polymer per triplicate with n> 3 measurements.

- Size measurements, polymer solutions were prepared under different conditions (ddH_2O, phosphate buffers or salt containing solutions, at different concentrations and temperatures), automatic optimization of beam focusing and attenuation was applied for each sample.
- Critical aggregation concentration was evaluated through an already described method[53] using DLS by plotting the scattered intensity (mean count rate (kcps)) *vs.* the concentration.

III.4.2.8. Cryo-TEM.

Samples were vitrified in an FEI's vitrobot: A 60 μL drop of an aqueous suspension of the material was placed on a TEM holey carbon copper grid, excess of water was blotted away at the vitrobot with filter paper and the grid were freeze-plunged in liquid ethane. Samples were then transferred under liquid nitrogen atmosphere to a Gatan TEM cryo-holder equipped with a liquid nitrogen reservoir. After that, samples were transferred to a Tecnai T20 (FEI company) operated at 200 KV. All observations were done at low temperature (100 K).

III.4.2.9. Small Angle Neutron Scattering (SANS)

Small-angle neutron scattering (SANS) experiments were performed on the D11 instrument at the Institute Laue-Langevin (ILL) in Grenoble, France. Sample solutions were prepared at a conjugate concentration of 10 mg mL^{-1} on a 1ml scale in D_2O (pH=5.5, 0.1M phosphate buffer) and placed in 2mm path length quartz cells, mounted in a sample

changer thermostatted at 37°C (± 0.2). Scattering data were corrected for the scattering and transmission of the solvent and quartz cell, and placed on an absolute intensity scale by reference to H_2O. Three sample detector distances were used to cover a Q range of 0.002 – 0.43 $Å^{-1}$. Data were analyzed by a model fit using SASview. [54]

III.4.3. Synthesis of polymer-AGM linkers

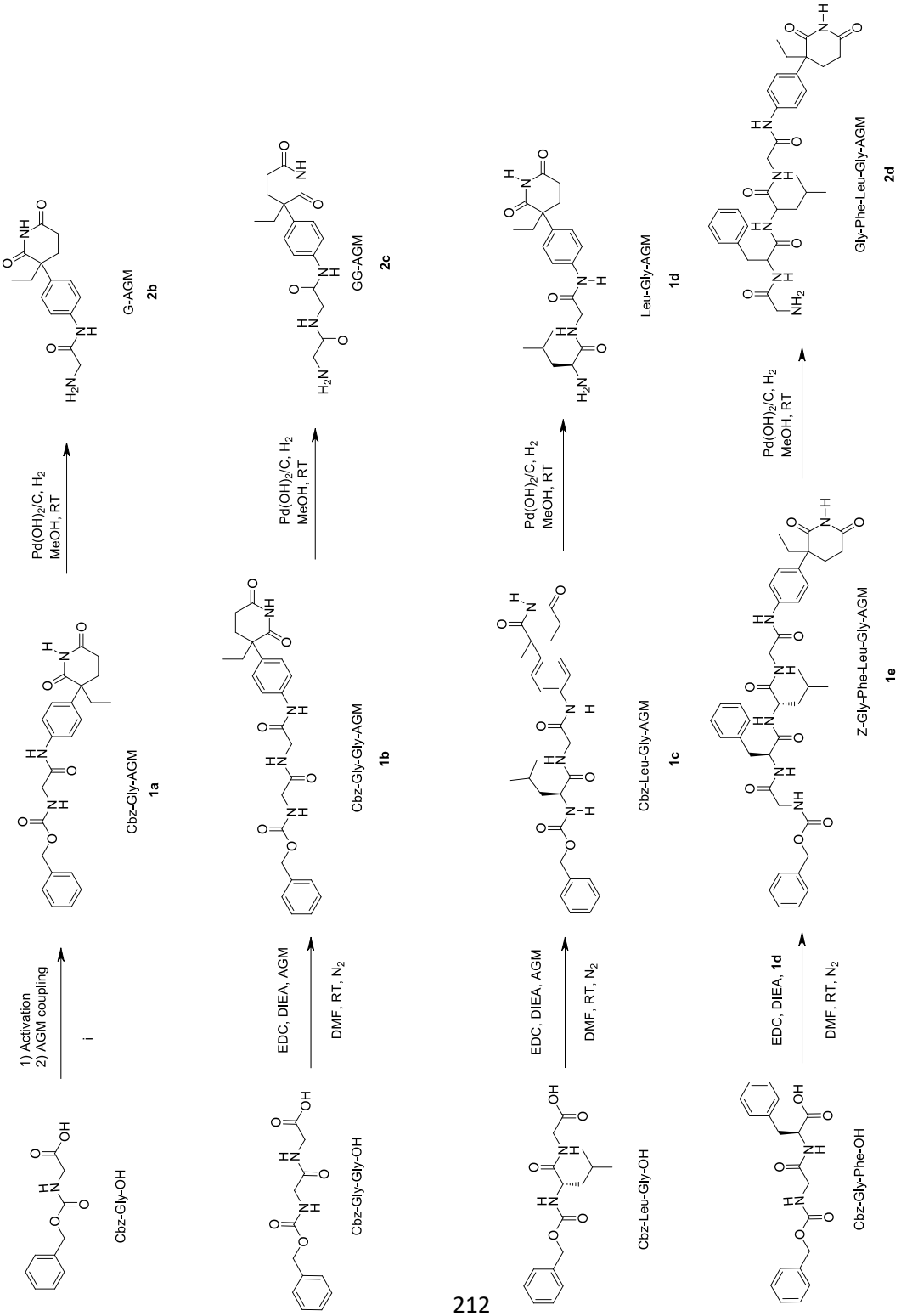

Figure 14. General synthetic scheme for the preparation of AGM-peptidyl derivatives

Synthesis of Cbz-Gly-AGM

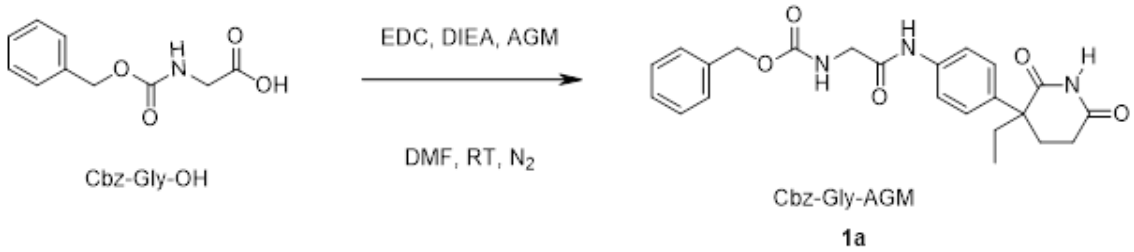

Figure 15. Synthetic scheme for the preparation of Cbz-Gly-AGM.

A solution of EDC (1.97 mmol, 377.8 mg) in dry DMF(1mL) was added dropwise to a solution of Cbz-Gly-OH (1.72 mmol, 361.12 mg) in dry DMF (10.0 ml). Activation was allowed to stand over an ice bath, under stirring and N_2 atmosphere. 10 minutes later, Aminoglutethimide (1.64 mmol, 582,3 mg) was added and once dissolved, pH of the solution was adjusted to 8.0 by addition of some drops of DIEA. Reaction proceeded during 24 hours at room temperature under N_2 atmosphere and then solvent was evaporated under reduced pressure. Viscose residue was partitioned between $CHCl_3$ and water. The organic phase was washed with dilute HCl solution, water and dilute sodium bicarbonate to be finally dried over sodium sulfate. Solvent was evaporated and final white/yellow powder was obtained (yield = 80,8%) **^{1}H NMR** (300 MHz, DMSO) δ 10.83 (s, 1H), 10.00 (s, 1H), 7.55 (dd, J = 17.1, 7.3 Hz, 5H), 7.25 (t, J = 10.7 Hz, 4H), 5.05 (s, 2H), 3.80 (s, J = 6.1 Hz, 2H), 2.49 – 2.25 (m, 2H), 2.24 – 2.01 (m, 2H), 1.97 – 1.63 (m, 2H), 0.75 (t, J = 7.3 Hz, 3H).**^{13}C NMR** (75 MHz, DMSO) δ 177.62 – 174.91 (s), 173.19 (d, J = 5.9 Hz), 168.76 (d, J = 48.6 Hz), 159.22 – 155.39 (m), 138.15 (t, J = 45.9 Hz), 136.46 – 133.53 (s), 121.07 – 117.54 (m), 68.34 – 63.76 (m), 51.90 – 48.89 (s), 44.34 (d, J = 23.7 Hz), 34.25 – 31.32 (s), 29.47 (d, J = 13.6 Hz), 27.49 – 25.09 (s), 11.04 – 7.81 (s). **MALDI-TOF:** $[M]^+$ + [Na+]= 446.13.

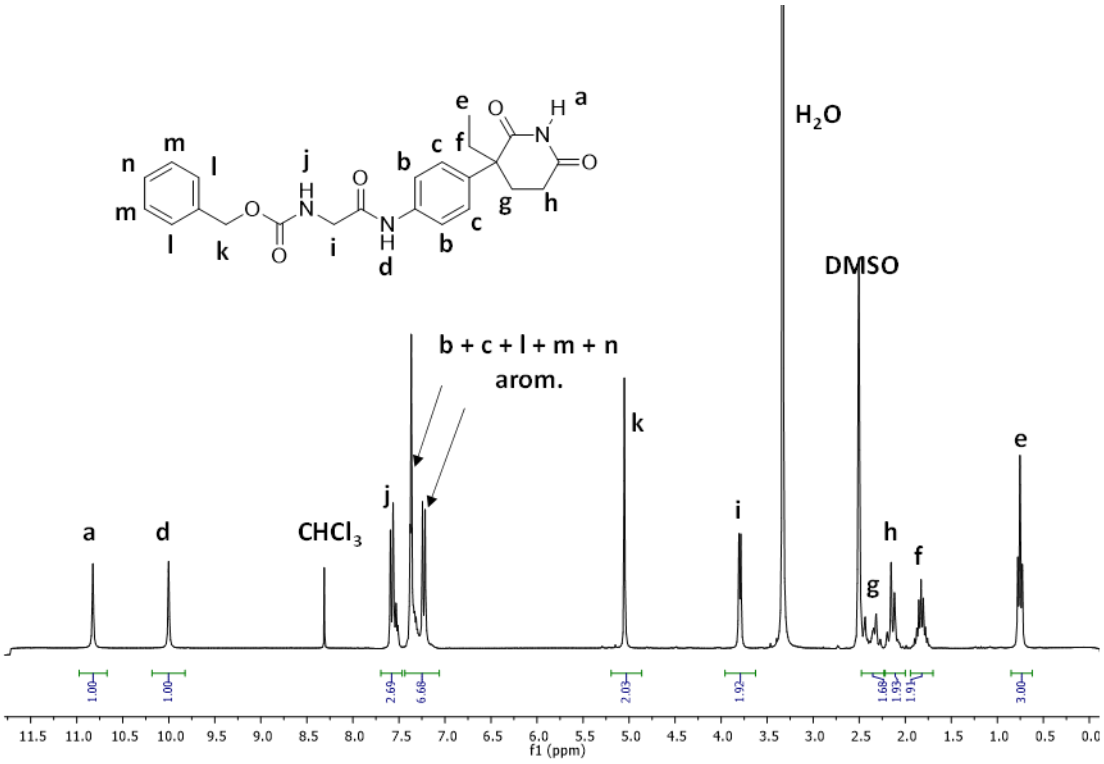

Figure 16. [1]H-NMR assignment for Cbz-Gly-AGM.

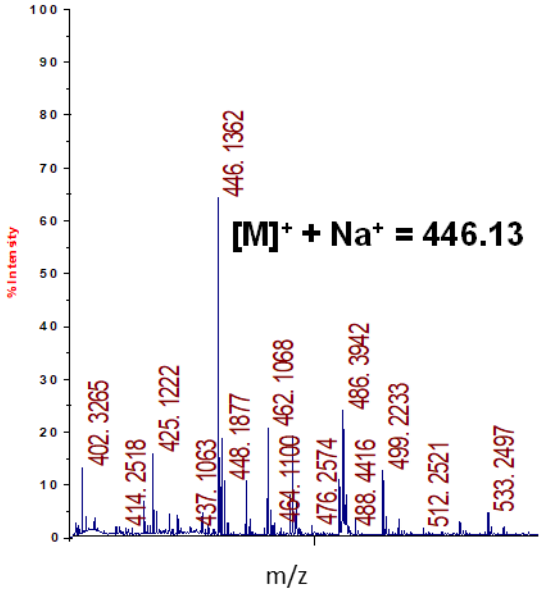

Figure 17. MALDI-TOF spectrum of Cbz-Gly-AGM.

Synthesis of Gly-AGM

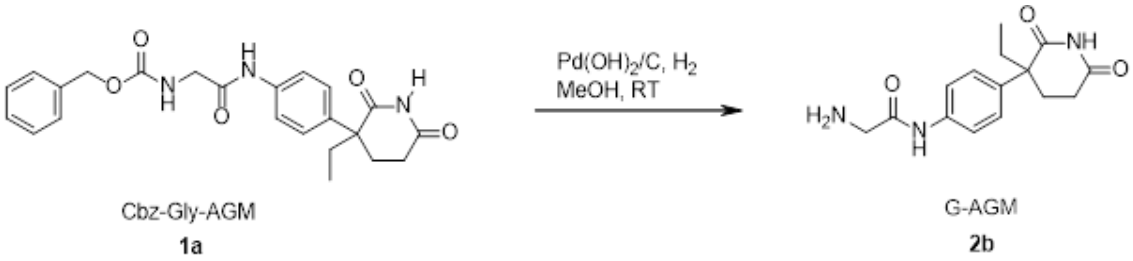

Figure 18. Synthetic scheme for the preparation of Gly-AGM.

200 mg of **1a** were dissolved in dry MeOH (20 mL) and a spoon of Pearlman's catalyst, $Pd(OH)_2$ over charcoal, was added. Reductive H_2 atmosphere was established by careful purging and priming the flask. Methanolic suspension was stirred in H_2 atmosphere overnight. Carbon was filtered off with celite and solvent was evaporated under reduced pressure to yield brownish fine powder (yield = 91%) was characterized by ^{1}H-NMR in d^6-DMSO. **^{1}H NMR** (300 MHz, DMSO) δ 10.84 (s, 1H), 10.72 (s, 1H), 8.42 – 8.06 (s, 2H), 7.71 – 7.50 (d, 2H), 7.28 (d, J = 9.0, 2.2 Hz, 2H), 3.76 (s, J = 10.5 Hz, 2H), 2.36 (m, 2H), 2.21 – 2.01 (m, 2H), 1.94 – 1.65 (m, 2H), 0.75 (t, J = 7.3 Hz, 3H).**^{13}C NMR** (75 MHz, DMSO) δ 178.14 – 174.91 (s), 174.61 – 171.61 (s), 167.03 – 162.97 (s), 137.43 (s), 136.24 – 133.76 (s), 129.18 – 125.65 (s), 121.37 – 117.84 (s), 52.65 – 48.07 (s), 33.72 – 30.79 (s), 29.85 (s), 26.63 (s), 8.50 (s). **MALDI-TOF:** $[M]^+ + [H^+]$= 290.13.

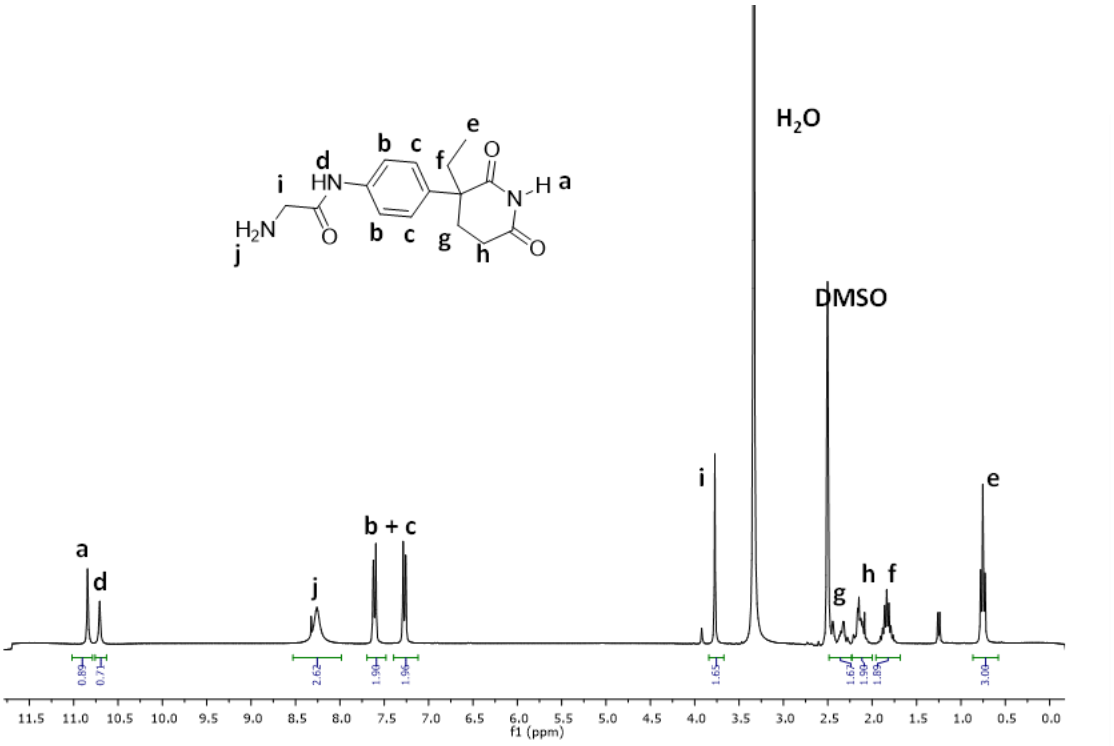

Figure 19. ^{1}H-NMR assignment for Gly-AGM.

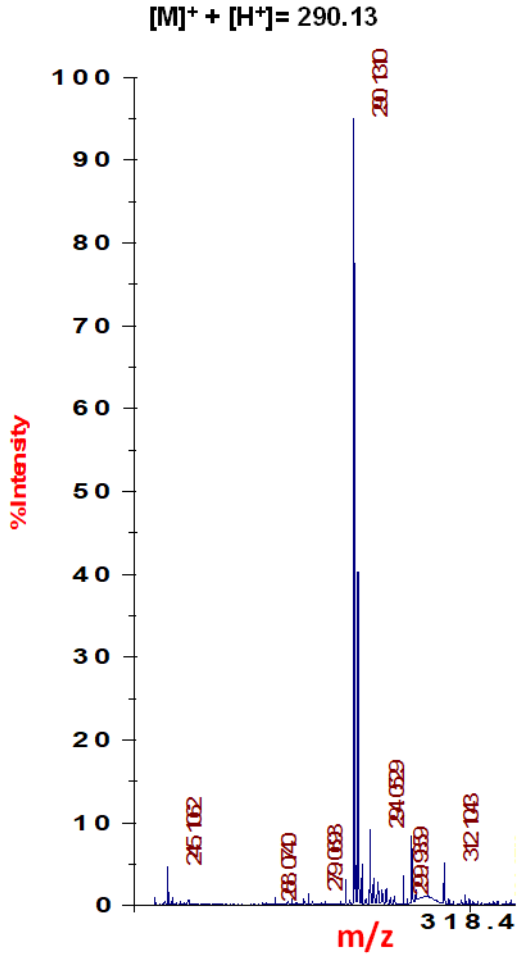

Figure 20. MALDI-TOF spectrum of Gly-AGM.

Synthesis of Cbz-Gly-Gly-AGM

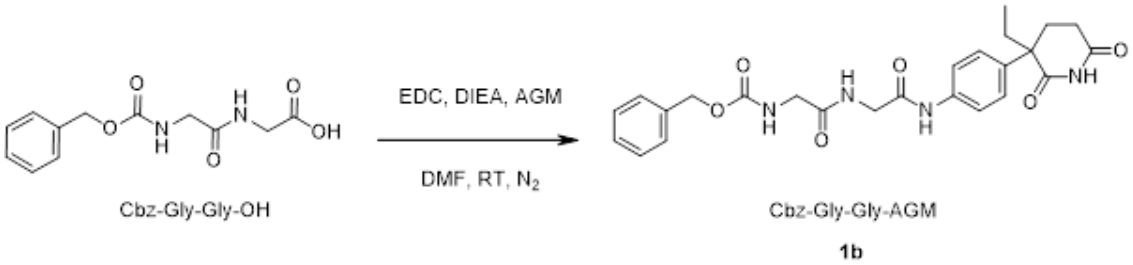

Figure 21. Synthetic scheme for the preparation of Cbz-Gly-Gly-AGM.

Synthesis of Cbz-Gly-Gly-AGM was carried out following the same procedure described for compound Cbz-Gly-AGM using Cbz-Gly-Gly-OH instead (1.72 mmol, 361.12 mg). (yield = 80,8%) **^{1}H NMR** (300 MHz, DMSO) δ 10.82 (s, 1H), 9.90 (s, 1H), 8.22 (t, J = 5.6 Hz, 1H), 7.56 (dd, J = 15.2, 7.3 Hz, 4H), 7.44 – 7.10 (m, 5H), 5.05 (s, 2H),

3.90 (d, J = 5.7 Hz, 2H), 3.69 (d, J = 6.1 Hz, 2H), 2.44 – 2.23 (m, 2H), 2.24 – 2.01 (m, 2H), 1.96 – 1.63 (m, 2H), 0.75 (t, J = 7.3 Hz, 3H).**^{13}C NMR** (75 MHz, DMSO) δ 175.61 (s), 174.61 – 172.21 (s), 169.73 (s), 168.01 (s), 159.22 (s), 137.48 (d, J = 47.7 Hz), 134.80 (s), 128.79 (s), 128.19 (s), 126.95 (d, J = 26.8 Hz), 121.37 (s), 67.82 (s), 52.65 (s), 45.06 – 41.31 (d), 32.14 (s), 29.22 (s), 27.79 (s), 11.27 (s). **MALDI-TOF:** $[M]^+ + [Na^+]$= 503.16.

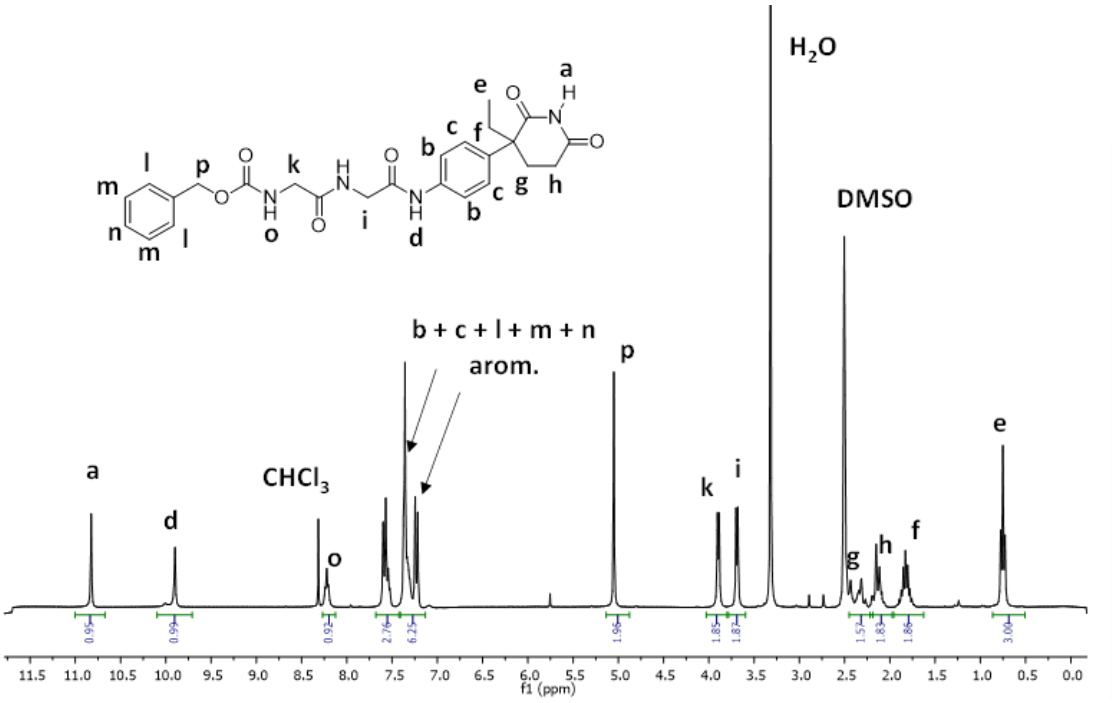

Figure 22. ^{1}H-NMR assignment for Cbz-Gly-Gly-AGM.

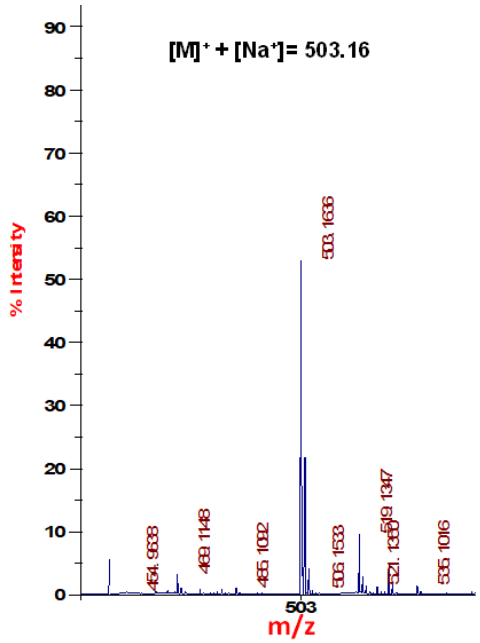

Figure 23. MALDI-TOF spectrum of Cbz-Gly-Gly-AGM.

Synthesis of Gly-Gly-AGM

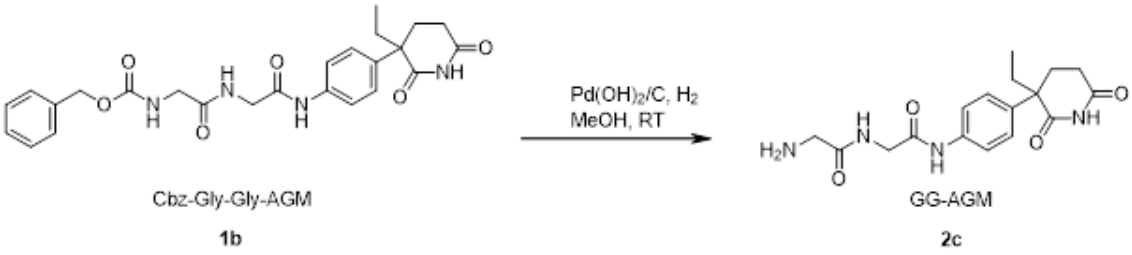

Figure 24. Synthetic scheme for the preparation of Gly-Gly-AGM.

Deprotection of Cbz-Gly-Gly-AGM was performed following the same procedure described for the deprotection of Cbz-Gly-AGM. Yield (76%) **^{1}H NMR** (300 MHz, DMSO) δ 10.76 (s, 1H), 10.21 (s, 1H), 8.72 (s, 1H), 7.66 – 7.48 (d, 2H), 7.31 – 7.10 (d, 2H), 3.99 (d, *J* = 2.9 Hz, 2H), 3.56 (d, *J* = 22.4 Hz, 2H), 2.34 (t, *J* = 24.8 Hz, 2H), 2.24 – 1.98 (m, 2H), 1.97 – 1.67 (m, 2H), 0.75 (t, *J* = 6.0 Hz, 3H). **^{13}C NMR** (75 MHz, DMSO) δ 176.24 (s), 173.01 (s), 168.90 (s), 138.01 (s), 135.56 (d, *J* = 90.9 Hz), 128.12 (s), 121.89 (s), 50.80 (s), 33.50 (s), 30.79 (s), 27.79 (s), 11.04 (s). **MALDI-TOF:** $[M]^{+}$ + $[Na^{+}]$= 379.07.

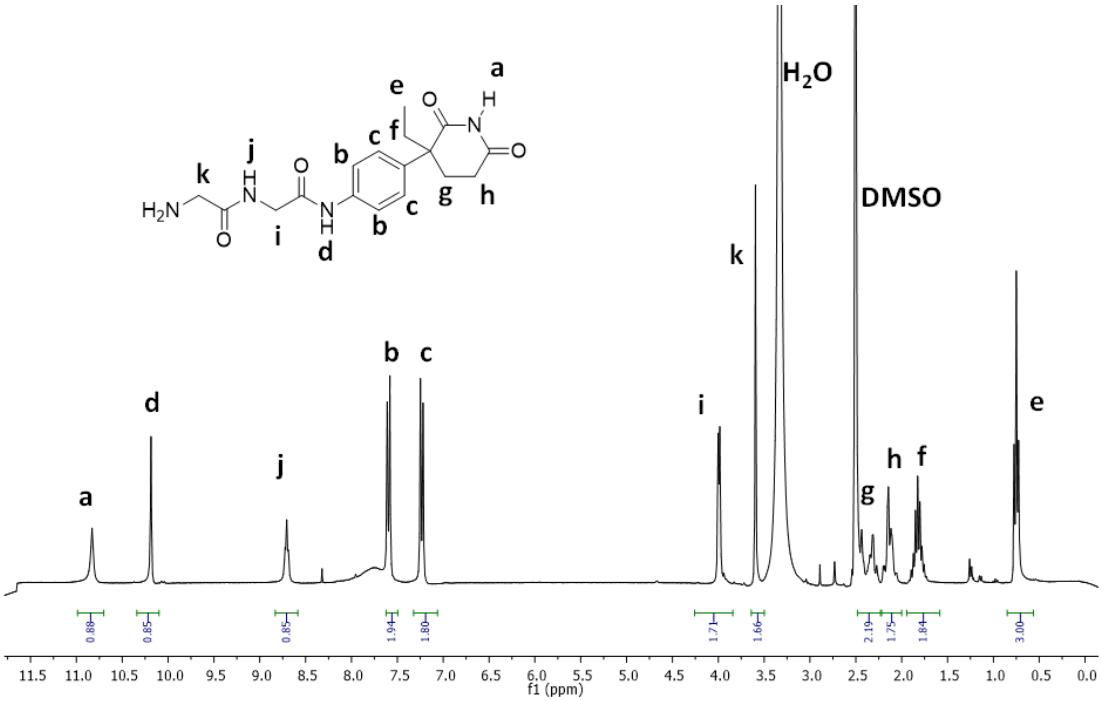

Figure 25. ^{1}H-NMR assignment for Gly-Gly-AGM.

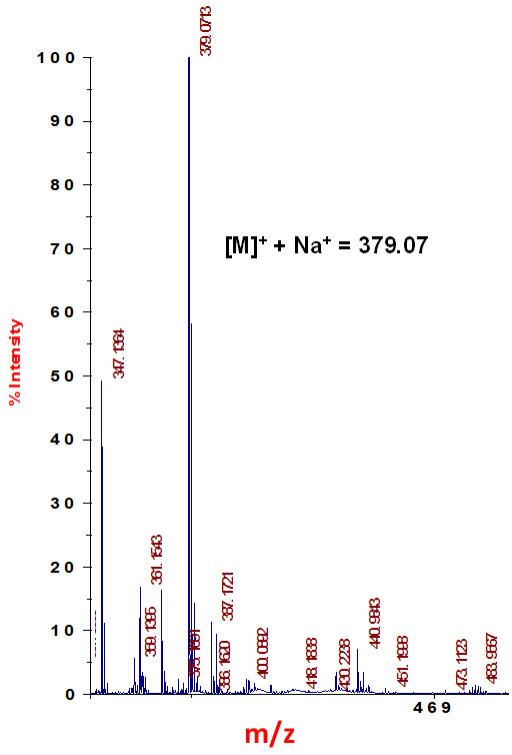

Figure 26. MALDI-TOF spectra of Gly-Gly-AGM.

Synthesis of Cbz-Leu-Gly-AGM

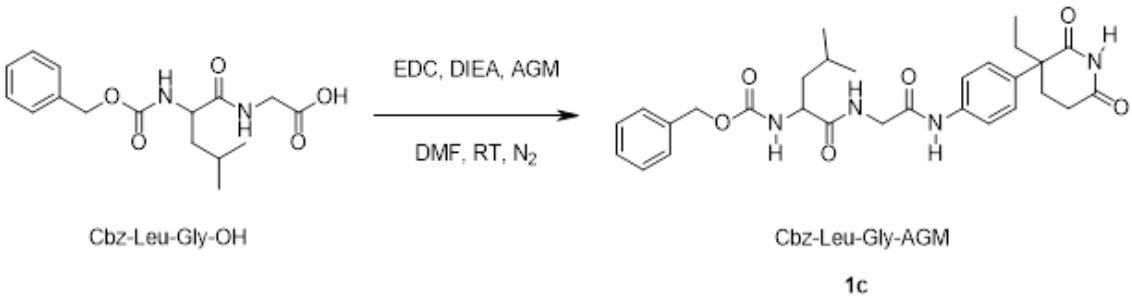

Figure 27. Synthetic scheme for the preparation of Cbz-Leu-Gly-AGM.

The general coupling procedure described for compound Cbz-Gly-AGM was used to synthesize compound Cbz-Leu-Gly-AGM using Cbz-Leu-Gly-OH instead (1.72 mmol, 361.12 mg). Yield=82%. **^{1}H NMR** (300 MHz, DMSO) δ 10.82 (s, 1H), 9.80 (s, 1H), 8.46 (m, 1H), 7.62(d, 3H), 7.34 (d, 2H), 7.25 (d, 4H), 5.16 (s, 2H), 4.06 (dd, J = 14.7, 8.1 Hz, 1H), 3.87 (d, J = 5.7 Hz, 2H), 2.38 (dd, J = 22.2, 4.9 Hz, 2H), 2.34 – 2.23 (m, 2H), 2.22 – 1.98 (m, 2H), 1.95 – 1.74 (m, 1H), 1.65 (dt, J = 13.1, 6.5 Hz, 2H), 1.57 – 1.36 (m, 1H), 0.88 (t, J = 6.8 Hz, 6H), 0.80 – 0.57 (m, 3H).**^{13}C NMR** (75 MHz, DMSO) δ 176.23 (s), 174.19 (s), 167.53 (s), 139.18 – 136.70 (m), 136.23 – 133.79 (m), 128.22 (dd, J = 42.8, 31.5 Hz), 127.75 – 126.37 (m), 120.81 (s), 80.58 (s), 65.71 (s), 54.79 (s), 50.04 (s), 43.99 (s), 32.58 (s), 29.43 (s), 26.35 (s), 24.54 (s), 23.37 (s), 21.93 (s), 8.88 (s).

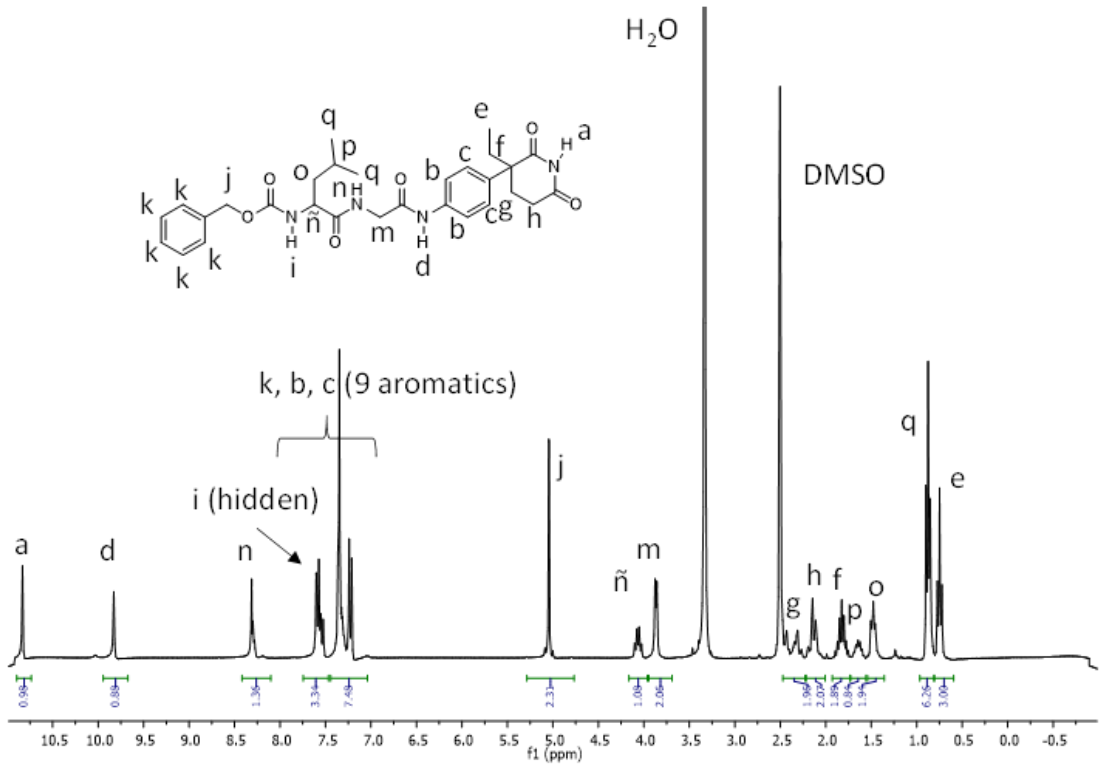

Figure 28. [1]H-NMR assignment for Cbz-Leu-Gly-AGM.

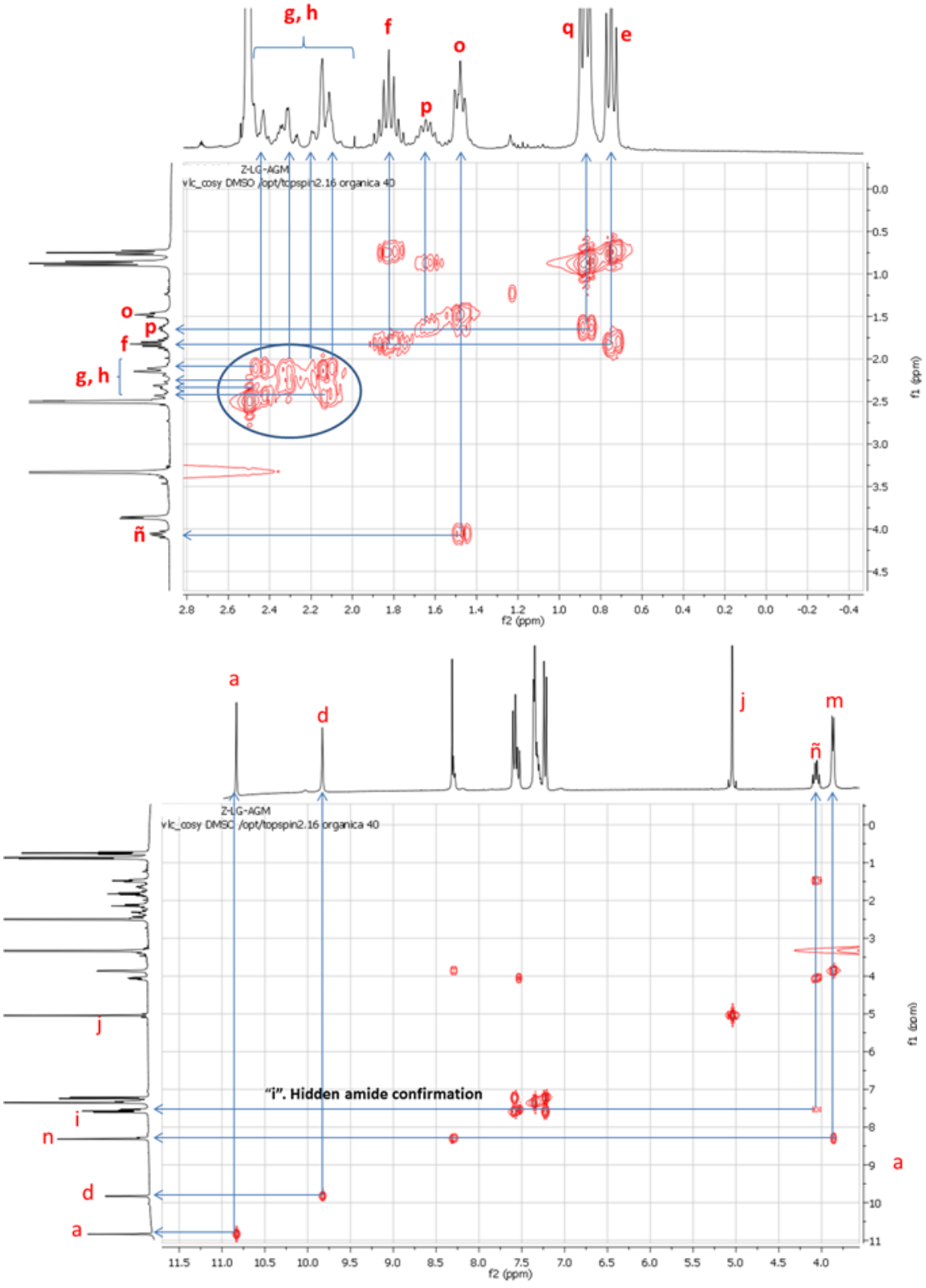

Figure 29. ^{1}H-^{1}H COSY NMR (two regions shown) spectra of Cbz-Leu-Gly-AGM.

Synthesis of Leu-Gly-AGM

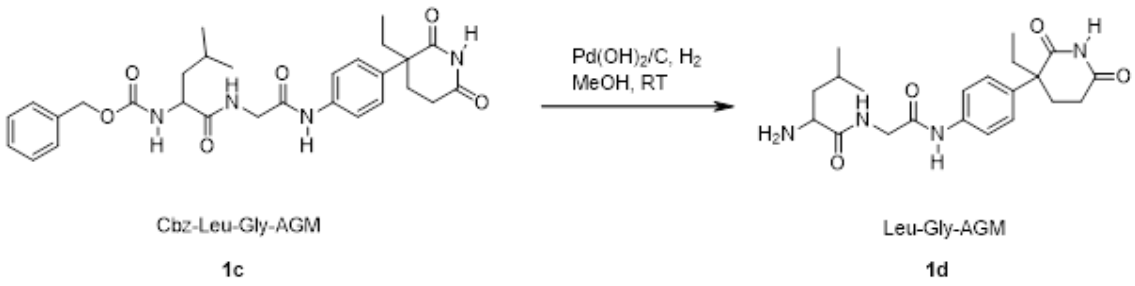

Figure 30. Synthetic scheme for the preparation of Leu-Gly-AGM.

Deprotection of Cbz-Leu-Gly-AGM was carried out following the same procedure described for deprotection of Cbz-Gly-AGM to yield Leu-Gly-AGM. Yield (79%). **^{1}H NMR** (300 MHz, DMSO) δ 10.83 (s, 1H), 10.24 (s, 1H), 8.94 (t, J = 5.7 Hz, 1H), 8.28 (s, 1H), 7.61 (d, J = 8.8 Hz, 2H), 7.23 (d, J = 8.8 Hz, 2H), 4.11 – 3.88 (m, 2H), 3.85 (s, 2H), 3.63 (dq, J = 13.1, 6.5 Hz, 1H), 2.45 – 2.27 (m, 2H), 2.25 – 1.97 (m, 2H), 1.93 – 1.79 (m, 1H), 1.76 – 1.62 (m, 2H), 1.57 (dt, J = 20.7, 7.0 Hz, 2H), 0.98 (t, J = 9.6 Hz, 2H), 0.92 (t, J = 6.1 Hz, 4H), 0.75 (t, J = 7.3 Hz, 3H).**^{13}C NMR** (75 MHz, DMSO) δ 177.53 (s), 172.90 (d, J = 47.0 Hz), 170.92 (s), 168.44 (s), 138.85 (s), 135.84 (s), 127.51 (d, J = 58.4 Hz), 121.58 (s), 51.15 (d, J = 24.0 Hz), 49.88 (d, J = 54.6 Hz), 44.07 (s), 32.57 (s), 30.70 (s), 23.98 (s), 23.76 (s), 23.05 (s), 22.54 (s), 9.38 (s). **MALDI-TOF:** $[M]^+ + [H^+]= 403.19$; $[M]^+ + [Na^+]= 425.18$.

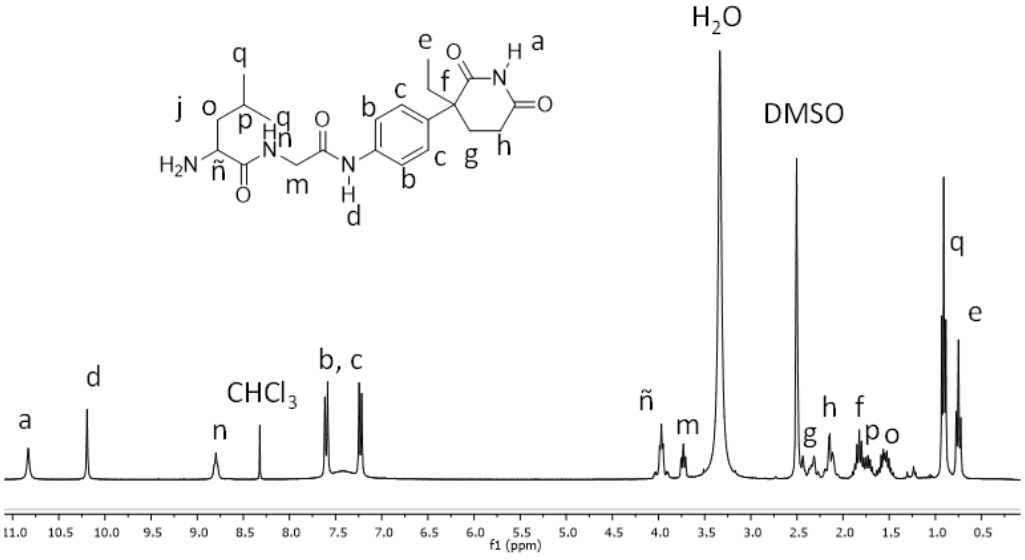

Figure 31. ^{1}H-NMR assignment for Leu-Gly-AGM.

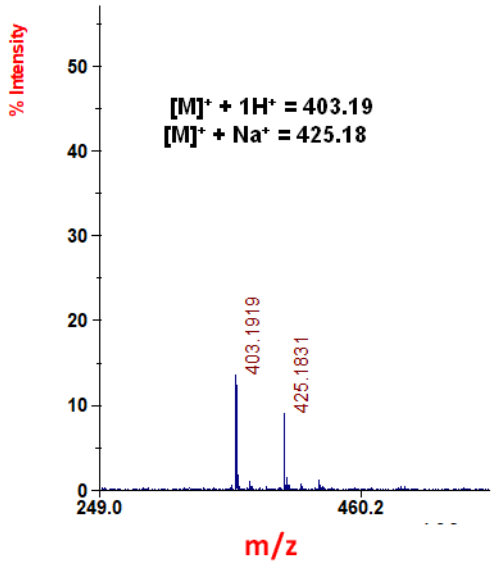

Figure 32. MALDI-TOF spectrum of Leu-Gly-AGM.

Synthesis of Cbz-Gly-Phe-Leu-Gly-AGM

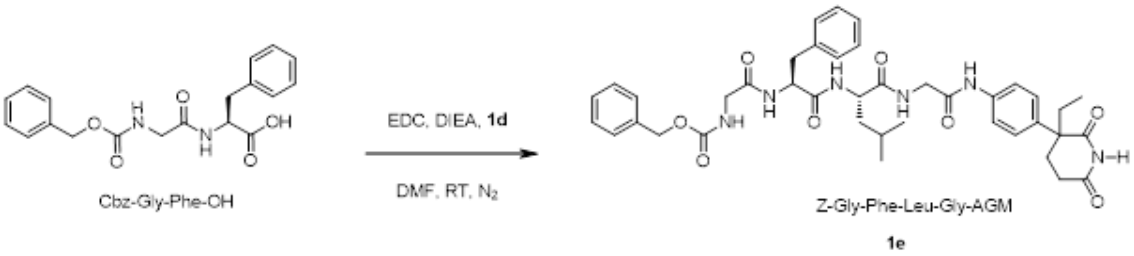

Figure 33. Synthetic scheme for the preparation of Cbz-Gly-Phe-Leu-Gly-AGM.

Cbz-Gly-Phe-Leu-Gly-AGM was synthesized following the general coupling procedure previously described using Cbz-Gly-Phe-OH (1.72 mmol, 361.12 mg) and compound Leu-Gly-AGM(1.64 mmol, 582,3 mg). Final purification by silica gel chromatography was performed with $CHCl_2$/MeOH 95/5 (v/v) as a mobile phase to yield the product as a fine brown oil (69% yield). **^{1}H NMR** (300 MHz, DMSO) δ 10.95(s), 10.04 (s, 1H), 8.27 (m, 2H), 8.09 – 7.90 (m, 1H), 7.75 – 7.52 (m, 4H), 7.49 – 7.05 (m, 10H), 5.24 (s, 1H), 4.71 (m, 1H), 4.41 – 4.19 (m, 1H), 3.98 – 3.73 (m, 2H), 3.73 – 3.46 (m, 2H), 3.13 – 2.66 (m, 2H), 2.42 – 2.27 (m, 2H), 2.24 – 2.01 (m, 2H), 1.95 – 1.72 (m, 2H), 1.69 – 1.57 (m, 1H), 1.55 – 1.44 (m, 2H), 0.99 – 0.81 (m, 6H), 0.80 – 0.62 (m, 3H).**^{13}C NMR** (75 MHz, DMSO) δ 176.19 (s) 173.13 (d, J = 13.5 Hz), 171.53 (s), 169.44

(s), 167.70 (d, J = 46.5 Hz), 138.84 – 136.95 (m), 134.86 (s), 129.66 (s), 129.36 – 127.54 (m), 127.54 – 126.28 (m), 120.34 – 118.29 (m), 80.44 – 78.22 (m), 65.37 (d, J = 84.2 Hz), 54.34 (d, J = 29.1 Hz), 51.28 – 49.39 (m), 32.59 (s), 29.55 (s), 26.51 (s), 24.55 (s), 23.44 (s), 22.06 (d, J = 11.5 Hz), 9.45 (d, J = 13.2 Hz). **MALDI-TOF:** $[M]^+ + [K^+]= 779.35$; $[M]^+ + [Na^+]= 763.18$.

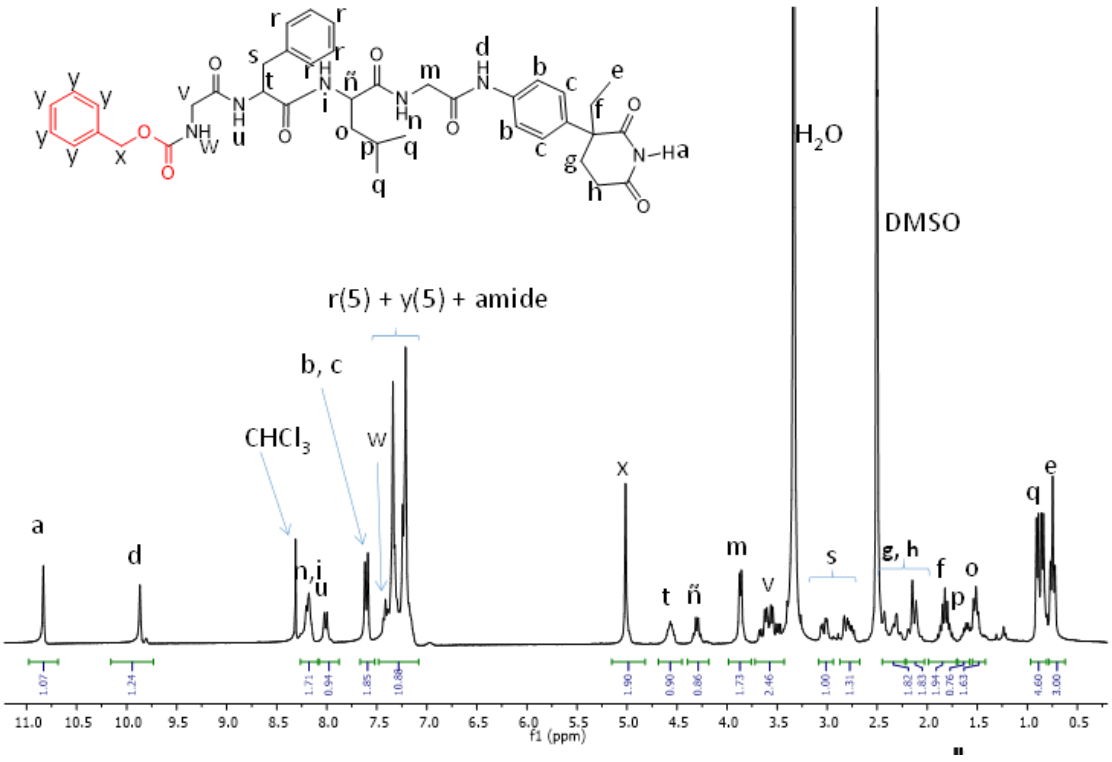

Figure 34. ^{1}H-NMR assignment for Cbz-Gly-Phe-Leu-Gly-AGM.

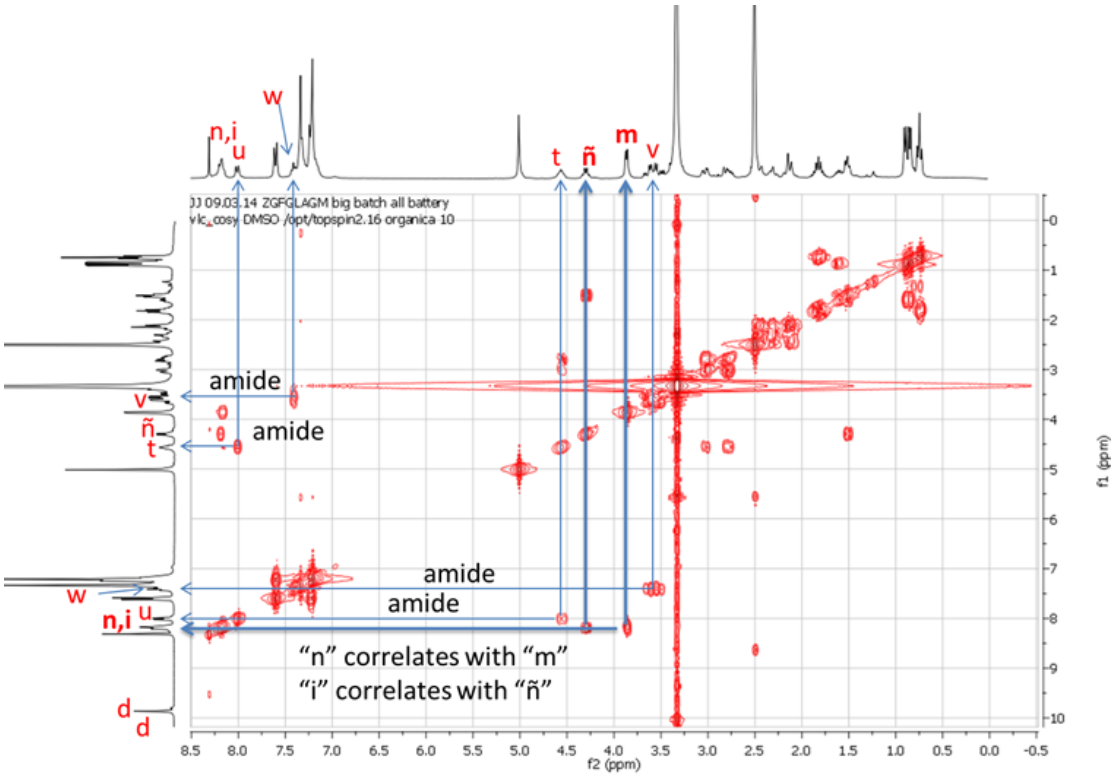

Figure 35. ^{1}H-^{1}H COSY NMR spectrum of for Cbz-Gly-Phe-Leu-Gly-AGM.

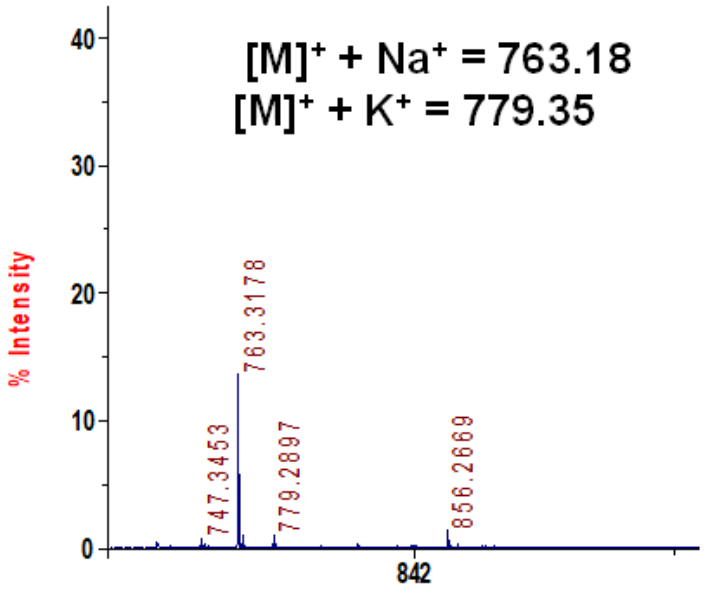

Figure 36. MALDI-TOF spectrum of Cbz-Gly-Phe-Leu-Gly-AGM.

Synthesis of Gly-Phe-Leu-Gly-AGM

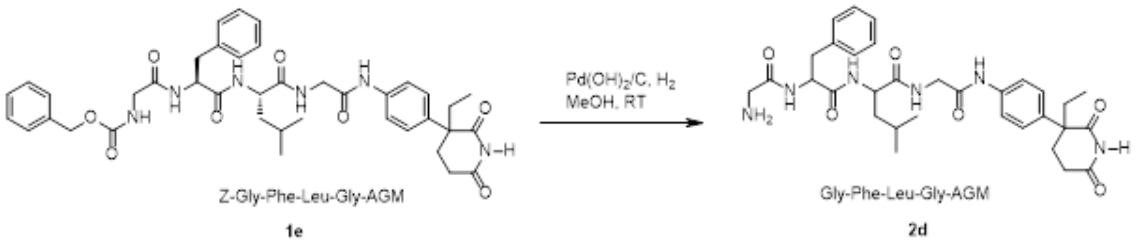

Figure 37. Synthetic scheme for the preparation of Gly-Phe-Leu-Gly-AGM.

Deprotection of Cbz-Gly-Phe-Leu-Gly was performed following the same procedure described for previous deprotection. No further purifications were required Yield=65%. **^{1}H NMR** (300 MHz, DMSO) δ 10.81 (S, 1H), 10.12 – 9.93 (d, 2H), 8.23 (m, 2H), 8.03 (s, 1H), 7.61 (dd, J = 8.7, 2.3 Hz, 4H), 7.42 – 7.02 (m, 10H), 4.83 – 4.52 (m, 1H), 4.32 (td, J = 14.4, 7.9 Hz, 1H), 4.05 – 3.74 (m, 2H), 3.60 – 3.42 (m, 2H), 3.25 – 2.67 (m, 2H), 2.46 – 2.23 (m, 2H), 2.23 – 2.01 (m, 2H), 1.70 – 1.59 (m, 2H), 1.55 (dd, J = 15.1, 7.7 Hz, 1H), 1.48 – 1.30 (m, 2H), 1.00 – 0.80 (m, 6H), 0.80 – 0.67 (m, 3H).**^{13}C NMR** (75 MHz, DMSO) δ 177.08 – 174.82 (m), 174.07 – 172.12 (m), 139.07 – 137.35 (m), 134.83 (s), 130.44 – 129.16 (m), 128.53 (s), 126.96 (d, J = 24.7 Hz), 120.82 – 118.80 (m), 63.30 – 61.79 (m), 55.19 – 53.68 (m), 52.71 – 51.21 (m), 50.98 – 49.25 (m), 34.16 – 31.75 (m), 30.03 – 28.30 (m), 27.02 – 25.29 (m), 25.07 – 22.82 (m), 22.59 – 21.39 (m), 9.97 – 8.55 (m). **MALDI-TOF:** $[M]^+ + [H^+]= 607.29$; $[M]^+ + [Na^+]= 629.27$.

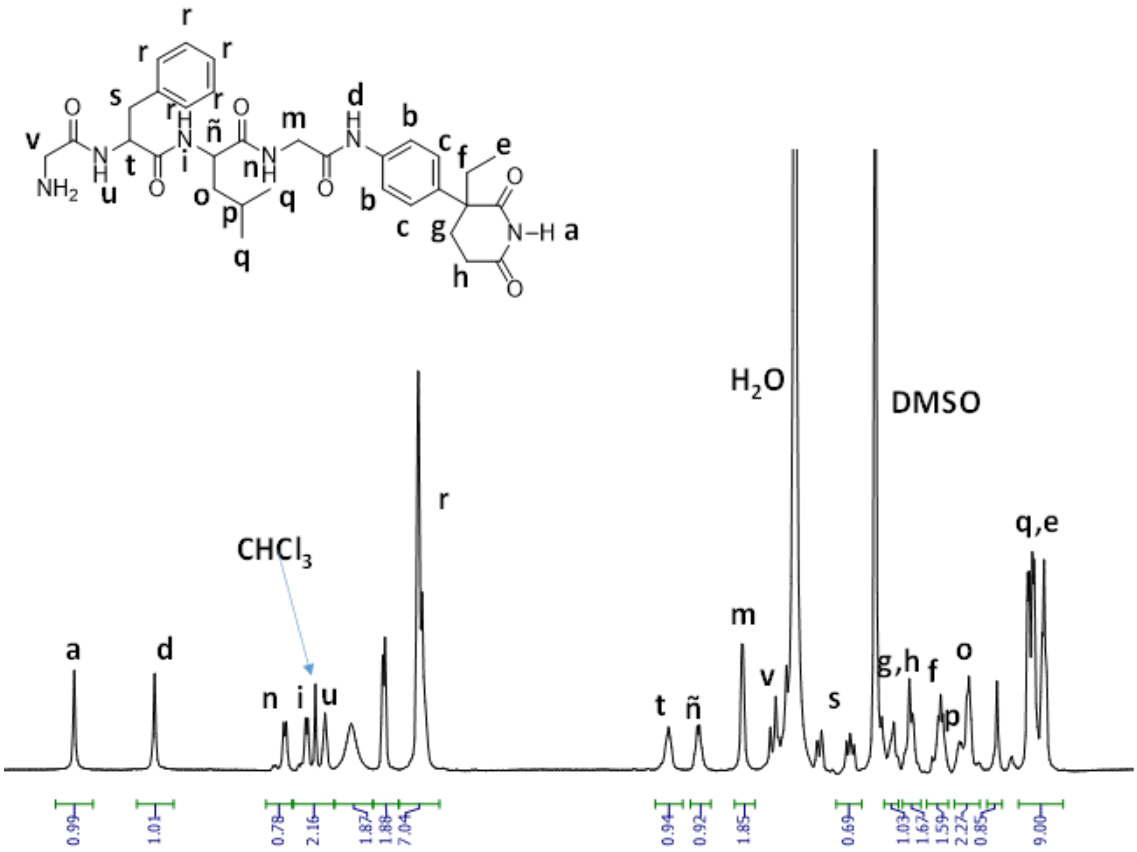

Figure 38. [1]H-NMR assignment for Gly-Phe-Leu-Gly-AGM.

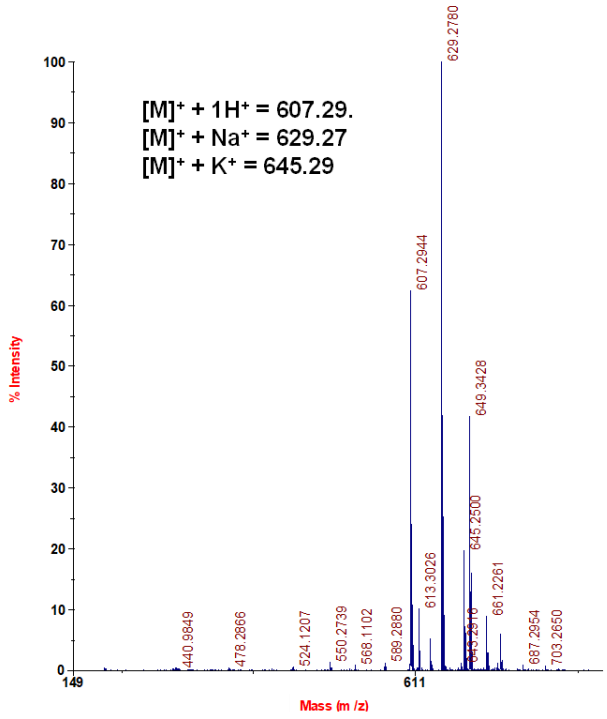

Figure 39. MALDI-TOF spectrum of Gly-Phe-Leu-Gly-AGM.

III.4.4. Synthesis of PGA conjugates as single and combination agents

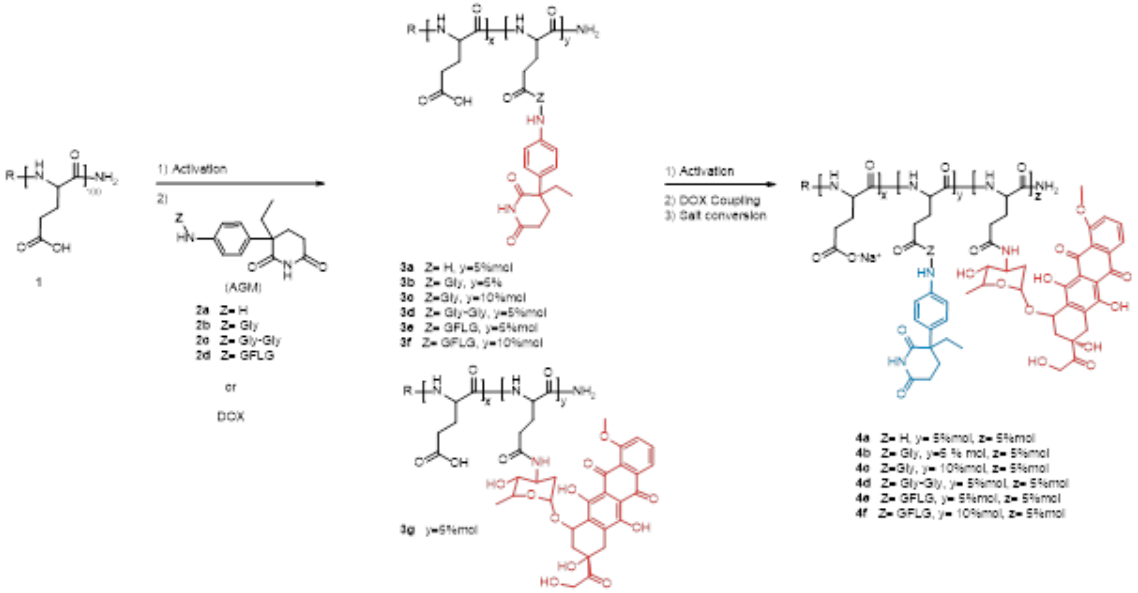

Figure 40. General synthetic scheme for the preparation of AGM-peptidyl derivatives

Synthesis of single PGA-X-AGM conjugates

Poly-L-glutamic acid (PGA) (0,51 mmol of glutamic acid units (GAU), 80,3 mg) was dissolved in anhydrous DMF (5 mL). Carboxylic groups were activated by adding DIC (0,808 mmol, 126,2 µL) and HOBt (0,808 mmol, 109 mg). After 15 min of activation, the required amount of compound **2** (0,0269 mmol eq. to GAU to reach 5 mol% modification, 0,0538 for 10% modification) was added. The pH was controlled and adjusted with DIEA to pH8. The reaction was monitored by TLC and was left to react for 36 h at RT, under stirring and dry N_2 atmosphere. Then, DMF was evaporated under reduced pressure and the conjugate was precipitated over cold Diethylether/Acetone 4/1. Precipitate was stirred and isolated by centrifugation and dried under vacuum. PGA-X-AGM sodium salt was obtained by dissolving in milliQ water with the addition of some drops of $NaHCO_3$ 1M until complete dissolution. Two purification steps (dialysis against water (membrane MWCO 3,5 KDa) and SEC in water (Sephadex G-25) were carried out in order to remove the excess of salt and any remaining impurities including free drug. After lyophilization, the reaction yields were 70-80 %.

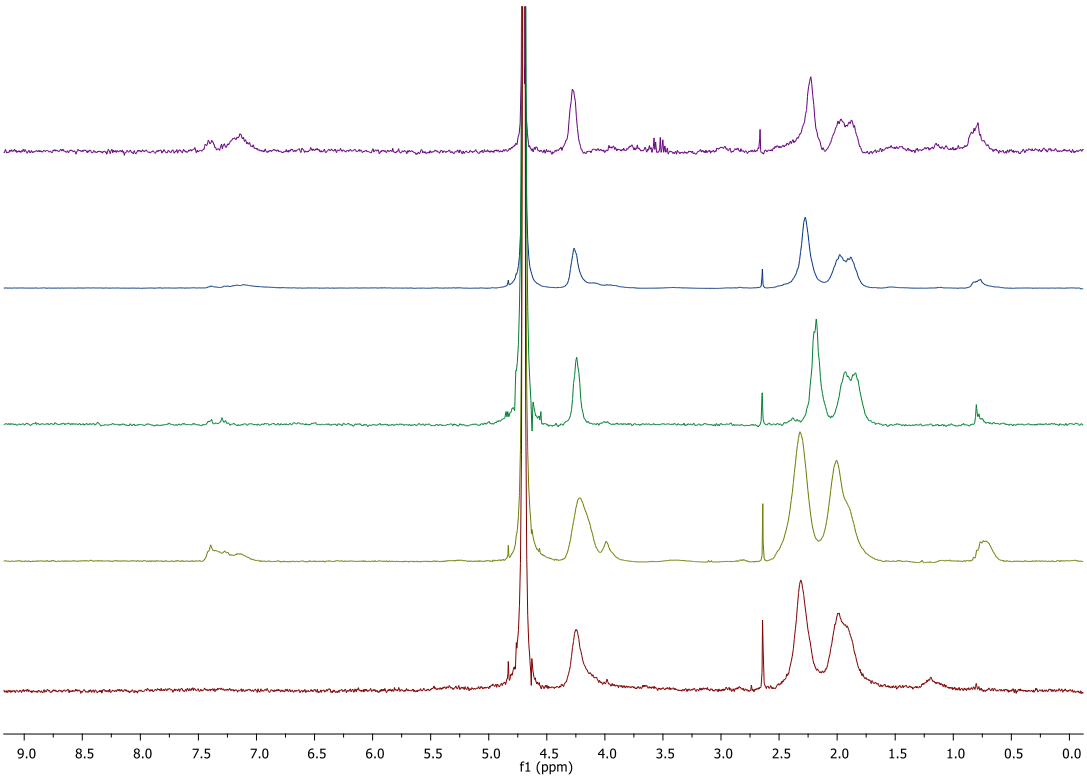

Figure 41. ^{1}H-NMR spectra of compounds 3 (PGA-X-AGM single conjugates. From top to bottom: **3e, 3f, 3b, 3c, 3g**).

Synthesis of single PGA-Dox conjugates

PGA (0,51 mmol of glutamic acid units (GAU), 80,3 mg) was dissolved in anhydrous DMF (5 mL). Carboxylic groups were activated by adding DIC (0,808 mmol, 126,2 µL) and HOBt (0,808 mmol, 109 mg). After 15 min of activation, DOX.HCl 0,0269 mmol, 14 mg) was incorporated to the reaction mixture and the pH was adjusted carefully with DIEA to 7.5-8. The reaction was monitored by TLC and left to stand for 36h at R.T. under stirring, dry N_2 atmosphere and protected from light. DMF was evaporated under los pressure and the conjugate was precipitated over cold Diethylether/Acetone 4/1. Precipitate was stirred and isolated by centrifugation and dried under vacuum. PGA-X-AGM sodium salt was obtained by dissolving in milliQ water with the addition of some drops of $NaHCO_3$ 1M until complete dissolution. Purification by SEC (Sephadex G-25, milliQ water as mobile phase) was carried out in order to remove the excess of salt and any remaining impurities including traces of activating agents or free drug. After lyophilization, the reaction yield was around 75%.

Conjugation and purity was confirmed by ^{1}H NMR (spectra of compounds **3a-f** can be found in supporting figures section, Figure SI9) and SEC-UV also provided evidences of homogeneous drug conjugation along the Mw population.

Synthesis of PGA-X-AGM-Dox combination conjugates

PGA (0,51 mmol of glutamic acid units (GAU), 80,3 mg) was dissolved in dry DMF (5 mL). Carboxylic groups were activated by adding DIC (0,808 mmol, 126,2 μL) and HOBt (0,808 mmol, 109 mg). After 15 min of activation, X-AGM (0,0269 mmol,) was added. The pH was controlled and adjusted with DIEA to pH8. The reaction was monitored by TLC and was left to react for 36 h at Rt, under stirring and dry N_2 atmosphere. Small fraction was isolated and purified apart for further determination of drug loading. Carboxylic groups were reactivated again by a new addition of DIC and HOBt following the same procedure described before and DOX.HCl was added. pH was adjusted again to 7.5 - 8 with DIEA and the reaction was left to react for 36h more at room temperature protected from light and keeping N_2 atmosphere and continuous stirring. The solvent was evaporated by high vacuum and polymer conjugate precipitated following the same protocol as for the single conjugates. Carboxylate salt form of the conjugate was obtained as described previously. Purification by SEC (Sephadex G25, milliQ water as mobile phase) was carried out in order to remove the excess of salt and any remaining impurities including traces of activating agents or free drug. After lyophilization, the reaction yield was around 75%. Conjugation and purity was confirmed by ^{1}H NMR (spectra of compounds **4a-f** can be found in supporting figures section, Figure SI10) and SEC-UV also provided evidences of homogeneous drug conjugation along the Mw population.

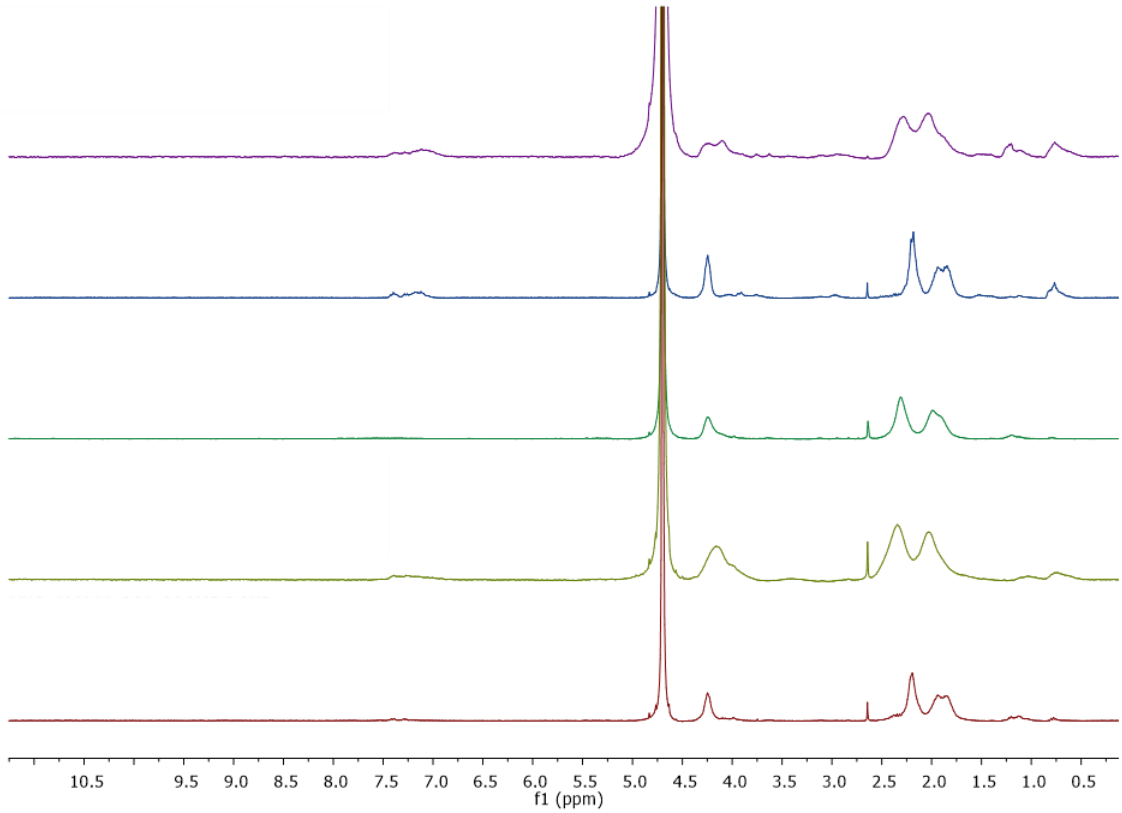

Figure 42. ^{1}H-NMR spectra of compounds 4 (PGA-X-AGM-DOX combination conjugates). From top to bottom: **4f, 4e, 4d, 4c, 4b**.

III.4.5. Histopathological analysis

Organs expected to develop metastasis or pathological alterations, were removed from just euthanized mice at desired relevant time points. All the organs were washed in fresh PBS, carefully dried, weighed and fixed in paraformaldehyde (PFA) at room temperature for 24h. PFA was eliminated by successive washing with PBS, replacing completely the wash every time (5 times of 20 min, fast agitation), Once washed, organs were stored in a cold solution of PBS with 0.05% of sodium azide and preserved at 4ºC and darkness. Further inclusion in paraffin was preceded by several dehydration steps of 2 min immersion in successive alcoholic solutions with increased degree (30%, 50% 70%, 96% and 99.9%) and two final washes of 100% xylol. Afterwards, paraffin blocks were cut in 3um slides and placed in SuperFrost-plus glass slides for the hematoxylin-eosin (HE) staining. For this staining, the remaining paraffin from tissue slides was previously removed with xylene and then slides were rehydrated with a successive ethanol solutions (99.9%, 96%, 70%) and water, followed by Dako hematoxylin staining for 2.5min. Then,

samples were washed with DEM water (1.5min), blueing buffer (1min), and water (1.5min). Tissue slides were next incubated for 2 min in lithium carbonate and hydrochloric acid 0.25% in ethanol 70% to remove the possible excess of hematoxylin staining. Following, tissue slides were incubated with Dako Eosin for 2 min and the final dehydration was performed by washing with 96% ethanol (0.5min) and 99.9% ethanol (2.5min). The slide was finally assembled with Eukitt. For the image capturing, tissue slides were observed under the microscope and the ones of interest were scanned with a Panoramic 250 Flash III (3DHISTECH Ltd, Budapest, Hungary) and processed with CaseViewer software, from the same company.

III.4.6. SANS Analysis

The data for all samples clearly consists of two regions. At low Q values (<0.01 $Å^{-1}$), data presents as a straight line. This is indicative of Porod scattering where the slope (n) is given by scattering from either a mass fractal (n=1-3) or surface fractal (n=3–4). At high Q, the scattering data has a different pattern, with the data showing a steady deviation from linearity or, in some cases, exhibiting a small peak at Q ~ 0.06. Peaks such as these have been observed previously in scattering from unmodified polyglutamic acid at similar solution concentrations,[37, 55] with the exact Q value being dependent upon polymer concentration and degree of polymerization. Data were fitted according to a broad peak model,[52] described in equation 1, where the first term accounts for scattering at low Q (arising from larger polymer clusters). $I_p(0)$ is the scattering intensity at q = 0 and *n* the fractal dimension. For long rigid structures n=1, increasing to 2 for Gaussian chains and tending towards 3 for collapsed polymer systems. The second term describes scattering from the solvated polymer chains. $I_L(0)$ is the scattering intensity at q = 0, ξ the correlation length, m the fractal dimension and Q_0 the peak position. When no peak is present $Q_0 = 0$ and the model is reduced to that of the typical correlation length model.[56]

For the PGA-$(G\text{-}AGM)_{LL}$-DOX data, it can be seen on the figure that the scattering profile starts to curve at low Q values (< 0.0043 $Å^{-1}$) with the intensity plateauing. This is indicative of the particle size approaching the Guinier regime and the overall polymer size being on the length scale accessible on the SANS Q range. In this instance, more information can be extracted and therefore, in place of the Porod component of equation 1, an excluded polymer chain equation has been used giving

equation 2. V is the excluded volume parameters, a the statistical length of the polymer chain and n the degree of polymerization.[57]

The fitting parameters obtained from this model are the Porod exponent, n, which is related to the excluded volume parameter as m = 1/v and has the same meaning as in equation 1, and the radius of gyration though the equation 3. Fits to these models are presented in the figure and fit parameters given in the table above.

	Rg (±10 Å)	n	m	ξ ± 2 Å	Q_0 / Å^{-1}	$I_L(0)$	$I_P(0)$	B_{inc} /cm^{-1}
PGA-(GG-AGM)$_{LL}$-Dox	n/a	3.2	1.4	16	0.062	0.0168	4.30E-08	0.042
PGA-(G-AGM)$_{LL}$-Dox	n/a	2.8	1.8	15.6	0.043	0.0257	1.66E-06	0.042
PGA-(G-AGM)$_{HL}$-Dox	680	3	1.8	25.942	n/a	0.11	30.1*	0.04
PGA-(AGM)$_{LL}$-Dox	n/a	2.2	2.2	34	n/a	0.23712	5.80E-06	0.049

*For PGA-(G-AGM)$_{HL}$-DOX, IP(0) refers to the scale factor of the excluded volume portion of equation 2

Equation 1

$$I(Q) = \frac{I_P(0)}{Q^n} + \frac{I_L(0)}{1+(|Q-Q_0|\xi)^m} + bkg$$

Equation 2

$$I(Q) = 2\int_0^1 dx(1-x)\exp\left[-\frac{Q^2a^2}{6}n^{2v}x^{2v}\right] + \frac{I_L(0)}{1+(|Q-Q_0|\xi)^m} + bkg$$

Equation 3

$$R_g^2 = \frac{a^2n^{2v}}{(2v+1)(2v+2)}$$

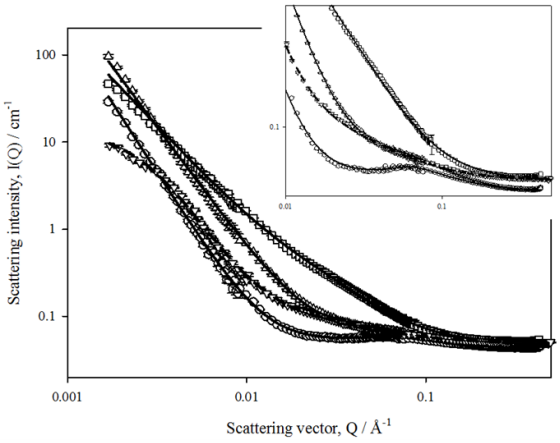

Figure 43: Sans Analysis: top) fitting parameters for selected conjugates; bottom left) equations employed for the fitting; bottom right) The scattering data obtained for PGA-(AGM)$_{LL}$-(Dox), PGA-(G-AGM)$_{LL}$-(Dox), PGA-(G-AGM)$_{HL}$-(Dox) and PGA-(GG-AGM)$_{LL}$-(Dox) are shown on a log-log plot in.

III.4.7. DLS analysis in terms of intensity and volume

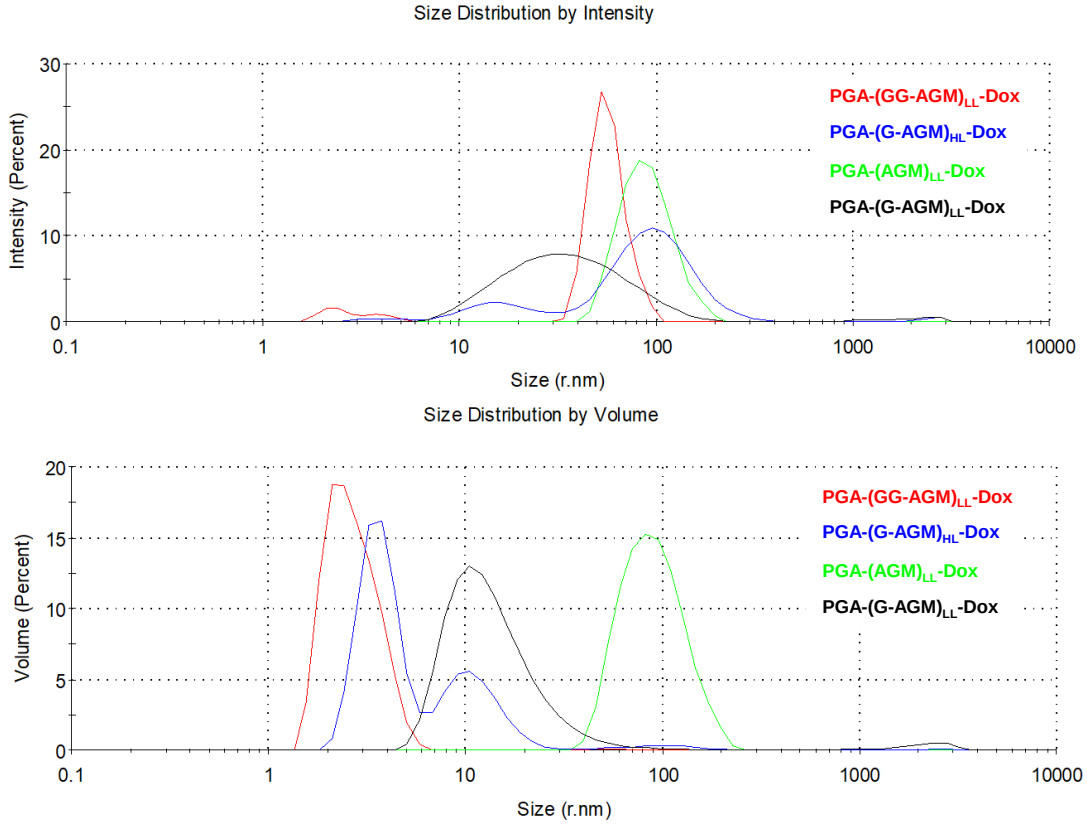

Figure 44: Size by DLS of selected conjugates in terms of Intensity and Volume

III.4.8. Critical Aggregation Concentration of selected polymer-drug conjugates

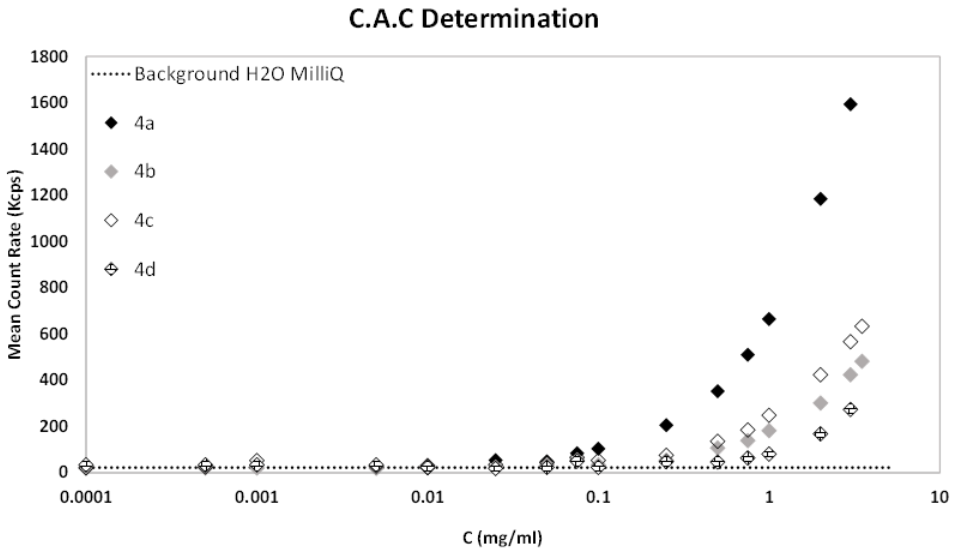

Figure 45: Critical Aggregation Concentration of selected polymer-drug conjugates

III.5. References

[1] Arroyo-Crespo Juan J, Deladriere C, Nebot Vicent J, Charbonnier D, Masiá E, Paul A, et al. Anticancer Activity Driven by Drug Linker Modification in a Polyglutamic Acid-Based Combination-Drug Conjugate. Advanced Functional Materials. 2018;28:1800931.
[2] Duncan R, Vicent MJ, Greco F, Nicholson RI. Polymer-drug conjugates: towards a novel approach for the treatment of endrocine-related cancer. Endocrine-related cancer. 2005;12 Suppl 1:S189-99.
[3] Greco F, Vicent M. Polymer-drug conjugates: Current status and future trends2008.
[4] Dai W, Wang X, Song G, Liu T, He B, Zhang H, et al. Combination antitumor therapy with targeted dual-nanomedicines. Advanced Drug Delivery Reviews. 2017;115:23-45.
[5] He B, Lu C, Zheng G, He X, Wang M, Chen G, et al. Combination therapeutics in complex diseases. Journal of cellular and molecular medicine. 2016;20:2231-40.
[6] Vogus DR, Krishnan V, Mitragotri S. A review on engineering polymer drug conjugates to improve combination chemotherapy. Current Opinion in Colloid & Interface Science. 2017;31:75-85.
[7] Burrell RA, McGranahan N, Bartek J, Swanton C. The causes and consequences of genetic heterogeneity in cancer evolution. Nature. 2013;501:338-45.
[8] Ronson A, Tvito A, Rowe JM. Liposomal cytarabine and daunorubicin (CPX-351) for treatment of acute myeloid leukemia. Expert Opinion on Orphan Drugs. 2017;5:369-74.
[9] Maeda H. Tumor-selective delivery of macromolecular drugs via the EPR effect: background and future prospects. Bioconjugate chemistry. 2010;21:797-802.
[10] Maeda H, Tsukigawa K, Fang J. A Retrospective 30 Years After Discovery of the Enhanced Permeability and Retention Effect of Solid Tumors: Next-Generation Chemotherapeutics and Photodynamic Therapy--Problems, Solutions, and Prospects. Microcirculation (New York, NY : 1994). 2016;23:173-82.
[11] Ojha T, Pathak V, Shi Y, Hennink WE, Moonen CTW, Storm G, et al. Pharmacological and physical vessel modulation strategies to improve EPR-mediated drug targeting to tumors. Advanced Drug Delivery Reviews. 2017;119:44-60.
[12] Nino-Pariente A, Nebot VJ, Vicent MJ. Relevant Physicochemical Descriptors of "Soft Nanomedicines" to Bypass Biological Barriers. Current pharmaceutical design. 2016;22:1274-91.
[13] Tajes M, Ramos-Fernández E, Weng-Jiang X, Bosch-Morató M, Guivernau B, Eraso-Pichot A, et al. The blood-brain barrier: Structure, function and therapeutic approaches to cross it. Molecular Membrane Biology. 2014;31:152-67.
[14] Canal F, Sanchis J, Vicent MJ. Polymer–drug conjugates as nano-sized medicines. Current Opinion in Biotechnology. 2011;22:894-900.
[15] Duncan R. Polymer therapeutics as nanomedicines: new perspectives. Current opinion in biotechnology. 2011;22:492-501.
[16] Greco F, Vicent MJ. Combination therapy: Opportunities and challenges for polymer–drug conjugates as anticancer nanomedicines. Advanced Drug Delivery Reviews. 2009;61:1203-13.
[17] Zagorodko O, Arroyo-Crespo JJ, Nebot VJ, Vicent MJ. Macromol. Biosci. 1/2017. Macromolecular Bioscience. 2017;17.
[18] Nel AE, Mädler L, Velegol D, Xia T, Hoek EMV, Somasundaran P, et al. Understanding biophysicochemical interactions at the nano–bio interface. Nature Materials. 2009;8:543-57.
[19] C. Deladriere AA, E. Masiá, R. Lucas, M.J. Vicent Rationally Designed Polymer-based Combination Therapy Demonstrates Anti-tumor Synergism in Aggressive orthotopic Breast Cancer Model. Br J Cancer 2018;In Preparation.
[20] Greco F, Vicent MJ, Gee S, Jones AT, Gee J, Nicholson RI, et al. Investigating the mechanism of enhanced cytotoxicity of HPMA copolymer–Dox–AGM in breast cancer cells. Journal of Controlled Release. 2007;117:28-39.

[21] Vicent MJ, Greco F, Nicholson RI, Paul A, Griffiths PC, Duncan R. Polymer Therapeutics Designed for a Combination Therapy of Hormone-Dependent Cancer. Angewandte Chemie International Edition. 2005;44:4061-6.
[22] Duncan R. Polymer therapeutics at a crossroads? Finding the path for improved translation in the twenty-first century. Journal of Drug Targeting. 2017;25:759-80.
[23] Hehir S, Cameron NR. Recent advances in drug delivery systems based on polypeptides prepared fromN-carboxyanhydrides. Polymer International. 2014;63:943-54.
[24] Weinstock-Guttman B, Nair KV, Glajch JL, Ganguly TC, Kantor D. Two decades of glatiramer acetate: From initial discovery to the current development of generics. Journal of the Neurological Sciences. 2017;376:255-9.
[25] Duncan R, Vicent MJ. Polymer therapeutics-prospects for 21st century: The end of the beginning. Advanced Drug Delivery Reviews. 2013;65:60-70.
[26] Duncan R. Polymer therapeutics: Top 10 selling pharmaceuticals — What next? Journal of Controlled Release. 2014;190:371-80.
[27] Bernabeu E, Cagel M, Lagomarsino E, Moretton M, Chiappetta DA. Paclitaxel: What has been done and the challenges remain ahead. International Journal of Pharmaceutics. 2017;526:474-95.
[28] Zhao J, Koay EJ, Li T, Wen X, Li C. A hindsight reflection on the clinical studies of poly(l-glutamic acid)-paclitaxel. 2018;10:e1497.
[29] Baabur-Cohen H, Vossen LI, Krüger HR, Eldar-boock A, Yeini E, Landa-Rouben N, et al. In vivo comparative study of distinct polymeric architectures bearing a combination of paclitaxel and doxorubicin at a synergistic ratio. Journal of Controlled Release. 2017;257:118-31.
[30] Markovsky E, Baabur-Cohen H, Satchi-Fainaro R. Anticancer polymeric nanomedicine bearing synergistic drug combination is superior to a mixture of individually-conjugated drugs. Journal of controlled release : official journal of the Controlled Release Society. 2014;187:145-57.
[31] Eldar-Boock A, Miller K, Sanchis J, Lupu R, Vicent MJ, Satchi-Fainaro R. Integrin-assisted drug delivery of nano-scaled polymer therapeutics bearing paclitaxel. Biomaterials. 2011;32:3862-74.
[32] Khan SR, Baghdasarian A, Nagar PH, Fahlman R, Jurasz P, Michail K, et al. Proteomic profile of aminoglutethimide-induced apoptosis in HL-60 cells: Role of myeloperoxidase and arylamine free radicals. Chem Biol Interact. 2015;239:129-38.
[33] Johnston SRD, Dowsett M. Aromatase inhibitors for breast cancer: lessons from the laboratory. Nature Reviews Cancer. 2003;3:821-31.
[34] Min Y, Caster JM, Eblan MJ, Wang AZ. Clinical Translation of Nanomedicine. Chemical Reviews. 2015;115:11147-90.
[35] Vicent MJ, Pérez-Payá E. Poly-l-glutamic acid (PGA) Aided Inhibitors of Apoptotic Protease Activating Factor 1 (Apaf-1): An Antiapoptotic Polymeric Nanomedicine. Journal of Medicinal Chemistry. 2006;49:3763-5.
[36] Reddy Chichili VP, Kumar V, Sivaraman J. Linkers in the structural biology of protein-protein interactions. Protein Science. 2013;22:153-67.
[37] Nickels JD, Perticaroli S, Ehlers G, Feygenson M, Sokolov AP. Rigidity of poly-L-glutamic acid scaffolds: Influence of secondary and supramolecular structure. Journal of Biomedical Materials Research Part A. 2015;103:2909-18.
[38] Rinaudo M, Domard A. Interchain correlation observed in neutron-scattering experiments on poly(α-L-glutamic acid) solutions. Journal of Polymer Science: Polymer Letters Edition. 1977;15:411-5.
[39] Duncan R. Design of Polymeric Drug Delivery Systems for Controlled Release of Antitumour Agents. Encapsulation and Controlled Release: Elsevier; 2005. p. 13-7.
[40] Chou TC. Theoretical Basis, Experimental Design, and Computerized Simulation of Synergism and Antagonism in Drug Combination Studies. Pharmacological Reviews. 2006;58:621-81.

[41] Khan SR, Baghdasarian A, Nagar PH, Fahlman R, Jurasz P, Michail K, et al. Proteomic profile of aminoglutethimide-induced apoptosis in HL-60 cells: Role of myeloperoxidase and arylamine free radicals. Chemico-Biological Interactions. 2015;239:129-38.
[42] Turk V, Stoka V, Vasiljeva O, Renko M, Sun T, Turk B, et al. Cysteine cathepsins: From structure, function and regulation to new frontiers. Biochimica et Biophysica Acta (BBA) - Proteins and Proteomics. 2012;1824:68-88.
[43] Mezö G, Reményi J, Kajtár J, Barna K, Gaál D, Hudecz F. Synthesis and conformational studies of poly(l-lysine) based branched polypeptides with Ser and Glu/Leu in the side chains. Journal of Controlled Release. 2000;63:81-95.
[44] Li M, Song W, Tang Z, Lv S, Lin L, Sun H, et al. Nanoscaled Poly(l-glutamic acid)/Doxorubicin-Amphiphile Complex as pH-responsive Drug Delivery System for Effective Treatment of Nonsmall Cell Lung Cancer. ACS Applied Materials & Interfaces. 2013;5:1781-92.
[45] Bae Y, Diezi TA, Zhao A, Kwon GS. Mixed polymeric micelles for combination cancer chemotherapy through the concurrent delivery of multiple chemotherapeutic agents. Journal of Controlled Release. 2007;122:324-30.
[46] Van S, Das SK, Wang X, Feng Z, Jin Y, Hou Z, et al. Synthesis, characterization, and biological evaluation of poly(L-γ-glutamyl-glutamine)- paclitaxel nanoconjugate. Int J Nanomedicine2010. p. 825-37.
[47] Pulaski BA, Ostrand-Rosenberg S. Mouse 4T1 Breast Tumor Model. Current Protocols in Immunology: John Wiley & Sons, Inc.; 2001.
[48] Mei K-C, Bai J, Lorrio S, Wang JT-W, Al-Jamal KT. Investigating the effect of tumor vascularization on magnetic targeting in vivo using retrospective design of experiment. Biomaterials. 2016;106:276-85.
[49] Duro-Castano A, England RM, Razola D, Romero E, Oteo-Vives M, Morcillo MA, et al. Well-Defined Star-Shaped Polyglutamates with Improved Pharmacokinetic Profiles As Excellent Candidates for Biomedical Applications. Molecular Pharmaceutics. 2015;12:3639-49.
[50] Lai J, Huang Y. Fibril aggregates of the poly(glutamic acid)–drug conjugate. RSC Advances. 2015;5:48856-60.
[51] Duro-Castano A, Nebot VJ, Niño-Pariente A, Armiñán A, Arroyo-Crespo JJ, Paul A, et al. Nanocarriers: Capturing “Extraordinary” Soft-Assembled Charge-Like Polypeptides as a Strategy for Nanocarrier Design (Adv. Mater. 39/2017). Advanced Materials. 2017;29.
[52] Horkay F, Hammouda B. Small-angle neutron scattering from typical synthetic and biopolymer solutions. Colloid and Polymer Science. 2008;286:611-20.
[53] Khuphe M, Kazlauciunas A, Huscroft M, Thornton PD. The formation of biodegradable micelles from a therapeutic initiator for enzyme-mediated drug delivery. Chemical Communications. 2015;51:1520-3.
[54] http://www.sasview.org/.
[55] Rinaudo M, Domard A. INTERCHAIN CORRELATION OBSERVED IN NEUTRON-SCATTERING EXPERIMENTS ON POLY(ALPHA-L-GLUTAMIC ACID) SOLUTIONS. Journal of Polymer Science Part C-Polymer Letters. 1977;15:411-5.
[56] Hammouda B, Ho DL, Kline S. Insight into clustering in poly(ethylene oxide) solutions. Macromolecules. 2004;37:6932-7.
[57] Hammouda B. SANS FROM HOMOGENEOUS POLYMER MIXTURES - A UNIFIED OVERVIEW. Advances in Polymer Science. 1993;106:87-133.

Chapter IV

TUMOR MICROENVIRONMENT-TARGETED POLY-L-GLUTAMIC ACID-BASED COMBINATION CONJUGATE FOR ENHANCED TRIPLE NEGATIVE BREAST CANCER TREATMENT

IV.1. Antecedents and Background

The hypoxic and acidic environment of the tumor microenvironment (TME) promotes the survival of cancer cells in comparison to normal cells [1] and represents a crucial target for the newest generation of anticancer drug delivery systems (DDS). The higher glycolytic rate of tumor cells generates and sustains the acidic character of the TME [2] and provides a rationale for the specific design of targeted DDS. If properly engineered, nanoscale DDS passively accumulate within the TME of adequately vascularize tumors [3-5] by the enhanced permeability and retention (EPR) effect and the presence of pH-labile linkers within the DDS can then trigger conjugated drug release. Other than TME-targeting of pH-labile DDS, endocytic internalization promotes lysosomal degradation [6] of polymers such as poly-L-glutamatic acid (PGA), thanks to the presence of hydrolytic enzymes such as Cathepsin B [7].

Our laboratory recently reported the development of PGA-based combination conjugates bearing a synergistic ratio of the anthracycline drug doxorubicin (Dox) and the aromatase inhibitor Aminoglutethimide (AGM) [8]. Specific engineering of the three-dimensional (3D) conformation permitted similar optimal release rates for Dox and AGM, with release rate representing the parameter controlling drug-drug synergism [8, 9]. This synergism translated to an enhanced antitumor efficacy in the orthotopic 4T1 triple negative breast cancer (TNBC) preclinical model [10]. The release of both drugs via protease-cleavable drug linkers relied on the heterogeneous expression of various hydrolytic enzymes within the TME activity (at both the patient [11] and tumor level [12]). This fact highlights the need for patient stratification in DDS treatment cohorts, a requirement exemplified by clinical data obtained for Opaxio®, which displayed optimal activity in phase III clinical trials in premenopausal women with optimally high levels of estrogen to promote cathepsin B activity [13].

We aimed to potentiate the therapeutic capacity of our previously described PGA-combination conjugates by also promoting metastasis inhibition through the incorporation of a pH-labile linker for Dox (simple hydrazone moiety or complex EMCH [N-ε-maleimidocaproic acid hydrazide] moiety), while retaining the optimized glycine-based linking chemistry for AGM [8], using our metastatic TNBC mice as preclinical model [10]. Of note, TME-targeting represents a promising alternative means to inhibit

metastasis in TNBC, a particularly aggressive breast cancer subtype that features a unique microenvironment distinct from that of other subtypes, especially when compared to Luminal A [14, 15]. Furthermore, due to molecular complexity and heterogeneity, TNBC lacks the targeted treatments available for other breast cancer subtypes.

During this study, we discovered that low Dox loading and shorter hydrazone linkers yielded optimal antitumor and antimetastatic effects in our TNBC model. RNA sequencing (RNA-seq) analysis employed to explore the mechanism of action of TME-targeted conjugates revealed the inhibition of metastatic pathways and the importance of immunomodulation. This powerful genomics tool allowed us to elucidate the functional aspects of gene expression driving cell death at the genome-wide level and the establishment of relationships with the physico-chemical descriptors. To the best of our knowledge, this study represents one of the few studies of this type within polymer therapeutics and demonstrates the enormous potential of polymer genomics [16] to elucidate the molecular mechanism of action and identify promising molecular targets.

IV.2. Results and Discussion

IV.2.1. Synthesis and Characterization of Polymer-drug Conjugates

We previously demonstrated optimal therapeutic benefit with PGA-AGM-Dox combination conjugates presenting a differential (faster) Dox release rate when compared to AGM in an orthotopic TNBC model [10]. To enhance this effect, we incorporated hydrazone-based pH-sensitive linkers for Dox conjugation while retaining the original optimized linking chemistry for AGM (Gly-AGM).

As demonstrated in **Figure 1** and **2**, we employed two different pH-sensitive hydrazone linkers: we used the direct conjugation through the C-13 Dox ketone [17] or conjugation employing a flexible, hydrophobic, and longer maleimido linker (EMCH) that we hypothesized would provide even faster Dox release. Direct conjugation required the previous modification of the PGA backbone with tert-butylcarbazate (**Figures 3** and **4**). The EMCH spacer required the previous modification of Dox to obtain EMCH-Dox as well as previous modification of the PGA backbone with a PD moiety. The last stage involved the reduction of the disulfide bond to yield the conjugate through the thioether derivative (**Figure 1**). This Dox-linker strategy (**Figure 5** and **6**) has its origin in the development of Aldoxorubicin (formerly, INNO-206, EMCH-Dox) as a bovine serum albumin (BSA)-binding-Dox prodrug [18] and has been reported previously for a PGA-based combination conjugate [19].

Additionally, to explore the effect of different Dox loadings and encouraged by preliminary results demonstrating enhanced cytotoxicity in the lower Dox loading range [8], we fixed G-AGM content in all combination conjugates at 10% mol, but varied Dox loading from 1% mol (Low Loading [LL]) to 3% mol (High Loading [HL]) (**Table 1**)**.** Unfortunately, we could not generate the single conjugate incorporating a high loading of the bulky EMCH moiety (PGA-EMCH$_{HL}$), most probably due to steric impediments. We performed the direct attachment of G-AGM and the precursor moieties (tert-buthylcarbazate and PD) by carbodiimide coupling to achieve our combination (**Figure 1**) and single conjugates (**Figure 2**)**.**

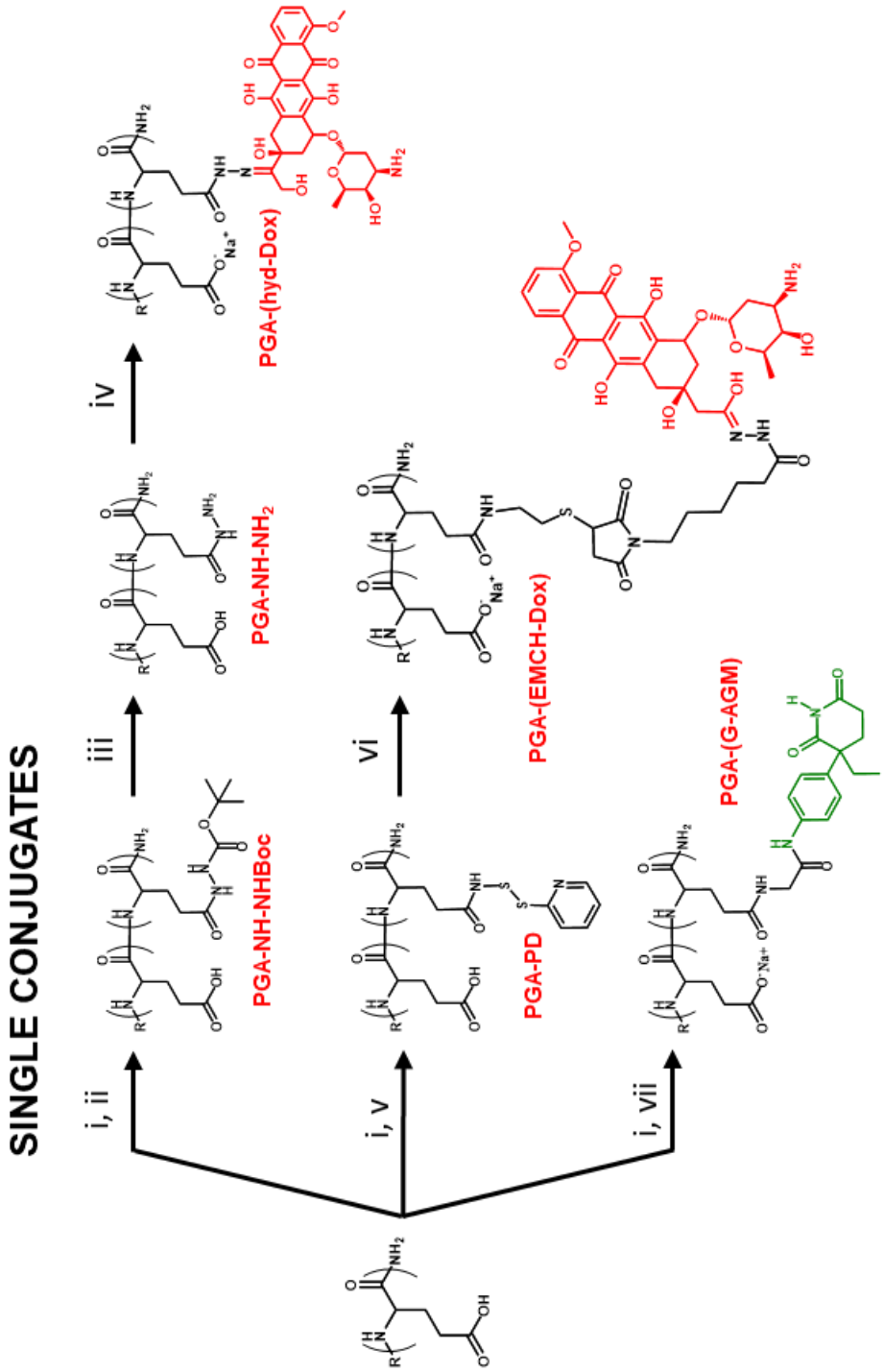

Figure 1. Synthetic Scheme followed to achieve for Polyglutamate (PGA)-based single conjugates. **i)** DMTMM.BF_4, DIEA, ahn-DMF, 15min, R.T. **ii)** t-butylcarbazate, 24h, pH=8, R.T.; **iii)** TFA, 30min, R.T.; **iv)** DOX.HCL, CH_3COOH (cat.), 36h. and $NaHCO_3$ (dil) **v)** Piridildithiol, 24h, pH=8, R.T.; **vi.a)** EMCH-Dox, TCEP (cat.) and $NaHCO_3$ (dil) **vii)** G-AGM and $NaHCO_3$ (dil).

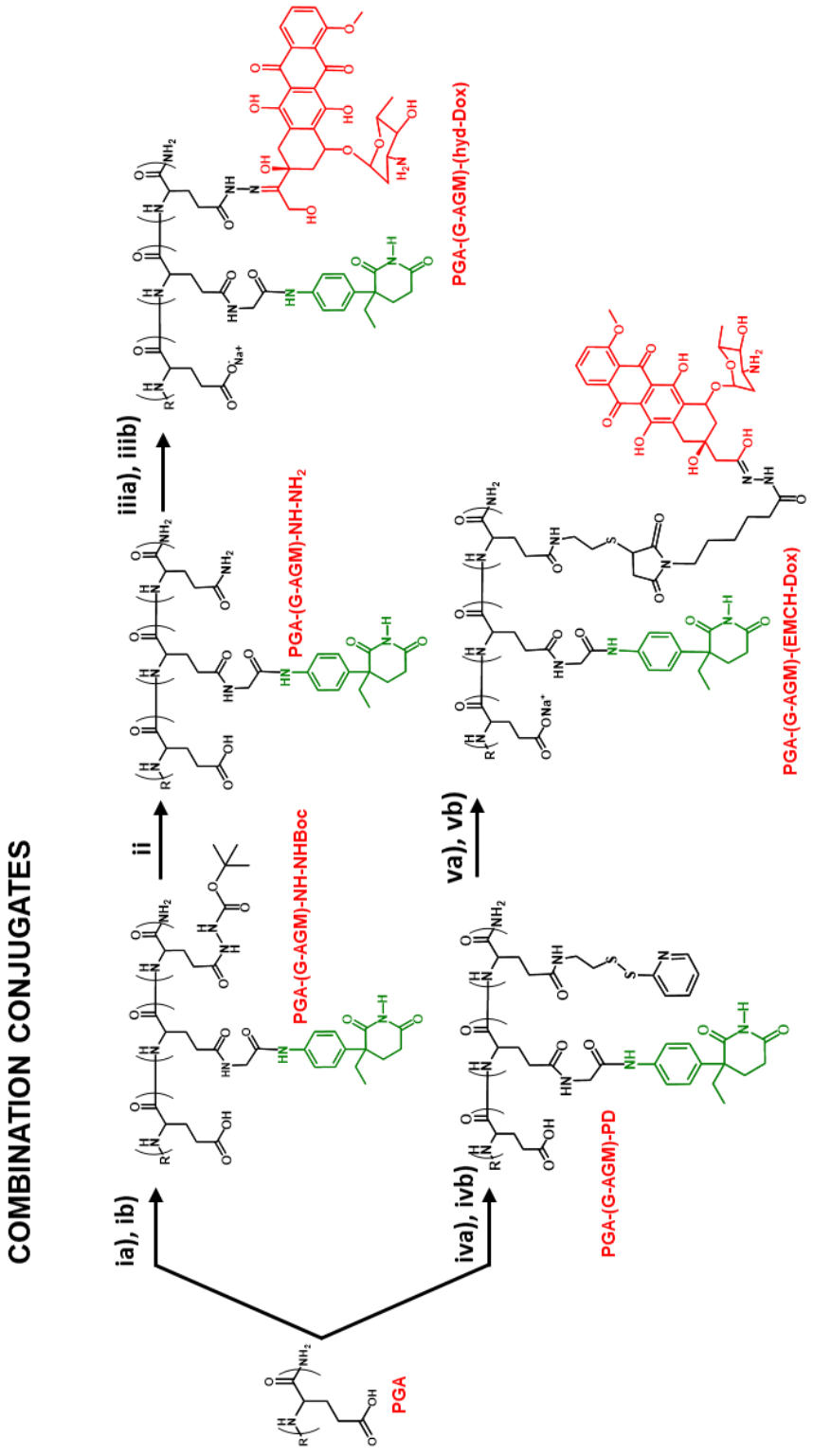

Figure 2. Synthetic scheme followed to generate poly-L-glutamate (PGA)-based combination conjugates. **i. a)** DMTMM.BF_4, DIEA, ahn-DMF, 15min, R.T. **i. b)** t-butyl carbazate, G-AGM, 24h, pH=8, R.T.; **ii)** TFA, 30min, R.T.; **iii. a)** DOX.HCL, CH_3COOH (cat.), 36h. **iii. b)** $NaHCO_3$ (dil) **iv. a)** DMTMM.BF_4, DIEA, ahn-DMF, 15min, R.T. **iv. b)** Piridildithiol, G-AGM, 24h, pH=8, R.T.; **v. a)** EMCH-Dox, TCEP (cat.); **v. b)** $NaHCO_3$ (dil).

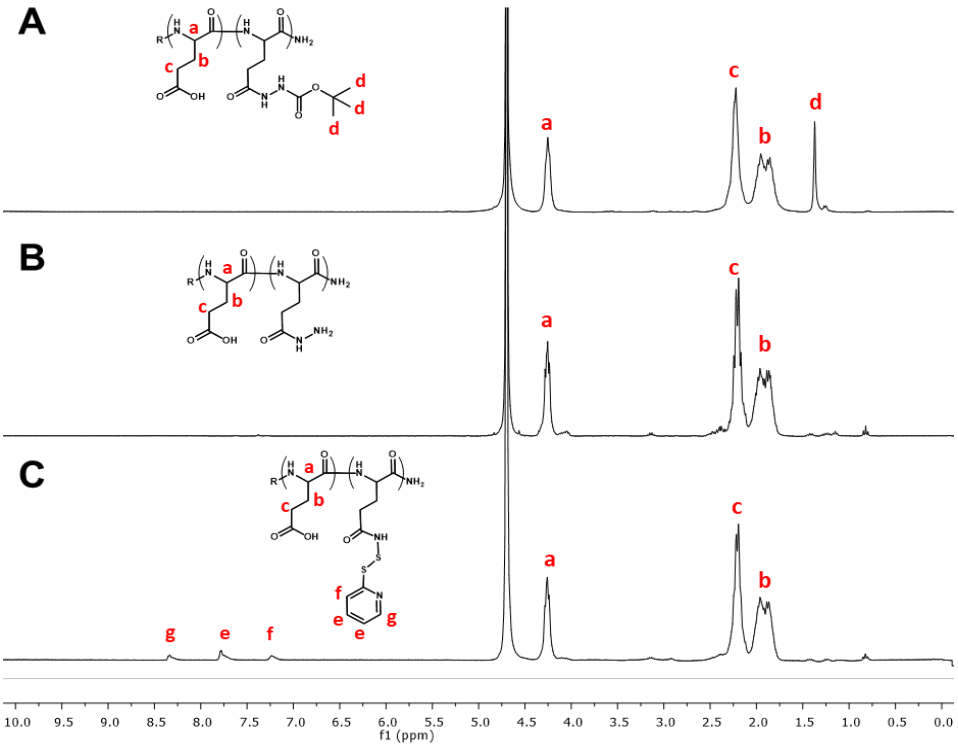

Figure 3. ^{1}H-NMR characterization of intermediate products: **A)** PGA-NH-Boc, **B)** PGA-NH-NH$_2$, and **C)** PGA-PD

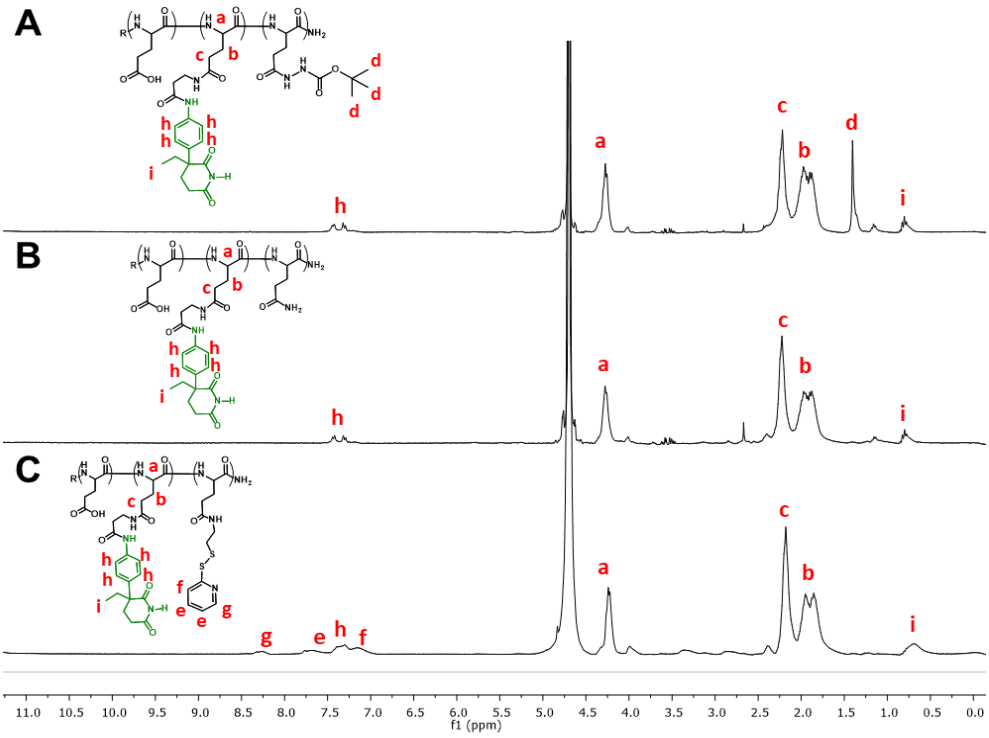

Figure 4. ^{1}H-NMR characterization of intermediate products: **A)** PGA-(G-AGM)-NH-Boc, **B)** PGA-(G-AGM)-NH-NH$_2$, and **C)** PGA-(G-AGM)-PD

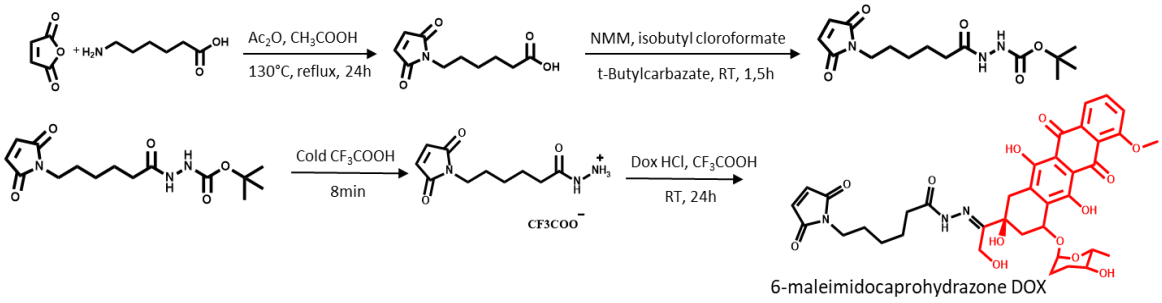

Figure 5. EMCH-Dox synthetic scheme.

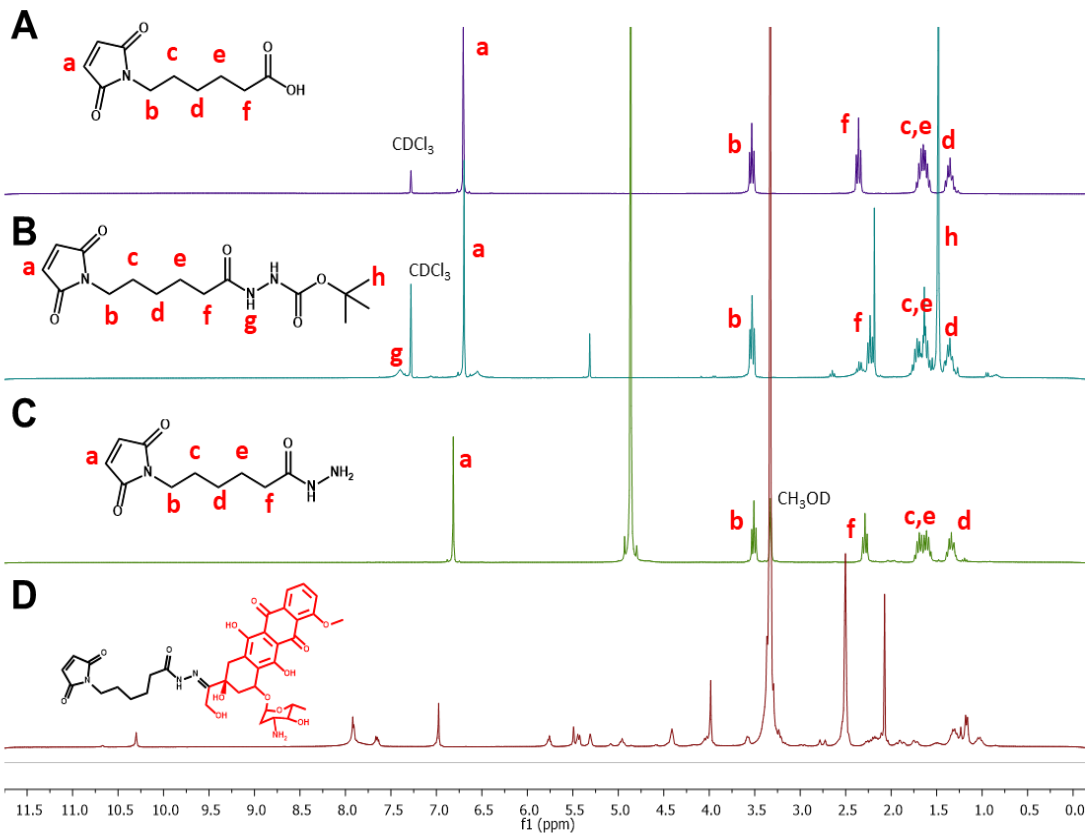

Figure 6. EMCH-Dox and corresponding precursors. ^{1}H-NMR characterization: **A)** 6-maleimidocaproic acid (300 MHz, $CDCl_3$). **B)** Tert-butyl 6-maleimidocaprohydrazinecarboxylate (300 MHz, $CDCl_3$). **C)** 6-maleimidocaprohydrazide (300 MHz, MeOD). **D)** 6-maleimidocaprohydrazone-Dox (300 MHz. d^6-DMSO).

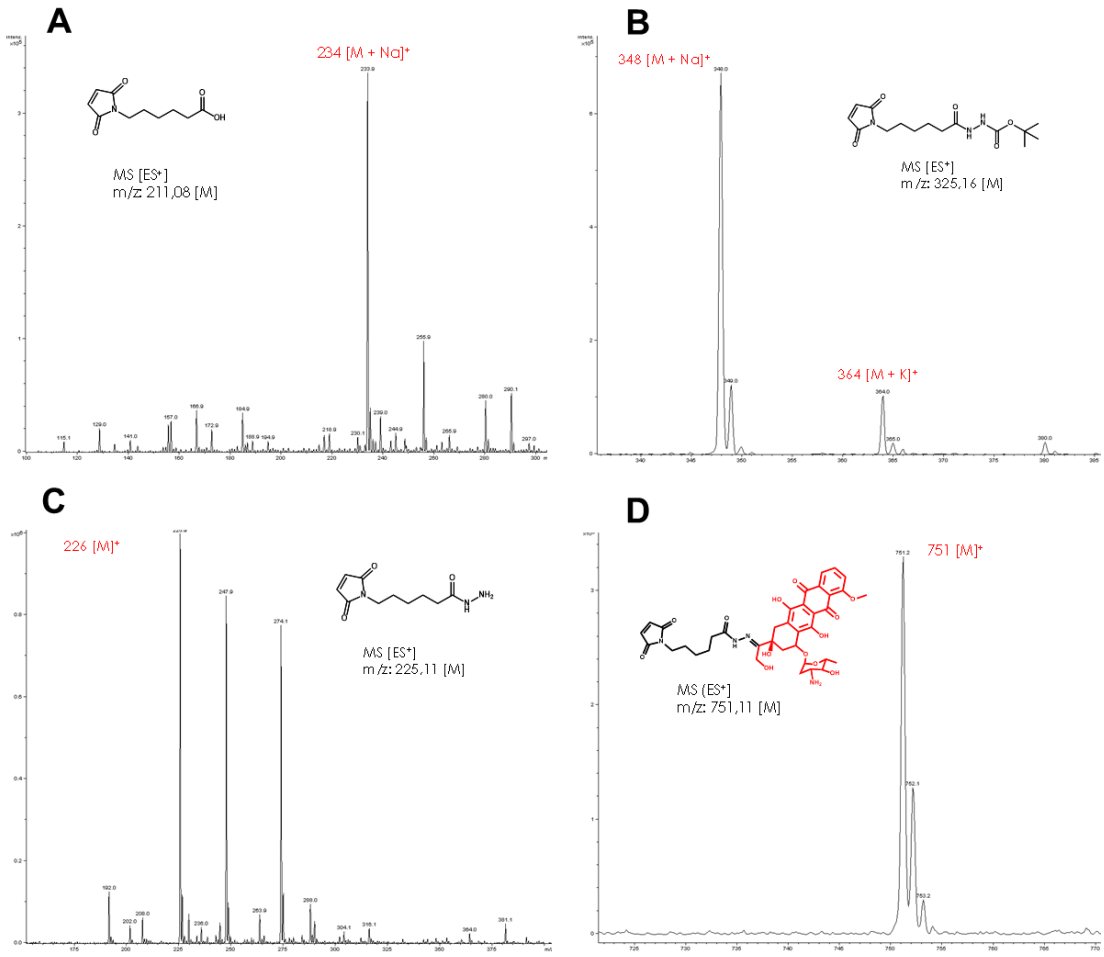

Figure 7. MALDI-TOF characterization of EMCH-Dox and corresponding precursors: **A)** 6-maleimidocaproic acid, **B)** Tert-butyl 6-maleimidocaprohydrazinecarboxylate, **C)** 6-maleimidocaprohydrazide, and **D)** 6-maleimidocaprohydrazone-Dox.

We then carried out the physico-chemical characterization of all synthesized conjugates. **Figure 8** depicts the spectra of representative conjugates with chemical shifts attributed to the incorporation of one or both drugs. The signal corresponding to the ethylene group (δ 0.75ppm) and those at the aromatic region (δ 7.5 ppm) indicated the presence of G-AGM. Dox aromatic rings signals appeared in the region of δ 7.0-8.0 ppm and the methylene group of the amino-sugar moiety at δ 1.25ppm. The conjugates bearing EMCH-Dox presented a characteristic ethylene signal of the EMCH spacer (δ 3.3ppm) also present in the combination conjugate; however, the aromatic signals of the drug practically disappeared. Additionally, the broadening of polymer signals also represented an indication for polymer conjugation.

PGA conjugates	Dox Loading (mol%)[A]	AGM Loading (mol%)[B]	Size by DLS (D_h, nm)[C]	Theoretical Mw (KDa)[D]
PGA-(G-AGM)$_{10}$	-	9.9	3.2	14830
PGA-(hyd-Dox)$_1$	1.3	n/a	390.0	13090
PGA-(hyd-Dox)$_3$	3.1	n/a	4.2	14100
PGA-(EMCH-Dox)$_1$	0.9	n/a	6.5	12900
PGA-(G-AGM)$_{10}$-(hyd-Dox)$_1$	2.9	9.1	4.4	14620
PGA-(G-AGM)$_{10}$-(hyd-Dox)$_3$	1.1	10.4	3.6	14860
PGA-(G-AGM)$_{10}$-(EMCH-Dox)$_1$	0.9	8.1	17.7	14900
PGA-(G-AGM)$_{10}$-(EMCH-Dox)$_3$	2.9	9.4	3.2	15250

Table 1. Physico-chemical characteristics of PGA-drug conjugates. [A]Calculated spectrophotometrically by UV-VIS, [B]Averaged form ^{1}H-NMR and UV measurements, [C]Size by Number, and [D]Calculated according to the drug loading.

We also employed ^{1}H-NMR to evaluate single conjugates precursors, PGA-PD, PGA-NH-NHBoc, PGA-NH-NH$_2$ (**Figure 3**), and the combination conjugates precursors PGA-(G-AGM)-PD, PGA-(G-AGM)-NH-NHBoc, and PGA-(G-AGM)-NH-NH$_2$ (**Figure 4**). Additional ^{1}H-NMR assignments of final conjugates (**Figures 8** and **12)** can be compared with the corresponding spectra of the free parent drugs, demonstrating the presence of the drug within the nanoconjugate structure (**Figure 9**).

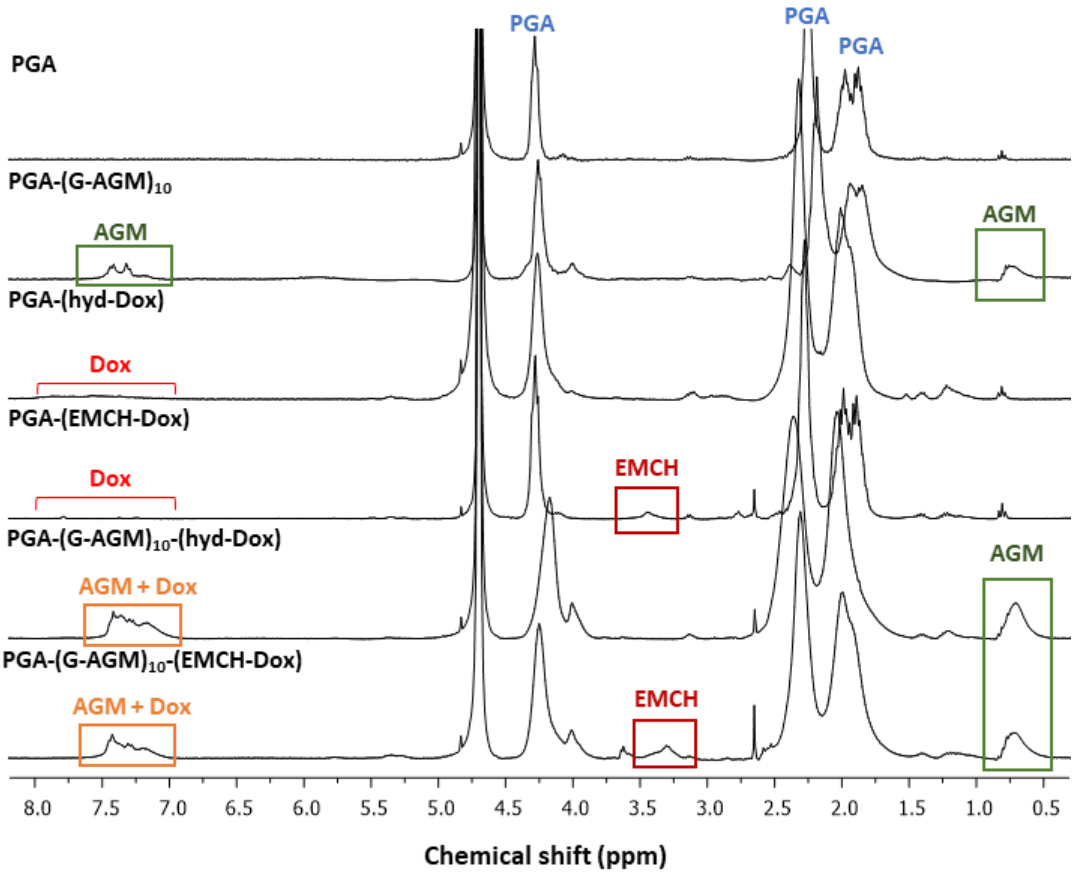

Figure 8. ^{1}H-NMR spectra of representative single and combination conjugates.

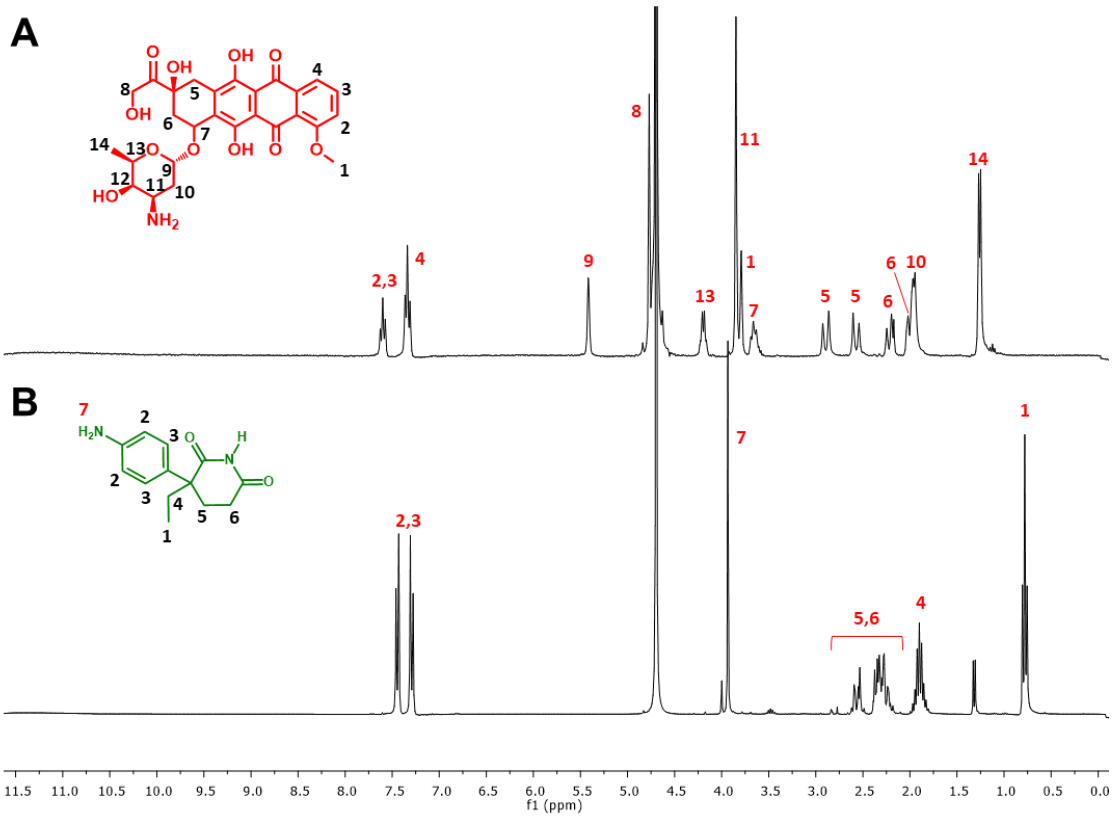

Figure 9. : Dox (**A**) and AGM (**B**) ^{1}H-NMR signal assignments.

Size-exclusion chromatography (SEC) elugrams demonstrated single homogeneous Mw distribution by refractive index (RI), and no evidence of free drug presence (**Figure 10**). We note that the conjugation of one or both drugs did not significantly modify the D_h in solution by DLS (number), and most of the conjugates exhibited a monomodal averaged D_h of ~3-6 nm, except in the case of the single conjugate PGA-(Hyd-Dox)$_{LL}$ (D_h ~290nm) and the combination conjugate PGA-(G-AGM)-(EMCH-Dox)$_{LL}$ (D_h ~18nm).

Interestingly, DLS measurements regarding intensity (**Figure 12**), revealed a bimodal population distribution indicating the coexistence of unimers and aggregates. Although we expected the higher Dox-loaded conjugates and those bearing the hydrophobic EMCH linker to aggregate given the overall increased hydrophobicity, we observed greater aggregation behavior for those with the lowest Dox content.

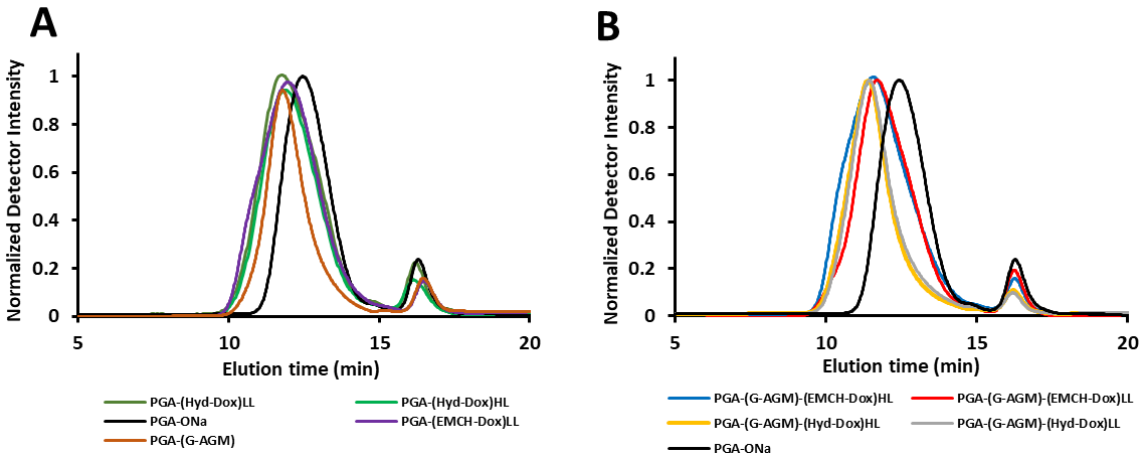

Figure 10. SEC elugrams for parental PGA compared with single conjugates and combination conjugates, respecttively (RI detection, peak at 17.1 min corresponds to the counter-cation Na^+).

This counterintuitive finding may indicate that the overall aqueous solution conformation is driven by a complex interplay of dynamic factors (including the polyelectrolyte effect [20, 21]) and not only imposed by the hydrophobicity of the loaded drugs as a single factor [8]. We aim to undertake additional studies involving complementary techniques, such as in-flow fractionation techniques [20, 22] to reveal the contribution of both, hydrophobicity and polyelectrolyte effect to the global spatial arrangement of conjugated macromolecules.

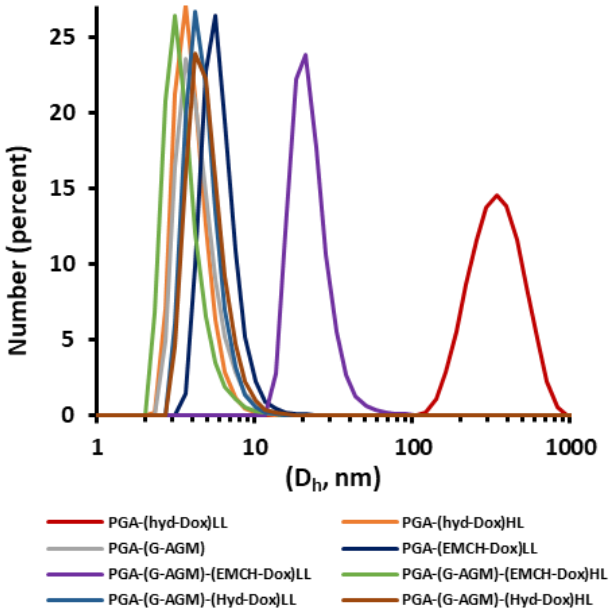

Figure 11. Size distribution graphs in number obtained by DLS in PBS at 5.0 mg·mL^{-1}.

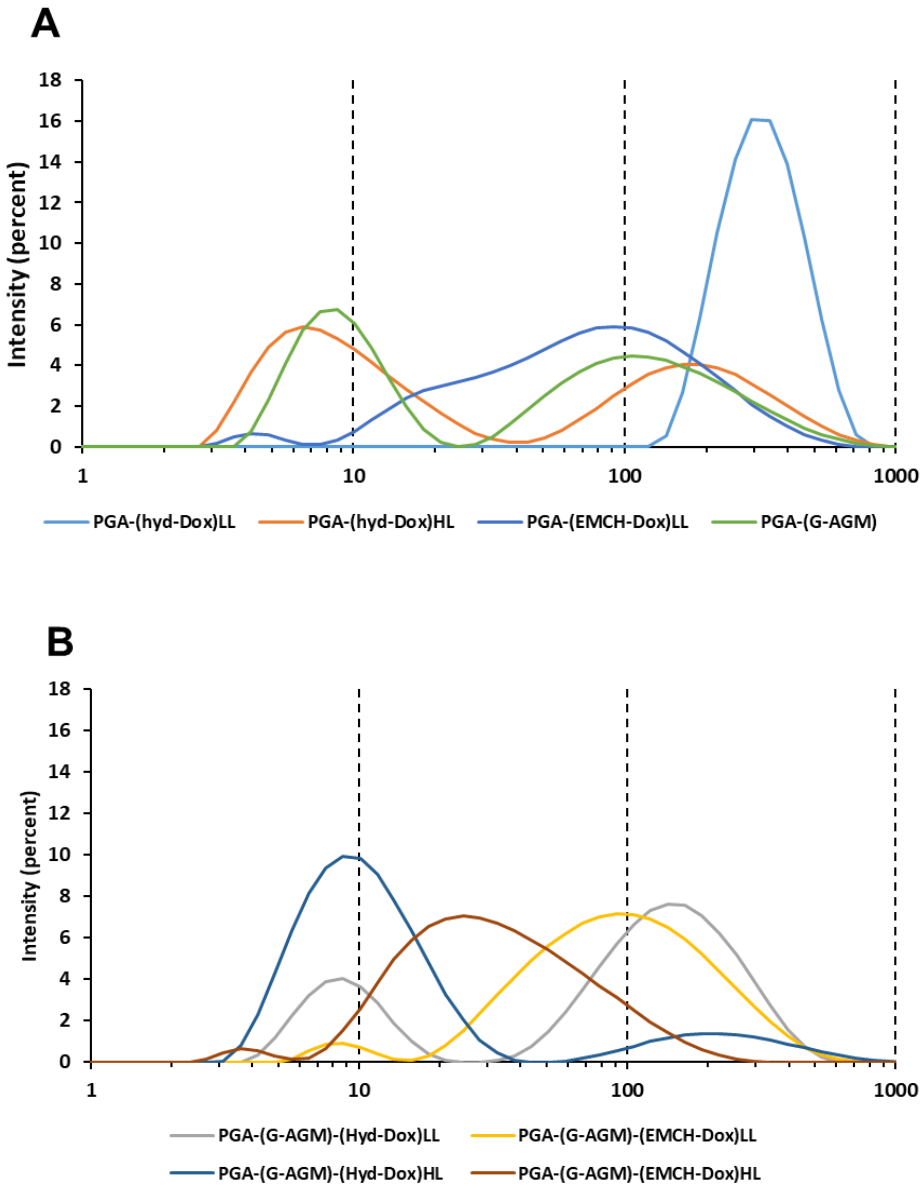

Figure 12. DLS measurements of single (**A**) and combination conjugates (**B**) by Intensity means.

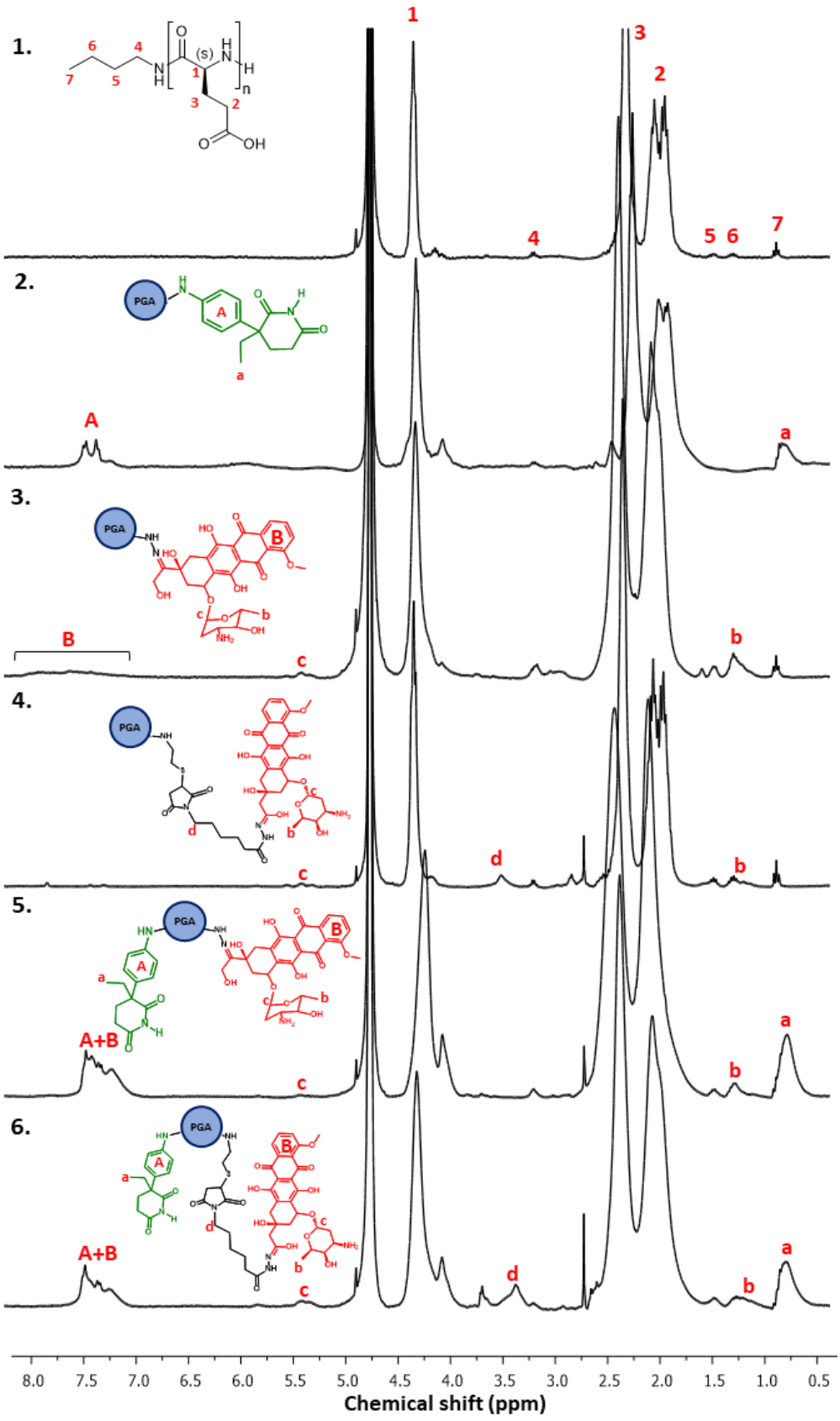

Figure 13. ^{1}H-NMR assignments of representative drug signals for the single (2. to 4.) and combination (5. and 6.) conjugates.

IV.2.2. Dox Release Kinetics as a Crucial Feature Driving in vitro Output

To understand the biological implications of different drug-linker use and drug loading/ratio in our conjugates, we performed cell toxicity assays in 4T1 murine breast cancer cells. **Figure 14** depicts the *in vitro* effect of the PGA-(G-AGM)-$(Hyd\text{-}Dox)_{HL}$, PGA-(G-AGM)-$(Hyd\text{-}Dox)_{LL}$, PGA-(G-AGM)-$(EMCH\text{-}Dox)_{HL}$, and PGA-(G-AGM)-$(EMCH\text{-}Dox)_{LL}$ combination conjugates. Cell viability assays demonstrated higher cytotoxicity for the PGA-(G-AGM)-$(Hyd\text{-}Dox)_{LL}$, PGA-(G-AGM)-$(Hyd\text{-}Dox)_{HL}$, and PGA-(G-AGM)-$(EMCH\text{-}Dox)_{LL}$ combination conjugates when compared with PGA-(G-AGM)-$(EMCH\text{-}Dox)_{HL}$, which displayed very low cytotoxicity.

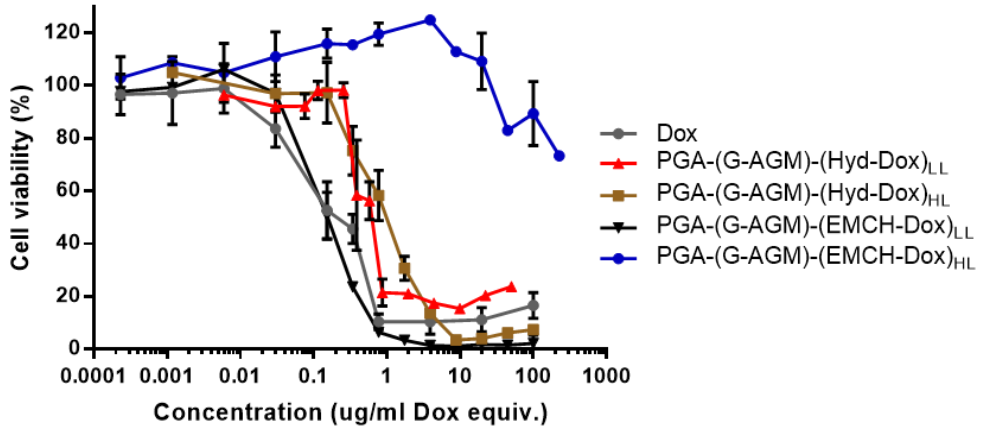

Figure 14. Cell viability and drug release kinetic analyses for combination conjugates. Cell viability measured by MTS assay after 72 hours of treatment with PGA-(G-AGM)-(Hyd-Dox)LL, PGA-(G-AGM)-(Hyd-Dox)HL, PGA-(G-AGM)-(EMCH-Dox)L, PGA-(G-AGM)-(Hyd-Dox)HL or free Dox. Data expressed as mean ± SEM, at least n = 3 experiments per treatment.

Although cytotoxicity assays provided non-statistically-significant differences at the range of concentrations tested, both combination conjugates incorporating low Dox loadings presented with trends towards higher cytotoxicity (IC_{50} = 0.13 μg/mL and 0.45 μg/mL for PGA-(G-AGM)-$(EMCH\text{-}Dox)_{LL}$ and PGA-(G-AGM)-$(Hyd\text{-}Dox)_{LL}$, respectively, vs. IC_{50}=0.79 μg/mL for PGA-(G-AGM)-$(Hyd\text{-}Dox)_{HL}$) (**Figure 15**). In contrast with our previously reported PGA-(G-AGM)-Dox family [8], we did not observe any significant differences in cell toxicity between the single and the combination conjugates (**Figure 16**), indicating a lack of AGM:Dox synergism at the drug ratios present upon hydrazone-mediated conjugation.

	IC_{50} (µg/ml Dox equiv)
Dox	0,1265
PGA-(G-AGM)-(Hyd-Dox)$_{LL}$	0,4579
PGA-(G-AGM)-(Hyd-Dox)$_{HL}$	0,7898
PGA-(G-AGM)-(EMCH-Dox)$_{LL}$	0,1323
PGA-(G-AGM)-(EMCH-Dox)$_{HL}$	191

Figure 15. IC50 values for free Dox and polymer-drug conjugates in the mouse 4T1 breast cancer cell line.

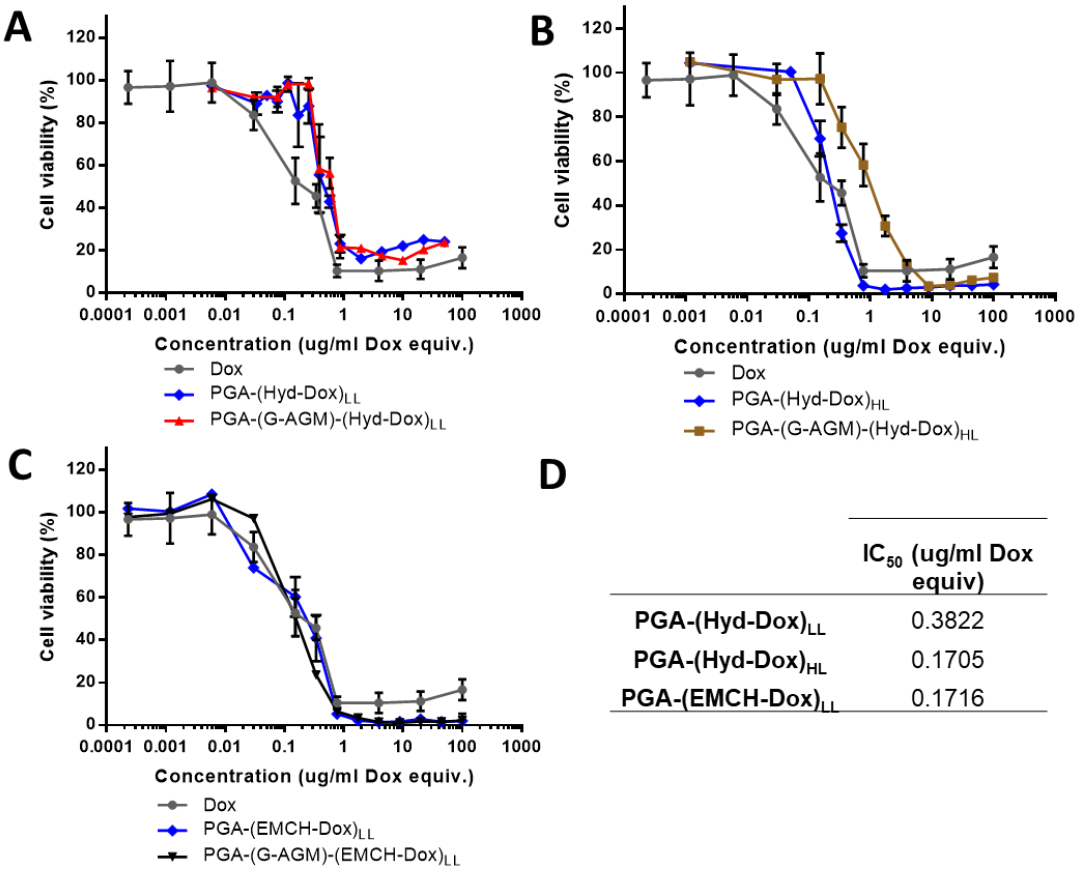

	IC_{50} (ug/ml Dox equiv)
PGA-(Hyd-Dox)$_{LL}$	0.3822
PGA-(Hyd-Dox)$_{HL}$	0.1705
PGA-(EMCH-Dox)$_{LL}$	0.1716

Figure 16. Comparative cell viability study for the single and combination conjugates in mouse 4T1 breast cancer cell line demonstrating lack of drug synergism. **A)** PGA-(Hyd-Dox)$_{LL}$ vs. PGA-(G-AGM)-(Hyd-Dox)$_{LL}$, **B)** PGA-(Hyd-Dox)$_{HL}$ vs. PGA-(G-AGM)-(Hyd-Dox)$_{HL}$, **C)** PGA-(EMCH-Dox)$_{LL}$ vs. PGA-(G-AGM)-(EMCH-Dox)$_{LL}$, and **D)** IC_{50} values of the single conjugates.

To explain this biological/therapeutic output, we evaluated Dox release from the combination conjugates at physiological and acidic pH, as well as in the presence of Cathepsin B (**Figure 17**). As expected, we found differential release profiles depending on Dox loading and linker length. For the EMCH-derivatives, the PGA-(G-AGM)-

(EMCH-Dox)$_{LL}$ combination conjugate displayed rapid Dox release at pH 5.0 during the first 8 h, reaching a maximum of 16%, and a slower Dox release (~2%) at physiological pH (7.4). Remarkably, the corresponding combination conjugate with higher Dox loading, PGA-(G-AGM)-(EMCH-Dox)$_{HL}$, displayed almost no Dox release at pH 5 or 7.4 (<1%) during the same time period (**Figure 19**). These results, together with DLS measurements (by number) (**Figure 11**), suggest a distinct conjugate solution conformation due to a different spatial arrangement of Dox molecules as a function of loading. We hypothesize that high loading of EMCH-Dox promotes a more condensed structure (lower D_h), with the hydrazone bond hidden from the acidic environment and thereby hindering Dox release. This may also explain the difficulty we faced when attempting to increase Dox loading. Therefore, we also hypothesize that low loadings of EMCH-Dox correlate with a more swollen structure (higher D_h), promoting a higher level of hydrazone exposure and Dox release.

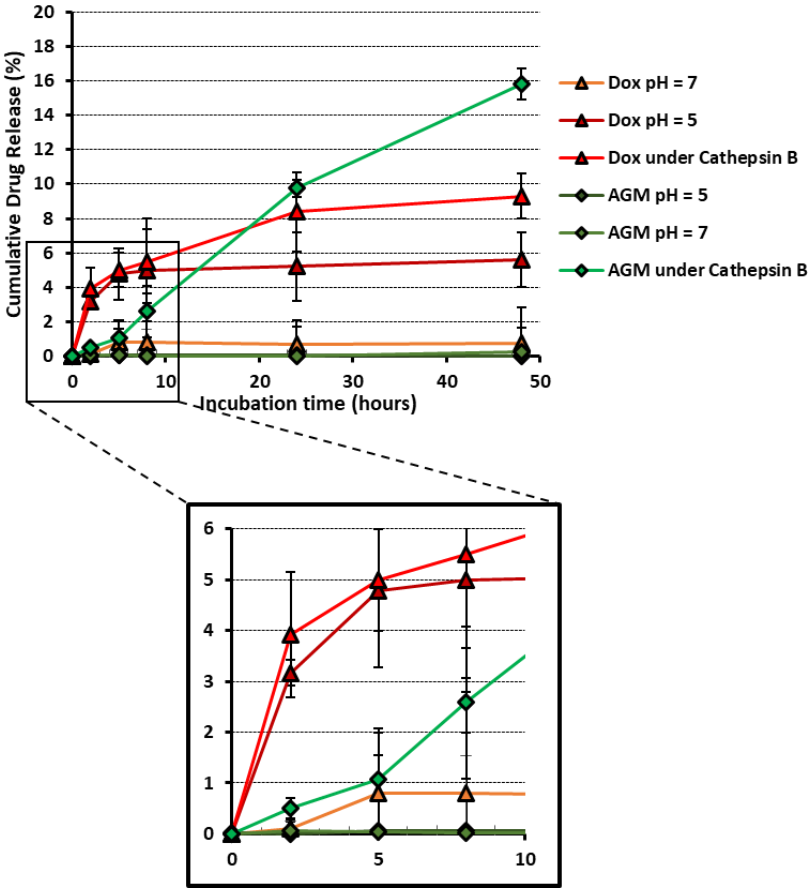

Figure 17. Kinetics of drug(s) release from PGA-(G-AGM)-(Hyd-Dox)$_{LL}$ under hydrolytic and proteolytic (cathepsin B) conditions; n = 3 experiments per assay.

Conjugates obtained by direct conjugation displayed similar Dox loading-related release behavior (**Figure 18**). The PGA-(G-AGM)-(Hyd-Dox)$_{LL}$ combination conjugate exhibited up to 10% Dox released at pH 5.0 within 8 h and less than 1% at pH 7.4. In contrast, the PGA-(G-AGM)-(Hyd-Dox)$_{HL}$ combination conjugate displayed only 2% Dox release at pH 5.0 within the same time frame. Independently of the Dox linking chemistry employed, lower loading correlated higher release rates, thereby explaining the differential cytotoxicity observed. For hydrazone-derivative conjugates, we did not find any differences by DLS regarding number. However, measurement by intensity suggested a higher aggregation tendency (larger D_h) for the combination conjugate bearing the lower Dox loading (PGA-(G-AGM)-(Hyd-Dox)$_{LL}$ when compared to the corresponding conjugate with higher Dox loading (PGA-(G-AGM)-(Hyd-Dox)$_{HL}$.

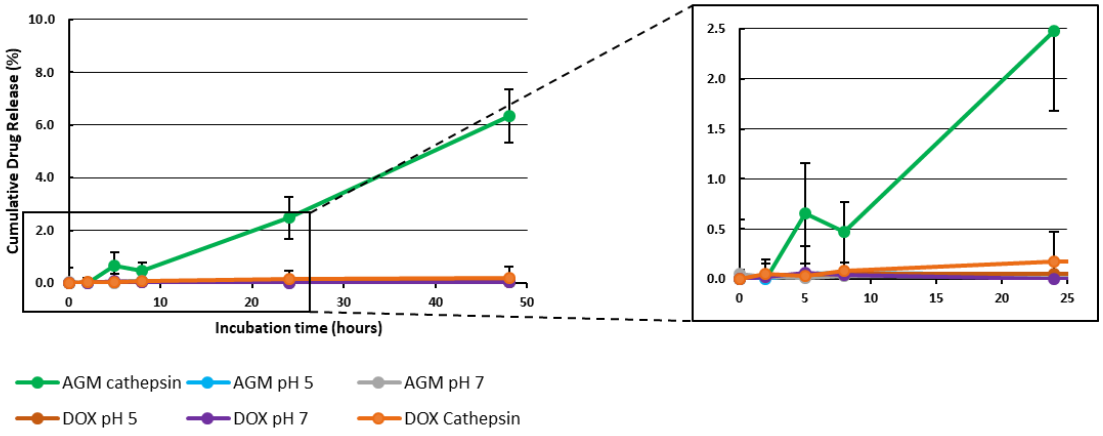

Figure 18. pH-dependent and Cathepsin B-dependent Dox and AGM releases of PGA-(G-AGM)-(Hyd-Dox)$_{HL}$; n = 3 experiments per assay.

As we conjugated AGM through a pH-stable chemical bond, we expect AGM release from the PGA mainchain by cathepsin B-driven degradation [8]. Therefore, we expected much faster overall Dox release rates from Dox-hydrazone-bearing conjugates than AGM release (only influenced by protease presence). However, cathepsin B degradation studies with (PGA-(G-AGM)-(Hyd-Dox)$_{HL}$ (**Figure 17**) clearly demonstrated that this assumption was wrong and that the final conjugate solution conformation again was critical. The greater AGM bioavailability *vs.* Dox obtained for

this conjugate could be responsible for the lack of activity as well as drug synergism discovered. In the case of the most active conjugate, (PGA-(G-AGM)-(Hyd-Dox)$_{LL}$, we observed similar results, however in this particular case, and we believe is the reason for the enhanced activity, Dox release profile was faster at very early time-points (at pH 5 as well as in the presence of cathepsin B, showing the preferential hydrolytic mechanism triggering Dox release) most probably due to a greater accessibility of the hydrazine triggered by a less compact structure. The final relative release profile comparing Dox *vs.* AGM could also explain the absence of drug synergism as we obtained an inverse relative bioavailable AGM:Dox ratio from that previously identified as synergistic [8].

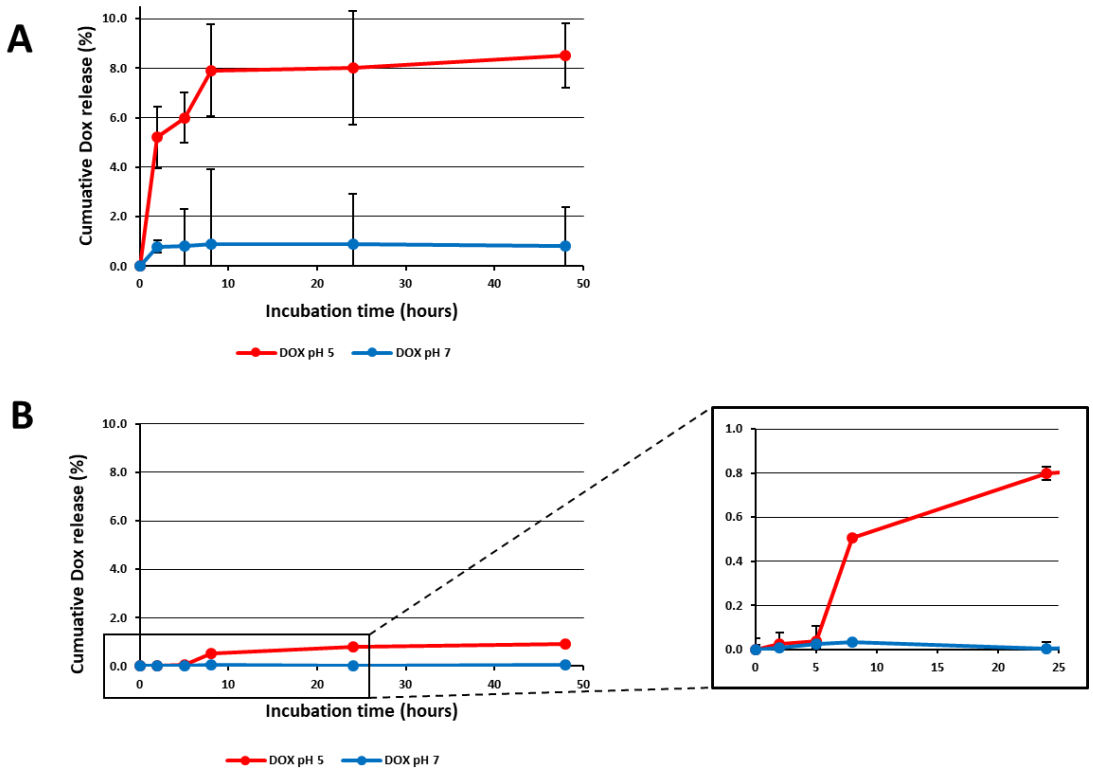

Figure 19. A) pH-dependent Dox release of PGA-(G-AGM)-(EMCH-Dox)$_{LL}$. **B)** pH-dependent Dox release of PGA-(G-AGM)-(EMCH-Dox)$_{HL.}$ n = 3 experiments per assay.

In summary, the release kinetics findings correlate with *in vitro* results: the combination conjugate displaying the highest IC_{50} (PGA-(G-AGM)-(EMCH-Dox)$_{HL}$) demonstrated almost no Dox release, while the conjugate showing the highest Dox release (PGA-(G-AGM)-(EMCH-Dox)$_{LL}$) corresponded to the highest cytotoxicity. As demonstrated previously [8, 23], the selection of drug linkers, drug ratios, and drug loadings in a polymer-drug combination conjugate can drastically modify the entire

macromolecular configuration, varying key parameters, including hydrodynamic size and drug release kinetics, which directly influence biological readout.

IV.2.3. Study of Combination Conjugates Antitumor Activity and Safety in a Spontaneously Metastatic TNBC Murine Model

The antitumor/antimetastatic effect of polymer-drug combination conjugates requires accumulation within the tumor site by passive (EPR effect) accumulation and/or active targeting. We and others have previously described the spontaneously metastatic 4T1 TNBC murine model developed in immunocompetent BALB/c mice [10, 24, 25], which included the study of EPR effect [4]. This preclinical model faithfully mimics the human clinical scenario, offering an opportunity for reliable DDS *in vivo* testing [10].

To examine combination conjugate antitumor efficacy, we randomly distributed tumor-bearing mice whose volumes had reached ~0.1cm^3 (maximal EPR effect [10]) into representative groups and scheduled four treatments every three days with the conjugates showing the best cytotoxic activity (at 10 mg/kg Dox equivalents) (**Figure 20A**). In addition, we administered Dox to a control group at 5 mg/kg and unconjugated PGA as a vehicle control at 25 mg/kg (maximum concentration used for the conjugates as a carrier). Both PGA-(G-AGM)-(Hyd-Dox)$_{LL}$ and PGA-(G-AGM)-(EMCH-Dox)$_{LL}$ combination conjugates exhibited substantial antitumor activity (50% tumor reduction compared with PBS-treated mice). Furthermore, we noted a similar decrease in tumor volume in the free Dox-treated animals. However, treatment with unconjugated PGA and PGA-(G-AGM)-(Hyd-Dox)$_{HL}$ did not significantly diminish tumor growth when compared with PBS-treated mice. In good agreement with our *in vitro* findings, we did not find improvements in efficacy when we administered the physical mixture of single conjugates (PGA-(G-AGM) + PGA-(Hyd-Dox)$_{LL}$) or the combination conjugate PGA-(G-AGM)-(Hyd-Dox)$_{LL}$ in comparison to the administration of the PGA-(Hyd-Dox)$_{LL}$ single conjugate, suggesting, in this case, that the presence of AGM plays a relatively minor role. As stated above, this result could be explained by the differential bioavailable drug ratio employed when compared to previous protease labile PGA-AGM-Dox conjugates [8] (**Figure 17**).

To further understand the effect of our combination conjugates on tumor growth, we studied tumor density (**Figure 20A**) and the relationship between proliferation (via Ki-67 immunostaining of axial sections) and tumor necrosis (**Figure 21A**) at the

experimental endpoint. We did not observe significant tumor necrosis within the free Dox-treated animals, perhaps due to lower levels of drug persistence within the tumor stroma. However, treatment with the two combination conjugates displaying the most promising therapeutic effects (PGA-(G-AGM)-(Hyd-Dox)$_{LL}$ and PGA-(G-AGM)-(EMCH-Dox)$_{LL}$) led to the appearance of large necrotic tumor cores (**Figure 21A**) and optimal tumor growth inhibition (**Figure 20A**). Furthermore, these two combination conjugates inhibited the proliferation of viable outer cells (**Figure 21A**), indicating possible cell-cycle arrest induced by prolonged Dox exposure driven by both passive conjugate accumulation and sustained stromal release [26, 27]. Although necrosis is typically related with hypodense tissue regions, our analyses demonstrated higher necrosis in the denser tumors (~1.9g/cm^3 *vs.* placebo ~1.4g/cm^3). PGA-(G-AGM)-(Hyd-Dox)$_{HL}$ treated tumors presented the lowest density, similar to the PBS control group (~1.3g/cm^3) (**Figure 20B**). Of note, 4T1 tumors develop coagulative necrosis [28, 29] characterized by the preservation of the basic structural outline of the affected cells in a compact network and the accumulation of inflammatory cells [30]. Dox-related hypoxia [31] may lead to tumor tissue ischemia and thus to more hypoxic tumors resulting in increased coagulative necrosis and therefore, denser tumors.

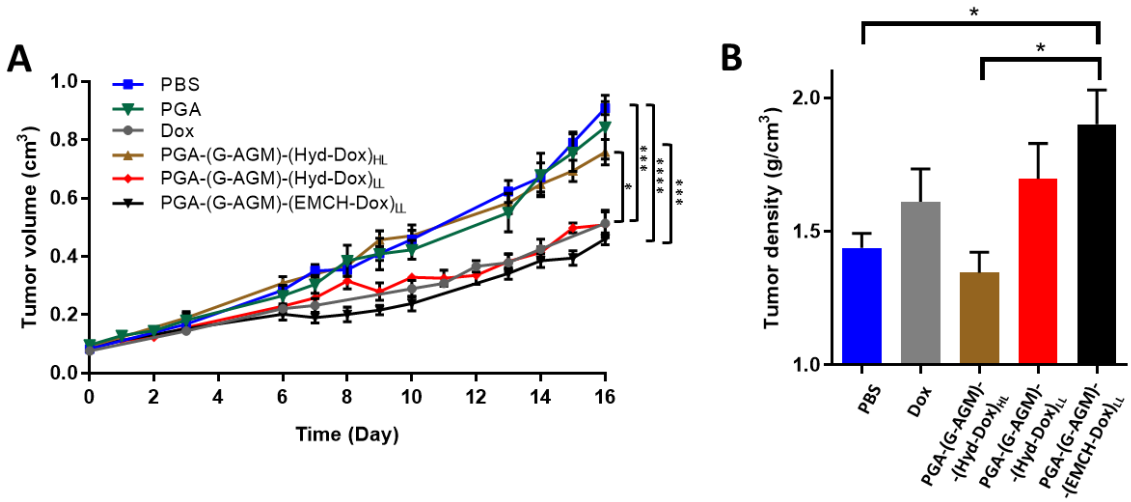

Figure 20. A) Tumor growth inhibition of previously selected polymer-drug conjugates. Data represent mean ± SEM. Statistical significance was determined using an ANOVA t-test, (* p<0.05, ** p<0.01, *** p<0.001). **B)** Evaluation of tumor density after different treatments.

To assess safety, we systematically evaluated, body weight, general aspect, behavior, and post-mortem major organ weights of all animals employed. We observed no significant alterations in body weight of animals treated with PGA-(G-AGM)-(Hyd-

Dox)$_{LL,}$ PGA-(G-AGM)-(Hyd-Dox)$_{HL,}$ or Dox, which displayed a 100% survival rate (**Figure 21B**). However, PGA-(G-AGM)-(EMCH-Dox)$_{LL}$ treated presented with lethargy, weakness, and slight dyspnea immediately following the third and fourth iv. administration, with only 50% of animals surviving (**Figure 22A**). Post-mortem organ analysis revealed increased relative liver weight in all animals compared to healthy (non-tumor bearing animals) noting the largest relative liver weight increase in animals treated with PGA-(G-AGM)-(EMCH-Dox)$_{LL}$. However, we note that animals treated with PGA-(G-AGM)-(Hyd-Dox)$_{LL,}$ PGA-(G-AGM)-(Hyd-Dox)$_{HL,}$ and Dox exhibited smaller increases in relative liver weight when compared to the PBS-treated (tumor-bearing) control animals, suggesting better overall anti-tumor activity.

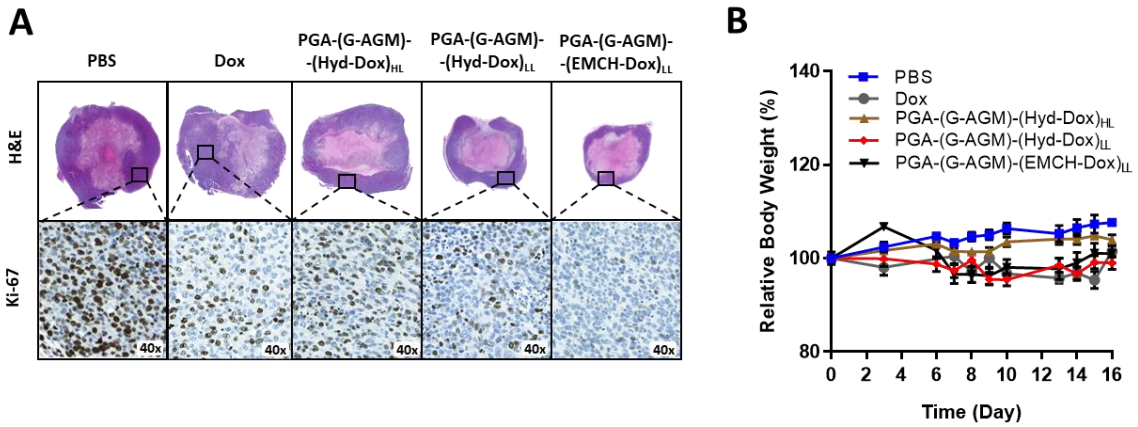

Figure 21.) A) Comparisons of H&E and Ki-67 axial sections of tumors with different treatments at the experimental endpoint. **B)** Relative mice body weight during treatments.

Of the organs studied, histopathological analyses revealed treatment-related adverse effects in the liver, as noted, and the heart, one of the key organs that present anthracycline-related pathologies [32, 33]. The liver presented significant hydropic degeneration, suggesting possible treatment-associated toxicity (**Figure 23**) and hearts of animals treated with Dox presented with myocardial fiber tortuosity, interfibrillar edema, and abundant fibrosis as major cardiomyopathies (**Figure 22C**). Although we discovered some disperse regions presenting minor levels of fibrosis, we observed no other major Dox-related cardiomyopathies in animals treated with two most effective antitumor treatments (PGA-(G-AGM)-(EMCH-Dox)$_{LL}$ or PGA-(G-AGM)-(Hyd-Dox)$_{LL}$).

All combination conjugates demonstrated safer *in vivo* therapeutic characteristics in terms of body weight and cardiotoxicity compared to free Dox (at even half dosage).

Nevertheless, the PGA-(G-AGM)-(EMCH-Dox)$_{LL}$ combination conjugate-treated animals demonstrated low overall survival and some degree of hepatotoxicity. Of note, the PGA-(G-AGM)-(EMCH-Dox)$_{LL}$ combination conjugate exhibited the lowest Dox loading, and so, we required highly concentrated doses of the conjugate to reach desired Dox equivalents, which increased the final solution viscosity; a parameter with the potential to affect proper blood distribution. Second, the larger size and heightened ability of this combination conjugate to aggregate in solution might promote accumulation in other organs, as well as in the tumor.

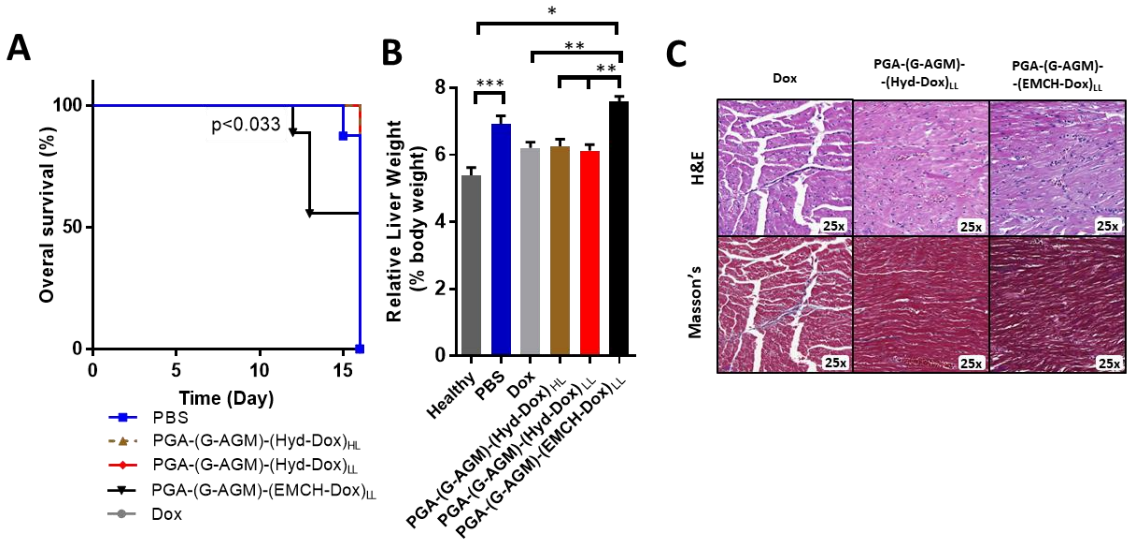

Figure 22. A) Kaplan-Meyer survival curves demonstrating the safety of the combination conjugates with the exception of PGA-(G-AGM)-(EMCH-Dox)$_{LL}$, that shows only 50% of mice survival. **B)** Relative liver weight by treatments demonstrating tumor-related hepatomegaly in the PBS group, which was partially improved with Dox, PGA-(G-AGM)-(Hyd-Dox)$_{HL}$, PGA-(G-AGM)-(Hyd-Dox)$_{LL}$. Greater organ weight was related to the treatment PGA-(G-AGM)-(EMCH-Dox)$_{LL}$. Statistical significance was determined using an ANOVA t-test (* $p<0.05$, ** $p<0.01$, *** $p<0.001$). C**)** Mice-treated heart sections showing Dox-induced cardiotoxicity using H&E and Masson's immunostaining compared with the cardio-safety displayed by the combination conjugates.

Livers from animals receiving PGA-(G-AGM)-(EMCH-Dox)$_{LL}$, developed even higher hydropic degeneration (vacuolar degeneration), coinciding with organ swelling (**Figure 23**) when compared with free Dox treatment [32]. Chemotherapeutic drug-induced hydropic degeneration occurs by direct and indirect toxicity mechanisms. The direct action causes increased cell membrane injury [34] leading to cellular injury (e.g., cisplatin and Dox). The indirect action includes the release of highly toxic and reactive free radicals [35] causing lipid peroxidation and cell membrane damage [36] with the

increased influx of sodium and water causing cellular swelling. Therefore, enhanced liver toxicity and reduced overall survival might be the result of a sum of factors, such as the possible accumulation of this conjugate and corresponding Dox-associated toxicity in the liver.

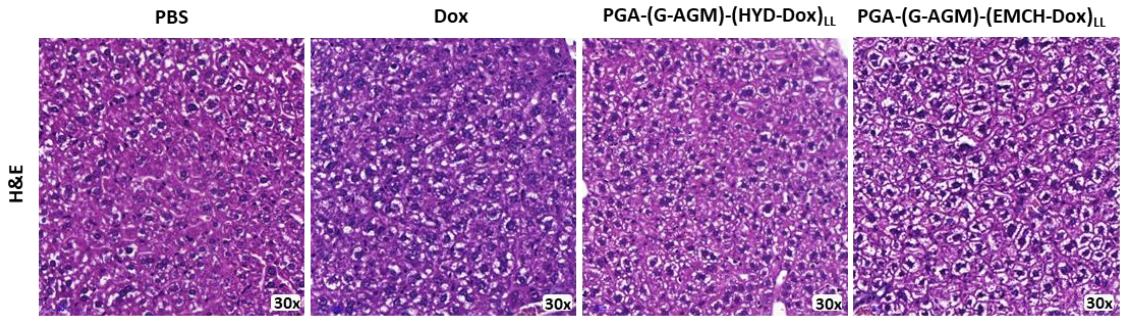

Figure 23. H&E staining of liver sections after the most relevant treatments**.**

Overall, the PGA-(G-AGM)-(Hyd-Dox)$_{LL}$ combination conjugate displayed the greatest antitumor activity and the most significant inhibition of tumor cell proliferation without impairing safety, thereby demonstrating the benefits of the rationally designed polymer conjugation-based strategies.

IV.2.4. Study of Antimetastatic Activity of Combination Conjugates and Effects on Extramedullary Hematopoiesis and Leukemoid Reaction

Lung metastasis is the most common complication of breast cancer patients and is identified in 60-70% of all cancer patients [37]. During primary tumor progression, cancer cells escape from the tumor stroma and travel through the bloodstream or lymphatic system to generate metastatic foci within the lung parenchyma or in the subpleural region. The 4T1 orthotopic TNBC BALB/c murine model is suitable for antimetastatic nanomedicines validation as it faithfully mimics the human clinical scenario, including spontaneously metastatic to the lung [10, 24]. This model develops the first signs of lung metastasis around day three after cell implantation, although our scheduled treatment began on day eight (max EPR). As depicted in **Figure 24A**, the PGA-(G-AGM)-(Hyd-Dox)$_{LL}$ combination conjugate displayed optimal antimetastatic activity: a 90% reduction in lung metastasis when compared with non-treated mice. The EMCH-based conjugate incorporating the lowest Dox loading (PGA-(G-AGM)-(EMCH-Dox)$_{LL}$)

displayed the same antimetastatic potential as free Dox. Further histopathological analysis confirmed these results (**Figure 24B**); animal receiving PGA-(G-AGM)-(Hyd-Dox)$_{LL}$ treatment (optimal antitumor combination conjugate) also displayed reduced subpleural and intraparenchymatous metastatic foci when compared with other treatments.

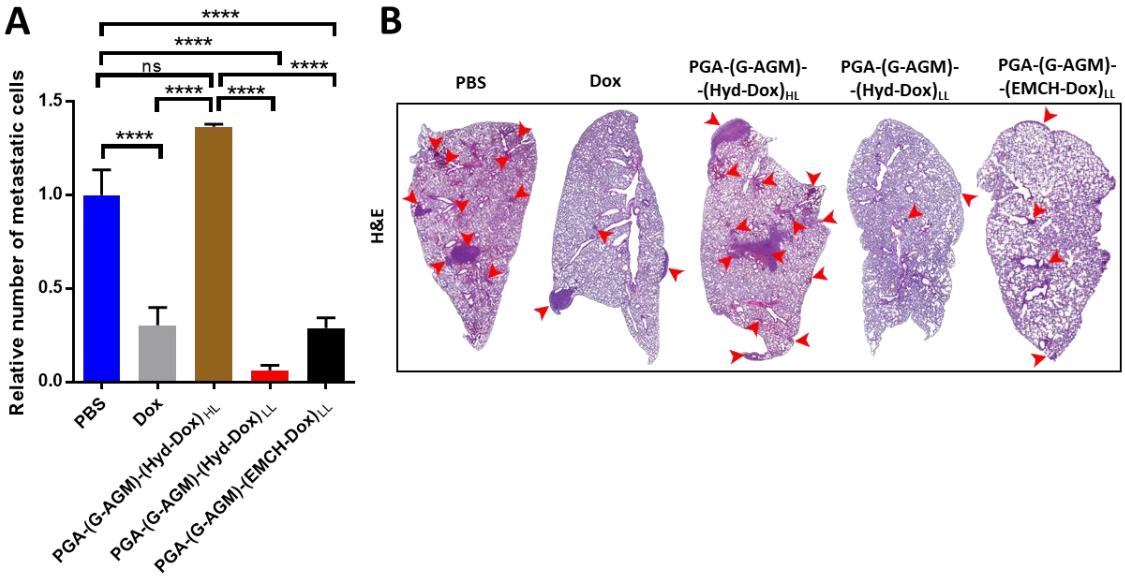

Figure 24. A) Quantification of lung metastasis in response to treatment - metastasis was significantly decreased after the treatment with PGA-(G-AGM)-(Hyd-Dox)$_{LL}$**,** PGA-(G-AGM)-(EMCH-Dox)$_{LL}$ and free Dox. Statistical significance was determined using an ANOVA t-test (* p<0.05, ** p<0.01, *** p<0.001). **B)** H&E histological analysis of representative lung lobes receiving different treatments. Red arrowheads indicate metastatic nodules identified under the microscope.

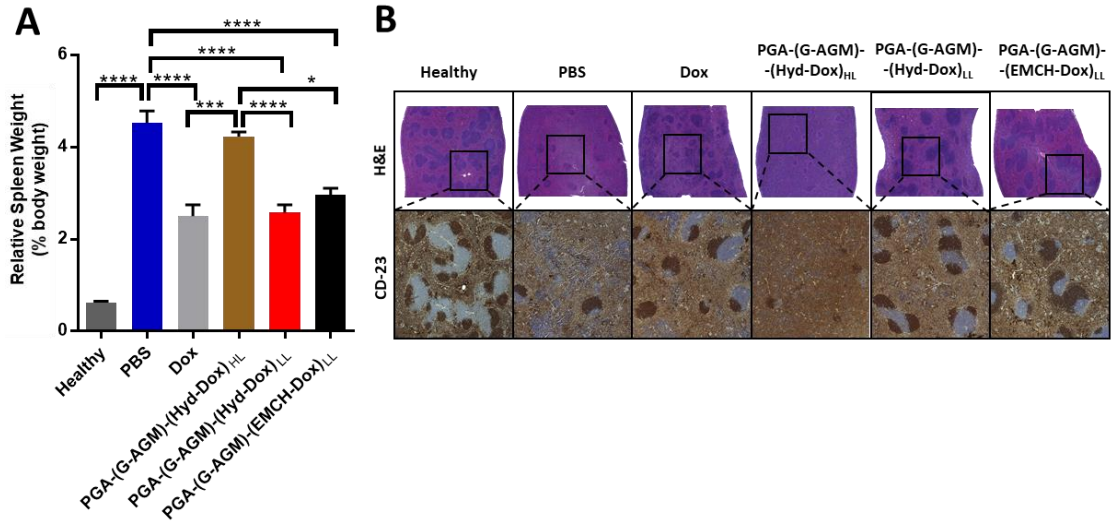

Figure 25. A) Tumor-induced splenomegaly, demonstrating the maximum weight of spleen in control animals (PBS) and those treated with PGA-(G-AGM)-(Hyd-Dox)$_{HL}$. Spleens of mice treated with Dox,

PGA-(G-AGM)-(Hyd-Dox)$_{HL}$ or PGA-(G-AGM)-(Hyd-Dox)$_{LL}$, demonstrated significant spleen weight reduction. **B)** Histopathological examination of spleens of mice treated with different conjugates. Splenomegaly correlates with congested red pulp as demonstrated by H&E and CD23.

4T1 tumor development blocks medullar erythropoiesis and, as a consequence, causes splenic and hepatic erythropoiesis which promotes acute splenomegaly in mice [10, 38, 39]. We evaluated the capacity of combination conjugates to reduce this secondary effect of tumor progression by examining spleen weights and histopathological features. As depicted in **Figure 25A**, we observed significant decreases in spleen weight in mice treated with PGA-(G-AGM)-(Hyd-Dox)$_{LL}$, PGA-(G-AGM)-(EMCH-Dox)$_{LL}$, or free Dox (the most effective antitumor treatments), with spleen weight in the PGA-(G-AGM)-(Hyd-Dox)$_{HL}$ treated animals similar to PBS (tumor-bearing) animals. Further histopathological analyses confirmed previous findings (**Figure 25B)**.

We discovered severe congestion of the red pulp and hyperplasia due to elevated reactive hematopoiesis in the spleens of PBS control mice and the combination conjugate PGA-(G-AGM)-(EMCH-Dox)$_{HL}$ treated mice. Spleens from mice treated with Dox, PGA-(G-AGM)-(Hyd-Dox)$_{LL}$, or PGA-(G-AGM)-(EMCH-Dox)$_{LL}$ displayed a partially restored splenic parenchyma. However, the severe leukemoid (leukocytosis) reaction observed in the PBS treated mice developed to a lesser extent in animals treated with Dox or with PGA-(G-AGM)-(Hyd-Dox)$_{LL}$ (**Figure 26A-C**), in line with the slower overall disease progression.

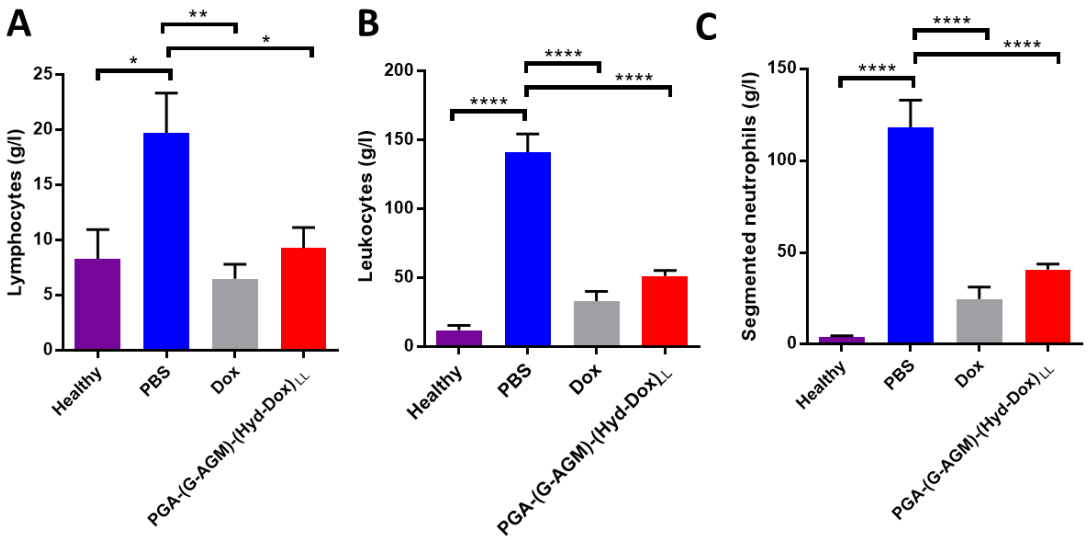

Figure 26. 4T1 tumor development produced acute lymphocytosis and leukocytosis (with major proportion of segmented neutrophils) as seen in the PBS-treated mice (**A, B, C**). Animals treated with Dox and PGA-(G-AGM)-(Hyd-Dox)$_{LL}$ demonstrated a recovery to the normal levels of lymphocytes, leukocytes and segmented neutrophils. Statistical significance was determined using an ANOVA t-test (* $p<0.05$, ** $p<0.01$, *** $p<0.001$ and ****$p<0.0001$).

The reduction in metastasis at the experimental endpoint might imply two different antimetastatic mechanisms induced by our combination conjugates. Greater anti-tumor activity (primary tumor), a reduction of tumor growth and tumor cell proliferation, may inhibit metastatic-related processes, including angiogenesis, migration, and/or epithelial-mesenchymal transition of tumor cells. Additionally, given the enhanced size in solution of the conjugates, the higher ability to aggregate and the accelerated Dox release kinetics of the low loading combination conjugates could promote accumulation in the lungs [40], leading to a direct effect on metastatic tumor cells. We hope that additional experiments focused on lung accumulation will corroborate these hypotheses.

In summary, the combination conjugates with lower Dox loading exhibit higher antitumor and antimetastatic activity, coinciding with higher Dox release influenced by the conjugate solution conformation and tumor stromal features.

IV.2.5. Transcriptomic study of Combination Conjugates

IV.2.5.1. Gene Ontology Analysis

To understand the molecular basis of the responses to the different combination conjugates, we performed RNA-seq analysis of tumors derived from treated animals and compared genes differentially expressed between each possible pair-wise comparison (**Figure 27**). In agreement with the above-described physiological characterization assays, we found that the highest number of differentially expressed genes, compared to the PBS control group, corresponded to the PGA-(G-AGM)-(Hyd-Dox)$_{LL}$ and PGA-(G-AGM)-(EMCH-Dox)$_{LL}$ combination conjugates. Of note, the PGA-(G-AGM)-(Hyd-Dox)$_{HL}$ combination conjugate, which demonstrated no differences in tumor growth inhibition with respect to PBS control, displayed significantly lower numbers of differentially expressed genes when compared to other treatments. Therefore, we concentrated our functional enrichment analysis on PGA-(G-AGM)-(Hyd-Dox)$_{LL}$, and

PGA-(G-AGM)-(EMCH-Dox)$_{LL}$ treatments to understand similarities and differences in molecular responses.

A

	UP	DOWN
PGA-(G-AGM)-(Hyd-Dox)^{HL} vs PBS	0	0
PGA-(G-AGM)-(Hyd-Dox)^{LL} vs PBS	196	173
PGA-(G-AGM)-(EMCH-Dox)^{LL} vs PBS	194	273
PGA-(G-AGM)-(Hyd-Dox)^{HL} vs PGA-(G-AGM)-(Hyd-Dox)^{LL}	427	616
PGA-(G-AGM)-(EMCH-Dox)^{LL} vs PGA-(G-AGM)-(Hyd-Dox)^{LL}	177	171

B

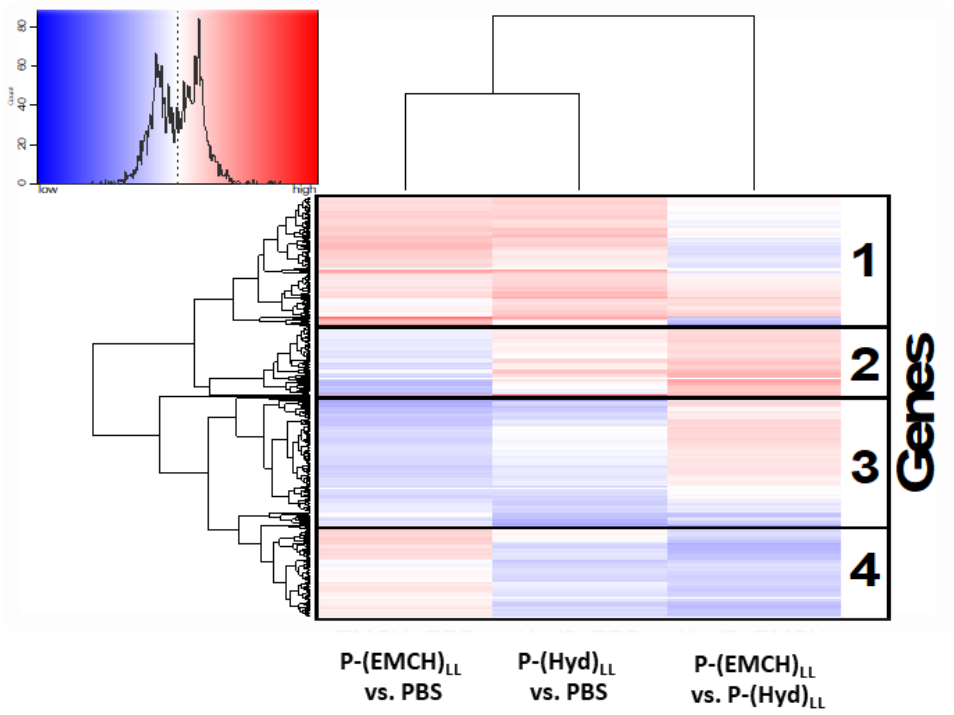

Figure 27. A) Differentially expressed genes in different comparisons between conjugate-based treatments and PBS. **B)** Heat map of selected differentially regulated genes between P-(EMCH)$_{LL}$ vs. PBS, P-(Hyd)$_{LL}$ vs. PBS and P-(EMCH)$_{LL}$vs. P-(Hyd)$_{LL}$. P-(EMCH)$_{LL}$ = PGA-(G-AGM)-(EMCH-Dox)$_{LL}$; P-(Hyd)$_{LL}$ = PGA-(G-AGM)-(Hyd-Dox)$_{LL}$.

GO enrichment analysis revealed the enrichment of 62 and five terms in genes that were up- or down-regulated, respectively, when comparing (PGA-(G-AGM)-(Hyd-Dox)$_{LL}$ and PGA-(G-AGM)-(EMCH-Dox)$_{LL}$) transcriptional responses (**Figure 28**),

while 11 and 10 GO terms were enriched in up- or down-regulated genes between the two conjugates.

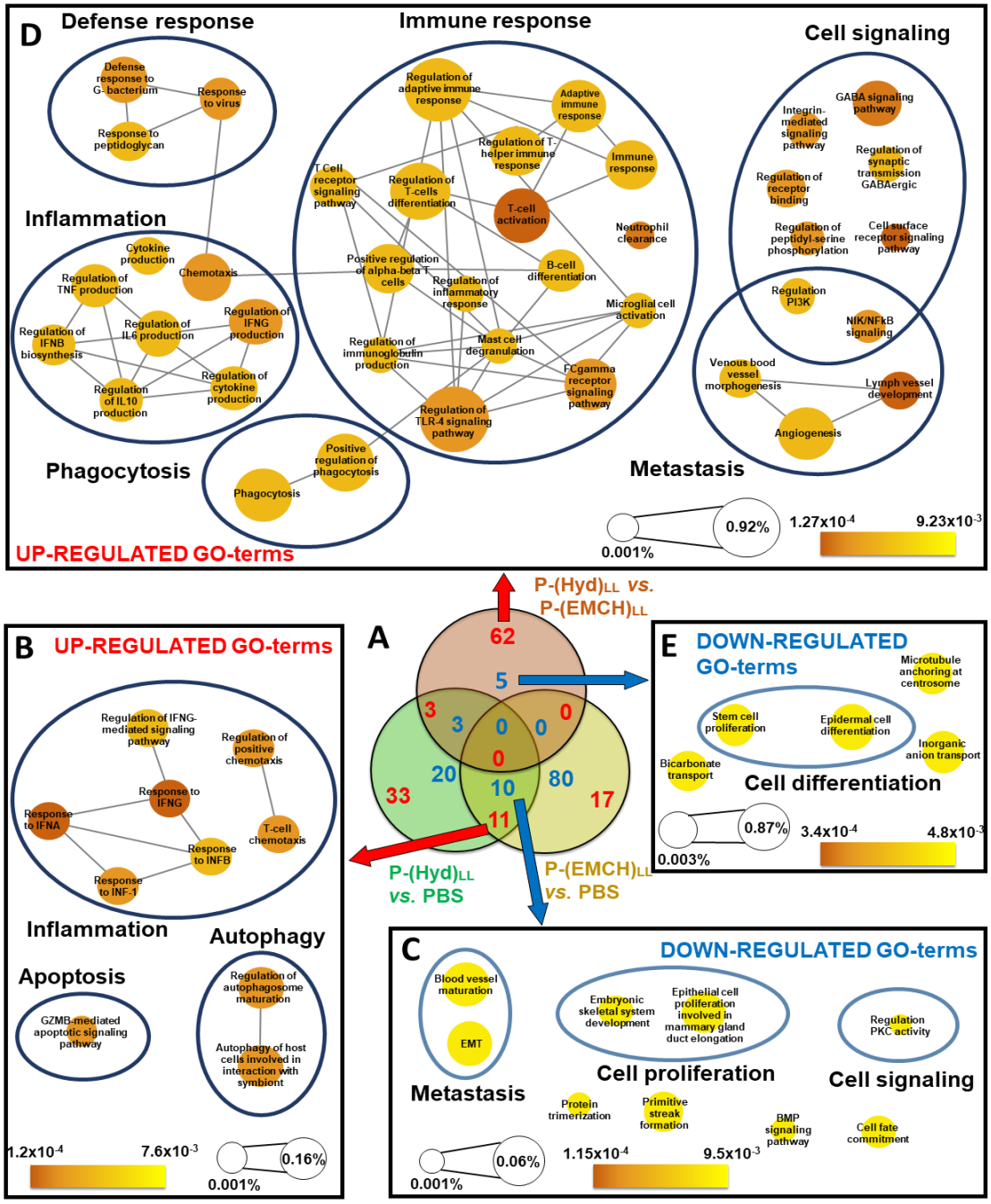

Figure 28. Network visualization of the statistically significant GO terms grouped by hyper-categories. **A**) Venn diagram comparing the GO terms up or downregulated between PGA-(G-AGM)-(Hyd-Dox)$_{LL}$- PBS; PGA-(G-AGM)-(EMCH-Dox)$_{LL}$ – PBS and PGA-(G-AGM)-(Hyd-Dox)$_{LL}$- PGA-(G-AGM)-(EMCH-Dox)$_{LL}$ paired comparisons. Red numbers: upregulated GO terms; blue numbers: downregulated genes. Networks were constructed from these results, and the more relevant are demonstrating similarities (**C,E**) and differences (**B,D**) between the two drug conjugates. Networks constructed through REVIGO web server using EBI-GOA database. The darker the color the lower the p-value, as an indication of significance

level. Nodes size indicates the frequency of the GO term in the EBI-GOA database. Edges indicates highly similar GO terms regarding the number of genes shared. (PGA-(G-AGM)-(Hyd-Dox)$_{LL}$: P-(Hyd)$_{LL}$,PGA-(G-AGM)-(EMCH-Dox)$_{LL}$: P-(EMCH)$_{LL}$).

Upregulated processes common for PGA-(G-AGM)-(Hyd-Dox)$_{LL}$ and PGA-(G-AGM)-(EMCH-Dox)$_{LL}$ include chemotaxis, positive regulation of interferon-gamma-mediated (IFN-γ) signaling pathway, response to interferon alpha (IFN-α), granzyme (GZMB)-mediated apoptotic signaling pathway, and autophagy of host cells, amongst others (**Fig. 28D**), indicating that treatment induced a shared activation signature related to inflammation, apoptosis induction and autophagy activation.

Interferon signaling pathways (IFN-α and IFN-γ) are involved in immune response, inhibition of cell proliferation, inflammation, immune surveillance and tumor suppression by inducing the transcription of a number of IFN-stimulated genes [41]. Binding of IFN-γ and IFN-α to their respective receptors promotes the activation of PI3K/AKT and JAK/STAT pathways [41, 42], resulting in the synthesis of several pro-apoptotic factors, but also inhibiting the synthesis of anti-apoptotic genes [43]. We also detected the upregulation of the GZMB-mediated pathway, a process that involves T-cell mediated cytotoxicity and perforin (PRF1)-GZMB-dependent killing of the cell through the induction of apoptosis [44], found in our enrichment results. Additionally, we identified the upregulation of autophagy, which is a different type of active programmed cell death [45]. Interestingly, both treatments caused a marked upregulation of T-cell chemotaxis; T-cell trafficking to and increasing the T-cell frequency at the TME is one of the major challenges for adoptive immunotherapy as a new strategy against tumor development and metastasis [46].

Taken together, these upregulated pathways indicate the contribution of different cell death mechanisms, including processes leading to apoptosis and others mediating autophagy, in both PGA-(G-AGM)-(Hyd-Dox)$_{LL}$ and PGA-(G-AGM)-(EMCH-Dox)$_{LL}$ treatments.

Both treatments also provoked the downregulation of processes related to cell proliferation, intercellular signaling and metastasis, blood vessel development (angiogenesis), epithelial-mesenchymal transition (EMT), epithelial cell proliferation involved in mammary gland duct elongation, and positive regulation of protein kinase C (**Figure 28C**).

The link between angiogenesis and EMT is widely accepted, as the same factors that drive endothelial cells toward a pro-angiogenic phenotype may also drive epithelial cells toward a mesenchymal stem cell (MSC) phenotype. Thus, angiogenesis can be accomplished through endothelial sprouting or non-sprouting microvascular growth, similarly to how endothelial cells gain invasive and migratory properties to become MSCs [47]. In this context, EMT and angiogenesis have emerged as integral processes in the promotion of carcinogenesis [48, 49].

Genes related to "epithelial cell proliferation" involved in mammary gland duct elongation also displayed downregulated expression. This GO term includes may genes playing an important role in mammary gland organogenesis and development [50]. The mammary gland epithelium passes through several cycles of proliferation and cell death during pregnancy, lactation, and involution. However, many of the signaling mechanisms that control the initial invasion of the fat pad by the epithelium and regulate its continuing plasticity can be harnessed or corrupted by tumor cells to support their aberrant growth and progression towards invasion [51]. Accordingly, we hypothesize that at least part of the anti-cancer activity of our conjugates might be mediated by the inhibition in the proliferation of mammary gland cells. Additionally, the PGA-(G-AGM)-$(Hyd\text{-}Dox)_{LL}$ and PGA-(G-AGM)-$(EMCH\text{-}Dox)_{LL}$ combination conjugates downregulate the protein kinase C (PKC) pathway, which could imply deactivation of NF-κB signaling [52]. Overexpression of the factor NF-κB is frequently found in cancer and other inflammatory diseases, and a potential inhibition of NF-κB here could be an additional anticancer effect of our combinatorial therapy.

As mentioned, we discovered a total of 67 GO terms (5 downregulated terms and 62 upregulated terms) enriched in a comparison between PGA-(G-AGM)-$(Hyd\text{-}Dox)_{LL}$ and PGA-(G-AGM)-$(EMCH\text{-}Dox)_{LL}$ treated tumors. This indicates a stronger and more general effect of PGA-(G-AGM)-$(Hyd\text{-}Dox)_{LL}$ when treating tumor cells compared to PGA-(G-AGM)-$(EMCH\text{-}Dox)_{LL}$. PGA-(G-AGM)-$(EMCH\text{-}Dox)_{LL}$ involves fewer targeted processes, such as stem cell proliferation and epidermal cell differentiation, indicating a role of this combination conjugate in reducing cancer cell growth (**Figure 28D**). PGA-(G-AGM)-$(Hyd\text{-}Dox)_{LL}$ specifically activates general processes such as defense/immune responses, inflammation, phagocytosis, cell signaling and metastasis

(**Figure 28E**), suggesting that the PGA-(G-AGM)-(Hyd-Dox)$_{LL}$ is more effective in provoking a general immune response that might contribute to fight tumor progression, improve health status of the individual and increase survival rates. In this sense, we observed higher survival rates of mice treated with PGA-(G-AGM)-(Hyd-Dox)$_{LL}$, which corroborates this assumption.

IV.2.5.2. Pathway Analysis Highlights Mechanistic Differences between PGA-(G-AGM)-(Hyd-Dox)$_{LL}$ and PGA-(G-AGM)-(EMCH-Dox)$_{LL}$

We used the PaintOmics 3 tool to create a mechanistic representation of some of the processes involved in the PGA-(G-AGM)-(Hyd-Dox)$_{LL}$ and PGA-(G-AGM)-(EMCH-Dox)$_{LL}$ modes of action. PaintOmics 3 analysis confirmed and expanded GO enrichment results in relation to cell survival/apoptosis (**Figure 29A**) and inflammation, angiogenesis, and metastasis (**Figure 29B**), revealing additional similarities and differences between the two conjugates.

We uncovered evidence of both conjugates inducing apoptosis through the activation of the GZMB) signaling pathway. Indeed, we found strong upregulation of GZMB and PRF1 for both treatments (**Figure 29A**, see first two columns of gene heatmaps); however, we also detected activation of the apoptosis extrinsic pathway, which involves the activation of cell surface death receptors (FAS, TNFR) by extracellular ligands such as FAS-L or TNF, resulting in the cleavage or activation of caspase-8 and a signaling cascade that culminates in cell death [53]. We note the strong upregulating of all these markers for both conjugates (**Figure 29A**). Additionally we demonstrated the differences between the two conjugates in the third column of the gene heatmaps (**Figure 29A**). PGA-(G-AGM)-(Hyd-Dox)$_{LL}$ exhibits consistent activation of typical pro-apoptotic markers such as tubulin alpha 1b (TUBA1B), poly(ADP-Ribose) polymerase 1 (PARP1), beta-actin (ACTB), and myeloid cell leukemia sequence 1 (MCL1) (red in gene heatmaps).

However, PGA-(G-AGM)-(EMCH-Dox)$_{LL}$ more frequently triggers the overexpression of cell survival and anti-apoptotic genes, including as B-cell lymphoma 2 (BCL2), growth arrest and DNA damage-inducible alpha (GADD45A), baculoviral IAP

repeat containing 2 (BIRC2), mouse double minute 2 homolog (MDM2), and TNF receptor-associated factor 1 (TRAF1) (blue in gene heatmaps).

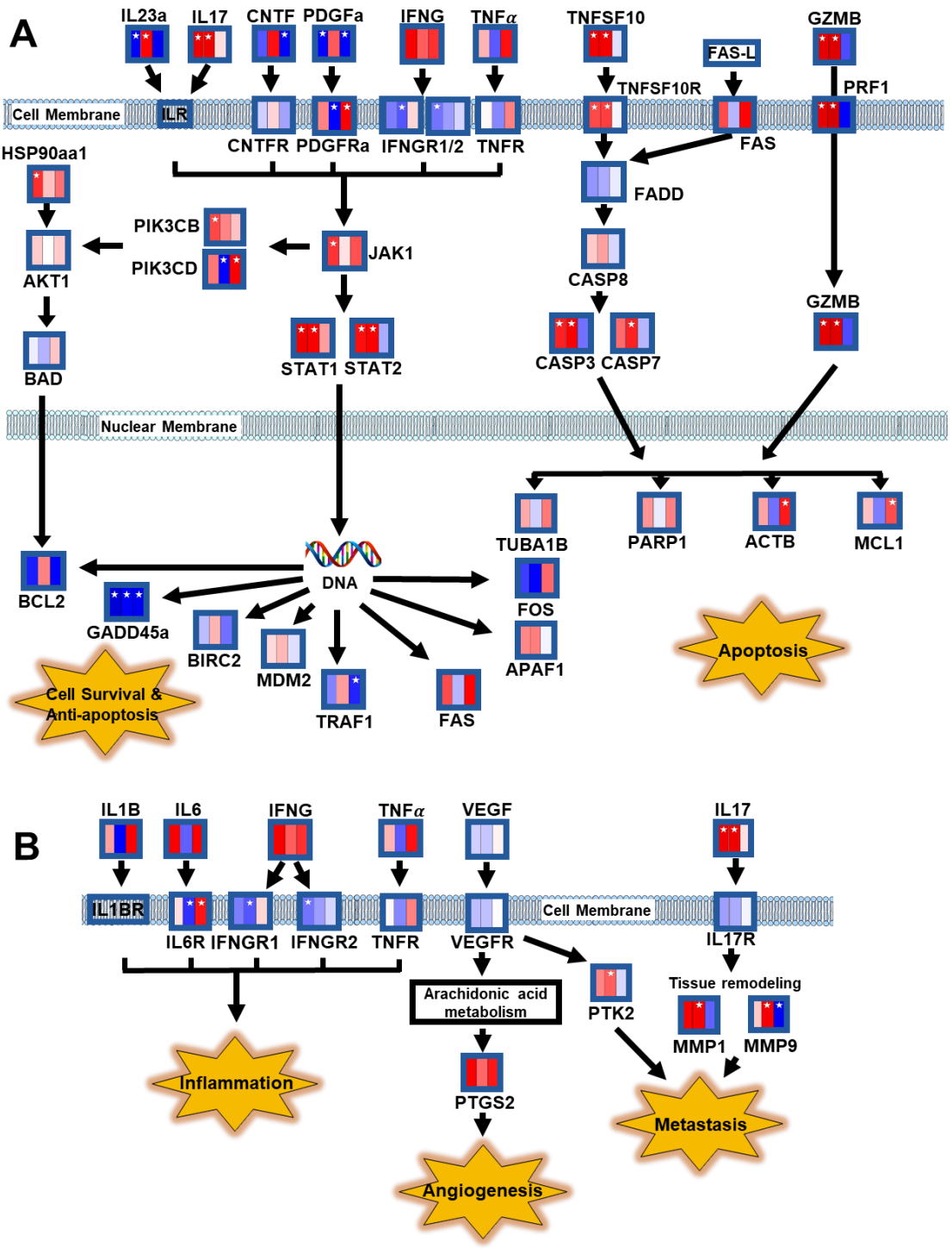

Figure 29. Simplified representation of genes involved in processes affected for the PGA-(G-AGM)-(Hyd-Dox)$_{LL}$ and PGA-(G-AGM)-(EMCH-Dox)$_{LL}$ conjugates. **A)** Processes related to cell survival and apoptosis and **B)** Inflammation, angiogenesis, and metastasis. Genes represented as heat maps: from left to right, log2-fold change values between PGA-(G-AGM)-(Hyd-Dox)$_{LL}$- PBS; PGA-(G-AGM)-(EMCH-Dox)$_{LL}$ – PBS and PGA-(G-AGM)-(Hyd-Dox)$_{LL}$- PGA-(G-AGM)-(EMCH-Dox)$_{LL}$ paired comparisons respectively.

Blue: downregulation in the first treatment of the pair; red: upregulation in the first treatment of the pair; blunt ends: negative relationship; arrowheads: positive relationship; green-background stars: Statistically significant differences between that pair in that gene ($p < 0.01$).

From these observations, we hypothesize that PGA-(G-AGM)-$(Hyd\text{-}Dox)_{LL}$ treatment is not only stronger in provoking apoptosis through upregulation of proapoptotic processes, but also reduces the expression of genes related to cell survival and anti-apoptosis, jointly contributing to a robust apoptotic response.

Pathway enrichment analysis also revealed stronger angiogenesis and inflammation activities for PGA-(G-AGM)-$(Hyd\text{-}Dox)_{LL}$ treatment than for PGA-(G-AGM)-$(EMCH\text{-}Dox)_{LL}$ (**Figure 28D**). Prostaglandin-endoperoxide synthase 2 (PTGS2), a marker of pro-angiogenesis processes [54] that, although overexpressed for both conjugates, exhibited higher levels for PGA-(G-AGM)-$(Hyd\text{-}Dox)_{LL}$ treatment (**Figure 29B**). Similarly, although inflammation was a hallmark of both treatments (**Figure 28B**), selected inflammatory biomarkers such as Interleukin (IL)1B, IL6, Interferon-γ and TNF-α were upregulated following PGA-(G-AGM)-$(Hyd\text{-}Dox)_{LL}$ treatment compared to PGA-(G-AGM)-$(EMCH\text{-}Dox)_{LL}$ (**Figure 29B**), which might mediate the differential inflammatory response between the two conjugates.

Protein tyrosine kinase 2 (PTK2) and the matrix metallopeptidases 1 and 9 (MMP1 and MMP9) displayed higher levels in PGA-(G-AGM)-$(EMCH\text{-}Dox)_{LL}$ treatment (**Figure 29B**), suggesting that these genes might mediate the increased trend for heightened metastatic activity observed in PGA-(G-AGM)-$(EMCH\text{-}Dox)_{LL}$ treated tumors when compared to PGA-(G-AGM)-$(Hyd\text{-}Dox)_{LL}$.

IV.3. Conclusions

Both experimental results and transcriptional analysis indicate that the two most effective conjugates, PGA-(G-AGM)-$(Hyd\text{-}Dox)_{LL}$ and PGA-(G-AGM)-$(EMCH\text{-}Dox)_{LL}$, target the TME to trigger a cascade of molecular events that promote tumor cell death (apoptosis and autophagy) and inhibit tumor-related activities, including metastasis and cell proliferation.

However, we also highlight significant differences between the two combination conjugates: PGA-(G-AGM)-$(Hyd\text{-}Dox)_{LL}$ triggers a more intense immune response that might explain why recipient mice display a higher survival rate. Also, PGA-(G-AGM)-$(Hyd\text{-}Dox)_{LL}$ leads to higher pro-apoptotic activity, lower anti-apoptotic signals, and inhibition of metastasis, which support the overall response to this treatment.

We have also demonstrated the relative importance of targeting the TME for drug release and optimizing the bioavailable drug ratio in a combination therapy, highlighting the importance of a chemical rationale for polymer-drug(s) linker design. Adequate drug release kinetics represents a crucial parameter towards achieving an adequate safety:efficacy ratio and may secure an adequate therapeutic window for future treatments.

Finally, this study also demonstrates the utility of side-by-side transcriptional analysis that serves to understand our results and promote the future design of advanced polymer-based DDS for the treatment of metastatic TNBC among others.

IV.4. Materials and Methods

IV.4.1. Materials

All reagent grade chemicals purchased from Sigma-Aldrich were used without any purification. Poly-(alpha-L-glutamic acid) (Mw: 12900Da, PDI: 1.2, 100 subunits per polymer, PGA_{100u}) was obtained from Polypeptide Therapeutic Solutions SL (Valencia, Spain). Doxorubicin hydrochloride salt was purchased from Xingcheng Chempharm Co. Ltd (Zhejiang, China). Aminoglutethimide was purchased from Sigma-Aldrich. Anhydrous N,N-dimethylformamide (DMF, ≥99.8% anhydrous) was purchased from Scharlab SL (Sentmenat, Spain). MTS reagent was supplied by Promega (Spain). Ultrapure Milli-Q water with a resistance of 18 MΩ.cm was used in all aqueous preparations (Millipore). Preparative size-exclusion chromatography (SEC) was performed using Sephadex® G-25 or Sephadex® LH-20 purchased from GE Healthcare Bio-Sciences AB (Uppsala, Sweden). Tert-butyl-carbazate and N,N-diisopropylethylamine were purchased from Sigma-Aldrich. Dulbecco's Modified

Eagle's Medium (DMEM), phosphate buffer saline (PBS), fetal bovine serum (FBS) medium 200, low serum growth supplement (LSGS), and trypsin were provided from Gibco.

IV.4.2. Synthesis of Single Conjugates

Synthesis of PGA-Hyd-Dox

We employed an optimized protocol derived from a previously described strategy by Van Heeswijk in order to generate PGA-Hyd-Dox conjugates [17].

Synthesis of PGA-NH-NHBoc

PGA (300mg, 2.32 mmol, 1.0 equivalents (eq.), 100 units, Mw~13 KDa) was dissolved in 10 ml of anhydrous DMF in an inert atmosphere with gently stirring. Then, the eq. for the required modification of 4-(4,6-dimethoxy-1,3,5-triazin-2-yl)-4-methyl-morpholinium tetrafluoroborate salt (DMTMM.BF_4) was added (i.e. 15.34 mg, 0.116 mmol, 0.05 eq. for 5% modification) to activate the carboxylic acid of the polymer. After 15 minutes (min), tert-butyl-carbazate (NH_2-NHBoc) (18.38 mg, 0.139 mmol, 0.06 eq. for 5% modification) was added and the pH of the reaction fixed to 8 by dropwise addition of N,N-diisopropylethylamine (DIEA) as a non-nucleophilic base. After 24 hours (h), the solvent was concentrated under reduced pressure and the oily product was isolated by three precipitations over cold diethyl ether. The resulting solid was washed with acidified water (pH~3) to remove traces of DMTMM activated ester. After freeze-drying, 5 mg of the resulting PGA-NH-NHBoc were dissolved in 500 µl of 1.0 M deuterated sodium hydrogen carbonate ($NaDCO_3$) and analyzed by NMR to ensure purity and to calculate the % of modification by ^{1}H-NMR (**Figure 3**).

Synthesis of PGA-NH-NH_2

Deprotection of the primary amine from PGA-NH-NHBoc was carried out by dissolving the resulting solid in trifluoroacetic acid (TFA) and stirring in a round bottom flask at room temperature (RT) for 30 min. The solution was precipitated twice over diethyl ether, washed twice with water, and then freeze-dried. The final % of hydrazine of PGA-HN-NH_2 was determined by TNBSA (trinitrobenzene sulfonic acid) assay (**Figure 30**) and correlated with the previous estimation of Boc loading by ^{1}H-NMR.

Synthesis of PGA-hyd-Dox

Conjugation of Dox through an N-acyl-hydrazone bond was performed by dissolving 200 mg (1.55 mmol, 1.0 eq.) of PGA-NH-NH_2 in 8 ml of anhydrous dimethylsulfoxide (DMSO) in an inert atmosphere with gently stirring. Dox (543.52 g/mol, 1.5 eq. with respect to free –NH_2 groups) was dissolved and 20 µl of glacial acetic acid added dropwise to act as a catalyst. The reaction was allowed to proceed in darkness for 48 h at RT. The solution was then concentrated under reduced pressure and the viscose product precipitated twice over acetone/chloroform (4:1). The removal of unreacted Dox was performed twice by SEC with DMF as the mobile phase using a LH-20 gel. The first eluting fraction, corresponding to the acid form of the final conjugate, was collected and dried under vacuum and the water-soluble sodium salt form of the final product was obtained by dissolving the resulting solid in 0.25M $NaHCO_3$. The last purification step was performed by SEC in Milli-Q water with G-25 resin. The first fraction containing the salt form of the final conjugate was collected and freeze-dried obtaining a red fine powder.

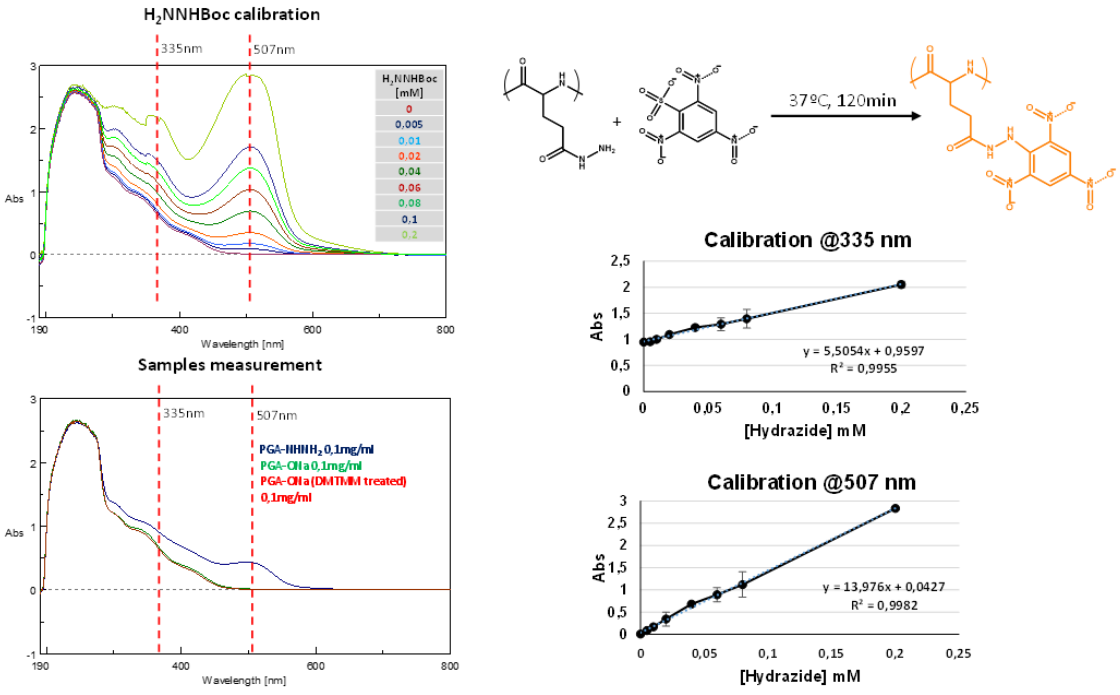

Figure 30. Hydrazine content quantification by 2,4,6-trinitrobenzene sulfonic acid (TNBSA) assay. Representative example.

Synthesis of PGA-(G-AGM)

G-AGM and PGA-(G-AGM) were synthesized and characterized following a previously described protocol [8].

Synthesis of PGA-EMCH-Dox

EMCH-Dox was prepared following a procedure developed by Willner and co-workers [55] including some improvements to increase yield [56]. Final characterization (including ^{1}H-NMR spectrum and matrix-assisted laser desorption/ionization time-of flight (MALDI-TOF) analysis) of all the intermediate products (as well as EMCH-Dox), matched previously described data (**Figures 5-7**).

Synthesis of PGA-Pyridyl disulfide (PD)

PGA (300mg, 2.32 mmol, 1.0 eq., 100 units, Mw~13 KDa) was dissolved in 10 ml of anhydrous DMF in an inert atmosphere with gently stirring. Then, the eq. for the aimed modification of DMTMM.BF_4 was added (i.e. 15.34 mg, 0.116 mmol, 0.05 eq. for 5% modification) to activate the carboxylic acid of the polymer. After 15 min, pyridyl disulfide cysteamine HCl Salt (PD) (30.9 mg, 0.139 mmol, 0.06 eq. for 5% modification) was dissolved and the pH of the reaction was fixed to 8 by the dropwise addition of DIEA. 24h later, the solvent was concentrated under high vacuum and the resultant product was purified by three precipitations over cold diethyl ether. The excess of activated DMTMM ester was removed by two washings with acidic water (pH~3). Once dried, 5 mg of resulting PGA-PD was dissolved in 1M $NaDCO_3$ to ensure purity and to determine the % of modification by ^{1}H-NMR. Additional measurement of PD modification was performed by full reduction of the disulfide and direct spectrophotometric measurement of the pyridine-2-thione released (**Figures 3 and 33**).

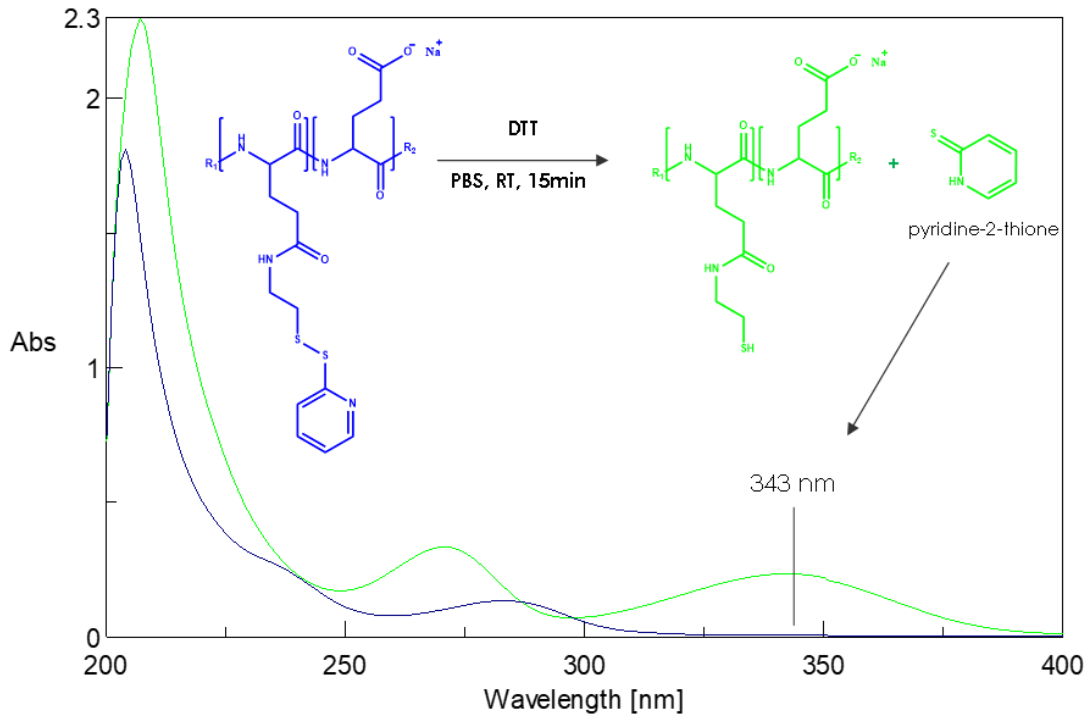

Figure 33. Representative example of indirect measurement of PD content of pyridyl disulfide by complete reduction to pyridine-2-thione

Synthesis of PGA-EMCH-Dox

PGA-PD (1.55 mmol, 1.0 eq) was dissolved in 10 ml of anhydrous DMF in an inert atmosphere. EMCH-Dox (750.76 g/mol, 1.5 eq. with respect to PD modification) was added to the solution and the reaction was initiated by the addition of tris(2-carboxyethyl)phosphine (TCEP) (0.15 eq. with respect to the PD modification) as a reducing agent. The reaction was allowed to proceed for 48 h in the dark at RT. After this step, the solvent was evaporated under reduced pressure and the resulting viscose product was purified and analyzed by the same procedure previously described for the conjugate PGA-hyd-Dox.

IV.4.3. Synthesis of Combination Conjugates

Synthesis of PGA-(G-AGM)-Hyd-Dox

We employed an optimized protocol derived from a previously described strategy by Van Heeswijk in order to generate PGA-Hyd-Dox conjugates [17]. Hydrazone-based combination conjugates were synthesized by one-pot direct attachment of G-AGM and

tert-butyl-carbazate. Further Boc deprotection of the amino-group allowed final Dox coupling. PGA (300 mg, 2.32 mmol, 1.0 eq., 100 units, Mw ~13 KDa) was dissolved in 10 ml of anhydrous DMF in an inert atmosphere. DMTMM.BF_4 (0.3 eq.) was added to the solution and 15 min later G-AGM (0.164 mmol, 58.2 mg) and tert-butyl-carbazate (18.38 mg, 0.139 mmol, 0.06 eq. for 5% modification) were added. The reaction proceeded for 48 h and the workup was performed as already described procedure for the workup of PGA-NH-NHBoc. Once the stability of G-AGM in TFA was ensured (**Figure 34**), Boc release was performed as for the synthesis of PGA-NH-NH_2 (see section 2.3.1.2) and Dox was coupled through a hydrazone bond following the same procedure as for the synthesis of PGA-hyd-Dox.

Synthesis of PGA-(G-AGM)-EMCH-Dox

EMCH-Dox-based combination conjugates were synthesized by one-pot direct attachment of G-AGM and PD and further EMCH-Dox coupling through the reduction of PD. PGA (300mg, 2.32 mmol, 1.0 eq., 100 units, Mw~13 KDa) was dissolved in 10 ml of anhydrous DMF in an inert atmosphere. DMTMM.BF_4 (i.e. 15.34 mg, 0.116 mmol, 0.05 eq. for 5% modification) was added to the solution and 15 min later G-AGM (0.164 mmol, 58.2 mg) and PD (30.9 mg, 0.139 mmol, 0.06 eq. for 5% modification) were added. The reaction proceeded for 48 h and the workup was performed as for the PGA-NH-NHBoc. An aliquot was isolated for G-AGM and PD loading determination. For EMCH-Dox attachment, PGA-(G-AGM)-PD was dissolved in anhydrous DMF and EMCH-Dox (750.76 g/mol, 1.5 eq. with respect to PD modification) was dissolved and TCEP (0.15 eq. with respect to the PD modification) was finally added as reducing agent. Boc release was performed as for the synthesis of PGA-NH-NH_2 and Dox was coupled through a hydrazone bond following the same procedure as for the synthesis of PGA-hyd-Dox.

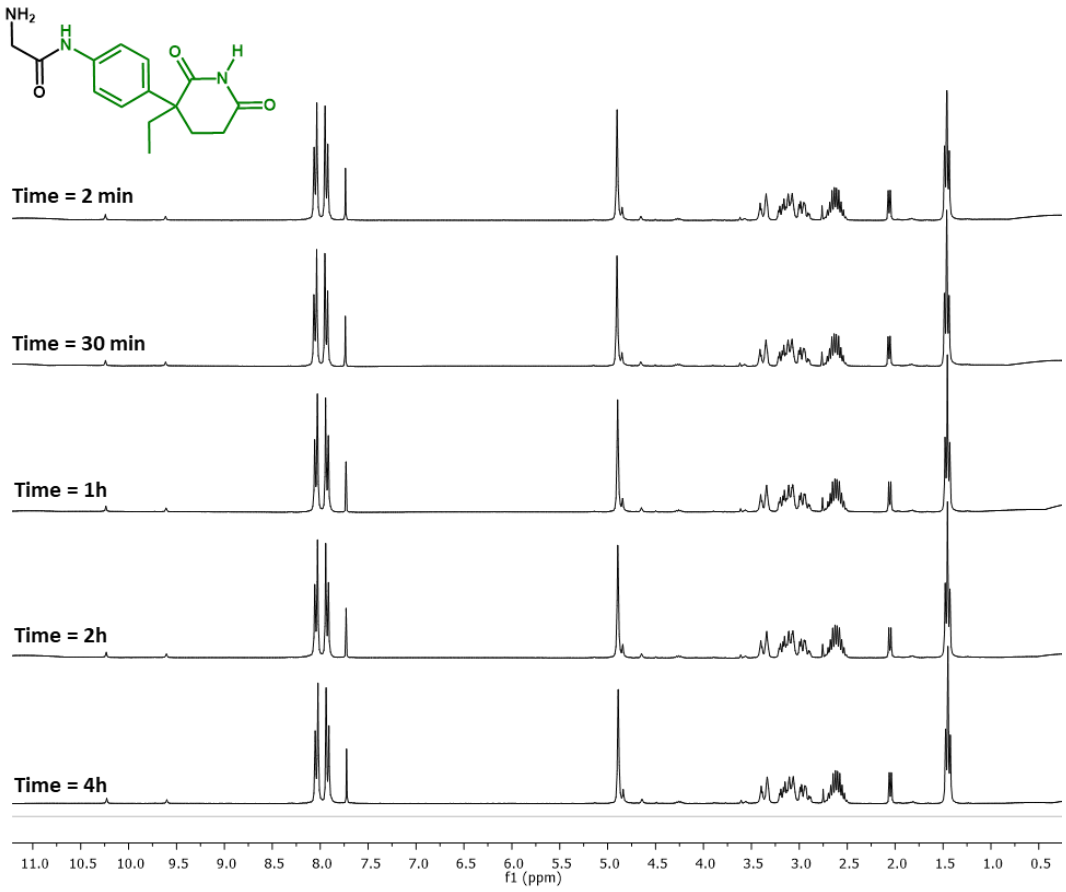

Figure 34. 1H-NMR proof of stability of G-AGM under TFA conditions for 4h.

IV.4.4. Physico-chemical Characterization

Quantification of Drug Loading

AGM loading in single conjugates was determined by UV and ^{1}H-NMR analyses. In the case of combination conjugates, AGM was quantified prior to the incorporation of Dox by the same procedure. A small aliquot of the final PGA-(G-AGM) or the precursors PGA-(G-AGM)-NH-NHBoc / PGA-(G-AGM)-PD were isolated, converted into salt form as described before, and purified. Samples were split and AGM loading was determined either by ^{1}H-NMR or UV-VIS spectrophotometry. For NMR quantification, 500 □l of 10 mg/ml solution in D_2O of each conjugate were prepared and protons from aromatic signals and from the methylene group allowed quantification. For UV quantification, a calibration curve of G-AGM in DMSO 50% (v/v) was performed with dilutions ranging from 0.05 to 0.065 mg/ml, measuring the absorbance at 246 nm using a JASCO V-630 spectrophotometer. Three aliquots of 0.1, 0.25, and 0.5 mg/ml of each

conjugate were prepared and the AGM loading was calculated from the absorbance and the calibration curve.

Dox loading in both single and combination conjugates was determined by measuring the absorbance of three aliquots of the conjugate (0.1, 0.25, and 0.5 mg/ml) in DMSO 50% (v/v) (λ = 480 nm) and by the use of molar absorbance of Dox in this solvent (20.280 L $mol^{-1}cm^{-1}$).

Identity and purity confirmation by 1H-NMR

NMR spectra were recorded at 27°C (300K) on an Advance III 500MHz Bruker spectrometer equipped with a 5mm TBI broadband probe or a 300 Ultrashield^{TM} from Bruker (Billerica MA, USA). Data were processed with the software Mestrenova (Bruker GmbH, Karlsruhe, Germany). Samples were prepared at the desired concentration in D_2O.

Uniformity and Mw distribution by Analytical Size Exclusion Chromatography (SEC)

SEC measurements were performed using PBS as mobile phase in an AF2000 system from Postnova Analytics. The system was configured to work on SEC mode with an isocratic pump (PN1130) an autosampler (PN5300), and a refractive index (RI, PN3150) detector. A flow rate of 0.7 mL/min at 30°C was employed with one TSKgel G3000PWXL (Tosoh) column.

Size measurements by Dynamic Light Scattering (DLS)

DLS measurements were performed using a Malvern ZetaSizer NanoZS instrument with a 633 nm laser at a fixed emission angle of 173°. Conjugate solutions in PBS were sonicated until complete dissolution, filtered through a 0.45 µm cellulose membrane filter, and allowed to stabilize for 10-15 min prior to measurement. Size distribution was determined for each conjugate in triplicate. Automatic optimization of beam focusing and attenuation was applied for each sample. Each solution was analyzed 6-8 times depending on the correlogram quality. Unless stated, the term size refers to hydrodynamic diameter (Dh).

IV.4.5. Cell Culture and In vitro Cytotoxicity Analysis of Conjugate

The 4T1 cell line was maintained in RPMI supplemented with 10% heat inactivated FBS at 37ºC in a controlled atmosphere of air / CO_2 (95/5 vol./vol.). Media was replaced every 48 - 72 hours and underwent passaging when 80% cell confluence was reached. Cytotoxic assays were performed according to a previously described protocol [8]. In brief, cells were seeded in sterile 96-well microtiter plates at concentration of 6,250 cells/cm^2. Plates were incubated for 24 h and then solutions of free drugs and conjugates were tested at final concentrations ranging from 0 to 0.1 mg/ml of drug equivalents. After 72 h of treatment, cell viability was determined suing a Cell Titer 96 Aqueous non-radioactive cell proliferation assay accordingly to manufacturer's guidance. The optical density of each well was measured at 490 nm in a Wallac 1420 spectrophotometer. Cell viability was expressed as a percentage of the viability of untreated cells established as control.

IV.4.5.1. pH-dependent Drug Release

Specific Dox release under mild acidic conditions was demonstrated *in vitro* by liquid-liquid extraction and further quantification by reversed-phase high-performance liquid chromatography (RP-HPLC). The conjugates were incubated in 50 mM PBS at pH 7.4 and pH 5.0, mimicking the blood and tumor (and/or lysosomal) environment respectively. At determined time points, 100 µl aliquots were made up to 1 ml with phosphate buffer pH 7.4 in a 15 ml tube. Then, 5 ml of $CHCl_3$ was added and the mixture was vortexed for 60 seconds (s). The aqueous phase was removed and the organic phase was evaporated using a Speedvac concentrator. The resulting pellet was dissolved in 200 µl MeOH HPLC-grade and 20µl aliquots were analyzed by RP-HPLC (Mobile phase: formate buffer pH 3.5 / Acetonitrile, 69:31 v/v, flow rate: 1.0 ml/min, diode array detector: 480nm, fluorescence detector: λ_{ex} = 480nm, λ_{em} = 565 nm). A calibration curve was performed by successive analysis of samples ranging from 0.005 to 0.065 mg/ml of pure Dox in MeOH under the same experimental conditions. Retention time of Dox was found to be 4.4 min.

IV.4.5.2. Cathepsin B-dependent Drug Release Kinetics

Cathepsin B (5 U) was added to a solution of 2 mg of each conjugate, in 1 mL of a pH 6 buffer composed of 20 mM sodium acetate, 2 mM ethylenediaminetetraacetic acid (EDTA), and 5 mM dithiothreitol (DTT). The incubation was carried out at 37°C. Aliquots (100 μl) were taken at times up to 48 h, immediately frozen in liquid nitrogen, and stored in the dark until assayed by HPLC as described above for pH-dependent drug release assay. The free drug (0.75 mg/mL) was also incubated under same conditions and later used as the reference control.

IV.4.6. Establishment of Highly Metastatic 4T1 murine Breast Cancer Model and in vivo Validation of Conjugates

6-8 week old female BALB/c mice used for all experimental procedures were purchased from Envigo Laboratories Inc. (Spain, EU). 4T1 orthotopic tumors were induced by the subdermal inoculation of 5×10^5 4T1 early passage cells suspended in 100 μl of sterile Matrigel™ in the second left mammary fat pad of females under inhalatory anesthesia (3% sevoflurane in 100% oxygen). Tumors were morphometrically evaluated daily with an electronic caliper and tumor volumes were obtained by considering tumor shape as spheroids [8, 10].

IV.4.6.1. *In vivo* study at 10 mg/Kg Dox-equivalent dose

Eight days before induction, tumor sizes reached 0.1 cm^3 and mice were split into representative groups. Conjugate-based treatments were dissolved in sterile PBS and immediately injected intravenously (i.v.) in four doses of 10 mg/Kg of Dox equivalents every three days. Free Dox was dissolved in saline and administered at 5 mg/Kg as control, following the same schedule. Tumors were measured daily with a digital caliper before every treatment and daily after the last dose with tumor volumes calculated considering spherical growth by applying the formula: 4/3 x Π x (height /2 x length / 2 x width /2). When tumors of untreated animals reached 1.0 cm^3 or 24 days after cells

implantation, mice were sacrificed using a CO_2 atmosphere and major organs, tumors, and blood were extracted for further analysis.

IV.4.6.2. Hematological Study

Blood was extracted immediately after sacrificing mice by cardiac puncture with a 1.0 ml heparinized syringe and transferred to a 2 ml Eppendorf tube. Blood was gently homogenized and left to reach RT and then kept at 4 ºC until analysis (within the first 30 min after extraction). Serum was isolated by centrifugation (4000 rpm, 10 min, 4 ºC) and analyzed using an automated hematologic analyzer (Sysmex XT-2000i).

IV.4.6.3. Histopathological Study

All tissues were washed in fresh PBS, carefully dried, weighed, and fixed in paraformaldehyde (PFA) at room temperature for 24 h. PFA was eliminated by successive washing with PBS (5 times x 20 min, rapid agitation). Once washed, tissues were stored in a solution of PBS with 0.05% of sodium azide as preservant at 4 ºC protected from light. Bone marrow samples were derived from femurs decalcified by immersion in Osteodec (BioOptica) for 8 h. A common dehydration and paraffin-inclusion procedure was carried out [10] leading to blocks that were sliced into 3-µm sections. Hematoxylin-Eosin staining [10] and immunostaining were performed as required and the slides were assembled with Eukitt. Tissue slides were observed under the microscope and those of interest were scanned with a Panoramic 250 Flash III slide scanner and processed with CaseViewer software (both from 3DHISTECH Ltd, Budapest, Hungary).

IV.4.6.4. Safety Evaluation of Treatments

Treatments safety was evaluated by tracking body weight and comparisons with control and healthy animals, as well as further histopathological studies of key organs. The mice under study were examined daily in the search for any pain-related behavior or

conduct modification. Postmortem, major organs were also analyzed histopathologically for any treatment-derived damage.

IV.4.6.5. Tumor Density

Tumor density was obtained by simple arithmetic calculation and allowed us to elucidate differential stromal arrangement due to the different treatments.

IV.4.7. Evaluation of the Antimetastatic Effect of Conjugates in the Lung

Lung metastasis was evaluated following a previously described protocol [57] with several improvements. Lungs were removed immediately after animal sacrifice and washed in PBS. Tissues were then transferred to a P-6 plate previously filled with 3 ml of cold Hank's Balanced Salt Solution 1X (HBSS - Gibco) and washed twice. Over a new empty P-6 plate, organs were mixed with surgical scissors for 2 min and 2.5 ml of cold collagenase Type IV (Gibco 17104-019) was added to each well. The tissue mixture was transferred into a 15 ml falcon tube and incubated at 4°C for 90 min in a rotatory shaker at maximum speed. Once the digestion was finished, the largest tissue pieces were broken down and the final mixture was filtered by gravity through a 70□m nylon filter (Fisher). The filtered suspension was collected by adding 5 ml of HBSS 1X in the falcon and then centrifuged at 1,500 rpm (10°C, 5 min). Supernatant was removed and the pellet was washed twice with 10 ml of HBSS and the pellet was then suspended in 10 mL of medium (RPMI1640 + 10% FBS + penicillin/streptomycin + fungizone) and seeded in P-6 plates (1.4 ml each). The cells were incubated at 37ºC under 5% CO_2 allowing uniform growth.

After 5 days, every well was washed 3 times with PBS. 6-thioguanine resistant-cells adhered to the plate and other cells could be easily removed. 2 mL of fresh medium and 2 μl 6-thioguanine were added back and incubation was allowed to continue.

Eleven days after seeding, cells were washed twice with PBS, trypsinized (700 μl of trypsin), and resuspended in 800 μl of medium. Finally, cells were counted with trypan blue in a dilution according with the degree of confluency.

IV.4.7.1. Extraction of RNA from Frozen Tumors and Sequencing

Total RNA isolation was performed from 50 mg of previously pulverized frozen tumor employing the PureLink RNA Mini kit (Ambion-Life Technologies) following manufacturer's recommendations. The On-column PureLink DNase Kit (Invitrogen) was used to purify the DNA-free RNA. The qualification and integrity of total RNA was performed with an Agilent Technologies 2100 Bioanalyzer (or 4200 Tape Station). TruSeq Stranded mRNA libraries were constructed and sequenced at Macrogen (Seoul, Korea) using an Illumina HiSeq4000 platform (paired-end with a length of 100 bp).

IV.4.7.2. Mapping and Quantification

Raw paired-end sequences were mapped against the mouse reference genome with STAR aligner software [58]. There was no need to trim or filter due to the high quality of the samples, checked with FastQC tool (URL: https://www.bioinformatics.babraham.ac.uk/projects/fastqc/). The mapping step was completed with a mean of an 88% of uniquely mapped reads. The quantification of the transcripts was performed with RSEM software [59].

IV.4.7.3. RNA-seq Data Analysis

Low count genes in RNA-seq count data were filtered with NOISeq package [60] and kept for the statistical analysis the 14,323 genes having an average of more than one read count per million reads in any of the four experimental groups. The resulting count matrix was normalized by the sequencing depth to make samples comparable. Data were transformed with the Voom approach [61] to get a normal distribution. The limma R package [62], which is based on linear models, was used to obtain the differentially expressed genes among experimental groups. We performed 5 different comparisons: PGA-(G-AGM)-(EMCH-Dox)$_{LL}$, PGA-(G-AGM)-(Hyd-Dox)$_{LL}$ and PGA-(G-AGM)-(Hyd-Dox)$_{HL}$ *versus* PBS (control), PGA-(G-AGM)-(Hyd-Dox)$_{LL}$ *versus* PGA-(G-AGM)-(Hyd-Dox)$_{HL}$, and PGA-(G-AGM)-(Hyd-Dox)$_{LL}$ *versus* PGA-(G-AGM)-(EMCH-Dox)$_{LL}$. For each comparison, genes with a false-detection rate (FDR) adjusted

p-value [63] lower than 0.05 and an absolute log fold-change value higher than 0.5 were declared as differentially expressed.

IV.4.7.4. Functional Analysis

Gene Ontology functional enrichment analysis using the Fisher's exact test was performed for genes selected (nominal p-value <0.01) at each of the above comparisons. Additionally, the log2-fold change at each pair wise comparison was calculated and exported to PaintOmics 3 [64] for KEGG pathway analysis. KEGG pathways were manually edited to improve interpretation of functional analysis results.

IV.5. References

[1] Wang M, Zhao J, Zhang L, Wei F, Lian Y, Wu Y, et al. Role of tumor microenvironment in tumorigenesis. J Cancer. Sydney2017. p. 761-73.

[2] Feng L, Ziliang D, Danlei T, Yicheng Z, Zhuang L. The acidic tumor microenvironment: a target for smart cancer nano-theranostics. National Science Review. 2018;5:269-86.

[3] Maeda H. Tumor-Selective Delivery of Macromolecular Drugs via the EPR Effect: Background and Future Prospects. Bioconjugate Chemistry. 2010;21:797-802.

[4] Maeda H, Tsukigawa K, Fang J. A Retrospective 30 Years After Discovery of the Enhanced Permeability and Retention Effect of Solid Tumors: Next-Generation Chemotherapeutics and Photodynamic Therapy--Problems, Solutions, and Prospects. Microcirculation (New York, NY : 1994). 2016;23:173-82.

[5] Ojha T, Pathak V, Shi Y, Hennink WE, Moonen CTW, Storm G, et al. Pharmacological and physical vessel modulation strategies to improve EPR-mediated drug targeting to tumors. Advanced drug delivery reviews. 2017;119:44-60.

[6] Kou L, Sun J, Zhai Y, He Z. The endocytosis and intracellular fate of nanomedicines: Implication for rational design. Asian Journal of Pharmaceutical Sciences. 2013;8:1-10.

[7] Johnson DE, Ostrowski P, Jaumouillé V, Grinstein S. The position of lysosomes within the cell determines their luminal pH. The Journal of Cell Biology. 2016;212:677-92.

[8] Arroyo-Crespo JJ, Deladriere C, Nebot VJ, Charbonnier D, Masiá E, Paul A, et al. Anticancer Activity Driven by Drug Linker Modification in a Polyglutamic Acid-Based Combination-Drug Conjugate. Advanced Functional Materials. 2018;28:1800931.

[9] Paul A, Vicent MJ, Duncan R. Using Small-Angle Neutron Scattering to Study the Solution Conformation of N-(2-Hydroxypropyl)methacrylamide Copolymer−Doxorubicin Conjugates. Biomacromolecules. 2007;8:1573-9.

[10] Arroyo-Crespo JJ, Armiñan A, Charbonnier D, Forteza J, Palomino-Schatzlein M, Pineda-Lucena A, et al. Triple-negative Breast Cancer Preclinical Models Provide Functional Evidence of Metastatic Progression and Suitability for Nanomedicine Evaluation Cancer Research. 2018;Under Review.

[11] Zhong Y, Zhao J, Gu Yj, Zhao Y-f, Zhou Y-w, Fu G-X. Differential levels of cathepsin B and L in serum between young and aged healthy people and their association with matrix metalloproteinase 2. Archives of Gerontology and Geriatrics. 2015;61:285-8.
[12] Atkinson S, Andreu Z, Vicent M. Polymer Therapeutics: Biomarkers and New Approaches for Personalized Cancer Treatment. Journal of Personalized Medicine. 2018;8:6.
[13] Chipman SD, Oldham FB, Pezzoni G, Singer JW. Biological and clinical characterization of paclitaxel poliglumex (PPX, CT-2103), a macromolecular polymer-drug conjugate. International journal of nanomedicine. 2006;1:375-83.
[14] Yu T, Di G. Role of tumor microenvironment in triple-negative breast cancer and its prognostic significance. Chinese journal of cancer research = Chung-kuo yen cheng yen chiu. 2017;29:237-52.
[15] Xie HY, Shao ZM, Li DQ. Tumor microenvironment: driving forces and potential therapeutic targets for breast cancer metastasis. Chinese journal of cancer. 2017;36:36.
[16] Kabanov AV. Polymer genomics: An insight into pharmacology and toxicology of nanomedicines. Advanced Drug Delivery Reviews. 2006;58:1597-621.
[17] van Heeswijk WAR, Stoffer T, Eenink MJD, Potman W, van der Vijgh WJF, v.d. Poort J, et al. Synthesis, Characterization and Antitumor Activity of Macromolecular Prodrugs of Adriamycin. In: Anderson JM, Kim SW, editors. Recent Advances in Drug Delivery Systems. Boston, MA: Springer US; 1984. p. 77-100.
[18] Walker L, Perkins E, Kratz F, Raucher D. Cell penetrating peptides fused to a thermally targeted biopolymer drug carrier improve the delivery and antitumor efficacy of an acid-sensitive doxorubicin derivative. International journal of pharmaceutics. 2012;436:825-32.
[19] Markovsky E, Baabur-Cohen H, Satchi-Fainaro R. Anticancer polymeric nanomedicine bearing synergistic drug combination is superior to a mixture of individually-conjugated drugs. Journal of controlled release : official journal of the Controlled Release Society. 2014;187:145-57.
[20] Patterson JP, Robin MP, Chassenieux C, Colombani O, O'Reilly RK. The analysis of solution self-assembled polymeric nanomaterials. Chemical Society Reviews. 2014;43:2412-25.
[21] Duro-Castano A, Nebot VJ, Nino-Pariente A, Arminan A, Arroyo-Crespo JJ, Paul A, et al. Capturing "Extraordinary" Soft-Assembled Charge-Like Polypeptides as a Strategy for Nanocarrier Design. Advanced materials. 2017;29.
[22] Dionzou M, Morere A, Roux C, Lonetti B, Marty JD, Mingotaud C, et al. Comparison of methods for the fabrication and the characterization of polymer self-assemblies: what are the important parameters? Soft matter. 2016;12:2166-76.
[23] Vicent MJ, Greco F, Nicholson RI, Paul A, Griffiths PC, Duncan R. Polymer therapeutics designed for a combination therapy of hormone-dependent cancer. Angewandte Chemie. 2005;44:4061-6.
[24] DuPre SA, Redelman D, Hunter KW, Jr. The mouse mammary carcinoma 4T1: characterization of the cellular landscape of primary tumours and metastatic tumour foci. International journal of experimental pathology. 2007;88:351-60.
[25] Arminan A, Palomino-Schatzlein M, Deladriere C, Arroyo-Crespo JJ, Vicente-Ruiz S, Vicent MJ, et al. Metabolomics facilitates the discrimination of the specific anti-cancer effects of free- and polymer-conjugated doxorubicin in breast cancer models. Biomaterials. 2018;162:144-53.
[26] Lupertz R, Watjen W, Kahl R, Chovolou Y. Dose- and time-dependent effects of doxorubicin on cytotoxicity, cell cycle and apoptotic cell death in human colon cancer cells. Toxicology. 2010;271:115-21.
[27] Bar-On O, Shapira M, Hershko DD. Differential effects of doxorubicin treatment on cell cycle arrest and Skp2 expression in breast cancer cells. Anti-cancer drugs. 2007;18:1113-21.
[28] Peixoto RC, Miranda-Vilela AL, de Souza Filho J, Carneiro ML, Oliveira RG, da Silva MO, et al. Antitumor effect of free rhodium (II) citrate and rhodium (II) citrate-loaded maghemite nanoparticles on mice bearing breast cancer: a systemic toxicity assay. Tumour biology : the

journal of the International Society for Oncodevelopmental Biology and Medicine. 2015;36:3325-36.
[29] Zhou M, Ku G, Pageon L, Li C. Theranostic probe for simultaneous in vivo photoacoustic imaging and confined photothermolysis by pulsed laser at 1064 nm in 4T1 breast cancer model. Nanoscale. 2014;6:15228-35.
[30] Caruso RA, Branca G, Fedele F, Irato E, Finocchiaro G, Parisi A, et al. Mechanisms of coagulative necrosis in malignant epithelial tumors (Review). Oncology letters. 2014;8:1397-402.
[31] Chawla SP, Cranmer LD, Tine BAV, Reed DR, Okuno SH, Butrynski JE, et al. Phase II Study of the Safety and Antitumor Activity of the Hypoxia-Activated Prodrug TH-302 in Combination With Doxorubicin in Patients With Advanced Soft Tissue Sarcoma. Journal of Clinical Oncology. 2014;32:3299-306.
[32] Shivakumar P, Rani MU, Reddy AG, Anjaneyulu Y. A study on the toxic effects of Doxorubicin on the histology of certain organs. Toxicology international. 2012;19:241-4.
[33] Tacar O, Sriamornsak P, Dass CR. Doxorubicin: an update on anticancer molecular action, toxicity and novel drug delivery systems. The Journal of pharmacy and pharmacology. 2013;65:157-70.
[34] Alves AC, Magarkar A, Horta M, Lima J, Bunker A, Nunes C, et al. Influence of doxorubicin on model cell membrane properties: insights from in vitro and in silico studies. Scientific reports. 2017;7:6343.
[35] Thorn CF, Oshiro C, Marsh S, Hernandez-Boussard T, McLeod H, Klein TE, et al. Doxorubicin pathways: pharmacodynamics and adverse effects. Pharmacogenetics and genomics. 2011;21:440-6.
[36] Hrelia S, Fiorentini D, Maraldi T, Angeloni C, Bordoni A, Biagi PL, et al. Doxorubicin induces early lipid peroxidation associated with changes in glucose transport in cultured cardiomyocytes. Biochimica et biophysica acta. 2002;1567:150-6.
[37] Gao D, Du J, Cong L, Liu Q. Risk Factors for Initial Lung Metastasis from Breast Invasive Ductal Carcinoma in Stages I–III of Operable Patients. Japanese Journal of Clinical Oncology. 2009;39:97-104.
[38] Liu M, Jin X, He X, Pan L, Zhang X, Zhao Y. Macrophages support splenic erythropoiesis in 4T1 tumor-bearing mice. PloS one. 2015;10:e0121921.
[39] DuPre SA, Hunter KW, Jr. Murine mammary carcinoma 4T1 induces a leukemoid reaction with splenomegaly: association with tumor-derived growth factors. Experimental and molecular pathology. 2007;82:12-24.
[40] Perry JL, Reuter KG, Luft JC, Pecot CV, Zamboni W, DeSimone JM. Mediating Passive Tumor Accumulation through Particle Size, Tumor Type, and Location. Nano letters. 2017;17:2879-86.
[41] Platanias LC. Mechanisms of type-I- and type-II-interferon-mediated signalling. Nature reviews Immunology. 2005;5:375-86.
[42] de Weerd NA, Samarajiwa SA, Hertzog PJ. Type I interferon receptors: biochemistry and biological functions. The Journal of biological chemistry. 2007;282:20053-7.
[43] Arellano G, Ottum PA, Reyes LI, Burgos PI, Naves R. Stage-Specific Role of Interferon-Gamma in Experimental Autoimmune Encephalomyelitis and Multiple Sclerosis. Frontiers in immunology. 2015;6:492.
[44] Elmore S. Apoptosis: a review of programmed cell death. Toxicologic pathology. 2007;35:495-516.
[45] Yin Z, Pascual C, Klionsky DJ. Autophagy: machinery and regulation. Microbial cell. 2016;3:588-96.
[46] Slaney CY, Kershaw MH, Darcy PK. Trafficking of T Cells into Tumors. Cancer Research. 2014;74:7168-74.
[47] Ribatti D. Epithelial-mesenchymal transition in morphogenesis, cancer progression and angiogenesis. Experimental cell research. 2017;353:1-5.

[48] Sanchez-Garcia I. The crossroads of oncogenesis and metastasis. The New England journal of medicine. 2009;360:297-9.
[49] Holderfield MT, Hughes CCW. Crosstalk Between Vascular Endothelial Growth Factor, Notch, and Transforming Growth Factor-β in Vascular Morphogenesis. Circulation Research. 2008;102:637-52.
[50] Montévil M, Speroni L, Sonnenschein C, Soto AM. Modeling mammary organogenesis from biological first principles: Cells and their physical constraints. Progress in Biophysics and Molecular Biology. 2016;122:58-69.
[51] Lanigan F, O'Connor D, Martin F, Gallagher WM. Common Molecular Mechanisms of Mammary Gland Development and Breast Cancer. Cellular and Molecular Life Sciences. 2007;64:3159-84.
[52] Garg A, Aggarwal BB. Nuclear transcription factor-kappaB as a target for cancer drug development. Leukemia. 2002;16:1053-68.
[53] Strasser A, O'Connor L, Dixit VM. Apoptosis signaling. Annual review of biochemistry. 2000;69:217-45.
[54] Balzano L, Diez N. Mecanismos asociados a la agresividad tumoral y su empleo para diagnosticar este fenómeno. RET Revista de Estudios Transdisciplinarios. 2010;2:77-86.
[55] Willner D, Trail PA, Hofstead SJ, King HD, Lasch SJ, Braslawsky GR, et al. (6-Maleimidocaproyl)hydrazone of doxorubicin. A new derivative for the preparation of immunoconjugates of doxorubicin. Bioconjugate Chemistry. 1993;4:521-7.
[56] Cai T, Chen Y, Wang Y, Wang H, Liu X, Jin Q, et al. Functional 2-methylene-1,3-dioxepane terpolymer: a versatile platform to construct biodegradable polymeric prodrugs for intracellular drug delivery. Polymer Chemistry. 2014;5:4061-8.
[57] Pulaski BA, Ostrand-Rosenberg S. Mouse 4T1 breast tumor model. Current protocols in immunology. 2001;Chapter 20:Unit 20 2.
[58] Dobin A, Davis CA, Schlesinger F, Drenkow J, Zaleski C, Jha S, et al. STAR: ultrafast universal RNA-seq aligner. Bioinformatics. 2013;29:15-21.
[59] Li B, Dewey CN. RSEM: accurate transcript quantification from RNA-Seq data with or without a reference genome. BMC Bioinformatics. 2011;12:323.
[60] Tarazona S, Furió-Tarí P, Turrà D, Pietro AD, Nueda MJ, Ferrer A, et al. Data quality aware analysis of differential expression in RNA-seq with NOISeq R/Bioc package. Nucleic Acids Research. 2015;43:e140-e.
[61] Law CW, Chen Y, Shi W, Smyth GK. voom: precision weights unlock linear model analysis tools for RNA-seq read counts. Genome Biology. 2014;15:R29.
[62] Smyth GK. Linear models and empirical bayes methods for assessing differential expression in microarray experiments. Statistical applications in genetics and molecular biology. 2004;3:Article3.
[63] Benjamini Y, Hochberg Y. Controlling the False Discovery Rate: A Practical and Powerful Approach to Multiple Testing. Journal of the Royal Statistical Society Series B (Methodological). 1995;57:289-300.
[64] Hernandez-de-Diego R, Tarazona S, Martinez-Mira C, Balzano-Nogueira L, Furio-Tari P, Pappas GJ, Jr., et al. PaintOmics 3: a web resource for the pathway analysis and visualization of multi-omics data. Nucleic acids research. 2018.

CHAPTER V

RATIONALLY DESIGNED PGA-BASED COMBINATION CONJUGATES OF SMALL MOLECULE INHIBITORS OF TYROSINE KINASE AND TOPOISOMERASE FOR THE TREATMENT OF METASTATIC TNBC

The experimental basis and research presented in this Thesis chapter correspond to a project nearing full development in the laboratory. Given the novelty, patentability, and robust antitumor and antimetastatic activities of one of the developed combination conjugates, we have protected some of the proceeding data.

To this end, we have purposely omitted certain parts of the materials and methods, citations, chemical entities, drug structures and NMR assignations. Furthermore, some parts of the physicochemical characterization of the drug precursors and the final conjugates have been purposely removed to protect the identity of both drugs and the chemical modifications employed for the combination conjugates.

We have purposely omitted the names of the two drugs involved in this study; these drugs are a Tyrosine-Kinase Inhibitor and a Topoisomerase Inhibitor. Therefore, we used the acronyms “TKI” and “TI” to refer both drugs, respectively, throughout.

Despite this fact, we hope that the information provided will suffice for a complete understanding of the research rationale. Even given the relative incompleteness of our data, our initial findings encouraged us to present the research in its current state.

V.1. Antecedents and Background

As already stated in previous Chapters, the primary complication in the treatment of TNBC results from a lack of expression of the ER, PR, and HER2 hormonal receptors that impedes the administration of targeted therapies [1]. Owing to intrinsic characteristics such as extensive clinical heterogeneity, high metastatic capacity, rapid growth rates, and high risk of early relapse, monotherapies based on chemotherapy (topoisomerase inhibitors or TIs, in particular) represent the first line treatment for this aggressive breast cancer subtype [2].

Importantly, several studies have revealed low antitumor responses with single agents-based treatments, including chemotherapeutics, epigenetic treatments, or immunotherapies in most of TNBC subtypes. However, the co-administration of chemotherapeutic agents in a synergistic ratio can substantially improve clinical outcomes [3].

Among the therapeutic approaches for TNBC, the family of SRC (Proto-oncogene Tyrosine-protein Kinase) Inhibitors, a specific type of tyrosine kinase inhibitor (TKIs) deserves particular interest. SRC plays critical roles in cell adhesion and motility [4], which both represent important mechanisms for cancer progression and invasiveness. Accordingly, TNBC cell lines display high sensitivity to certain TKIs in preclinical studies [5]. Additional studies have indicated a heightened sensitivity of the mesenchymal-like TNBC subtype to TKIs [6], which may be explained by the overexpression of genes related to cell motility in this particular TNBC subtypes and the crucial role of SRC-family kinases in cell migration.

Studies have reported robust drug synergism between TIs and TKIs [7]; however, only a few examples in the literature discuss combinations conjugated to drug delivery systems (DDS) for the treatment of breast cancer. These studies include non-biodegradable polyethylene glycol (PEG)-ylated peptidic nanocarriers [8] or micelles [9] where the DDS physically entraps one or both drugs.

The conjugation of active agents to a biodegradable polymer provides distinct advantages over physical entrapment, including the ability to fine-tune drug release

kinetics through the rational design of stimuli-responsive linking chemistry and the co-delivery of both drugs at a desired synergistic ratio.

We previously discussed both the advantages of combination therapies based on polymer-drug conjugates for breast cancer (**Chapters 1, 3, and 4**) and the importance of the rational design of newer biodegradable conjugates with enhanced drug linkers that permit improved spatiotemporal control on release profiles (a prerequisite for the maximization of synergistic effects) and, therefore, improved antitumorigenic capacity.

Herein, we present the rational design of poly-L-glutamic acid-(PGA) based combination conjugates bearing a synergistic combination of a TI and a TKI, engineered with optimized drug linkers to maximize drug synergism. Additionally, we demonstrate cytotoxic effects *in vitro* and the antitumor and antimetastatic properties *in vivo* of selected combination conjugates.

We focused on the mesenchymal-like TNBC subtype, which represents around 20% of total TNBC cases. This particularly aggressive subtype is characterized by the expression of factors involved in cell motility, extracellular receptor interaction, cell differentiation pathways, and growth factor signaling pathways [10]. To reproduce the mesenchymal-like TNBC-subtype clinical scenario, we employed the human MDA-MB-231-Luc cell line to test the cytotoxicity of our combination conjugates and to develop a spontaneously metastatic immunocompromised orthotopic murine model in NOD/SCID mice for validation purposes.

V.2. Results and Discussion

V.2.1. Synthesis and Characterization of Combination Conjugates

The conjugation of anticancer drugs to a biodegradable polymeric DDS through stimuli-responsive drug linkers that allow modulable release kinetics represents a proven approach for the effective synergistic co-delivery of drugs. We took advantage of the expertise acquired during this Thesis with regards to the development of different drug linkers (pH-stable amide, acid-sensitive hydrazone, and pH-sensitive ester linkers) to develop a new combination conjugate incorporating two synergistic anticancer drugs with optimal release kinetics to achieve drug synergism both *in vitro* and *in vivo.*

The first synthetic approach (**See Section V.2.3.**) involved the direct attachment of both drugs to the polymeric backbone; the TI through an amide bond, employing the same procedure previously described (based on carbodiimide coupling) (**See Chapter III**), and the TKI through an ester bond. After the evaluation of the first approach, we decided to incorporate two different drug linkers to fine-tune combination conjugate pharmacokinetics; we attached the TI through the previously described hydrazone bond (**see Chapter IV**) while we modified the TKI with different alpha amino acids (α-aa) to achieve an ester bond of different stability (**see section 2.4 and Materials and Methods**). **Figure 1** exhibits the synthetic scheme for the development of single and combination conjugates.

As the UV spectra of the drugs employed presented overlapping profiles (**Figure 2**) and so the peaks cannot be exclusively attributable to a single drug, we could not determine the drug loadings of the combination conjugates by direct measurement. Therefore, we implemented an elaborated procedure that allows this determination: we measured calibration curves of the TKI (λ_{max} = 324nm) and the TI (λ_{max} = 480nm) in DMSO 50% as shown in **Figure 2A, B**. These curves allowed for the determination of the molar extinction coefficient of both drugs at their respective absorption maximum. Then, we measured the absorption of the combination conjugate at 324 nm (λ_{max} of the TKI) and we calculated the contribution of the TI at the same wavelength. Finally, by applying the Lambert-Beer equation, we calculated the concentration and, therefore, the total drug loading of both drugs as well as the conjugation efficiency (**See Table 1**).

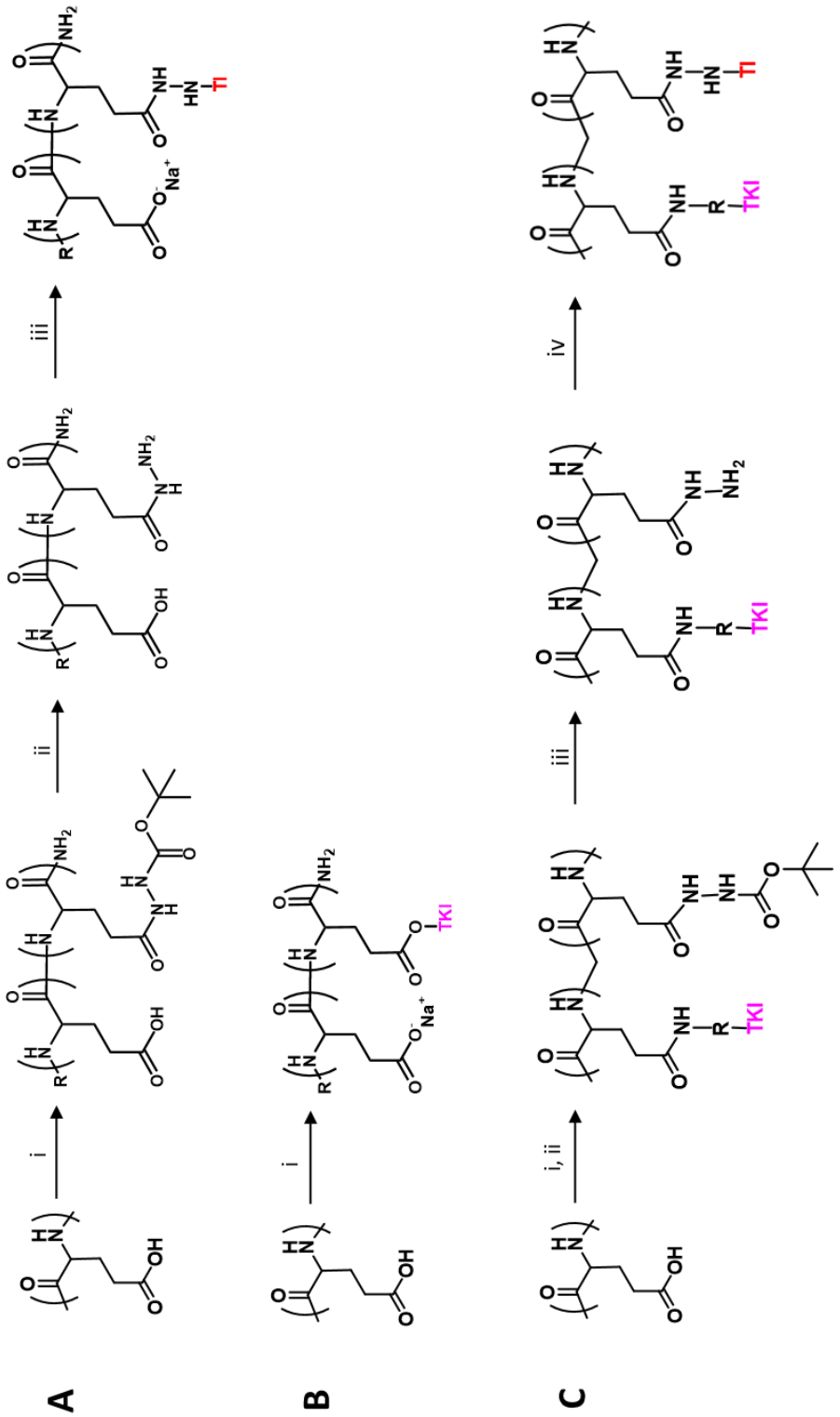

Figure 1: Synthetic Scheme used to obtain single polyglutamate (PGA)-based conjugates (A and B) and combination PGA-based conjugates (C). A) i) t-butyl carbazate, anh. DMF, 24 h, pH=8, R.T. **ii)** TFA, 30 min, R.T. **iii)** TI, CH_3COOH (cat.), 36h. and $NaHCO_3$ (dil) **B**) i) TKI / aa-TKI, EDC, DMAP, **C)** i) t-butyl carbazate, anh. DMF. **ii)** TKI derivative, 24h, pH=8, R.T. **iii)** TFA, 30min, R.T. **iv)** TI, CH_3COOH (cat.), 36 h and $NaHCO_3$ (dil). R= amino acid-TKI derivative in each case. R = 0 for direct TKI attachment.

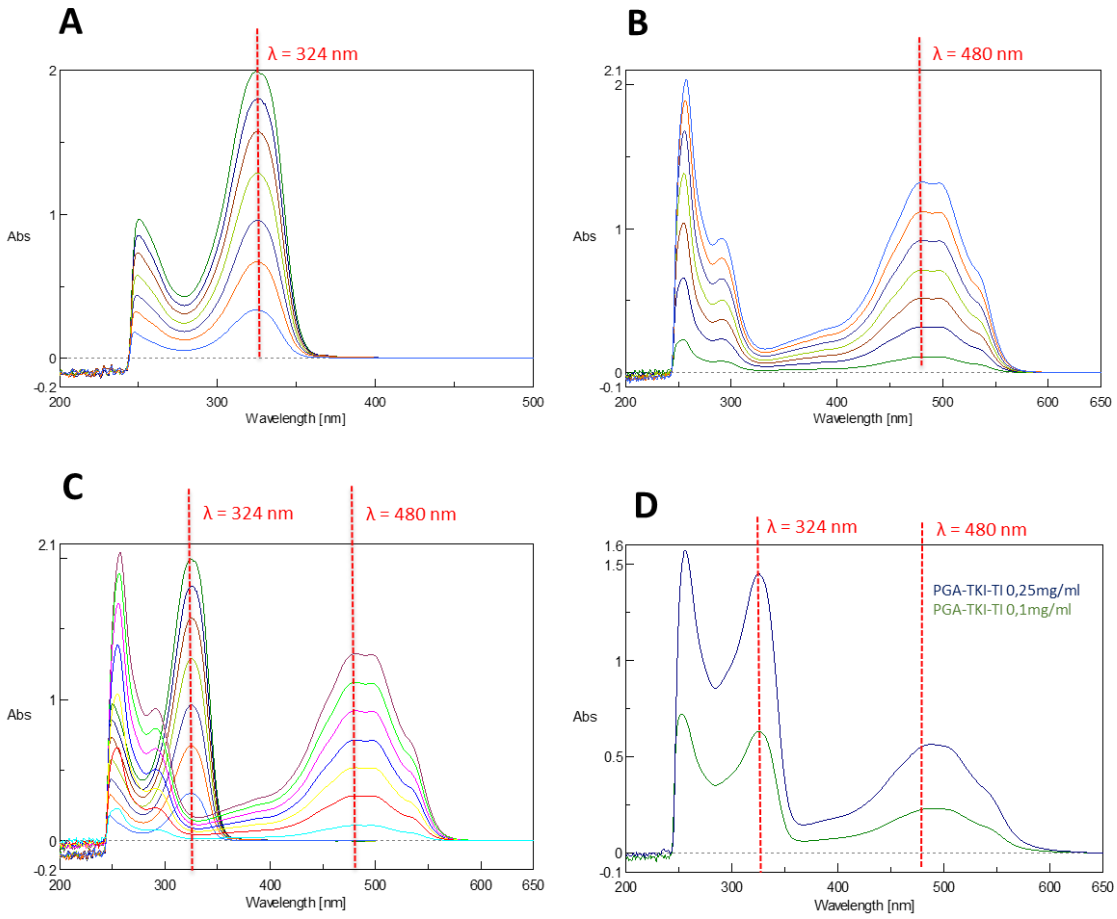

Figure 2. UV-VIS spectra of the TKI (**A**), the TI (**B**) and the overlapping of both spectra (**C**), demonstrating the overlapping signals of both species. **D**) Representative UV-VIS spectra of the combination conjugate PGA-TKI-TI at 0.1 and 0.25 mg.mL^{-1}.

We carried out the identification and characterization of all synthesized conjugates by ^{1}H-NMR and studied the size in solution and z-potential via dynamic light scattering (DLS). As shown in **Table 1,** we aimed for highly efficient conjugation as demonstrated by achieving 5 mol% drug loadings in all conjugates both for the TKI and the TI with great conjugation efficiencies. However, the direct conjugation of the TKI resulted in a reduced yield reaction in both the single and the combination conjugates after several improvement trials most probably due to steric hindrance. Interestingly, the yield improved significantly after the attachment of an amino acid linker.

We also evaluated the hydrodynamic radius (Rh) in phosphate buffer (PB) and Milli-Q water (**see Table 1**). We observed an average Rh of 33-88 nm for conjugates in water. All the conjugates demonstrated smaller Rh in PB (around 3-10nm), as expected due to the polyelectrolyte effect [11], except PGA-TKI and PGA-Phe-TKI single

conjugates, probably due to intramolecular interactions. The analysis of z-potential revealed an overall negative charge for the polypeptide, with values ranging from -11 to -43 mV without a distinct relationship with the nature of the incorporated moieties.

Polymer-conjugate	TI loading (mol%)	TKI loading (mol%)	Theor. MW (kDa)	Rh by DLS (H_2O) (nm)	Rh by DLS (PB) (nm)	Z-pot (mV)	C.E. (%)
PGA-TKI	n/a	2.6	16.1	77	30	-43	43
PGA-Gly-TKI	n/a	4.4	17.3	33	4	-36	87
PGA-Ala-TKI	n/a	4.5	17.4	69	3	-28	90
PGA-Abu-TKI	n/a	4.8	17.7	58	3	-28	92
PGA-Val-TKI	n/a	4.8	17.7	38	4	-11	98
PGA-Leu-TKI	n/a	5.1	18	71	4	-15	98
PGA-Phe-TKI	n/a	4.5	17.8	88	54	-38	91
PGA-Hyd-TI	3.7	n/a	16.5	n/a	4	-20	80
PGA-TI-TKI	3.5	3.8	17.9	n/a	10	-27	71
PGA-(Gly-TKI)-(Hyd-TI)	3.8	4.7	18.2	9	3	-32	69
PGA-(Val-TKI)-(Hyd-TI)	3.6	4.6	18.5	35	5	-33	79

Table 1. Characteristics of PGA-TKI-TI polymer-drug conjugates. DLS determined by Number. C.E.= conjugation efficiency

V.2.2. Establishment of an Optimized TI:TKI Ratio to Achieve Synergism

On the basis of previous studies demonstrating drug synergism between TKIs and TIs in different breast cancer cell lines [7], we *in vitro* corroborated the results in two representative TNBC cell models: the murine 4T1 and the human MDA-MB-231-Luc models. The first columns in **Figure 3** depict the cytotoxicity of both drugs administered simultaneously in both cell lines.

Thanks to the versatility of polymer-drug combination conjugates and the rational design of drug linkers, we can optimize the entire system to promote the release of drugs at an adjusted ratio and relative controlled release kinetics always seeking for drug synergism.

From our previous experience in this area, polymer-drug combination conjugates bearing certain TIs demonstrated enhanced antitumor effect following a high TI release over a very short period of time. Accordingly, we compared the simultaneous treatment

with both drugs *vs.* the treatment of the TKI following an initial treatment with the TI alone. To determine the optimal synergistic ratio, we computed the combination index (CI) for each separate treatment schedule (CI >1 antagonism, CI <1 synergism).

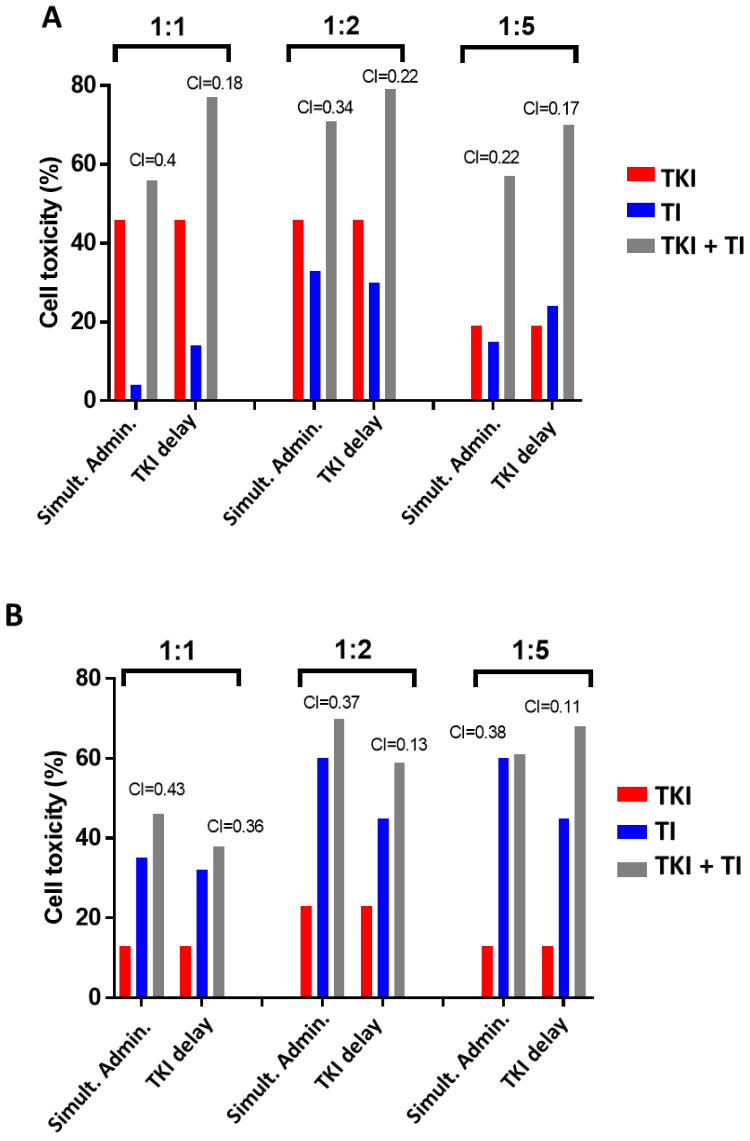

Figure 3. Assessment of the TKI and the TI combination *in vitro* cytotoxicity in 4T1 (**A**) and MDA-MB-231-Luc (**B**) tested at different TKI/TI ratios. Data represents the cell toxicity when both drugs were administered simultaneously ("Simult. Admin.") and with 24 h delay for the TKI administration ("TKI delay").

As depicted in **Figure 3A,** MDA-MB-231-Luc cells displayed higher sensitivity to the TI than to the TKI *in vitro* (as single agents). Co-treatment enhanced cytotoxicity at all ratios employed, thereby demonstrating drug synergism; however, TI treatment combined with delayed (24 hours) TKI treatment resulted in even higher percentage of cell death. Overall, although non-significant, we found the highest drug synergism

(lowest CI) for a TI:TKI ratio of 1:5 and with delayed administration of TKI (**Figure 3A**). Following a similar assessment in 4T1 cells, we discovered that the TKI demonstrated higher cytotoxicity than the TI, while co-treatment led to higher cytotoxicity (and therefore better drug synergism) than that observed in MDA-MB-231-Luc cells. We also found in this case that the drug synergism at a 1:1 ratio was similar to that for TI:TKI 1:5 and not significantly different were found with a delay in the TKI administration (**Figure 3B**).

Considering these results, we sought to improve synergistic effects by means of polymer conjugation under the hypothesis that anticancer activity will benefit from a 1:1 TI:TKI ratio and ideally a non-simultaneous release preferentially being TI release required first.

V.2.3. Synthesis and *in vitro* Evaluation of a TKI-TI Combination Conjugate via Direct Conjugation

Trying to proof our hypothesis, and once we established a drug ratio that provided optimal synergism (1:1 TKI:TI), we directly attached (absence of drug linkers) both drugs to the PGA backbone. This procedure represented the most straightforward approach for chemical conjugation and allowed the assessment of possible drug synergism. We synthesized (**see Figure 1**) and characterized (**see Table 1**) a combination conjugate employing an ester bond for the TKI conjugation and a pH-stable amide bond for the TI conjugation.

When studying the *in vitro* toxicity of our combination conjugate in MDA-MB-321-Luc cells, we found similar cytotoxicity to treatments with a PGA-TKI single conjugate, the sum of single PGA-TKI and PGA-TI conjugates, and co-treatment with free drugs (**Figure 4**). While we found similar results in the 4T1 cell line, we did observe higher sensitivity to the combination of free drugs (**Figure 5)**, in agreement with previous data. The lack of significant differences between conjugates and free drugs suggested the rapid release of the TKI and the absence of TI release from single or combination conjugates (**Figures 4 and 5**).

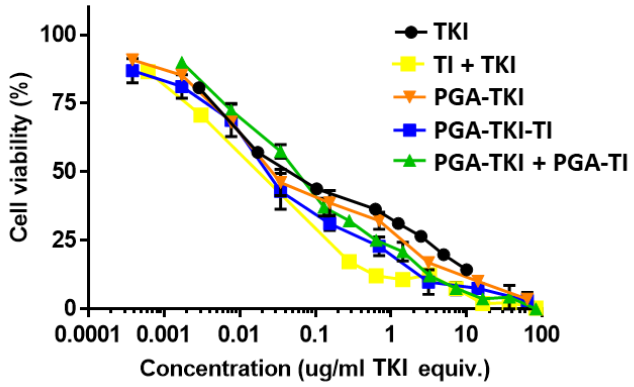

	IC50 (ug/ml TKI equiv.)	CI
TKI	0.05	n/a
TI + TKI	0.03	0.44
PGA-TKI	0.26	n/a
PGA-TKI + PGA-TI	0.1	3.57
PGA-TKI-TI	0.03	0.39

Figure 4. *In vitro* cytotoxicity of PGA-TKI-TI combination conjugate, the corresponding single conjugates, and the free drugs in the MDA-MB-231-Luc cell line.

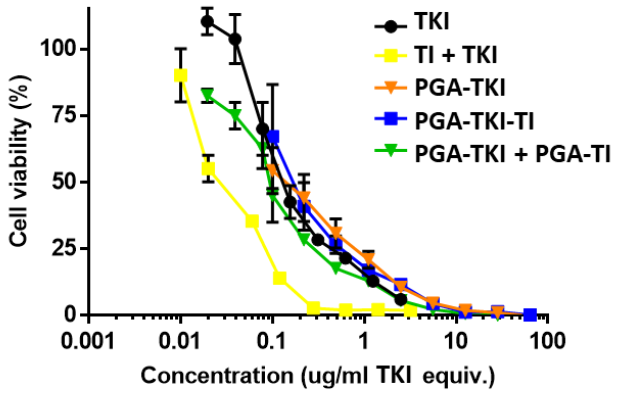

	IC50 (ug/ml TKI equiv.)	CI
TKI	0.07	n/a
TI + TKI	0.01	0.26
PGA-TKI	0.48	n/a
PGA-TKI + PGA-TI	0.1	0.28
PGA-TKI-TI	0.14	2.68

Figure 5. *In vitro* cytotoxicity of a PGA-TKI-TI combination conjugate, the corresponding single conjugates, and the free drugs in the 4T1 cell line.

To explain our *in vitro* data and to mimic the degradative environment of the endocytic pathway, we performed *in vitro* drug release assays in the presence of the cathepsin B proteolytic enzyme. We discovered a fast TKI release and almost no TI

release from the directly coupled combination conjugate (**Figure 6**) in support of previous *in vitro* data.

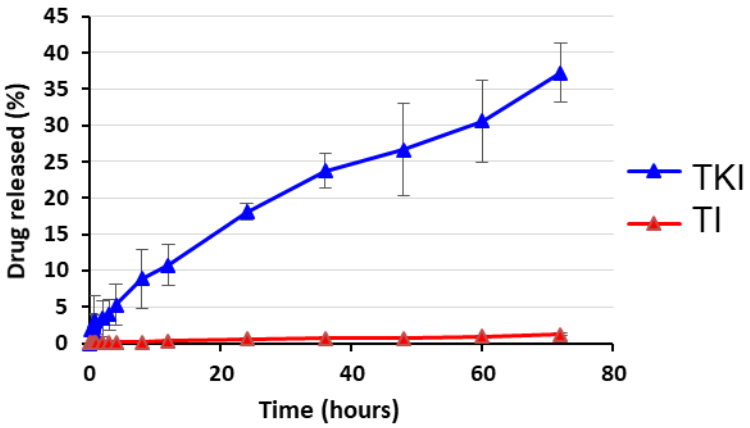

Figure 6. Drug release kinetics from PGA-TKI-TI in the presence of cathepsin B. Data expressed as mean ± SEM, with at least n = 3 experiments per treatment.

Taken together, these data establish several design implications for an advanced combination conjugate. First, a combination conjugate would benefit from a higher and more rapid TI release, as demonstrated by the *in vitro* assays (See **Figure 3**). Second, as previous studies demonstrated, a greater drug synergism would be achieved by a drug-linker that could slow down TKI release.

In **Chapter III**, we implemented two different length hydrazone-based Dox linkers for its specific release in an acidic environment. The shorter hydrazone linker demonstrated not only more straightforward chemistry but also a safer *in vivo* profile and better *in vivo* performance. Consequently, we decided to incorporate a short hydrazone linker to enhance the TI release in this case; however, the incorporation of a drug-linker that delays the TKI release represented a more challenging task.

V.2.4. Optimization of Polyglutamate-TKI Linker Looking For a Slow TKI Release

In the hope of a modulated TKI release, we considered the incorporation of simple α-aa between TKI and the PGA backbone, in such way that stabilizes the ester bond, reducing its cleavage and consequently delaying its release.

Acid-catalyzed hydrolysis of esters takes place via an $A_{AC}2$ (acidic, acyl, bimolecular) mechanism as depicted in **Figure 7.** Although the hydrolysis rate is a complicated process dependent on factors such as the electrostatic effects of the surrounding substituents, the resonant effect, or the hydrogen bonding effect [12], it is assumed that the presence of bulky groups in the alpha position of the ester bond (R_1 in **Figure 7**) decreases the decomposition rate [13, 14].

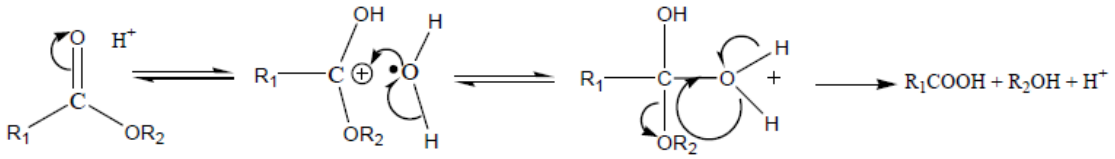

Figure 7: General scheme of the most common mechanism for acid-catalyzed ester hydrolysis, proceeding through a tetrahedral intermediate and acyl cleavage.

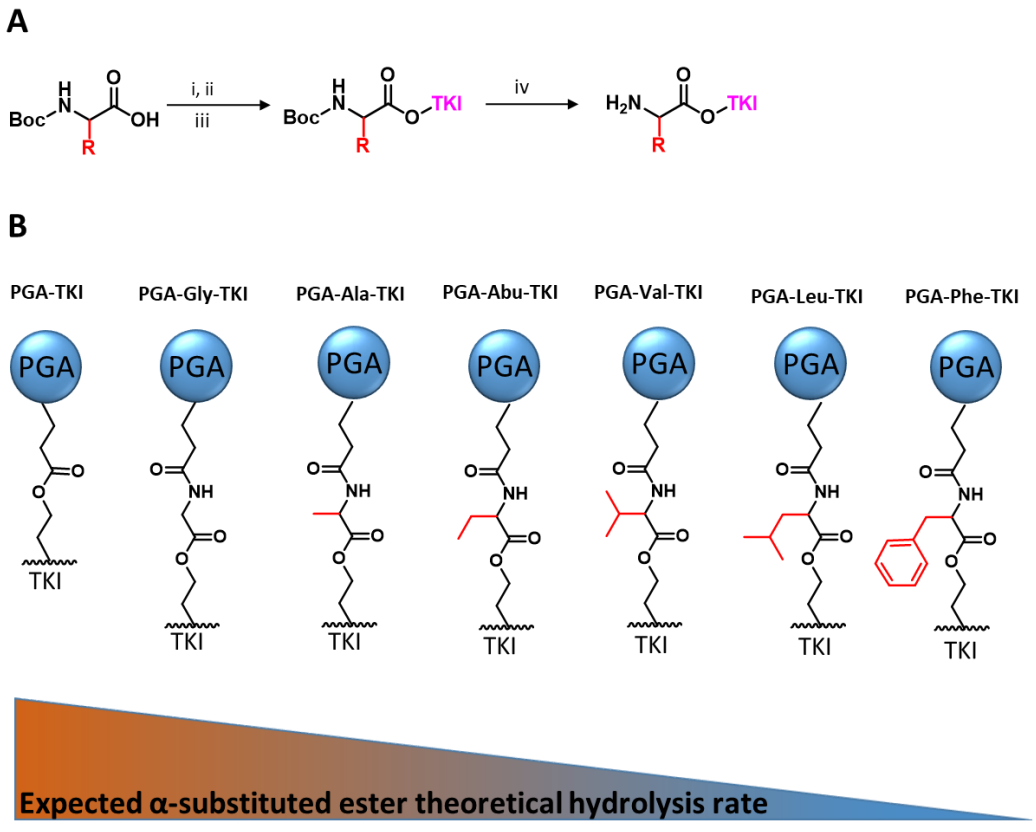

Figure 8. A) General scheme for preparation of α-aa-TKI derivative. **i)** anh. DMF, **ii)** EDAC, DMAP **iii)** TKI, 8h, pH=8, R.T.; **iv)** TFA, 30 min, R.T. Gly-TKI, R= 0; Ala-TKI, R= CH_3; Abu-TKI, R= CH_2-CH_3; Leu-TKI, R= CH_2-CH-$(CH_3)_2$; Val-TKI, R= CH-$(CH_3)_2$; Phe-TKI, R= CH_2-C_6H_5; **B)** Schematic representation of incorporation of α-aa with crescent bulkiness as TKI drug linker and the expected decrease in the hydrolysis rate according to the amino acid bulkiness.

Therefore, we hypothesized that the modification of the TKI through an ester bond, with α-aa of different bulkiness could yield a range of α-aa-TKI with different hydrolysis rates. Subsequent conjugation of prodrugs to PGA through a stable amide bond would then generate pH-sensitive single conjugates of the TKI derivatives.

To this end, we selected six α-aa's substituents with increasing volume in the alpha position and we expected decreasing hydrolysis rate of the ester as displayed in **Figure 8** as the aa volume increased from Glycine (R = 0), Alanine (R = methyl), alpha-aminobutyric acid (R = methyl), Valine (R = isopropyl), Leucine (R = isobutyl), and finally Phenylalanine (R = benzyl).

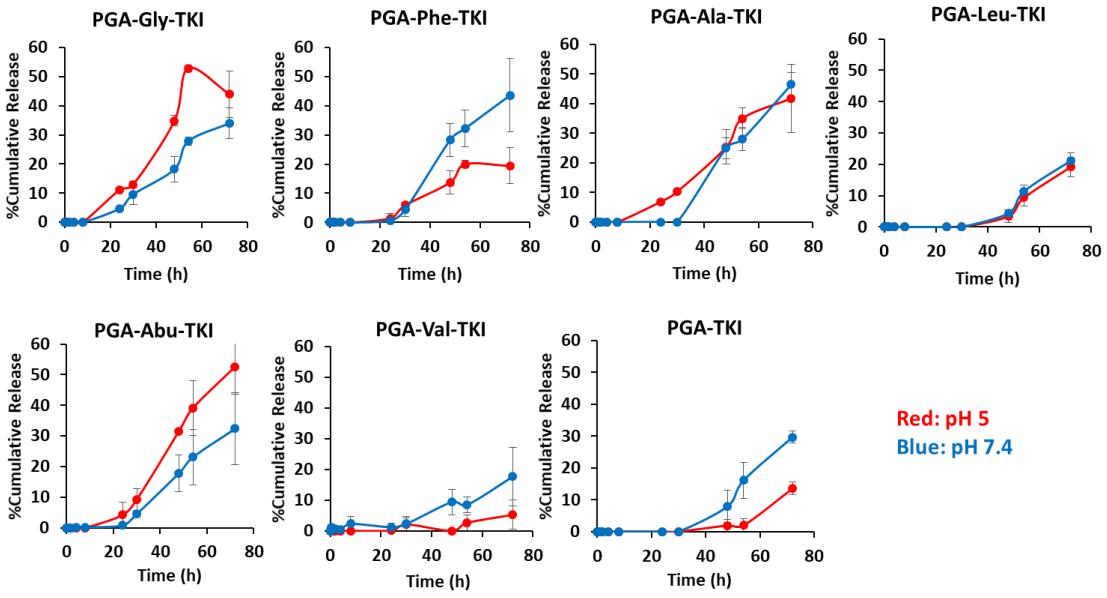

Figure 9. pH-dependent release profiles of PGA-α-aa-TKI single conjugates.

Once synthesized and adequately characterized (**See Subsequent Section and Characterization table**), we screened hydrolytic drug release at physiological pH (7.4) and at a pH characteristic of the tumor microenvironment (pH ~5). As seen in **Figure 9** a non-linear relationship between bulkiness of the α-substituent and drug release kinetics at acidic pH was encountered. This highlights the multiple factors driving the overall conjugate solution conformation and how a simple amino acid incorporation can alter the conjugate tridimensional conformation, thereby varying the exposure of the drug linker modifying, therefore, the pH sensitivity (**see chapter III**). Among the observed pH-dependent drug release profiles displayed in **Figure 9** corresponding to different PGA-α-

aa-TKI single conjugates, the bulky amino acid valine promoted the slowest TKI release under the mildly acidic conditions compared to the other single conjugates. Furthermore, the PGA-Val-TKI single conjugate demonstrated the highest stability at physiological pH, a crucial requirement for any DDS to protect the cargo during blood circulation. For all these reasons, we proposed that the Val approach could meet the requirements for the new combination conjugates.

We also studied the *in vitro* cytotoxicity of this family of PGA-α-aa-TKI single conjugates, to determine how the differences observed in the release kinetics could affect the *in vitro* activity. Even though we expected greater differences given the wide range of α-aa-modified-TKI conjugates, we found similar toxicity profiles (**Figure 10**). However, a closer look when we examined the IC50 values allow to discuss several rational correlations with TKI release rates. PGA-Gly-TKI showed the lowest IC50, similar to free TKI (IC50=0.026 and IC50=0.025, respectively), in agreement with the fastest TKI release rate that correlates with the least hidden ester. PGA-Ala-TKI (IC50=0.035), PGA-Abu-TKI (IC50=0.039), PGA-Leu-TKI (IC50=0.041), PGA-Phe-TKI (IC50=0.039) and PGA-TKI (IC50=0.033) showed slightly greater IC50 values corresponding to bulkier aa volumes and therefore greater ester protection. Finally, whereas PGA-Val-TKI is not the bulkiest aa, it showed the highest IC50 value (IC50=0.103) nicely correlating with the slowest TKI release. Therefore, it is clear that apart from alpha substitution there are other design features that drives ester stability [13, 14], as for example the degree of substitution in the beta position of the aa (Val is the most substituted in such position (R = isopropyl) (**Figures 7, 8**)).

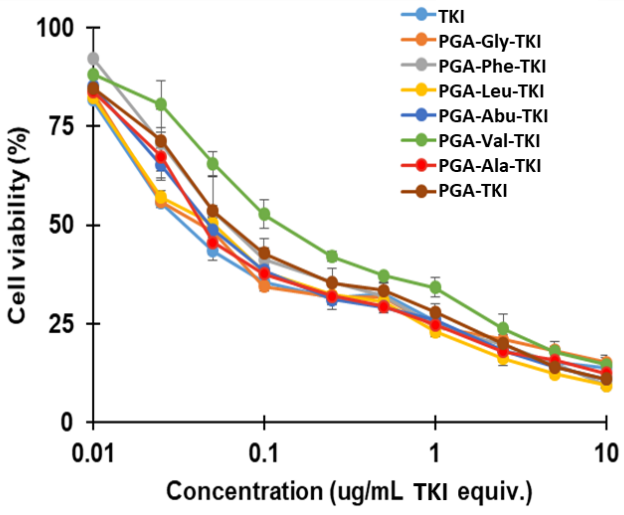

	Concentration (ug/mL TKI equiv.)
TKI	0.025
PGA-Gly-TKI	0.026
PGA-Phe-TKI	0.054
PGA-Leu-TKI	0.041
PGA-Abu-TKI	0.039
PGA-Val-TKI	0.103
PGA-Ala-TKI	0.035
PGA-TKI	0,033

Figure 10. *In vitro* evaluation of the single PGA-α-aa-TKI in the MDA-MB-231-Luc cell line.

On the basis of these findings, we decided to synthesize a combination conjugate with a pH-sensitive hydrazone for the TI and the Val-linker for the TKI.

V.2.5. *In Vitro* Activity of TI-TKI Combination Conjugate with optimally designed linkers. Study of Drug Release Kinetics

Initial *in vitro* cytotoxicity assays of the PGA-(Val-TKI)-(Hyd-TI) combination conjugate and the corresponding single conjugates in the MDA-MB-231-Luc cell line demonstrated enhanced biological performance for the combination conjugate as shown in **Figure 11** (drug concentrations expressed in TI equivalents) and **Figure 12** (drug concentrations expressed in TKI equivalents). Overall, the combination conjugate displayed slightly higher cytotoxicity than the physical mixture of the single conjugates. However, when computing the CI (**See Tables in Figures 11 and 12**), we noted a higher drug synergism for the combination conjugate, demonstrating the advantages of polymer-based combination strategies.

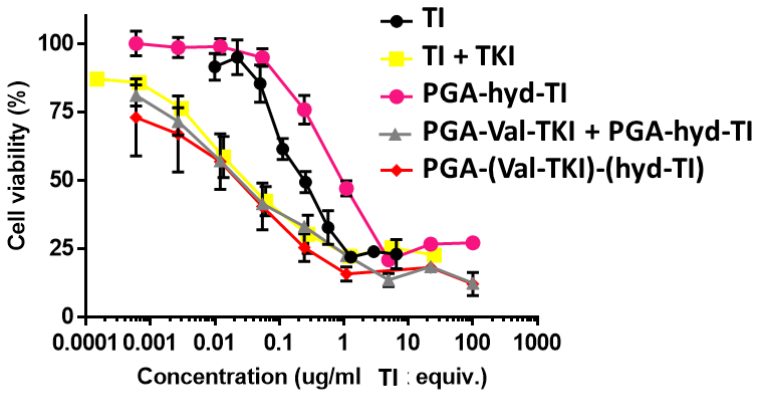

	IC50 (ug/ml TI equiv.)	CI
TI	0.14	n/a
TI + TKI	0.02	0.44
PGA-Hyd-TI	0.48	n/a
PGA-Val-TKI + PGA-Hyd-TI	0.04	0.98
PGA-(Val-TKI)-(Hyd-TI)	0.04	0.52

Figure 11. Cytotoxicity in TI equivalents and combination index. n/a: not-applicable

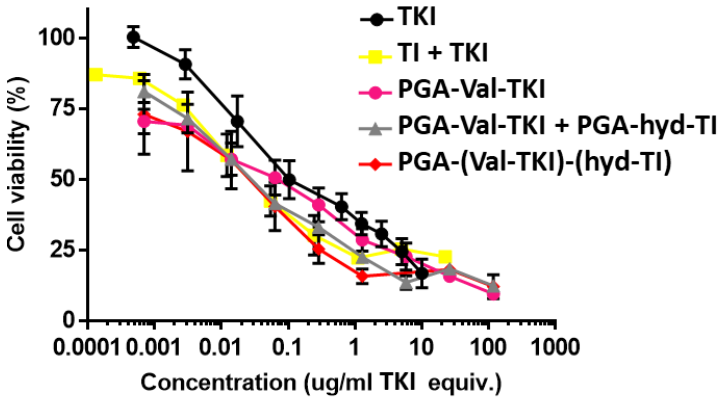

	IC50 (ug/ml TKI equiv.)	CI
TKI	0.04	n/a
TI + TKI	0.02	0.44
PGA-Val-TKI	0.26	n/a
PGA-Val-TKI + PGA-Hyd-TI	0.04	0.98
PGA-(Val-TKI)-(Hyd-TI)	0.05	0.52

Figure 12. Cytotoxicity in TKI equivalents and combination index. n/a: not-applicable

Drug release in the biological medium is driven by a complex interplay of physicochemical factors, including tridimensional conformation of the conjugate, interaction with blood proteins, or blood shear stress. [15-17] However, the study of drug release kinetics *in vitro* in the presence of the proteolytic enzyme cathepsin B (overexpressed in most solid tumors) provides a suitable model system to study pharmacokinetics for a lysosomotropic delivery mechanism.

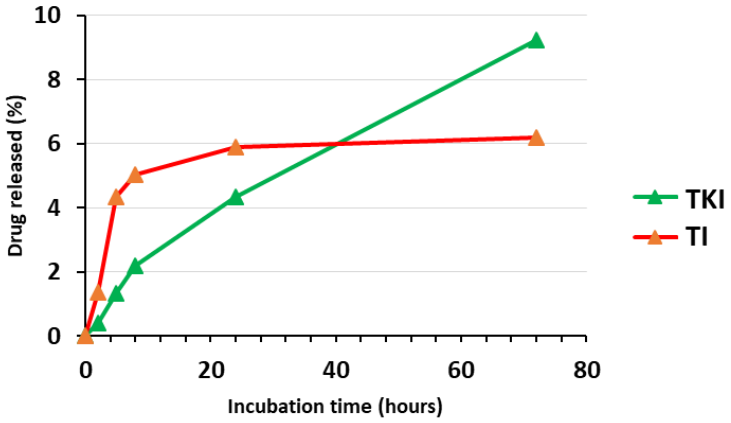

Figure 13. Drug release kinetics of the combination conjugate PGA-(Val-TKI)-(Hyd-TI) in the presence of cathepsin B.

In vitro drug release kinetics of the PGA-(Val-TKI)-(Hyd-TI) combination conjugate demonstrated a sudden and rapid TI release over the first 8 h of incubation and a sustained release up to 72 h (6%). In contrast, the release profile of the TKI demonstrated a delayed and progressive release with respect to the TI, reaching 9% of drug release over 72 h. These results support the rational linker design approach followed, as the hydrazone linker incorporated for the TI promoted the required early faster release than the TKI, which presented an impaired release rate by the valine linker.

Overall, we developed a combination conjugate bearing two anticancer drugs via rationally designed bioresponsive linkers that allow to deliver them at the appropriate relative bioavailable ratio to promote an enhanced synergistic effect.

V.2.6. *In Vivo* Antitumor Activity of PGA-(Val-TKI)-(Hyd-TI) combination conjugate.

To explore the antitumor effect of the developed conjugates, we employed previously established murine model (**See Chapter II**). We randomly split mice inoculated with the luciferase-transfected MDA-MB-231-Luc cells into representative groups and scheduled six treatments every four days with selected combination conjugates and their corresponding single conjugates at the optimized drug equivalents. We administered the TI and the TKI as free agents in a control group at the maximum non-lethal doses. Analysis of tumor growth *vs.* time (**Figure 14**) revealed high intragroup uniformity allowing us to evaluate the antitumor effect of the different treatments effectively. Treatment with the single conjugates bearing the TI, the TKI, the addition of either single conjugate, or free TI or TKI did not significantly affect tumor growth. However, we observed a significant reduction in primary tumor growth in animals treated with the combination conjugate PGA-(Val-TKI)-(Hyd-TI).

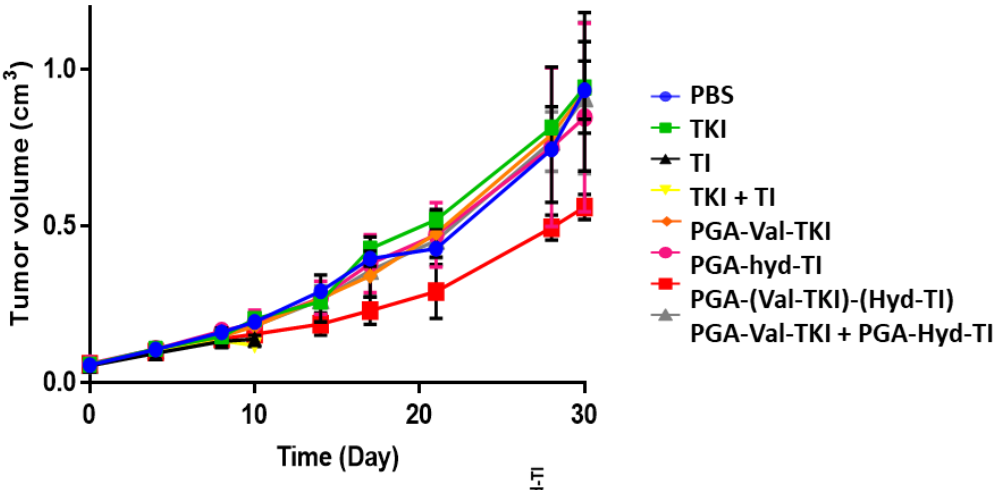

p-value at day 30	PBS	PGA-Val-TKI	PGA-Hyd-TI	PGA-(Val-TKI)-(Hyd-TI)	PGA-Val-TKI + PGA-Hyd-TI
PBS					
PGA-Val-TKI	ns				
PGA-Hyd-TI	ns	ns			
PGA-(Val-TKI)-(Hyd-TI)	**	**	*		
PGA-Val-TKI + PGA-Hyd-TI	ns	ns	ns	**	

Figure 14. *In vivo* evaluation of the combination conjugate PGA-(Val-TKI)-(Hyd-TI) and related single conjugates in an orthotopic MDA-MB-231-Luc murine model.

We also assessed safety profiles for all tested drugs and polymer-drug conjugates by means of body weight monitoring and general wellbeing. We did not observe significant alterations in body weight in any of the animals treated with single or combination conjugates except a slight weight loss in the group of animals treated with PGA-(Val-TKI)-(Hyd-TI) (**Figure 15A**). However, the administration of free TI or the sum of the TI + the TKI at the same doses as the conjugates (in drug equivalents) led to an abrupt weight loss following the first dose that enhanced with the second dose (> 10% weigth loss) that resulted in some animals dead and obliged us to sacrifice the rest of the animals of those groups before day 10. Subsequent analysis of survival rates (**Figure 15B**) demonstrated a low survival rate for animals treated with free TI (both groups, TI and TI + TKI). In contrast, 100% of the animals survived following PGA-conjugate-related treatments.

Taken altogether, these data demonstrated the therapeutic improvements obtained first upon polypeptide conjugation (safety), and more importantly following the incorporation of two synergistic bioactive agents in the same biodegradable polymeric carrier (therapeutic activity).

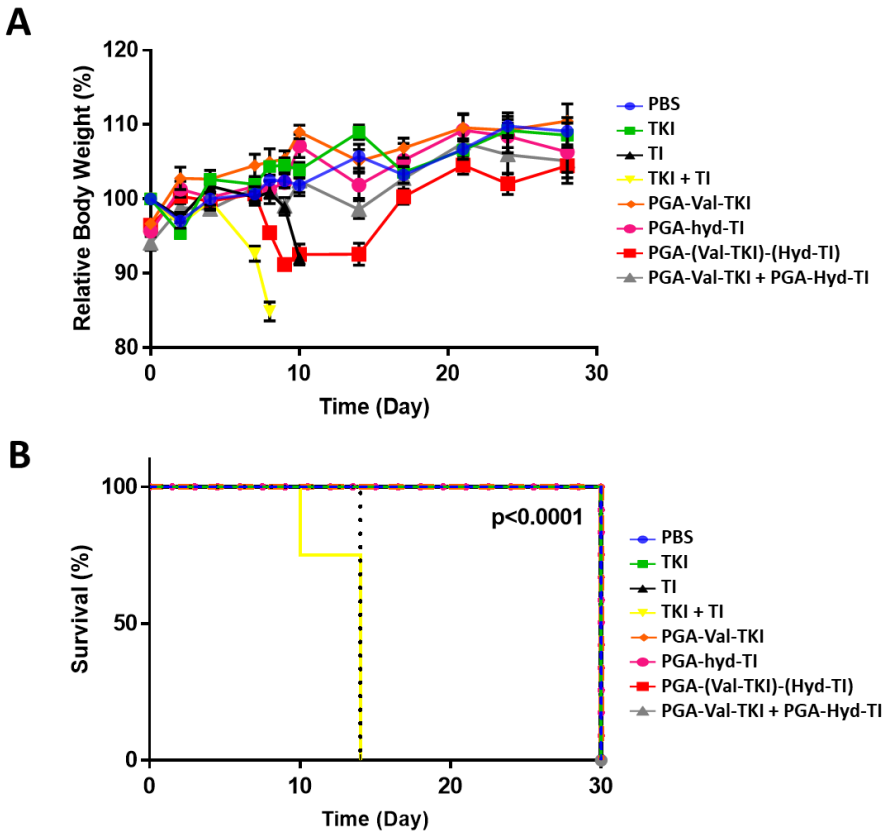

Figure 15. Proof of safety of the polymer-drug conjugates: **A)** Body weight loss (relative to the initial body weight) during the experiment. **B)** Kaplan-Meyer survival rates of different treatments.

V.2.7. *In Vivo* Antimetastatic Activity of PGA-(Val-TKI)-(Hyd-TI) combination conjugate.

The MDA-MB-231-Luc orthotopic TNBC NOD/SCID murine model is suitable for antimetastatic nanomedicine validation as it faithfully mimics the human clinical scenario, including spontaneous metastasis to the lung (**see Chapter II**). This model develops profuse lung metastasis with concomitant axillary lymph node (ANL) invasion. Thanks to the luciferase transfection of MDA-MB-231 cell line, metastatic cells can be monitored by bioluminescence (BLI)-based imaging. As depicted in **Figure 16**, the PGA-(Val-TKI)-(Hyd-TI) combination conjugate displayed optimal antimetastatic activity: a 90% reduction in lung metastasis (**Figure 16A**) when compared with the single

conjugates, the sum of single conjugates, and control (non-treated) mice. Additionally, the conjugate demonstrated better antimetastatic efficiency in ALN (**Figure 16B**). Interestingly, the single conjugates administered alone or in a physical mixture, produced an increase in either lung metastasis or ALN metastasis. Additional experiments are currently underway in order to understand this undesired effect.

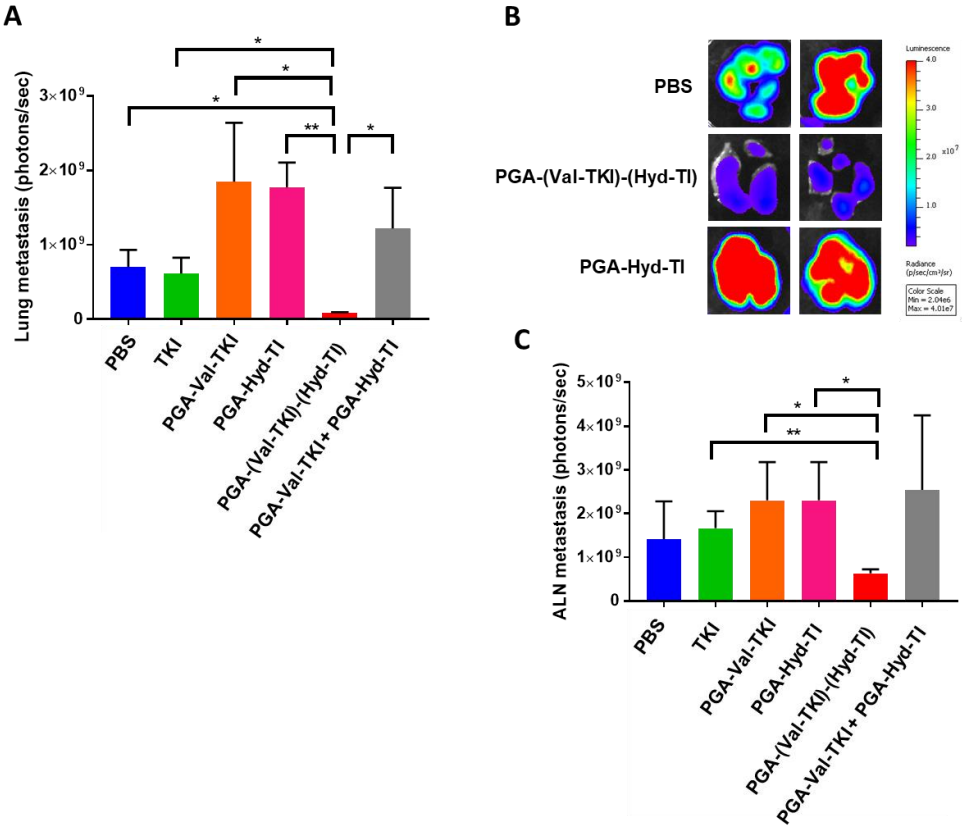

Figure 16. Study of metastasis inhibition. **A)** Lung metastasis; **B**) Ex-vivo lung metastasis by means of BLI **C)** ALN metastasis

V.3. Conclusions

Effective systemic treatments for TNBC require multiple targeted approaches, given its heterogeneity and molecular complexity. Encouraged from promising studies in the laboratory, we incorporated two synergistic drugs: a TI (having the ability to kill cells undergoing DNA replication, stopping the reading of the DNA for protein production, and blocking repair of DNA damage) and a TKI, (that compete with the ATP binding site of the catalytic domain of several oncogenic tyrosine kinases, impairing key processes in tumor cell proliferation as growth, migration, differentiation, and extracellular

communication) to a biodegradable polymeric carrier, polyglutamate, that accumulates specifically in the tumor after i.v. administration, once the EPR takes place.

The polymer-drug conjugate arose from the direct drug attachment to the polymer lacked for drug synergism due to an inappropriate pharmacokinetics. Taking advantage of the multivalency of the PGA as carrier, we followed a rational design to promote and improve drug synergism by the incorporation of a hydrazone linker for the TI (that promoted a fast TI release as seen in Chapter IV) and a Val linker for the TKI (that delayed TKI release), meeting, therefore, the design requirements previously observed in our *in vitro* studies with free drugs. This optimized combination conjugate demonstrated an enhanced anticancer effectiveness in a human TNBC immunodeficient mice model, leading to a 50% of primary tumor growth reduction with almost total remission of lung metastasis.

In order to complement this research, additional histopathological studies are currently being conducted, looking for cancer cell proliferation in primary tumors and metastasized lungs and the possible damage/improvement on major organs.

Interestingly, after treatments with both of our single conjugates PGA-Val-TKI and PGA-Hyd-TI separately or in physical mixture, we observed an apparently pro-metastatic behavior in lungs, while we do not found antitumor benefit for those conjugates. Because metastatic disease is the major cause of cancer-related mortality and is currently incurable, it is critical that we develop strategies to prevent progression of cancer to the metastatic stage and to prevent further spread from already existing metastatic foci. Our combination conjugate succeeds in metastasis inhibition, but the fact that our single conjugates positively modulates metastatic spread, suggest the possible activation of any prometastatic mechanism related to the physicochemical properties of the conjugates, their pharmacokinetics or combination of both, and this must be elucidated.

Several studies with anticancer treatments such as paclitaxel and other chemotherapies modulate the tumor microenvironment and promote breast cancer cell intravasation and dissemination to distant sites [18-20]. To explain this, is generally proposed a mechanism through which tumor cells from primary breast lesions may intravasate and disseminate at sites of microanatomical structures called tumor

microenvironment of metastases (TMEM). The particular physico-chemical characteristics or drug-release kinetics of our single conjugates could modulate the tumor microenvironment in this way. Other possible explanation could involve the activity of tumor macrophages.[21] As response to the presence of the tumor, classically activated (M1) macrophages are activated by IFN-γ, LPS or TLR ligands, secrete pro-inflammatory cytokines and play tumouricidal roles. Alternatively activated (M2) macrophages are activated by IL-4 and IL-13, secrete anti-inflammatory cytokines IL-10 and TGF-β and play tumourigenic roles. However, the so called tumor-associated macrophages (TAMs) display M2-like phenotype and exhibit pro-tumourigenic features. It has also been described how certain chemotherapies could reprogram these TAMs and how TAMs are able to facilitate metastasis progression. [22]

In order to explain this behavior, additional deeper *in vivo* validation of our treatments in an immunocompetent TNBC mice model is currently being accomplished, with the aim of evaluate the effects of the treatment at immune system level and reveal its possible relationship with cancer cell dissemination.

V.4. Materials and Methods

V.4.1. Materials.

All chemicals were reagent grade and used without further purification, unless otherwise indicated. All solvents were of analytical grade. Preparative SEC was performed using Sephadex G-25 medium from GE as well as PD MiniTrap G-10 ™ columns containing 2.1 mL of Sephadex™ G-10.

V.4.2. Characterization Techniques.

NMR spectroscopy, DLS, ^{1}H-NMR and UV were performed using the equipments and techniques according to previous chapters.

V.4.3. Synthetic Protocols.

V.4.3.1. General Procedure for The Synthesis of TKI-Derivatives

This section has been hidden purposely

Workup

Reaction mixture was transferred to a 50 ml falcon tube and remaining traces were washed out with some new DMF. Then, milliQ water was added until reaction mixture precipitate is observed. The heterogeneous mixture was transferred to a 500ml separation funnel and remaining traces were washed out with a mixture of DMF and water. Aqueous part was extracted 3 times with 100ml AcOEt and the organic part was kept apart. Then, all organic fractions were mixed and washed with 100 ml of diluted $NaHCO_3$. Next, a new wash with 100 ml of milli-Q water was carried out. Organic phase was finally separated into a 1000ml Erlenmeyer flask and allow to dry by adding anhydrous $MgSO_4$. Then, a final white fine powder was obtained by evaporating the solvent under rotatory evaporator (yield: 90-95% depending on the amino acid).

Flash-Column

Mobile phase was prepared by mixing CH_2Cl_2, MeOH and $NH_4(OH)$ (100/7/1) (v/v). Some of the TKI-derivatives were directly soluble in the mobile phase, but others were seeded as a suspension. Column progression could be followed under UV light (λ = 366nm). All fractions were analysed by TLC and selected ones are placed together and evaporated using rotatory evaporator. ^{1}H-NMR will confirm the identity and purity of the compound.

Boc-Deprotection

Boc-aa-TKI derivative was placed in a 25 ml round bottomed flask and a deprotection solution is prepared before, to avoid local decrease of pH that could degrade the ester bond. 1,2 ml of HCl in dioxane solution (4M) was diluted in 5 ml of EtOAc and the mixture was added in the flask containing the Boc-aa-TKI provided with a magnetic stirrer. Deprotection was allowed to proceed for 90-120 min and the solid adhered in the flask walls was scratched to put all the solid in suspension. After this time, reaction was transferred into a 50 ml falcon tube and washed with more EtOAc. To improve precipitation, 5ml of hexane was also added and the mixture was centrifuged. The supernatant was taken off and the solid pellet was washed again with 20 ml of hexane and

a new centrifugation was carried out. The supernatant was discarded and the solid was dried under vacuum for 1 hour. After that a solution of 30ml Milli-Q water and dil. $NaHCO_3$ was added in order to neutralize the remaining HCl and once well mixed, some drops of $NaHCO_3$ 1,0M solution were also added up to pH = 7-8. After 24h of freeze drying the solid, its identity can be ensured by ^1H NMR and COSY experiments.

V.4.3.2. General Procedure for Conjugates Synthesis

TKI-derivatives are provided with terminal amines. Therefore, the conjugation was performed according to the previously described conjugation protocols (**Chapter III and IV**). Similarly, the TI was conjugate following the synthetic protocols described in **Chapter IV**)

V.4.4. Biological Evaluation of the Polymer-Drug Conjugates

V.4.4.1. Cathepsin B-Mediated Drug Release Kinetics

Drug release kinetics in presence of cathepsin B was accomplished as explained in **Chapters III and IV.**

V.4.4.2. *In vitro* evaluation

Cell culture experiments to determine cytotoxicity and combination index in the 4T1 cell line were performed as described in previous chapters. Alternatively, MDA-MB-231-Luc cells were seeded in sterile 96-well microtiter plates at concentration of 7,500 cells/cm^2 under standard culture conditions. Plates were incubated for 24 h and then solutions of free drugs and conjugates were tested at final concentrations ranging from 0.0001 to 1000 µg/ml of drug equivalents.

V.4.4.3. *In vivo* evaluation

Animal experiments to determine antitumor and antimetastatic activities of the conjugates have been accomplished following the same ethical regulations and experimental procedures already explained in previous chapters.

V.5. References

[1] Bianchini G, Balko JM, Mayer IA, Sanders ME, Gianni L. Triple-negative breast cancer: challenges and opportunities of a heterogeneous disease. Nature reviews Clinical oncology. 2016;13:674-90.
[2] Wahba HA, El-Hadaad HA. Current approaches in treatment of triple-negative breast cancer. Cancer biology & medicine. 2015;12:106-16.
[3] Lee A, Djamgoz MBA. Triple negative breast cancer: Emerging therapeutic modalities and novel combination therapies. Cancer Treatment Reviews. 2018;62:110-22.
[4] Gelman IH. Src-family tyrosine kinases as therapeutic targets in advanced cancer. Frontiers in bioscience (Elite edition). 2011;3:801-7.
[5] This reference has been ommited purposely
[6] Lehmann BD, Bauer JA, Chen X, Sanders ME, Chakravarthy AB, Shyr Y, et al. Identification of human triple-negative breast cancer subtypes and preclinical models for selection of targeted therapies. The Journal of clinical investigation. 2011;121:2750-67.
[7] This reference has been ommited purposely
[8] This reference has been ommited purposely
[9] This reference has been ommited purposely
[10] Ahn SG, Kim SJ, Kim C, Jeong J. Molecular Classification of Triple-Negative Breast Cancer. Journal of Breast Cancer. 2016;19:223-30.
[11] Cameron GG. Polyelectrolytes: formation, characterization and application. H. Dautzenberg, W. Jaeger, J. Kötz, B. Philipp, Ch. Seidel and D. Stscherbina. Carl Hanser Verlag, Munich, 1994. pp. xiv + 343, price DM168.00. ISBN 1-56990-127-9. ISBN 3-446-17127-4. Polymer International. 1995;38:106-.
[12] Norcross BE. Advanced Organic Chemistry: Reactions, Mechanisms, and Structure, 4th ed. (March, Jerry). Journal of Chemical Education. 1993;70:A51.
[13] Wolfe NL, Steen WC, Burns LA. Phthalate ester hydrolysis: Linear free energy relationships. Chemosphere. 1980;9:403-8.
[14] Carboxylic Acids and Esters (1969). John Wiley & Sons, Ltd.; 1969.
[15] Zagorodko O, Arroyo-Crespo JJ, Nebot VJ, Vicent MJ. Polypeptide-Based Conjugates as Therapeutics: Opportunities and Challenges. Macromolecular bioscience. 2016;17:1600316.
[16] Duro-Castano A, Nebot VJ, Nino-Pariente A, Arminan A, Arroyo-Crespo JJ, Paul A, et al. Capturing "Extraordinary" Soft-Assembled Charge-Like Polypeptides as a Strategy for Nanocarrier Design. Advanced materials (Deerfield Beach, Fla). 2017;29.
[17] Arroyo-Crespo Juan J, Deladriere C, Nebot Vicent J, Charbonnier D, Masiá E, Paul A, et al. Anticancer Activity Driven by Drug Linker Modification in a Polyglutamic Acid-Based Combination-Drug Conjugate. Advanced Functional Materials. 2018;28:1800931.
[18] Karagiannis GS, Pastoriza JM, Wang Y, Harney AS, Entenberg D, Pignatelli J, et al. Neoadjuvant chemotherapy induces breast cancer metastasis through a TMEM-mediated mechanism. Science translational medicine. 2017;9:eaan0026.
[19] Karagiannis GS, Condeelis JS, Oktay MH. Chemotherapy-induced metastasis: mechanisms and translational opportunities. Clinical & experimental metastasis. 2018.
[20] DeMichele A, Yee D, Esserman L. Mechanisms of Resistance to Neoadjuvant Chemotherapy in Breast Cancer. The New England journal of medicine. 2017;377:2287-9.
[21] Aras S, Zaidi MR. TAMeless traitors: macrophages in cancer progression and metastasis. British journal of cancer. 2017;117:1583.
[22] Genard G, Lucas S, Michiels C. Reprogramming of Tumor-Associated Macrophages with Anticancer Therapies: Radiotherapy versus Chemo- and Immunotherapies. Frontiers in Immunology. 2017;8:828.

General Discussion

GENERAL DISCUSSION

Current statistics show that around one in eight women will suffer from breast cancer. Growing incidence, increasing clinical costs derived from breast cancer care, and a general lack of effective therapeutics highlight the urgent need for novel treatment approaches [1]. Although postmenopausal age and hereditary predisposition remain critical risk factors, weight, alcohol consumption, diet, and lifestyle represent controllable risk factors [2]. Breast cancer is a systemic disease encompassing a very large group of illnesses characterized by abnormal cell growth. However, the existence of multiple subtypes, presenting differential signatures (e.g., hormone receptor expression, proliferative rate, invasiveness) requires effective and adaptive therapies for such a complex disease. The treatment approaches employed for breast cancer treatment currently depend on the stage and molecular subtype. Local treatment at early stages includes surgery and radiation therapy, while advanced stages of the disease may require systemic treatments based on chemotherapy, hormone therapy, and targeted therapy [3].

Around 15% of diagnosed breast cancers are considered triple negative (TNBC), a subtype associated with high metastasis incidence (and decreased overall survival) and affects mainly young women (<40) [4]. Among breast cancer subtypes, TNBC (lacking expression of hormone receptors) displays the most heterogeneous molecular features, which translates into a complex clinical presentation and differential response to standardized treatments. The lack of hormone receptors makes targeted or hormone therapy ultimately inadequate, and although some reports suggest that TNBC responds to chemotherapy better than other types of breast cancer, prognosis remains poor in most cases [5]. Therefore, research efforts into the design of effective treatments usually require a drug-combination strategy, rather than a monotherapy approach, to affect different cancer cell pathways.

During the preparation of this Thesis, we aimed to understand the complex pathology of TNBC through the establishment of two relevant preclinical TNBC murine models. Additionally, we also took on the challenging task of developing effective combination therapies for advanced stage TNBC.

Research using animal models has been instrumental in delivering improved therapies for breast cancer and generating new insights into the mechanisms that underpin the disease development [6]. However, the lack of accurately characterized multistage animal models (those capable of mimicking progressive stages of the human disease) that faithfully simulate the pathological features of human TNBC, including spontaneous metastasis or multiple side alterations, frequently hampers research [7]. Currently employed metastatic mouse models mimic advanced stages of the disease, but the requirement for infusions of high concentrations of aggressive breast cancer cells [7], the need to resect the primary tumor to allow metastasis, or slow metastatic development limits the application of these models.

Herein, we have described two preclinical spontaneously metastatic TNBC orthotopic murine models for the evaluation of advanced therapeutics: an immunodeficient human MDA-MB-231-Luc model and an immunocompetent mouse 4T1 model. These models offer a useful platform for testing/validation of advanced anticancer therapeutics, especially for the treatment of patients presenting with both primary tumors and metastasis. We took advantage of these preclinical models to evaluate the therapeutic potential of polymer-drug conjugate families, including the study of primary tumor growth inhibition, tumor characterization after treatment, and their evaluation of antimetastatic activity in lungs and axillary lymph nodes (ALN).

The immunocompetent model (BALB/c - 4T1) exhibited aggressive primary tumor evolution as densely packed masses with slight anemia, thrombocytosis, and reticulocytosis in the short term, and an acute leukemoid reaction that led to bone marrow failure and subsequent extramedullary hematopoiesis in the spleen and liver (splenomegaly and liver). Immunological disorders included lymphocytosis and complement system activation in the mid-to-long term. Additional tumor-related hematological disorders included β- and γ-immunoglobulinemia, increased neutrophil-to-lymphocytes (NLR) ratio, and increased levels of G-CSF correlating with a metastatic switch. After systemic administration of our polymer-drug conjugates, such cancer-derived pathologies represent biomarkers for tumor progression and as “therapeutic checkpoints” to evaluate the effectiveness of our preclinical treatments. As observed throughout the preparation of this Thesis, the knowledge and understanding of both models have advanced in parallel with the development of successive families of

conjugates, and new therapeutic checkpoints have arisen and then subsequently incorporated into our analyses. Accordingly, we employed the immunocompetent model for conjugate evaluations in **Chapter III** and **Chapter IV.** This model was used to demonstrate not only antitumor efficacy (primary tumor and metastasis progression) but also safety of selected treatments, including as drugs aminogluthethimide (endocrine) and doxorubicin (chemotherapy) and poly-L-glutamic acid (PGA) as carrier. A comprehensive analyses, concerning the antimetastatic activity of the conjugates both in lungs and ALN, modulation of tumor density and necrosis between treatments, and the decrease in tumor cell proliferation rate was performed. We also observed improvements at the immunological level following the most effective treatment, observing a reduction in leukocytosis and confirming a significant reduction in extramedullary hematopoiesis.

We later incorporated the immunosuppressed model (NOD/SCID MDA-MB-231-Luc) to evaluate conjugates in human-derived orthotopic breast cancer tumors. This model offers a new testing perspective, as it allowed us to explore TNBC therapies in the absence of an immune system, even if mice display a natural weakness and tolerate lower doses of chemotherapeutics [8]. We used this model to evaluate the efficacy of the combination conjugates based on a tyrosine kinase inhibitor (TKI) and a topoisomerase inhibitor (TI) (**Chapter V**) and tracked antimetastatic effect in lungs and ALN by non-invasive imaging techniques (BLI) thanks to the luciferin transfection of the MDA-MB-231 cell line. Interestingly, we found cancer associated adipocytes (CAA) in primary tumors of this model (**Chapter II**) and a partial restoration of the immune system at late stages of the disease. We hope that further experiments will explore the effect of our anticancer combination in the presence of cancer-associated adipocytes (CAA) and its role on immune restoration. Additional experiments will encompass the full histological characterization of critical organs and the analysis of cytokine levels from frozen serum.

As a functional tool for the characterization of disease progression, we employed NMR-metabolomics analysis of metastatic lungs and tumors. Metabolomic analysis can help us to understand the biochemical alterations sustaining the onset and progression of pathological processes, and the molecular mechanisms involved in response to new therapies. We previously reported a metabolomic study concerning functional comparisons of tumor tissue following treatments with the free form of Dox and HPMA-Dox (PK1), the first polymer-drug conjugate to reach the clinic [9]. Employing NMR-

metabolomics, we discovered that polymer conjugation leads to increased apoptosis, reduced glycolysis, and reduced levels of phospholipids when compared to the free Dox which all represent indicators of enhanced antitumor activity.

The metabolomic comparison of 4T1 and MDA-MB-231-Luc primary tumors suggested that specific metabolic alterations could explain the differences observed in growth rates, being much faster and aggressive the 4T1 model. We also confirmed that lipid metabolism alterations closely associate with TNBC malignancy and metastatic progression to lungs. Moreover, the metabolomic signature for lung metastases in each model reflected the different molecular and biochemical mechanisms associated with metastatic spread and, therefore, could be employed as a biomarker for disease monitoring during preclinical evaluation. Given the robust nature of NMR-metabolomics and the description of a metabolic signature of primary tumors and metastasis in our preclinical models, we now plan to extend the analysis to different organs and biofluids in mice treated with the most effective combination conjugates to correlate therapeutic benefit with metabolic alterations.

Our combination conjugates are part of one of the most successful classes of nanomedicine, polymer therapeutics (PT), which have been proposed as a valid therapeutic platform towards the development of viable breast cancer treatments. PT are considered new chemical entities with 24 products currently on the market, including PEGylated proteins, polymeric drugs, and one polymer-drug conjugate, and a growing pipeline in clinical development [10-13].

The intrinsic features of PT offer strategic advantages to overcome the main limitations of low molecular weight drugs. These features include (i) improved pharmacokinetic (PK) profiles and enhanced plasma half-life, (ii) the incorporation of targeting moieties for active targeting, (iii) carrier multivalency for tunable drug(s) loading capacity and drug combinations, (iv) controlled and sustained release of conjugated drugs via bioresponsive linkers; and (v) chemical stability, reduced immunogenicity of the bioactive compound, and optimal size in the nanoscale for tissue penetration [10].

Towards the development of a new generation PT, we followed the following guidelines: (i) the employment of biodegradable polymeric carriers, such as polyglutamates, which allow chronic treatments and avoids biopersistence and polymer-derived side effects, (ii) the use of sophisticated physico-chemical characterization methodologies in relevant biological media, allowing a better control of the final product and a broader and more reliable understanding of the developed systems. This characterization also allows for constant PT improvement via feedback to the original design from the observed physico-chemical behaviors, and (iii) the use of combination therapy as a primary tool to enhance therapeutic potential via drug synergism.

A growing number of polymeric conjugates are already implemented in preclinical and clinical trials in combination with free drugs or radiotherapy [14]. The importance of anticancer combination therapies has been corroborated via the development of VYEOXS™ (already in post-marketing observational study) by Celator Pharmaceuticals (now in Jazz Pharmaceuticals). VYXEOS™ (formerly CPX-351) employs a liposomal strategy (Combiplex®) that physically entraps a combination of cytarabine and daunorubicin in a synergistic ratio for the successful treatment of acute myeloid leukemia [15] and represents a clear example in which rational design provides benefits to the patient. Combination therapy may provide further benefit when compared to physical entrapment, as the presence of bio-responsive polymer-drug linker(s) allows better control of drug PK and improved therapeutic output. Of note, the incorporation of drug combinations into the same polymeric carrier represents the only strategy that ensures the transport of both drugs to the same target cell within the same timeframe [16].

The Polymer Therapeutics Laboratory at CIPF, Valencia, currently works in the development of polymer-based combination conjugates for the treatment of hormone-dependent advanced (metastatic) breast cancer. The first attempt to develop a combination conjugate employed the copolymer 2-(hydroxypropyl) methacrylamide (HPMA), bearing a combination of endocrine (aromatase inhibitor, aminogluthethimide (AGM)) and chemotherapy (Dox) for the treatment of breast cancer in postmenopausal patients [17, 18].

We based the design of HPMA-AGM-Dox on two main pillars: (i) the demonstrated activity of the copolymer HPMA-Dox (PK1) in phase II clinical trials in

chemoresistant breast cancer patients [19], and (ii) aromatase inhibitors act synergistically with chemotherapy [20]. HPMA-AGM-Dox displayed enhanced *in vitro* breast cancer cell toxicity compared to a combination of the unconjugated drugs or individual polymer-drug conjugates [17, 18]. Recently, *in vivo* proof of concept for antitumor drug synergism with the combination conjugate has been achieved in an aggressive metastatic 4T1 murine breast cancer model [21]. Enhanced activity appeared primarily due to improved drug release kinetics and the bioavailability of both drugs in the same cell at the same time. Importantly, tumor sample protein expression analysis demonstrated robust differences in tumor-associated angiogenesis pathways, which could be explained by the estrogen inhibition induced by AGM. This effect was enhanced by an autophagic cell death mechanism only associated with the combination conjugate [9, 18]. These results demonstrated for the first time that the rational design of a combination PT could significantly enhance safety as well as therapeutic drug output. This concept has been further explored and reinforced both *in vitro* and *in vivo* through studies in our laboratory and other research groups [22].

However, limitations with existing polymeric systems, such as a lack of biodegradability, biocompatibility, and multifunctionality, inevitably lead to side effects and poor patient compliance. A new generation of biodegradable polymers are excellent candidates for drug delivery, as they can overcome the previously mentioned limitations. Particularly polypeptides, since clinical benefits have been achieved with polymeric drugs, such as Copaxone [23] (one of the top ten selling drugs) [10, 24] and PGA-based anticancer therapeutics such as Opaxio™ [25], designated as orphan drug in combination with radiotherapy and temozolomide for the treatment of glioblastoma multiforme.

Encouraged by the successful application of PGA in the conjugation of single chemotherapeutic drugs [25] and their combination [22, 26], as well as our prior studies combining endocrine and chemotherapy [17, 18], we directed the first efforts of this Thesis towards the development of the first PGA-based combination conjugates bearing chemotherapeutic and estrogen modulating agents for the treatment of breast cancer (**Chapter III**). Furthermore, we took this opportunity to explore how the incorporation of different polymer-drug linkers influences conjugate characteristics and biological fate.

AGM is a commercially available first-generation aromatase inhibitor, and its chemical structure permits simple derivatization and easy conjugation to PGA. For these reasons, we considered the application of AGM as a means to achieve proof of concept. AGM has been superseded by more potent inhibitors, including the triazoles class (anastrozole and letrozole), although these lack the functional groups required for conjugation, and the steroid exemestane (currently being explored in the lab).

Keeping invariable the direct attachment of Dox through an amide bond, we studied the influence of the incorporation of two drug ratios (5:5 (LL) and 10:5 (HL) AGM: Dox) for AGM via small drug linkers. At the *in vitro* level, we found that the addition of small, short, and flexible Gly or Gly–Gly linker led to enhanced cytotoxicity when compared to a more bulky GFLG linker or the direct linkage of AGM. We also observed a synergistic *in vivo* antitumor effect in animals treated with the PGA-(G-AGM)$_{LL}$-Dox and PGA-(G-AGM)$_{HL}$-Dox combination conjugates, as compared with the single conjugates (alone or added simultaneously).

The study of *in vitro* drug release represented a vital point of this research. When we compared the release profiles of both drugs under the same experimental conditions (i.e. in the presence of cathepsin B mimicking lysosomotropic delivery), we noted a strong influence of the linking chemistry and drug ratio on drug release kinetics. Interestingly, when we compared the two most relevant combination conjugates which differed only in their level of AGM loading, the PGA-(G-AGM)$_{HL}$-Dox combination conjugate with high loading displayed diminished drug release kinetics when compared to the PGA-(G-AGM)$_{LL}$-Dox combination conjugate with lower loading, perhaps due to structural modifications in the polymer chain. However, we noted a similar cytotoxic effect for both LL and HL conjugates, suggesting that they mediate their effect through different molecular mechanisms. While attempting to understand this behavior, we realized that the degradation process requires efficient cellular uptake and access of the proteolytic trigger (mainly cathepsin B) to cleave the polymer-drug linker [27]. Molecular access is directly correlated with the 3D spatial disposition of the polypeptide, which, in turn, may be influenced by structural factors such as the conjugated moieties [27], drug loadings [28], drug ratios [29], linking chemistry, and physicochemical descriptors ruling the nano-bio interface [30].

To establish direct structure-activity relationships (SAR), we looked for critical physico-chemical descriptors driving *in vitro* and *in vivo* output of PGA-AGM-Dox conjugates. Circular dichroism (CD) and Small Angle Neutron Scattering (SANS) analysis of the most effective AGM-Dox combination conjugate (PGA-(G-AGM)$_{LL}$-Dox) revealed the impact of the Gly linker on the structure of the whole macromolecule. The Gly linker partially shifts the secondary structure to alpha helix, when compared to the parent conjugate with direct attachment of both drugs. Also, this conjugate presented with smaller and more compact aggregates with no evidence of internal ordering. Overall, the data provided by CD, DLS, and SANS, can correlate structure and conformation with drug release and biological output. Results from *in vitro* and *in vivo* experiments suggest that the drug release that drives the antitumor activity of AGM-Dox conjugates can be modulated by the rational design and of polymer-drug linking chemistry.

After the development of this first family of conjugates, we next aimed to further enhance its antitumor activity. We discovered that faster release of Dox, the more active agent, when compared to AGM boosted drug synergism. Also, we noted that the release of both drugs relied exclusively on the heterogeneous expression (at both the patient [31] and tumor level [32]) of various proteolytic enzymes within the tumor microenvironment (TME). This highlights the need for patient stratification in PT treatment cohorts, a requirement exemplified by clinical data obtained for Opaxio®, which displayed optimal activity in phase III clinical trials in premenopausal women with levels of estrogen high enough to promote cathepsin B activity [33].

With these considerations, alongside the acidic nature of the TME [34], we decided to implement pH-sensitive hydrazone Dox linkers to the PGA carrier and maintained the linking chemistry for AGM. We employed two different pH-sensitive hydrazone linkers: the direct conjugation through the C-13 Dox ketone [35-37] or conjugation employing a flexible, hydrophobic, and longer maleimido linker (EMCH). This Dox-linker strategy has its origin on the development of Aldoxorubicin (formerly, INNO-206, EMCH-Dox) as a *bovine serum albumin* (*BSA*)-binding-Dox prodrug [38] and has been reported previously for a PGA-based combination conjugate [22].

To understand the biological implications of different drug linkers and drug loading/ratio in our conjugates, we performed cell toxicity assays. Interestingly, and in

contrast with our previously reported PGA-(G-AGM)-Dox family [39], we did not observe significant differences in cell toxicity between the single and the combination conjugates (for the most relevant combination conjugate, PGA-(G-AGM)-$(Hyd\text{-}Dox)_{LL}$), indicating a lack of AGM:Dox synergism at the drug ratios employed achieved hydrazone-mediated conjugation. While we considered that drug synergism required the balanced co-delivery of the drug combination and rapid Dox release via a hydrazone linker, the cathepsin B degradation studies instead indicated the critical nature of the final conjugate solution conformation. In the case of the most active conjugate, (PGA-(G-AGM)-$(Hyd\text{-}Dox)_{LL}$), the more rapid Dox release at very early time-points at pH 5 and in the presence of cathepsin B demonstrated the preferential hydrolytic mechanism triggering Dox release offering the greatest antitumor effect. However, the final relative release profile comparing Dox *vs.* AGM (with greater overall AGM bioavailability) could explain the absence of drug synergism as we obtained an inverse relative bioavailable AGM: Dox ratio from that previously identified as synergistic [8].

Concerning the *in vivo* evaluation, the combination conjugate (PGA-(G-AGM)-$(Hyd\text{-}Dox)_{LL}$ presented similar antitumor activity as the combination conjugate (PGA-(G-AGM)-$(EMCH\text{-}Dox)_{LL}$. Additionally, we demonstrated improved antitumor and antimetastatic activity with hydrazone-based combination conjugates when compared with the direct conjugation. [39] However, the observed reduction of the overall survival (OS) in mice motivated us to discard the EMCH-based subfamily of conjugates. We proposed two different explanations for the observed associated toxicity of the combination conjugate. The first relates to the increased final solution viscosity (due to the high conjugate concentration needed to reach the desired Dox equivalents), a parameter with the potential to affect proper blood distribution. The second relates to the larger size and heightened ability of this combination conjugate to aggregate in solution, which might promote accumulation in other organs, as well as in the tumor. Additionally, this increased in size may also promote certain protein corona aggregation upon arrival to the bloodstream, while this effect could also enhance the size and promote undesired side effects, leading to systemic toxicity. The higher hydropic degeneration supports both explanations (vacuolar degeneration) observed in livers from animals treated with this conjugate. Although none of our experiments demonstrated any apparent AGM effect, our murine model may be too aggressive, and we postulated whether the application of

these conjugates in other models (towards chronic application) could display additional benefits from AGM.

To understand the molecular basis of the responses to the different combination conjugates, we implemented a battery of RNA-seq analysis of tumor tissues derived from treated animals and compared genes differentially regulated between each possible pair-wise comparison. Through this experiments, we observed a more general effect of PGA-(G-AGM)-$(Hyd\text{-}Dox)_{LL}$ when treating tumor cells compared to PGA-(G-AGM)-$(EMCH\text{-}Dox)_{LL}$. PGA-(G-AGM)-$(EMCH\text{-}Dox)_{LL}$ involves fewer targeted processes, such as stem cell proliferation and epidermal cell differentiation, indicating a role of this combination conjugate in reducing cancer cell growth. Additionally, PGA-(G-AGM)-$(Hyd\text{-}Dox)_{LL}$ specifically activates general processes such as defense/immune responses, inflammation, phagocytosis, cell signaling and metastasis, suggesting that this combination conjugate is more effective in triggering a general immune response that might contribute to stall tumor progression, improve health status of the individual, and increase survival rates.

Finally, we decided to exploit all the expertise acquired and techniques implemented to develop a more challenging PGA-based combination conjugate. Among the therapeutic approaches devised for TNBC treatment, inhibition of SRC (proto-oncogene tyrosine-protein kinase) deserves particular interest due to critical roles in cell adhesion and motility [40], which both represent essential mechanisms for cancer progression and invasiveness. Accordingly, TNBC cell lines display high sensitivity to tyrosine kinase inhibitors (TKIs) in preclinical studies [41]. Additional data have indicated a heightened sensitivity of the mesenchymal-like TNBC subtype to TKIs [42, 43], which may be explained by the overexpression of genes related to cell motility in this particular TNBC subtypes and the crucial role of SRC-family kinases in cell migration. Recent research have demonstrated robust drug synergism between TIs and TKIs. However, only a few examples in the literature discuss combinations of such drugs within polymer backbones for the treatment of breast cancer. These studies include non-biodegradable polyethylene glycol (PEG)-ylated peptidic nanocarriers [44] or micelles [45] where the polymer physically entraps one or both drugs. On this basis, we believed that we could enhance the already reported drug synergism by the rational design of responsive polymer-drug(s) linkers towards the development of the PGA-combination

conjugate for a TKI and a TI. A first conjugate employing direct conjugation of both drugs (amide linker for the TI and ester linker for the TKI) lacked drug synergism due to an inappropriate pharmacokinetics. As a consequence, we took advantage of the multivalency of PGA as carrier, and rationally designed drug linkers to promote and improve drug synergism by the incorporation of two modifications: a hydrazone linker for the TI (to achieve fast TI release) and a simple amino acid (Val) [46] linker for TKI (to diminish TKI release).

This optimized combination conjugate demonstrated elevated *in vitro* drug synergism in two TNBC cell lines (4T1 and MDA-MB-231-Luc). Importantly, we observed enhanced *in vivo* safety as at 1.5mg/Kg drug equivalents, the TI resulted lethal at the second dose, while animals treated with the PGA-(Val-TKI)-(Hyd-TI) did not suffer any visible treatment-related toxicity even after six doses. As well as anticancer effects *in vivo*, leading to 50% of primary tumor growth reduction and almost total remission of lung metastasis. Although this research currently remains unfinished, we demonstrate a significantly improved *in vivo* output, and we hope the additional ongoing histopathological studies to analyze cancer cell proliferation in primary tumors, metastasized lungs and major organs, will allow a better understanding of the therapeutic value of such conjugates.

Undesirably, after treatments with our non-active single conjugates PGA-Val-TKI and PGA-Hyd-TI separately or as physical sum, we observed pro-metastatic behavior in the lungs. Several studies of anticancer treatments have demonstrated that some chemotherapeutics modulate the tumor microenvironment and promote breast cancer cell intravasation and dissemination to distant sites [47-49]. Following treatment, tumor cells from primary breast lesions may intravasate and disseminate at sites of microanatomical structures called tumor microenvironment of metastases (TMEM). The particular physico-chemical characteristics or drug-release kinetics of our single conjugates could modulate the tumor microenvironment in this way. Other possible explanation could involve the activity of tumor macrophages [50]. In response to tumor presence, classically activated (M1) macrophages activate, secrete pro-inflammatory cytokines, and play tumouricidal roles. Alternatively activated (M2) macrophages secrete anti-inflammatory cytokines IL-10 and TGF-β and play tumourigenic roles. However, so-called tumor-associated macrophages (TAMs) display the M2-like phenotype and exhibit pro-

tumourigenic features. Studies have described how chemotherapies could reprogram these TAMs to facilitate metastasis progression [51]. A series of further experiments are ongoing to investigate the possibilities with the hope of controlling undesired effects.

In conclusion, we suggest that the results presented indicate that the development of these PGA-based combination conjugates paves the way for the construction of more effective rationally-designed treatments for breast cancer, and in particular, metastatic TNBC.

References

[1] Blumen H, Fitch K, Polkus V. Comparison of Treatment Costs for Breast Cancer, by Tumor Stage and Type of Service. American Health & Drug Benefits. 2016;9:23-32.
[2] http://www.breastcancer.org.
[3] http://www.cancer.org.
[4] Tano SV, Kavanaugh MM, Peddi P, Mansour RP, Shi R, Burton GV. Triple negative breast cancer (TNBC): Analysis of age and stage distribution and survival between African American and Caucasian women in a predominant low-income population. Journal of Clinical Oncology. 2017;35:e12586-e.
[5] Wahba HA, El-Hadaad HA. Current approaches in treatment of triple-negative breast cancer. Cancer Biology & Medicine. 2015;12:106-16.
[6] Holen I, Speirs V, Morrissey B, Blyth K. In vivo models in breast cancer research: progress, challenges and future directions. 2017;10:359-71.
[7] Manning HC, Buck JR, Cook RS. Mouse Models of Breast Cancer: Platforms for Discovering Precision Imaging Diagnostics and Future Cancer Medicine. Journal of Nuclear Medicine. 2016;57:60S-8S.
[8] Wunderlich M, Mizukawa B, Chou F-S, Sexton C, Shrestha M, Saunthararajah Y, et al. AML cells are differentially sensitive to chemotherapy treatment in a human xenograft model. Blood. 2013;121:e90-e7.
[9] Arminan A, Palomino-Schatzlein M, Deladriere C, Arroyo-Crespo JJ, Vicente-Ruiz S, Vicent MJ, et al. Metabolomics facilitates the discrimination of the specific anti-cancer effects of free- and polymer-conjugated doxorubicin in breast cancer models. Biomaterials. 2018;162:144-53.
[10] Duncan R. Polymer therapeutics: Top 10 selling pharmaceuticals - what next? Journal of controlled release : official journal of the Controlled Release Society. 2014;190:371-80.
[11] Garnock-Jones KP. Naloxegol: a review of its use in patients with opioid-induced constipation. Drugs. 2015;75:419-25.
[12] Thomas J, Levy H, Amato S, Vockley J, Zori R, Dimmock D, et al. Pegvaliase for the treatment of phenylketonuria: Results of a long-term phase 3 clinical trial program (PRISM). Molecular genetics and metabolism. 2018;124:27-38.
[13] Konkle BA, Stasyshyn O, Chowdary P, Bevan DH, Mant T, Shima M, et al. Pegylated, full-length, recombinant factor VIII for prophylactic and on-demand treatment of severe hemophilia A. Blood. 2015;126:1078-85.
[14] Canal F, Sanchis J, Vicent MJ. Polymer--drug conjugates as nano-sized medicines. Current opinion in biotechnology. 2011;22:894-900.
[15] Tolcher AW, Mayer LD. Improving combination cancer therapy: the CombiPlex((R)) development platform. Future oncology (London, England). 2018;14:1317-32.

[16] Eldar-Boock A, Miller K, Sanchis J, Lupu R, Vicent MJ, Satchi-Fainaro R. Integrin-assisted drug delivery of nano-scaled polymer therapeutics bearing paclitaxel. Biomaterials. 2011;32:10.1016/j.biomaterials.2011.01.073.
[17] Vicent MJ, Greco F, Nicholson RI, Paul A, Griffiths PC, Duncan R. Polymer therapeutics designed for a combination therapy of hormone-dependent cancer. Angewandte Chemie (International ed in English). 2005;44:4061-6.
[18] Greco F, Vicent MJ, Gee S, Jones AT, Gee J, Nicholson RI, et al. Investigating the mechanism of enhanced cytotoxicity of HPMA copolymer-Dox-AGM in breast cancer cells. Journal of controlled release : official journal of the Controlled Release Society. 2007;117:28-39.
[19] Vasey PA, Kaye SB, Morrison R, Twelves C, Wilson P, Duncan R, et al. Phase I clinical and pharmacokinetic study of PK1 [N-(2-hydroxypropyl)methacrylamide copolymer doxorubicin]: first member of a new class of chemotherapeutic agents-drug-polymer conjugates. Cancer Research Campaign Phase I/II Committee. Clinical cancer research : an official journal of the American Association for Cancer Research. 1999;5:83-94.
[20] Bauerfeind I, Elling D, Heinemann V. Lapatinib in the Treatment of Hormone Receptor-Positive/ErbB2-Positive Breast Cancer. Breast Care. 2010;5:13-5.
[21] C. Deladriere PT, University of Valencia, Spain 2013.
[22] Markovsky E, Baabur-Cohen H, Satchi-Fainaro R. Anticancer polymeric nanomedicine bearing synergistic drug combination is superior to a mixture of individually-conjugated drugs. Journal of controlled release : official journal of the Controlled Release Society. 2014;187:145-57.
[23] Weinstock-Guttman B, Nair KV, Glajch JL, Ganguly TC, Kantor D. Two decades of glatiramer acetate: From initial discovery to the current development of generics. Journal of the neurological sciences. 2017;376:255-9.
[24] Greco F, Vicent MJ. Combination therapy: opportunities and challenges for polymer-drug conjugates as anticancer nanomedicines. Advanced drug delivery reviews. 2009;61:1203-13.
[25] Bernabeu E, Cagel M, Lagomarsino E, Moretton M, Chiappetta DA. Paclitaxel: What has been done and the challenges remain ahead. International journal of pharmaceutics. 2017;526:474-95.
[26] Baabur-Cohen H, Vossen LI, Kruger HR, Eldar-Boock A, Yeini E, Landa-Rouben N, et al. In vivo comparative study of distinct polymeric architectures bearing a combination of paclitaxel and doxorubicin at a synergistic ratio. Journal of controlled release : official journal of the Controlled Release Society. 2017;257:118-31.
[27] Giménez V, James C, Armiñán A, Schweins R, Paul A, Vicent MJ. Demonstrating the importance of polymer-conjugate conformation in solution on its therapeutic output: Diethylstilbestrol (DES)-polyacetals as prostate cancer treatment. Journal of Controlled Release. 2012;159:290-301.
[28] Li M, Song W, Tang Z, Lv S, Lin L, Sun H, et al. Nanoscaled poly(L-glutamic acid)/doxorubicin-amphiphile complex as pH-responsive drug delivery system for effective treatment of nonsmall cell lung cancer. ACS Appl Mater Interfaces. 2013;5:1781-92.
[29] Yunzhu L, Lingling W, Qingrong Q. Synthesis of Novel Peptide Dendrimers PDL-GB2 and PDL-G2. The Scientific World Journal. 2015;2015:907859.
[30] Zagorodko O, Arroyo-Crespo JJ, Nebot VJ, Vicent MJ. Polypeptide-Based Conjugates as Therapeutics: Opportunities and Challenges. Macromolecular bioscience. 2016;17:1600316.
[31] Zhong Y, Zhao J, Gu Yj, Zhao Y-f, Zhou Y-w, Fu G-X. Differential levels of cathepsin B and L in serum between young and aged healthy people and their association with matrix metalloproteinase 2. Archives of Gerontology and Geriatrics. 2015;61:285-8.
[32] Atkinson S, Andreu Z, Vicent M. Polymer Therapeutics: Biomarkers and New Approaches for Personalized Cancer Treatment. Journal of Personalized Medicine. 2018;8:6.
[33] Chipman SD, Oldham FB, Pezzoni G, Singer JW. Biological and clinical characterization of paclitaxel poliglumex (PPX, CT-2103), a macromolecular polymer-drug conjugate. International journal of nanomedicine. 2006;1:375-83.

[34] Feng L, Ziliang D, Danlei T, Yicheng Z, Zhuang L. The acidic tumor microenvironment: a target for smart cancer nano-theranostics. National Science Review. 2018;5:269-86.
[35] van Heeswijk WAR, Stoffer T, Eenink MJD, Potman W, van der Vijgh WJF, v.d. Poort J, et al. Synthesis, Characterization and Antitumor Activity of Macromolecular Prodrugs of Adriamycin. In: Anderson JM, Kim SW, editors. Recent Advances in Drug Delivery Systems. Boston, MA: Springer US; 1984. p. 77-100.
[36] Quan L, Zhang Y, Crielaard BJ, Dusad A, Lele SM, Rijcken CJF, et al. Nanomedicines for Inflammatory Arthritis: Head-to-Head Comparison of Glucocorticoid-Containing Polymers, Micelles, and Liposomes. ACS nano. 2013;8:458-66.
[37] Pang X, Jiang Y, Xiao Q, Leung AW, Hua H, Xu C. pH-responsive polymer–drug conjugates: Design and progress. Journal of Controlled Release. 2016;222:116-29.
[38] Walker L, Perkins E, Kratz F, Raucher D. Cell penetrating peptides fused to a thermally targeted biopolymer drug carrier improve the delivery and antitumor efficacy of an acid-sensitive doxorubicin derivative. International journal of pharmaceutics. 2012;436:825-32.
[39] Arroyo-Crespo JJ, Deladriere C, Nebot VJ, Charbonnier D, Masiá E, Paul A, et al. Anticancer Activity Driven by Drug Linker Modification in a Polyglutamic Acid-Based Combination-Drug Conjugate. Advanced Functional Materials. 2018;28:1800931.
[40] Gelman IH. Src-family tyrosine kinases as therapeutic targets in advanced cancer. Frontiers in bioscience (Elite edition). 2011;3:801-7.
[41] This reference has been ommited purposely
[42] Lehmann BD, Bauer JA, Chen X, Sanders ME, Chakravarthy AB, Shyr Y, et al. Identification of human triple-negative breast cancer subtypes and preclinical models for selection of targeted therapies. The Journal of clinical investigation. 2011;121:2750-67.
[43] This reference has been ommited purposely
[44] This reference has been ommited purposely
[45] This reference has been ommited purposely
[46] Vogus DR, Evans MA, Pusuluri A, Barajas A, Zhang M, Krishnan V, et al. A hyaluronic acid conjugate engineered to synergistically and sequentially deliver gemcitabine and doxorubicin to treat triple negative breast cancer. Journal of controlled release : official journal of the Controlled Release Society. 2017;267:191-202.
[47] Karagiannis GS, Pastoriza JM, Wang Y, Harney AS, Entenberg D, Pignatelli J, et al. Neoadjuvant chemotherapy induces breast cancer metastasis through a TMEM-mediated mechanism. Science translational medicine. 2017;9:eaan0026.
[48] Karagiannis GS, Condeelis JS, Oktay MH. Chemotherapy-induced metastasis: mechanisms and translational opportunities. Clinical & experimental metastasis. 2018.
[49] DeMichele A, Yee D, Esserman L. Mechanisms of Resistance to Neoadjuvant Chemotherapy in Breast Cancer. The New England journal of medicine. 2017;377:2287-9.
[50] Aras S, Zaidi MR. TAMeless traitors: macrophages in cancer progression and metastasis. British journal of cancer. 2017;117:1583.
[51] Genard G, Lucas S, Michiels C. Reprogramming of Tumor-Associated Macrophages with Anticancer Therapies: Radiotherapy versus Chemo- and Immunotherapies. Frontiers in Immunology. 2017;8:828.

Final Conclusions

FINAL CONCLUSIONS

The objectives achieved during the development of this Thesis have significant relevance for the treatment of triple-negative breast cancer (TNBC) with biodegradable polymer-based combination conjugates. We highlight the main conclusions below:

1. We have characterized two spontaneously metastatic and preclinically relevant murine models of TNBC for testing and validation of nanomedicine. In summary, we have studied metastasis progression via hematological analysis, identified specific biomarkers of metastasis via nuclear magnetic resonance (NMR) metabolomics, histopathologically characterized relevant organs presenting pathologies as a consequence of tumor development, and finally detected the modulation of tumor cytokines in plasma and identified descriptors that allow advanced antitumor treatment evaluation.

2. We have developed three families of polymer-drug combination conjugates, based on the biodegradable carrier poly-L-glutamic acid incorporating two drugs in a synergistic ratio for treatment of TNBC.

3. To improve and optimize drug release and potentiate synergism, we have developed and fully characterized polymer-drug linkers that are sensitive to different biological stimuli. These included peptide bonds (degraded by proteolytic enzymes overexpressed in most solid tumors and tumor cell lysosomes), ester bonds, (sensitive to pH and esterases), and pH-sensitive bonds, (for drug release drugs at the required ratio and quantity in the slightly acidic conditions of the tumor microenvironment and/or endosome/lysosome).

4. We employed advanced characterization techniques in biologically relevant solutions to physicochemically characterize our developed conjugates, thereby establishing structure-activity relationships (SARs).

5. We have evaluated *in vitro* the developed conjugates in clinically relevant breast cancer cell lines. Studies of cytotoxicity, synergism, cellular internalization, and drug release (in biologically relevant conditions in the presence of degrading enzymes) have provided crucial information permitting advances in conjugate design.

6. We then *in vivo* evaluated promising conjugates in our established preclinical murine models, demonstrating antitumor/antimetastatic efficacy and safety. Furthermore, we monitored previously identified disease descriptors that permitted assessment of the therapeutic potential of polymer-drug combination conjugates.

7. Finally, we studied primary tumor at transcriptomic and metastasized lungs at transcriptomic and metabolomic level. The transcriptomic analysis clarified cell death mechanisms following conjugate treatments and allowed us to establish direct relationships between cell death mechanisms and physicochemical descriptors of the polymer-drug combination conjugates. The metabolomic results identified significant differences in the production/consumption of critical metabolites during metastatic development, allowing us a complete understanding of the molecular mechanisms at play.

APPENDIX

THESIS PROJECT, OBJECTIVES,

MAIN METHODOLOGY,

RESULTS AND CONCLUSIONS IN SPANISH

1. INTRODUCCIÓN, ANTECEDENTES Y MARCO TEMÁTICO DE LA TESIS

El cáncer de mama es el cáncer más frecuente en mujeres y la segunda causa de muerte después de las enfermedades cardiovasculares. La supervivencia a esta enfermedad ha mejorado sustancialmente en la última década gracias a la incorporación de nuevas terapias y desarrollo de nuevas herramientas para el diagnóstico precoz [1]. Sin embargo, este porcentaje no ha mejorado en tumores metastásicos (estadío avanzado de la enfermedad). Se trata de una patología altamente heterogénea que presenta gran diversidad genética que se traduce en diferencias en cuanto al comportamiento biológico y, por lo tanto, grandes diferencias en las respuestas terapéuticas entre los pacientes ante un mismo tratamiento [2-4]. Ante este escenario, se hacen necesaria la aplicación de diferentes abordajes terapéuticos que actúen sobre diferentes vías de desarrollo de la enfermedad.

Entre los diferentes subtipos de cáncer de mama se encuentra el cáncer de mama triple negativo (CMTN) que representa entre un 15-20% de todos los carcinomas de mama [5]. El CMTN se caracteriza, molecularmente, por la falta de expresión del receptor de estrógeno (ER), el receptor de progesterona (PR) y el receptor-2 del factor de crecimiento epidérmico humano (HER2) y presenta un mal pronóstico clínico debido a la agresividad clínica del tumor primario, a la alta tasa de metástasis y a la deficiente detección temprana de la enfermedad. La mayoría de los pacientes con CMTN mantiene la enfermedad residual después del tratamiento, por lo que existe un alto riesgo de reincidencia y por lo tanto, hay una disminución en la supervivencia después de los 3-5 años del tratamiento. Los pacientes de CMTN presentan una esperanza de vida menor a 5 años desde el diagnóstico [2].

Actualmente, existe poca información en la que basarse para la selección del tratamiento adecuado para CMTN. Éste subtipo de cáncer es insensible a algunos de los tratamientos más eficaces disponibles para el cáncer de mama, incluyendo la terapia dirigida al HER2 (trastuzumab), los tratamientos endocrinos (tamoxifeno), o los inhibidores de la aromatasa. Los tratamientos convencionales quimioterapéuticos suelen ser el tratamiento de elección ya que se ha aceptado que los CMTN muestran alta quimiosensibilidad [5].

Entre los fármacos más frecuentemente utilizados se emplean principalmente las antraciclinas y los taxanos, que han demostrado en estudios clínicos fase I ser efectivos en los estadios tempranos de la enfermedad [6]. Sin embargo, los pacientes en estadíos avanzados de la enfermedad han mostrado una baja respuesta a este tipo de terapia debido a resistencias a múltiples fármacos (MDR). Estos motivos justifican la necesidad del desarrollo de nuevos fármacos dirigidos a nuevas dianas terapéuticas [5].

En la última década los avances en nanotecnología y ciencia de materiales han permitido el desarrollo de sistemas innovadores de liberación controlada de fármacos y técnicas de imagen que han aportado importantes beneficios para la salud humana y han abierto nuevos mercados a la industria farmacéutica [7, 8]. Los Polímeros Terapéuticos han sido considerados una de las nanomedicinas más ventajosas. Estas nuevas entidades químicas engloban una variedad de sistemas macromoleculares complejos cuya característica común es la presencia de un enlace químico (covalente) entre el agente(s) bioactivo y el transportador polimérico soluble en medio acuoso.

Como principales beneficios, la conjugación de fármacos a transportadores poliméricos, (i) aumenta su solubilidad acuosa y (ii) cambia la farmacocinética del fármaco tanto a nivel sistémico como a nivel celular, con la posibilidad de mejorar claramente el valor terapéutico de los fármacos. Además, (iii) el uso de nanoconjugados ofrece un alta especificidad tumoral debido al efecto de permeabilidad y retención aumentada (EPR,‘enhanced permeability and retention effect’) [9, 10] y por tanto (iv) una menor toxicidad sistémica. Asimismo, (v) permiten la superación de mecanismos quimioresistentes, al emplear la endocitosis como principal mecanismo de internalización celular. Gracias a sus características intrínsecas a nanoescala (controlada multifuncionalidad, arquitectura, y presencia de elementos biosensibles), esta clase de nanofármacos pueden ser diseñados para que expongan características únicas. (vi) Son capaces de alcanzar lugares a los que otros 'nanotransportadores’ más grandes (i.e. liposomas) no se pueden llegar. (vii) Son capaces de cruzar barreras biológicas naturales y muestran un tráfico celular específico dependiente de las arquitecturas químicas que posean. Por último y no menos importante, (viii) permiten un mayor control de la farmacocinética de el/los fármaco/s conjugado/s gracias a la incorporación de enlaces polímero-fármaco biosensible [11].

A día de hoy, fruto de la investigación translacional en el ámbito de Polímeros Terapéuticos, se han transferido exitosamente 24 productos al mercado. Dos de ellos, -Glatiramer (Sanofi Aventis-Teva) y Neulasta (Amgen)- para el tratamiento de esclerosis múltiple y para tratamientos anticancerígenos respectivamente, se hallan dentro de los 10 fármacos más vendidos en EEUU [12]; demostrando así su beneficio clínico. Entre los productos comercializados se encuentran fármacos poliméricos [13], conjugados polímero-proteína [14] (37) y conjugados polímero-aptamero [15] que actualmente se encuentran en uso clínico, y un conjugado polímero-fármaco (Movantik) para uso oral. [16]

Debido a la complejidad molecular de las patologías humanas a menudo se emplean múltiples fármacos en combinación que son administrados simultáneamente para atacar diferentes dianas farmacológicas y de este modo mejorar la eficacia a la vez que disminuye la resistencia. Por este motivo surge la llamada terapia de combinación polimérica [17]. Los conjugados polímero-fármaco son excelentes herramientas para el desarrollo de este interesante concepto [18].

Un creciente número de conjugados poliméricos ya han sido probados clínicamente en combinación con fármacos libres o radioterapia [18, 19]. Sin embargo, el empleo de polímeros que contienen múltiples fármacos conjugados a través de enlaces biodegradables, permite tener un mayor control en la liberación de los fármacos, siendo además la única estrategia que asegura el transporte efectivo de ambos fármacos a la misma célula tumoral con adecuada farmacocinética [19, 20] haciendo esta estrategia más eficiente con respecto al resto. El laboratorio de Polímeros Terapéuticos es pionero en el desarrollo de conjugados de combinación para el tratamiento de cáncer de mama hormono-dependiente avanzado (metastásico). Este concepto fue demostrado con el conjugado modelo basado en el transportador no biodegradable (copolimero 2-(Hidroxipropil) metacrilamida (HPMA)-(AGM)-Dox, que transporta una combinación de terapia endocrina (el inhibidor de aromatasa aminoglutetimida, AGM) indicado para pacientes postmenopáusicas) y quimioterapia (Dox) para el tratamiento de cáncer de mama [17]. Su diseño se basó en dos observaciones principalmente: (i) el copolímero HPMA-Dox (PK1) es un conjugado en fase clínica II con demostrada actividad en pacientes con tumores de mama quimioresistentes [21] y (ii) los inhibidores de aromatasa

pueden actuar de forma sinérgica con quimioterapia [22] especialmente en mujeres postmenopáusicas (77% incidencia). A pesar de que AGM es un inhibidor de aromatasa de primera generación, presentaba una funcionalización química muy adecuada para ser conjugado al polímero y estaba disponible comercialmente. Por tanto era un fármaco adecuado en esta primera fase de prueba de concepto [23]. Actualmente, AGM ha sido reemplazado por inhibidores más potentes pertenecientes a la clase de los triazoles (anatrozol y letrozol) (no adecuados para conjugación) y, recientemente, por el inactivador esteroidal exemestano (explorado actualmente en el laboratorio). Estos fármacos presentan un mejor perfil de toxicidad y una mayor actividad antitumoral cuando se compara con la terapia convencional.

El conjugado de combinación (HPMA-AGM-Dox) demostró un aumento muy marcado de citotoxicidad en modelos celulares de cáncer de mama positivos en receptores de estrógenos (ER+) (MCF-7 y MCF-7ca (transfectada de forma estable con el gen humano aromatasa)) y también *in vivo* en un modelo de cáncer de mama metastásico (4T1), cuando dicha citotoxicidad se comparó con los conjugados individuales por separado (HPMA-Dox) o una mezcla física de ambos (HPMA-Dox + HPMA-AGM). Diferentes estudios mecanísticos comparativos entre HPMA-Dox y HPMA-AGM-Dox demostraron que esta sinergia es únicamente observable cuando los dos fármacos se hallan covalentemente unidos al mismo portador polimérico. Además de ello, se observó una biodistribución diferente entre los dos conjugados, una cinética de liberación distinta cuando los dos fármacos están en el mismo portador polimérico, e incluso un cambio en su mecanismo molecular (autofagia *vs.* apoptosis e inhibición de procesos angiogénicos (VEGF, iNOS)) [24].

Cabe destacar que, la importancia de este tipo de terapia de combinación anticancerígena ha sido corroborada en clínica (Combiplex® aprobada por la FDA en 2017 para leucemia mieloide aguda) con los estudios realizados por Celator Pharmaceuticals Inc. (ahora Jazz Pharmaceuticals) en los cuales se ha empleado un liposoma de combinación ofreciendo ventajas significativas frente a tratamientos individuales [25].

A lo largo de esta Tesis hemos tomado como base de partida el conocimiento aportado a lo largo del desarrollo conjugado de combinación HPMA-AGM-Dox para desarrollar conjugados análogos basados en el polímero biodegradable ácido

poliglutámico (PGA) de posible mayor relevancia clínica debido a su biodegradabilidad. Adicionalmente, hemos hecho especial hincapié en la caracterización fisicoquímica de los conjugados, investigado la influencia de la incorporación de diferentes enlaces polímero-fármaco en la biofísica de la macromolécula y cómo esos cambios promueven diferentes efectos conformacionales y consecuentemente biológicos *in vitro* e *in vivo*.

Finalmente, se ha mejorado el conocimiento y la caracterización de un modelo murino inmunocompetente previamente descrito (4T1) y se ha desarrollado un modelo nuevo inmunodeprimido (MDA-MB-231-Luc), clínicamente más relevante. Los modelos animales capaces de reproducir varias etapas del desarrollo de cáncer de mama representan plataformas de investigación translacional cruciales para evaluar y validar terapias experimentales. Sin embargo, la falta de modelos caracterizados con precisión que imiten fielmente las características patológicas del CMTN humano, incluyendo la metástasis espontánea o las alteraciones colaterales múltiples, con frecuencia dificultan la investigación [26, 27]. Los modelos de ratones metastásicos actualmente empleados imitan la enfermedad en estadío avanzado, pero el requisito de infusiones de altas concentraciones de células de cáncer de mama agresivas [26], la necesidad de extirpar el tumor primario para permitir la metástasis o el desarrollo metastásico lento limita la aplicación de estos modelos.

2. OBJETIVOS DE LA INVESTIGACIÓN

Los objetivos del presente trabajo de Tesis se centran en el diseño y desarrollo de varias familias de conjugados de combinación polímero-fármaco basado en el uso de polímeros biocompatibles y biodegradables para su aplicación en el tratamiento de cáncer de mama triple negativo (CMTN) en estadío avanzado o metastásico. Este objetivo global enmarca los siguientes objetivos específicos:

1. El desarrollo y la caracterización exahustiva de dos modelos animales ortotópicos de cáncer de mama, espontáneamente metastásicos y preclínicamente relevantes, como plataformas para la validación de terapias avanzadas.

2. Síntesis, caracterización fisicoquímica completa y evaluación biológica de conjugados de combinación de fármacos basados en ácido poli-L-glutámico (PGA) que incorporan fármacos en una relación adecuada, así como enlaces polímero-fármaco biosensibles de para lograr la sinergia en modelos de TNBC.

El diseño racional de los conjugados de combinación implicará:

i) Investigación de enlaces polímero-fármaco de diferente naturaleza bioreactiva (proteasa frente a respuesta al pH).

ii) Estudios de relación estructura-actividad (SAR) en medios biológicamente relevantes.

iii) Estudios *in vitro* e *in vivo* (seguridad, farmacocinética y actividad anticancerígena) en modelos preclínicamente relevantes (Objetivo 1).

3. Implementación de técnicas -ómicas (metabolómica y transcriptómica) en el desarrollo de conjugados poliméricos de combinación para comprender, no solo el mecanismo de acción molecular sino también identificar biomarcadores relevantes y descriptores fisicoquímicos que nos ayuden a avanzar hacia enfoques de terapia personalizada.

3. METODOLOGÍA

3.1. Materiales e instrumentación.

3.1.1. Materiales.

Todos los reactivos usados durante el desarrollo de la presente Tesis fueron de grado analítico, superior, y se usaron sin purificación adicional, a no ser que se indique en el correspondiente apartado. Los disolventes usados también eran de grado analítico, superior, o HPLC, cuando fue necesario y se secaron previamente a su uso. De manera general, las reacciones llevadas a cabo en disolventes orgánicos se realizaron bajo atmósfera inerte de nitrógeno o argón.

Los métodos más frecuentemente empleados para el aislamiento y purificación de los conjugados poliméricos fueron la diálisis (con membranas de 1, 3, 5 o 10 kDa), ultrafiltración (usando Vivaspin®) o cromatografías por exclusión de tamaño, usando resina Sephadex® LH-20 medium para disolventes orgánicos o Sephadex® G-25 medium en el caso de purificaciones en fase acuosa.

Los animales de experimentación empleados a lo largo de la Tesis, se adquirieron en Envigo Laboratories Inc. (España). Se utilizaron ratones hembras de 6 a 8 semanas de las cepas BALB/c OlaHsd y NOD.CB17-Prkdcscid / NCrHsd.

3.1.2. Instrumentación.

Espectroscopía de Resonancia Magnética Nuclear (NMR). Los espectros ^{1}H NMR y DOSY NMR se llevaron a cabo en un sistema Bruker Advance AC 300 (300 MHz) o V500 (500 MHz) utilizando para ello al menos 5 mg de compuesto, temperatura ambiente y disolventes deuterados. Los datos obtenidos se analizaron mediante el software MestreNova 6.2.

Espectroscopia por Dicroísmo circular. Se realizó en un espectrómetro J-815 CD Spectrometer (JASCO Corporation) equipado con un soporte de celda termostatizado (PTC-423, JASCO Corporation), un refrigerante (JULABO F250, JASCO Corporation) y flujo controlado de nitrógeno (~2.7 L.min-1) (Afriso Euro-Index). Las muestras se midieron en agua desionizada o PB 7.4 para polímeros en la forma sal sódica. Las medidas se realizaron en cubetas de cuarzo, de d= 0.1 cm y por triplicado.

Dispersión de Luz Dinámica (DLS). Las medidas tanto de tamaño de partícula como de potencial ζ se realizaron a 25˚C en un dispositivo Malvern Zetasizer Nano ZS equipado con un láser (532 nm) a un ángulo de dispersión fijo de 90˚. La celda utilizada fue DTS 1070. Para las medidas de tamaño, el tiempo de equilibrado fue de 0 min con atenuación automática. El índice de refracción del disolvente, en este caso agua, fue 1,330 y, por lo tanto, la viscosidad fue 0,8872. Para el análisis de los diferentes polímeros se utilizó el índice de refracción del látex de poliestireno (1,590). Cada muestra se midió tres veces con 10 submedidas. El potencial ζ se calculó a través del modelo Smoluchowski. Se utilizaron entre 10 y 20 medidas de 10 s cada una a 25˚C (n=3).

Espectroscopía Ultravioleta-Visible (UV-Vis). Los espectros se adquirieron en un espectrofotómetro Jasco V-630 UV/Vis a 25˚C con celdas de plástico o cuarzo (en su caso) de 1 cm y ancho de banda de 0.5 nm.

Microscopía Electrónica de Transmisión (TEM). Las imágenes se adquirieron en un microscopio de transmisión electrónica FEI Tecnai G2 Spirit (FEI Europe, Eindhoven, Netherlands) usando una cámara digital Morada (Olympus Soft Image Solutions GmbH, Münster, Germany). Para su preparación, las muestras se adsorbieron en rejillas de cobre recubiertas por una película de carbón de 200 mallas. Tras ello, se realizó una tinción de contraste negativo con una disolución de acetato de uranilo al 2%.

Victor2 Wallace^{TM} para medidas de absorbancia o fluorescencia. Para determinar absorbancias o fluorescencias en fracciones de purificación o ensayos celulares se usó un equipo Victor2 Wallac 1420 Multilabel HTS Counter Perkin Elmer (Northwolk, CT, EEUU) utilizando placas de 96 pocillos y las correspondientes longitudes de onda (emisión/excitación) propias de cada compuesto.

Dispersión de Neutrones de Ángulo Pequeño (SANS).

Los experimentos de SANS se llevaron a cabo utilizando el difractómetro D11 del Instituto Laue-Langevin (ILL, Grenoble) y los difractómetros SANS2d y LOQ en ISIS pallation Neutron Source (Didcot, UK). Todas las disoluciones fueron preparadas en disolventes deuterados a la concentración máxima de 1 wt% y se colocaron en celdas de cuarzo de 2 mm de camino óptico. Los volúmenes de muestra fueron aproximadamente de 0,6 cm^3. Los datos fueron recogidos y corregidos de la transmisión y dispersión de la celda y del disolvente y se pusieron en una escala de intensidad absoluta. Los datos de dispersión fueron expresados en función del vector de dispersión Q, el cual viene dado por $Q = 4n\pi/\lambda \sin(\theta/2)$ en el que n es el índice de refracción para los neutrones ($n \approx 1$), λ es la longitud de onda, y θ es el ángulo de dispersión.

3.2. Consideraciones éticas

Los experimentos con animales se realizaron en conformidad con las directrices del Consejo de la Comunidad Europea (86/609/CCE) y con el Real Decreto español

1201/2005. Todos los procedimientos experimentales fueron aprobados por el comité institucional sobre el cuidado y uso de animales y realizados por personal acreditado y capacitado, que cumplen con las normas de cuidado de los animales. Todos los ratones se mantuvieron en una instalación libre de patógenos específicos (SPF), a temperatura y humedad controlada y utilizando un ciclo de luz y oscuridad de 12 horas. Se proporcionó pienso estandarizado libre de alfalfa como alimento y agua *ad-libitum* durante todos los experimentos. En todos los casos se evaluó el aspecto general, la conducta de acicalamiento, el tamaño del tumor, el peso corporal y el comportamiento general desde el comienzo del experimento para garantizar el bienestar de los animales. El desarrollo del tumor no produjo pérdida de peso en los animales, ni se observó ningún comportamiento relacionado con el dolor.

3.3. Métodos más relevantes.

3.3.1. Acoplamientos peptídicos.

Protocolo 1. En un matraz de fondo redondo equipado con un agitador magnético y entrada y salida de nitrógeno seco se disuelven 200 mg de PGA forma ácida (1.55 mmol, 1 eq.) en 10 mL de DMF anhidro. Seguidamente se añade la correspondiente cantidad de DMTMM·BF4 como activante de ácidos carboxílicos, para el porcentaje de modificación deseado (para un 10% de modificación, 0.1 equivalentes). Tras 10 minutos, se añade el doble de eq. que de DMTMM·BF4 de la correspondiente amina a conjugar (para un 10 % de modificación 0.3 eq.). Se ajusta el pH a 8, y la mezcla se deja reaccionar durante 16 horas a temperatura ambiente. Tras ello, se realizan las purificaciones estándar usando diálisis, o exclusión molecular, o precipitación ácido-base. El producto se caracteriza por RMN y por las técnicas espectrofotométricas correspondientes.

Protocolo 2. En un matraz provisto de un agitador magnético y una entrada y salida de nitrógeno, se pesa PGA forma ácida (0.225 mmol UAG, 1 eq.) y se disuelve en DMF anhidro bajo atmósfera de nitrógeno. A continuación, se añade DIC (i.e. 0.15 eq. para una modificación de un 10 %) y se deja reaccionar durante 5 minutos a temperatura ambiente. Tras ello, se añade HOBt (0.15 eq. para una modificación del 10 %). La reacción se deja transcurrir durante 10 minutos más y se añade a continuación 0.10 eq. de la amina correspondiente. Se ajusta el pH a 8 mediante la adición de DIEA. La mezcla se deja

reaccionar durante 48 horas. Finalmente, el disolvente se elimina a vacío, y el producto se convirtió en la forma sal mediante la adición de bicarbonato sódico. Tras ello, se procede a su purificación mediante los métodos estándar de diálisis, G25 o precipitación ácido-base.

3.3.2. Determinación de la concentración de agregación crítica (CAC) de los conjugados poliméricos mediante DLS.

Se disolvieron los polímeros basados en PGA en PBS 7.4 a diferentes concentraciones dentro de un rango de 0.004-2 $mg \cdot mL^{-1}$. Se usó PGA lineal como control negativo. Cada solución se preparó fresca para las medidas, se sonicó durante 5 minutos y se dejó 24 horas para su estabilización. Las medidas de DLS se hicieron por triplicado con parámetros fijados para todas las muestras. Los datos se expresaron en Kcps *vs* concentración, donde la intersección entre las curvas nos da el valor de CAC. Los estudios de co-ensamblaje de diferentes polímeros se llevaron a cabo de igual forma, pero añadiendo a cada serie de concentraciones, una cantidad por debajo de su CAC del polímero con quien se quiere averiguar el co-ensamblaje.

3.3.3. Ensayos *In vitro*.

Degradaciones con Catepsina B. La biodegradabilidad de varios poliglutamatos en presencia de la enzima lisosomal catepsina B se evaluó *in vitro*. Brevemente, se prepararon disoluciones de 2 mg·mL-1 de polímero en tampón acetato (para 3 mg de polímero, 700 µL de tampón acetato 20 mM, pH 6, 100 µL de EDTA 2 mM, 100 µL de DTT 5 mM). Finalmente, se añadieron 6.25 unidades de Catepsina B disueltas en 100 µL de tampón acetato pH 6 20 mM). Las mezclas se mantuvieron a 37 °C bajo agitación, y se tomaron alícuotas a diferentes tiempos (0, 0.5, 1, 2, 4, 8, 24, 48 y 72 h). La concentración de fármaco liberada en cada caso se analiza mediante técnicas espectrofotométricas o HPLC en cada caso.

Cultivos celulares. La línea celular de cáncer de mama humano dependiente de estrógenos MCF-7ca (transfectada con aromatasa humana) se mantuvo en DMEM complementado con Suero Bovino Fetal (SFBS) inactivado al 10% (SFBS) con estradiol y 0,75 mg / mL de geneticina G418 sobre condiciones de cultivo celular estándar (37ºC y 5% de CO_2). Las células 4T1 se mantuvieron en RPMI suplementado con 10% de Suero Bovino Fetal (FBS) inactivado por calor sobre condiciones estándar de cultivo de tejidos. Las células humanas de cáncer de mama MDA-MB-231-Luc se mantuvieron de forma rutinaria en el medio de Eagle modificado por Dulbecco / Mezcla de nutrientes F-12, DMEM/F12, (Gibco) suplementado con 10% FBS y 500ug/mL de Geneticina a 37 ° C en una atmósfera humidificada con 5% de CO_2. En todos los casos, los medios se reemplazaron cada 2 - 3 días y se sometieron a pases una vez que las células alcanzaron el 80% de confluencia.

Ensayos MTS de viabilidad celular. Las líneas celulares se sembraron en placas de 96 pocillos estériles a la concentración de 12500 células / cm^2 para MCF-7ca, 6250 células / cm^2 para 4T1 y 7.500 células / cm^2 para MDA-MB-231-Luc. Las placas se incubaron durante 24 h y posteriormente se analizaron los fármacos libres y los conjugados se analizaron en las concentraciones finales que varían de 0 a 0,1 mg / ml de equivalentes del fármaco. Después de 72 h de tratamiento, se midió la viabilidad celular usando el ensayo de proliferación celular no radiactiva Acuático Cell Titer 96 (Promega, Corporation, España, UE) de acuerdo con las instrucciones del fabricante. La densidad óptica de cada pocillo se midió a 490 nm usando una estación de trabajo Wallac 1420 (PerkinElmer, MA, EE. UU.). La viabilidad celular se expresó como un porcentaje de la viabilidad de las células de control no tratadas.

3.3.4. Ensayos *in vivo*.

Desarrollo de modelos ortotópicos de cáncer de mama triple negativo. Para la inducción de los tumores en el modelo 4T1 se inocularon subdérmicamente d 5 x 10^5 células de pase temprano suspendidas en 100 µl de Matrigel (20%) en la segunda mama izquierda inferior de hembras BALB/c (BALB/cOlaHsd) bajo anestesia inhalatoria (sevoflurano al 3% en oxígeno al 100%). Siguiendo las mismas condiciones experimentales, se establecieron los tumores MDA-MB-231-Luc usando 3 x 10^6 células de paso temprano en ratones

NOD/SCID (NOD.CB17-Prkdcscid/NCrHsd). Los tumores se evaluaron morfométricamente diariamente con un calibre electrónico y se obtuvieron volúmenes tumorales considerando la forma del tumor esferoidal. Las metástasis en órganos de interés en el modelo 4T1 se aislaron y evaluaron siguiendo un protocolo previamente descrito.

Estudio de la actividad antitumoral y antimetastásica de los conjugados poliméricos en ambos modelos murinos previamente implementados. Después de 8 días tras la inoculación celular, cuando el tamaño del tumor alcanzó 0,1 cm^3, los ratones se dividieron en grupos representativos y los conjugados se inyectaron por vía intravenosa (iv) en tres/cuatro dosis (según el caso) en los correspondientes equivalentes de fármaco cada tres días. Los fármacos libres libre se disolvieron en solución salina y se usaron como un control de fármaco libre, administrados siguiendo el mismo esquema. Los tumores se midieron cada 3 días con un calibre digital y se obtuvieron volúmenes considerando el crecimiento de esferoides, aplicando la fórmula (altura / 2 x longitud / 2 x ancho / 2)^3 x (4/3 Pi). Una vez que los tumores alcanzaron 1,0 cm^3 (16 días después del primer tratamiento), los ratones se sacrificaron en atmósfera de CO_2 y se recogieron la sangre, los órganos principales y los tumores para su posterior análisis histopatológico.

Tomografía de Emisión de Positrones (PET). El análisis PET-CT empleó el equipo Albira (Bruker, EE. UU.) Ubicado dentro del CIPF. Para el análisis PET-CT, los animales se mantuvieron en ayunas durante 14 h antes de la administración del radiotrazador para PET y se alojaron a 21ºC constantes. El peso promedio del ratón fue de 19.2 ± 0.7 g, mientras que el nivel promedio de glucosa en sangre fue de 47.2 ± 10.1 $mg.dl^{-1}$. La anestesia se indujo por inhalación de isoflurano (4% en oxígeno al 100%) y se mantuvo en (1,5% en oxígeno al 100%). La resolución de la tomografía híbrida PET / CT se fijó en 1,5 mm con un campo axial de 9 cm y transaxial de 8 cm. Una vez que los parámetros fueron arreglados, los animales fueron inyectados de manera i.v. con 18F-FDG con una actividad de 4.5 ± 0.1MBq a través de un catéter en la vena de la cola. La dosis promedio de 18F-FDG fue 4516.2 KBq ± 236.3. Los experimentos dinámicos de PET se realizaron mediante la adquisición de 28 cuadros de 60 minutos de longitud total (6 x 10 s, 6 x 30 s, 6 x 60 s, 5 x 120 s, 4 x 300 s y 1 x 1200 s). Las imágenes de PET se reconstituyeron utilizando el algoritmo Método de Estimación de Máxima Verosimilitud (MLEM, 12

iteraciones) y se aplicaron correcciones de desintegración, dispersión y aleatorias cuando fue necesario.

Estudio de bioluminscencia (BLI) mediante IVIS. Las células MDA-MB-231-Luc transfectadas con luciferasa presentes en el cuerpo del animal se trazaron utilizando la tecnología IVIS Spectrum. Para la obtención de imágenes de bioluminiscencia (BLI), los ratones se anestesiaron con sevoflurano al 3% en oxígeno y recibieron una inyección subdérmica de 150 mg / kg de D-luciferina. La adquisición se realizó con el sistema de espectrometría IVIS 10 min después de la administración de D-luciferina. Las imágenes se adquirieron usando la configuración automática de la cámara y los datos BLI se cuantificaron con el software Living Image en términos de fotones por segundo.

Biodistribución de los conjugados poliméricos. Se usaron ratones con 0,1 cm^3 de tumor (desarrollados como se detalla anteriormente) para el estudio de biodistribución. Los conjugados de interés fueron iv. administrados a la adecuada concentración y los grupos de animales (n = 6) fueron sacrificados en diferentes tiempos (0, 8, 24, 48 y 72 horas). Se recogieron la sangre, los principales órganos y el tumor y se congelaron y almacenaron a -80 °C hasta su posterior análisis. Posteriormente, Los órganos y el tumor se suspendieron en 2 ml de PBS frío y se mezclaron enérgicamente mediante el uso de un mezclador Ultraturrax. El pH de la mezcla homogénea resultante se ajustó a 8,5 añadiendo algunas gotas de tampón de formiato de amonio 1 M y seguidamente se extrajo tres veces con 5,0 ml de una mezcla de CH_3Cl/iPrOH 4:1 (v/v). Las fases acuosas se descartaron y los sobrenadantes se concentraron hasta sequedad bajo corriente de N_2. Los residuos finales se disolvieron en 100 µl de MeOH de grado HPLC y las muestras se analizaron mediante RP-HPLC siguiendo el mismo método para la determinación de fármaco libre ya descrito. Las mediciones fluorescentes finales relacionadas con el fármaco de interés se estandarizaron según el peso del tejido.

4. RESULTADOS

4.1. Modelos preclínicos de cáncer de mama triple negativo que proporcionan evidencias funcionales de progresión metastásica y su adecuación para la evaluación de nanomedicinas (Capítulo II, *manuscrito en revisión (Int. J. Cancer)*).

El desarrollo acelerado de terapias avanzadas anticancerígenas requiere modelos preclínicos que permitan la identificación de biomarcadores funcionales para facilitar la traslación clínica [28] y la estratificación de pacientes [29]. A lo largo del presente trabajo de Tesis, se presenta una caracterización amplia y detallada de dos modelos murinos de cáncer de mama triple negativo (CMTN) espontáneamente metastásicos y preclínicamente relevantes (un modelo de células humanas MDA-MB-231-Luc desarrollado en un ratón inmunodeficiente y un modelo 4T1 murino desarrollado en ratón inmunocompetente) con un enfoque especial en su uso como plataformas vivas para el desarrollo de nanomedicinas anticancerígenas. Ambos modelos desarrollan homogéneos tumores primarios con posterior metástasis en nódulo linfático axilar (ALN) y pulmones, reproduciendo fielmente las características más determinantes de la patología humana. Nuestras comparaciones han revelado descriptores importantes con respecto a los procesos tisulares / moleculares interconectados que conducen el avance de la enfermedad hacia la metástasis. Los descriptores incluyen diseminación metastásica por vía linfática, remodelación del sistema inmune, adipocitos asociados al cáncer y alteraciones metabólicas relevantes. Asimismo, hemos identificado características distintivas que pueden representar biomarcadores funcionales para la progresión de la enfermedad o incluso como herramientas de diagnóstico molecular. Por lo tanto, estos modelos ofrecen una plataforma útil para la prueba / validación de terapias contra el cáncer, especialmente para el tratamiento de pacientes que se presentan con ambos tumores primarios y metástasis.

4.2. Actividad anticancerígena promovida por modificaciones en el enlace polímero-fármaco en un conjugado de combinación basado en ácido poliglutámico (PGA) (Capítulo III, *Arroyo-Crespo et al. Adv. Funct. Mat. 2018*)

Tal y como se ha comentado y discutido anteriormente a lo largo de este trabajo de Tesis, las nanoterapias de combinación para el tratamiento de cáncer de mama se benefician del efecto sinérgico de los fármacos incorporados en el nanosistema [30]. Sin embargo, la mayoría de los transportadores poliméricos poseen baja biodegradabilidad, limitada sinergia de los fármacos combinados, ineficaz regulación de la liberación de dichos fármacos, y una falta de control en la conformación en solución de la macromolécula final (que define el potencial biológico) lo que limita la aplicación de esta estrategia de forma más amplia.

A lo largo de este Capítulo de Tesis, hemos diseñado una amplia familia de conjugados polímero-fármaco con buenos resultados en actividad anticancerígena, incorporando la antraciclina doxorrubicina (Dox) y el inhibidor de aromatasa aminoglutetimda (AGM). Con esta nueva familia de conjugados PGA-AGM-Dox, se ha ratificado la importancia de la presencia de ambos fármacos en el mismo portador polimérico para asegurar su liberación simultánea en la misma célula.

Hemos prestado especial atención a la interacción entre el comportamiento biológico y las propiedades fisicoquímicas de los conjugados en solución acuosa. Como esperábamos, la proporción de los fármacos conjugados es una característica clave a la hora de controlar la actividad biológica tal y como hemos podido observar en las comparativas PGA-(G-AGM)$_{HL}$-Dox frente a PGA-(G-AGM)$_{LL}$-Dox. Quizá más importante es el hecho de descubrir que la presencia de un pequeño y flexible espaciador de Glicina (Gly) entre AGM y el polímero (el aminoácido más pequeño, que supone menos del 1% del peso molecular total del conjugado) juega un papel decisivo en la estructura de toda la macromolécula y por lo tanto, influye significativamente en la actividad biológica. Igualmente, la introducción de Gly induce un cambio significativo en la cinética de liberación del fármaco, tamaño hidrodinámico, estructura secundaria y disposición interna del esqueleto polipeptídico, tal y como hemos podido observar tras los análisis de dicroísmo circular (CD), dispersión dinámica de luz (DLS), y estudios de Dispersión de Neutrones de Ángulo Pequeño (SANS). La distinta configuración molecular proporcionada por el espaciador de Gly (Gly o Gly-Gly) parece modificar la disposición espacial del conjugado de tal manera que se ve favorecido el acceso de la enzima proteolítica catepsina B, lo que se traduce en una liberación diferencial de AGM frente a Dox y esto determina el resultado terapéutico final. Por otro lado, se reafirma la

idea de que la cinética de la liberación del fármaco es uno de los principales descriptores fisicoquímicos a tener en cuenta al diseñar terapias combinadas basadas en polipéptidos.

Como hemos podido demostrar en este trabajo, la elección de los enlaces empleados en la conjugación de agentes activos en un conjugado de combinación polimérico puede dotar al complejo sistema macromolecular con propiedades mejoradas con respecto a la conjugación directa. En esta familia de conjugados los mejores resultados biológicos se obtuvieron con PGA-(G-AGM)$_{HL}$-Dox, en el cual la relación molar de fármacos es 2:1 (AGM:Dox) y empleando Gly como enlace para AGM. Este conjugado ha demostrado significativamente mayor efecto antitumoral que PGA-(G-AGM)$_{LL}$-Dox (1:1 AGM:Dox en mol) e incluso mayor, comparado con los conjugados derivados de unión de AGM directa. Nuestros resultados sientan las bases para avanzar hacia el diseño eficiente de nuevos enlaces polímero-fármaco que permitan un control espaciotemporal mejorado en los perfiles de liberación, mejorando los efectos sinérgicos y, por lo tanto, mejorando la actividad antitumoral. Nuestros resultados también resaltan la importancia de caracterización supramolecular exhaustiva para comparar adecuadamente evaluaciones *in vitro* e *in vivo.*

4.3. Conjugado de combinación basado en PGA dirigido al microambiente tumoral para el tratamiento del cáncer de mama triple negativo (Capítulo IV, *manuscrito en revisión (Biomaterials)*).

Tras los resultados positivos obtenidos con la conjugación de AGM y Dox, empleando para ambos fármacos enlaces peptídicos, se observó una mejoría terapéutica cuando la presencia de los enlaces polímero-fármaco promovían la liberación más rápida de Dox frente a la de AGM. Sobre esta base se desarrolló una nueva familia de conjugados poliméricos similares, incorporando un enlace hidrazona sensible al pH con el objetivo de promover una mayor liberación de este fármaco en el microentorno tumoral.

Tanto los resultados experimentales como el análisis transcripcional de tejido tumoral realizado a posteriori, indicaron que los dos conjugados más efectivos, PGA-(G-AGM)-(Hyd-Dox)$_{LL}$ y PGA-(G-AGM)-(EMCH-Dox)$_{LL}$, se dirigen al microentorno

tumoral (TME) para desencadenar un cascada de eventos moleculares que promueven la muerte de las células tumorales (principalmente mediante apoptosis y autofagia) e inhiben las actividades relacionadas con progresión del tumor, incluyendo metástasis y la proliferación celular. Sin embargo, también descubrimos diferencias significativas entre los dos conjugados de combinación: PGA-(G-AGM)-$(Hyd\text{-}Dox)_{LL}$ desencadena una respuesta inmune más intensa que podría explicar por qué los ratones receptores muestran una mayor tasa de supervivencia. Además, PGA-(G-AGM)-$(Hyd\text{-}Dox)_{LL}$ conduce a una mayor actividad proapoptótica, señales antiapoptóticas más bajas e inhibición de la metástasis, que respaldan la respuesta global a este tratamiento.

También hemos demostrado la importancia de dirigir el tratamiento al TME para la liberación del fármaco *in situ* y optimizar la proporción del fármaco biodisponible en una terapia de combinación, destacando la importancia del diseño racional de enlaces biosensibles efectivos. La cinética adecuada de liberación del fármaco representa un parámetro crucial para lograr una adecuada relación seguridad / eficacia y puede asegurar una ventana terapéutica adecuada para tratamientos futuros. Finalmente, este estudio también demuestra la utilidad del análisis transcripcional de tejido tumoral sometido a tratamiento sistémico, que sirve para mejorar la comprensión de nuestros resultados y promover el diseño futuro de sistemas de liberación de fármacos avanzados basados en polímeros para el tratamiento de CMTN metastásico, entre otros.

4.4. Diseño racional de conjugados de combinación basados en poliglutamato, incorporando inhibidores de la tirosina-quinasa e inhibidores de la topoisomerasa para el tratamiento de CMTN metastásico (Capítulo V, *manuscrito en preparación*).

Finalmente, se han aplicado los conocimientos adquiridos a lo largo del desarrollo de esta Tesis para el diseño de un nuevo conjugado de combinación (PGA-TKI-TI), que tiene como objetivo la liberación controlada de dos fármacos anticancerígenos sinérgicos (un inhibidor de la tirosina-quinasa (TKI) y un inhibidor de la topoisomerasa (TI)). Para desarrollar este conjugado, se ha empleado la química previamente optimizada, dotando al conjugado de un enlace sensible al pH (hidrazona) para la liberación de TI en el microentorno tumoral. Adicionalmente, se ha comprobado que la conjugación directa del TKI al polímero no resultaba en una adecuada cinética de liberación y como consecuencia inducia efectos terapéuticos no deseados. En consecuencia, se han sintetizado una serie

de conjugados PGA-aa-TKI simples, incorporando aminoácidos de distinta naturaleza (hidrofobicidad cadena lateral) entre el polímero y el fármaco, con el fin de obtener una modulación en la liberación del fármaco. Una vez evaluada la familia de conjugados simples en términos de liberación de fármaco *in vitro* y actividad citotóxica, se ha elegido el aminoácido valina como el mejor enlace para intercalar entre el TKI y el polímero. El conjugado de combinación obtenido, PGA-(Val-TKI)-(hyd-TI) fue evaluado *in vitro*, en dos líneas celulares de CMTN y demostró una mayor citotoxicidad que los conjugados simples administrados por separado y la suma física de ambos, y una mayor sinergia entre ambos fármacos demostrándose la ventaja de la conjugación de dos fármacos al mismo portador polimérico. Seguidamente, se evaluó su capacidad antitumoral y antimetastásica en un modelo murino inmunodeprimido de CMTN, cuyo desarrollo se expone en el **Capítulo II**. El conjugado de combinación PGA-(Val-TKI)-(hyd-TI) demostró una mayor capacidad antitumoral (un ~50% de reducción de crecimiento de tumor primario con respecto al control sin tratar) y una mayor capacidad de reducción de metástasis en pulmón y ALN un ~90% de reducción en pulmón y un 60% en ALN) con respecto al control sin tratar. Se demostró nuevamente, una mayor sinergia entre fármacos en el conjugado de combinación y un mayor efecto terapéutico que al administrar los conjugados simples por separado o la suma física de ambos, demostrándose la ventaja de la conjugación de dos fármacos al mismo portador polimérico. Finalmente, se validó el conjugado en un modelo murino (también definido en el **Capítulo II**) inmunocompetente, con resultados similares. Además, en éste modelo hemos podido observar otras mejorías con respecto a los animales sin tratar, como una reducción de la esplenomegalia asociada al tumor, y una inhibición de la secreción de algunas citoquinas tumorales.

5. CONCLUSIONES.

Durante el desarrollo de la presente Tesis, se han logrado una serie de objetivos, haciendo de éste trabajo innovador y con relevancia en el ámbito de la terapia de combinación basada en polímeros biodegradables para el tratamiento de CMTN. Las principales conclusiones se destacan a continuación:

1. Se han caracterizado en detalle dos modelos murinos de cáncer de mama ortotópicos, espontáneamente metastásicos y preclínicamente relevantes,

para ser empleados como plataformas de testeo y validación de conjugados polimérico-fármaco. Se han estudiado las repercusiones del avance de la metástasis, mediante análisis hematológicos. Se han identificado biomarcadores específicos de metástasis para cada modelo mediante metabolómica por resonancia magnética nuclear (RMN). También se han caracterizado histopatológicamente los órganos más relevantes que presentaban patologías como consecuencia del desarrollo del tumor. Finalmente, se ha detectado una modulación de citoquinas tumorales en plasma y, se han podido identificar diferentes descriptores que permiten evaluar la eficacia de los tratamientos antitumorales en el ámbito de la nanomedicina y en particular, de los Polímeros Terapéuticos.

2. Se han desarrollado tres familias de conjugados de combinación polímero-fármaco, basados en ácido poliglutámico, incorporando dos fármacos en proporciones sinérgicas para tratamiento de CMTN.

3. Con el fin de mejorar y optimizar las cinéticas de liberación de los fármacos y mejorar su sinergia, se han desarrollado y caracterizado enlaces polímero-fármaco sensibles a distintos estímulos biológicos, incluyendo enlaces peptídicos (degradables bajo la actividad proteolítica de enzimas sobreexpresadas en los lisosomas de las células tumorales), enlaces éster, (sensibles a variaciones del pH y a la presencia de esterasas), y enlaces sensibles al pH, (destinados a liberar específicamente los fármacos en la proporción y cantidad adecuada en el microentorno tumoral y/o a lo largo del proceso endosomolítico, ambos ambientes ligeramente ácidos).

4. Se han caracterizado fisicoquímicamente las familias de conjugados desarrollados, mediante técnicas avanzadas de caracterización en soluciones biológicamente relevantes, que han permitido establecer relaciones estructura-actividad de los diferentes conjugados en la mayoría de los casos.

5. Se han evaluado *in vitro* los conjugados previamente desarrollados, en varias líneas celulares de cáncer de mama clínicamente relevantes. Estos ensayos han incluido estudios de citotoxicidad, estudios de sinergia e

internalización celular y han proporcionado información decisiva para avanzar en el diseño de los conjugados. Asimismo, se han estudiado *in vitro* las cinéticas de liberación de fármaco en diferentes ambientes biológicamente relevantes y en presencia de enzimas degradantes.

6. Los conjugados poliméricos previamente desarrollados que han demostrado los mejores resultados preliminares *in vitro*, se han evaluado *in vivo* (en los modelos murinos preclínicos establecidos). Esta evaluación ha demostrado su actividad antitumoral y antimetastásica, así como su seguridad, y se han podido monitorizar diversos descriptores de la enfermedad, identificados previamente, que han permitido valorar el potencial terapéutico de nuestros conjugados de combinación.

7. Finalmente, se han estudiado diversas muestras biológicas (tumor primario y pulmones metastatizados) mediante transcriptómica y proteómica. Estas dos potentes herramientas analíticas han permitido esclarecer algunos aspectos funcionales de la expresión génica responsables de la muerte celular a nivel genómico tras los tratamientos, y ha permitido establecer relaciones directas entre los mecanismos de muerte celular y algunos descriptores físico-químicos de los conjugados poliméricos. Por su parte, los resultados metabolómicos han permitido identificar diferencias significativas en la producción/consumo de metabolitos clave en el desarrollo de la metástasis, con diferencias claras entre los dos modelos murinos empleados y ha permitido comprender los mecanismos moleculares implicados en los procesos metastásicos.

6. REFERENCIAS.

[1] McGuire A, Brown JA, Malone C, McLaughlin R, Kerin MJ. Effects of age on the detection and management of breast cancer. Cancers. 2015;7:908-29.

[2] Duggan MA, Anderson WF, Altekruse S, Penberthy L, Sherman ME. The Surveillance, Epidemiology and End Results (SEER) Program and Pathology: Towards Strengthening the Critical Relationship. The American journal of surgical pathology. 2016;40:e94-e102.

[3] Dawood S. Triple-negative breast cancer: epidemiology and management options. Drugs. 2010;70:2247-58.

[4] Camacho-Rivera M, Kalwar T, Sanmugarajah J, Shapira I, Taioli E. Heterogeneity of breast cancer clinical characteristics and outcome in US black women--effect of place of birth. The breast journal. 2014;20:489-95.

[5] Dai X, Li T, Bai Z, Yang Y, Liu X, Zhan J, et al. Breast cancer intrinsic subtype classification, clinical use and future trends. American journal of cancer research. 2015;5:2929-43.

[6] Andre F, Zielinski CC. Optimal strategies for the treatment of metastatic triple-negative breast cancer with currently approved agents. Annals of oncology : official journal of the European Society for Medical Oncology. 2012;23 Suppl 6:vi46-51.

[7] Petros RA, DeSimone JM. Strategies in the design of nanoparticles for therapeutic applications. Nature reviews Drug discovery. 2010;9:615-27.

[8] Duncan R, Gaspar R. Nanomedicine(s) under the Microscope. Molecular pharmaceutics. 2011;8:2101-41.

[9] Maeda H, Nakamura H, Fang J. The EPR effect for macromolecular drug delivery to solid tumors: Improvement of tumor uptake, lowering of systemic toxicity, and distinct tumor imaging in vivo. Advanced drug delivery reviews. 2013;65:71-9.

[10] Maeda H, Tsukigawa K, Fang J. A Retrospective 30 Years After Discovery of the Enhanced Permeability and Retention Effect of Solid Tumors: Next-Generation Chemotherapeutics and Photodynamic Therapy--Problems, Solutions, and Prospects. Microcirculation (New York, NY : 1994). 2016;23:173-82.

[11] Duncan R. Polymer therapeutics as nanomedicines: new perspectives. Current opinion in biotechnology. 2011;22:492-501.

[12] Duncan R. Polymer therapeutics: Top 10 selling pharmaceuticals - what next? Journal of controlled release : official journal of the Controlled Release Society. 2014;190:371-80.

[13] Dhal PK, Polomoscanik SC, Avila LZ, Holmes-Farley SR, Miller RJ. Functional polymers as therapeutic agents: concept to market place. Advanced drug delivery reviews. 2009;61:1121-30.

[14] Veronese FM, Pasut G. PEGylation, successful approach to drug delivery. Drug discovery today. 2005;10:1451-8.

[15] Kneller R. The importance of new companies for drug discovery: origins of a decade of new drugs. Nature reviews Drug discovery. 2010;9:867-82.

[16] Garnock-Jones KP. Naloxegol: a review of its use in patients with opioid-induced constipation. Drugs. 2015;75:419-25.

[17] Vicent MJ, Greco F, Nicholson RI, Paul A, Griffiths PC, Duncan R. Polymer therapeutics designed for a combination therapy of hormone-dependent cancer. Angewandte Chemie (International ed in English). 2005;44:4061-6.

[18] Canal F, Sanchis J, Vicent MJ. Polymer--drug conjugates as nano-sized medicines. Current opinion in biotechnology. 2011;22:894-900.

[19] Greco F, Vicent MJ. Combination therapy: opportunities and challenges for polymer-drug conjugates as anticancer nanomedicines. Advanced drug delivery reviews. 2009;61:1203-13.

[20] Eldar-Boock A, Miller K, Sanchis J, Lupu R, Vicent MJ, Satchi-Fainaro R. Integrin-assisted drug delivery of nano-scaled polymer therapeutics bearing paclitaxel. Biomaterials. 2011;32:10.1016/j.biomaterials.2011.01.073.

[21] Vasey PA, Kaye SB, Morrison R, Twelves C, Wilson P, Duncan R, et al. Phase I clinical and pharmacokinetic study of PK1 [N-(2-hydroxypropyl)methacrylamide copolymer doxorubicin]: first member of a new class of chemotherapeutic agents-drug-polymer conjugates. Cancer Research Campaign Phase I/II Committee. Clinical cancer research : an official journal of the American Association for Cancer Research. 1999;5:83-94.
[22] Johnston SR, Dowsett M. Aromatase inhibitors for breast cancer: lessons from the laboratory. Nature reviews Cancer. 2003;3:821-31.
[23] Goss PE, Strasser K. Tamoxifen Resistant and Refractory Breast Cancer. Drugs. 2002;62:957-66.
[24] Greco F, Vicent MJ, Gee S, Jones AT, Gee J, Nicholson RI, et al. Investigating the mechanism of enhanced cytotoxicity of HPMA copolymer-Dox-AGM in breast cancer cells. Journal of controlled release : official journal of the Controlled Release Society. 2007;117:28-39.
[25] Feldman EJ, Lancet JE, Kolitz JE, Ritchie EK, Roboz GJ, List AF, et al. First-in-man study of CPX-351: a liposomal carrier containing cytarabine and daunorubicin in a fixed 5:1 molar ratio for the treatment of relapsed and refractory acute myeloid leukemia. Journal of clinical oncology : official journal of the American Society of Clinical Oncology. 2011;29:979-85.
[26] Manning HC, Buck JR, Cook RS. Mouse Models of Breast Cancer: Platforms for Discovering Precision Imaging Diagnostics and Future Cancer Medicine. Journal of Nuclear Medicine. 2016;57:60S-8S.
[27] Francia G, Cruz-Munoz W, Man S, Xu P, Kerbel RS. Mouse models of advanced spontaneous metastasis for experimental therapeutics. Nature Reviews Cancer. 2011;11:135-41.
[28] Pio R, Corrales L, Lambris JD. The Role of Complement in Tumor Growth. Advances in Experimental Medicine and Biology: Springer New York; 2013. p. 229-62.
[29] Inra CN, Zhou BO, Acar M, Murphy MM, Richardson J, Zhao Z, et al. A perisinusoidal niche for extramedullary haematopoiesis in the spleen. Nature. 2015;527:466-71.
[30] Tanei T, Choi DS, Rodriguez AA, Liang DH, Dobrolecki L, Ghosh M, et al. Antitumor activity of Cetuximab in combination with Ixabepilone on triple negative breast cancer stem cells. Breast cancer research : BCR. 2016;18:6.